High-Throughput Compatible Catalyst Development Towards Sustainable Direct Alkenylation Reaction Discovery and Optimization

by

Nahiane Pipaon Fernández
B.Sc., University of Navarra, 2016
M.Sc., Chemical Institute of Sarria (IQS), Ramon Lull University, 2018

A Dissertation Submitted for Fulfillment of the
Requirements for the Degree of

DOCTOR OF PHILOSOPHY

in the Department of Chemistry

© Nahiane Pipaon Fernández, 2024
University of Victoria

All rights reserved. This dissertation may not be reproduced in whole or in part, by photocopy or other means, without the permission of the author.

We acknowledge and respect the Lək^{w}əŋən (Songhees and Esquimalt) Peoples on whose territory the university stands, and the Lək^{w}əŋən and W̱SÁNEĆ Peoples whose historical relationships with the land continue to this day.

Supervisory Committee

High-Throughput Compatible Catalyst Development Towards Sustainable Direct Alkenylation Reaction Discovery and Optimization

by

Nahiane Pipaon Fernández
B.Sc., University of Navarra, 2016
M.Sc., Chemical Institute of Sarria (IQS), Ramon Lull University, 2018

Supervisory Committee

Dr. David C. Leitch, Supervisor
Department of Chemistry

Dr. Lisa Rosenberg, Departmental Member
Department of Chemistry

Dr. Cornelia Bohne, Departmental Member
Department of Chemistry

Dr. John Burke, Outside Member
Department of Biochemistry and Microbiology

Abstract

The direct C–H functionalization of heteroaromatic compounds such as pyridine, furan, thiophenes, thiazoles, and others have been developed as effective methods for making Csp^2–Csp^2 linkages which are often found in biologically active compounds and π-conjugated functional materials. More specifically, the development of palladium catalysts that can selectively activate specific C–H bonds is key for late-stage functionalization of pharmaceutically-relevant compounds. Mechanistic studies of the catalytic system, reaction intermediates and evaluation of the reaction parameters allows chemists maximize the reaction performance.

This thesis explores direct C–H alkenylation reactions from both a catalyst and substrate perspective, and exploits modifications to the generally accepted direct alkenylation mechanism. Furthermore, this work shows how systematic, hypothesis-driven High-Throughput Experimentation of reaction conditions, palladium sources and ancillary ligands enables the development of new reactivity, optimization of catalytic systems and exploration of the chemical space of direct alkenylation of heterocycles.

Finally, this work also highlights the versatility of palladacyclic precatalysts in the selective C–H functionalization of challenging but pharmaceutically relevant heterocycles such as pyrazoles and thiazoles. New synthetic procedures have been described toward the development of single-component precatalyst systems, and they have been used for the synthesis of two pharmaceutical compounds: GSK3368715, a PRMT1 inhibitor, and fatostatin, a lipid accumulation inhibitor.

Table of Contents

The quantification, via ^{1}H NMR spectroscopy, of the dialkenylated product when hydroxypyridone or 4-benzyloxy-2(1H)-pyridone was not possible as the signals overlap with the additives; however, the generally low reactivity of these X-type ligands make this quantification basically irrelevant. Pivalic acid is still the additive with higher selectivity, but does show lower reactivity when compared with 2-ethylhexanoic acid. In terms of L-type ligands, lutidine showed lower reactivity than the phosphine ligands $P(tBu)_3$, XPhos and PPh_3.

List of Figures

List of Tables

List of Abbreviations

2EHA ..... 2-Ethylhexanoic acid
AMLA ..... Ambiphilic metal-ligand activation
Ar ..... Aromatic ring
API ..... Active pharmaceutical ingredient
Bn ..... Benzyl group
Boc ..... *Tert*-Butyloxycarbonyl group
CMD ..... Concerted metallation deprotonation
Cp ..... Cyclopentadienyl ligand
CPET ..... Concerted proton-electron transfer
CPME ..... Cyclopentyl methyl ether
COD 1,5-Cyclooctadiene
COX ..... Cyclooxygenase isoenzymes
Cy ..... Cyclohexyl group
DoE ..... Design of Experiments
DAB ..... *N,*'-diaryldiazabutadiene
DBU ..... 1,8-diazabicyclo[5.4.0]undec-7-ene
DFT ..... Density functional theory
DIPEA ..... *N,N*'-diisopropylethylamine
DMA ..... Dimethylacetamide
eCMD ..... Electrophilic Concerted metallation deprotonation
EDG ..... Electron donating group
ESI-HRMS ..... High resolution electrospray ionization mass spectrometry
Et ..... Ethyl group
ET-PT ..... Electron transfer-proton transfer
EWG ..... Electron withdrawing group
HAT ..... Hydrogen atom transfer
HetAr ..... Heteroaromatic ring
HMBC ..... Heteronuclear Multiple Bond Correlation
HRMS ..... High-resolution mass spectrometry
HSQC ..... Heteronuclear Single Quantum Coherence

HTE ..... High-throughput experimentation
*i*Pr ..... Isopropyl group
L ..... Ligand
LCAP ..... Liquid chromatography area percent
LCMS ..... Liquid chromatography–mass spectrometry
LLHT ..... Ligand to ligand hydrogen transfer
M ..... Metal
MAH ..... Maleic anhydride
Me ..... Methyl group
MS ..... Mass Spectrometry
NBS ..... N-Bromosuccinimide
NMP N-Methyl-2-pyrrolidone
NCS ..... N-Chlorosuccinimide
NMR ..... Nuclear magnetic resonance
Nu ..... Nucleophile
OAc ..... Acetoxy group
OFAT ..... One Factor at a time
OVAT ..... One variable at a time
O*t*Bu ..... *Tert*-butoxide
OTf ..... Trifluoromethanesulfonate
o-tol ..... *Ortho*-tolyl group
PCET ..... Proton-coupled electron transfer
Pd ..... Palladium
PivOH ..... Pivalic acid
Ph ..... Phenyl group
PPAR ..... Peroxisome proliferator-activated receptor
PRMT ..... Protein arginine methyltransferase
PS ..... Photosensitizer
R ..... Organic Substituent
R&D ..... Research and Development
R_3P ..... Tertiary phosphines
TAA ..... *Tert*-amyl alcohol

THF ..... Tetrahydrofuran
THP ..... Tetrahydropyran
TBME ..... Methyl *tert*-butyl ether
TMB 1,3,5-Trimethoxybenzene
TMEDA ..... Tetramethylethylenediamine
*t*Bu ..... *Tert*-butyl
TON ..... Turnover number
UPLC ..... Ultra-performance liquid chromatography
VT ..... Variable temperature
X ..... Halogen
XRD ..... X-ray diffraction
$\Delta G^{\ddagger}$ ..... Free energies of activation

Acknowledgements

I would like to express my sincere gratitude to my supervisor, Dr. David Leitch, for his invaluable guidance, unwavering support, and insightful feedback throughout the course of this research.

I am also deeply thankful to our industrial collaborators at GSK, particularly Damian Hruszkewycz and Brennan Rose, for their expertise, and provision of resources. Their practical insights have significantly enriched the applicability and relevance of my findings.

Dr. Violeta Iosub, I want to express my sincere gratitude for your exceptional support as a mentor. Your guidance has help me explore and develop my passion for teaching. I truly appreciate your encouragement and insights you have shared.

Furthermore, I extend my appreciation to all the members of the Leitch group, Kushal, Jingjun, Jingru, Joe, Greg, Kyla, Austin, Bennett and Gilian, it has been an amazing experience being able to work and learn aside you. I am also thankful to the undergraduate students that have contributed to this work, Odhran, Sarah and Hailey.

I am grateful to my family and friends for their unwavering support, encouragement and understanding throughout this journey. Vanessa, your support in and out of university has made you a forever friend. Dominic and Elena, you helped me look at my research from a different perspective and to give value to the PhD experience as a whole. Angel, I really appreciate your unconditional support and understanding throughout this challenging yet rewarding journey. You have been key in helping me navigate the challenges and have celebrated all the successes along the way. I am incredibly fortunate to have you by my side.

Dedication

To the women of my family, for your unwavering encouragement and love.

Ama, Ainhoa, Mari Luz, nigan duzuen sinesmena nire indarrik handiena izan da.

CHAPTER 1. Introduction to C–H Activation and High-Throughput Experimentation

1.1 C–H Functionalization in Organic Chemistry

The development of new transformations for the functionalization of organic compounds has been key for the synthesis of more complex molecules such as polymers, biomolecules and organometallic compounds.[1] Still, hydrocarbons, and especially alkanes, are an important class of organic molecules for which functionalization remains a challenge.[2] Alkanes are organic molecules consisting of saturated carbon and hydrogen bonds, and lack any other functional groups. The simplest example is methane (CH_4), with extended alkanes having longer carbon chains that form more complex molecules such as paraffins (carbon chain with 17 to 35 carbons) that can be used as anti-corrosive agents.[3] Alkanes are usually obtained from oil and natural gas. Natural gas contains primarily methane (70-90%) and some larger chain alkanes such as ethane, propane and butane. All organic molecules are based on chains of carbon-hydrogen units, and are the basis of most of the materials found in everyday life. For example, methanol, the backbone of plastics and paint can be synthesized from methane in the presence of metal salts.[4] Alkenes, alkynes and aromatic hydrocarbons are more complex hydrocarbons built from C–H units but contain multiple C–C bonds which functionalization is essential for the development of polymers and other materials.[5]

Hydrocarbons pose a challenge for functionalization due to their generally poor reactivity and difficulties in achieving selectivity.[6] The characteristics of the C–H bond are the reason for these challenges. C–H bonds are strong, with bond dissociation enthalpies (BDEs) between 90-100 kcal/mol. They also have very low acidity (estimated alkane C–H pK_a between 45 and 60) due

to similar electronegativity of both atoms (χ_C 2.55 and χ_H 2.1 in Pauling scale).[7,8] The backbone of most organic molecules contain C–H bonds that have similar characteristics. Despite decades of research, few reagents can selectively activate specific C–H bonds in organic molecules.[9] When considering alkenes and alkynes, these functional groups have π-bonds that can be more reactive than the C–H bond, potentially leading to side reactivity and undesired products. The major aim of C–H functionalization reactions is to form new bonds at specific positions of the molecule selectively and efficiently (Figure 1.1).

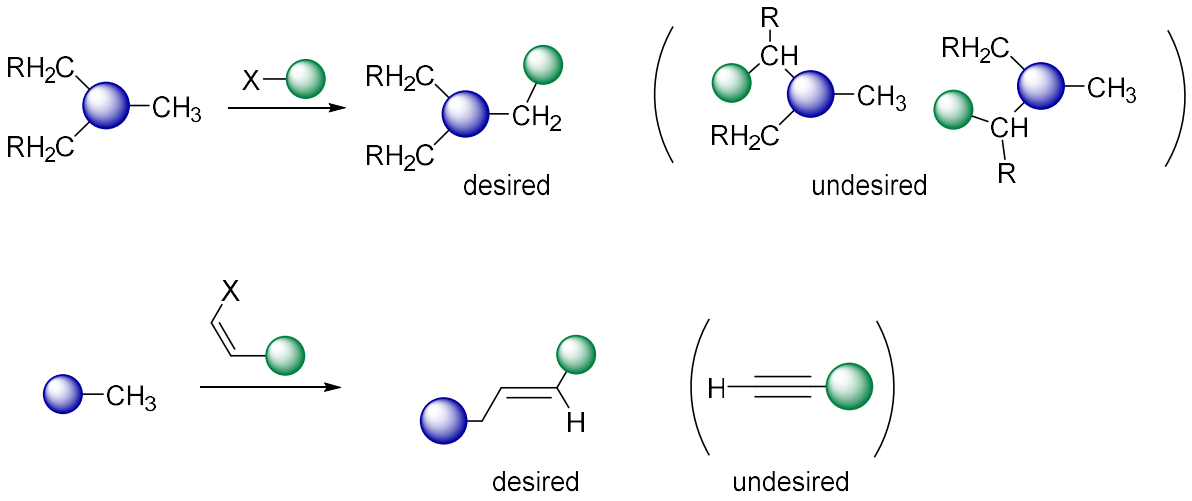

Figure 1.1. Selective C–H functionalization of molecules with several inequivalent C–H bonds and more reactive C–C multiple bonds.

C–H functionalization reactions have allowed chemists to synthesize a variety of molecules from otherwise unreactive hydrocarbons, an otherwise inefficiently used synthetic handle.[10] The synthetic community remains interested in the development of new reactions to selectively activate C–H bonds.[11] This is because current examples still cannot be applied broadly across many compound classes, and the established reaction conditions are far from optimal.[12] They usually

involve high temperatures, high catalyst loadings and the use of corrosive or toxic additives. In spite of that, chemists in academia and industry have included C–H functionalization in the synthesis of drug candidates, natural products and late-stage functionalization.[1,13,14]

Developing new synthetic approaches for the C–H bond cleavage or functionalization into more reactive functional groups requires an understanding of their reactivity. Alkanes and other hydrocarbons are abundant in nature and relatively inexpensive, as they are the (by)products of several industrial processes. Their reactivity and functionalization would widen the starting materials available for further transformation. As a result, selective C–H bond functionalization has long been considered a "Holy Grail" of organic chemistry,[15] as greater understanding of the transformation and development of reagents capable of selective reactivity would allow chemists to bypass intermediate functional group interconversions, and significantly reduce the formation of waste byproducts. Thus, direct C–H functionalization has potential to be an atom and step efficient alternative to traditional synthetic pathways (Figure 1.2).[16,17]

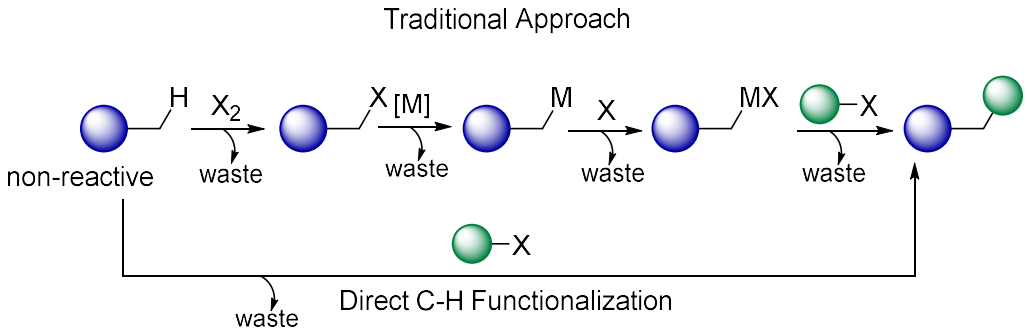

Figure 1.2. Traditional approach toward C–H functionalization vs direct C–H functionalization.

Beginning in the 1980s, the development of new metal complexes and salts able to activate C–H bonds in diverse molecules led to C–H functionalization reactions progressively being more

used in synthesis.[18,19] These first reactions required stoichiometric amounts of metal additives and several reaction intermediates to generate the target molecule. Subsequent advances in catalytic C–H functionalization has made these reactions more practical. As a result, many different direct C–H functionalization reactions have been developed. These include the formation of C-C, C-O, C-N and C-Si bonds.[20] They can be applied to functionalize small molecules such as methane, obtaining methanol or methyl bisulfate,[11] as well as in the synthesis of natural products,[21,22] pharmaceutical compounds,[18] and late stage functionalization.[19,23] Overall, C–H functionalization reactions are attractive tools for organic chemists, as they allow new disconnections for the synthesis of organic molecules with a great variety of functionalization.

1.2 Classes of C–H Functionalization Reactions

From an application point of view, C–H functionalization reactions can be categorized as "first functionalization" and "further functionalization" types (Figure 1.3).[10] First functionalization involves simple hydrocarbons (*e.g.* methane, *n*-alkanes, benzene) that can be converted into new starting materials for other reactions. Due to these compounds often containing many similar C–H bonds, and the high bond strength of these C–H bonds, over-functionalization, high catalyst loadings, and narrow scope of application are persistent challenges. [14] Further functionalization reactions use starting materials that already contain functional groups for the synthesis of complex molecules, such as in late-stage functionalization. While these starting materials have more distinct C–H bonds, this approach requires of the development of tolerant and selective reaction conditions that can operate in the presence of such functional groups.

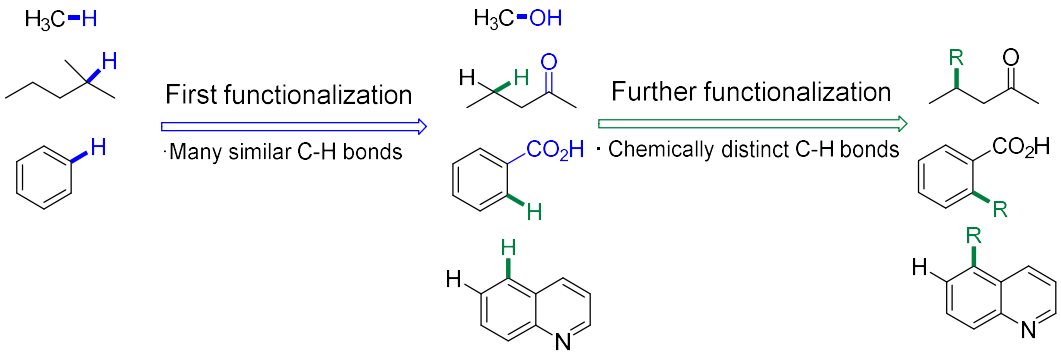

Figure 1.3. First functionalization and further functionalization of organic molecules.

The variety of applications for C–H functionalization is due to the diverse ways in which the C–H bond can be transformed. Specific C–H functionalization reactions range from commonly known electrophilic aromatic substitution and C–H bond oxidation, to more recently developed methods such as carbene/nitrene C–H insertion, photochemical C–H activation, and organometallic reactions.

Electrophilic aromatic substitution is widely utilized and cost-effective formal C–H functionalization reaction.[13] The reaction proceeds via electrophilic attack of the π-system of the aryl ring, forming a cationic intermediate (also known as a Wheland intermediate). This is followed by C–H deprotonation and formation of the final product by rearomatization. Although extensively used, there are several limitations to this reaction. One major drawback is related to the selectivity of the reaction, both in terms of site-selectivity and as well as formation of byproducts due to side reactivity of the reactive electrophiles (Figure 1.4).[24]

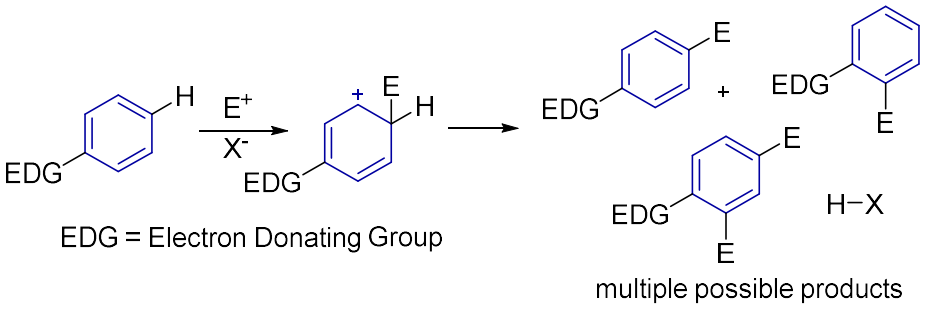

Figure 1.4. C–H functionalization by electrophilic aromatic substitution (S_EAr).

C–H oxidation reactions are powerful transformations to include reactive functional groups into otherwise unreactive molecules.[25] The most common oxidizing agents include those based on oxygen, halogens, and nitrogen. Halogenating reagents include elemental halogens (Cl_2, Br_2, I_2)[26,27] and *N*-halogenated imides (NBS or NCS).[28] Oxygen based oxidants (O_2 and peroxides/peracids)[29,30] are less often used than halogens in organic synthesis because of their hazardous nature. When oxygen gas is used as a reagent, the reaction conditions usually require the use of a reductant present to control the formation of intermediate peroxides, as their accumulation in the reaction mixture can be dangerous. Additionally, the concentration of oxygen in the headspace of the reactor has to be controlled to reduce the risk of combustion (fuel/air mixture).[31] Nitrogen-based oxidants, such as nitric acid or p-dodecylPhSO_2N_3,[32–34] are also hazardous. One of the reasons to avoid these chemicals is that reaction intermediates are prone to decompose at low temperatures via Beckmann rearrangement. Another general challenge with oxidation reactions is that over-oxidation is an issue if an intermediate oxidation state (*e.g.* –CH_2–OH) is desired over a higher oxidation state (*e.g.* –COOH) (Figure 1.5).

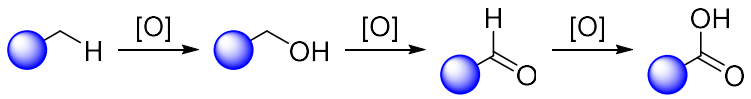

Figure 1.5. Progressive C–H oxidation of hydrocarbons. Common overoxidation products are represented.

Photochemical reactions have also been applied to C–H functionalization.[35] They can involve either the transfer of a hydrogen free radical (a neutral hydrogen atom), hydrogen atom transfer (HAT) or the transfer of a H^+ and an e^- for the functionalization of the molecule, proton-coupled electron transfer (PCET) reactions.[35] Photochemical transformations often require photosensitizers, such as 1,2,4,5-tetracyanobenzene, anthraquinone and other smaller organic molecules including benzophenone or acetophenone.[36–38] The most common options for functionalizing unactivated C–H bonds are concerted proton-electron transfer (CPET) and stepwise electron transfer-proton transfer (ET-PT) (Figure 1.6).[39] The mechanism will depend on the properties of the photosensitizer (PS) and the substrate. Some of the specific challenges of photochemical C–H functionalization include the need for high energy light to activate the photosensitizers, and low site-selectivity due to similar characteristics of the many available C–H bonds. Photocatalytic species have emerged as a solution to these challenges, but a discussion of these is beyond the scope of this thesis.[40–42]

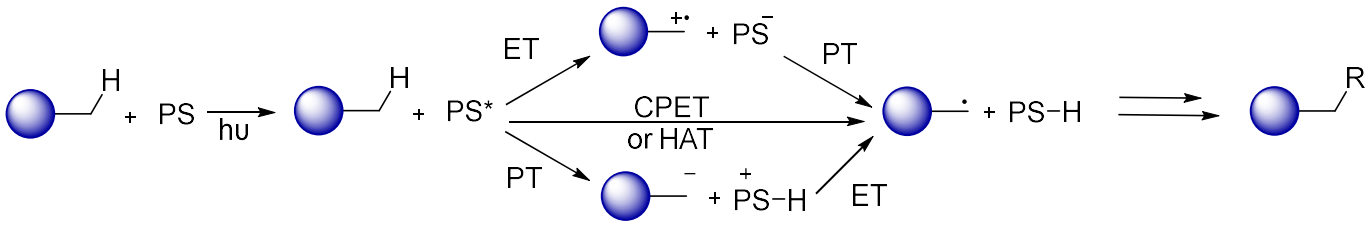

Figure 1.6. General mechanisms of photochemical C–H functionalization reactions.

C–H insertion reactions are another prominent class of C–H functionalization reactions. Carbenes are reactive organic molecules capable of C–H insertion, and contain a neutral carbon atom with a lone pair of electrons.[43] Many carbenes are extremely reactive and have short lifetimes, but are capable of activating C–H bonds.[44] However, the high reactivity of these species make the reaction generally unselective and hard to control. An approach to this challenge is to use metal-carbenoid induced C–H insertion.[45] In these reactions, a reactive M-carbene fragment achieves C–H insertion. In contrast to organometallic C–H activation reactions (discussed below), the metal atom of the carbenoid does not interact directly with the C–H bond. These carbenoids are usually formed from reactions between metal centers and diazo compounds, which are themselves carbene precursors (Figure 1.7). The metal complex performs the C–H insertion is regenerated, making these transformations catalytic. [46]

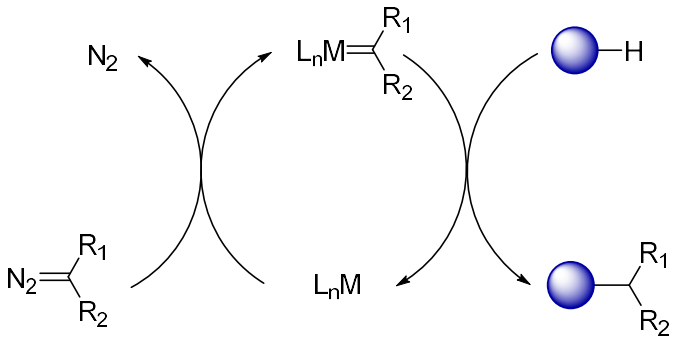

Figure 1.7. General mechanism of metal-*c*arbenoid induced C–H insertion.

Both intramolecular[43,47,48] and intermolecular[49,50] examples of C–H insertions have been developed. Their reactivity depends on the substituents present in the substrate(s).[51,52] If electron withdrawing groups are present, the carbene becomes more electrophilic and it will exhibit poor regioselectivity. If strong electron donating groups are present, the carbenoid will not be

electrophilic enough to achieve efficient C–H insertion.[45] Both of these factors can limit the scope of the reaction. Finally, analogous nitrene/nitrenoid C–H insertion reactions can be used to form C–N bonds.[53]

1.3 Organometallic C–H Activation Reactions

C–H activation and C–H functionalization are terms that are often used inconsistently in the literature. For this thesis, C–H *activation* is defined as a step (or series of steps) in a reaction mechanism that involves the cleavage of a C–H bond. It is *not* the elongation of the C–H bond. C–H *functionalization* is any reaction where a hydrogen from a C–H bond is replaced by another atom or group of atoms (Figure 1.8). In other words, C–H activation is one of the reaction steps involved in a C–H functionalization reaction. Organometallic C–H activation reactions are a subset of C–H activation that involve the cleavage of a C–H bond *via* a transition metal, resulting in a new metal-carbon (M–C) bond. The new organometallic M–C fragment is referred to as the activated state.

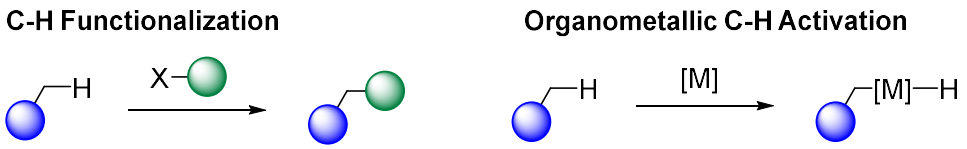

Figure 1.8. Difference between C–H activation and C–H functionalization.

Organometallic C–H activation is an important feature of many C–H functionalization pathways. The properties of the metal complex can enable site-selective functionalization of

simple hydrocarbons and, in recent years, has been applied to the synthesis of complex targets. The power of organometallic C–H activation is due to the reactivity of the new M–C bond, which can be used to achieve further functionalization. Organometallic C–H activation is therefore often used as part of catalytic cycles. Catalytic C–H functionalization is a powerful tool in organic synthesis as it can eliminate the need for functionalized synthetic intermediates, and can also decrease the amount of waste generated in a synthetic process. These transformations allow the rapid and direct synthesis of functionalized products and therefore, they have allowed the conversion of relatively simple hydrocarbons into more complex molecules.

1.3.1 C–H Sigma Complexes

Organometallic C–H activation reactions occur through diverse mechanisms, but many have in common the initial coordination between the metal and the C–H bond. The formed complex is a high energy organometallic intermediate – termed a C–H sigma complex or σ-complex – that polarizes the C–H bond allowing for further cleavage and functionalization.[54] The bonding interaction involves donation of electron density from the C–H σ-bond to an empty *d*-type orbital on the metal center. Back donation from a filled *d*-type orbital into the C–H σ* orbital is also possible (Figure 1.9).[55] If the σ-donation is too weak, the C–H sigma complex will not form. In contrast, a high degree of back donation further weakens the C–H bond, enabling faster C–H activation.[56]

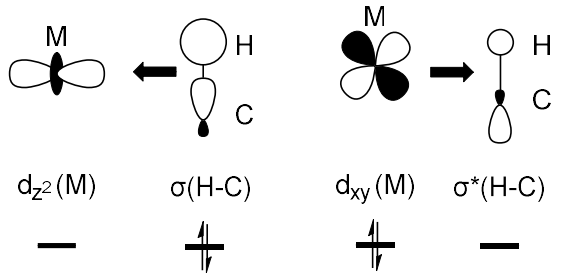

Figure 1.9. Simplified bonding picture of metal and C–H orbital overlap in C–H sigma complexes.

Depending on the nature of the metal complex and organic C–H fragment, there are examples of characterized sigma complexes as well as complexes with C–H agostic interactions. The difference between these two intermediates is in the origin of the C–H bond. Sigma complexes are formed from intermolecular M---C–H interactions, whereas agostic complexes, a term formulated by Brookhart and Green,[57] are intramolecular M---C–H interactions. Figure 1.10 shows two examples such complexes: a rhodium sigma complex with methane, and a titanium agostic complex with an ethyl ligand.[58,59]

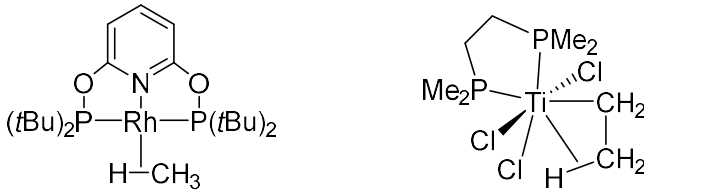

Figure 1.10. Examples of σ-complex (intermolecular C–H activation intermediate) and agostic complex (intramolecular C–H activation intermediate).

Complexes with sigma (σ) interactions are not limited to C–H bonds. They can also involve H–H, B–H or Si–H bonds that act as two electron donors to the metal center, resulting in a 3-center-2-electron bond.[54,60] Sigma interactions are usually weak, especially for C–H sigma complexes, and therefore the complexes are generally not isolable; however, they have been observed through infrared spectroscopy.[55,58]

Agostic interactions form as a result of intramolecular bonding to give the same kind of 3-center-2-electron interaction involving a C–H bond and an unsaturated metal. The term 'agostic' refers specifically to interactions involving M---C–H groups and no other 3-center-2-electron interactions. At the same time, not all M---C–H interactions are agostic, as C–H bonds can also be weak hydrogen-bond donors.[58,61] Agostic interactions are characterized by relatively short M---H distances (≈1.8-2.3 Å) and small M---H–C bond angles (≈90-140º).[61] They also show specific NMR spectroscopic features, with low $^{1}J_{CH}$ values (50-100Hz). As well, chemical shifts of agostic hydrogens are typically upfield from the uncoordinated group.[62] Agostic interactions can significantly affect the structures and stabilities of reaction intermediates and transition states.[57]

Intermolecular coordination of C–H bonds is entropically less favored than agostic interactions. As a result, direct observation of intermolecular sigma complexes is far less common than for agostic complexes. Nevertheless, formation of the sigma (or agostic) complex is proposed as a common first step in all organometallic C–H activation reactions. Depending on the steps involved in the breaking of the C–H bond, there are five distinct proposed mechanisms (Figure 1.11). These include:

- **Sigma-bond metathesis** reacts through a four-centered transition state, and the hydrogen atom is transferred to another hydrocarbon or hydride.
- **Metalloradical** activation is a less common example of C–H activation. These are proposed to proceed from a bimetallic species that undergoes homolytic M–M bond cleavage prior to C–H activation.
- **1,2-Addition** occurs when the C–H bond adds across a M=E π-bond to form a new M–C bond. The process usually involves early transition metals.
- **Oxidative addition** is one of the most studied C–H activation reactions. It generally involves low valent, electron-rich transition metals with strong donating ligands. The oxidation state of the metal centers increases by two, with formation of new M–C and M–H bonds.
- **Electrophilic mechanisms** generally occur at less electron-rich metal centers, and the metal's oxidation state does not change during the C–H activation step.[9,63] Basic X-type ligands receive the hydrogen atom, generating HX as a byproduct.

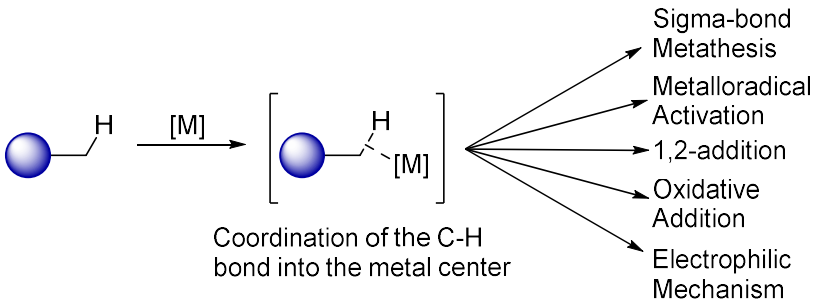

Figure 1.11. σ-Complexes or agostic complex as a common intermediate for organometallic C–H activation mechanisms.

For all organometallic C–H activation reactions, the rate determining step is often coordination of the C–H bond to generate the sigma complex. The following sections will describe the subsequent steps for each of the five mechanism types, and the situations where these mechanisms operate.

1.3.2 Sigma-Bond Metathesis

Sigma-bond metathesis is a concerted exchange of a metal-ligand σ-bond with the C–H bond from the substrate undergoing C–H activation. The reaction proceeds via a [2σ+2σ] cycloaddition-type transition state involving the two sigma bonds (Figure 1.12).[64] This transformation is generally specific to early transition metals with d^0 electron counts (*e.g.* Sc(III), Ti(IV), *etc.*) and lanthanide complexes with higher oxidation states.[65,66] These metals, which do not have an accessible +2 oxidation state, can undergo sigma-bond metathesis to achieve X-type ligand exchange reactions (*e.g.* alkyl, aryl, hydride *etc.*). Such ligand exchange reactions often proceed via oxidative addition followed by reductive elimination at late transition metal centers, whereas metal centers that cannot access higher oxidation states can benefit from the concerted nature of the sigma-bond metathesis mechanism. Studies indicate that more electrophilic metal centers are more reactive in sigma-bond metathesis reactions.[66]

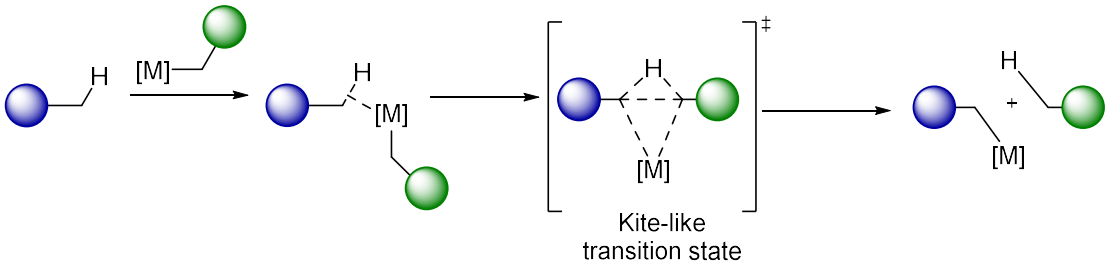

Figure 1.12. Sigma bond metathesis C–H activation mechanism.

Computational studies have indicated that the structure of the transition state is closer to a so-called kite-like transition state (C---H---C angle > 90°) than a more symmetric square or rectangular shape (Figure 1.12).[67,68] The strained transition state requires that substrates undergoing σ-bond metathesis have orbitals that can overlap in continuous bonding between the metal center and the carbon. The relative rates for C–H bond activation follow the trend C*sp*–H > Csp^2–H > Csp^3–H. In other words, the more *s* character the C–H bond has, the greater the overlap with the metal center, which lowers the energy of the transition state.[69]

An example of C–H activation via sigma-bond metathesis applied in catalysis is the zirconium-catalyzed coupling of propene and α-picoline (Figure 1.13). The zirconium complex reacts with unsaturated substrates via alkene insertion into the Zr–C bond, producing a metallacyclic structure. The catalytic activity of the zirconium complex was moderate (1-2 turnovers/hour), but it can achieve a total turnover number of 40.[70]

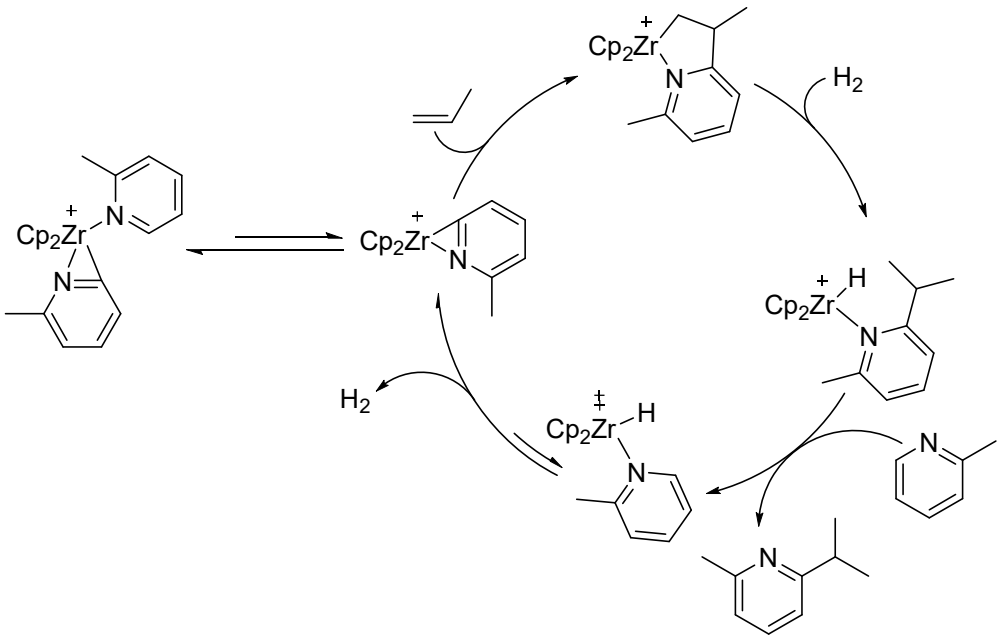

Figure 1.13. Catalytic alkylaton of 2-methylpyridine with a zirconium catalyst.

A second example was developed in 1990 for the catalytic oligomerization of terminal alkynes by lanthanide catalysts (Figure 1.14). These catalysts were successful for the regioselective C–H activation of terminal alkynes, followed by oligomerization via alkyne insertion in to the M–C bond. The extent of the oligomerization depends on the metal source and the substituents on the alkyne substrate. NMR studies indicate the formation of lanthanide acetylides by σ-bond metathesis are the active catalytic species in the catalytic cycle.[71]

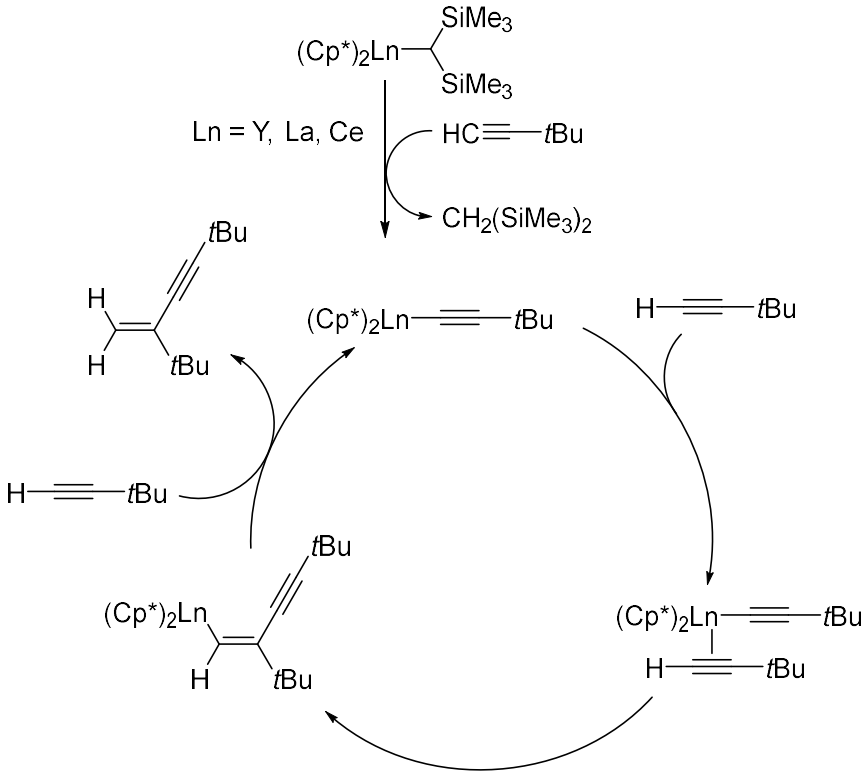

Figure 1.14. Oligomerization of terminal alkynes by lanthanide catalyst.

1.3.3 Metalloradical Activation

Metalloradical species are metal complexes with unpaired *d*-electrons that can participate in single electron reaction mechanisms. Such homolytic mechanisms have several advantages compared to two electron mechanisms. They can lead to higher reactivity under mild conditions, function in several types of solvent (including water), and can be less sensitive to the electronic and steric properties of the substrates. Metalloradical C–H activation proceeds by a one-electron stepwise mechanism that generally initiates with the homolytic bond scission of dimeric metal complexes, followed by the coordination of the C–H bond to the metalloradical center (radical addition) generating a four center linear transition state. The C–H bond is then broken generating

the two products (Figure 1.15).[72] For metalloradical activation of C–H bonds, the C–H BDE is a critical determinant in the selectivity of the reactions.

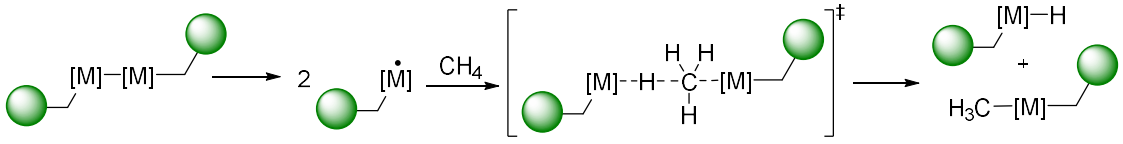

Figure 1.15. Metalloradical C–H activation mechanism

Metalloradical species usually have an odd number of d-electrons, such as Co(II), Rh(II), or Ir(II) (d^7).[73] Common substrates include linear and small hydrocarbons.[74] An early example of metalloradical activation of C–H bonds involved a Rh(II)-based catalyst capable of homolytically activating methane and toluene (Figure 1.16).[75,76] Many metalloradical species for C–H activation use porphyrin ligands, which are heterocyclic macrocycles consisting of interconnected pyrrole units. These ligands have a near-planar geometry with the nitrogen atoms facing inward providing a coordination pocket. It is a rigid and stable ligand, with a high degree of aromaticity. Porphyrin ligands are chelating ligands that can bind in a bi-dentate or tetradentate manner. The selective activation of C–H bonds has been attributed to the ability of porphyrin ligands to stabilize the metalloradical intermediate.[77] Even though metalloradical catalysts have been used to functionalize C–H bonds in organic compounds, challenges with selectivity and the discovery of suitable catalyst systems has limited their use in organic synthesis.[78]

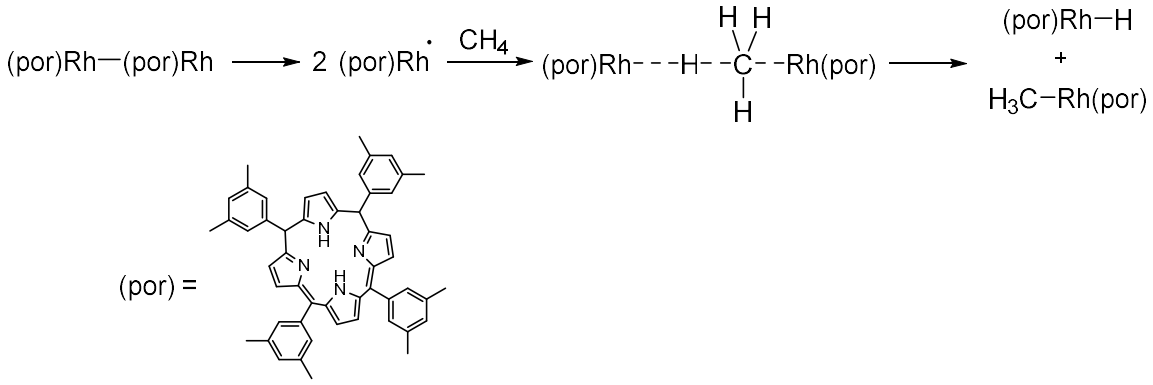

Figure 1.16. Porphyrin ligated rhodium catalyzed metalloradical activation of methane.

1.3.4 1,2-Addition

Activation of C–H bonds by 1,2-addition results in cleavage of the C–H and transfer of the hydrogen atom onto a reactive metal-ligand multiple bond. The symmetrical 1s orbital of the hydrogen allows the overlap with both metal and ligated atom (Figure 1.17). The transition state is four-membered, similar to that of sigma-bond metathesis. In this case, it is a [2π+2σ] cycloaddition, with electron density from the metal-ligand π-system donated into the C–H σ* orbital. Activation by 1-2 addition occurs at early transition metal alkylidene, alkylidyne and imido complexes.[9] A major factor influencing the rate of 1,2-addition is the metal-ligand bond polarity of the alkylidene/alkylidyne/imido, where a highly polarized metal-ligand bonds allows for a better interaction with the C–H bond.[79]

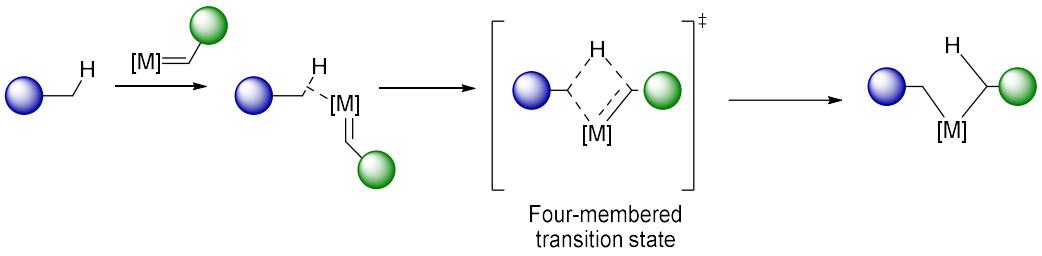

Figure 1.17. General mechanism for 1,2 addition of C–H bonds.

The formation of the required metal-ligand multiple bonds can be challenging, and as a result active catalysts can be hard to isolate. The high reactivity of metal-element multiple bonds can also lead to low selectivity, catalyst decomposition, and/or formation of undesired byproducts. This limits the applicability of this specific mechanism for organic synthesis. The most common complexes that undergo 1,2-addition are based on Ti(IV) and Zr(IV). Wolczanski demonstrated that Zr-imidos can activate simple hydrocarbons such as methane and more complex arylated benzene rings (Figure 1.18).[80]

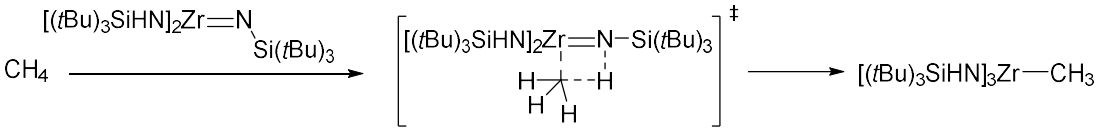

Figure 1.18. 1,2-Addition of methane into unsaturated zirconium catalyst.

More recently, Mindiola and Baik studied titanium alkylidyne-mediated intermolecular activation of aryl and alkyl C–H bonds. Although they were able to develop a route to a reactive, transient titanium alkylidyne intermediate able to react with unactivated C–H bonds, they also observed C–H bond activation of the reaction solvent (Figure 1.19).[81]

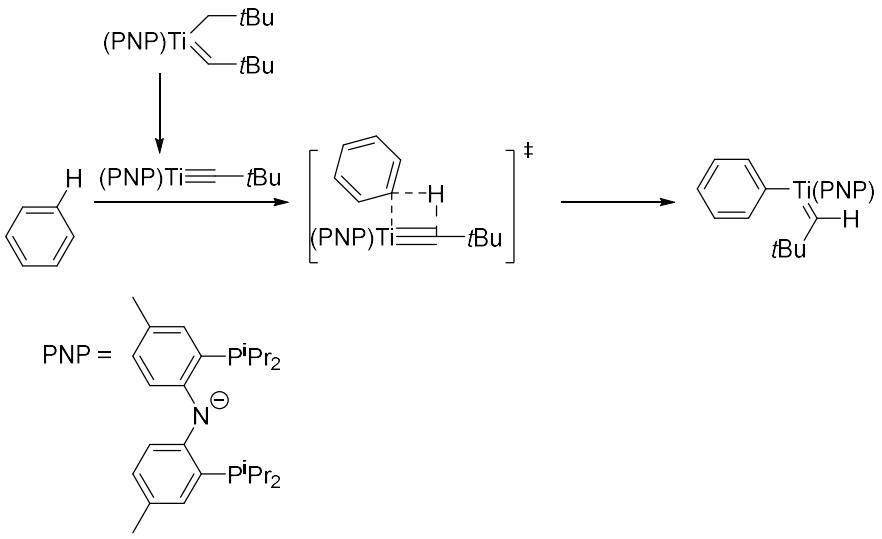

Figure 1.19. 1,2-Addition of benzene to titanium alkylidyne.

1.3.5 Oxidative Addition

Oxidative addition is one of the most common and well-studied organometallic transformations.[16] Oxidative addition occurs when a metal center inserts into a bond of an organic fragment, leading to both the oxidation state of the metal and its coordination number increasing by two. Specifically for C–H activation by oxidative addition, the metal center inserts into the C–H bond, resulting in the formation of both M–C and M–H bonds. For this to occur, the metal must have at least one empty coordination site, as well as the ability to increase its oxidation state.[82] The transition state closely resembles a C–H σ-complex (Figure 1.20).

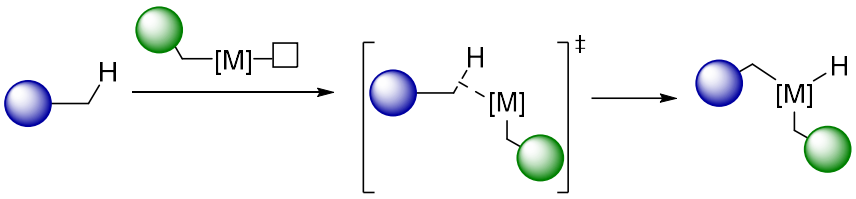

Figure 1.20. General C–H bond oxidative addition mechanism.

In terms of ligand effects, bulky, electron-rich ligands generally favour C–H activation by oxidative addition. Pincer ligands, such as the PCP or POCOP class, are a key example: they are bulky enough to protect an open coordination site, but also rigid to allow the coordination of the C–H bond (Figure 1.21).[83,84] Another key feature of these ligands is the inclusion of *tert*-butyl substituents on the phosphines, which also allow an open coordination site.[85,86] A common characteristic of these two types of ligands is their strong electron donation to the metal center. This destabilizes the low oxidation state starting material, and stabilizes the oxidative addition product, favoring the forward reaction.[87,88] In terms of catalytic applications, C–H oxidative addition is a key step in reactions such as alkane dehydrogenation, and C–H borylation.[89]

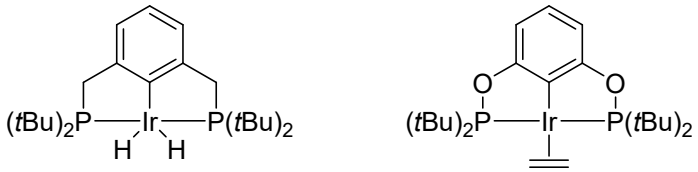

PCP Iridium complex POCOP Iridium complex

Figure 1.21. PCP and POCOP iridium complexes.

Computational studies have demonstrated that although the transition states for oxidative addition of C–C bonds and C–H bonds containing pincer ligands are similar, the activation of C–C bonds can be kinetically and thermodynamically preferred over C–H bonds in some cases.[90,91] This can represent a challenge for selective C–H activation. The preference for C–C activation could be due to a better metal positioning for the insertion into the C–C sigma bond versus the C–H bond. This selectivity can be tuned by the reaction solvent: acetonitrile can coordinate to the metal center, blocking the vacant coordination site and generating a bulky intermediate that hinders the C–C bond coordination to the metal. Some strategies to optimize the C–H bond activation vs

the C–C bond activation include specific solvent, ligand and temperature conditions (Figure 1.22). Furthermore, when trying to isolate C–H bond oxidation products, the removal of solvent can result in conversion to the C–C activated product,[92] which is stabilized by the shorter bonds between the ligands and the metal center and the presence of two five-membered chelate rings. These two factors make C–C oxidative addition thermodynamically preferred in this case.

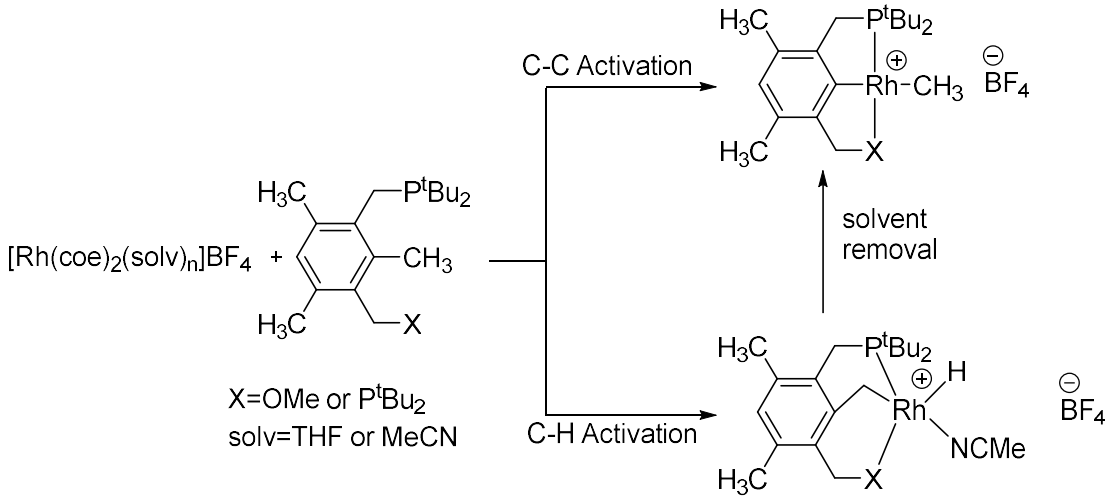

Figure 1.22. C–C vs C–H activation via oxidative addition with Rh(I).

1.3.6 Electrophilic Mechanism (EM)

The electrophilic activation of C–H bonds involves a mechanism where a lone pair from a basic X-type ligand deprotonates the C–H bond during the transition state (Figure 1.23). A key feature of this mechanism is that the metal-heteroatom bond is not directly involved in the C–H cleavage.

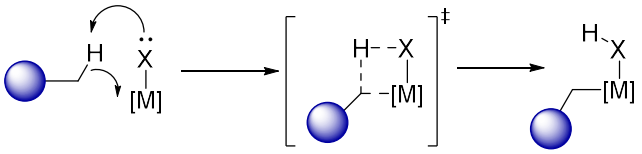

Figure 1.23. General mechanism of Electrophilic Activation of C–H bond.

The electrophilic mechanism, as for all other C–H activation mechanisms, starts with the coordination of the C–H bond to the metal center. Once the sigma complex has formed, the basic X-type ligand (often a carboxylate) deprotonates the carbon atom, leading to the formation of a new M–C bond and an X–H bond. The oxidation state of the metal center does not change during the C–H activation step.[93] While the transition state can be similar to the one formed in sigma bond metathesis, there are several key differences. First, electron donation from the X ligand to the hydrogen atom further polarizes the coordinated C–H bond through hydrogen bonding. Second, the basic atom responsible for deprotonation is not required to be directly bonded to the metal center, allowing variation in the number of atoms involved in the transition state. Carboxylate ligands often enable six-membered transition states rather than four-membered ones (Figure 1.24).

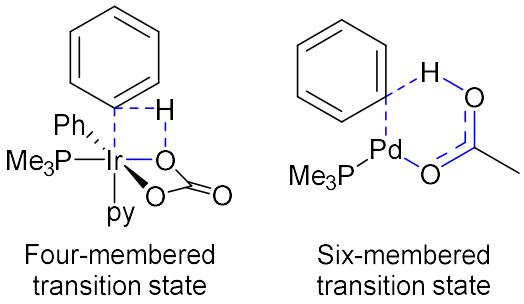

Figure 1.24. Comparison between four- and six-membered transition states in electrophilic C–H activation mechanisms.

The metals that usually participate in electrophilic activation of C–H bonds are d^6 or higher metals; a lower number of valence electrons would lead to ligand-to-metal donation by the X ligand lone pair, impeding the X---H interaction. At the same time, due to the electrophilic characteristic of the mechanism a higher number of valence of electrons would impede coordination of the C–H bond to the metal center. Therefore, a compromise between the electrophilicity of the metal center and the affinity for the lone pair of the X ligand must be found. Common metals for electrophilic C–H activation include Pt(II) and Pd(II).[94]

Depending on the electrophilic or nucleophilic characteristics of the transition state, different electrophilic mechanism types have been proposed. These include ambiphilic metal-ligand activation (AMLA), concerted metallation deprotonation (CMD) and ligand-to-ligand hydrogen transfer (LLHT) (Figure 1.25)[95]. CMD transition states are electrophilic with respect to the C–H bond, whereas LLHT transition states are nucleophilic with respect to the C–H bond. AMLA transition states are both electrophilic and nucleophilic (hence, ambiphilic), where the transfer of electrons between the metal, the X-type ligand, and the C–H bond is small, balancing the charge density of the process.

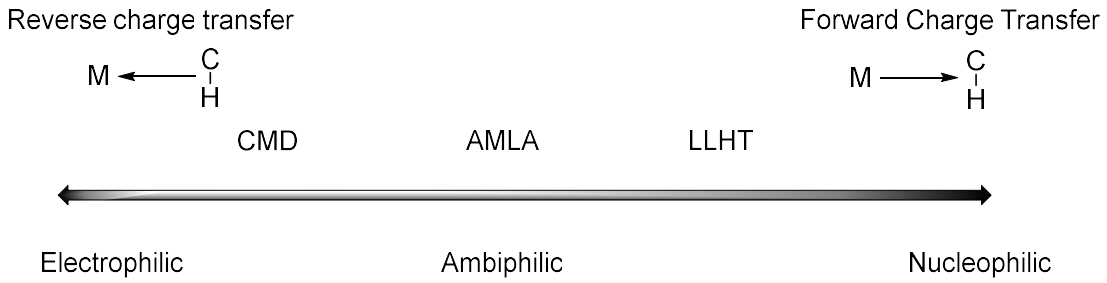

Figure 1.25. Representation of the continuum charge transfer and transition state characteristic in C–H electrophilic mechanisms.

The main difference between CMD and AMLA mechanism resides on the nature of the transition state.[9,96] AMLA mechanisms are less oxidative in nature, the transition state is both electrophilic and nucleophilic, and CMD mechanisms are more electrophilic (Figure 1.26).[97] Another difference resides in the transition states: AMLA has two possible transition state geometries, either four or and six membered, whereas CMD mechanisms are specific to carboxylate and related ligands that undergo six membered transition states (Figure 1.26). Ligand to ligand hydrogen transfer (LLHT) mechanisms are characterized by C–H transfer to coordinated alkynes or allenes, and is specific for first-row transition metals [9] It is also a concerted mechanism, where the hydrogen is transferred between coordinated ligands (Figure 1.26).[98] A key feature of this C–H activation process is that it does not require a basic X-type ligand.[99]

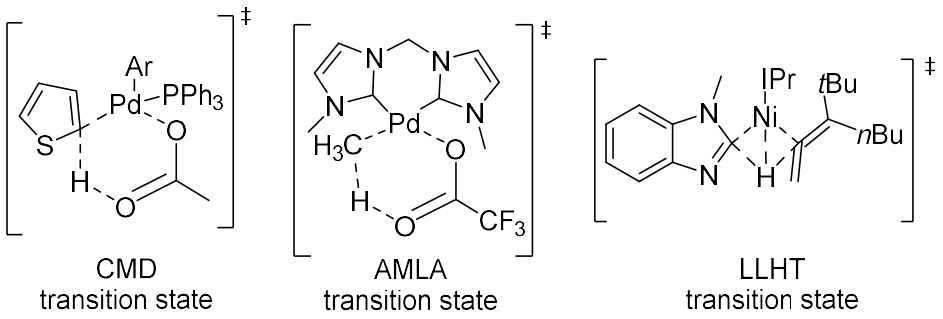

Figure 1.26. Examples of transition states for electrophilic activations: concerted metallation-deprotonation, ambiphillic metal-ligand activation and ligand to ligand hydrogen transfer.

1.3.7 Concerted Metallation Deprotonation (CMD)

CMD is one of the most important C–H activation mechanisms in the context of organic synthesis. As a result, extensive study of the CMD mechanism has allowed the understanding of crucial steps in organometallic catalytic C–H functionalization.[97,100,101] Several of the most common catalyst types are palladium acetate derivatives, where the acetate ligand is responsible for

cleavage of the C–H bond. Other catalyst systems include different carboxylate ligands, such as pivalate (added to the reaction mixture as the carboxylic acid) that can improve reactivity. As a result, carboxylate bases generally show better reactivity in C–H functionalization via CMD than amine or hydroxide bases. [102]

The CMD mechanism is a useful model to explain the selectivity observed in Pd-catalyzed C–H functionalization reactions. Goreslky and co-workers have deeply studied the activation barriers using Density Functional Theory (DFT) calculations for diverse C–H bonds on different heterocycles. Using distortion-interaction analysis, they quantified the different contributions to the CMD barrier.[103–105] There is an initial energetic cost, the distortion energy (ΔE_{dist}) associated with the distortion of the palladium complex and C–H bond to obtain the geometry needed for the interaction between the C–H bond and the metal center. Once both fragments interact, there is a decrease in energy, which corresponds to the interaction energy (ΔE_{int}) (Figure 1.27).[100,106,107]

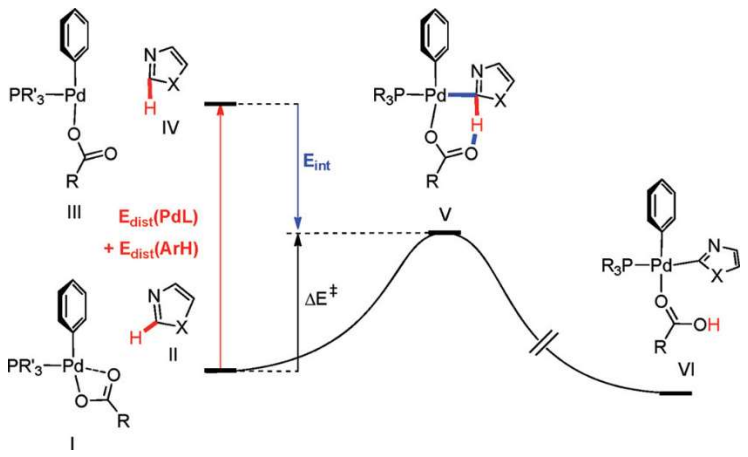

Figure 1.27. Distortion-Interaction analysis for the CMD transition states of azoles. Reprinted with permission from *Organometallics* **2012**, *31*, 794–797. Copyright {2012} American Chemical Society.[107]

The distortion-interaction analysis identifies geometric and electronic contributions to the activation of specific C–H bonds, allowing an understanding of the reactivity and regioselectivity of organometallic C–H functionalization. The distortion energy is the cost associated with the distortion of the ground state geometries into their transition state geometries. Related to the C–H bond, it can be separated in two components: the elongation of the C–H bond, and the out-of-plane bending of the C–H bond. It can be approximated to the C–H deprotonation energy.[97] The electronic interactions between the Pd–OAc catalyst and the C–H bond from the (hetero)aryl component explain the energy released by the formation of the Pd–C bond and the O–H bond.

Based on the analysis of the distortion-interaction energies of C–H bond activation through the CMD pathway, (hetero)aryl substrates can be divided into three classes (Figure 1.28). This classification depends on which of the energies controls the regioselectivity of the C–H activation.[107]

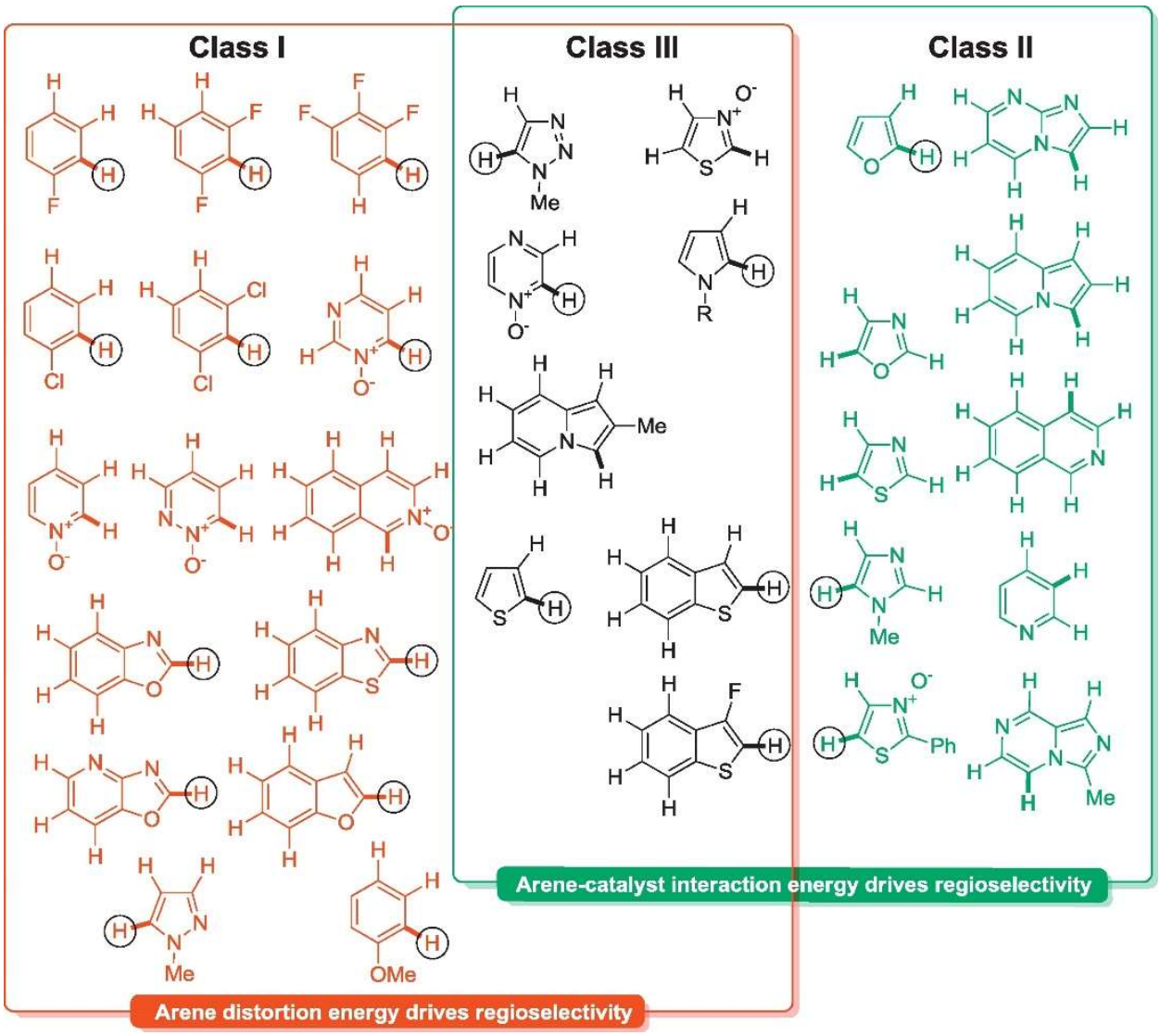

Figure 1.28. Classification of heterocyclic substrates in terms of contributions to regioselectivity of C–H bond via CMD pathway based on their reactivity with [Pd(C_6H_5)(PMe_3)(OAc)]. Reprinted with permission from *Organometallics* **2012**, *31*, 794–797. Copyright {2012} American Chemical Society.[107]

Class I includes arenes and heterocycles for which the aryl distortion energy controls the regioselectivity of the reaction. Most of these arenes are electron-deficient, though there are exceptions (*e.g.* anisole). An example is 1-methylpyrazole, where C5 is the major site of C–H

activation both experimentally and based on the calculation of barrier energy ($\Delta G^{\ddagger}_{298\ K}$ = 27.3 kcal/mol). C5–H is more reactive than the C3–H ($\Delta G^{\ddagger}_{298\ K}$ = 31.3 kcal/mol) or C4–H ($\Delta G^{\ddagger}_{298\ K}$ 28.5 kcal/mol) (Figure 1.29). This preference is directly related to the distortion energy, as C5-H is the bond with the lowest energetic cost when adopting the required geometry. If interaction energies were guiding reactivity, the C4–H bond would be the most reactive, as it is the one with a higher energetic release when the transition state is formed.

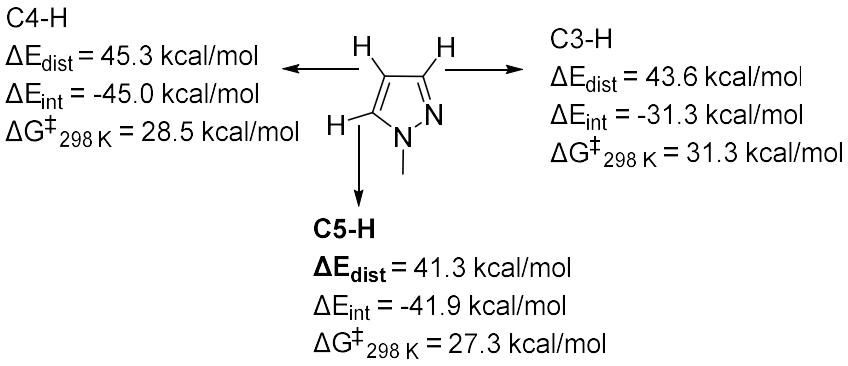

Figure 1.29. Distortion and interaction energies and Gibbs free energy of different C–H bonds of 1-methylpyrazole.

Site selectivity for Class II heterocycles is defined by the catalyst-arene interaction energy (ΔE_{int}). A specific example is furan, where the Cα–H bond is the most reactive ($\Delta G^{\ddagger}_{298\ K}$ = 25.3 kcal/mol) in comparison with Cβ–H ($\Delta G^{\ddagger}_{298\ K}$ = 28.7 kcal/mol) (Figure 1.30). In this case, there is an insignificant difference in the distortion energies needed to obtain the geometries to allow the interaction between the C–H bond and palladium center. However, the interaction energy once the transition state is formed is more favourable at the α *vs* the β C–H bond (-4.8 kcal/mol).

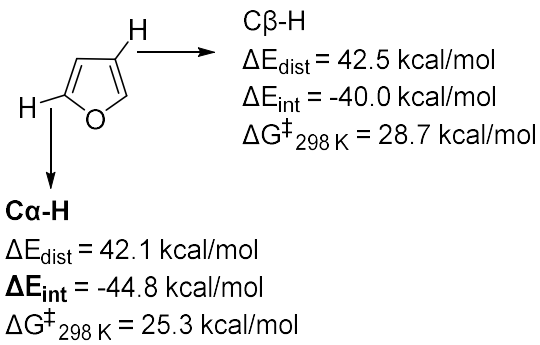

Figure 1.30. Distortion and interaction energies and Gibbs free energy of different C–H bonds of furan.

Class III substrates include examples of heterocycles where both distortion and interaction energies add to the selectivity of a particular C–H bond. This clearly can be observed for thiophene, where both energies are lower for the Cα–H bond. In this case, there is a smaller distortion energy cost (ΔE = 1.9 kcal/mol) for this bond to adopt the required geometry to interact with the metal and at the same time it releases the most energy (ΔE = -3.6 kcal/mol) when the transition state is formed (Figure 1.31).

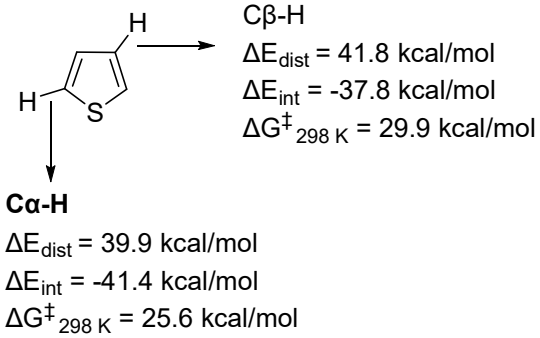

Figure 1.31. Distortion and interaction energies and Gibbs free energy of different C–H bonds of thiophene.

The C–H bond activation selectivity usually correlates with most acidic C–H bond. [108,109] This trend is observed with electron poor substrates; however, DFT calculations have shown that for electron rich arenes, the original CMD model is inconsistent with experimental outcomes. In this context, Carrow *et al.*, proposed the electrophilic concerted metallation-deprotonation mechanism (eCMD) for substrates that are exceptions to the acidity trend. According to their calculations, these substrates still undergo a concerted, base-assisted mechanism. The selectivity for electron-rich substrates is proposed to be determined from the metal-carbon bond formation rather than the C–H bond cleavage. This can lead to otherwise unexpected reactivity patterns.[110]

There is not a clear line that separates if a specific substrate/catalyst combination undergoes a CMD or eCMD pathway. Carrow presented a continuum of transition state structures which, depending on the characteristics of the substrate and the metal catalyst, may be more electrophilic or nucleophilic (Figure 1.32). The transition states of the metals undergoing CMD are characterized by the presence of phosphine ligands (leading to more electron-rich and nucleophilic metal centers), whereas the eCMD transition states contain nitrogen or oxygen based ligands (leading to more electron-deficient and electrophilic metal centers).

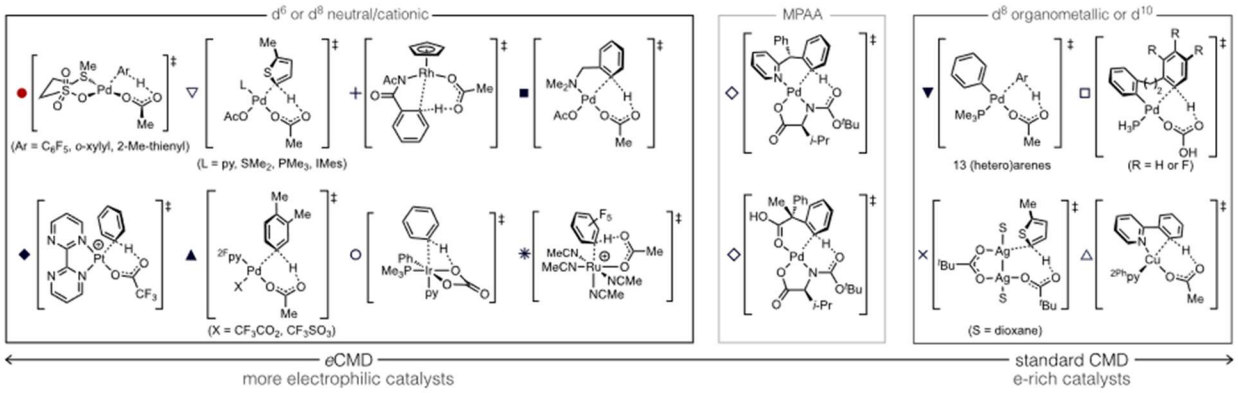

Figure 1.32. Transition states of CMD mechanisms classified as electrophilic concerted metallation deprotonation or standard concerted metallation deprotonation mechanisms. Reprinted with permission from *ACS Catal*. **2019**, *9*, 6821–6836. Copyright 2019 American Chemical Society.[108]

There is a high complexity on the mechanism by which C–H bonds are activated. However, C–H activation is recognized as an increasingly viable tool towards the development of new products or new synthetic pathways towards known molecules in pharmaceutical chemistry, drug discovery and material sciences. Advances in this field move toward selective functionalization under industrially reproducible mild conditions.[20] Specific catalytic applications of C–H bond activation towards pharmaceutical compounds will be discussed in the introductions to Chapter 2 and Chapter 3.

1.4 High Throughput Experimentation for Reaction Discovery and Optimization

Chemical reaction systems depend on many different factors/variables that must be optimized to reach a successful and generally applicable protocol. Variables such as the identities of solvent(s), additives, catalysts/ligands, among many others, can have a huge impact on both

reactivity (yield, scope) and selectivity (chemo, regio, stereo) of a reaction. The traditional approach to reaction optimization is the analysis of each variable individually using One Factor at a Time (OFAT) or One Variable at a Time (OVAT) optimization. This has been the primary approach in academia for a long time: it is simple to follow, conceptually intuitive, and does not require more advanced experimental design or data analysis. It does require, to some extent, scientific intuition to decide which are the most important factors. After the best value/setting for one variable is identified, it is fixed and another variable is analyzed. Optimizing one variable at a time often leads to local maxima, as this experimental design implicitly assumes that there are no interactions between variables (Figure 1.33).[111] This leads to an inefficient exploration of the variable space, and does not reveal key features of how the variables interact.

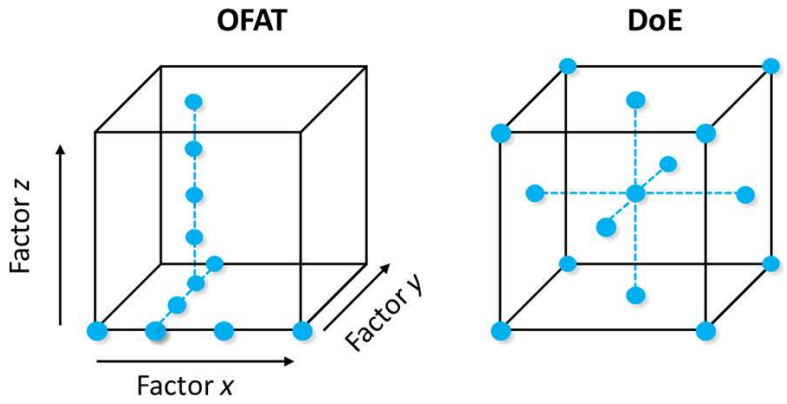

Figure 1.33. Expected variable space exploration comparison of OFAT versus multivariate approaches (here Design of Experiments).

An alternative approach is multivariate experimentation, where multiple factors are explored simultaneously, hence evaluating the effect that each variable has on the system. One example is to use Design of Experiments (DoE), where multiple factors are systematically changed to efficiently explore a variable space. Unfortunately, in many chemical systems, the need to study a

large number of variables leads to the need to perform a large amount of experiments. As a simple example, studying a reaction with five variables (catalyst, solvent, base, concentration, temperature) at four settings each would require $5^4 = 625$ experiments! Bayesian models have been proposed as iterative optimization algorithm that outperforms human decision making in optimization efficiency and consistency. This experiment design approach could facilitate more efficient synthetic pathways by enabling better-informed and data driven decisions about which experiments to run.[112] However, Bayesian and other optimization logarithm models can also lead to local maxima, as the information it uses to build the prediction can overshadow the data and bias the results. High-Throughput Experimentation (HTE) is a solution to this problem. Chemists in both industry and academia are increasingly using HTE to set, run and analyze a large number of reactions rapidly, while minimizing the amount of substrates, catalysts, solvents, etc. used for each individual experiment. Overall, HTE accelerates the exploration of multiple variables simultaneously, leading to more efficient and economic optimization of reactions.

1.4.1 High-Throughput Experimentation in Industry and Academia

A general HTE cyclic workflow involves a five-step process: experimental design, array set up, reaction execution, chemical analysis, and data collation to inform the design of the next array of experiments. To make this process feasible and chemically efficient, specific automation and analysis systems and methods for reaction miniaturization have been developed (Figure 1.34).[113,114]

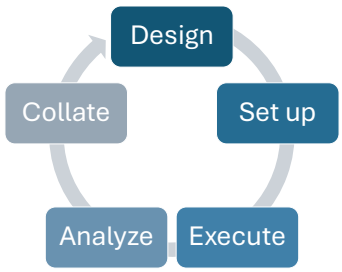

Figure 1.34. General steps in the HTE process.

The need for specific equipment has resulted in a gap between industrial and academic uptake of HTE in chemistry research. The key difference is the level of infrastructure that each sector is able to assemble and operate (Figure 1.35).[115] For example, large pharmaceutical companies can operate sophisticated and expensive automated instruments specifically designed for HTE. This has allowed these companies to perform in-depth studies of chemical transformations. Some recent examples include the optimization of a Suzuki-Miyaura cross-coupling reaction by Pfizer,[116] and the development of a screening platform for the metallophotoredox catalysis by Merck.[117] Beyond catalytic reactions, HTE is also used for chiral salt resolution, solvent/base combinations, and metal-scavenger screening.

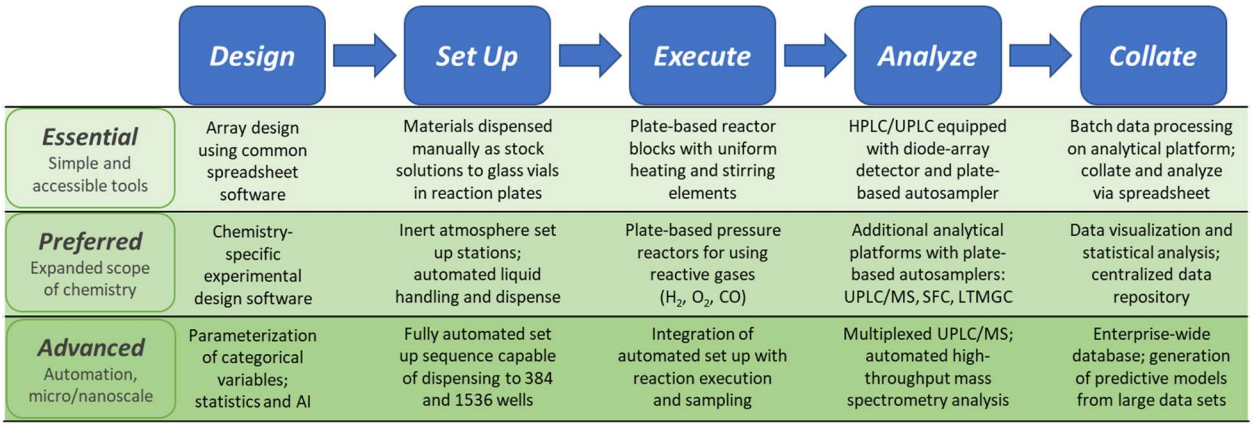

Figure 1.35. A general workflow of HTE in chemistry laboratories with types of infrastructure required. Reprinted with permission from *Comprehensive Organometallic Chemistry IV*, Oxford **2022**; pp 502-555. Copyright 2022 Elsevier.[115]

Apart from reaction set-up, the analysis of the reaction outcome is often the major challenge of processing HTE screens.[118] There are two main strategies to deal with this bottleneck: run multiple assays in parallel, or reduce the time for each individual assay (Figure 1.35).[115] High- or Ultrahigh-Performance Liquid Chromatography (HPLC, UPLC) is an ideal technique for high-throughput analysis, allowing the development of fast analysis methods (30 seconds in some cases) while still maintaining high-quality quantitative data. The main advantage is the ability to run a high number of analyses in a short amount of time. By itself, liquid chromatography is a separation technique; however, it is usually coupled to a detection apparatus (such as UV-Vis absorption) for quantification of the components in small scale reactions. Mass spectrometers are also commonly coupled to these systems. Mass spectrometry (MS) is one of the most sensitive detection methods. Its applicability ranges from the development and discovery of new drugs, to overall structure determination and characterization.[119]

Historically within the pharmaceutical industry, HTE work is performed by specialist teams due to the complexity of the automation platforms required. Lately, more user-friendly and modular systems have been developed, expanding the use of HTE to non-specialists.[120] This has also allowed some academic groups to direct their research towards HTE, and has also led to academic/industry partnerships.[121] As a result the gap between industry and academia regarding HTE has decreased.[122]

1.4.2 High-Throughput Experimentation in Organometallic Chemistry and Catalysis

Regarding reactions studied by HTE in process chemistry, a report from 2022 indicates 67% of these are organometallic reactions (Figure 1. 36).[122] This analysis included some of the biggest

pharmaceutical companies, including Amgen, AstraZeneca, Bristol-Myers Squibb, GSK, Eli Lilly, Merck and Pfizer. It is notable that among these many examples, Pd-catalyzed C–H functionalization reactions were only a small fraction of the reactions studied (1%), despite the large volume of recent academic publications on these reactions. However, this trend is expected to change in the next years. Six out of eight HTE process chemistry departments reported in the same paper that they anticipate C–H functionalization reactions will be in their top 10 screened reaction types going forward.

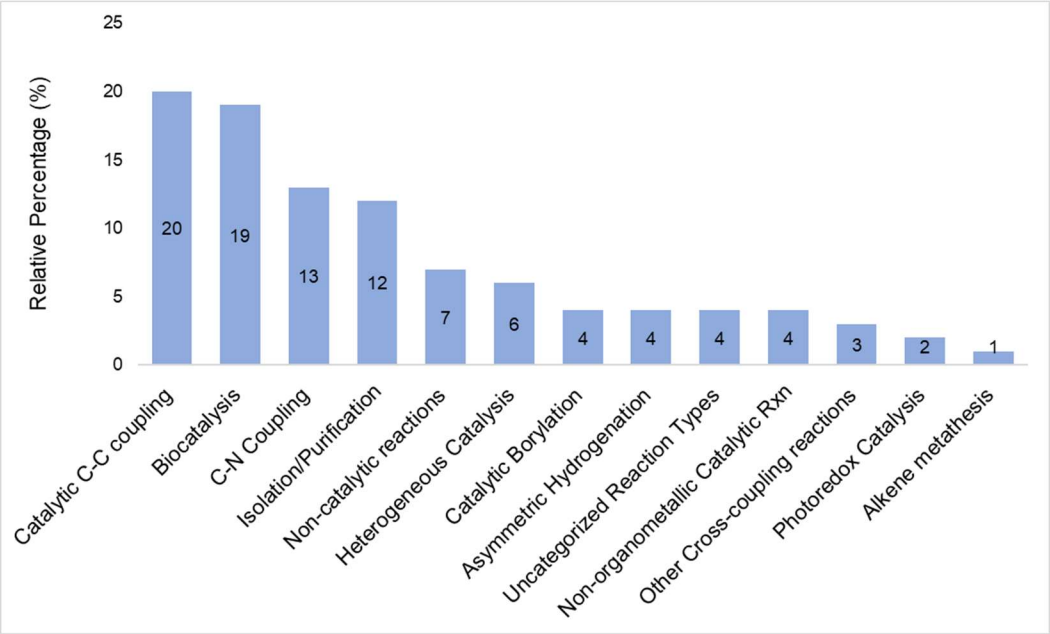

Figure 1.36. Relative Percent of the Most Common Reaction Types Studied by HTE Groups in Process Chemistry.

Foremost among the expected increase in C–H functionalization reactions are direct C–H arylations. These are a broad class of cross-coupling reaction in which C–H bonds are converted into C–C bonds to other aryl groups. The resulting products contain motifs commonly present in pharmaceutical molecules and also conjugated materials (Figure 1.37).[123,124]

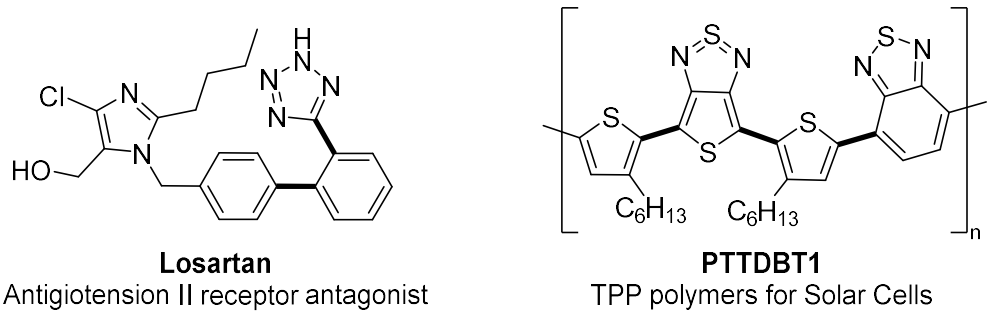

Figure 1.37. Examples of direct C–H arylation used to make molecules or materials.

HTE can be applied to three distinct research approaches in organic chemistry: reaction discovery, reaction optimization, and reaction scope evaluation. Reaction discovery for cross-coupling reactions generally involves screening combinations of precatalysts and ligands to set the initial reaction conditions that can be further optimized. In this case, researchers can rapidly explore a wide range of conditions to identify those that lead to *any* formation of product, even only a small amount. This can significantly accelerate the discovery process, as many initial attempts to observe a new reaction fail.

An example of HTE-enabled reaction discovery for C–H functionalization is the development of a nickel-catalyzed arylation of benzoxazole and oxazoles with arylhalides reported by Merck.[125] HTE identified $Ni(COD)_2$ and dcype or NiXantphos as active catalyst/ligand combinations. At the same time, they identified an interaction between the choice of base and the substrate structure. This led to further optimization of each system individually, rather than trying to find one general set of conditions (Figure 1.38).

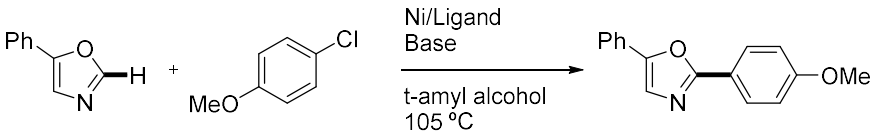

ligands/bases	L1	L2	L3	L4	L5	L6
K_3PO_4	38	41	32	25	18	36
Cs_2CO_3	11	41	8	16	8	9
LiOtBu	28	75	19	31	11	61
NaOtBu	26	35	25	12	18	62
P_2Et	60	82	56	23	39	87

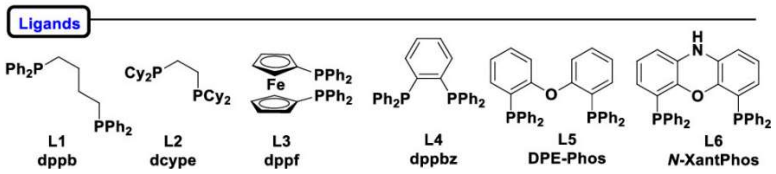

Figure 1.38. HTE applied to reaction discovery of nickel catalyzed direct functionalization of oxazole. Figure adapted from *J. Org. Chem*. **2019**, *84*, 13092–13103. Copyright 2019 American Chemical Society.

Researchers at Merck and UPenn also applied HTE techniques to the discovery of reaction conditions for the synthesis of diarylmethyl phosphine oxides from benzyl phosphine oxides via C–H arylation.[126] This was envisioned as an alternative to other reaction pathways such as Michaelis-Arbuzov, Michaelis-Becker reactions or the use of organolithium bases and phosphine halides. They initially screened twenty-four ligands with the same palladium source to assess the product formation and obtained initial hits for reaction discovery.

Once establishing this basis for reactivity, they moved to the reaction optimization stage, using HTE to screen two palladium sources, two ligands, four solvents and six bases (Figure 1.39). The goal of reaction optimization is to determine the ideal setting for each factor and, to more

thoroughly explore interactions between factors. In this case, specific catalyst/solvent/base combinations are needed to achieve good reactivity.

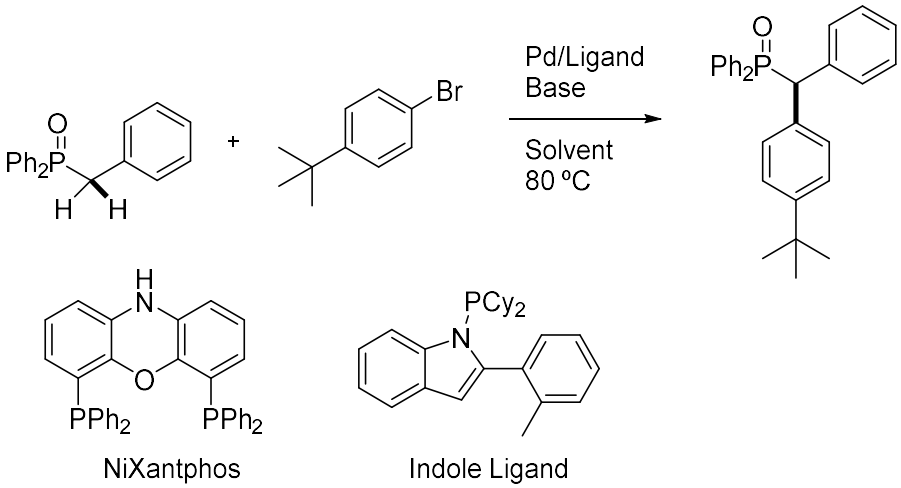

	Pd(OAc)2								
	NiXantPhos				Indole Ligand				
	CPME	Dioxane	THF	Toluene	CPME	Dioxane	THF	Toluene	
LiHMDS	0.09	0.92	0.22	1.37	0	0.62	0.16	0.41	LiHMDS
NaHMDS	2.08	1.41	0.76	1.94	0	0.71	0.21	0	NaHMDS
KHMDS	0	0	0	0.42	0	0	0	0	KHMDS
LiOTbu	0.25	0	0.27	0	0	1.51	0.16	0	LiOTbu
NaOtBu	1.78	0.15	1.18	0	0	0.91	0.59	0	NaOtBu
KOtBu	0	0	0	0.23	0	0	0	0	KOtBu
LiHMDS	0.44	0	0	0.53	0	0.33	0.2	0	LiHMDS
NaHMDS	2.34	1.49	0.84	0	0	0	0.24	0.32	NaHMDS
KHMDS	0	0.16	0	0	0	0	0	0	KHMDS
LiOTbu	0	0	0.25	0	0	0	1.9	0	LiOTbu
NaOtBu	0	0	0.95	0	1.86	1.66	0	1.22	NaOtBu
KOtBu	0	0	0	0	0	0	0	0	KOtBu
	CPME	Dioxane	THF	Toluene	CPME	Dioxane	THF	Toluene	
	NiXantPhos				Indole Ligand				
	Pd(dba)2								

Figure 1.39. HTE results of reaction discovery of palladium catalyzed alpha-arylation of benzylic phosphine oxides.

As another example, researchers at Bristol Myers Squibb optimized the reaction conditions for late-stage selective C–H functionalization of a quinazoline, examining a wide range of many different factors in a large HTE campaign. These studies indicated that addition of any phosphine, pyridine or phosphite would lead to the inhibition of catalysis. Therefore, they proceeded with a 'ligandless' catalyst system of just Pd(OAc) to achieve the synthesis of BMS-919373, a potent I_{Kur} current blocker (Figure 1.40).[126,127]

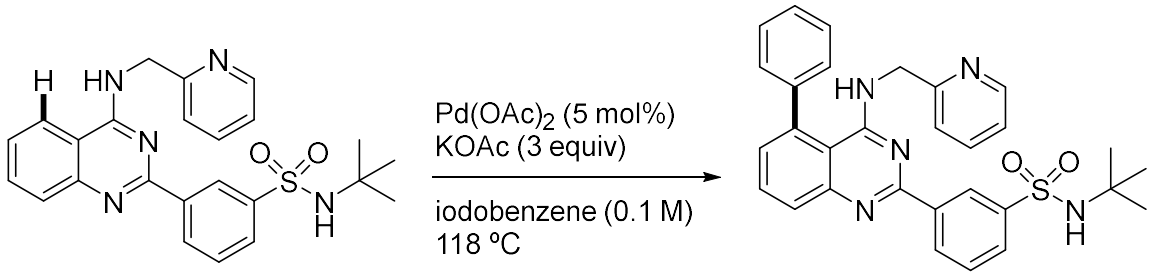

Solvents:
Dioxane
Anisole
DMA
NMP
Toluene
Xylene
Trifluorotoluene
Chlorobenzene
t-Amyl alcohol
Propylene Carbonate

Substrate:
Iodobenzene
Phenyl triflate
Bromobenzene

Bases:
$KHCO_3$
Cs_2CO_3
K_2CO_3
$NaHCO_3$
Na_2CO_3
K_3PO_4
K_2HPO_4
KH_2PO_4
CsF
KF
NaOMe
KOAc
KOtBu
KOPiv
TMAOAc
NEt_3
2,6-lutidine
Cy_2NMe

Acid (equiv)
HOAc (0.005-3.0)
PivOH (0.1-0.3)
2-Ph-Benzoic Acid (0.1-0.3)
Dibenzyl phosphate (0.1-0.3)

Pd Source:
$Pd(OAc)_2$
$Pd(RFA)_2$
$Pd(OPiv)_2$
$(MeCN)_2PdCl_2$
$Pd_2(dba)_3$

Ligands (5-10 mol%)
Monodentate phosphines
Bidentate phosphines
Diketocompounds
Substituted pyridines
Phosphites

Figure 1.40. Optimization of synthesis of BMS-919373. Analyzed HTE variables including solvents, substrate, bases, acids, palladium sources and ligands. Optimized reaction conditions on reaction scheme.

HTE can also be used to evaluate the scope and/or robustness of a newly developed reaction. This involves identification of the limits of the reaction with respect to the substrate structures and/or tolerance of functional groups. A representative example is the catalytic C–H functionalization of fused- and bridged- secondary amines with heteroaromatic halides. HTE allowed the synthesis of complex scaffolds and the understanding of substrate scope. This resulted in the successful cross-coupling of twenty-one heteroaryl iodides including thiophenes, indoles, pyridines, benzothiazoles and other nitrogen containing heterocycles. As a result thirty one products were synthesized and isolated. At the same time, they were able to analyze the limits of reactivity and discovered seventeen unsuccessful heteroaryl iodides (Figure 1.41).[128]

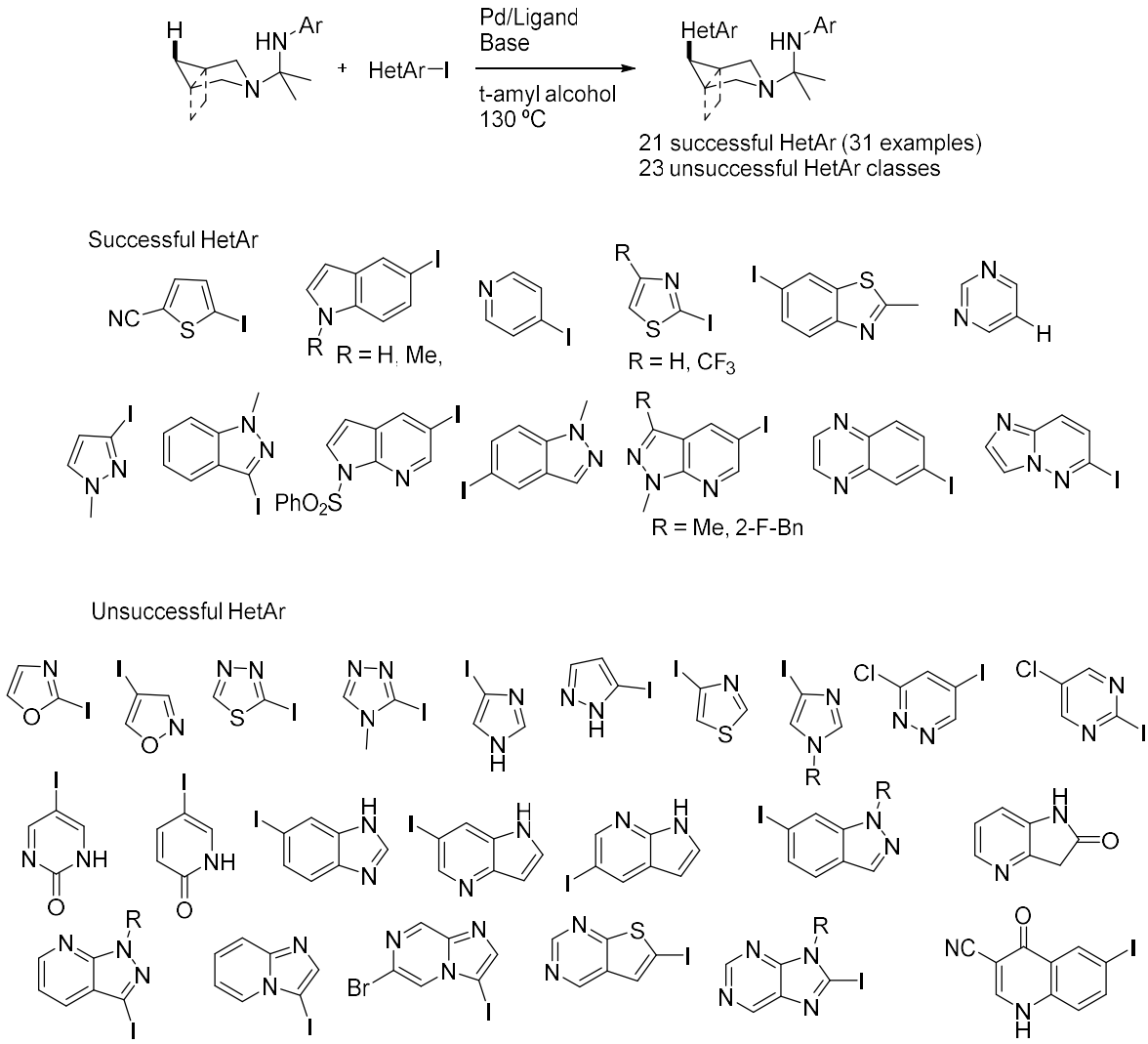

Figure 1.41. HTE driven reaction scope evaluation of cross-coupling reaction of fused- or bridged-secondary amines and diverse heterocycles.

1.5 Thesis Scope and Objectives

Given the versatility and potential of C–H functionalization reactions for the synthesis of pharmaceutical compounds, the development of industrially applicable, robust reaction conditions for a broad scope of substrates is essential. At the same time, understanding the mechanism that guides selective C–H activation is necessary for the development of active catalysts. High-

throughput experimentation allows for a rapid screening of reactivity, optimization of systems, and chemical space mapping. Applying this set of techniques to further develop C–H functionalization reactions would therefore have a positive impact on the possible routes to prepare pharmaceutically relevant molecules (Figure 1.42). This thesis describes the use of all these techniques to develop Pd-catalyzed direct C–H functionalization reactions.

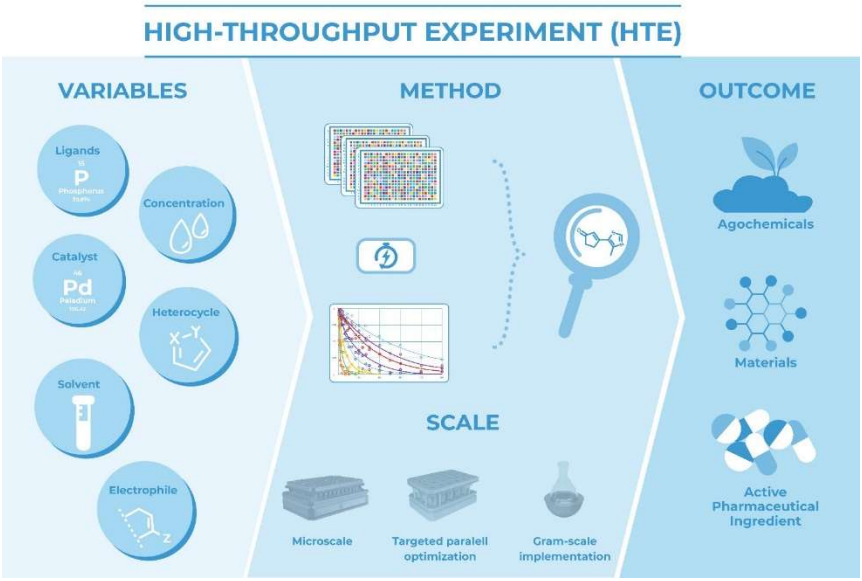

Figure 1.42. Application of HTE to C–H functionalization reactions

Chapter 2 focuses on the development of a reactive system for C–H functionalization of heterocycles. Specifically, it covers the first examples of palladium catalyzed tandem C–O/C–H activation using enol pivalate electrophiles. This specific pool of substrates allowed for the development of homogeneous reaction conditions to yield 30 isolated products. C–O bond activation, although challenging, allowed for the exploration of a new substrate pool and also avoids the need for external carboxylate additives or bases. As a result, *in situ* NMR spectroscopy is viable to observe the formed organometallic intermediates. Finally, several of the isolated

molecules share structural features with bioactive molecules that have been studied for a variety of diseases including retinal degeneration or hypoadiponectinemia.

Mechanistically, examining the oxidative addition of the C–O bond from the enol pivalate substrate brought to the surface a key challenge: reversible C–O oxidative addition that is shifted towards palladium(0) under the reaction conditions. The reversibility of the oxidative addition step translated into limitations in terms of scope, which highlighted the need to develop another catalytic system with the aim of a broadly applicable reaction protocol that can react with a large variety of heterocycle classes.

Chapter 3 focuses on applying HTE to the optimization of C–H functionalization of heterocycles. Including the substrate structure as a variable in HTE reaction optimization enabled discovery of the interrelation between solvent/base and substrate factors. The optimization of nine heterocyclic classes (12 examples in total) led to a small four-condition array (two solvents and two bases) that will allow a rapid assessment of palladium catalyzed direct functionalization using (pseudo)halides. All the heterocycles included in the screening are commonly present in pharmaceutical compounds. Our industrial collaborators, GSK, applied the optimized system to the synthesis of a key intermediate of **GSK3368715**, a type I PRMT inhibitor for advanced-stage solid tumors.[129] The overall catalytic procedure was proven to be industrially scalable. This should enable other research groups both in academia and industry to take advantage of the reported HTE approach for the synthesis of bioactive molecules.

During optimization of direct alkenylation of heterocycles in Chapter 3, selectivity challenges were identified for two heterocycles. Specifically in the case of thiazoles, three products were formed: two regioisomers and a dialkenylated product. Regioselectivity is closely linked to

the structure of the (pre)catalyst. In Chapter 4, a dimeric *tert*-butyl-based palladacycle is described, whose structure allowed for the exploration of the effect of eleven L type ligands (ten phosphines and one nitrogen-based ligand) and two carboxylates on the regioselectivity of direct functionalization of thiazoles. Only the L-type ligands showed a correlation with the number of products formed. At the same time, the electronic features of the heterocycles heavily influence the regioselectivity of the reaction.

During the synthesis of palladacycle precatalysts containing diverse phosphine ligands, I discovered that a commonly used phosphine ligand class, BRIDP ligands, undergo C–H activation reactions and form six membered palladacycles. Chapter 5 discusses investigations on whether the active catalytic species is the palladacycle, and describes palladacycle formation from the mixture of $Pd(OAc)_2$ and phosphine. These palladacycles are also investigated as potential precatalysts for a variety of cross-coupling reactions, including C–H functionalization.

Overall, the research described in this thesis exemplifies the versatility of HTE in academic chemistry research, and the advantages that this experimentation approach imparts in reaction discovery, optimization and chemical space evaluation. The HTE approach also enabled studies of C–H functionalization selectivity when using heterocyclic substrates relevant to the synthesis of pharmaceutical compounds. Finally, mechanistic studies on these C–H functionalization reactions have given information about catalytic intermediates, and allowed the development of new palladacycle precatalysts for diverse cross-coupling reactions.

1.6 References

(1) Dalton, T.; Faber, T.; Glorius, F. C–H Activation: Toward Sustainability and Applications. *ACS Cent Sci* **2021**, *7*, 245–261. https://doi.org/10.1021/acscentsci.0c01413.

(2) Waltz, K.; Hartwig. J. Selective Functionalization of Alkanes by Transition-Metal Boryl Complexes. *Science* **1997**, *277*, 211-213 https://doi.org/10.1126/science.277.5323.211.

(3) Yan, L.; Yao, X.; Zhang, T.; Jiang, F.; Shui, Y.; Xie, H.; Xiang, Z.; Li, Y.; Lin, L. Passivation Effect of the Chlorinated Paraffin Added in the Cutting Fluid on the Surface Corrosion Resistance of the Stainless Steel. *Molecules* **2023**, *28*, 3648. https://doi.org/10.3390/molecules28093648.

(4) Newhouse, T.; Baran, P. S. If C–H Bonds Could Talk – Selective C–H Bond Oxidation. *Angew Chem Int Ed Engl* **2011**, *50* (15), 3362–3374. https://doi.org/10.1002/anie.201006368.

(5) Yamazaki, M. Industrialization and Application Development of Cyclo-Olefin Polymer. *Journal of Molecular Catalysis A: Chemical* **2004**, *213*, 81–87. https://doi.org/10.1016/j.molcata.2003.10.058.

(6) Dick, A. R.; Sanford, M. S. Transition Metal Catalyzed Oxidative Functionalization of Carbon–Hydrogen Bonds. *Tetrahedron* **2006**, *62*, 2439–2463. https://doi.org/10.1016/j.tet.2005.11.027.

(7) Pauling, L. *The Nature of the Chemical Bond and the Structure of Molecules and Crystals: An Introduction to Modern Structural Chemistry*; Cornell University Press, 1960.

(8) Yao, X.-Q.; Hou, X.-J.; Jiao, H.; Xiang, H.-W.; Li, Y.-W. Accurate Calculations of Bond Dissociation Enthalpies with Density Functional Methods. *J. Phys. Chem. A* **2003**, *107*, 9991–9996. https://doi.org/10.1021/jp0361125.

(9) Altus, K. M.; Love, J. A. The Continuum of Carbon–Hydrogen (C–H) Activation Mechanisms and Terminology. *Commun Chem* **2021**, *4*, 1–11. https://doi.org/10.1038/s42004-021-00611-1.

(10) Engle, K. M.; Mei, T.-S.; Wasa, M.; Yu, J.-Q. Weak Coordination as a Powerful Means for Developing Broadly Useful C–H Functionalization Reactions. *Acc. Chem. Res.* **2012**, *45*, 788–802. https://doi.org/10.1021/ar200185g.

(11) Gunsalus, N. J.; Koppaka, A.; Park, S. H.; Bischof, S. M.; Hashiguchi, B. G.; Periana, R. A. Homogeneous Functionalization of Methane. *Chem. Rev.* **2017**, *117*, 8521–8573. https://doi.org/10.1021/acs.chemrev.6b00739.

(12) Taylor, A. P.; Robinson, R. P.; Fobian, Y. M.; Blakemore, D. C.; Jones, L. H.; Fadeyi, O. Modern Advances in Heterocyclic Chemistry in Drug Discovery. *Org. Biomol. Chem.* **2016**, *14*, 6611–6637. https://doi.org/10.1039/C6OB00936K.

(13) Zhang, L.; Ritter, T. A Perspective on Late-Stage Aromatic C–H Bond Functionalization. *J. Am. Chem. Soc.* **2022**, *144*, 2399–2414. https://doi.org/10.1021/jacs.1c10783.

(14) Shah, T. A.; Sarkar, T.; Kar, S.; Maharana, P. K.; Talukdar, K.; Punniyamurthy, T. Transition-Metal-Catalyzed Directed C−H Functionalization in/on Water. *Chemistry – An Asian Journal* **2024**, *19*, e202300815. https://doi.org/10.1002/asia.202300815.

(15) Arndtsen, B. A.; Bergman, R. G.; Mobley, T. A.; Peterson, T. H. Selective Intermolecular Carbon-Hydrogen Bond Activation by Synthetic Metal Complexes in Homogeneous Solution. *Acc. Chem. Res.* **1995**, *28*, 154–162. https://doi.org/10.1021/ar00051a009.

(16) Janowicz, A. H.; Bergman, R. G. Carbon-Hydrogen Activation in Completely Saturated Hydrocarbons: Direct Observation of M^+ R-H .Fwdarw. M(R)(H). *J. Am. Chem. Soc.* **1982**, *104*, 352–354. https://doi.org/10.1021/ja00365a091.
(17) Trost, B. M. Atom Economy—A Challenge for Organic Synthesis: Homogeneous Catalysis Leads the Way. *Angew. Chem. Int. Ed.* **1995**, *34*, 259–281. https://doi.org/10.1002/anie.199502591.
(18) de Jesus, R.; Hiesinger, K.; van Gemmeren, M. Preparative Scale Applications of C−H Activation in Medicinal Chemistry. *Angew. Chem. Int. Ed.***2023**, *62*, e202306659. https://doi.org/10.1002/anie.202306659.
(19) Shim, S. Y. Late-Stage C−H Activation of Drug (Derivative) Molecules with Pd(Ll) Catalysis. *Chem. Eur. J.***2023**, *29*, e202302620. https://doi.org/10.1002/chem.202302620.
(20) Rogge, T.; Kaplaneris, N.; Chatani, N.; Kim, J.; Chang, S.; Punji, B.; Schafer, L. L.; Musaev, D. G.; Wencel-Delord, J.; Roberts, C. A.; Sarpong, R.; Wilson, Z. E.; Brimble, M. A.; Johansson, M. J.; Ackermann, L. C–H Activation. *Nat. Rev. Methods Primers* **2021**, *1*, 43. https://doi.org/10.1038/s43586-021-00041-2.
(21) Zhang, Y.; Szostak, M. Synthesis of Natural Products by C−H Functionalization of Heterocycless. *Chem. Eur. J.* **2022**, *28*, e202104278. https://doi.org/10.1002/chem.202104278.
(22) Yamaguchi, J.; Yamaguchi, A. D.; Itami, K. C−H Bond Functionalization: Emerging Synthetic Tools for Natural Products and Pharmaceuticals. *Angew. Chem. Int. Ed.***2012**, *51*, 8960–9009. https://doi.org/10.1002/anie.201201666.
(23) Guillemard, L.; Kaplaneris, N.; Ackermann, L.; Johansson, M. J. Late-Stage C–H Functionalization Offers New Opportunities in Drug Discovery. *Nat. Rev. Chem.* **2021**, *5*, 522–545. https://doi.org/10.1038/s41570-021-00300-6.
(24) Gasco, A.; Boulton, A. J. Furazans and Furazan Oxides. Part IV. The Structures and Tautomerism of Some Unsymmetrically Substituted Furoxans. *J.C.S. Perkin II*, **1973**. 1613-1617. https://doi.org/10.1039/P29730001613
(25) Caron, S.; Dugger, R. W.; Ruggeri, S. G.; Ragan, J. A.; Ripin, D. H. B. Large-Scale Oxidations in the Pharmaceutical Industry. *Chem. Rev.* **2006**, *106*, 2943–2989. https://doi.org/10.1021/cr040679f.
(26) Stuk, T. L.; Assink, B. K.; Bates, Ronald C.; Erdman, D. T.; Fedij, V.; Jennings, S. M.; Lassig, J. A.; Smith, R. J.; Smith, T. L. An Efficient and Cost-Effective Synthesis of Pagoclone. *Org. Process Res. Dev.* **2003**, *7*, 851–855. https://doi.org/10.1021/op034060b.
(27) Barnett, C. J.; Wilson, T. M.; Kobierski, M. E. A Practical Synthesis of Multitargeted Antifolate LY231514. *Org. Process Res. Dev.* **1999**, *3*, 184–188. https://doi.org/10.1021/op9802172.
(28) Duquette, J.; Zhang, M.; Zhu, L.; Reeves, R. S. A Scalable Asymmetric Synthesis of (R)-2-Amino-1-(3-Pyridinyl)Ethanol Dihydrochloride via an Oxazaborolidine Catalyzed Borane Reduction. *Org. Process Res. Dev.* **2003**, *7*, 285–288. https://doi.org/10.1021/op0340208.
(29) Watson, D. J.; Dowdy, E. D.; DePue, J. S.; Kotnis, A. S.; Leung, S.; O'Reilly, B. C. Development of a Safe and Scalable Oxidation Process for the Preparation of 6-Hydroxybuspirone: Application of In-Line Monitoring for Process Ruggedness and Product Quality. *Org. Process Res. Dev.* **2004**, *8*, 616–623. https://doi.org/10.1021/op049918r.

(30) Ohta, T.; Zhang, H.; Torihara, Y.; Furukawa, I. Improved Synthetic Route to Dexamethasone Acetate from Tigogenin. *Org. Process Res. Dev.* **1997**, *1*, 420–424. https://doi.org/10.1021/op9700338.
(31) Kelly, R. J. Review of Safety Guidelines for Peroxidizable Organic Chemicals. *Chem. Health Saf.* **1996**, *3*, 28–36. https://doi.org/10.1021/acs.chas.8b03515.
(32) Bodurow, C. C.; Boyer, B. D.; Brennan, J.; Bunnell, C. A.; Burks, J. E.; Carr, M. A.; Doecke, C. W.; Eckrich, T. M.; Fisher, J. W.; Gardner, J. P.; Graves, B. J.; Hines, P.; Hoying, R. C.; Jackson, B. G.; Kinnick, M. D.; Kochert, C. D.; Lewis, J. S.; Luke, W. D.; Moore, L. L.; Morin, J. M.; Nist, R. L.; Prather, D. E.; Sparks, D. L.; Vladuchick, W. C. An Enantioselective Synthesis of Loracarbef (LY163892/KT3777). *Tetrahedron Lett.* **1989**, *30*, 2321–2324. https://doi.org/10.1016/S0040-4039(01)80388-9.
(33) Salzmann, T. N.; Ratcliffe, R. W.; Christensen, B. G.; Bouffard, F. A. A Stereocontrolled Synthesis of (+)-Thienamycin. *J. Am. Chem. Soc.* **1980**, *102*, 6161–6163. https://doi.org/10.1021/ja00539a040.
(34) am Ende, D. J.; Brown Ripin, D. H.; Weston, N. P. Thermal Stability Investigation of Pyridine Substituted Tosyl Oximes. *Thermochimica Acta.* **2004**, *419*, 83–88. https://doi.org/10.1016/j.tca.2004.01.032.
(35) Field, M. J.; Sinha, S.; Warren, J. J. Photochemical Proton-Coupled C−H Activation: An Example Using Aliphatic Fluorination. *Phys. Chem. Chem. Phys.* **2016**, *18*, 30907–30911. https://doi.org/10.1039/C6CP06418C.
(36) Bloom, S.; Knippel, J. L.; Lectka, T. A Photocatalyzed Aliphatic Fluorination. *Chem. Sci.* **2014**, *5*, 1175–1178. https://doi.org/10.1039/C3SC53261E.
(37) Kee, C. W.; Chin, K. F.; Wong, M. W.; Tan, C.-H. Selective Fluorination of Alkyl C–H Bonds via Photocatalysis. *Chem. Commun.* **2014**, *50*, 8211–8214. https://doi.org/10.1039/C4CC01848F.
(38) Xia, J.-B.; Zhu, C.; Chen, C. Visible Light-Promoted Metal-Free Sp^3-C−H Fluorination. *Chem. Commun.* **2014**, *50*, 11701–11704. https://doi.org/10.1039/C4CC05650G.
(39) Warren, J. J.; Tronic, T. A.; Mayer, J. M. Thermochemistry of Proton-Coupled Electron Transfer Reagents and Its Implications. *Chem. Rev.* **2010**, *110*, 6961–7001. https://doi.org/10.1021/cr100085k.
(40) Capaldo, L.; Ravelli, D. Hydrogen Atom Transfer (HAT): A Versatile Strategy for Substrate Activation in Photocatalyzed Organic Synthesis. *Eur. J. Org. Chem.***2017**, *2017* (15), 2056–2071. https://doi.org/10.1002/ejoc.201601485.
(41) Protti, S.; Fagnoni, M.; Ravelli, D. Photocatalytic CH Activation by Hydrogen-Atom Transfer in Synthesis. *ChemCatChem.* **2015**, *7*, 1516–1523. https://doi.org/10.1002/cctc.201500125.
(42) Capaldo, L.; Quadri, L. L.; Ravelli, D. Photocatalytic Hydrogen Atom Transfer: The Philosopher's Stone for Late-Stage Functionalization? *Green Chem.* **2020**, *22*, 3376–3396. https://doi.org/10.1039/D0GC01035A.
(43) Doyle, M. P.; Forbes, D. C. Recent Advances in Asymmetric Catalytic Metal Carbene Transformations. *Chem. Rev.* **1998**, *98*, 911–936. https://doi.org/10.1021/cr940066a.
(44) Davies, H. M. L.; Morton, D. Guiding Principles for Site Selective and Stereoselective Intermolecular C–H Functionalization by Donor/Acceptor Rhodium Carbenes. *Chem. Soc. Rev.* **2011**, *40* (4), 1857–1869. https://doi.org/10.1039/C0CS00217H.

(45) Davies, H. M. L.; Beckwith, R. E. J. Catalytic Enantioselective C−H Activation by Means of Metal−Carbenoid-Induced C−H Insertion. *Chem. Rev.* **2003**, *103*, 2861–2904. https://doi.org/10.1021/cr0200217.
(46) Xia, Y.; Qiu, D.; Wang, J. Transition-Metal-Catalyzed Cross-Couplings through Carbene Migratory Insertion. *Chem. Rev.* **2017**, *117*, 13810–13889. https://doi.org/10.1021/acs.chemrev.7b00382.
(47) Estevan, F.; Herbst, K.; Lahuerta, P.; Barberis, M.; Pérez-Prieto, J. Chiral Dirhodium(II) Catalysts with Orthometalated Aryl Phosphine Ligands: Synthesis and Application for Enantioselective C−H Insertion of α-Diazo Ketones. *Organometallics* **2001**, *20*, 950–957. https://doi.org/10.1021/om0010060.
(48) Doyle, M. P.; McKervey, M. A. Recent Advances in Stereoselective Synthesis Involvingdiazocarbonyl Intermediates. *Chem. Commun.* **1997**, 11, 983–990. https://doi.org/10.1039/A604927C.
(49) Davies, H. M. L.; Matasi, J. J.; Ahmed, G. Divergent Pathways in the Intramolecular Reactions between Rhodium-Stabilized Vinylcarbenoids and Pyrroles: Construction of Fused Tropanes and 7-Azabicyclo[4.2.0]Octadienes. *J. Org. Chem.* **1996**, *61*, 2305–2313. https://doi.org/10.1021/jo952127q.
(50) Davies, H. Catalytic Asymmetric C—H Activation of Sp3-Hybridized C—H Bonds by Means of Carbenoid C—H Insertions: Applications in Organic Synthesis. *J. Mol. Catal. A Chem.* **2002**, *189*, 125–135. https://doi.org/10.1016/S1381-1169(02)00201-7.
(51) Taber, D. F.; Ruckle, R. E. Cyclopentane Construction by Dirhodium Tetraacetate-Mediated Intramolecular C–H Insertion: Steric and Electronic Effects. *J. Am. Chem. Soc.* **1986**, *108* (24), 7686–7693. https://doi.org/10.1021/ja00284a037.
(52) Wang, P.; Adams, J. Model Studies of the Stereoelectronic Effect in Rh(II) Mediated Carbenoid C–H Insertion Reactions. *J. Am. Chem. Soc.* **1994**, *116*, 3296–3305. https://doi.org/10.1021/ja00087a016.
(53) García-Cárceles, J.; Bahou, K. A.; Bower, J. F. Recent Methodologies That Exploit Oxidative Addition of C–N Bonds to Transition Metals. *ACS Catal.* **2020**, *10*, 12738–12759. https://doi.org/10.1021/acscatal.0c03341.
(54) Perutz, R. N.; Sabo-Etienne, S. The σ-CAM Mechanism: σ Complexes as the Basis of σ-Bond Metathesis at Late-Transition-Metal Centers. *Angew. Chem. Int. Ed.***2007**, *46*, 2578–2592. https://doi.org/10.1002/anie.200603224.
(55) Young, R. D. Characterisation of Alkane σ-Complexes. *Chem. Eur. J.***2014**, *20*, 12704–12718. https://doi.org/10.1002/chem.201403485.
(56) Bernskoetter, W. H.; Schauer, C. K.; Goldberg, K. I.; Brookhart, M. Characterization of a Rhodium(I) σ-Methane Complex in Solution. *Science.* **2009**, *326*, 553–556. https://doi.org/10.1126/science.1177485.
(57) Brookhart, M.; Green, M. L. H. Carbon−hydrogen-Transition Metal Bonds. *J. Organomet. Chem.* **1983**, *250*, 395–408. https://doi.org/10.1016/0022-328X(83)85065-7.
(58) Knighton, R. C.; Emerson-King, J.; Rourke, J. P.; Ohlin, C. A.; Chaplin, A. B. Solution, Solid-State, and Computational Analysis of Agostic Interactions in a Coherent Set of Low-Coordinate Rhodium(III) and Iridium(III) Complexes. *Chem. Eur. J.* **2018**, *24*, 4927–4938. https://doi.org/10.1002/chem.201705990.
(59) Dawoodi, Z. Evidence for a Direct Bonding Interaction between Titanium and a β-C–H Moiety in a Titanium-Ethyl Compound; X-Ray Crystal Structure of

[Ti(Me,PCH,CH,PMe,)EtCI,]. *J. Chem. Soc., Chem. Commun.* **1982**, *14*, 802-803. https://doi.org/10.1039/C39820000802.
(60) Chadwick, F. M.; Krämer, T.; Gutmann, T.; Rees, N. H.; Thompson, A. L.; Edwards, A. J.; Buntkowsky, G.; Macgregor, S. A.; Weller, A. S. Selective C–H Activation at a Molecular Rhodium Sigma-Alkane Complex by Solid/Gas Single-Crystal to Single-Crystal H/D Exchange. *J. Am. Chem. Soc.* **2016**, *138*, 13369–13378. https://doi.org/10.1021/jacs.6b07968.
(61) Lein, M. Characterization of Agostic Interactions in Theory and Computation. *Coordination Chemistry Reviews* **2009**, *253* (5), 625–634. https://doi.org/10.1016/j.ccr.2008.07.007.
(62) Brookhart, M.; Green, M. L. H.; Parkin, G. Agostic Interactions in Transition Metal Compounds. *Proc. Natl. Acad. Sci. USA.* **2007**, *104*, 6908–6914. https://doi.org/10.1073/pnas.0610747104.
(63) Labinger, J. A.; Bercaw, J. E. Understanding and Exploiting C–H Bond Activation. *Nature* **2002**, *417* (6888), 507–514. https://doi.org/10.1038/417507a.
(64) Waterman, R. σ-Bond Metathesis: A 30-Year Retrospective. *Organometallics* **2013**, *32*, 7249–7263. https://doi.org/10.1021/om400760k.
(65) Watson, P. L. Methane Exchange Reactions of Lanthanide and Early-Transition-Metal Methyl Complexes. *J. Am. Chem. Soc.* **1983**, *105*, 6491–6493. https://doi.org/10.1021/ja00359a023.
(66) Thompson, M. E.; Baxter, S. M.; Bulls, A. R.; Burger, B. J.; Nolan, M. C.; Santarsiero, B. D.; Schaefer, W. P.; Bercaw, J. E. ..Sigma.-Bond Metathesis for Carbon-Hydrogen Bonds of Hydrocarbons and Sc-R (R = H, Alkyl, Aryl) Bonds of Permethylscandocene Derivatives. Evidence for Noninvolvement of the .Pi. System in Electrophilic Activation of Aromatic and Vinylic C–H Bonds. *J. Am. Chem. Soc.* **1987**, *109*, 203–219. https://doi.org/10.1021/ja00235a031.
(67) Perrin, L.; Maron, L.; Eisenstein, O. A DFT Study of SiH_4 Activation by Cp_2LnH. *Inorg. Chem.* **2002**, *41*, 4355–4362. https://doi.org/10.1021/ic011275y.
(68) Maron, L.; Eisenstein, O. DFT Study of H−H Activation by Cp_2 LnH d^0 Complexes. *J. Am. Chem. Soc.* **2001**, *123*, 1036–1039. https://doi.org/10.1021/ja0033483.
(69) Balcells, D.; Clot, E.; Eisenstein, O. C—H Bond Activation in Transition Metal Species from a Computational Perspective. *Chem. Rev.* **2010**, *110*, 749–823. https://doi.org/10.1021/cr900315k.
(70) Jordan, R. F.; Taylor, D. F. Zirconium-Catalyzed Coupling of Propene and .Alpha.-Picoline. *J. Am. Chem. Soc.* **1989**, *111*, 778–779. https://doi.org/10.1021/ja00184a081.
(71) Heeres, H. J.; Teuben, J. H. Catalytic Oligomerization of Terminal Alkynes by Lanthanide Carbyls $(\eta^5\text{-}C_5Me_5)_2LnCH(SiMe_3)_2$ (Ln = Y, La, Ce). *Organometallics* **1991**, *10*, 1980–1986. https://doi.org/10.1021/om00052a052.
(72) Puschmann, F. F.; Grützmacher, H.; Bruin, B. de. Rhodium(0) Metalloradicals in Binuclear C−H Activation. *J. Am. Chem. Soc.* **2010**, *132* (1), 73–75. https://doi.org/10.1021/ja909022p.
(73) Lu, H.; Jiang, H.; Wojtas, L.; Zhang, X. P. Selective Intramolecular C−H Amination through the Metalloradical Activation of Azides: Synthesis of 1,3-Diamines under Neutral and Nonoxidative Conditions. *Angew. Chem. Int. Ed.* **2010**, *49*, 10192–10196. https://doi.org/10.1002/anie.201005552.
(74) Cui, W.; Li, S.; Wayland, B. B. Factors Contributing to One-Electron Metalloradical Activation of Ethene and Carbon Monoxide Illustrated by Reactions of Co(II), Rh(II), and

Ir(II) Porphyrins. *J. Organomet. Chem.* **2007**, *692*, 3198–3206. https://doi.org/10.1016/j.jorganchem.2007.01.018.
(75) Wayland, B. B.; Ba, S.; Sherry, A. E. Activation of Methane and Toluene by Rhodium(II) Porphyrin Complexes. *J. Am. Chem. Soc.* **1991**, *113*, 5305–5311. https://doi.org/10.1021/ja00014a025.
(76) Sherry, A. E.; Wayland, B. B. Metalloradical Activation of Methane. *J. Am. Chem. Soc.* **1990**, *112*, 1259–1261. https://doi.org/10.1021/ja00159a064.
(77) Thompson, S. J.; Brennan, M. R.; Lee, S. Y.; Dong, G. Synthesis and Applications of Rhodium Porphyrin Complexes. *Chem. Soc. Rev.* **2018**, *47*, 929–981. https://doi.org/10.1039/C7CS00582B.
(78) Lee, W.-C. C.; Zhang, X. P. Metalloradical Catalysis: General Approach for Controlling Reactivity and Selectivity of Homolytic Radical Reactions. *Angew. Chem. Int. Ed.***2024**, *63*, e202320243. https://doi.org/10.1002/anie.202320243.
(79) Wolczanski, P. T. Activation of Carbon–Hydrogen Bonds via 1,2-RH-Addition/-Elimination to Early Transition Metal Imides. *Organometallics* **2018**, *37*, 505–516. https://doi.org/10.1021/acs.organomet.7b00753.
(80) Cummins, C. C.; Baxter, S. M.; Wolczanski, P. T. Methane and Benzene Activation via Transient (Tert-Bu3SiNH)2Zr:NSi-Tert-Bu3. *J. Am. Chem. Soc.* **1988**, *110*, 8731–8733. https://doi.org/10.1021/ja00234a044.
(81) Bailey, B. C.; Fan, H.; Huffman, J. C.; Baik, M.-H.; Mindiola, D. J. Intermolecular C−H Bond Activation Reactions Promoted by Transient Titanium Alkylidynes. Synthesis, Reactivity, Kinetic, and Theoretical Studies of the Ti⋮C Linkage. *J. Am. Chem. Soc.* **2007**, *129*, 8781–8793. https://doi.org/10.1021/ja070989q.
(82) Labinger, J. A. Tutorial on Oxidative Addition. *Organometallics* **2015**, *34*, 4784–4795. https://doi.org/10.1021/acs.organomet.5b00565.
(83) Kundu, S.; Choliy, Y.; Zhuo, G.; Ahuja, R.; Emge, T. J.; Warmuth, R.; Brookhart, M.; Krogh-Jespersen, K.; Goldman, A. S. Rational Design and Synthesis of Highly Active Pincer-Iridium Catalysts for Alkane Dehydrogenation. *Organometallics* **2009**, *28*, 5432–5444. https://doi.org/10.1021/om900568f.
(84) Findlater, M.; Schultz, K. M.; Bernskoetter, W. H.; Cartwright-Sykes, A.; Heinekey, D. M.; Brookhart, M. Dihydrogen Complexes of Iridium and Rhodium. *Inorg. Chem.* **2012**, *51*, 4672–4678. https://doi.org/10.1021/ic202630x.
(85) van der Boom, M. E.; Milstein, D. Cyclometalated Phosphine-Based Pincer Complexes: Mechanistic Insight in Catalysis, Coordination, and Bond Activation. *Chem. Rev.* **2003**, *103*, 1759–1792. https://doi.org/10.1021/cr960118r.
(86) Gunanathan, C.; Milstein, D. Bond Activation and Catalysis by Ruthenium Pincer Complexes. *Chem. Rev.* **2014**, *114*, 12024–12087. https://doi.org/10.1021/cr5002782.
(87) Liu, F.; Pak, E. B.; Singh, B.; Jensen, C. M.; Goldman, A. S. Dehydrogenation of N-Alkanes Catalyzed by Iridium "Pincer" Complexes: Regioselective Formation of α-Olefins. *J. Am. Chem. Soc.* **1999**, *121*, 4086–4087. https://doi.org/10.1021/ja983460p.
(88) Choi, J.; MacArthur, A. H. R.; Brookhart, M.; Goldman, A. S. Dehydrogenation and Related Reactions Catalyzed by Iridium Pincer Complexes. *Chem. Rev.* **2011**, *111*, 1761–1779. https://doi.org/10.1021/cr1003503.

(89) Larsen, M. A.; Hartwig, J. F. Iridium-Catalyzed C–H Borylation of Heteroarenes: Scope, Regioselectivity, Application to Late-Stage Functionalization, and Mechanism. *J. Am. Chem. Soc.* **2014**, *136*, 4287–4299. https://doi.org/10.1021/ja412563e.
(90) Rybtchinski, B.; Vigalok, A.; Ben-David, Y.; Milstein, D. A Room Temperature Direct Metal Insertion into a Nonstrained Carbon−Carbon Bond in Solution. C−C vs C−H Bond Activation. *J. Am. Chem. Soc.* **1996**, *118*, 12406–12415. https://doi.org/10.1021/ja962253r.
(91) Gandelman, M.; Vigalok, A.; Konstantinovski, L.; Milstein, D. The First Observation and Kinetic Evaluation of a Single Step Metal Insertion into a C−C Bond. *J. Am. Chem. Soc.* **2000**, *122*, 9848–9849. https://doi.org/10.1021/ja993108r.
(92) Rybtchinski, B.; Oevers, S.; Montag, M.; Vigalok, A.; Rozenberg, H.; Martin, J. M. L.; Milstein, D. Comparison of Steric and Electronic Requirements for C−C and C−H Bond Activation. Chelating vs Nonchelating Case. *J. Am. Chem. Soc.* **2001**, *123*, 9064–9077. https://doi.org/10.1021/ja016126t.
(93) Stahl, S. S.; Labinger, J. A.; Bercaw, J. E. Homogeneous Oxidation of Alkanes by Electrophilic Late Transition Metals. *Angew. Chem. Int. Ed.***1998**, *37*, 2180–2192. https://doi.org/10.1002/(SICI)1521-3773(19980904)37:16<2180::AID-ANIE2180>3.0.CO;2-A.
(94) Oxgaard, J.; Tenn, W. J.; Nielsen, R. J.; Periana, R. A.; Goddard, W. A. Mechanistic Analysis of Iridium Heteroatom C−H Activation: Evidence for an Internal Electrophilic Substitution Mechanism. *Organometallics* **2007**, *26*, 1565–1567. https://doi.org/10.1021/om061189b.
(95) Munz, D.; Meyer, D.; Strassner, T. Methane CH Activation by Palladium Complexes with Chelating Bis(NHC) Ligands: A DFT Study. *Organometallics* **2013**, *32*, 3469–3480. https://doi.org/10.1021/om400232u.
(96) Boutadla, Y.; Davies, D. L.; Macgregor, S. A.; Poblador-Bahamonde, A. I. Mechanisms of C–H Bond Activation: Rich Synergy between Computation and Experiment. *Dalton Trans.* **2009**, *30*, 5820-5831. https://doi.org/10.1039/b904967c.
(97) Gorelsky, S. I.; Lapointe, D.; Fagnou, K. Analysis of the Palladium-Catalyzed (Aromatic)C–H Bond Metalation–Deprotonation Mechanism Spanning the Entire Spectrum of Arenes. *J. Org. Chem.* **2012**, *77*, 658–668. https://doi.org/10.1021/jo202342q.
(98) Liu, Y.; Wang, K.; Ling, B.; Chen, G.; Li, Y.; Liu, L.; Bi, S. Theoretical Elucidation of the Multi-Functional Synthetic Methodology for Switchable Ni(0)-Catalyzed C–H Allylations, Alkenylations and Dienylations with Allenes. *Catal. Sci. Technol.* **2020**, *10*, 4219–4228. https://doi.org/10.1039/D0CY00965B.
(99) Guihaumé, J.; Halbert, S.; Eisenstein, O.; Perutz, R. N. Hydrofluoroarylation of Alkynes with Ni Catalysts. C–H Activation via Ligand-to-Ligand Hydrogen Transfer, an Alternative to Oxidative Addition. *Organometallics* **2012**, *31*, 1300–1314. https://doi.org/10.1021/om2005673.
(100) Gorelsky, S. I. Reactivity and Regioselectivity of Palladium-Catalyzed Direct Arylation in Noncooperative and Cooperative Processes. *Organometallics* **2012**, *31*, 4631–4634. https://doi.org/10.1021/om300230b.
(101) Tan, Y.; Barrios-Landeros, F.; Hartwig, J. F. Mechanistic Studies on Direct Arylation of Pyridine N-Oxide: Evidence for Cooperative Catalysis between Two Distinct Palladium Centers. *J. Am. Chem. Soc.* **2012**, *134*, 3683–3686. https://doi.org/10.1021/ja2122156.

(102) Lapointe, D.; Fagnou, K. Overview of the Mechanistic Work on the Concerted Metallation–Deprotonation Pathway. *Chem. Lett.* **2010**, *39*, 1118–1126. https://doi.org/10.1246/cl.2010.1118.
(103) Zeist, W.-J. van; Bickelhaupt, F. M. The Activation Strain Model of Chemical Reactivity. *Org. Biomol. Chem.* **2010**, *8*, 3118–3127. https://doi.org/10.1039/B926828F.
(104) Ess, D. H.; Houk, K. N. Distortion/Interaction Energy Control of 1,3-Dipolar Cycloaddition Reactivity. *J. Am. Chem. Soc.* **2007**, *129*, 10646–10647. https://doi.org/10.1021/ja0734086.
(105) Gorelsky, S. I.; Ghosh, S.; Solomon, E. I. Mechanism of N2O Reduction by the M4-S Tetranuclear CuZ Cluster of Nitrous Oxide Reductase. *J. Am. Chem. Soc.* **2006**, *128*, 278–290. https://doi.org/10.1021/ja055856o.
(106) Gorelsky, S. I. Tuning the Regioselectivity of Palladium-Catalyzed Direct Arylation of Azoles by Metal Coordination. *Organometallics* **2012**, *31*, 794–797. https://doi.org/10.1021/om2012612.
(107) Gorelsky, S. I. Origins of Regioselectivity of the Palladium-Catalyzed (Aromatic)CH Bond Metalation–Deprotonation. *Coordination Chemistry Reviews* **2013**, *257*, 153–164. https://doi.org/10.1016/j.ccr.2012.06.016.
(108) Wang, L.; Carrow, B. P. Oligothiophene Synthesis by a General C–H Activation Mechanism: Electrophilic Concerted Metalation–Deprotonation (eCMD). *ACS Catal.* **2019**, *9*, 6821–6836. https://doi.org/10.1021/acscatal.9b01195.
(109) Petit, A.; Flygare, J.; Miller, A. T.; Winkel, G.; Ess, D. H. Transition-State Metal Aryl Bond Stability Determines Regioselectivity in Palladium Acetate Mediated C–H Bond Activation of Heteroarenes. *Org. Lett.* **2012**, *14*, 3680–3683. https://doi.org/10.1021/ol301521n.
(110) Carrow, B. P.; Sampson, J.; Wang, L. Base-Assisted C−H Bond Cleavage in Cross-Coupling: Recent Insights into Mechanism, Speciation, and Cooperativity. *Isr. J. Chem.* **2020**, *60*, 230–258. https://doi.org/10.1002/ijch.201900095.
(111)Taylor, C. J.; Pomberger, A.; Felton, K. C.; Grainger, R.; Barecka, M.; Chamberlain, T. W.; Bourne, R. A.; Johnson, C. N.; Lapkin, A. A. A Brief Introduction to Chemical Reaction Optimization. *Chem. Rev.* **2023**, *123*, 3089–3126. https://doi.org/10.1021/acs.chemrev.2c00798.
(112) Shields, B.J., Stevens, J., Li, J. *et al.* Bayesian reaction optimization as a tool for chemical synthesis. *Nature,* **2021**, *590*, 89–96. https://doi.org/10.1038/s41586-021-03213-y
(113) Zeng, W.; Guo, L.; Xu, S.; Chen, J.; Zhou, J. High-Throughput Screening Technology in Industrial Biotechnology. *Trends Biotechnol* **2020**, *38*, 888–906. https://doi.org/10.1016/j.tibtech.2020.01.001.
(114) Pereira, D. A.; Williams, J. A. Origin and Evolution of High Throughput Screening. *Br. J. Pharmacol.* **2007**, *152*, 53–61. https://doi.org/10.1038/sj.bjp.0707373.
(115) Leitch, D. C.; Becica, J. 13.12 - High-Throughput Experimentation in Organometallic Chemistry and Catalysis. In *Comprehensive Organometallic Chemistry IV*; Parkin, G., Meyer, K., O'hare, D., Eds.; Elsevier: Oxford, 2022; pp 502–555. https://doi.org/10.1016/B978-0-12-820206-7.00111-6.
(116) McClure, K. F.; Piotrowski, D. W.; Petersen, D.; Wei, L.; Xiao, J.; Londregan, A. T.; Kamlet, A. S.; Dechert-Schmitt, A.-M.; Raymer, B.; Ruggeri, R. B.; Canterbury, D.; Limberakis, C.; Liras, S.; DaSilva-Jardine, P.; Dullea, R. G.; Loria, P. M.; Reidich, B.; Salatto, C. T.; Eng, H.; Kimoto, E.; Atkinson, K.; King-Ahmad, A.; Scott, D.; Beaumont, K.; Chabot,

J. R.; Bolt, M. W.; Maresca, K.; Dahl, K.; Arakawa, R.; Takano, A.; Halldin, C. Liver-Targeted Small-Molecule Inhibitors of Proprotein Convertase Subtilisin/Kexin Type 9 Synthesis. *Angew. Chem. Int. Ed.* **2017**, *56*, 16218–16222. https://doi.org/10.1002/anie.201708744.

(117) Twilton, J.; Christensen, M.; DiRocco, D. A.; Ruck, R. T.; Davies, I. W.; MacMillan, D. W. C. Selective Hydrogen Atom Abstraction through Induced Bond Polarization: Direct α-Arylation of Alcohols through Photoredox, HAT, and Nickel Catalysis. *Angew. Chem. Int. Ed.* **2018**, *57*, 5369–5373. https://doi.org/10.1002/anie.201800749.

(118) Welch, C. J. High Throughput Analysis Enables High Throughput Experimentation in Pharmaceutical Process Research. *React. Chem. Eng.* **2019**, *4*, 1895–1911. https://doi.org/10.1039/C9RE00234K.

(119) Glish, G. L.; Vachet, R. W. The Basics of Mass Spectrometry in the Twenty-First Century. *Nat Rev Drug Discov* **2003**, *2*, 140–150. https://doi.org/10.1038/nrd1011.

(120) Allen, C. L.; Leitch, D. C.; Anson, M. S.; Zajac, M. A. The Power and Accessibility of High-Throughput Methods for Catalysis Research. *Nat. Catal.* **2019**, *2*, 2–4. https://doi.org/10.1038/s41929-018-0220-4.

(121) Schultz, D.; Campeau, L.-C. Harder, Better, Faster. *Nat. Chem.* **2020**, *12*, 661–664. https://doi.org/10.1038/s41557-020-0510-8.

(122) Mennen, S. M.; Alhambra, C.; Allen, C. L.; Barberis, M.; Berritt, S.; Brandt, T. A.; Campbell, A. D.; Castañón, J.; Cherney, A. H.; Christensen, M.; Damon, D. B.; Eugenio de Diego, J.; García-Cerrada, S.; García-Losada, P.; Haro, R.; Janey, J.; Leitch, D. C.; Li, L.; Liu, F.; Lobben, P. C.; MacMillan, D. W. C.; Magano, J.; McInturff, E.; Monfette, S.; Post, R. J.; Schultz, D.; Sitter, B. J.; Stevens, J. M.; Strambeanu, I. I.; Twilton, J.; Wang, K.; Zajac, M. A. The Evolution of High-Throughput Experimentation in Pharmaceutical Development and Perspectives on the Future. *Org. Process Res. Dev.* **2019**, *23*, 1213–1242. https://doi.org/10.1021/acs.oprd.9b00140.

(123) Umeyama, T.; Watanabe, Y.; Miyata, T.; Imahori, H. Synthesis of Thienothiadiazole–Benzothiadiazole Alternating Copolymers and Their Application to Bulk Heterojunction Solar Cells. *Chem. Lett.* **2014**, *43*, 1876–1878. https://doi.org/10.1246/cl.140822.

(124) Larsen, R. D.; King, A. O.; Chen, C. Y.; Corley, E. G.; Foster, B. S.; Roberts, F. E.; Yang, C.; Lieberman, D. R.; Reamer, R. A.; Tschaen, D. M.; Verhoeven, T. R.; Reider, P. J.; Lo, Y. S.; Rossano, L. T.; Brookes, A. S.; Meloni, D.; Moore, J. R.; Arnett, J. F. Efficient Synthesis of Losartan, A Nonpeptide Angiotensin II Receptor Antagonist. *J. Org. Chem.* **1994**, *59*, 6391–6394. https://doi.org/10.1021/jo00100a048.

(125) Larson, H.; Schultz, D.; Kalyani, D. Ni-Catalyzed C–H Arylation of Oxazoles and Benzoxazoles Using Pharmaceutically Relevant Aryl Chlorides and Bromides. *J. Org. Chem.* **2019**, *84*, 13092–13103. https://doi.org/10.1021/acs.joc.9b02094.

(126) Montel, S.; Jia, T.; Walsh, P. J. Palladium-Catalyzed α-Arylation of Benzylic Phosphine Oxides. *Org. Lett.* **2014**, *16*, 130–133. https://doi.org/10.1021/ol403124g.

(127) Wisniewski, S. R.; Stevens, J. M.; Yu, M.; Fraunhoffer, K. J.; Romero, E. O.; Savage, S. A. Utilizing Native Directing Groups: Synthesis of a Selective IKur Inhibitor, BMS-919373, via a Regioselective C–H Arylation. *J. Org. Chem.* **2019**, *84*, 4704–4714. https://doi.org/10.1021/acs.joc.8b02254.

(128) Li, Z.; Dechantsreiter, M.; Dandapani, S. Systematic Investigation of the Scope of Transannular C–H Heteroarylation of Cyclic Secondary Amines for Synthetic Application in

Medicinal Chemistry. *J. Org. Chem.* **2020**, *85*, 6747–6760. https://doi.org/10.1021/acs.joc.0c00870.

(129) El-Khoueiry, A. B.; Clarke, J.; Neff, T.; Crossman, T.; Ratia, N.; Rathi, C.; Noto, P.; Tarkar, A.; Garrido-Laguna, I.; Calvo, E.; Rodón, J.; Tran, B.; O'Dwyer, P. J.; Cuker, A.; Abdul Razak, A. R. Phase 1 Study of GSK3368715, a Type I PRMT Inhibitor, in Patients with Advanced Solid Tumors. *Br. J. Cancer.* **2023**, *129*, 309–317. https://doi.org/10.1038/s41416-023-02276-0.

CHAPTER 2. Palladium-Catalyzed Direct C–H Alkenylation with Enol Pivalates Proceeds via Reversible C–O Oxidative Addition to Pd(0)

This chapter has been adapted from:

Nahiane Pipaon Fernandez, Gregory Gaube, Kyla J. Woelk, Mathias Burns, Damian P. Hruszkewycz, and David C. Leitch. *ACS Catal*. **2022**, *12*, 6997-7003.

Contributions:

Reaction discovery and optimization, scope, and reaction monitoring experiments were performed by Nahiane Pipaon Fernandez. Products **3x** and **3ad** were synthesized and isolated by Kyla J. Woelk. Products **3a-3ad** were synthesized by Nahiane Pipaon Fernandez and isolated by Nahiane Pipaon Fernandez, Greg Gaube and Kyla J. Woelk. Starting materials **1i** and **1j** were synthesized by Mathias Burns.

2.1 Abstract

A tandem C–O/C–H activation approach to C–C bond formation using palladium catalysis is reported. This reaction combines C–O oxidative addition at enol pivalates with concerted metallation deprotonation of functionalized heterocycles to achieve base-free direct C–H alkenylation (Figure 2.1). Preliminary mechanistic studies indicate that the C–O oxidative addition to Pd(0) is reversible under these conditions, and that C–H activation occurs directly from the Pd(II) C–O oxidative addition product. *In situ* $^{31}P\{1H\}$ NMR spectroscopy further reveals that the $(Cy_3P)_2Pd(alkenyl)(OPiv)$ species is a major catalyst resting state during the reaction.

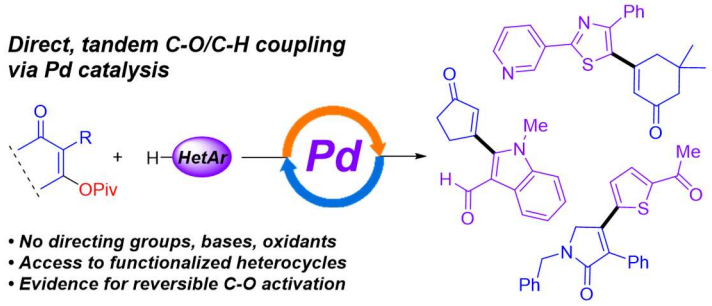

Figure 2.1: Tandem C-O/C–H activation via palladium catalysis.

2.2 Introduction

The synthesis of pharmaceuticals and pharmaceutically-relevant compounds is a major motivation for reaction development in organic chemistry. A summary of the composition of the US FDA approved small molecule drugs revealed that a high percentage of them have aromatic moieties (78%). It also revealed that a high percentage contain heterocycles: 58% of the molecules contain nitrogen heterocycles, 39% contain oxygen heterocycles, and 19% contain sulfur heterocycles.[1] The development of reaction conditions for the functionalization of aromatic heterocycles is therefore key to the synthesis of current drugs, as well as to enable new approaches for the synthesis of investigational compounds.

As stated in Chapter 1, selective functionalization of aromatic and heteroaromatic C–H bonds is a powerful tool for the synthesis of organic molecules. Transition metal catalyzed C–H functionalization is a key strategy to achieve this for preparing complex molecules. Direct functionalization of C–H bonds has several advantages compared to traditional functionalization, including high atom economy and good functional group tolerance. Direct arylation and alkenylation reactions are two specific direct functionalization approaches that allow C–C bond formation between heteroaromatic substrates and organic electrophiles.

2.2.1 Direct Arylation and Alkenylation Reactions

Palladium-catalyzed direct arylation (R = aryl) or alkenylation (R = vinyl) is proposed to proceed through a catalytic mechanism that involves oxidative addition, salt metathesis, C–H activation, and finally reductive elimination (Figure 2.2). Even though various mechanisms have been proposed for Pd-mediated C–H activation,[2] concerted metallation deprotonation (CMD) is the most commonly accepted pathway for a wide range of electron-rich and electron-poor aromatic compounds.[3] The salt metathesis step that precedes CMD is needed to install the reactive carboxylate ligand. Even though work has been done to elucidate the mechanism, there is a lack of research about how the structure of the heterocycle influences the reaction outcome, and what molecular features lead to successful reactions. Establishing how the heterocycle structure affects reactivity in CMD mechanisms would improve our understanding of how to design appropriate sets of reaction conditions for the synthesis of heterocycle-containing molecules.

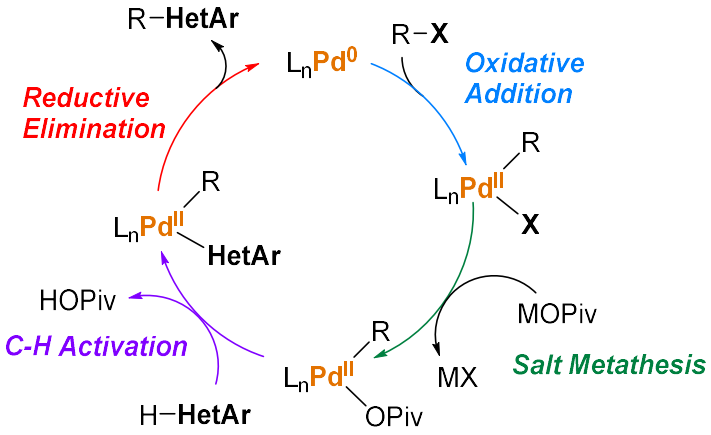

Figure 2.2. Generally accepted *catalytic* mechanism for *Pd-catalyzed* direct arylation and alkenylation reactions.

The difference between direct arylation and alkenylation reactions is in the identity of the electrophile. Direct arylation involves the use of aryl halides, whereas direct alkenylation reactions have an activated alkene or alkenyl halide. The product of many direct arylation reactions is the preparation of biaryl compounds. A wide range of heteroatom-containing biaryl structures have been successfully synthesized including (benzo)thiophenes[4], furans[5], (benz)oxazoles[6], indoles[7], pyrroles[8], (benz)imidazoles[9], (benzo)thiazoles[10], triazoles[11], indolizines[12], purines[13] and pyrazine[14] derivatives. This reaction will be further discussed in Chapter 5.

Direct alkenylation reactions have been developed as a simpler synthetic pathway to access alkenylarene derivatives as they are important scaffolds found in biologically active compounds.[15–18] In contrast with the diaryl products, the double bond on the alkenylarenes can be further functionalized to access unsaturated, tetrahedral sp^3-hybridized C or oxidized to further expand the carbon chain.

Other cross-coupling reactions for the direct functionalization of alkenes include Fujiwara-Moritani coupling and the Heck reaction (Figure 2.3). The first catalytic example was reported by Moritani and Fujiwara[19] in the synthesis of stilbene from styrene and benzene. The reaction requires an appropriate oxidant. Another challenge associated with this transformation is its low regioselectivity.[20] Heck reactions are also known to be prone to polymerization and homocoupling side reactions.[21]

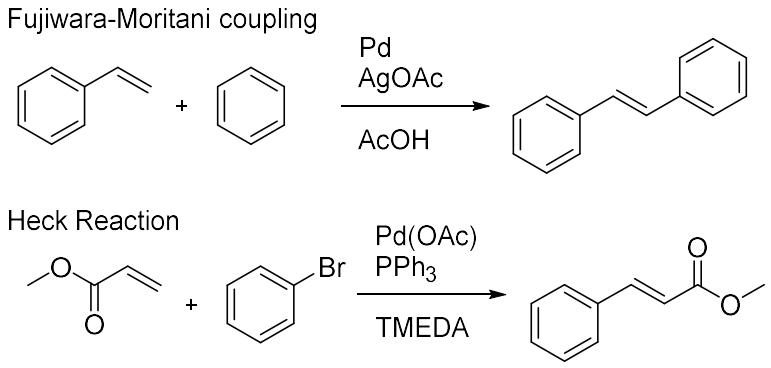

Figure 2.3. Palladium catalyzed Fujiwara-Moritani and Heck coupling examples of direct alkene C–H functionalization reactions.

Palladium catalyzed direct alkenylation reactions involving alkenyl electrophiles (halides or pseudohalides) allow the synthesis of π-conjugated molecules with great advantages. They offer excellent functional-group tolerance, relatively low catalyst loadings and robust reaction conditions.[22] However, there is still need for the development of broadly applicable reaction conditions, especially with respect to expanding the scope of suitable alkenyl electrophiles.

2.2.2 C–O Bond Activation

Aryl halides are the most common class of electrophiles used in cross-coupling reactions. Triflates and other sulfonate-based pseudohalides are also commonly employed in this transformation. Unfortunately, triflates are often unstable, and their formation requires expensive starting materials. Non-sulfonate C–O electrophiles, such as carboxylates, possess several advantages compared to the halides and pseudohalides. They are naturally abundant species and

come from a different feedstock, the use of toxic halogens is avoided, and they can be easily installed.[23,24]

Kinetically, the activation of C–O bonds is a challenge as they are quite strong (BDE ~100-110 kcal/mol).[25] However the organometallic oxidative addition of C–O bonds should be thermodynamically favoured as they would make a stronger metal-oxygen bond. To be able to promote C–O cross coupling reactions, the development of catalytic systems with good reactivity and the design of more reactive and stable C–O electrophiles is necessary.

Aside from triflates, there are other C–O electrophiles that have been able to undergo oxidative addition to palladium catalysts (Figure 2.4). A review on palladium-catalyzed cross-couplings by C–O bond activation from 2020 reported esters as unreactive electrophiles.[26] Although several examples of Pd mediated C–O activation have been published recently,[27,28] there is a significant challenge in the use of carboxylates as electrophiles.

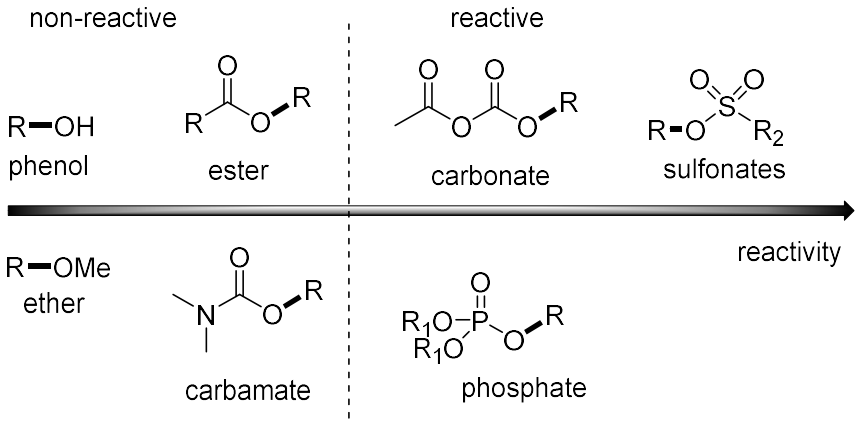

Figure 2.4. Relative order of reactivity of C–O electrophiles in Pd-catalyzed cross-coupling reactions. Activated C–O bond bolded.

Carboxylates contain two C–O bonds that can be activated, making selective coupling more challenging. The C(acyl)–O bonds are significantly weaker (BDE ~80 kcal/mol), and activation of these bonds would lead to acyl substitution and not the desired coupling product. Examples of C_{acyl}–O activation include nickel and metal catalyzed cross-coupling reactions[29–31] and more common direct acyl substitution when nucleophiles are used.[32,32] The goal of this project is to break the stronger C–O bond (BDE ~100 kcal/mol), which is thermodynamically favoured, as it results in a stronger M–O bond (Figure 2.5).[33]

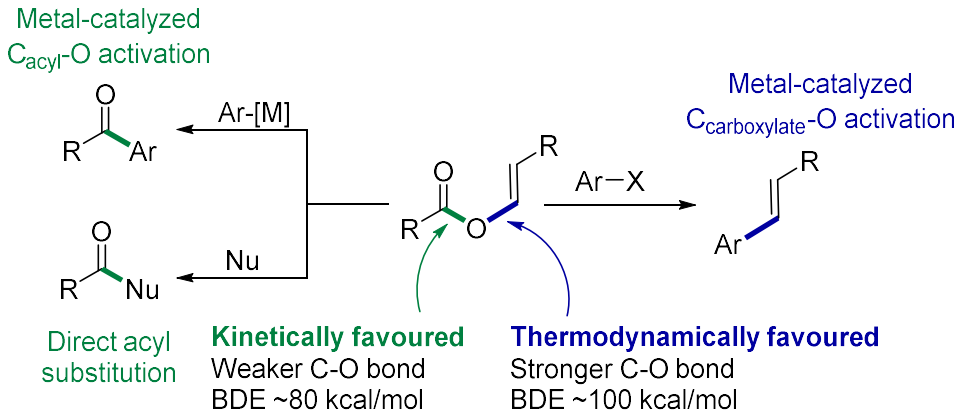

Figure 2.5. Metal-catalyzed cross-coupling with carboxylate-based electrophiles.

The combination of C–O and C–H activation in a catalytic process could result in fewer synthetic steps and greater mass efficiency in the overall process, as well as unlocking new feedstocks and building blocks.[34,35] Accordingly, considerable effort has been devoted to incorporating C–H [36–44] or C–O[25,27,32,45–51] bond activation in redox-neutral cross-coupling catalysis. Far less developed are catalytic processes that combine multiple strong bond activations into a single transformation.[52]

2.2.3 Tandem C-O/C–H Activation

Tandem C–O/C–H activation to form new C–C bonds is a particularly attractive synthetic approach for the synthesis or pharmaceutical molecules. One method is to take advantage of C_{acyl}–O activation of activated carboxylic acid derivatives, followed by decarbonylation of the resulting metal-acyl intermediate (Figure 2.6).[32] Rh catalysis involving directing-group assisted C–H activation is the major reported method.[53–60] For reactions without C–H directing groups, Ni catalysis[61] and more recently tandem Pd/Cu catalysis[62,63] have been reported.

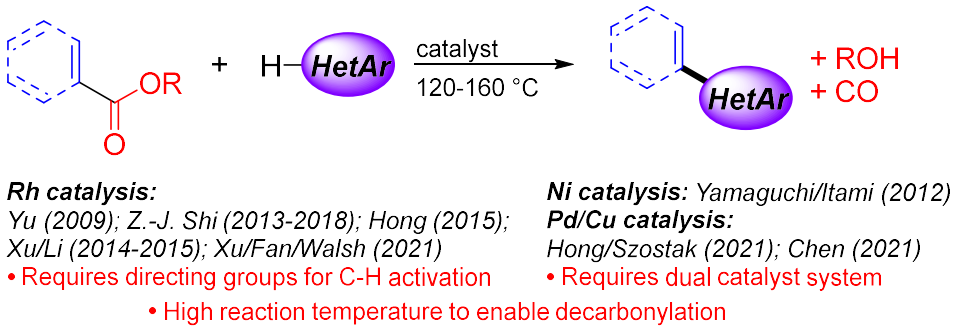

Figure 2.6. Decarbonylative C–O/C–H coupling.

A more direct method is tandem C–O/C–H activation involving ester, ether, or carbamate leaving groups. The major challenge is that this requires activating a considerably stronger C–O bond.[25] Itami and co-workers first demonstrated this approach with Ni-catalysis to couple aryl pivalates with azoles.[64] Later studies further explored the synthetic and mechanistic aspects of this catalysis.[65–68] Song and Ackermann reported a Co-system for directed C–H arylation with carbamate substrates,[69] with follow-up work on other alkenyl electrophiles.[70] Since these initial reports, very few additional direct C–O/C–H coupling methods have appeared: Shi and co-workers disclosed a dual Ni/Cu system for perfluoroarene C–H functionalization with aryl carbamates;[71]

Zhao, Ong and co-workers reported a Ni-based coupling of aryl ethers with imidazoles;[72] Dong and co-workers reported a Rh-catalyzed system for unselective alkenylation of 7-azaindoles;[73] and Toupalas and Morandi recently reported one example of Ni-catalyzed coupling between an aryl carbamate and benzoxazole (Figure 2.7).[74] Despite the success of Pd catalysis for direct arylation using (pseudo)halide electrophiles,[75] no Pd systems for direct C–O/C–H coupling with these less reactive electrophiles have been reported.[27,48]

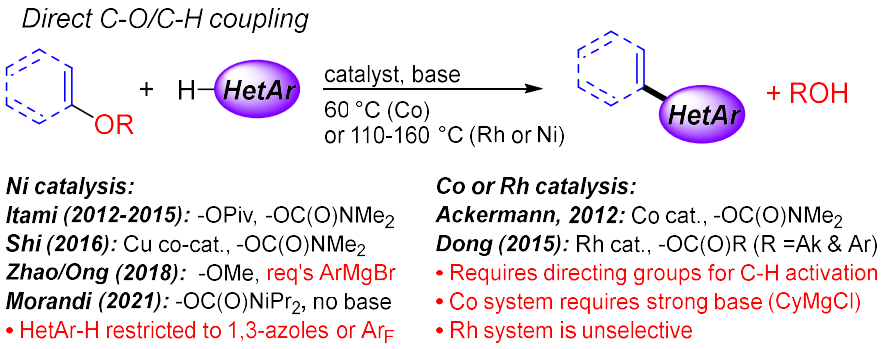

Figure 2.7. Direct C–O/C–H coupling for the formation of new C–C bonds.

In this chapter, a palladium-catalyzed tandem C–O/C–H activation process for the direct alkenylation of aromatic heterocycles using enol pivalates (Figure 2.8) is reported. In contrast to nearly all the methods mentioned before, this coupling proceeds without the need for bases, additives, or co-catalysts. This is possible because of the direct formation of the key Pd(II) pivalate intermediate *via* C–O oxidative addition, which then activates the HetAr–H bond *via* concerted metallation deprotonation (CMD).[76] Mechanistic studies confirm that this proposed sequence of steps is viable, with the observation of the Pd(II) pivalate species as the major catalyst resting state.

Importantly, it has been established that the key C–O oxidative addition is reversible under these conditions, what is an added challenge in tandem C-O/C–H activation.

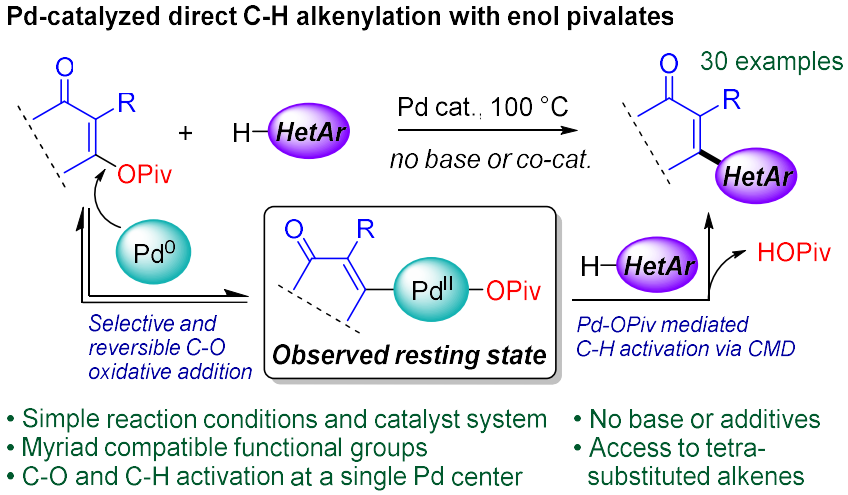

Figure 2.8. Pd-catalyzed direct C–O/C–H coupling via selective and reversible C–O activation and subsequent concerted metallation deprotonation (CMD).

2.3 Results and Discussion

2.3.1 High-Throughput Experimentation for Reaction Condition Optimization

To explore the possibility of Pd-catalyzed heterocycle C–H alkenylation using enol ester substrates, we designed a series of multivariate high-throughput screening experiments[77–80] for the C–H alkenylation of benzothiophene (**2a**) with a dimedone-derived enol pivalate (**1a**). First, an initial 24-reaction screen was conducted to discover potential Pd catalysts (Figure 2.9). In addition to $Pd(OAc)_2$, $[Pd(allyl)Cl]_2$, and freshly prepared and recrystallized $Pd_2dba_3•CHCl_3$,[81] we included a recently developed palladium source, DAB–Pd–MAH, as an alternate Pd(0) source.[82] Six phosphines were chosen based on their known utility for Pd-catalyzed direct arylation.[36,75,83,84] *N*,*N*-dimethylacetamide (DMA) was fixed as the solvent,[75] and *N*,*N*-diisopropylethylamine (DIPEA) was added to quench the pivalic acid generated from the coupling. Among the Pd/ligand

combinations screened, only PCy_3 paired with $Pd(OAc)_2$ or DAB–Pd–MAH gave **3a**, with the latter Pd source giving 34% solution yield.

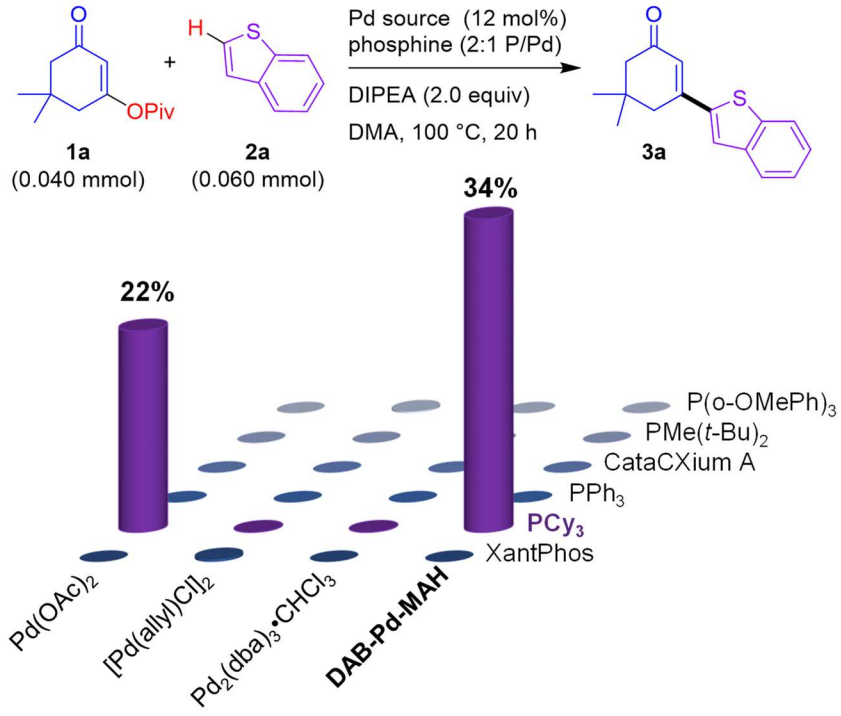

Figure 2.9. Initial Reaction and Catalyst discovery screen and for Pd-catalyzed tandem C–O/C–H coupling. Yields determined by HPLC UV/Vis absorbance using a calibration curve for **3a**.

Using DAB–Pd–MAH as the Pd source, we then undertook an extensive multifactor screen to evaluate the combination of ligand (18 phosphines), solvent (DMA and cyclopentylmethyl ether – CPME), and base (DIPEA, 1,8-diazabicyclo[5.4.0]undec-7-ene – DBU – and no base). Due to the relatively low reactivity observed in the initial screen, we increased the catalyst loading to 24 mol% (Figure 2b). Across these conditions, PCy_3 again emerged as the only effective ligand, giving 33-40% solution yield of **3a** with DMA and either DIPEA or no added base (Figure 2.10).

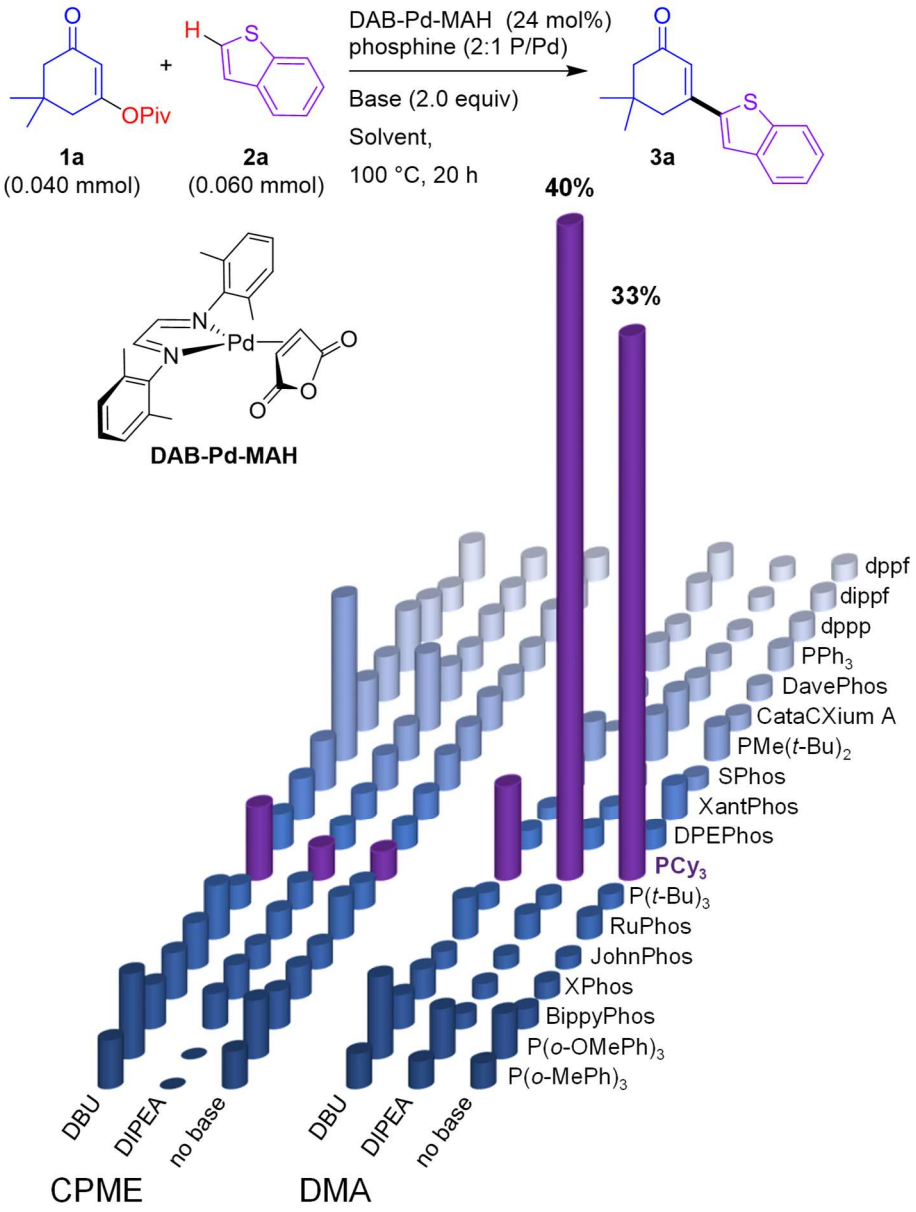

Figure 2.10. Extensive ligand survey using DAB-Pd-MAH and multiple base/solvent combinations. Yields determined by HPLC UV/Vis absorbance using a calibration curve for **3a**.

The stabilizing ligands from the DAB–Pd–MAH precursor could be inhibiting C–O oxidative addition. Based on prior success with $Pd(PCy_3)_2$ as a single-component catalyst for coupling with C–O electrophiles,[28,85] this specific palladium source was evaluated on the coupling

of **1a** and **2a** on 0.10 mmol scale using OFAT approach. At a reduced catalyst load of 10 mol% Pd, a 66% solution yield of **3a** was observed (^{1}H NMR spectroscopy versus internal standard). After a targeted optimization of Pd loading, base, concentration, and stoichiometry (Figure 2.11), it was determined that 6 mol% Pd performs similarly to 10 mol% over the 20 h reaction time, the addition of DIPEA has no effect on the reaction outcome, and a higher overall reaction concentration (0.50 M) combined with an increased loading of heterocycle (3 equiv) results in 91% solution yield of **3a**.

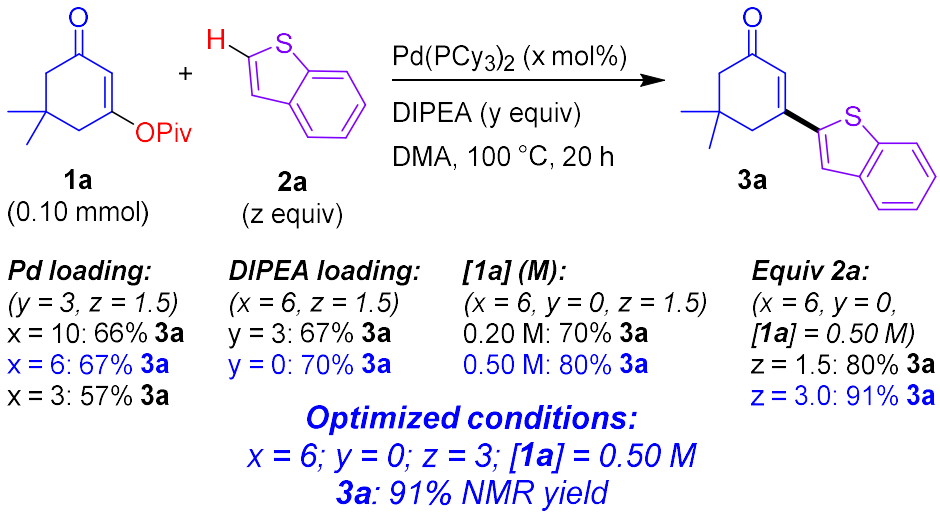

Figure 2.11. Targeted reaction optimization for Pd-catalyzed tandem C–O/C–H coupling. Analyzed variables are palladium loading (x), DIPEA loading (y), concentration of **1a** and equivalents of **2a** (z). Yields determined by ^{1}H NMR spectroscopy versus internal standard (1,3,5-trimethoxybenzene).

2.3.2 Reaction Scope

Once effective reaction conditions for the formation of **3a** were identified, the reactivity of various enol pivalates and heterocycles in this tandem C–O/C–H coupling was evaluated (Figure 2.12). Preparative scale synthesis of **3a** using the conditions from Figure 2.11 proceeds in 86%

isolated yield after chromatography. A series of other heterocycles also perform well in combination with **1a**, including an electron-deficient thiophene (**3b**) and sterically-hindered thiazoles (**3c**-**e**). Other thiophene and benzothiophene derivatives with potentially reactive aldehyde and enolizable ketone functional groups undergo coupling to an unsubstituted cyclohexenyl pivalate substrate (**3f**-**i**). A pyrone-derived pivalate is compatible for heterocycle/heterocycle couplings, though modest yields are obtained in these cases (**3j**, **k**), due to incomplete consumption of substrate.

A variety of substituted cyclopentenone products were also synthesized using this methodology through C–H functionalization of thiophene and thiazole heterocycles (**3l**-**p**), as well as 1-methyl-3-formylindole (**3q**). 2-alkylcyclopentenone substrates can be successfully arylated, despite the additional steric bulk on the ring (**3r**-**w**). While the yields are modest, cross-coupling to form tetrasubstituted alkenes is known to be challenging.[86,87] In addition to 5-membered carbocycles, *γ*-lactone (**3x**-**y**) and *γ*-lactam (**3z**-**ad**) substrates are successfully arylated, generating multisubstituted α,β-unsaturated *γ*-lactone and *γ*-lactam compounds with (benzo)thiophene and thiazole substituents.

Overall, this method provides access to functionalized heterocycles with a variety of functional groups. This includes sensitive and/or reactive functional groups such as aldehyde, ketone, ester, amide, nitrile, pyridine, thiophene, thiazole, and indole. The highly-functionalized products would allow further reactivity on multiple points of the structure. This method allowed the coupling between two five-membered rings, what has been a challenge in cross-coupling reactions.[88] These coupled structures of two five membered rings or five and six membered rings have been demonstrated to be interesting for biologically active compounds.

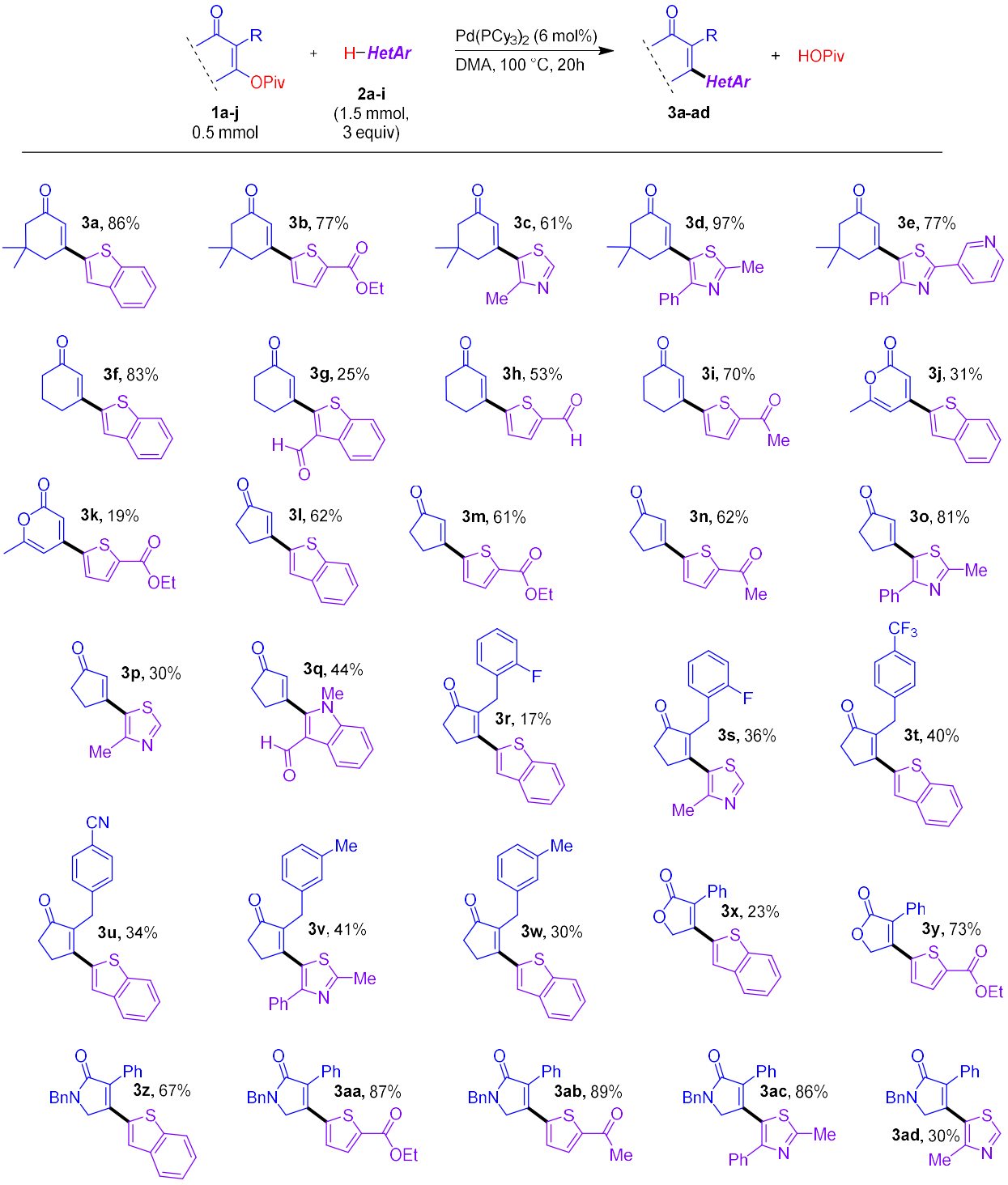

Figure 2.12. Reaction scope of the Pd-catalyzed direct arylation of alkenyl pivalates, with isolated product yields obtained after purification by flash chromatography.

Cyclohexenone rings have been shown to have adenylyl cyclase and anthrax edema factor inhibition activity (Figure 2.13).[89] *γ*-Lactone and *γ*-lactam units are present in many biologically active compounds, including natural products,[90,91] synthetic pesticides,[92] and COX-2 inhibitors.[93] In figure 2.13 we can find some specific examples of indole containing *γ*-lactam molecules that are involved in the PPAR-regulating mechanism[94] and have been explored in the treatment of hypoadiponectinemia. Thiazole, thiophene containing *γ*-lactone small molecules have shown biological activity on the treatment of retinal degeneration[95] and are phosphodiesterase 10 inhibitors and have antiproliferative activity.[96,97]

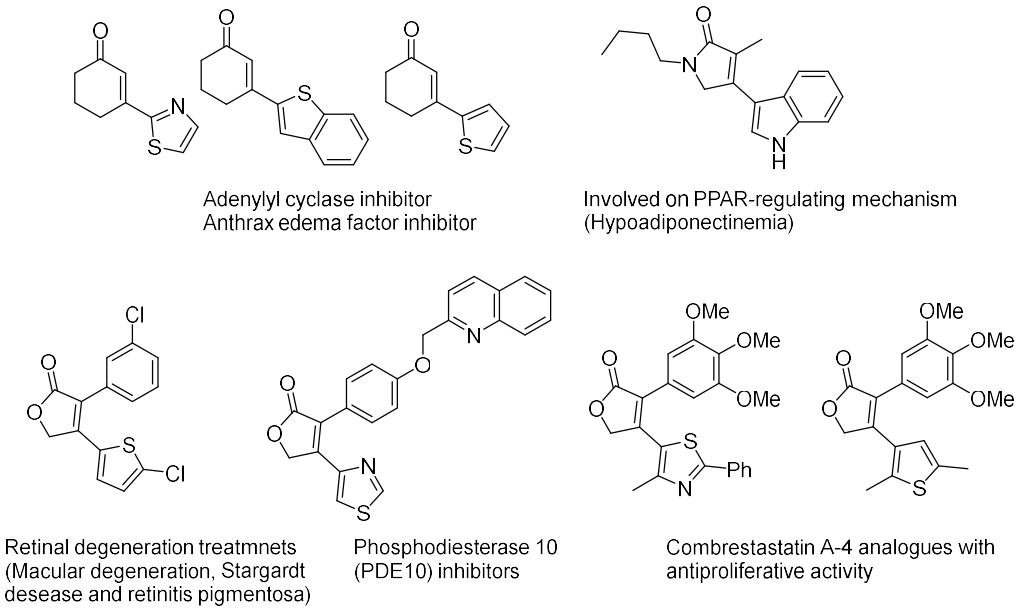

Figure 2.13. Examples of biologically active molecules that contain cyclohexenone or cyclopentenone cores with fused heterocycles.

2.3.3 Reaction Monitoring

2.3.3.1 Oxidative Addition

Based on the promising reactivity observed in this coupling chemistry, a series of organometallic mechanistic experiments were conducted. By analogy to previous work from our laboratory,[33] Complex **4** was successfully isolated (62% yield) from $Pd(PCy_3)_2$ using excess **1b** and extended heating in toluene (eq. 2.1). Compound **4** was fully characterized by solution and mass spectrometric methods, confirming the structure as the monomeric bis(phosphine) complex rather than a mono(phosphine) η^2-carboxylate complex,[98] or a carboxylate-bridged dimer.[99]

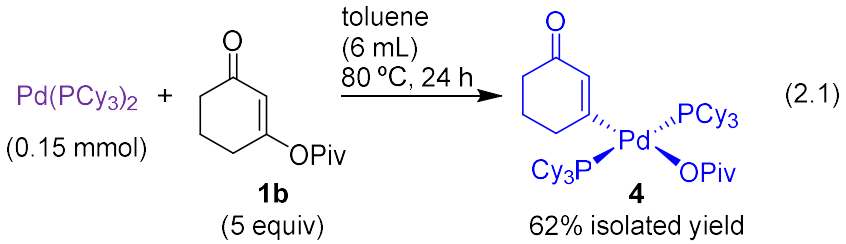

(2.1)

To better mimic the catalytic reaction conditions, the oxidative addition reaction was monitored by *in situ* $^{31}P\{1H\}$ NMR spectroscopy in a DMA/THF solvent mixture (Figure 2.14). This binary solvent system was used to ensure complete dissolution of $Pd(PCy_3)_2$, which is poorly soluble in DMA at room temperature. A capillary containing PPh_3 in C_6D_6 was use as internal standard. The consumption of $Pd(PCy_3)_2$ is clearly observed (decrease in signal at 40 ppm), along with the formation of the oxidative addition complex (increase in signal at 19 ppm). The equilibrium between both palladium species establishes after 45 minutes.

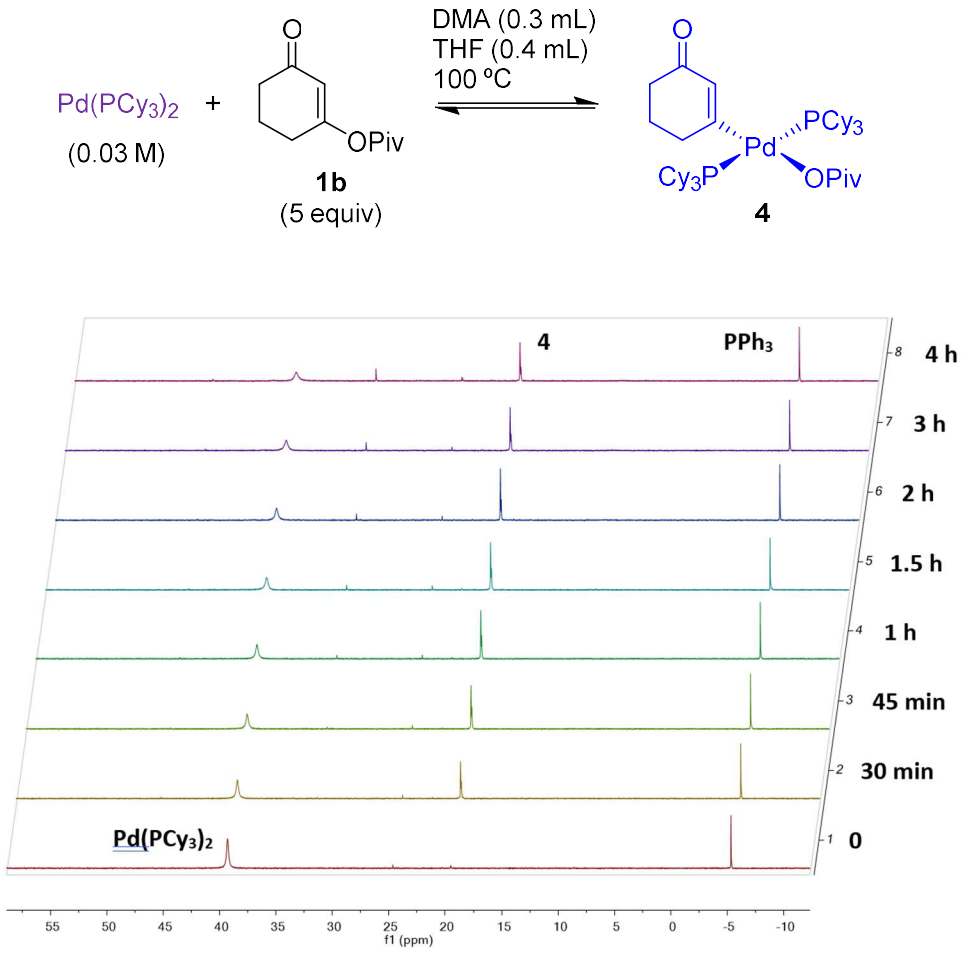

Figure 2.14. $^{31}P\{1H\}$ NMR spectroscopy monitoring of C–O oxidative addition with 5 equivalents of 3-oxocyclohex-1-en-1-yl pivalate (**1b**) and $Pd(PCy_3)_2$ in DMA/THF.

During the formation of **4**, a peak shoulder can be observed slightly upfield from the signal for **4** in the ^{31}P NMR spectrum. This could be the product of the insertion of palladium into the acyl C–O bond instead of the alkenyl C–O bond (Figure 2.15). This is the kinetic product that would be in equilibrium with Pd(0). The observation of this species may be due to the temperature of the NMR probe being at room temperature (23-25 ºC) instead of the catalytic reaction

temperature. However, it will be shown that during the thermal decomposition of **4** we do not observe formation of this second species.

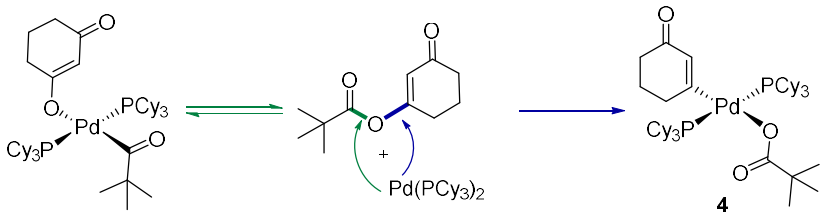

Figure 2.15. Palladium oxidative addition products of palladium $Pd(PCy_3)_2$ and **1b**.

In the reaction of **1b** (5 equiv, 0.15 M) to $Pd(PCy_3)_2$ (0.030 M) in DMA/THF at 100 °C, the reaction proceeds to a maximum of ~40% **4** within 60 min, with >50% $Pd(PCy_3)_2$ remaining unreacted even after extended reaction times. Doubling the initial concentration of **1b** to 0.30 M (10 equiv) leads to an increased oxidative addition rate and extent of reaction, and the equilibrium is reached faster (30 minutes); however, the reaction again fails to reach full conversion (Figure 2.16).

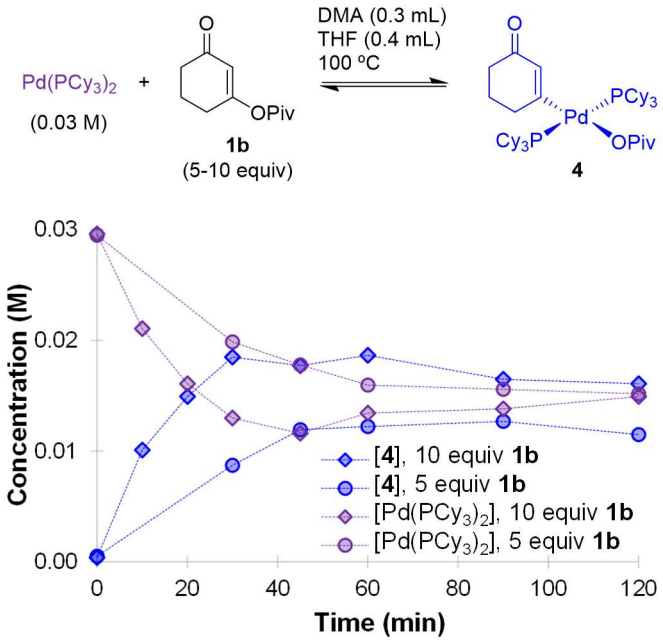

Figure 2.16. Reaction progress monitoring via $^{31}P\{1H\}$ NMR spectroscopy of: a) the oxidative addition of **1b** to $Pd(PCy_3)_2$ in DMA/THF solvent to generate **4**.

2.3.3.2 Thermal Decomposition of Oxidative Addition Complex 4

The thermal decomposition of **4** in the same solvent mixture was monitored as a possible reason for the establishment of an equilibrium is the reversible C–O oxidative addition (Figure 2.17). Complex **4** was dissolved in a DMA/THF mixture, heated in an oil bath, and monitored over time. At time-zero, the formation of Pd(0) can be observed at 40 ppm. That signal increases as the time progresses while complex **4** is consumed. The formation of the suspected constitutional isomer from Figure 2.15 is not observed under these conditions. At the end of the monitoring, 3-oxocyclohex-1-en-1-yl pivalate (**1b**) was observed by LCMS comparing the reaction crude with the purified starting material.

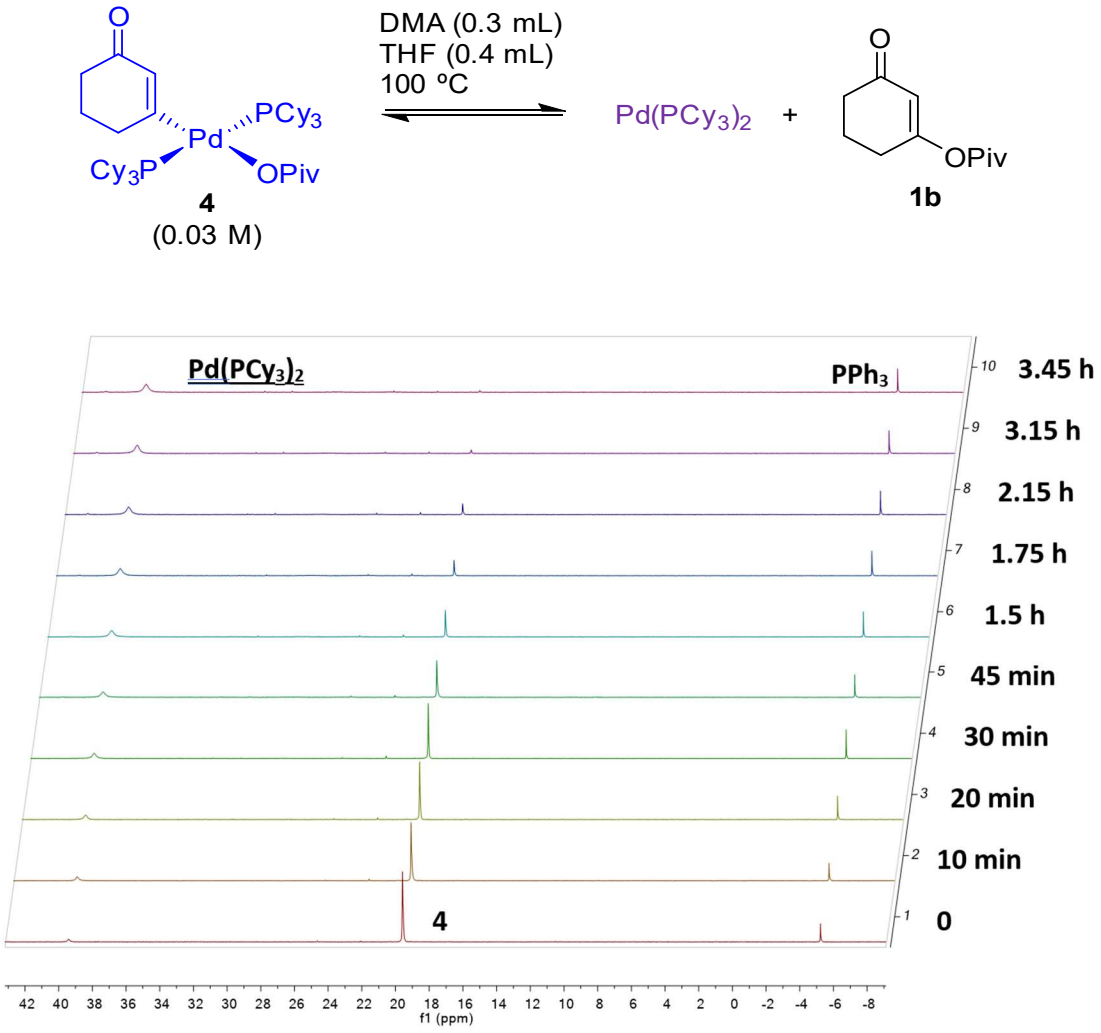

Figure 2.17. $^{31}P\{1H\}$ NMR spectroscopy monitoring of reversible C–O oxidative addition from thermolysis of complex **4** in DMA/THF.

When plotting the concentrations of species **4** and Pd(0), a first-order decay of **4** over ~3h is observed, with proportional formation of $Pd(PCy_3)_2$ and **1b** (Figure 2.18). This outcome confirms the reversible nature of the C–O oxidative addition, pointing to an additional kinetic challenge in achieving catalytic C–O/C–H coupling with Pd. Although the equilibrium between both palladium species is shifted towards the oxidative addition product, if as the reaction advances and **1b** is

consumed, the equilibrium will shift towards the palladium (0) intermediate. The equilibrium between both palladium species could lead to a smaller energetic span[100] across intermediates. This would potentially lead to a faster catalytic cycle. However, one of the additional challenges of a Pd^0 resting state is a reversible out of cycle product inhibition (Section 2.3.3.5) and irreversible decomposition of $Pd(PCy_3)_2$. Other systems have also described that exothermic pre-equilibria, even without product inhibitions, are usually insensitive to temperature.[101] As a result the equilibria will probably slow the catalytic reaction and impede full conversion of **1b** into product.

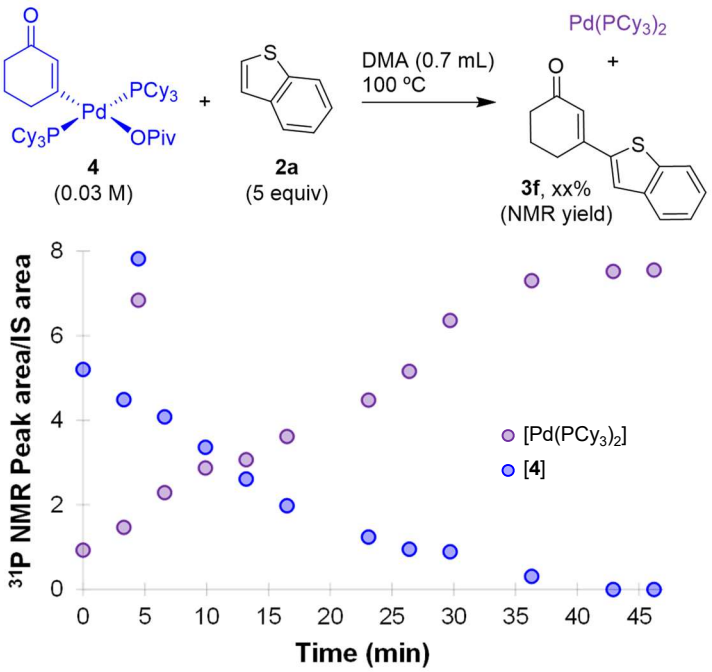

Figure 2.18. Reaction progress monitoring via $^{31}P\{1H\}$ NMR spectroscopy of the reductive elimination of **1b** from **4** to generate $Pd(PCy_3)_2$.

2.3.3.3 C–H Activation

Having established C–O activation as reversible, the formation of product **3f** from **4** and benzothiophene was monitored. The possible mechanism for the C–H activation step is a CMD process (Figure 2.19). In this case, the solubility of **4** allowed the use DMA as the only solvent. Removing THF as a lower-boiling co-solvent enabled to monitor the reaction progress with the NMR probe heated to 100 °C.

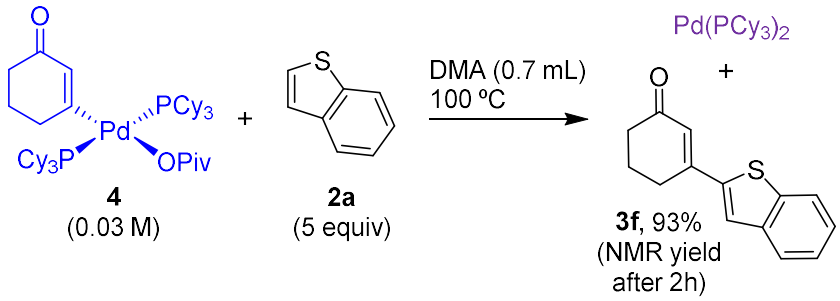

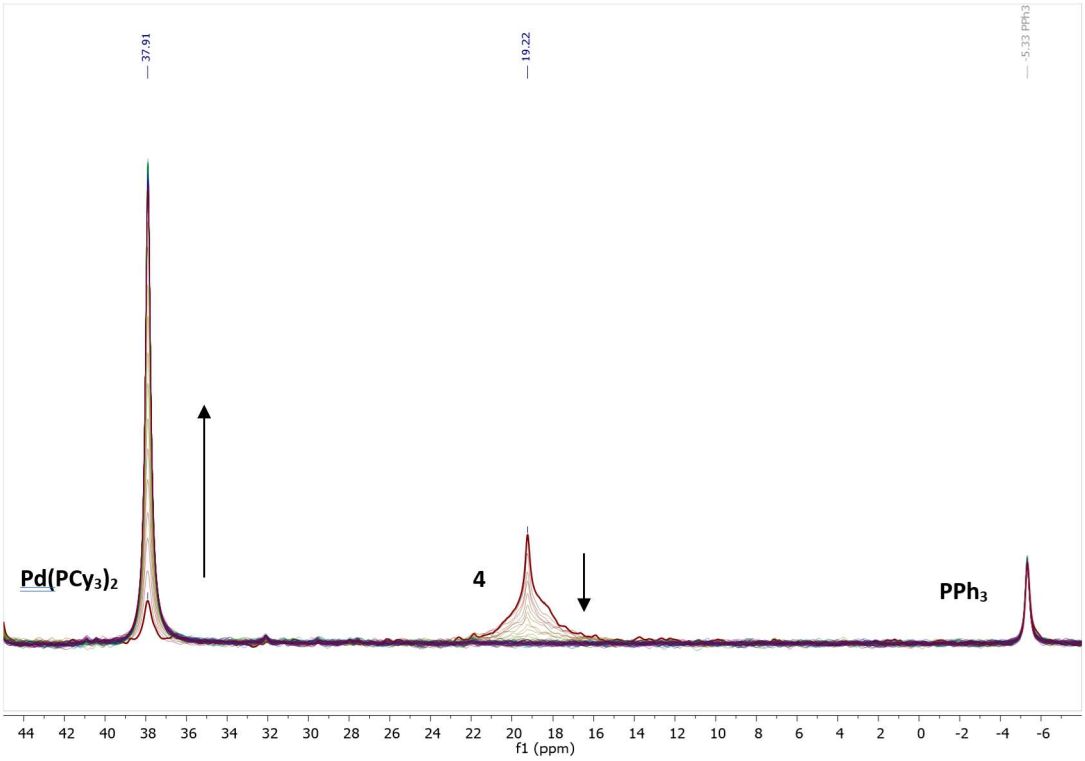

Figure 2.19. CMD reaction monitoring by $^{31}P\{^{1}H\}$ NMR spectroscopy at 100 °C (single scan spectra).

The complete conversion of **4** to $Pd(PCy_3)_2$ in less than 40 min can be observed by $^{31}P\{1H\}$ NMR spectroscopy (Figure 2.20). To assess whether this conversion results from the intended CMD/reductive elimination sequence to give **3f**, and/or from C–O reductive elimination to give **1b**, DMA was removed from the sample *in vacuo* after 2 hours and analyzed the resulting mixture by ^{1}H NMR spectroscopy. The formation of **3f** was determined to be 94% by ^{1}H NMR spectroscopy using 1,3,5-trimethoxybenzene as internal standard.

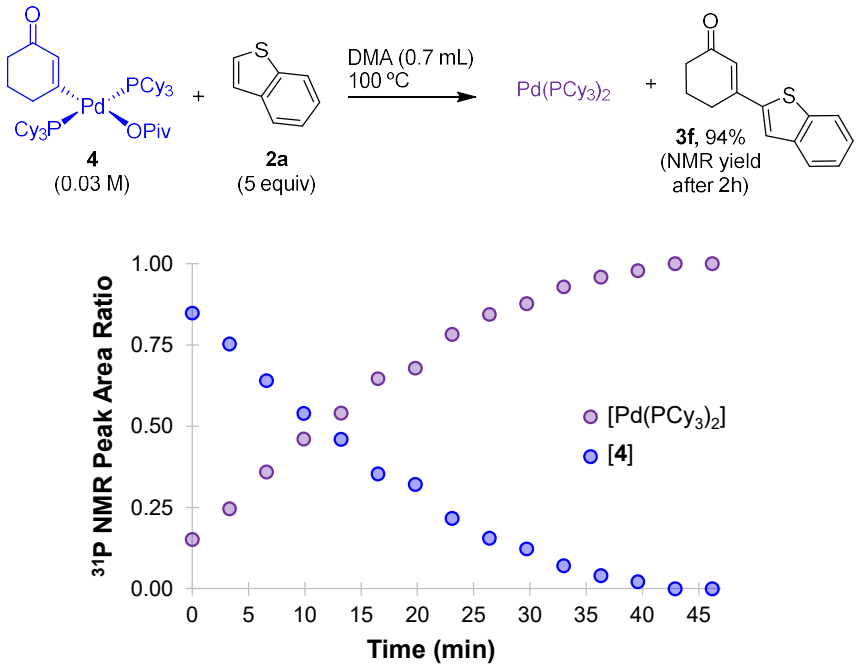

Figure 2.20. Reaction progress monitoring via $^{31}P\{^{1}H\}$ NMR spectroscopy of the formation of **3f** via CMD of **2a** by **4**.

2.3.3.5 Catalyst Resting State

Finally, to connect the stoichiometric chemistry observations to the catalytic system, $^{31}P\{^{1}H\}$ NMR spectroscopy was performed to observe the major phosphorus-containing species during the catalytic coupling of **1b** and **2a** (Figure 2.21). In the initial phase of the reaction, both $Pd(PCy_3)_2$ and **4** are present in solution, with the former species being fully depleted after 5 hours. As the reaction progresses, the amount of **4** also decreases and several new $^{31}P\{^{1}H\}$ NMR signals appear. These signals correspond to free PCy_3, $O{=}PCy_3$, and other so far unidentified phosphorous-containing species. The formation of Pd black was also observed, indicating catalyst decomposition. Based on the reversible nature of the C–O activation, the major resting state should shift from **4** to $Pd(PCy_3)_2$ as the alkenyl pivalate substrate is consumed.

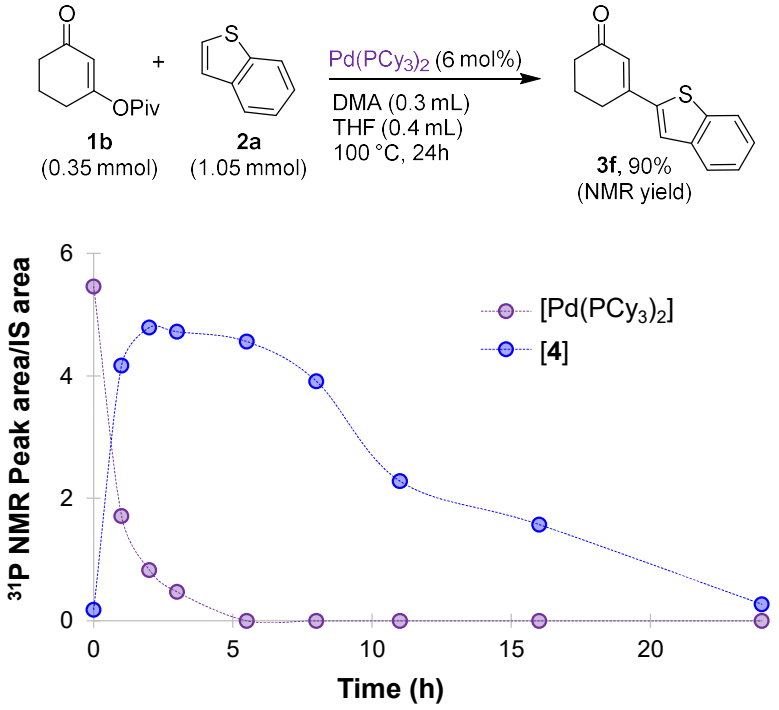

Figure 2.21. *In situ* $^{31}P\{1H\}$ NMR spectroscopy confirms **4** as a major catalyst resting state.

To account for the apparent absence of $Pd(PCy_3)_2$ in the later stages of the reaction, we suspected that the product enone **3f** could coordinate to Pd(0). To confirm this, we treated $Pd(PCy_3)_2$ with excess **3f**, resulting in disappearance of the $^{31}P\{^1H\}$ NMR signal at 39 ppm and appearance of two very broad signals centered at 30 and 40 ppm. This is consistent with reversible coordination of the product, causing $Pd(PCy_3)_2$ to be unobservable during later stages of the catalytic reaction as the concentration of **3f** increases.

2.3.4 Proposed Mechanism

Taking all the reaction monitoring experiments into account, the observations are consistent with the mechanistic proposal in Figure 2.22. $Pd(PCy_3)_2$ first undergoes reversible oxidative addition of the enol pivalate C–O bond to generate **4**, which is observed as a major catalytic resting

state. Subsequent C–H activation *via* CMD occurs directly from **4**, taking advantage of the already-installed pivalate ligand. This is followed by rapid reductive elimination to form the cross-coupled product and regenerate $Pd(PCy_3)_2$, which can also undergo reversible binding to the product **3f**. Further work is currently underway to fully elucidate the mechanistic details of this reaction.

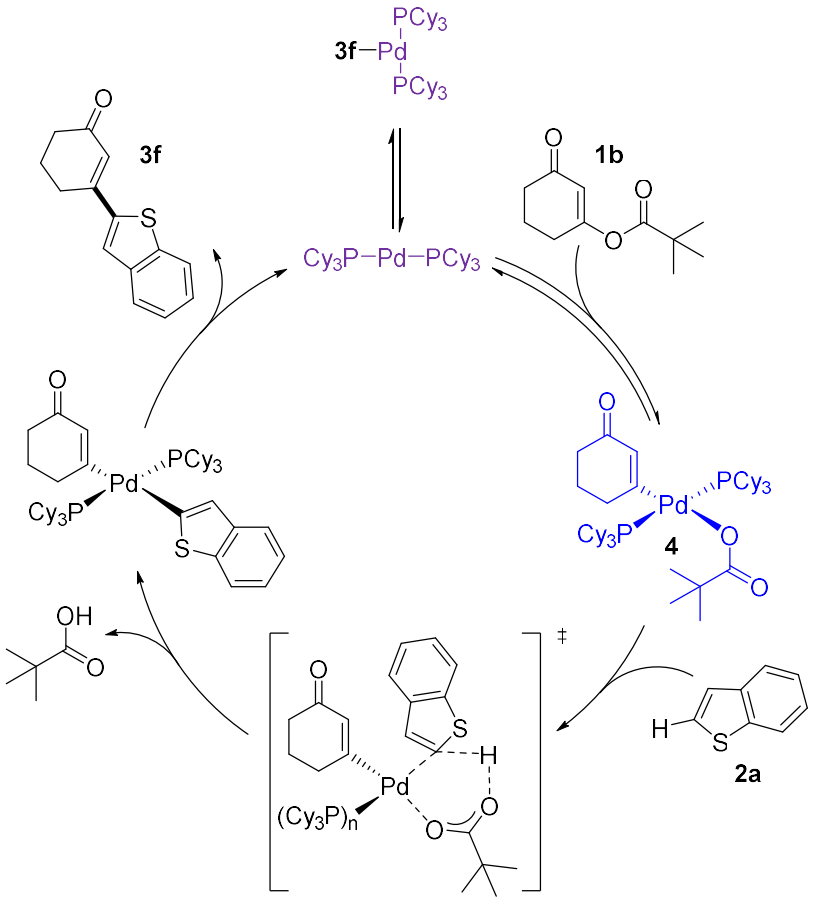

Figure 2.22. Simplified proposed catalytic cycle for Pd-catalyzed C–O/C–H coupling with reversible C–O activation.

2.4 Conclusions

In summary, the first Pd-catalyzed direct C–O/C–H coupling reaction has been developed, enabling the C–H alkenylation of heterocycles without the need for directing groups, co-catalysts, additives, oxidants, or any other reagents. By taking advantage of C–O oxidative addition of enol

pivalates to Pd(0), the carboxylate ligand required for C–H activation *via* CMD is directly installated, removing the need for exogenous base or carboxylic acid additives. We were able to synthesize and isolate the oxidative addition complex, what allowed us to monitor the reaction using $^{31}P\{1H\}$ NMR. According to our findings, the reaction proceeds through a reversible oxidative addition. This equilibrium is shifted towards Pd(0). This step is followed by the concerted-metallation-deprotonation of the heterocycle and its reductive elimination, yielding the desired product. The overall reaction monitoring indicates that the catalyst resting state is Pd(0). Overall, we opened the door to efficient catalytic C–H functionalization from new feedstocks and building blocks.

2.5 General Experimental Methods

Note: additional experimental details and images of relevant spectroscopic data are included in Appendix A.

2.5.1 High-Throughput Experiments for Reaction Screening

Preparation of Pd/ligand combinations:

Stock solutions of the catalysts were prepared by dissolving 0.1 mmol of the catalyst in 2.0 mL of THF. 120 μL or 240 μL of each stock solution was loaded into 1 mL shell vials in aluminum blocks. The solvent was removed by centrifugal evaporation.

Inside the glovebox, 0.154 mmol of each ligand was dissolved in 1.470 mL of THF in separate 4-dram vials. 183 μL (0.0192 mmol) of each ligand stock solution was dispensed into six wells (each containing a micro stir bar) corresponding to the experimental design using one 96-well plate and one 24-well plate. The reaction mixtures were stirred at room temperature for 20 minutes, before removing the volatiles by centrifugal evaporation.

Preparation and analysis of the reaction plate:

Inside the glovebox, two 20 mL vials were each charged with 5,5-dimethyl-3-oxocyclohex-1-en-1-yl pivalate **1a** (269.2 mg, 1.2 mmol), and benzothiophene **2a** (241.6 mg, 1.8 mmol, 1.5 equiv). 5.58 mL of either CPME or DMA were added to the vials with a stir bar. After stirring to ensure complete dissolution, 200 μL of the reaction mixture stock solution was added into each well according to the experimental design. Finally the bases were added as neat liquids to each well according to experimental design: *N*,*N*-diisopropylethylamine (DIPEA, 13.9 μL) or 1,8-diazabicyclo[5.4.0]undec-7-ene (DBU, 12.0 μL). The plates were sealed and removed from the glovebox. The plates were placed in a heat block on a tumble stirrer set to 300 rpm, and the reaction

mixtures stirred for 20 hours at 100 °C. Upon completion, the plates were cooled to room temperature before being opened. Acetonitrile (500 μL) was added to each well, followed by stirring for 10 minutes at room temperature to ensure complete dissolution. Aliquots of 40 μL of each diluted reaction mixture were then transferred to 24 different HPLC vials followed by the addition of 1 mL of acetonitrile. These 24 samples were analyzed by HPLC, with solution yields of **3a** determined by UV/Vis absorbance versus a calibration curve for **3a**.

2.5.2 Preparative-Scale Direct Alkenylation

Inside the glovebox, a 1-dram vial was charged with a stir bar. The enol pivalate substrate (0.5 mmol, 1 equiv) and heterocycle substrate (1.5 mmol, 3 equiv) were added, followed by bis(tricyclohexylphosphine)palladium(0) (20.0 mg, 0.03 mmol, 6 mol%) and anhydrous N,N-dimethylacetamide (1 mL). The vial was sealed with a Teflon-lined screw cap, and the reaction mixture stirred at 100 °C for 20 h. After cooling to room temperature, the solvent was removed by centrifugal evaporation. The resulting crude mixture was purified by automated column chromatography using a hexanes/ethyl acetate gradient elution.

2.6 References

(1) Das, P.; Delost, M. D.; Qureshi, M. H.; Smith, D. T.; Njardarson, J. T. A Survey of the Structures of US FDA Approved Combination Drugs. J. Med. Chem. **2019**, 47.

(2) Ackermann, L. Carboxylate-Assisted Transition-Metal-Catalyzed C−H Bond Functionalizations: Mechanism and Scope. *Chem. Rev*. **2011**, 111, 1315–1345. https://doi.org/10.1021/cr100412j.

(3) Gorelsky, S. I.; Lapointe, D.; Fagnou, K. Analysis of the Palladium-Catalyzed (Aromatic)C–H Bond Metalation–Deprotonation Mechanism Spanning the Entire Spectrum of Arenes. *J. Org. Chem*. **2012**, 77, 658–668. https://doi.org/10.1021/jo202342q.

(4) Hagui, W.; Besbes, N.; Srasra, E.; Roisnel, T.; Soulé, J.-F.; Doucet, H. Short Synthesis of Sulfur Analogues of Polyaromatic Hydrocarbons through Three Palladium-Catalyzed C–H Bond Arylations. *Org. Lett.* **2016**, 18, 4182–4185. https://doi.org/10.1021/acs.orglett.6b01735.

(5) Nakano, M.; Tsurugi, H.; Satoh, T.; Miura, M. Palladium-Catalyzed Perarylation of 3-Thiophene- and 3-Furancarboxylic Acids Accompanied by C−H Bond Cleavage and Decarboxylation. *Org. Lett.* **2008**, 10, 1851–1854. https://doi.org/10.1021/ol800466b.

(6) Yamada, S.; Murakami, K.; Itami, K. Regiodivergent Cross-Dehydrogenative Coupling of Pyridines and Benzoxazoles: Discovery of Organic Halides as Regio-Switching Oxidants. Org. Lett. **2016**, 18 (10), 2415–2418. https://doi.org/10.1021/acs.orglett.6b00932.

(7) Yang, Y.; Gao, P.; Zhao, Y.; Shi, Z. Regiocontrolled Direct C−H Arylation of Indoles at the C4 and C5 Positions. *Angew. Chem. Int. Ed.***2017**, 56, 3966–3971. https://doi.org/10.1002/anie.201612599.

(8) Roger, J.; Doucet, H. Regioselective C-2 or C-5 Direct Arylation of Pyrroles with Aryl Bromides Using a Ligand-Free Palladium Catalyst. *Advanced Synthesis & Catalysis* **2009**, 351, 1977–1990. https://doi.org/10.1002/adsc.200900196.

(9) Li, H.; Huang, H.-Y.; Roisnel, T.; Doucet, H. Regiocontrolled Palladium-Catalyzed Direct C2-Arylation of a Difluorobenzo[d]Imidazole. *Tetrahedron Lett. ,* **2021**, 153112. https://doi.org/10.1016/j.tetlet.2021.153112.

(10) P, S.; Sau, S. C.; Vardhanapu, P. K.; Mandal, S. K. Halo-Bridged Abnormal NHC Palladium(II) Dimer for Catalytic Dehydrogenative Cross-Coupling Reactions of Heteroarenes. *J. Org. Chem.* **2018**, 83, 9403–9411. https://doi.org/10.1021/acs.joc.8b01053.

(11) Yu, X.; Huang, Z.; Liu, W.; Shi, S.; Kuang, C. Palladium-Catalyzed Oxidative C–H/C–H Cross-Coupling of 1-Substituted 1,2,3-Triazoles with Furans and Thiophenes. *Org. Biomol. Chem*. **2015**, 13, 4459–4465. https://doi.org/10.1039/C5OB00102A.

(12) Park, C.-H.; Ryabova, V.; Seregin, I. V.; Sromek, A. W.; Gevorgyan, V. Palladium-Catalyzed Arylation and Heteroarylation of Indolizines. *Org. Lett.* **2004**, 6, 1159–1162. https://doi.org/10.1021/ol049866q.

(13) Čerňa, I.; Pohl, R.; Klepetářová, B.; Hocek, M. Direct C−H Arylation of Purines: Development of Methodology and Its Use in Regioselective Synthesis of 2,6,8-Trisubstituted Purines. *Org. Lett.* **2006**, 8, 5389–5392. https://doi.org/10.1021/ol062324j.

(14) Abdo, N. I.; El-Shehawy, A. A.; El-Barbary, A. A.; Lee, J.-S. Palladium-Catalyzed Direct C–H Arylation of Thieno[3,4- b]Pyrazines: Synthesis of Advanced Oligomeric and Polymeric Materials. *Eur. J. Org. Chem*. **2012**, 28, 5540–5551. https://doi.org/10.1002/ejoc.201200769.

(15) van den Berg, D.; Zoellner, K. R.; Ogunrombi, M. O.; Malan, S. F.; Terre'Blanche, G.; Castagnoli, N.; Bergh, J. J.; Petzer, J. P. Inhibition of Monoamine Oxidase B by Selected Benzimidazole and Caffeine Analogues. *BMC* **2007**, 15, 3692–3702. https://doi.org/10.1016/j.bmc.2007.03.046.
(16) Van der Walt, E. M.; Milczek, E. M.; Malan, S. F.; Edmondson, D. E.; Castagnoli, N.; Bergh, J. J.; Petzer, J. P. Inhibition of Monoamine Oxidase by (E)-Styrylisatin Analogues. *BMCL* **2009**, 19, 2509–2513. https://doi.org/10.1016/j.bmcl.2009.03.030.
(17) Vlok, N.; Malan, S. F.; Castagnoli, N.; Bergh, J. J.; Petzer, J. P. Inhibition of Monoamine Oxidase B by Analogues of the Adenosine A2A Receptor Antagonist (E)-8-(3-Chlorostyryl) Caffeine (CSC). *BMC* **2006**, 14, 3512–3521. https://doi.org/10.1016/j.bmc.2006.01.011.
(18) Zeng, F.; Alagille, D.; Tamagnan, G. D.; Ciliax, B. J.; Levey, A. I.; Goodman, M. M. Synthesis and In Vitro Evaluation of Imidazo[1,2-b]Pyridazines as Ligands for β-Amyloid Plaques. *ACS Med. Chem. Lett.* **2010**, 1, 80–84. https://doi.org/10.1021/ml100005j.
(19) Moritani, I.; Fujiwara, Y. Arohatic Sdbstitution Of Styreke-Palladium Chiletide Complex. *Tetrahedron Lett.* , **1967**, 12, 1119-1122.
(20) Fujiwara, Y.; Moritani, I.; Matsuda, M.; Teranishi, S. Aromatic Substitution of Olefin. IV Reaction with Palladium Metal and Silver Acetate. *Tetrahedron Lett.* **1968**, 9, 3863–3865. https://doi.org/10.1016/S0040-4039(01)99121-X.
(21) Dieck, H. A.; Heck, R. F. Organophosphinepalladium Complexes as Catalysts for Vinylic Hydrogen Substitution Reactions. *J. Am. Chem. Soc.* **1974**, 96, 1133–1136. https://doi.org/10.1021/ja00811a029.
(22) Dombrowski, A. W.; Gesmundo, N. J.; Aguirre, A. L.; Sarris, K. A.; Young, J. M.; Bogdan, A. R.; Martin, M. C.; Gedeon, S.; Wang, Y. Expanding the Medicinal Chemist Toolbox: Comparing Seven $C(Sp^2)$–$C(Sp^3)$ Cross-Coupling Methods by Library Synthesis. *ACS Med. Chem. Lett.* **2020**, 11, 597–604. https://doi.org/10.1021/acsmedchemlett.0c00093.
(23) Shi, S.; Nolan, S. P.; Szostak, M. Well-Defined Palladium(II)–NHC Precatalysts for Cross-Coupling Reactions of Amides and Esters by Selective N–C/O–C Cleavage. *Acc. Chem. Res.* **2018**, 51, 2589–2599. https://doi.org/10.1021/acs.accounts.8b00410.
(24) Bisz, E.; Szostak, M. Iron-Catalyzed C−O Bond Activation: Opportunity for Sustainable Catalysis. *ChemSusChem.* **2017**, 10, 3865–3865. https://doi.org/10.1002/cssc.201701888.
(25) Yu, D.-G.; Li, B.-J.; Shi, Z.-J. Exploration of New C−O Electrophiles in Cross-Coupling Reactions. *Acc. Chem. Res.* **2010**, 43, 1486–1495. https://doi.org/10.1021/ar100082d.
(26) Zhou, T.; Szostak, M. Palladium-Catalyzed Cross-Couplings by C–O Bond Activation. *Catal. Sci. Technol.* **2020**, 10, 5702–5739. https://doi.org/10.1039/D0CY01159B.
(27) Becica, J.; Leitch, D. C. C–O Bond Activation as a Strategy in Palladium-Catalyzed Cross-Coupling. *Synlett* **2021**, 32, 641–646. https://doi.org/10.1055/a-1306-3228.
(28) Gaube, G.; Pipaon Fernandez, N.; Leitch, D. C. An Evaluation of Palladium-Based Catalysts for the Base-Free Borylation of Alkenyl Carboxylates. *New J. Chem.* **2021**, 45, 20095–20098. https://doi.org/10.1039/D1NJ04008A.
(29) Ben Halima, T.; Zhang, W.; Yalaoui, I.; Hong, X.; Yang, Y.-F.; Houk, K. N.; Newman, S. G. Palladium-Catalyzed Suzuki–Miyaura Coupling of Aryl Esters. *J. Am. Chem. Soc.* **2017**, 139, 1311–1318. https://doi.org/10.1021/jacs.6b12329.
(30) Lei, P.; Meng, G.; Shi, S.; Ling, Y.; An, J.; Szostak, R.; Szostak, M. Suzuki–Miyaura Cross-Coupling of Amides and Esters at Room Temperature: Correlation with Barriers to Rotation

around C–N and C–O Bonds. *Chem. Sci*. **2017**, 8, 6525–6530. https://doi.org/10.1039/C7SC02692G.
(31) Tatamidani, H.; Kakiuchi, F.; Chatani, N. A New Ketone Synthesis by Palladium-Catalyzed Cross-Coupling Reactions of Esters with Organoboron Compounds. *Org. Lett*. **2004**, 6, 3597–3599. https://doi.org/10.1021/ol048513o.
(32) Guo, L.; Rueping, M. Decarbonylative Cross-Couplings: Nickel Catalyzed Functional Group Interconversion Strategies for the Construction of Complex Organic Molecules. *Acc. Chem. Res*. **2018**, 51, 1185–1195. https://doi.org/10.1021/acs.accounts.8b00023.
(33) Becica, J.; Gaube, G.; Sabbers, W. A.; Leitch, D. C. Oxidative Addition of Activated Aryl-Carboxylates to Pd(0): Divergent Reactivity Dependant on Temperature and Structure. *Dalton Trans*. **2020**, 49, 16067-16071. https://doi.org/10.1039/D0DT01119C.
(34) Qiu, Z.; Zeng, H.; Li, C.-J. Coupling without Coupling Reactions: En Route to Developing Phenols as Sustainable Coupling Partners via Dearomatization–Rearomatization Processes. *Acc. Chem. Res*. **2020**, 53, 2395–2413. https://doi.org/10.1021/acs.accounts.0c00479.
(35) Dalton, T.; Faber, T.; Glorius, F. C–H Activation: Toward Sustainability and Applications. *ACS Cent. Sci.* **2021**, 7, 245–261. https://doi.org/10.1021/acscentsci.0c01413.
(36) Alberico, D.; Scott, M. E.; Lautens, M. Aryl−Aryl Bond Formation by Transition-Metal-Catalyzed Direct Arylation. *Chem. Rev.* **2007**, 107, 174–238. https://doi.org/10.1021/cr0509760.
(37) Chen, X.; Engle, K. M.; Wang, D.-H.; Yu, J.-Q. Palladium(II)-Catalyzed C–H Activation/C–C Cross-Coupling Reactions: Versatility and Practicality. *Angew. Chem. Int. Ed.***2009**, 48, 5094–5115. https://doi.org/10.1002/anie.200806273.
(38) Wencel-Delord, J. Towards Mild Metal-Catalyzed C–H Bond Activation. 2011.
(39) Engle, K. M.; Mei, T.-S.; Wasa, M.; Yu, J.-Q. Weak Coordination as a Powerful Means for Developing Broadly Useful C–H Functionalization Reactions. *Acc. Chem. Res.* **2012**, 45, 788–802. https://doi.org/10.1021/ar200185g.
(40) Gorelsky, S. I. Origins of Regioselectivity of the Palladium-Catalyzed (Aromatic)CH Bond Metalation–Deprotonation. *Coordination Chemistry Reviews* **2013**, 257, 153–164. https://doi.org/10.1016/j.ccr.2012.06.016.
(41) Giri, R.; Thapa, S.; Kafle, A. Palladium-Catalysed, Directed C−H Coupling with Organometallics. *Advanced Synthesis & Catalysis* **2014**, 356, 1395–1411. https://doi.org/10.1002/adsc.201400105.
(42) Gensch, T.; Hopkinson, M. N.; Glorius, F.; Wencel-Delord, J. Mild Metal-Catalyzed C–H Activation: Examples and Concepts. *Chem Soc Rev* **2016**, 45, 2900-2936. https://doi.org/10.1039/c6cs00075d
(43) Rogge, T.; Kaplaneris, N.; Chatani, N.; Kim, J.; Chang, S.; Punji, B.; Schafer, L. L.; Musaev, D. G.; Wencel-Delord, J.; Roberts, C. A.; Sarpong, R.; Wilson, Z. E.; Brimble, M. A.; Johansson, M. J.; Ackermann, L. C–H Activation. *Nat Rev Methods Primers* **2021**, 1, 43. https://doi.org/10.1038/s43586-021-00041-2.
(44) Carrow, B. P.; Sampson, J.; Wang, L. Base-Assisted C−H Bond Cleavage in Cross-Coupling: Recent Insights into Mechanism, Speciation, and Cooperativity. *Isr. J. Chem.* **2020**, 60, 230-258. https://doi.org/10.1002/ijch.201900095.
(45) Rosen, B. M.; Quasdorf, K. W.; Wilson, D. A.; Zhang, N.; Resmerita, A.-M.; Garg, N. K.; Percec, V. Nickel-Catalyzed Cross-Couplings Involving Carbon−Oxygen Bonds. *Chem. Rev*. **2011**, 111, 1346–1416. https://doi.org/10.1021/cr100259t.

(46) Li, B.-J.; Yu, D.-G.; Sun, C.-L.; Shi, Z.-J. Activation of "Inert" Alkenyl/Aryl C−O Bond and Its Application in Cross-Coupling Reactions. *Chem. Eur. J.***2011**, 17, 1728–1759. https://doi.org/10.1002/chem.201002273.
(47) Mesganaw, T.; Garg, N. K. Ni- and Fe-Catalyzed Cross-Coupling Reactions of Phenol Derivatives. *Org. Process Res. Dev*. **2013**, 17, 29–39. https://doi.org/10.1021/op300236f.
(48) Tobisu, M.; Chatani, N. Nickel-Catalyzed Cross-Coupling Reactions of Unreactive Phenolic Electrophiles via C–O Bond Activation. *Top Curr Chem (Z)* **2016**, 374, 41. https://doi.org/10.1007/s41061-016-0043-1.
(49) Takise, R. Cross-Coupling of Aromatic Esters and Amides. *Chem Soc Rev*., **2017**, 46, 5864-5888. https://doi.org/10.1039/c7cs00182g
(50) Qiu, Z.; Li, C.-J. Transformations of Less-Activated Phenols and Phenol Derivatives via C–O Cleavage. *Chem. Rev.* **2020**, 120, 10454–10515. https://doi.org/10.1021/acs.chemrev.0c00088.
(51) Zheng, Y.-L. Cross-Coupling Reactions with Esters, Aldehydes, and Alcohols. *Chem. Commun.,* **2021**, 57, 2591-2604. https://doi.org/10.1039/d0cc08389e
(52) Zhao, B.; Prabagar, B.; Shi, Z. Modern Strategies for C–H Functionalization of Heteroarenes with Alternative Coupling Partners. *Chem. Commun.* **2021**, 7, 2585–2634. https://doi.org/10.1016/j.chempr.2021.08.001.
(53) Jin, W.; Yu, Z.; He, W.; Ye, W.; Xiao, W.-J. Efficient Rh(I)-Catalyzed Direct Arylation and Alkenylation of Arene C−H Bonds via Decarbonylation of Benzoic and Cinnamic Anhydrides. *Org. Lett.* **2009**, 11, 1317–1320. https://doi.org/10.1021/ol9000729.
(54) Pan, F.; Lei, Z.-Q.; Wang, H.; Li, H.; Sun, J.; Shi, Z.-J. Rhodium(I)-Catalyzed Redox-Economic Cross-Coupling of Carboxylic Acids with Arenes Directed by N-Containing Groups. *Angew. Chem. Int. Ed.***2013**, 52, 2063–2067. https://doi.org/10.1002/anie.201208362.
(55) Zhang, L.; Xue, X.; Xu, C.; Pan, Y.; Zhang, G.; Xu, L.; Li, H.; Shi, Z. Rhodium-Catalyzed Decarbonylative Direct C2-Arylation of Indoles with Aryl Carboxylic Acids. *Chem. Cat. Chem.* **2014**, 6, 3069–3074. https://doi.org/10.1002/cctc.201402534.
(56) Qiu, X.; Wang, P.; Wang, D.; Wang, M.; Yuan, Y.; Shi, Z. PIII-Chelation-Assisted Indole C7-Arylation, Olefination, Methylation, and Acylation with Carboxylic Acids/Anhydrides by Rhodium Catalysis. *Angew. Chem. Int. Ed.***2019**, 58, 1504–1508. https://doi.org/10.1002/anie.201813182.
(57) Zhang, L. Rh(I)-Catalyzed Decarbonylative Direct C2-Olefination of Indoles with Vinyl Carboxylic Acids. *Chem. Cat. Chem.* **2014**, 6, 3069 – 3074. https://doi.org/10.1002/cctc.201402534
(58) Qiu, R.; Zhang, L.; Xu, C.; Pan, Y.; Pang, H.; Xu, L.; Li, H. Rhodium-Catalyzed Decarbonylative Direct Olefination of Arenes with Vinyl Carboxylic Acids. *Advanced Synthesis & Catalysis* **2015**, 357, 1229–1236. https://doi.org/10.1002/adsc.201401020.
(59) Kwon, S.; Kang, D.; Hong, S. RhI-Catalyzed Site-Selective Decarbonylative Alkenylation and Arylation of Quinolones under Chelation Assistance. *European Journal of Organic Chemistry,* **2015** 17, 3671–3678. https://doi.org/10.1002/ejoc.201500187.
(60) Zhao, H.; Xu, J.; Xu, X.; Pan, Y.; Yu, Z.; Xu, L.; Fan, Q.; Walsh, P. J. Rh(I)-Catalyzed Direct C6−H Arylation of 2-Pyridones with Aryl Carboxylic Acids. *Advanced Synthesis & Catalysis* **2021**, 363, 3995–4001. https://doi.org/10.1002/adsc.202100596.

(61) Amaike, K.; Muto, K.; Yamaguchi, J.; Itami, K. Decarbonylative C–H Coupling of Azoles and Aryl Esters: Unprecedented Nickel Catalysis and Application to the Synthesis of Muscoride A. *J. Am. Chem. Soc.* **2012**, 134, 13573–13576. https://doi.org/10.1021/ja306062c.
(62) Liu, C.; Ji, C.-L.; Zhou, T.; Hong, X.; Szostak, M. Bimetallic Cooperative Catalysis for Decarbonylative Heteroarylation of Carboxylic Acids via C–O/C–H Coupling. *Angew.Chem.Int*. Ed. **2021**, 60,10690–10699. https://doi.org/10.1002/anie.202100949.
(63) Xiang, K.; Zhang, S.; Liu, L.; Huang, T.; Tang, Z.; Li, C.; Xu, K.; Chen, T. Tunable C–H Arylation and Acylation of Azoles with Carboxylic Acids by Pd/Cu Cooperative Catalysis. *Org. Chem. Front.* **2021**, 8, 2543–2550. https://doi.org/10.1039/D1QO00380A.
(64) Muto, K.; Yamaguchi, J.; Itami, K. Nickel-Catalyzed C–H/C–O Coupling of Azoles with Phenol Derivatives. *J. Am. Chem. Soc.* **2012**, 134, 169–172. https://doi.org/10.1021/ja210249h.
(65) Muto, K.; Yamaguchi, J.; Lei, A.; Itami, K. Isolation, Structure, and Reactivity of an Arylnickel(II) Pivalate Complex in Catalytic C–H/C–O Biaryl Coupling. *J. Am. Chem. Soc.* **2013**, 135, 16384–16387. https://doi.org/10.1021/ja409803x.
(66) Meng, L.; Kamada, Y.; Muto, K.; Yamaguchi, J.; Itami, K. C−H Alkenylation of Azoles with Enols and Esters by Nickel Catalysis. *Angewandte Chemie* **2013**, 125, 10232–10235. https://doi.org/10.1002/ange.201304492.
(67) Xu, H.; Muto, K.; Yamaguchi, J.; Zhao, C.; Itami, K.; Musaev, D. G. Key Mechanistic Features of Ni-Catalyzed C–H/C–O Biaryl Coupling of Azoles and Naphthalen-2-Yl Pivalates. *J. Am. Chem. Soc.* **2014**, 136, 14834–14844. https://doi.org/10.1021/ja5071174.
(68) Muto, K.; Hatakeyama, T.; Yamaguchi, J.; Itami, K. C–H Arylation and Alkenylation of Imidazoles by Nickel Catalysis: Solvent-Accelerated Imidazole C–H Activation. *Chem. Sci.* **2015**, 6, 6792–6798. https://doi.org/10.1039/C5SC02942B.
(69) Song, W.; Ackermann, L. Cobalt-Catalyzed Direct Arylation and Benzylation by C–H/C–O Cleavage with Sulfamates, Carbamates, and Phosphates. *Angew. Chem. Int. Ed.***2012**, 51, 8251–8254. https://doi.org/10.1002/anie.201202466.
(70) Moselage, M.; Sauermann, N.; Richter, S. C.; Ackermann, L. C–H Alkenylations with Alkenyl Acetates, Phosphates, Carbonates, and Carbamates by Cobalt Catalysis at 23 °C. *Angew. Chem. Int. Ed.***2015**, 54, 6352–6355. https://doi.org/10.1002/anie.201412319.
(71) Wang, Y.; Wu, S.-B.; Shi, W.-J.; Shi, Z.-J. C–O/C–H Coupling of Polyfluoroarenes with Aryl Carbamates by Cooperative Ni/Cu Catalysis. *Org. Lett.* **2016**, 18, 2548–2551. https://doi.org/10.1021/acs.orglett.6b00819.
(72) Wang, T.-H.; Ambre, R.; Wang, Q.; Lee, W.-C.; Wang, P.-C.; Liu, Y.; Zhao, L.; Ong, T.-G. Nickel-Catalyzed Heteroarenes Cross Coupling via Tandem C–H/C–O Activation. *ACS Catal*. **2018**, 8, 11368–11376. https://doi.org/10.1021/acscatal.8b03436.
(73) Li, S.-S.; Wang, C.-Q.; Lin, H.; Zhang, X.-M.; Dong, L. Rhodium(III)-Catalyzed C–C Coupling of 7-Azaindoles with Vinyl Acetates and Allyl Acetates. *Org. Biomol. Chem*. **2015**, 14, 229–237. https://doi.org/10.1039/C5OB02096D.
(74) Toupalas, G.; Morandi, B. Non-Innocent Electrophiles Unlock Exogenous Base-Free Coupling Reactions. *Nat Catal* **2022**, 5, 324–331. https://doi.org/10.1038/s41929-022-00770-x.
(75) Liégault, B.; Lapointe, D.; Caron, L.; Vlassova, A.; Fagnou, K. Establishment of Broadly Applicable Reaction Conditions for the Palladium-Catalyzed Direct Arylation of

Heteroatom-Containing Aromatic Compounds. *J. Org. Chem.* **2009**, 74, 1826–1834. https://doi.org/10.1021/jo8026565.
(76) Lapointe, D.; Fagnou, K. Overview of the Mechanistic Work on the Concerted Metallation–Deprotonation Pathway. *Chem. Lett.* **2010**, 39, 1118–1126. https://doi.org/10.1246/cl.2010.1118.
(77) Shevlin, M. Practical High-Throughput Experimentation for Chemists. *ACS Med. Chem. Lett.* **2017**, 8, 601–607. https://doi.org/10.1021/acsmedchemlett.7b00165.
(78) Allen, C. L.; Leitch, D. C.; Anson, M. S.; Zajac, M. A. The Power and Accessibility of High-Throughput Methods for Catalysis Research. *Nat Catal* **2019**, 2, 2–4. https://doi.org/10.1038/s41929-018-0220-4.
(79) Mennen, S. M.; Alhambra, C.; Allen, C. L.; Barberis, M.; Berritt, S.; Brandt, T. A.; Campbell, A. D.; Castañón, J.; Cherney, A. H.; Christensen, M.; Damon, D. B.; Eugenio de Diego, J.; García-Cerrada, S.; García-Losada, P.; Haro, R.; Janey, J.; Leitch, D. C.; Li, L.; Liu, F.; Lobben, P. C.; MacMillan, D. W. C.; Magano, J.; McInturff, E.; Monfette, S.; Post, R. J.; Schultz, D.; Sitter, B. J.; Stevens, J. M.; Strambeanu, I. I.; Twilton, J.; Wang, K.; Zajac, M. A. The Evolution of High-Throughput Experimentation in Pharmaceutical Development and Perspectives on the Future. *Org. Process Res. Dev.* **2019,** 23, 1213–1242. https://doi.org/10.1021/acs.oprd.9b00140.
(80) Isbrandt, E. S.; Sullivan, R. J.; Newman, S. G. High Throughput Strategies for the Discovery and Optimization of Catalytic Reactions. *Angew. Chem. Int. Ed.***2019,** 58, 7180–7191. https://doi.org/10.1002/anie.201812534.
(81) Zalesskiy, S. S.; Ananikov, V. P. Pd2(Dba)3 as a Precursor of Soluble Metal Complexes and Nanoparticles: Determination of Palladium Active Species for Catalysis and Synthesis. *Organometallics* **2012,** 31, 2302–2309. https://doi.org/10.1021/om201217r.
(82) Huang, J.; Isaac, M.; Watt, R.; Becica, J.; Dennis, E.; Saidaminov, M. I.; Sabbers, W. A.; Leitch, D. C. DMPDAB–Pd–MAH: A Versatile Pd(0) Source for Precatalyst Formation, Reaction Screening, and Preparative-Scale Synthesis. *ACS Catal.* **2021**, 11, 5636–5646. https://doi.org/10.1021/acscatal.1c00288.
(83) Bates, C. M.; Bates, F. S. 50th Anniversary Perspective: Block Polymers—Pure Potential. *Macromolecules* **2017**, 50, 3–22. https://doi.org/10.1021/acs.macromol.6b02355.
(84) Ji, Y.; Plata, R. E.; Regens, C. S.; Hay, M.; Schmidt, M.; Razler, T.; Qiu, Y.; Geng, P.; Hsiao, Y.; Rosner, T.; Eastgate, M. D.; Blackmond, D. G. Mono-Oxidation of Bidentate Bis-Phosphines in Catalyst Activation: Kinetic and Mechanistic Studies of a Pd/Xantphos-Catalyzed C–H Functionalization. *J. Am. Chem. Soc.* **2015**, 137, 13272–13281. https://doi.org/10.1021/jacs.5b01913.
(85) Becica, J.; Heath, O. R. J.; Zheng, C. H. M.; Leitch, D. C. Palladium-Catalyzed Cross-Coupling of Alkenyl Carboxylates. *Angew. Chem. Int. Ed.***2020**, 59, 17277–17281. https://doi.org/10.1002/anie.202006586.
(86) Flynn, A. B.; Ogilvie, W. W. Stereocontrolled Synthesis of Tetrasubstituted Olefins. *Chem. Rev.* **2007**, 107, 4698–4745. https://doi.org/10.1021/cr050051k.
(87) Polák, P.; Váňová, H.; Dvořák, D.; Tobrman, T. Recent Progress in Transition Metal-Catalyzed Stereoselective Synthesis of Acyclic All-Carbon Tetrasubstituted Alkenes. *Tetrahedron Lett.* **2016**, 57, 3684–3693. https://doi.org/10.1016/j.tetlet.2016.07.030.
(88) Badenock, J. C.; Gribble, G. W. Chapter Four - Metal-Catalyzed Coupling with Heterocycles. In Advances in Heterocyclic Chemistry; Scriven, E. F. V., Ramsden, C. A., Eds.; Heterocyclic

Chemistry in the 21st Century; *Academic Press*, **2016**; 120, 99–136. https://doi.org/10.1016/bs.aihch.2016.04.002.
(89) Jimenez, M. E.; Bush, K.; Pawlik, J.; Sower, L.; Peterson, J. W.; Gilbertson, S. R. Synthesis and Screening of Small Molecule Inhibitors of Anthrax Edema Factor. *Bioorganic & Medicinal Chem. Lett.* **2008**, 18, 4215–4218. https://doi.org/10.1016/j.bmcl.2008.05.059.
(90) Chatterjee, S.; Sahoo, R.; Nanda, S. Recent Reports on the Synthesis of γ-Butenolide, γ-Alkylidenebutenolide Frameworks, and Related Natural Products. *Org. Biomol. Chem.* **2021**, 19, 7298–7332. https://doi.org/10.1039/D1OB00875G.
(91) Caruano, J.; Muccioli, G. G.; Robiette, R. Biologically Active γ-Lactams: Synthesis and Natural Sources. *Org. Biomol. Chem.* **2016**, 14, 10134–10156. https://doi.org/10.1039/C6OB01349J.
(92) Nauen, R.; Jeschke, P.; Velten, R.; Beck, M. E.; Ebbinghaus-Kintscher, U.; Thielert, W.; Wölfel, K.; Haas, M.; Kunz, K.; Raupach, G. Flupyradifurone: A Brief Profile of a New Butenolide Insecticide. *Pest. Manag. Sci.* **2015**, 71, 850–862. https://doi.org/10.1002/ps.3932.
(93) Rattray, B.; Nugent, D. J.; Young, G. Rofecoxib as Adjunctive Therapy for Haemophilic Arthropathy. *Haemophilia* **2005**, 11, 240–244. https://doi.org/10.1111/j.1365-2516.2005.01087.x.
(94) Noh, Min Su; Shin, Jong Heon; Ahn, Seong Jin; Kwon, O Seok. Preparation of indole-γ-lactam compound for the treatment of disease related to hypoadiponectinemia. KR2022162059. December 7, **2022.**
(95) Palczewski, K.; Chen, Y.; Lipkovic, H. Compounds and Methods of Treating Retinal Degeneration. US 20200230119, January 11, **2018.**
(96) Yadykov, A. V.; Scherbakov, A. M.; Trofimova, V. V.; Lvov, A. G.; Markosyan, A. I.; Zavarzin, I. V.; Shirinian, V. Z. Photoswitching off the Antiproliferative Activity of Combretastatin A-4 Analogues. *Org. Lett.* **2019**, 21, 9608–9612. https://doi.org/10.1021/acs.orglett.9b03780.
(97) Ripka, A.; Shapiro, G.; Chesworth, R. 5- And 6-Membered Heterocyclic Compounds as Phosphodiesterase Inhibitors and Their Preparation, Pharmaceutical Compositions and Use in the Treatment of CNS Disorders and Disorders Affected by CNS Function. WO 2009158473, December 30, **2009**.
(98) Rousseaux, S.; Gorelsky, S. I.; Chung, B. K. W.; Fagnou, K. Investigation of the Mechanism of C(Sp3)−H Bond Cleavage in Pd(0)-Catalyzed Intramolecular Alkane Arylation Adjacent to Amides and Sulfonamides. *J. Am. Chem. Soc.* **2010**, 132, 10692–10705. https://doi.org/10.1021/ja103081n.
(99) Wakioka, M.; Nakamura, Y.; Montgomery, M.; Ozawa, F. Remarkable Ligand Effect of P(2-$MeOC_6H_4)_3$ on Palladium-Catalyzed Direct Arylation. *Organometallics* **2015**, 34, 198–205. https://doi.org/10.1021/om501052g.
(100) Kozuch S.; Shaik S. How to Conceptualize Catalytic Cycles? The Energetic Span Model. *Acc. Chem. Res.* **2011**, 44, 101-110. https://doi.org/10.1021/ar1000956
(101) Leitch D. C. ; Lam Y. C.; Labinger J. A.; Bercaw J. E. Upgrading Light Hydrocarbons via Tandem Catalysis: A Dual Homogeneous Ta/Ir System for Alkane/Alkene Coupling. *J. Am.. Chem. Soc.* **2013**, *135*, 10302-10305. https://doi.org/10.1021/ja405191a

CHAPTER 3: Direct Heterocycle C–H Alkenylation via Dual Catalysis Using a Palladacycle Precatalyst: Multifactor Optimization and Scope Exploration Enabled by High-Throughput Experimentation

This chapter has been adapted from:

Nahiane Pipaon Fernandez, Odhran Cruise, Sarah E. F. Easton, Justin M. Kaplan, John L. Woodard, Damian P. Hruszkewycz, and David C. Leitch. *J. Org. Chem.* **2024**, *ASAP*, DOI: 10.1021/acs.joc.3c02311

Contributions:

Synthesis of starting materials, high-throughput experiments and reaction optimization, reaction monitoring experiments, scope and the monitoring of palladium species were performed by Nahiane Pipaon Fernandez. High-throughput experiments and synthesis optimization of **1d**, **1e**, **1f** and **1g** were performed by Odhran Cruise. High-throughput experiments with **1k** and **1l** were performed by Sarah Easton. Initial reaction development and the larger scale synthesis were performed by John Woodard, Justin Kaplan and Damian Hruszkewycz of GSK.

3.1 Abstract

One of the major challenges in developing catalytic methods for C–C bond formation is the identification of generally applicable reaction conditions, particularly if multiple substrate structural classes are involved. Pd-catalyzed direct arylation reactions are powerful transformations that enable direct functionalization of C–H bonds; however, the corresponding direct alkenylation reactions, using vinyl (*pseudo*)halide electrophiles, are less well developed (Figure 3.1). Inspired by process development efforts toward **GSK3368715**, an investigational

active pharmaceutical ingredient, this chapter describes how a Pd(II) palladacycle derived from tri-*tert*-butylphosphine and $Pd(OAc)_2$ is an effective single-component precatalyst for a variety of direct alkenylation reactions. High-throughput experimentation identified optimal solvent/base combinations for a variety of HetAr–H substrate classes undergoing C–H activation without the need for co-catalysts or stoichiometric silver bases (e.g. Ag_2CO_3). This reaction is proposed to proceed *via* a dual cooperative catalytic mechanism, where *in situ* generated Pd(0) supports a standard Pd(0)/(II) cross-coupling cycle, and the palladacycle performs C–H activation *via* CMD in a redox-neutral cycle. In all, 192 substrate combinations were tested, with a hit-rate of approximately 40%, and 24 of these examples were isolated on preparative scale. Importantly, this method was applied to prepare a key intermediate in the synthesis of **GSK3368715** on multigram scale.

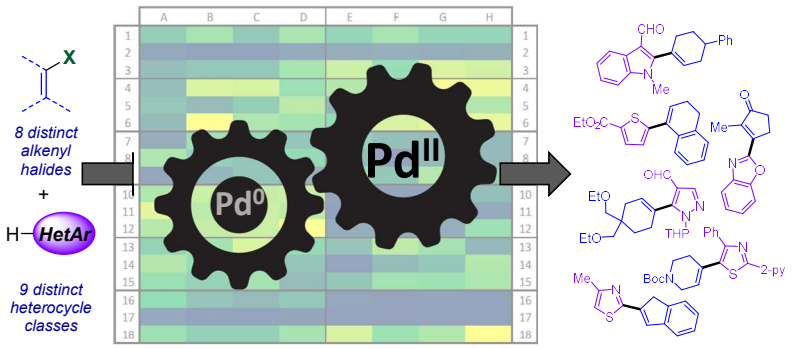

Figure 3.1. HTE mediated direct alkenylation of heterocycles reaction optimization and scope exploration.

3.2 Introduction

Catalytic C–H bond functionalization is a powerful and increasingly established method for complex molecule synthesis.[1–7] The ability to directly use C–H bonds as sites for reactivity means synthetic sequences toward biologically-active compounds are generally more atom- and step-efficient, which is critical for more sustainable syntheses.[8–13] One key C–H functionalization reaction that is becoming widely used in active pharmaceutical ingredient (API) syntheses is Pd-catalyzed direct arylation, especially for heterocycle functionalization.[14–20] Fagnou's seminal paper on general direct arylation conditions remains a go-to resource for many applications.[21]

Despite the general use of direct arylation reactions applied to synthetic problems, the corresponding direct *alkenylation* reactions are less common.[22–25] As discussed in Chapter 2, the ability to alkenylate (hetero)arenes leads to products with potential for further functionalization. For example, these reactions provide a two-step method to selectively alkylate a heterocycle, wherein the alkene is hydrogenated after C–C bond formation; in other words, a two-step, formal Csp^2–Csp^3 coupling. This is an alternative to direct catalytic Csp^2–Csp^3 coupling, such as Negishi coupling or Ni-catalyzed photoredox methods (Figure 3.2).[26]

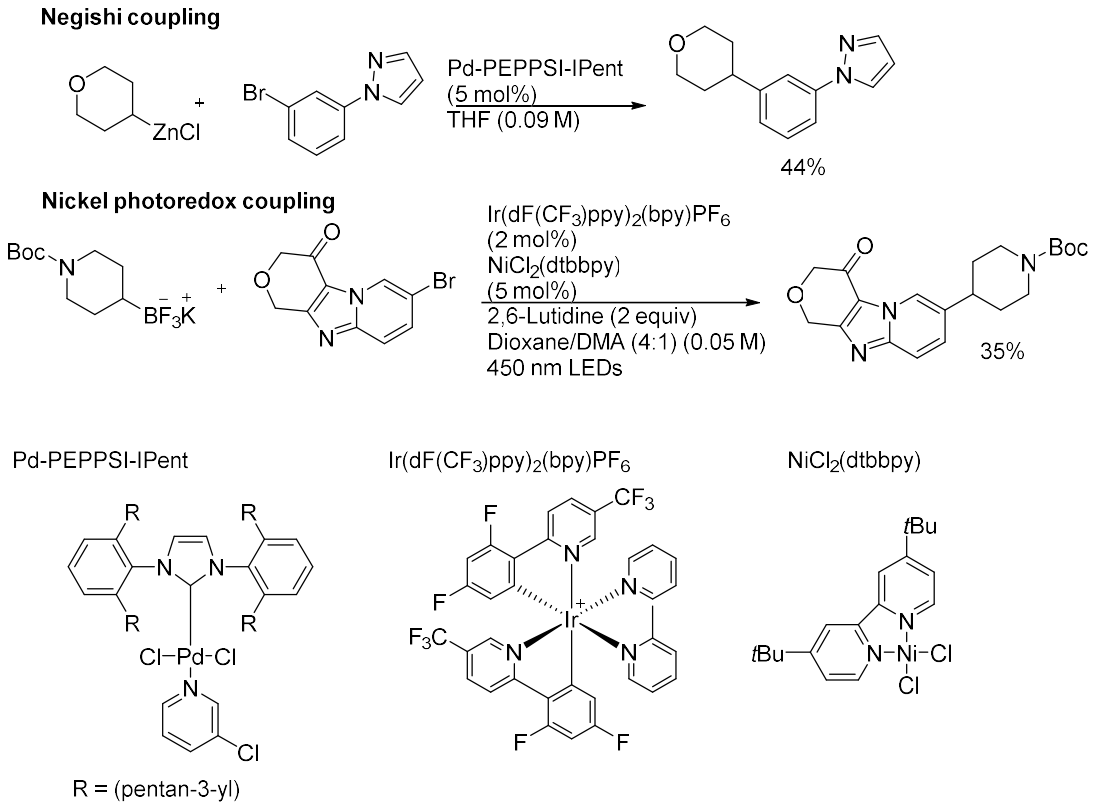

Figure 3.2. Examples of Negishi and Nickel photoredox coupling of Csp^2–Csp^3 bonds.

While these direct approaches are powerful, they often rely on use of alkyl organometallic intermediates and/or halogenated heteroarenes. If these substrates are not readily available, they can be difficult to synthesize or (in the case of reactive organometallics) be unstable. In contrast, direct alkenylation/hydrogenation requires only a suitable heterocycle and vinyl (*pseudo*)halide. Finally, alkenes are versatile synthetic handles for other functionalizations *via* addition reactions and other transformations. In the synthesis of **GSK3368715**, an investigational API reported in 2019 that contains an alkylated pyrazole as the key structural feature, instead of a Csp^2–Csp^3 coupling, direct alkenylation followed by hydrogenation of the alkene would facilitate its synthesis (Figure 3.3).[27]

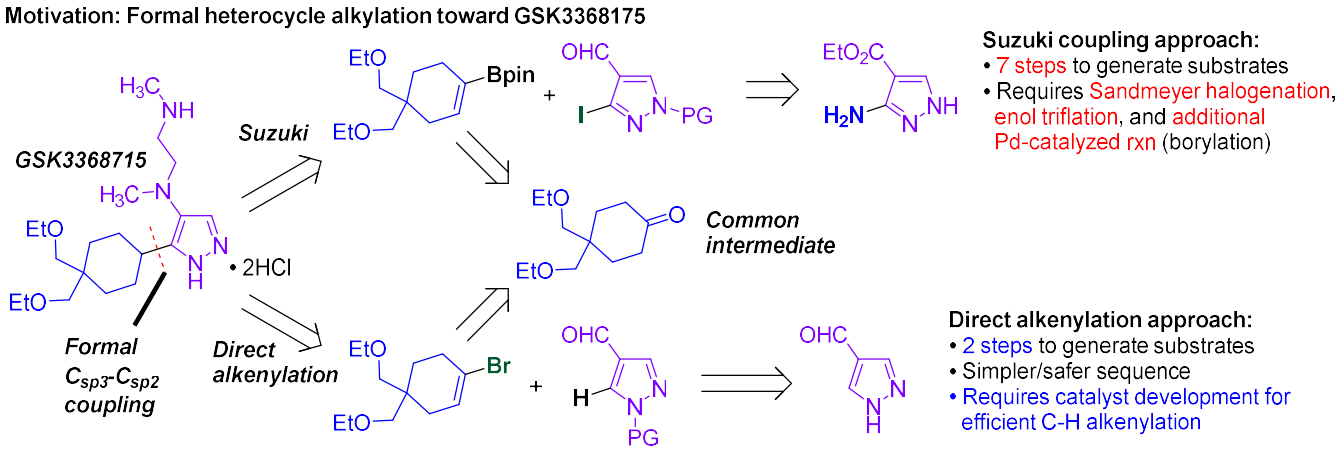

Figure 3.3. Approaches toward **GSK3368715** involving formal Csp^2–Csp^3 coupling, either through Suzuki coupling or direct alkenylation.

The initial supply synthesis of this compound relied on a Suzuki coupling to make the bond between the cyclohexyl ring and pyrazole, followed by hydrogenation. This approach requires 7 steps to generate the coupling partners from available starting materials, including a Sandmeyer iodination of the pyrazole, and triflation/borylation of the cyclohexenyl unit. Direct Csp^2–Csp^3 coupling would not offer any advantages on the amount of steps needed to access the coupling partners. In contrast, the coupling partners required for the direct alkenylation can be accessed in two simple steps each, and would avoid the challenges of the previously reported synthetic route, including the poor stability of the vinyl boronate, and safety concerns in the formation and iodination of the pyrazole diazonium intermediate.

Direct alkenylation of (hetero)aromatic C–H bonds with vinyl (*pseudo*)halides are reported with several catalyst systems, including Cu,[28–30] Ni,[31–34] Ru,[35–38] and predominantly Pd (Figure 3.4). The first Pd-catalyzed direct alkenylation was reported by Daugulis in 2005, using amide directing groups to achieve arene C–H activation.[39] Key contributions from Ackermann,[40–42] Alami,[43,44] Doucet,[45] Berteina-Raboin,[46] Moran,[47] Hoarau/Couve-Bonnaire/Pannecoucke/

Bischoff,[48–50] Piguel,[22,51] Charette,[52] Bouillon/Poisson,[53,54] and Lei/Kwong[55] have expanded the scope and efficiency of these reactions. Chapter 2 described the development of a Pd-catalyzed direct alkenylation of heterocycles using activated enol pivalates, which proceeds without the need for exogenous base.[56]

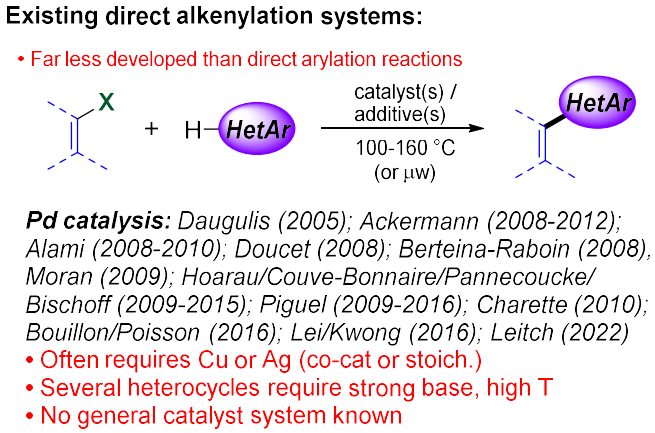

Figure 3.4. Prior work in Pd-catalyzed direct alkenylation reactions, characterized by substrate-dependent reaction conditions.

However, there are several issues with the reported examples. Many reactions require Cu or especially Ag additives, often in stoichiometric amounts (e.g. Ag-containing bases), likely to perform the C–H activation step (see below).[57–64] In addition, high reaction temperatures or microwave conditions are necessary, which are not compatible with large scale synthesis of the product. They also involve the use of strong bases that may be incompatible with sensitive functional groups. Furthermore, each class of heterocycle seems to require a specific catalyst/reaction system; there is no general system for a wide range of heterocycles. Finally, vinyl

electrophile side-reactivity has the potential to complicate reaction development and lead to lower yields/purification challenges.

From a mechanistic standpoint, the role of stoichiometric amounts of metal additives is still unclear. It is commonly proposed they act as halide scavengers or oxidants;[58] however, replacing the silver salts by other additives that should perform the same role often shuts down the reaction. This behaviour has raised a question about the role of silver in C–H activation. Recent mechanistic studies suggest that Ag complexes are responsible for C–H activation of electron-deficient arenes.[58] Deuteration experiments have shown that silver species are able to catalyze H/D exchange reactions with heterocycles, and therefore are able to perform C–H bond cleavage.[65] The same experiments with palladium sources did not show any H/D exchange.[66] Silver carboxylates can, therefore, bond with phosphines and promote the C–H activation step (Figure 3.5).

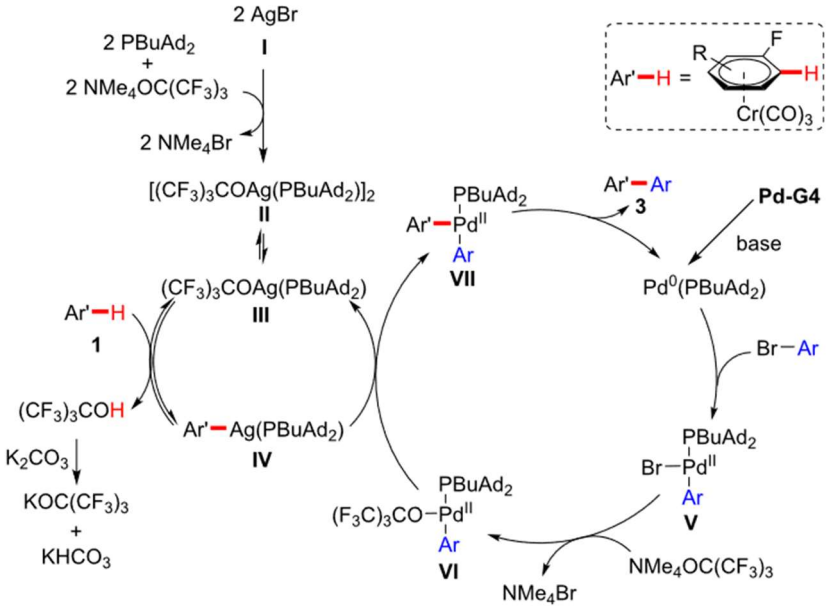

Figure 3.5. Proposed Mechanism for Ag(I)/Pd Cocatalyzed C–H arylation of fluorobenzene derivatives with bromoarenes. Reprinted with permission from *ACS Catal.* **2020**, *10*, 2100–2107. Copyright {2020} American Chemical Society.[59]

Recently, dual copper/palladium systems have been described. These catalyst systems enable the cooperative action of cooper and palladium for the synthesis of heterobiaryl compounds[60,67] with low catalyst loadings,[68] The proposed mechanism of these dual systems also claims that the C–H bond cleavage is done by the second metal catalyst, copper (Figure 3.6).

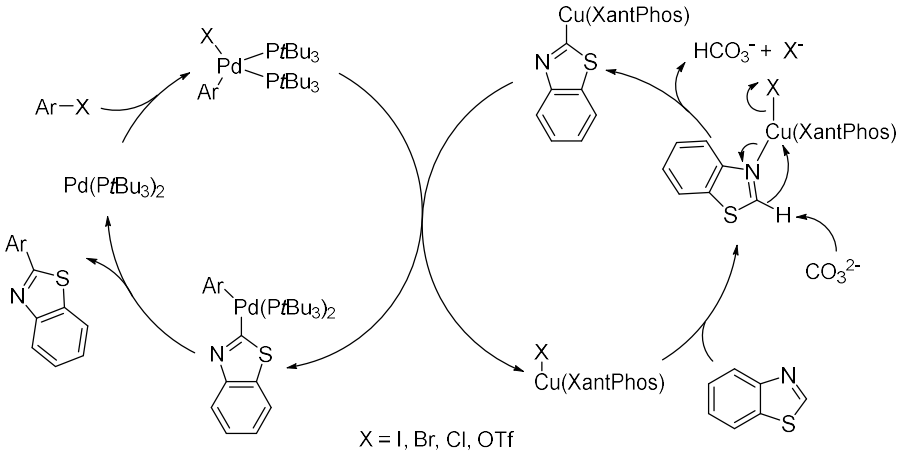

Figure 3.6. Proposed mechanism for Cu/Pd cocatalyzed direct arylation reaction.

The experimental observations conclude that the oxidative addition of the aryl halide or aryl carboxylate is done at the palladium center, while the copper catalyst facilitates deprotonation of the C–H bond on the heterocycle. The two catalytic cycles intersect during the transmetallation where the aryl species attached to the copper migrates to the palladium metal centre. Finally, C–C reductive elimination from palladium leads to the final product (Figure 3.7).[69]

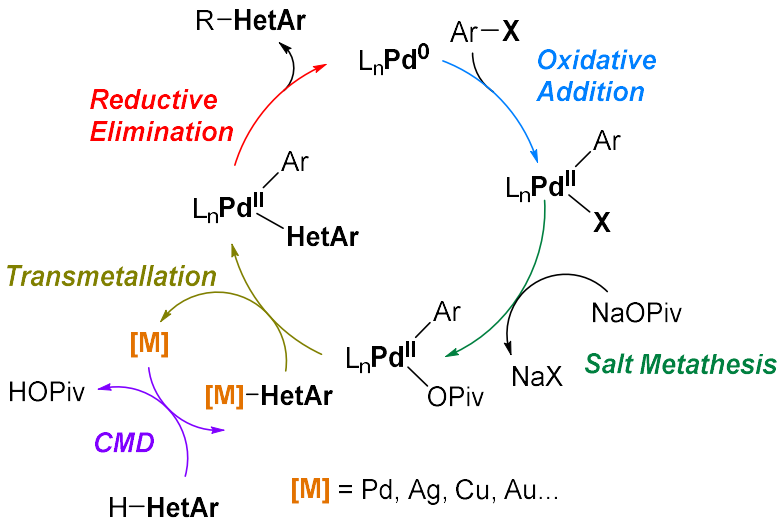

Figure 3.7. Suggested general mechanism for dual metal catalyzed C–H activation reactions.

3.3 Results and Discussion

In this work, a palladacycle derived from P(*t*Bu)$_3$, first reported by Stambuli in 2011[70], is reported as an active single-component precatalyst for a wide range of direct alkenylation reactions (Figure 3.8). Multifactor optimization by parallel-in-parallel microscale high-throughput experimentation[71–77] and larger scale Design of Experiments (DoE) studies[78–80] on multiple substrate combinations have identified optimal solvent/base combinations for 9 distinct heterocycle classes. Importantly, no co-catalysts or transition metal additives are required; the palladacycle precatalyst only requires a change of solvent and/or base to be widely applicable.[81]

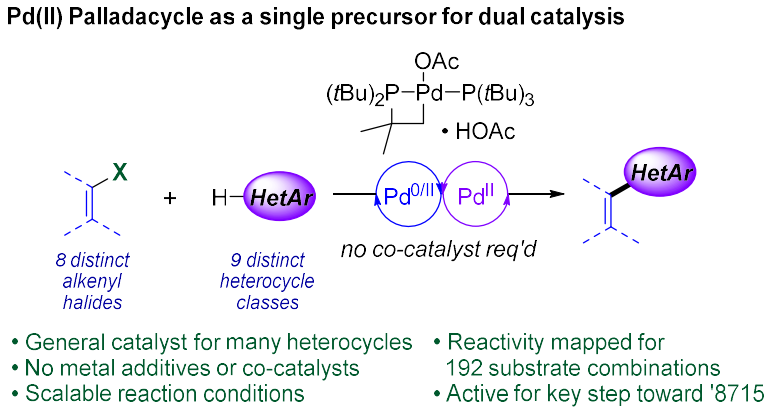

Figure 3.8. A palladacycle complex as a single-component precatalyst for diverse direct alkenylation reactions.

3.3.1 Catalyst Evaluation

Initial reaction development of the direct alkenylation toward the synthesis of **GSK3368715** (Figure 3.3) revealed several trends that informed the present study. Using a catalyst system resembling that reported by Fagnou[21], $Pd(OAc)_2$ / PCy_3, initial studies done at GSK revealed that stoichiometric Ag (0.6 equiv Ag_2CO_3) was required for catalysis to proceed. Furthermore, a large amount of PCy_3 was necessary, likely to coordinate both Pd and Ag.[59] While they were able to achieve 71% solution yield of the key intermediate using these conditions (eq. 3.1), serious challenges were discovered during the scale-up of the reaction. These include the formation of a thick slurry that made agitation difficult as the reaction proceeded, and formation of silver mirrors on the reactor walls. As a result, alternative reaction conditions were needed to proceed with scale-up.

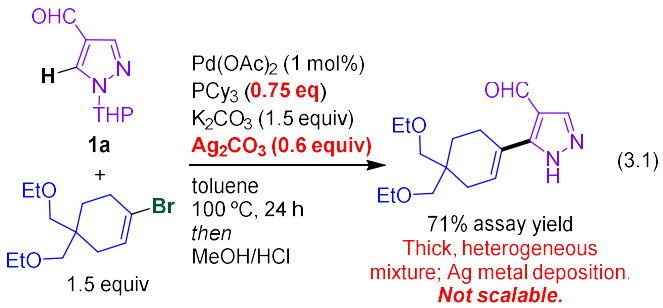

The first challenge that was targeted was the need for Ag additives. Exhaustive evaluation of phosphine ligands *via* high-throughput experimentation (HTE) in combination with $Pd(OAc)_2$ at GSK revealed P(*t*Bu)$_3$ and P(*o*-tol)$_3$ as uniquely effective in the absence of Ag additives. The reason behind the reactivity for these two specific ligands could be the formation of known palladacycles *via* cyclometalation.[70,82–86] Therefore, this research project was focused on direct alkenylation screening using four known single-component precatalysts (**I**-**IV**, Figure 3.9). A non-palladacycle system based on the Fagnou conditions – $Pd(PCy_3)_2(OAc)_2$ (**I**) – was included for comparison purposes. Stambuli showed that the combination of $Pd(OAc)_2$ and 2 equiv of P(*t*Bu)$_3$ in THF rapidly generates palladacycle **II**, which was isolated as reported and used as the acetic acid solvate.[70] The commercially available JohnPhos-based palladacycle (**III**) was included as another comparator with a different metallacycle structure. And finally, the well-known Herrmann-Beller catalyst was also included (**IV**, from P(*o*-tol)$_3$).[82,83]

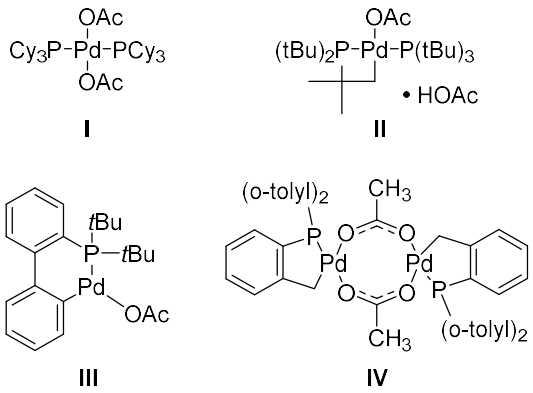

Figure 3.9. Single component precatalysts evaluated for direct alkenylation.

These four precatalysts were evaluated in a 96-experiment multifactor screen for the alkenylation of THP-protected pyrazole **1a** (Figure 3.10). Four solvents, three bases, and two model vinyl bromides (**2a** and **2b**) were tested for each catalyst. Polar and non-polar solvents with high boiling points were chosen: *N,N*-dimethylacetamide (DMA), toluene, cyclopentylmethyl ether (CPME) and *tert*-amyl alcohol (TAA). In addition to the three inorganic bases (K_3PO_4, K_2CO_3, and Cs_2CO_3), 2-ethylhexanoic acid (2-EHA, less volatile alternative to pivalic acid) was used as an additive to facilitate the CMD reaction.[87–90] Each reaction was carried out at high Pd loading (20 mol%), and subsequently analyzed by LCMS using area percent values (LC area percent: LCAP). For the initial evaluation, the consumption of **1a** was used to evaluate the success of the reaction (values in Figure 3.10) and product presence was confirmedby matching *m*/*z* values for **3aa** and **3ab** to peaks in the chromatograms. Several trends are apparent within the screening results. Catalyst **I** underperforms relative to the three palladacycle systems, likely due to the absence of Ag-containing additives that were required for good activity in preliminary experiments. K_2CO_3 significantly underperforms as a base relative to K_3PO_4 and Cs_2CO_3 regardless of the catalyst or solvent. No clear solvent trend is apparent, beyond DMA generally

underperforming relative to the other solvents. And finally, palladacycle **IV** seems to outperform catalysts **II** and **III** under these conditions involving high catalyst loading. More extensive comparisons of **II** and **IV** are in Appendix B (Fig. B2).

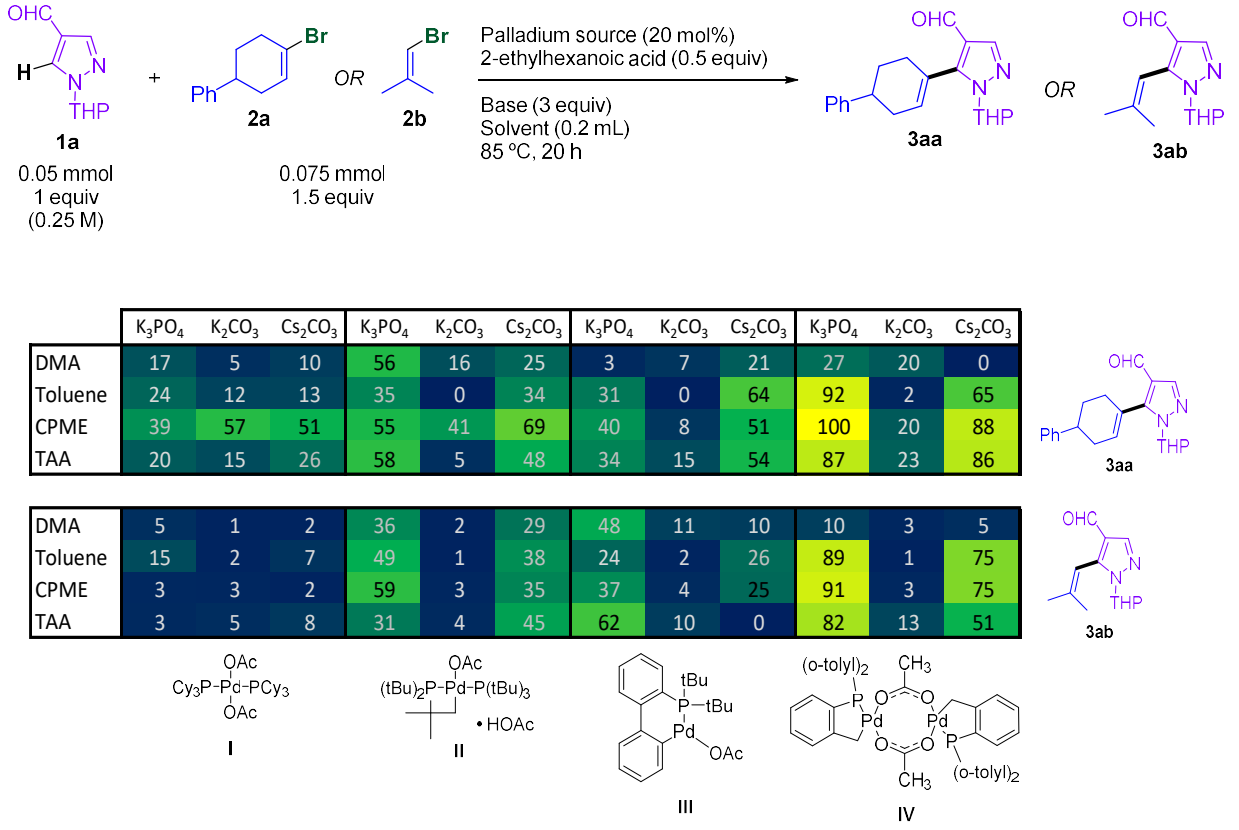

Figure 3.10. Multifactor evaluation of catalysts for direct alkenylation of pyrazole **1a** with two vinyl bromides (**2a** and **2b**), three bases (K_3PO_4, K_2CO_3, Cs_2CO_3), and four solvents (DMA, Toluene, CPME, and TAA). Outcome values correspond to % conversion of **1a** as measured by LCMS: 1.00 – [LCAP/LCAP0] • 100%.

While these screening results suggest Herrmann-Beller palladacycle **IV** is superior to the other Pd sources, we carried out several additional experiments under high Pd-loading HTE conditions (0.05 mmol, 20 mol% Pd, 47 reactions) and lower-Pd loading validation conditions

(0.10 mmol, 5 mol% Pd, 64 reactions). This enabled holistic comparison of the four Pd sources for multiple base/solvent combinations and coupling partners (see Tables B1-B13 in Appendix B for details). Figure 3.11 summarizes the average turnover number (TON) for each catalyst across these experiments, revealing the superiority of **II** at lower Pd loading. Our hypothesis is that the catalytic species generated from **II** are more stable under the reaction conditions, leading to more turnovers per catalytic site, and therefore a higher TON at lower loading. Further investigations to probe this possibility are underway. These results highlight the importance of validating several potential hits from HTE screening, rather than simply studying the one "best" set of conditions. Accordingly, we moved forward with palladacycle **II** for further study.

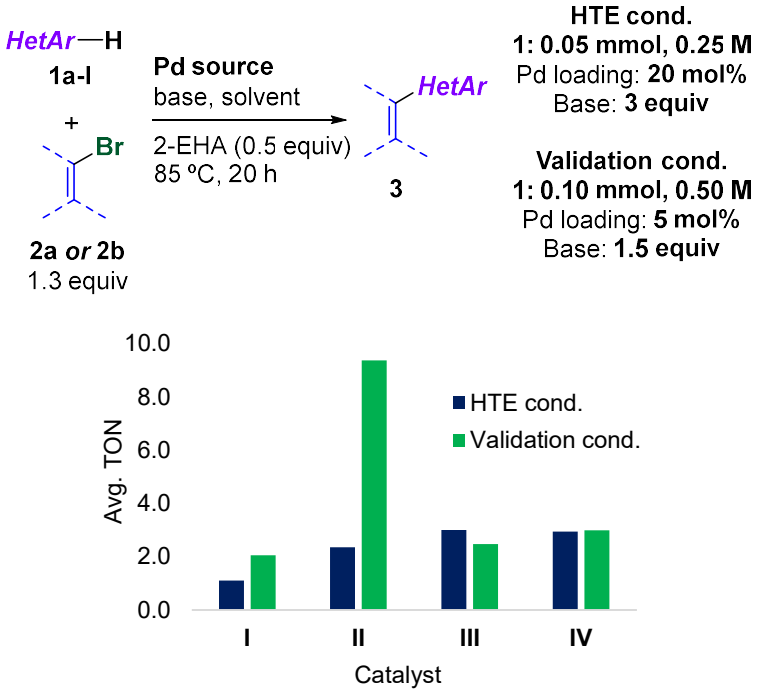

Figure 3.11. Catalyst comparison under two sets of conditions: HTE (high Pd, low [1a]) and validation (low Pd, high [1a]). Yields are obtained by ^{1}H NMR spectroscopy using 1,3,5-trimethoxybenzene as an internal standard; TON = [%yield] / [Pd mol%].

3.3.2 Multifactor optimization for different heterocycles.

Having established **II** as the most robust precatalyst across a range of reaction conditions, its reactivity towards a variety of heterocycle substrates was evaluated. As remarked in the introduction, although direct arylation has a general catalyst system ($Pd(OAc)_2/PCy_3$) for a broad scope of substrates,[21] the same case is not observed for direct alkenylation reactions. Rather than just apply the best solvent/base combination identified for the formation of **3aa** and/or **3ab**, a multifactor, 144-experiment array was carried out to evaluate four solvents and three bases in the direct alkenylation of twelve heterocycles (Figure 3.12). These include two pyrazoles (**1a**, **1b**), two thiazoles (**1c**, **1d**), two thiophenes (**1e**, **1f**), benzothiazole (**1g**), benzothiophene (**1h**), benzoxazole (**1i**), oxazole (**1j**), an indole (**1k**), and an imidazopyridine (**1l**). Because this study generated 12 different products, product formation was confirmed by LCMS and ^{1}H NMR spectroscopic analysis, and external calibration was used to calculate solution yields versus internal standard (1,3,5-trimethoxybenzene).

As expected for an array of many heterocycle classes, there is not one generally-optimal set of conditions. For pyrazoles **1a** and **1b**, it was observed that K_2CO_3 is inferior to K_3PO_4 and Cs_2CO_3, and several solvents give >50% solution yield. Thiazoles **1c** (both regioisomers observed) and **1d**, as well as benzothiazole **1g**, perform well under many different solvent/base combinations, including with K_2CO_3, giving quantitative yield in several cases. In contrast, thiophenes **1e** and **1f**, and especially benzothiophene **1h**, perform relatively poorly, with only a few solvent/base combinations reaching >50% yield (and none for **1h**). Benzoxazole **1i** generally outperforms oxazole **1j**. Finally, azoles **1k** and **1l** are unreactive with K_2CO_3, but work well with Cs_2CO_3 with a number of solvents.

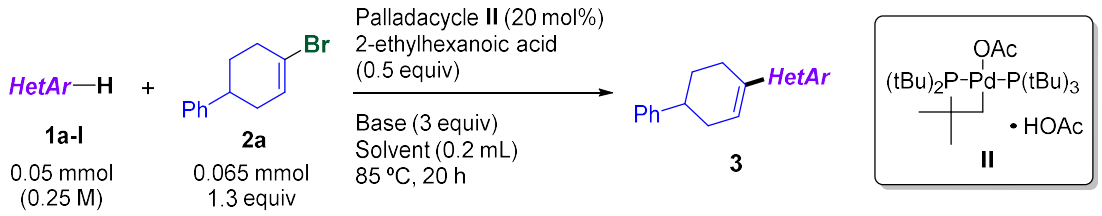

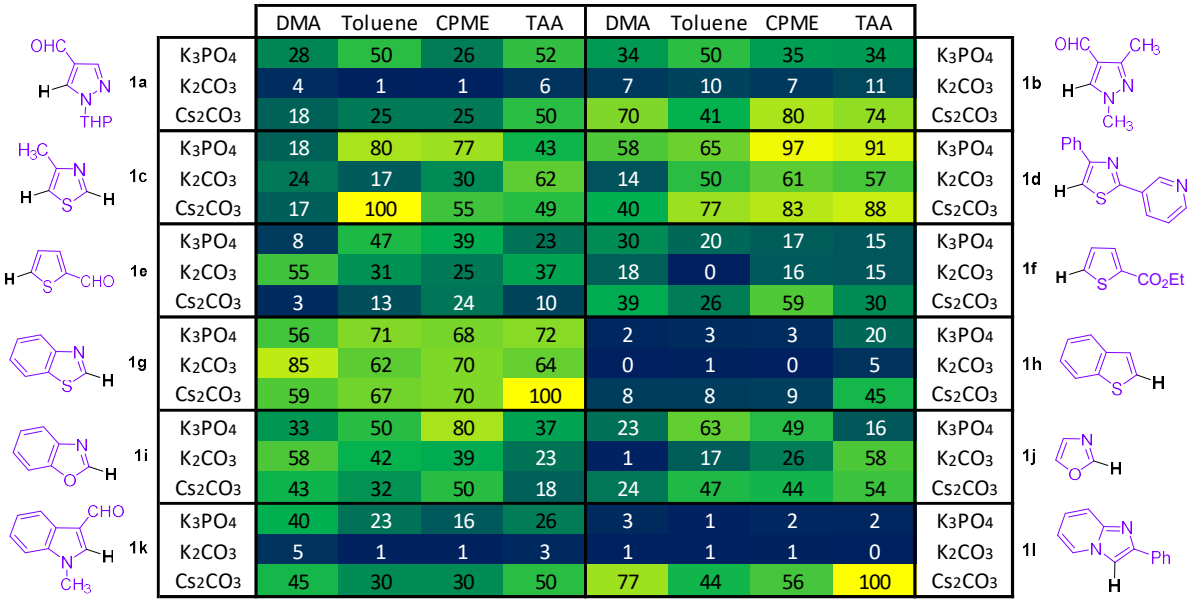

		DMA	Toluene	CPME	TAA	DMA	Toluene	CPME	TAA		
1a	K_3PO_4	28	50	26	52	34	50	35	34	K_3PO_4	1b
	K_2CO_3	4	1	1	6	7	10	7	11	K_2CO_3	
	Cs_2CO_3	18	25	25	50	70	41	80	74	Cs_2CO_3	
1c	K_3PO_4	18	80	77	43	58	65	97	91	K_3PO_4	1d
	K_2CO_3	24	17	30	62	14	50	61	57	K_2CO_3	
	Cs_2CO_3	17	100	55	49	40	77	83	88	Cs_2CO_3	
1e	K_3PO_4	8	47	39	23	30	20	17	15	K_3PO_4	1f
	K_2CO_3	55	31	25	37	18	0	16	15	K_2CO_3	
	Cs_2CO_3	3	13	24	10	39	26	59	30	Cs_2CO_3	
1g	K_3PO_4	56	71	68	72	2	3	3	20	K_3PO_4	1h
	K_2CO_3	85	62	70	64	0	1	0	5	K_2CO_3	
	Cs_2CO_3	59	67	70	100	8	8	9	45	Cs_2CO_3	
1i	K_3PO_4	33	50	80	37	23	63	49	16	K_3PO_4	1j
	K_2CO_3	58	42	39	23	1	17	26	58	K_2CO_3	
	Cs_2CO_3	43	32	50	18	24	47	44	54	Cs_2CO_3	
1k	K_3PO_4	40	23	16	26	3	1	2	2	K_3PO_4	1l
	K_2CO_3	5	1	1	3	1	1	1	0	K_2CO_3	
	Cs_2CO_3	45	30	30	50	77	44	56	100	Cs_2CO_3	

Figure 3.12. Multifactor optimization of direct alkenylation for 12 heterocycles using palladacycle **II**. Values given are yields and they are obtained by ^{1}H NMR spectroscopy using 1,3,5-trimethoxybenzene as an internal standard.

Taking a holistic view of these data, the success of various solvent/base combinations are tied to the specific class of heterocycle undergoing alkenylation. This is not surprising, since deprotonation of the reactive C–H bond is a key factor in the reaction mechanism.[87–90] Several heterocycles, particularly the azoles, require stronger bases: K_2CO_3 results in only 23% average yield across the array (compared to 39% and 43% for K_3PO_4 and Cs_2CO_3, respectively), and only 23% of K_2CO_3 containing reactions reach >50% yield (compared to 35% and 42% for the others).

Surprisingly, DMA – the solvent of choice in Fagnou's generally-applicable protocol[21] – is also generally poor in this array: the average yield of DMA-based reactions is only 29% (compared to 35-40% for the other solvents), and only 22% of DMA-based reactions reach >50% yield (compared to 33-39% for the other solvents).

Using clusters of the best performing solvent/base combinations for each heterocycle as a starting point, condition optimization was performed in each case under our validation conditions (5 mol% Pd, 0.50 M in limiting reagent). In several cases, these studies revealed a large drop in yield from 20 mol% Pd HTE conditions. Particularly evident case was benzoxazole **1i**, which dropped from 80% solution yield to only 10% at 5 mol% Pd. This could be due to several factors, including the solid/liquid heterogeneous nature of many of these reactions, and the change in vessel size/headspace volume from HTE to preparative scale.

A two-level, three-factor full factorial DoE study was performed to identify a combination of catalyst loading, reaction concentration, and base equivalents that would give a synthetically useful yield at reasonable Pd loading (Figure 3.13). From these data, success with 5 mol% Pd requires a combination of higher concentration (0.50 M) and 3 equiv base, reaching 55% yield; increasing the Pd loading to 10 mol% results in 80% yield. Two other heterocycles, thiazole (**1c**) and imidazopyridine (**1l**), also underwent full factorial DoE analysis and further optimization (Tables B15 and B16 in Appendix B).

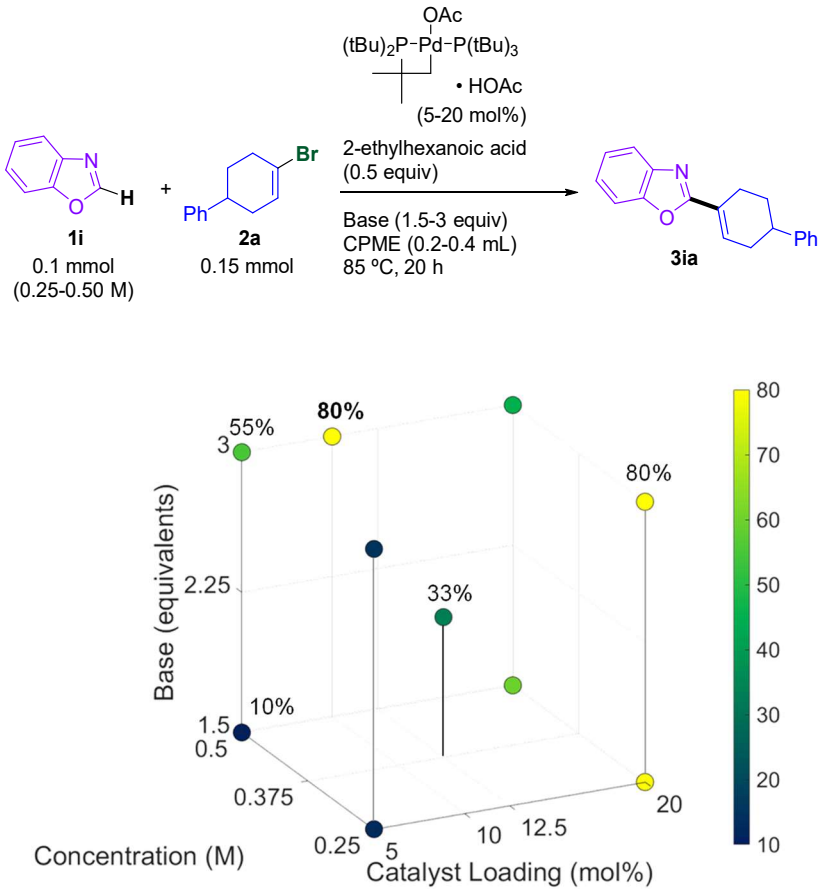

Figure 3.13. Full factorial analysis of direct alkenylation of **1i** with **2a**, revealing conditions for >50% yield at 5 mol% Pd. Yields determined by NMR spectroscopy.

The results of these validation/optimization studies led to a set of two solvents (CPME, TAA) and two bases (K_3PO_4, Cs_2CO_3) that were generally applicable across the various heterocycle classes. Figure 3.14 summarizes the solvent/base combinations and other modifications to the general conditions. For each heterocycle class, solution yields by ^{1}H NMR spectroscopy are given for exemplar alkenylation products. Even under optimized conditions, three products form when **1c** undergoes alkenylation: the major regioisomer is functionalized at C_2 (**3ca**, 30% yield), and C_5 alkenylation and dialkenylation (both C_2 and C_5) form in 15% yield each.

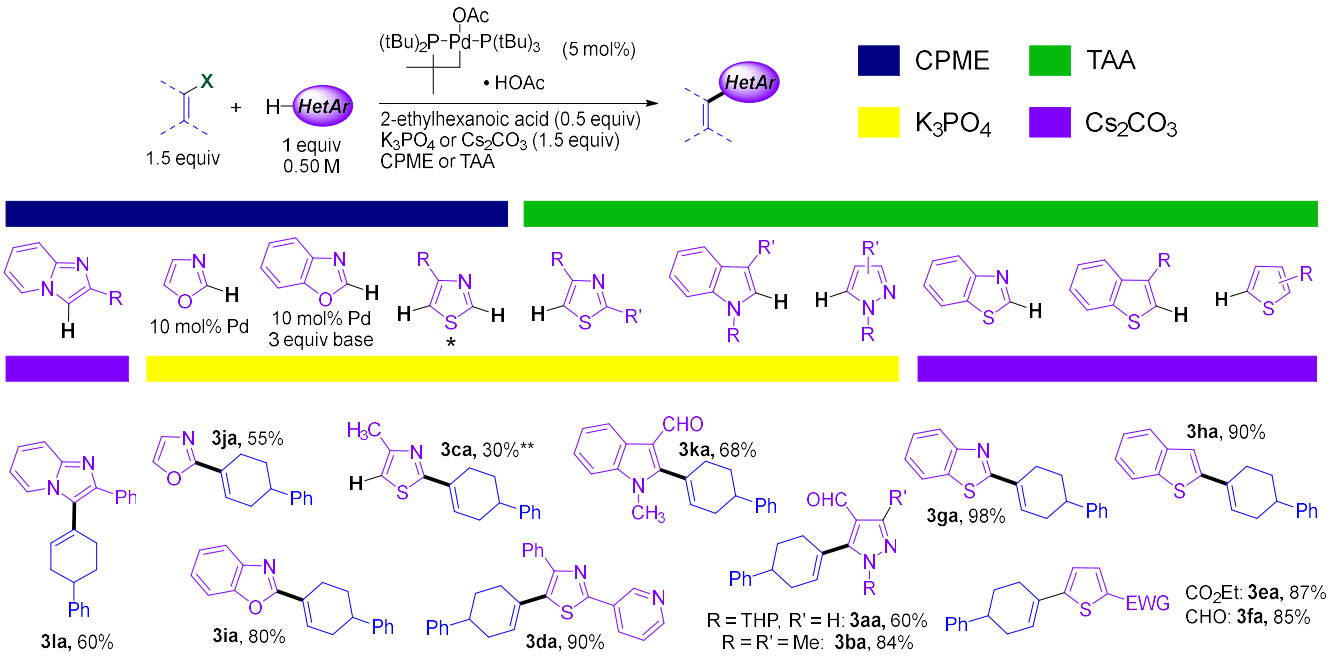

Figure 3.14. Optimized preparative scale conditions for direct alkenylation of each heterocycle class, organized by solvent/base combinations, with modifications indicated. Solution yields by ^{1}H NMR spectroscopy versus TMB internal standard are given for each optimized alkenylation with **1a**. *Alkenyl halide: 1 equiv, 0.25 M, thiazole: 1.5 equiv (concentration reduced and stoichiometry inverted to control selectivity). **Additional 15% of C_5 alkenylation, and 15% of C_2+C_5 alkenylation (see Table B18 in Appendix B for more details).

3.3.3 Evidence for cooperative dual catalytic mechanism.

Prior studies by Hartwig and co-workers on Pd-catalyzed direct arylation of pyridine *N*-oxide using P(*t*Bu)$_3$-based catalysts revealed that two distinct catalytic cycles operate in tandem (Figure 3.15).[91] Specifically, they propose that a palladacyclic species analogous to **II** is responsible for HetAr–H activation *via* CMD, while a separate Pd(0) species is responsible for C–X oxidative addition. Pd-to-Pd transmetalation of the HetAr group to the oxidative addition complex then enables C–C bond formation *via* reductive elimination. A key finding in the Hartwig study is that both Pd(II) and Pd(0) precatalysts – in the form of a palladacycle and Pd[P(*t*Bu)$_3$]$_2$, respectively – are required for catalytic direct arylation (Figure 3.15). In their case, the reaction rate was

proportional to only the Pd(II) palladacycle loading, and independent of the Pd[P(*t*Bu)$_3$]$_2$ loading; however, in all cases both Pd(II) and Pd(0) were added at the outset.

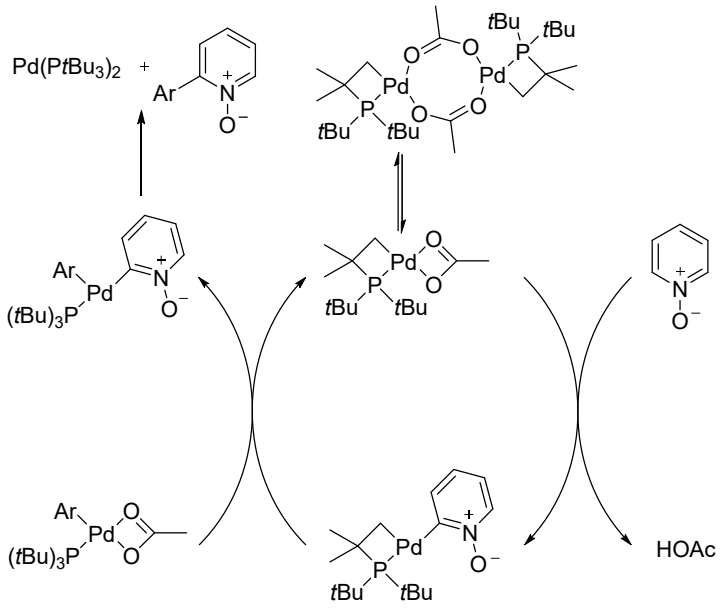

Figure 3.15. Proposed dual palladium mechanism for pyridine *N*-oxide direct arylation.

The reaction progress for three direct alkenylation reactions using three different (co)catalyst combinations (5 mol% total Pd): Pd(II) only, Pd(0) only, and a mix of Pd(II) and Pd(0) (Figure 3.16) was monitored. In each case, poor conversion at 20 hours using only Pd(0) is noticeable. This is not consistent with a traditional Pd(0)/(II) mechanism, where this precursor should be highly active. In addition, we observe essentially equal rates when using only Pd(II) and using a Pd(II)/Pd(0) co-catalyst mixture; in other words, there is no apparent benefit to adding a Pd(0) co-catalyst to this system.

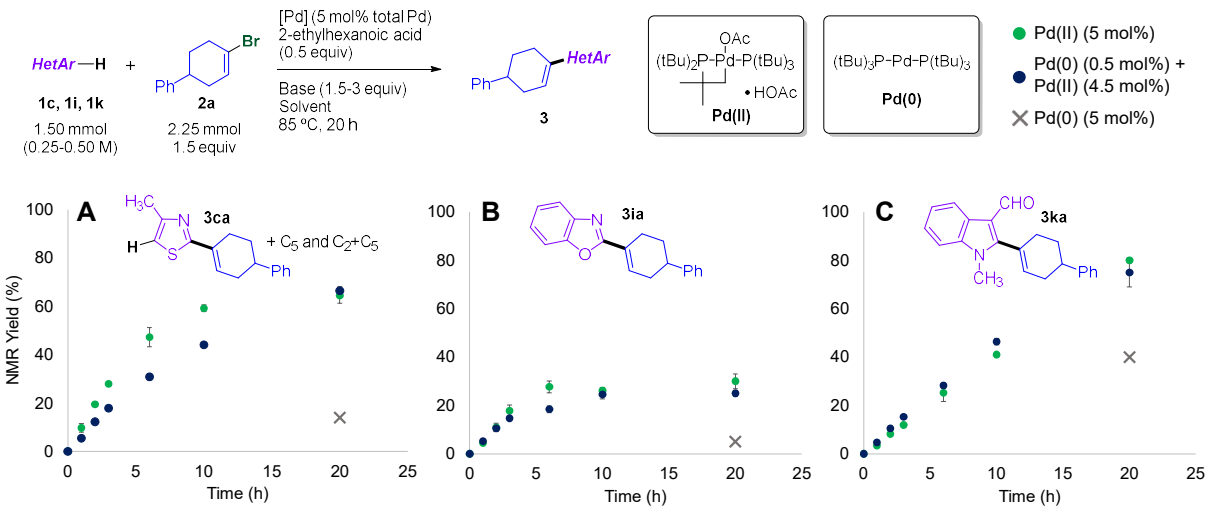

Figure 3.16. Reaction progress monitoring via 1H-NMR spectroscopy of three direct alkenylation reactions using different precatalyst mixtures. Data reveal no benefit to adding Pd(0) to Pd(II), nor in using Pd(0) as the precatalyst. Conditions:. A: **1c** (0.25 M), K_3PO_4 (1.5 equiv), CPME, yields are the sum of all coupling products (C_2, C_5, and C_2+C_5 alkenylation, see SI for more details). **B**: **1i** (0.5 M), K_3PO_4 (3 equiv), CPME. **C: 1k** (0.5 M), K_3PO_4 (1.5 equiv), DMA.

While the superiority of **II** as a catalyst precursor is consistent with Hartwig's prior findings of a cooperative dual catalyst system, it is not immediately clear why the addition of Pd(0) did not cause an increase in reaction rate, since Pd(0) is needed for the cross-coupling cycle. Stambuli noted that complex **II** does undergo spontaneous conversion to Pd[P(*t*Bu)$_3$]$_2$ when heated, though details of the extent and mass balance of this reaction were not provided.[70] I therefore studied the thermolysis of **II** in toluene at 85 °C for 24 h by $^{31}P\{^1H\}$ NMR spectroscopy to characterize all of the products. The formation of Pd[P(*t*Bu)$_3$]$_2$ is observed, accompanied by the formation of O=P(*t*Bu)$_3$, and a metallic Pd mirror (Figure 3.17).

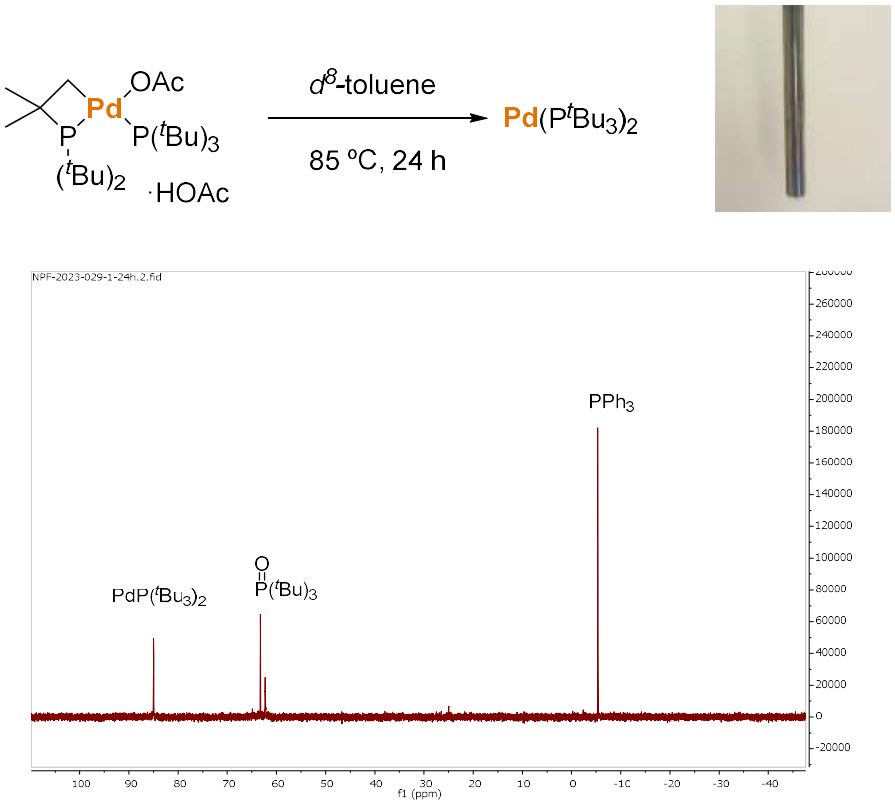

Figure 3.17. *In situ* reduction of complex **II** followed by $^{31}P\{^{1}H\}$ NMR spectroscopy. Palladium metallic mirror also observed in the NMR sample tube (top right image).

Presumably this reaction occurs through reduction of Pd(II) by P(*t*Bu)$_3$ and the equivalent of acetic acid present (due to **II** being isolated as the HOAc solvate) to generate [AcO–P(*t*Bu)$_3$]+[AcO]- and Pd[P(*t*Bu)$_3$] (Figure 3.18). The former would then hydrolyze with trace water present, while the latter disproportionates to Pd[P(*t*Bu)$_3$]$_2$ and Pd metal.[92–94] Under catalytic conditions, there is also the possibility of Pd-mediated oxidative C–H dimerization of the heterocyclic substrate, leading to Pd(0) *via* HetAr–HetAr reductive elimination.

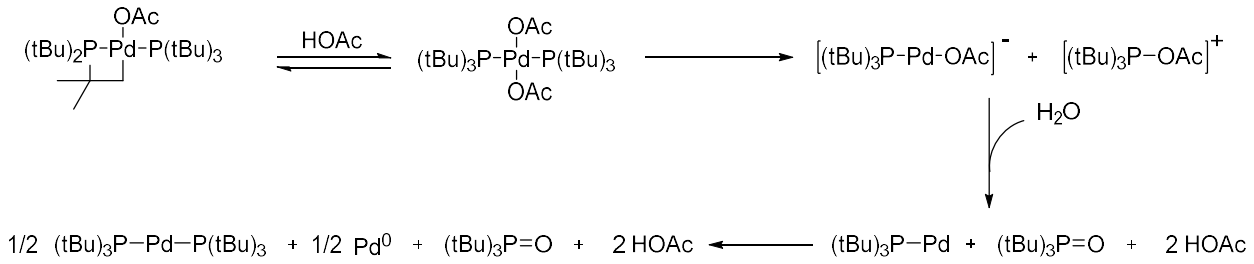

Figure 3.18. Proposed pathway for *in situ* reduction of complex **II.**

Under catalytic conditions, it is possible that a small amount of **II** undergoes *in situ* reduction to Pd[P(*t*Bu)$_3$]$_2$, which is then capable of supporting the Pd(0)/(II) part of the cooperative dual cycle. The majority of the Pd in solution remains as palladacycle species to perform CMD in the Pd(II) C–H activation cycle. *In situ* reaction monitoring of the direct alkenylation to form **3ea** by ^{31}P{H} NMR spectroscopy reveals signals consistent with this hypothesis (Figure 3.19).

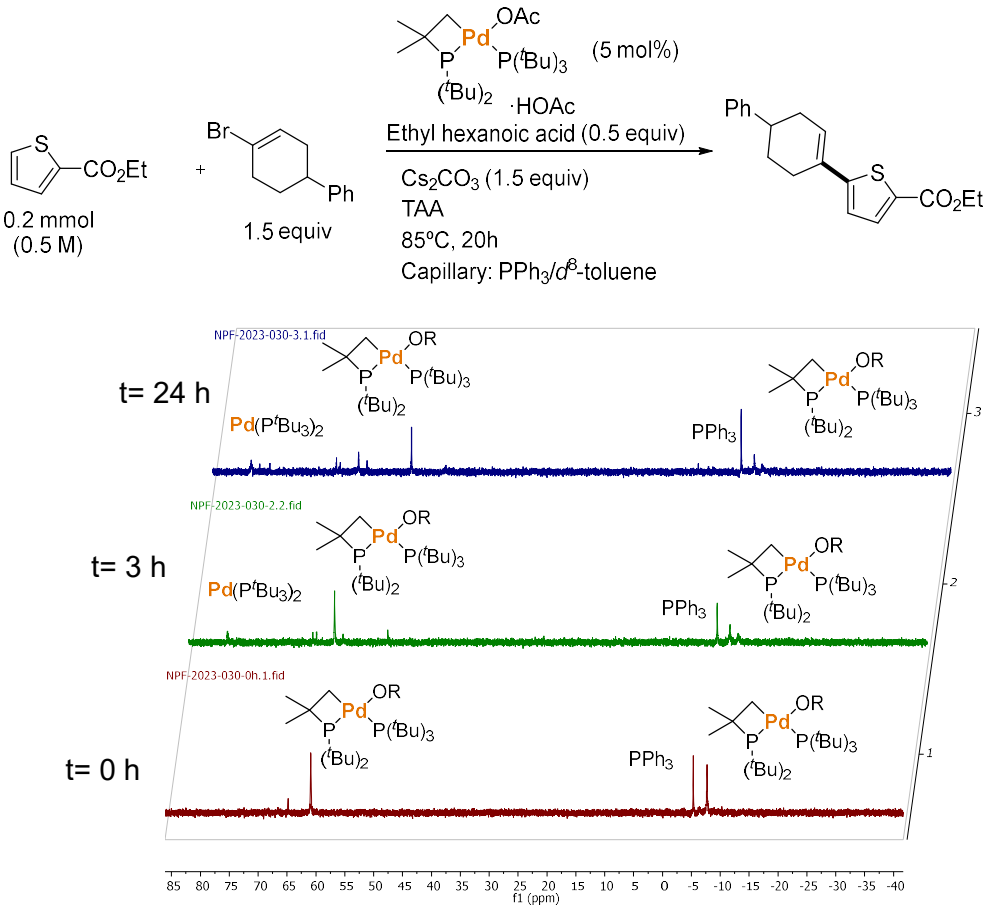

Figure 3.19. Reaction monitoring by $^{31}P\{^{1}H\}$ NMR spectroscopy of the direct alkenylation reaction between heterocycle **17** and vinyl halide **A**. PPh_3 is present as an internal standard (solution in d^8-toluene in a glass capillary).

A key practical advantage of this *in situ* reduction of **II** is that it can function as a single-component precatalyst, without the need for any co-catalysts or additives to assist with C–H activation. It also activates without any apparent induction period in the three systems monitored (Figure 3.14).

3.3.4 Proposed Mechanism

Based on prior work from Hartwig on C–H activation of pyridine *N*-oxides with analogous P(*t*Bu)$_3$-derived palladacycles,[91] and the reaction monitoring studies on catalytic reactions performed in this project, I propose complex **II** operates as a precatalyst for a tandem, dual-cooperative catalytic mechanism (Figure 3.20).[95–98] The C–H activation step is mediated by the Pd(II) palladacycle, while *in situ* reduction of Pd(II) by P(*t*Bu)$_3$ and a proton source generates the required Pd(0) species that supports the canonical Pd(0)/(II) catalytic cycle.

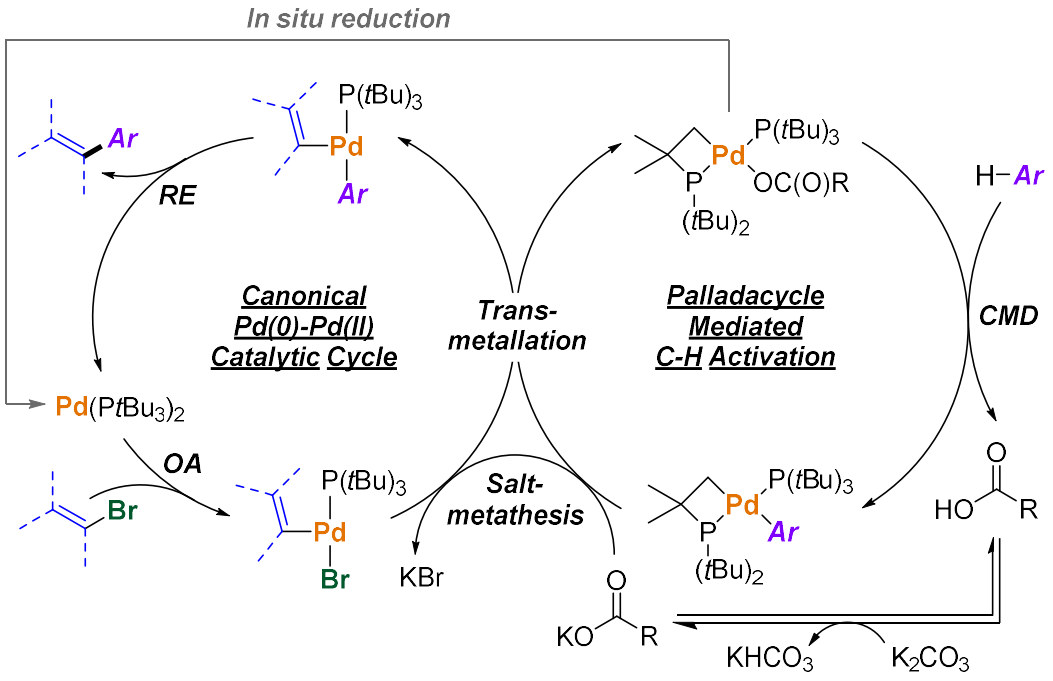

Figure 3.20. Tandem, dual-cooperative mechanism for direct alkenylation. A Pd(0)/(II) cycle involving oxidative addition (OA) and reductive elimination (RE) couples with a Pd(II)-only cycle for C–H activation via concerted metalation deprotonation (CMD).

3.3.5 Mapping Reaction Scope Through Combinatorial HTE.

To assess the generality of precatalyst **II** against a wide variety of substrate combinations, a 192-member array experiment combining 8 vinyl halides and 24 distinct heterocycles drawn from the 9 general classes (Figure 3.21) was performed. For each heterocycle class, the conditions established during screening/optimization (Figure 3.14) were used to ensure the array results are representative. Analysis was performed using LCMS to identify the presence of reaction products (matching *m*/*z* values) and estimate reaction progress using LCAP values. The reactions were categorized into three groups: 0-10 LCAP (blue entries), 10-30 LCAP (green entries), and >30 LCAP (yellow entries).

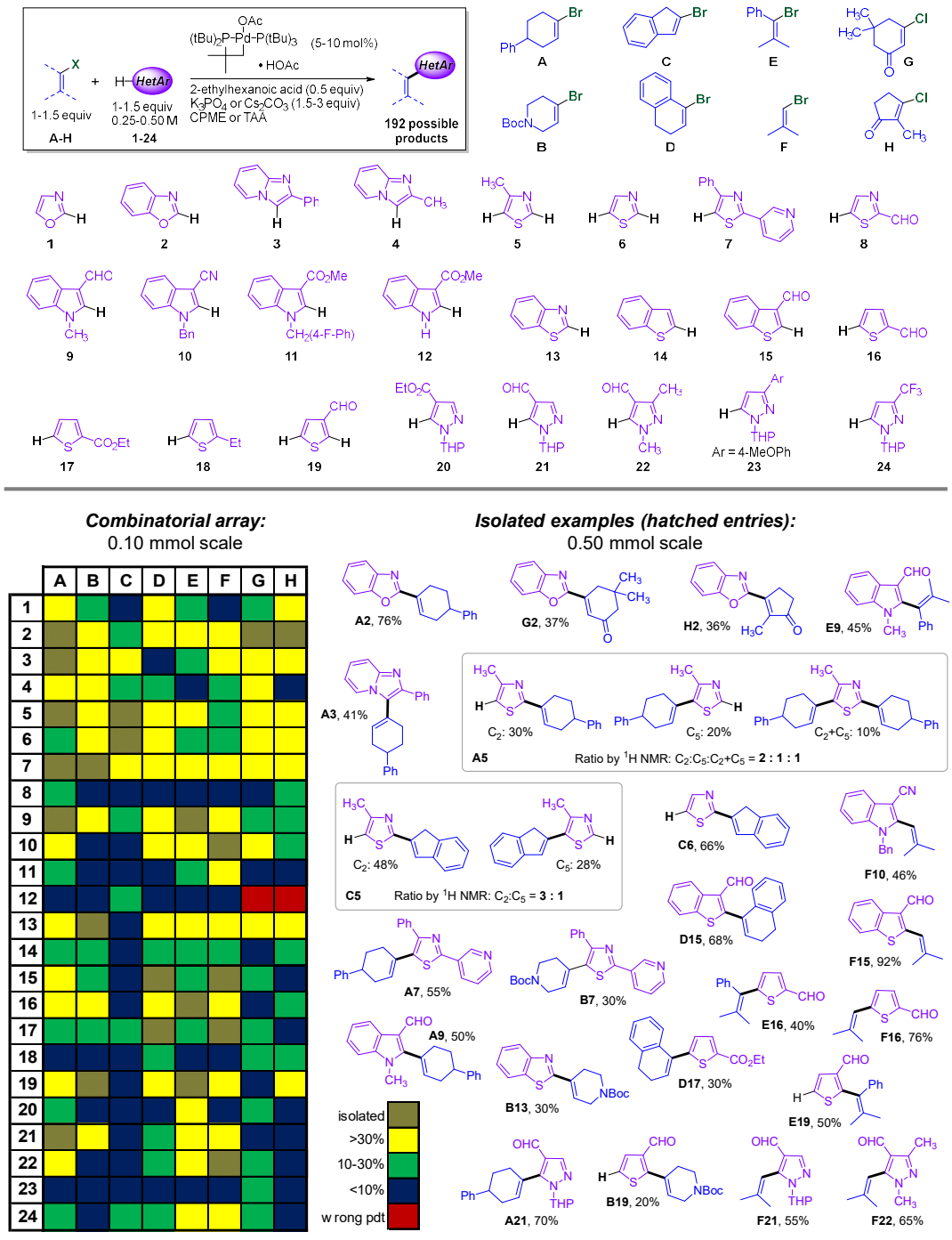

Figure 3.21. Combinatorial exploration of substrate scope for direct alkenylation of 24 heterocycles with 8 alkenyl halides (microscale, 0.10 mmol), with semi-quantitative analysis shown in array format: LCMS analysis based on LCAP values for peak(s) with target *m/z* value. Structures at right are isolated examples prepared on 0.50 mmol scale (hatched entries in array), with isolated yields after automated flash chromatography. Product ratios by ^{1}H NMR spectroscopy for **A5** and **C5** are obtained prior to purification. **G12** and **H12** revealed by NMR spectroscopic analysis to be N-alkenylation of the indole, rather than C_2-alkenylation.

The vinyl halide substrates include cyclic (Figure 3.21, **A**-**D**) and linear vinyl bromides (Figure 3.21, **E**-**F**) and activated cyclic vinyl chlorides (Figure 3.21, **G**-**H**). Notably, these two vinyl chlorides – which are vinylogous acyl chlorides – are susceptible to non-catalyzed nucleophilic attack (including hydrolysis back to the corresponding enol). The heterocycles also contain a variety of potentially sensitive functional groups, including aldehyde, ester, nitrile, methoxy, trifluromethyl, alkyl and (hetero)aryl groups. Potentially nucleophilic and/or basic nitrogens are protected with groups that are easily removed, such as Boc, THP or Bn, except for the unprotected indole **12**. Two experiments with unprotected indole gave "false positive" results, with matching *m*/*z* values observed, but the wrong structure apparent by ^{1}H NMR spectroscopy. The C–N coupling products were observed instead of the C–C coupling products (Figure 3.22).

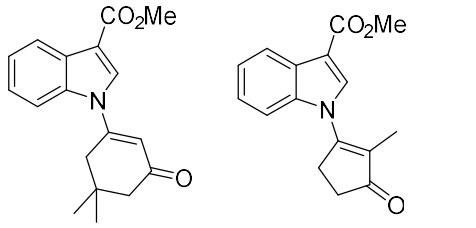

G12
observed product

H12
observed product

Figure 3.22. **G12** and **H12** coupling products.

As shown in the data visualization in Figure 3.21, there is a wide range of reactivity across the substrate combinations. Notably, nearly 70% of the reactions contained the desired product (132 entries with >10 LCAP of component with matching *m*/*z* value), and 43% of reactions have sufficient product formation to enable isolation (82 entries with >30 LCAP). This relatively good "hit rate" is likely because reaction conditions were optimized to each heterocycle class, rather than using a single set of conditions for all 192 experiments.[99] Even still, more than half of the

combinations failed or generated only small amounts of product. Many of these entries could likely be optimized further using higher catalyst loading and/or temperature, or exploring alternative catalyst systems.

Several structural trends are evident when examining the array. For the most part, vinyl bromides **A**-**F** perform similarly across the heterocycle array; however, indenyl bromide **C** fails more often, only giving isolable hits for imidazopyridine **3** and thiazole set **5**-**7** (all of which use CPME solvent). This could be due to side reactivity resulting from the activated methylene position that may be worsened by the more strongly basic conditions when using TAA as the solvent. Likewise, vinyl chlorides **G** and **H** perform well with (benz)oxazole and (benzo)thiazole substrates (generally run using CPME) but have generally poor reactivity across the other heterocycle classes (which mostly use TAA).

In general, the electronic nature of the heterocycles is a key attribute. Superior reactivity is observed for more electron-deficient substrates, consistent with the CMD mechanism and prior observations.[21,87–90] For example, the set of indoles **9**-**11** reveals that aldehyde and nitrile groups are suitable, while switching to an ester dramatically reduces reactivity. Within the set of substituted thiophenes **16**-**19**, aldehyde-functionalized rings work best, while the electron-rich 2-ethylthiophene fails to generate isolable amounts of product across all 8 electrophiles. Finally, the set of pyrazoles **20**-**24** also adheres to this trend, with the more electron rich 3-anisyl substrate **23** failing, and the ester-containing substrate **20** inferior to the aldehyde analogues **21** and **22**.

Using the reactivity array as a guide, key examples were isolated on 0.50 mmol scale, prioritizing isolating compounds from across the entire array, with each vinyl halide and each heterocycle class represented at least once, with 23 total examples (Figure 3.21, hatched entries).

Isolated yields are reported for each example after automated flash chromatography, and vary from 20% (**B19**) to 92% (**F15**), with an average of 50% across the set.

Notably, for 4-methylthiazole (**5**), regioisomeric product mixtures for both **A5** and **C5** were observed, with alkenylation favored at the C_2 position. Importantly, this is different than the regioselectivity reported for $Pd(OAc)_2/PCy_3$ as a catalyst, where C_5 is the favored position.[21,90] For **A5**, prior to purification a molar ratio of 2 : 1 : 1 for alkenylation at C_2 : C_5 : C_2+C_5 (dialkenylation) was observed by ^{1}H NMR spectroscopy. All three products were isolated to confirm their connectivity. For **C5**, both the C_2 (major) and C_5 (minor) alkenylation products were observed, with a molar ratio of 3 : 1 prior to purification. Likewise, both isomers were isolated to confirm connectivity by ^{1}H NMR spectroscopy. For simple thiazole (**6**), only one product was obtained when performing alkenylation with indenyl bromide **C**, with reactivity at C_2. This is again in contrast to the regiochemistry reported for $Pd(OAc)_2/PCy_3$.[21] Another heterocycle with potential for regioisomeric C–H alkenylation is thiophene-3-carboxaldehyde (**19**); however, only products functionalized at the C_2 position (**B19** and **E19**) were isolated.

3.3.6 Application toward the synthesis of GSK3368715.

A major motivation of this work was to develop a scalable catalytic method for direct alkenylation of pyrazole **1a** toward the PRMT1 inhibitor **GSK3368715**. The ease of access and stability of palladacycle **II**, combined with its ability to perform C–H alkenylation without the need for additives or co-catalysts – Ag-based or otherwise – made it an ideal option for this process. We therefore evaluated **II** for the coupling between **1a** and the vinyl bromide substrate **2i** (Figure 3.20). This vinyl bromide is prepared from the corresponding cyclohexanone (a common

intermediate in the previously reported synthesis of **GSK3368715**[27]) and used without further purification (~88-90% wt/wt purity, see Experimental section for details).

Initial development focused on the general solvent/base combination identified in Figure 3.12: TAA / K_3PO_4. However, GSK scientists determined the downstream chemistry functions best in ether-based solvents, so we altered the reaction conditions to use a mixed *t*BuOH/CPME solvent system (3:1 v/v). This enables straightforward removal of *t*BuOH during aqueous workup, leaving **3ai** as a solution in CPME. On ~110 mmol scale (20 g input of **1a**), we obtain a 78% assay yield (32 g) of **3ai** using 3.5 mol% of **II**. This material was then suitable to carry forward to **GSK3368715** using the previously reported synthetic endgame.[27]

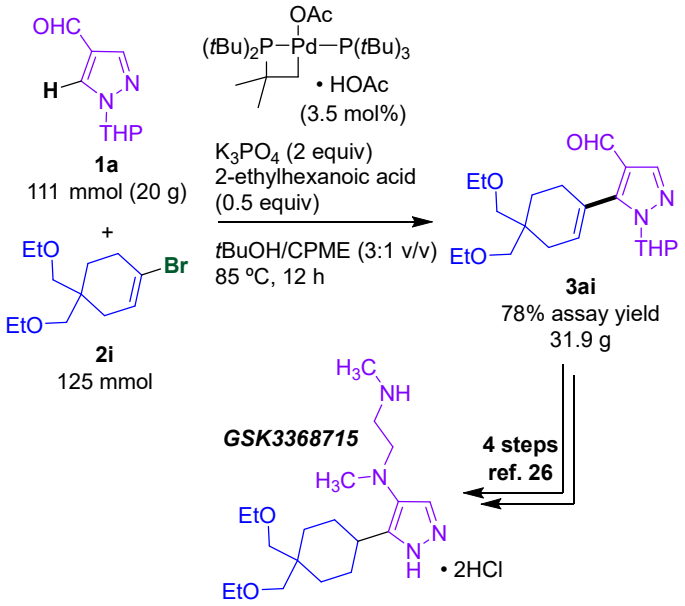

Figure 3.23. Large scale synthesis of **3ai** via Pd-catalyzed direct alkenylation using **II** as a single-component catalyst en route to **GSK3368715**.

3.4 Conclusions

Strategic use of catalytic C–H functionalization reactions have the potential to significantly shorten synthetic routes to complex molecule targets. In the case of **GSK3368715**, direct alkenylation of a protected pyrazole led to a 5 step shorter route to the key coupling partners as compared to a traditional Suzuki-coupling approach. While prior efforts in Pd-catalyzed direct alkenylation rely on the use of co-catalysts or stoichiometric additives (e.g. Ag-containing bases), this work shows that palladacycle **II** is an effective single-component precatalyst for alkenylation of many heterocycle classes. This precatalyst is easy to prepare,[70] and has previously been implicated in a cooperative dual catalytic mechanism for direct arylation.[91] We hypothesize that this aspect of **II**'s reactivity enables it to function with many different heterocycles, *if* the correct solvent/base combination is used. The selection guidelines in Figure 3.14 should provide an excellent starting point for reaction development across these heterocycle classes. Importantly, **II** exhibits complementary regioselectivity for thiazole alkenylation compared to the standard $Pd(OAc)_2/PCy_3$ conditions reported by Fagnou.[21] Exploring this selectivity trend is the subject of Chapter 4.

The present study was built on a foundation of data-rich high-throughput experimentation, which enabled a multi-factor/multi-substrate approach to reaction optimization. Several more general aspects of this type of workflow are worth highlighting here. One surprising aspect was the inability of the Hermann-Beller complex **IV** to perform well at lower catalyst loadings, despite its superior yields under high loading HTE conditions. Performing HTE with high (10-20 mol%) catalyst loading is common; clearly, it can lead to "fragile hits", where changes to the reaction conditions (such as lower catalyst loading) lead to poor performance. Two suggested methods to

combat this are to conduct HTE studies as close to the desired outcome conditions as possible (*i.e.* lower catalyst loadings) and/or ensure validation runs are conducted on several possible hits.

The second aspect of the HTE workflow worth noting is the importance of conducting extensive parallel-in-parallel screening,[72] where multiple substrate combinations are evaluated under arrays of reaction conditions. This is one way to "screen for generality"[100] in fragment coupling reactions: rather than identifying specific catalyst systems for each new substrate class, one catalyst may be generally effective if the other reaction conditions can be tuned.[81] The nearly 45% "hit rate" in our 192-product combinatorial array exemplifies the power of this multi-substrate, multi-condition screening approach, while also identifying gaps in the current methodology.[26] Finally, direct alkenylation catalyzed by precatalyst **II** is scalable, as demonstrated by the 30 g synthesis of **3ai**, a key intermediate *en route* to **GSK3368715**.

3.5 Experimental Procedures

3.5.1 General procedure for high-throughput experiments:

100 μL of 0.10 M solution of catalyst **I**, **II**, **III** or **IV** in THF and 100 μL of 0.050 M solution of 1,3,5-trimethoxybenzene (internal standard, IS) were added to 1 mL glass shell vials contained in aluminum reaction plates. The solvent was then removed by centrifugal evaporation. A micro parylene-coated stir-bar was added to each well. Inside the glovebox, ~3 equivalents of the corresponding base was added to each vial using calibrated plastic scoops: K_3PO_4 (30 mg), K_2CO_3 (20 mg) or Cs_2CO_3 (50 mg). Substrate stock solutions were prepared inside the glovebox: one containing the vinyl halide (0.65 M) and the others containing the heterocycle substrates (0.5 M) and 2-ethylhexanoic acid (0.25 M) in the desired solvent. Solvents include DMA, CPME, toluene,

or TAA. 0.1 mL of each stock solution was added into the corresponding 1 mL shell vial in the aluminum reaction plates. The plates were then sealed using a screwed-down lid with a Teflon liner and rubber spacer. The reaction plates were then heated on a tumble stirrer set to 500 rpm, at 85 °C for 20 h. Upon completion, the plates were cooled to room temperature before being opened. Acetonitrile (500 μL) was added to each vial, followed by stirring for 10 minutes at room temperature to ensure complete dissolution. The samples were centrifuged for 15 minutes. Aliquots (40 μL) of each diluted reaction mixture were then transferred to 96-well plastic analysis plate, followed by the addition of 0.7 mL of acetonitrile. The samples were analyzed by LCMS, using the product/IS area ratio. The reaction plates were then dried by centrifugal evaporation, and 20-25% of the wells were analyzed by ^{1}H NMR spectroscopy to confirm product presence, and to conduct external calibration of product/IS ratios to obtain yields.

3.5.2 General procedure for reaction monitoring experiments:

Inside the glovebox, three 1-dram vials were charged with a stir bar. Then, the following components were added: heterocycle substrate (1.5 mmol, 1 equiv), vinyl halide (1.5 equiv), 1,3,5-timethoxybenzene (10 mol%, IS), followed by the corresponding catalyst mixture: **II** (5 mol%), **II** (4.5 mol%) and Pd[P(*t*Bu)$_3$]$_2$ (0.5 mol%), or Pd(PtBu$_3$)$_2$ (5 mol%). Then, base (1.5 or 3 equivalents) and anhydrous solvent (3 mL) was added. The vial was sealed with a Teflon-lined screw cap, and the reaction mixture stirred at 85 °C for 20 h. Aliquots (10 μL) were taken in triplicate at the indicated times (0, 1, 2, 3, 6, 10 and 20 h). The aliquots were diluted with 1 mL of acetonitrile and analyzed using LCMS. Once the reactions reached completion (20 h), the solvent was evaporated under vacuum. The crude residue was redissolved in $CDCl_3$ to enable yields to be determined using ^{1}H NMR spectroscopy by relative integration with the internal standard.

3.5.3 General procedure for combinatorial scope array (Figure 3.21):

50 μL of 0.10 M solution of catalyst **II** in THF and 50 μL of 0.050 M solution of 1,3,5-trimethoxybenzene (IS) were added to 1 mL glass shell vials contained in aluminum reaction plates. The solvent was then removed by centrifugal evaporation. A micro parylene-coated stir-bar was added to each well. Inside the glovebox, ~3 equivalents of the corresponding base was added to each vial using calibrated plastic scoops: K_3PO_4 (30 mg), K_2CO_3 (20 mg) or Cs_2CO_3 (50 mg). Substrate stock solutions were prepared inside the glovebox: vinyl halides **A**–H (1.5 M) in CPME or TAA; and heterocycles **1**-**24** (1 M) with 2-ethylhexanoic acid (0.5 M) in CPME or TAA. 0.1 mL of the appropriate solution of vinyl halide and heterocycle were added to each 1 mL shell vial in the aluminum reaction plates. The plates were then sealed using a screwed-down lid with a Teflon liner and rubber spacer. The reaction plates were then heated on a tumble stirrer set to 500 rpm, at 85 °C for 20 h. Upon completion, the plates were cooled to room temperature before being opened. Acetonitrile (500 μL) was added to each vial, followed by stirring for 10 minutes at room temperature to ensure complete dissolution. The samples were centrifuged for 15 minutes. Aliquots (40 μL) of each diluted reaction mixture were then transferred to 96-well plastic analysis plates, followed by the addition of 0.7 mL of acetonitrile. The samples were analyzed by LCMS, using the product/IS area ratio.

3.5.4 General procedure for isolation of direct alkenylation products:

Inside the glovebox, a 1 dram vial was charged with a Teflon-coated stir bar. The heterocycle substrate (0.50 mmol, 1 equiv) and vinyl halide (1.5 mmol, 1.5 equiv) were added, followed by **II** (5 mol%), base (1.5 or 3 equivalents), 2-ethylhexanoic acid (0.5 equiv), and anhydrous solvents (1 mL). The vial was sealed with a Teflon-lined screw cap, and the reaction mixture stirred at 85 °C for 20 h. After cooling to room temperature, the solvent was removed by centrifugal evaporation.

The resulting crude mixture was purified by automated column chromatography using a hexanes/ethyl acetate gradient elution.

3.5.5 Synthesis of vinyl bromide 2i:

A 1 L Optimax reactor was charged with 4,4-bis(ethoxymethyl)cyclohexan-1-one (61.75 g, 288 mmol),[27] triethylamine (76 mL, 547 mmol), triphenylphosphite (128 mL, 490 mmol), and DCM (540 mL). The headspace was flushed with N_2, the reaction mixture temperature was set to -20 °C, and agitation (overhead stirring) was set to 400 rpm. Bromine (25.2 mL, 490 mmol) was drawn into a plastic syringe using a Teflon tube. Then, DCM was taken up into the syringe to make a total volume of 40 mL. Under an N_2 atmosphere in the Optimax reactor, the Teflon tube was passed through a rubber septum, and the end submerged in the agitating reaction mixture. A syringe pump was programmed to charge the Br_2 solution into the reaction mixture over 1.5 hr. After the Br_2 addition was complete, the reaction mixture was warmed to 25 °C over 90 min with continued stirring (400 rpm).

The reaction was quenched with a solution of sodium thiosulfate pentahydrate (21.45 g, 86 mmol) dissolved in water (200 mL), while maintaining a reaction temperature of 25 °C (4 h, stirring increased to 800 rpm). Stirring was then paused, and the aqueous layer was removed through the bottom valve. The organic layer was concentrated under vacuum inside the reactor. The resultant oil was diluted with MeOH (360 mL), and the contents were treated with sodium hydroxide (70.6 g, 1729 mmol) dissolved in water (360 mL), maintaining a reaction temperature of 55 °C (1.5 h, stirring at 800 rpm). After this, the reaction temperature was set to 25 °C. The mixture was diluted with heptane (420 mL, 20 min of stirring at 1000 rpm). Stirring was paused, and the aqueous/MeOH layer was removed. The heptane layer was extracted twice with water (2

x 240 mL, 20 min stirring at 800 rpm for each water treatment). The organic layer was concentrated under vacuum to yield **2i** as a crude oil (72.58 g, 88.6% w/w, 232 mmol, 81% yield). The purity of the crude oil was determined through quantitative HPLC by comparing the UV/Vis response of the crude oil vs. an authentic sample of **2i** isolated through vacuum distillation (bp = 128 °C at 7-9 torr). The crude **2i** was used without further purification in the direct alkenylation reactions.

3.5.6 Direct arylation of 1a with 2i using stoichiometric silver (eq. 1):

A 1 L OptiMax reactor was charged with potassium carbonate (27.3 g, 198 mmol, 1.5 equiv), silver carbonate (21.76 g, 78.9 mmol, 0.6 equiv), tricyclohexylphosphine (27.7 g, 98.8 mmol, 0.75 equiv), **1a** (23.7 g, 132 mmol), **2i** (54.7 g, 197 mmol, 1.5 equiv) and toluene (237 mL). The headspace was flushed with N_2, and overhead stirring commenced at 350 rpm. The reaction temperature was increased to 50 °C. Once the target temperature was reached, solid palladium acetate (0.295 g, 1.32 mmol, 0.01 equiv) was charged to the reactor. The reaction temperature was then increased to 100 °C, and the mixture stirred at this temperature for 24 h.

The reaction mixture was cooled 23 °C, followed by filtration of the suspension through a short pad of Celite in a disposable fritted filter. The filtrate was returned to the reactor and heated to 60 °C with stirring (350 rpm). A solution of *N*-acetyl cystine (8.59 g) in dilute NaOH (50% aq NaOH: 2.75 mL; water: 34 mL; pH ≈ 8.5) was added. The reaction mixture was stirred for 1 h, and then the layers were allowed to settle. Once there was a clear interface between layers, the aqueous layer was removed through the bottom valve. The organic layer was then washed with a second portion of *N*-acetyl cystine (8.59 g) in dilute NaOH (50% aq NaOH: 2.75 mL; water: 34 mL; pH ≈ 8.5). After stirring for 1 h, allowing layers to settle, and separation of the aqueous phase, the organic layer was then concentrated to ~50 mL under reduced pressure with stirring (350 rpm).

Once the desired reaction volume was achieved, the reaction temperature was set to 23 °C and stirring continued. Methanol (95 mL) was charged to the reactor. Concentrated HCl (96 mL, 24 equiv) was slowly charged to the reactor to control the exotherm and maintain an internal temperature of 23 °C. Once HCl was completely charged, the reaction mixture was stirred for 1 h. Then, the reaction mixture was sampled and analyzed by quantitative HPLC. This gave a solution yield of 71% for the deprotected pyrazole product. Characterization data matched those reported previously.[27]

3.5.7 Synthesis of 3ai using precatalyst II (Figure 3.23):

A 1 L jacketed lab reactor was charged with anhydrous 100 mesh K_3PO_4 (47.1 g, 222 mmol, 2 equiv, see Supporting Information for details on how to prepare this material with the required particle size), **1a** (20.0 g, 111 mmol), **2i** (39.0 g, 88.6% w/w, 125 mmol), 2-ethylhexanoic acid (7.85 g, 8.69 mL, 54.4 mmol, 0.5 equiv), CPME (inhibitor-free, anhydrous, 28 mL), and 80 mL *t*BuOH (80 mL). The reactor was then fitted with a condenser and sealed. The reactor contents were degassed by cycling vacuum and N_2 three times; the pressure of the reactor reached 100 torr during each evacuation, and the contents were stirred at 350 rpm with the reactor jacket temperature set to 25 °C. Once the degassing cycles were complete, the headspace was refilled with N_2, and the internal temperature was to 85 °C with continued stirring at 350 rpm. Palladacycle **II** (2.395 g, 3.81 mmol 3.5 mol%) was dissolved in *t*BuOH/CPME (10 mL / 2 mL) inside an N_2 filled glovebox. This solution was taken up into a syringe, removed from the glovebox, and transported to the reactor. With the reaction mixture temperature equilibrated to 85 °C, the precatalyst solution was injected into the reactor. The reaction mixture was stirred (350 rpm) at 85 °C for 22 h under an N_2 atmosphere.

Once the reaction time was complete, the internal temperature was lowered to 55 °C. Once cooled, the reactor was charged with water (140 mL), CPME (70 mL), and acetylcysteine (17.75 g, 109 mmol). The stir rate was increased to 500 rpm, and the mixture agitated for 2 h at 55 °C. The internal temperature was then lowered to 25 °C. Stirring was stopped and the layers allowed to settle. The aqueous layer was removed through the bottom valve. After the acetylcysteine treatment, the organic layer was washed with 1 M Tris-HCl solution (3 x 160 mL). Each Tris-HCl treatment was stirred at 25 °C, 500 rpm, for 1.5 h. The resulting organic solution was removed from the reactor, and a solution yield was determined through quantitative HPLC (31.9 g product, 78% yield). Characterization data matched those reported previously.[27]

3.6 References

(1) McMurray, L.; O'Hara, F.; Gaunt, M. J. Recent Developments in Natural Product Synthesis Using Metal-Catalysed C–H Bond Functionalisation. *Chem. Soc. Rev.* **2011**, *40*, 1885–1898. https://doi.org/10.1039/C1CS15013H.

(2) Gutekunst, W. R.; Baran, P. S. C–H Functionalization Logic in Total Synthesis. *Chem. Soc. Rev.* **2011**, *40*, 1976–1991. https://doi.org/10.1039/C0CS00182A.

(3) Engle, K. M.; Mei, T.-S.; Wasa, M.; Yu, J.-Q. Weak Coordination as a Powerful Means for Developing Broadly Useful C–H Functionalization Reactions. *Acc. Chem. Res.* **2012**, *45*, 788–802. https://doi.org/10.1021/ar200185g.

(4) Davies, H. M. L.; Morton, D. Recent Advances in C–H Functionalization. *J. Org. Chem.* **2016**, *81*, 343–350. https://doi.org/10.1021/acs.joc.5b02818.

(5) Dalton, T.; Faber, T.; Glorius, F. C–H Activation: Toward Sustainability and Applications. *ACS Cent Sci* **2021**, *7*, 245–261. https://doi.org/10.1021/acscentsci.0c01413.

(6) Rogge, T.; Kaplaneris, N.; Chatani, N.; Kim, J.; Chang, S.; Punji, B.; Schafer, L. L.; Musaev, D. G.; Wencel-Delord, J.; Roberts, C. A.; Sarpong, R.; Wilson, Z. E.; Brimble, M. A.; Johansson, M. J.; Ackermann, L. C–H Activation. *Nat. Rev. Methods Primers* **2021**, *1*, 43. https://doi.org/10.1038/s43586-021-00041-2.

(7) Holmberg-Douglas, N.; Nicewicz, D. A. Photoredox-Catalyzed C–H Functionalization Reactions. *Chem. Rev.* **2022**, *122*, 1925–2016. https://doi.org/10.1021/acs.chemrev.1c00311.

(8) Yamaguchi, J.; Yamaguchi, A. D.; Itami, K. C□H Bond Functionalization: Emerging Synthetic Tools for Natural Products and Pharmaceuticals. *Angew. Chem. Int. Ed.***2012**, *51*, 8960–9009. https://doi.org/10.1002/anie.201201666.

(9) Buskes, M. J.; Blanco, M.-J. Impact of Cross-Coupling Reactions in Drug Discovery and Development. *Molecules* **2020**, *25*. https://doi.org/10.3390/molecules25153493.

(10) Jana, R.; Begam, H. M.; Dinda, E. The Emergence of the C–H Functionalization Strategy in Medicinal Chemistry and Drug Discovery. *Chem. Commun.* **2021**, *57*, 10842–10866. https://doi.org/10.1039/D1CC04083A.

(11) Guillemard, L.; Kaplaneris, N.; Ackermann, L.; Johansson, M. J. Late-Stage C–H Functionalization Offers New Opportunities in Drug Discovery. *Nat. Rev. Chem.* **2021**, *5*, 522–545. https://doi.org/10.1038/s41570-021-00300-6.

(12) Zhang, Y.; Szostak, M. Synthesis of Natural Products by C−H Functionalization of Heterocycless. *Chem. Eur. J.***2022**, *28*, 1-40. https://doi.org/10.1002/chem.202104278.

(13) Docherty, J. H.; Lister, T. M.; Mcarthur, G.; Findlay, M. T.; Domingo-Legarda, P.; Kenyon, J.; Choudhary, S.; Larrosa, I. Transition-Metal-Catalyzed C–H Bond Activation for the Formation of C–C Bonds in Complex Molecules. *Chem. Rev.* **2023**, *123*, 7692–7760. https://doi.org/10.1021/acs.chemrev.2c00888.

(14) Alberico, D.; Scott, M. E.; Lautens, M. Aryl−Aryl Bond Formation by Transition-Metal-Catalyzed Direct Arylation. *Chem. Rev.* **2007**, *107*, 174–238. https://doi.org/10.1021/cr0509760.

(15) Satoh, T.; Miura, M. Catalytic Direct Arylation of Heteroaromatic Compounds. *Chem. Lett.* **2007**, *36*, 200–205. https://doi.org/10.1246/cl.2007.200.

(16) Hirano, K.; Miura, M. C−H Activation of Heteroaromatics. *Sustainable Catalysis*; John Wiley & Sons, Ltd, **2013**; pp 233–267. https://doi.org/10.1002/9781118354520.ch11.

(17) Ji, Y.; Plata, R. E.; Regens, C. S.; Hay, M.; Schmidt, M.; Razler, T.; Qiu, Y.; Geng, P.; Hsiao, Y.; Rosner, T.; Eastgate, M. D.; Blackmond, D. G. Mono-Oxidation of Bidentate Bis-

Phosphines in Catalyst Activation: Kinetic and Mechanistic Studies of a Pd/Xantphos-Catalyzed C–H Functionalization. *J. Am. Chem. Soc.* **2015**, *137*, 13272–13281. https://doi.org/10.1021/jacs.5b01913.

(18) Bien, J.; Davulcu, A.; DelMonte, A. J.; Fraunhoffer, K. J.; Gao, Z.; Hang, C.; Hsiao, Y.; Hu, W.; Katipally, K.; Littke, A.; Pedro, A.; Qiu, Y.; Sandoval, M.; Schild, R.; Soltani, M.; Tedesco, A.; Vanyo, D.; Vemishetti, P.; Waltermire, R. E. The First Kilogram Synthesis of Beclabuvir, an HCV NS5B Polymerase Inhibitor. *Org. Process Res. Dev.* **2018**, *22*, 1393–1408. https://doi.org/10.1021/acs.oprd.8b00214.

(19) Bream, R. N.; Clark, H.; Edney, D.; Harsanyi, A.; Hayler, J.; Ironmonger, A.; Mc Cleary, N.; Phillips, N.; Priestley, C.; Roberts, A.; Rushworth, P.; Szeto, P.; Webb, M. R.; Wheelhouse, K. Application of C–H Functionalization in the Development of a Concise and Convergent Route to the Phosphatidylinositol-3-Kinase Delta Inhibitor Nemiralisib. *Org. Process Res. Dev.* **2021**, *25*, 529–540. https://doi.org/10.1021/acs.oprd.0c00486.

(20) Yadav, P.; Velmurugan, N.; Luscombe, C. K. Recent Advances in Room-Temperature Direct C–H Arylation Methodologies. *Synthesis* **2023**, *55*, 1–26. https://doi.org/10.1055/a-1939-7052.

(21) Liégault, B.; Lapointe, D.; Caron, L.; Vlassova, A.; Fagnou, K. Establishment of Broadly Applicable Reaction Conditions for the Palladium-Catalyzed Direct Arylation of Heteroatom-Containing Aromatic Compounds. *J. Org. Chem.* **2009**, *74*, 1826–1834. https://doi.org/10.1021/jo8026565.

(22) Besselièvre, F.; Lebrequier, S.; Mahuteau-Betzer, F.; Piguel, S. C–H Bond Activation: A Versatile Protocol for the Direct Arylation and Alkenylation of Oxazoles. *Synthesis* **2009**, *2009*, 3511–3518. https://doi.org/10.1055/s-0029-1216987.

(23) Messaoudi, S.; Brion, J.-D.; Alami, M. Transition-Metal-Catalyzed Direct C–H Alkenylation, Alkynylation, Benzylation, and Alkylation of (Hetero)Arenes. *Eur. J. Org. Chem.***2010**, *2010*, 6495–6516. https://doi.org/10.1002/ejoc.201000928.

(24) Rossi, R.; Bellina, F.; Lessi, M. Alkenylation Reactions of Heteroarenes by Transition-Metal Catalysts. *Synthesis* **2010**, *2010*, 4131–4153. https://doi.org/10.1055/s-0030-1258262.

(25) Chen, S.; Ranjan, P.; Voskressensky, L. G.; Van der Eycken, E. V.; Sharma, U. K. Recent Developments in Transition-Metal Catalyzed Direct C–H Alkenylation, Alkylation, and Alkynylation of Azoles. *Molecules* **2020**, *25*, 4970. https://doi.org/10.3390/molecules25214970.

(26) Dombrowski, A. W.; Gesmundo, N. J.; Aguirre, A. L.; Sarris, K. A.; Young, J. M.; Bogdan, A. R.; Martin, M. C.; Gedeon, S.; Wang, Y. Expanding the Medicinal Chemist Toolbox: Comparing Seven $C(Sp^2)$–$C(Sp^3)$ Cross-Coupling Methods by Library Synthesis. *ACS Med. Chem. Lett.* **2020**, *11*, 597–604. https://doi.org/10.1021/acsmedchemlett.0c00093.

(27) Fedoriw, A.; Rajapurkar, S. R.; O'Brien, S.; Gerhart, S. V.; Mitchell, L. H.; Adams, N. D.; Rioux, N.; Lingaraj, T.; Ribich, S. A.; Pappalardi, M. B.; Shah, N.; Laraio, J.; Liu, Y.; Butticello, M.; Carpenter, C. L.; Creasy, C.; Korenchuk, S.; McCabe, M. T.; McHugh, C. F.; Nagarajan, R.; Wagner, C.; Zappacosta, F.; Annan, R.; Concha, N. O.; Thomas, R. A.; Hart, T. K.; Smith, J. J.; Copeland, R. A.; Moyer, M. P.; Campbell, J.; Stickland, K.; Mills, J.; Jacques-O'Hagan, S.; Allain, C.; Johnston, D.; Raimondi, A.; Porter Scott, M.; Waters, N.; Swinger, K.; Boriack-Sjodin, A.; Riera, T.; Shapiro, G.; Chesworth, R.; Prinjha, R. K.; Kruger, R. G.; Barbash, O.; Mohammad, H. P. Anti-Tumor Activity of the Type I PRMT Inhibitor, GSK3368715, Synergizes with PRMT5 Inhibition through MTAP Loss. *Cancer Cell* **2019**, *36*, 100-114. https://doi.org/10.1016/j.ccell.2019.05.014.

(28) Besselièvre, F.; Piguel, S.; Mahuteau-Betzer, F.; Grierson, D. S. Stereoselective Direct Copper-Catalyzed Alkenylation of Oxazoles with Bromoalkenes. *Org. Lett.* **2008**, *10*, 4029–4032. https://doi.org/10.1021/ol801512q.
(29) Das, B.; Reddy, G. C.; Balasubramanyam, P.; Salvanna, N. Copper-Catalyzed Direct Cross Coupling of 1,3,4-Oxadiazoles with Trans-β-Halostyrenes: Synthesis of 2-E-Vinyl 1,3,4-Oxadiazoles. *Tetrahedron* **2012**, *68*, 300–305. https://doi.org/10.1016/j.tet.2011.10.049.
(30) Rousée, K.; Schneider, C.; Bouillon, J.-P.; Levacher, V.; Hoarau, C.; Couve-Bonnaire, S.; Pannecoucke, X. Copper-Catalyzed Direct C–H Fluoroalkenylation of Heteroarenes. *Org. Biomol. Chem.* **2015**, *14*, 353–357. https://doi.org/10.1039/C5OB02213D.
(31) Meng, L.; Kamada, Y.; Muto, K.; Yamaguchi, J.; Itami, K. C□H Alkenylation of Azoles with Enols and Esters by Nickel Catalysis. *Angew. Chem. Int. Ed.***2013**, *52*, 10048–10051. https://doi.org/10.1002/anie.201304492.
(32) Muto, K.; Hatakeyama, T.; Yamaguchi, J.; Itami, K. C–H Arylation and Alkenylation of Imidazoles by Nickel Catalysis: Solvent-Accelerated Imidazole C–H Activation. *Chem. Sci.* **2015**, *6*, 6792–6798. https://doi.org/10.1039/C5SC02942B.
(33) Jagtap, R. A.; Vinod, C. P.; Punji, B. Nickel-Catalyzed Straightforward and Regioselective C–H Alkenylation of Indoles with Alkenyl Bromides: Scope and Mechanistic Aspect. *ACS Catal.* **2019**, *9*, 431–441. https://doi.org/10.1021/acscatal.8b04267.
(34) Patel, U. N.; Jagtap, R. A.; Punji, B. Scope and Mechanistic Aspect of Nickel-Catalyzed Alkenylation of Benzothiazoles and Related Azoles with Styryl Bromides. *Organometallics* **2019**, *38*, 2422–2430. https://doi.org/10.1021/acs.organomet.9b00060.
(35) Oi, S.; Fukita, S.; Hirata, N.; Watanuki, N.; Miyano, S.; Inoue, Y. Ruthenium Complex-Catalyzed Direct Ortho Arylation and Alkenylation of 2-Arylpyridines with Organic Halides. *Org. Lett.* **2001**, *3*, 2579–2581. https://doi.org/10.1021/ol016257z.
(36) Oi, S.; Ogino, Y.; Fukita, S.; Inoue, Y. Ruthenium Complex Catalyzed Direct Ortho Arylation and Alkenylation of Aromatic Imines with Organic Halides. *Org. Lett.* **2002**, *4*, 1783–1785. https://doi.org/10.1021/ol025851l.
(37) Oi, S.; Aizawa, E.; Ogino, Y.; Inoue, Y. Ortho-Selective Direct Cross-Coupling Reaction of 2-Aryloxazolines and 2-Arylimidazolines with Aryl and Alkenyl Halides Catalyzed by Ruthenium Complexes. *J. Org. Chem.* **2005**, *70*, 3113–3119. https://doi.org/10.1021/jo050031i.
(38) Hu, Z.; Belitz, F.; Zhang, G.; Papp, F.; Gooßen, L. J. Ru-Catalyzed (E)-Specific Ortho-C–H Alkenylation of Arenecarboxylic Acids by Coupling with Alkenyl Bromides. *Org. Lett.* **2021**, *23*, 3541–3545. https://doi.org/10.1021/acs.orglett.1c00956.
(39) Zaitsev, V. G.; Daugulis, O. Catalytic Coupling of Haloolefins with Anilides. *J. Am. Chem. Soc.* **2005**, *127*, 4156–4157. https://doi.org/10.1021/ja050366h.
(40) Ackermann, L.; Althammer, A.; Fenner, S. Palladium-Catalyzed Direct Arylations of Heteroarenes with Tosylates and Mesylates. *Angew. Chem. Int. Ed.***2009**, *48*, 201–204. https://doi.org/10.1002/anie.200804517.
(41) Ackermann, L.; Barfüsser, S.; Pospech, J. Palladium-Catalyzed Direct Arylations, Alkenylations, and Benzylations through C−H Bond Cleavages with Sulfamates or Phosphates as Electrophiles. *Org. Lett.* **2010**, *12*, 724–726. https://doi.org/10.1021/ol9028034.
(42) Ackermann, L.; Fenner, S. Direct Arylations of Electron-Deficient (Hetero)Arenes with Aryl or Alkenyl Tosylates and Mesylates. *Chem. Commun.* **2011**, *47*, 430–432. https://doi.org/10.1039/C0CC02360D.

(43) Sahnoun, S.; Messaoudi, S.; Peyrat, J.-F.; Brion, J.-D.; Alami, M. Microwave-Assisted $Pd(OH)_2$-Catalyzed Direct C−H Arylation of Free-(NH_2) Adenines with Aryl Halides. *Tetrahedron Lett.* **2008**, *49*, 7279–7283. https://doi.org/10.1016/j.tetlet.2008.10.021.
(44) Sahnoun, S.; Messaoudi, S.; Brion, J.-D.; Alami, M. Pd/Cu-Catalyzed Direct Alkenylation of Azole Heterocycles with Alkenyl Halides. *Eur. J. Org. Chem.***2010**, *31*, 6097–6102. https://doi.org/10.1002/ejoc.201000959.
(45) Gottumukkala, A. L.; Derridj, F.; Djebbar, S.; Doucet, H. Alkenyl Bromides: Useful Coupling Partners for the Palladium-Catalysed Coupling with Heteroaromatics via a C–H Bond Activation. *Tetrahedron Lett.* **2008**, *49*, 2926–2930. https://doi.org/10.1016/j.tetlet.2008.03.020.
(46) Koubachi, J.; El Kazzouli, S.; Berteina-Raboin, S.; Mouaddib, A.; Guillaumet, G. New and Efficient Palladium(0)-Mediated Microwave-Assisted Direct C3 Alkenylation of Imidazo[1,2- *a*]Pyridines. *Synthesis* **2008**, *2008* (16), 2537–2542. https://doi.org/10.1055/s-2008-1067181.
(47) Rodriguez, A.; Fennessy, R. V.; Moran, W. J. Palladium-Catalysed Direct Alkenylation of Sydnones. *Tetrahedron Lett.* **2009**, *50*, 3942–3944. https://doi.org/10.1016/j.tetlet.2009.04.075.
(48) Schneider, C.; Masi, D.; Couve-Bonnaire, S.; Pannecoucke, X.; Hoarau, C. Palladium- and Copper-Catalyzed Stereocontrolled Direct C−H Fluoroalkenylation of Heteroarenes Using Gem-Bromofluoroalkenes. *Angew. Chem. Int. Ed.***2013**, *52*, 3246–3249. https://doi.org/10.1002/anie.201209446.
(49) Verrier, C.; Hoarau, C.; Marsais, F. Direct Palladium-Catalyzed Alkenylation, Benzylation and Alkylation of Ethyl Oxazole-4-Carboxylate with Alkenyl-, Benzyl- and Alkyl Halides. *Org. Biomol. Chem.* **2009**, *7*, 647–650. https://doi.org/10.1039/B816374J.
(50) Muselli, M.; Baudequin, C.; Hoarau, C.; Bischoff, L. Pd-Catalyzed Direct C–H Functionalization of Imidazolones with Aryl- and Alkenyl Halides. *Chem. Commun.* **2014**, *51* (4), 745–748. https://doi.org/10.1039/C4CC07917E.
(51) Baladi, T.; Granzhan, A.; Piguel, S. Microwave-Assisted C-2 Direct Alk-enylation of Imidazo[4,5-b]Pyr-idines: Access to Fluorescent Purine Isosteres with Remarkably Large Stokes Shifts. *Eur. J. Org. Chem.***2016**, *14*, 2421–2434. https://doi.org/10.1002/ejoc.201600166.
(52) Mousseau, J. J.; Fortier, A.; Charette, A. B. Synthesis of 2-Substituted Pyrazolo[1,5-a]Pyridines through Cascade Direct Alkenylation/Cyclization Reactions. *Org. Lett.* **2010**, *12*, 516–519. https://doi.org/10.1021/ol902710f.
(53) Zhao, Q.; Besset, T.; Poisson, T.; Bouillon, J.-P.; Pannecoucke, X. Palladium-Catalysed Synthesis of α-(Trifluoromethyl)Styrenes by Means of Directed C–H Bond Functionalization. *Eur. J. Org. Chem.***2016**, *1*, 76–82. https://doi.org/10.1002/ejoc.201501217.
(54) Zhao, Q.; Tognetti, V.; Joubert, L.; Besset, T.; Pannecoucke, X.; Bouillon, J.-P.; Poisson, T. Palladium-Catalyzed Synthesis of 3-Trifluoromethyl-Substituted 1,3-Butadienes by Means of Directed C–H Bond Functionalization. *Org. Lett.* **2017**, *19*, 2106–2109. https://doi.org/10.1021/acs.orglett.7b00704.
(55) Fu, W. C.; Wu, Y.; So, C. M.; Wong, S. M.; Lei, A.; Kwong, F. Y. Catalytic Direct C2-Alkenylation of Oxazoles at Parts per Million Levels of Palladium/PhMezole-Phos Complex. *Org. Lett.* **2016**, *18*, 5300–5303. https://doi.org/10.1021/acs.orglett.6b02619.

(56) Pipaón Fernández, N.; Gaube, G.; Woelk, K. J.; Burns, M.; Hruszkewycz, D. P.; Leitch, D. C. Palladium-Catalyzed Direct C–H Alkenylation with Enol Pivalates Proceeds via Reversible C–O Oxidative Addition to Pd(0). *ACS Catal.* **2022**, *12*, 6997–7003. https://doi.org/10.1021/acscatal.2c01305.
(57) Lotz, M. D.; Camasso, N. M.; Canty, A. J.; Sanford, M. S. Role of Silver Salts in Palladium-Catalyzed Arene and Heteroarene C–H Functionalization Reactions. *Organometallics* **2017**, *36*, 165–171. https://doi.org/10.1021/acs.organomet.6b00437.
(58) Whitaker, D.; Burés, J.; Larrosa, I. Ag(I)-Catalyzed C–H Activation: The Role of the Ag(I) Salt in Pd/Ag-Mediated C–H Arylation of Electron-Deficient Arenes. *J. Am. Chem. Soc.* **2016**, *138*, 8384–8387. https://doi.org/10.1021/jacs.6b04726.
(59) Panigrahi, A.; Whitaker, D.; Vitorica-Yrezabal, I. J.; Larrosa, I. Ag/Pd Cocatalyzed Direct Arylation of Fluoroarene Derivatives with Aryl Bromides. *ACS Catal.* **2020**, *10*, 2100–2107. https://doi.org/10.1021/acscatal.9b05334.
(60) Huang, J.; Chan, J.; Chen, Y.; Borths, C. J.; Baucom, K. D.; Larsen, R. D.; Faul, M. M. A Highly Efficient Palladium/Copper Cocatalytic System for Direct Arylation of Heteroarenes: An Unexpected Effect of Cu(Xantphos)I. *J. Am. Chem. Soc.* **2010**, *132*, 3674–3675. https://doi.org/10.1021/ja100354j.
(61) Bay, K. L.; Yang, Y.-F.; Houk, K. N. Multiple Roles of Silver Salts in Palladium-Catalyzed C–H Activations. *J. Organomet. Chem.* **2018**, *864*, 19–25. https://doi.org/10.1016/j.jorganchem.2017.12.026.
(62) Bhaskararao, B.; Singh, S.; Anand, M.; Verma, P.; Prakash, P.; C, A.; Malakar, S.; Schaefer, H. F.; Sunoj, R. B. Is Silver a Mere Terminal Oxidant in Palladium Catalyzed C–H Bond Activation Reactions? *Chem. Sci.* **2019**, *11*, 208–216. https://doi.org/10.1039/C9SC04540F.
(63) Tlahuext-Aca, A.; Lee, S. Y.; Sakamoto, S.; Hartwig, J. F. Direct Arylation of Simple Arenes with Aryl Bromides by Synergistic Silver and Palladium Catalysis. *ACS Catal.* **2021**, *11*, 1430–1434. https://doi.org/10.1021/acscatal.0c05254.
(64) Tlahuext-Aca, A.; Hartwig, J. F. Site-Selective Silver-Catalyzed C–H Bond Deuteration of Five-Membered Aromatic Heterocycles and Pharmaceuticals. *ACS Catal.* **2021**, *11*, 1119–1127. https://doi.org/10.1021/acscatal.0c04917.
(65) Shimoyama, Y.; Kuwabara, J.; Kanbara, T. Mechanistic Study of Pd/Ag Dual-Catalyzed Cross-Dehydrogenative Coupling of Perfluoroarenes with Thiophenes. *ACS Catal.* **2020**, *10* (5), 3390–3397. https://doi.org/10.1021/acscatal.9b05326.
(66) Anand, M.; Sunoj, R. B.; Schaefer, H. F. Non-Innocent Additives in a Palladium(II)-Catalyzed C–H Bond Activation Reaction: Insights into Multimetallic Active Catalysts. *J. Am. Chem. Soc.* **2014**, *136* (15), 5535–5538. https://doi.org/10.1021/ja412770h.
(67) Fu, X.-P.; Xuan, Q.-Q.; Liu, L.; Wang, D.; Chen, Y.-J.; Li, C.-J. Dual C–H Activations of Electron-Deficient Heteroarenes: Palladium-Catalyzed Oxidative Cross Coupling of Thiazoles with Azine N-Oxides. *Tetrahedron* **2013**, *69*, 4436–4444. https://doi.org/10.1016/j.tet.2012.10.048.
(68) Piou, T.; Slutskyy, Y.; Kevin, N. J.; Sun, Z.; Xiao, D.; Kong, J. Direct Arylation of Azoles Enabled by Pd/Cu Dual Catalysis. *Org. Lett.* **2021**, *23*, 1996–2001. https://doi.org/10.1021/acs.orglett.1c00100.
(69) Liu, C.; Ji, C.-L.; Zhou, T.; Hong, X.; Szostak, M. Bimetallic Cooperative Catalysis for Decarbonylative Heteroarylation of Carboxylic Acids via C–O/C–H Coupling. *Angew. Chem. Int. Edition*, **2021**, 60, 10690–10699. https://doi.org/10.1002/anie.202100949.

(70) Henderson, W. H.; Alvarez, J. M.; Eichman, C. C.; Stambuli, J. P. Characterization, Reactivity, and Potential Catalytic Intermediacy of a Cyclometalated Tri -*Tert* - Butylphosphine Palladium Acetate Complex. *Organometallics* **2011**, *30*, 5038–5044. https://doi.org/10.1021/om2006936.
(71) Aldrichimica Acta 46.3. **2013**, *46*, 71–80.
(72) Buitrago Santanilla, A.; Regalado, E. L.; Pereira, T.; Shevlin, M.; Bateman, K.; Campeau, L.-C.; Schneeweis, J.; Berritt, S.; Shi, Z.-C.; Nantermet, P.; Liu, Y.; Helmy, R.; Welch, C. J.; Vachal, P.; Davies, I. W.; Cernak, T.; Dreher, S. D. Nanomole-Scale High-Throughput Chemistry for the Synthesis of Complex Molecules. *Science* **2015**, *347*, 49–53. https://doi.org/10.1126/science.1259203.
(73) Allen, C. L.; Leitch, D. C.; Anson, M. S.; Zajac, M. A. The Power and Accessibility of High-Throughput Methods for Catalysis Research. *Nat Catal* **2019**, *2*, 2–4. https://doi.org/10.1038/s41929-018-0220-4.
(74) Mennen, S. M.; Alhambra, C.; Allen, C. L.; Barberis, M.; Berritt, S.; Brandt, T. A.; Campbell, A. D.; Castañón, J.; Cherney, A. H.; Christensen, M.; Damon, D. B.; Eugenio de Diego, J.; García-Cerrada, S.; García-Losada, P.; Haro, R.; Janey, J.; Leitch, D. C.; Li, L.; Liu, F.; Lobben, P. C.; MacMillan, D. W. C.; Magano, J.; McInturff, E.; Monfette, S.; Post, R. J.; Schultz, D.; Sitter, B. J.; Stevens, J. M.; Strambeanu, I. I.; Twilton, J.; Wang, K.; Zajac, M. A. The Evolution of High-Throughput Experimentation in Pharmaceutical Development and Perspectives on the Future. *Org. Process Res. Dev.* **2019**, *23*, 1213–1242. https://doi.org/10.1021/acs.oprd.9b00140.
(75) Isbrandt, E. S.; Sullivan, R. J.; Newman, S. G. High Throughput Strategies for the Discovery and Optimization of Catalytic Reactions. *Angew. Chem. Int. Ed.***2019**, *58*, 7180–7191. https://doi.org/10.1002/anie.201812534.
(76) Cook, A.; Clément, R.; Newman, S. G. Reaction Screening in Multiwell Plates: High-Throughput Optimization of a Buchwald–Hartwig Amination. *Nat Protoc* **2021**, *16*, 1152–1169. https://doi.org/10.1038/s41596-020-00452-7.
(77) Leitch, D. C.; Becica, J. 13.12 - High-Throughput Experimentation in Organometallic Chemistry and Catalysis. In *Comprehensive Organometallic Chemistry IV*; Parkin, G., Meyer, K., O'hare, D., Eds.; Elsevier: Oxford, 2022; pp 502–555. https://doi.org/10.1016/B978-0-12-820206-7.00111-6.
(78) Weissman, S. A.; Anderson, N. G. Design of Experiments (DoE) and Process Optimization. A Review of Recent Publications. *Org. Process Res. Dev.* **2015**, *19*, 1605–1633. https://doi.org/10.1021/op500169m.
(79) Murray, P. M.; Bellany, F.; Benhamou, L.; Bučar, D.-K.; Tabor, A. B.; Sheppard, T. D. The Application of Design of Experiments (DoE) Reaction Optimisation and Solvent Selection in the Development of New Synthetic Chemistry. *Org. Biomol. Chem.* **2016**, *14*, 2373–2384. https://doi.org/10.1039/C5OB01892G.
(80) Taylor, C. J.; Pomberger, A.; Felton, K. C.; Grainger, R.; Barecka, M.; Chamberlain, T. W.; Bourne, R. A.; Johnson, C. N.; Lapkin, A. A. A Brief Introduction to Chemical Reaction Optimization. *Chem. Rev.* **2023**, *123*, 3089–3126. https://doi.org/10.1021/acs.chemrev.2c00798.
(81) Ghosh, I.; Shlapakov, N.; Karl, T. A.; Düker, J.; Nikitin, M.; Burykina, J. V.; Ananikov, V. P.; König, B. General Cross-Coupling Reactions with Adaptive Dynamic Homogeneous Catalysis. *Nature* **2023**, *619*, 87–93. https://doi.org/10.1038/s41586-023-06087-4.

(82) Herrmann, W. A.; Brossmer, C.; Öfele, K.; Reisinger, C.-P.; Priermeier, T.; Beller, M.; Fischer, H. Palladacycles as Structurally Defined Catalysts for the Heck Olefination of Chloro- and Bromoarenes. *Angew. Chem. Int. Ed.* **1995**, *34*, 1844–1848. https://doi.org/10.1002/anie.199518441.
(83) Herrmann, W. A.; Brossmer, C.; Reisinger, C.-P.; Riermeier, T. H.; Öfele, K.; Beller, M. Palladacycles: Efficient New Catalysts for the Heck Vinylation of Aryl Halides. *Chem. Eur. J.***1997**, *3*, 1357–1364. https://doi.org/10.1002/chem.19970030823.
(84) Bedford, R. B. Palladacyclic Catalysts in C–C and C–Heteroatom Bond-Forming Reactions. *Chem. Commun.* **2003**, *15*, 1787–1796. https://doi.org/10.1039/B211298C.
(85) Beletskaya, I. P.; Cheprakov, A. V. Palladacycles in Catalysis – a Critical Survey. *J. Organomet. Chem.* **2004**, *689*, 4055–4082. https://doi.org/10.1016/j.jorganchem.2004.07.054.
(86) Wu, L.; Hartwig, J. F. Mild Palladium-Catalyzed Selective Monoarylation of Nitriles. *J. Am. Chem. Soc.* **2005**, *127*, 15824–15832. https://doi.org/10.1021/ja053027x.
(87) Gorelsky, S. I.; Lapointe, D.; Fagnou, K. Analysis of the Concerted Metalation-Deprotonation Mechanism in Palladium-Catalyzed Direct Arylation Across a Broad Range of Aromatic Substrates. *J. Am. Chem. Soc.* **2008**, *130*, 10848–10849. https://doi.org/10.1021/ja802533u.
(88) Lapointe, D.; Fagnou, K. Overview of the Mechanistic Work on the Concerted Metallation–Deprotonation Pathway. *Chem. Lett.* **2010**, *39*, 1118–1126. https://doi.org/10.1246/cl.2010.1118.
(89) Ackermann, L. Carboxylate-Assisted Transition-Metal-Catalyzed C−H Bond Functionalizations: Mechanism and Scope. *Chem. Rev.* **2011**, *111*, 1315–1345. https://doi.org/10.1021/cr100412j.
(90) Gorelsky, S. I.; Lapointe, D.; Fagnou, K. Analysis of the Palladium-Catalyzed (Aromatic)C–H Bond Metalation–Deprotonation Mechanism Spanning the Entire Spectrum of Arenes. *J. Org. Chem.* **2012**, *77*, 658–668. https://doi.org/10.1021/jo202342q.
(91) Tan, Y.; Barrios-Landeros, F.; Hartwig, J. F. Mechanistic Studies on Direct Arylation of Pyridine N-Oxide: Evidence for Cooperative Catalysis between Two Distinct Palladium Centers. *J. Am. Chem. Soc.* **2012**, *134*, 3683–3686. https://doi.org/10.1021/ja2122156.
(92) Fors, B. P.; Krattiger, P.; Strieter, E.; Buchwald, S. L. Water-Mediated Catalyst Preactivation: An Efficient Protocol for C−N Cross-Coupling Reactions. *Org. Lett.* **2008**, *10*, 3505–3508. https://doi.org/10.1021/ol801285g.
(93) Wei, C. S.; Davies, G. H. M.; Soltani, O.; Albrecht, J.; Gao, Q.; Pathirana, C.; Hsiao, Y.; Tummala, S.; Eastgate, M. D. The Impact of Palladium(II) Reduction Pathways on the Structure and Activity of Palladium(0) Catalysts. *Angew. Chem. Int. Ed.***2013**, *52*, 5822–5826. https://doi.org/10.1002/anie.201210252.
(94) Wagschal, S.; Perego, L. A.; Simon, A.; Franco-Espejo, A.; Tocqueville, C.; Albaneze-Walker, J.; Jutand, A.; Grimaud, L. Formation of XPhos-Ligated Palladium(0) Complexes and Reactivity in Oxidative Additions. *Chem. Eur. J.***2019**, *25*, 6980–6987. https://doi.org/10.1002/chem.201900451.
(95) Fogg, D. E.; dos Santos, E. N. Tandem Catalysis: A Taxonomy and Illustrative Review. *Coordination Chemistry Reviews* **2004**, *248*, 2365–2379. https://doi.org/10.1016/j.ccr.2004.05.012.
(96) Wasilke, J.-C.; Obrey, S. J.; Baker, R. T.; Bazan, G. C. Concurrent Tandem Catalysis. *Chem. Rev.* **2005**, *105* (3), 1001–1020. https://doi.org/10.1021/cr020018n.

(97) Lohr, T. L.; Marks, T. J. Orthogonal Tandem Catalysis. *Nature Chem* **2015**, *7*, 477–482. https://doi.org/10.1038/nchem.2262.
(98) Kim, J.; Hong, S. H. Ligand-Promoted Direct C–H Arylation of Simple Arenes: Evidence for a Cooperative Bimetallic Mechanism. *ACS Catal.* **2017**, *7*, 3336–3343. https://doi.org/10.1021/acscatal.7b00397.
(99) Becica, J.; Hruszkewycz, D. P.; Steves, J. E.; Elward, J. M.; Leitch, D. C.; Dobereiner, G. E. High-Throughput Discovery and Evaluation of a General Catalytic Method for *N* -Arylation of Weakly Nucleophilic Sulfonamides. *Org. Lett.* **2019**, *21*, 8981–8986. https://doi.org/10.1021/acs.orglett.9b03380.
(100) Wagen, C. C.; McMinn, S. E.; Kwan, E. E.; Jacobsen, E. N. Screening for Generality in Asymmetric Catalysis. *Nature* **2022**, *610*, 680–686. https://doi.org/10.1038/s41586-022-05263-2.

CHAPTER 4: Assessing Ancillary Ligand Effects for the Pd-Catalyzed Direct Alkenylation of Thiazoles

This chapter is not yet published.

Nahiane Pipaon Fernández, Hailey Gray, Brennan Rose, Damian P. Hruszkewycz, and David C. Leitch. *Manuscript in preparation.*

Contributions:

Synthesis of starting materials and high-throughput experiments were performed by Nahiane Pipaon Fernandez. Synthesis and characterization of catalysts **I**, **II**, III, **VI**, **VII** were performed by Nahiane Pipaon Fernandez. Synthesis and characterization of catalyst **V** was performed by Hailey Gray. Isolation and characterization of coupling products were performed by Nahiane Pipaon Fernandez.

4.1 Abstract

The formation of multiple products during direct functionalization reactions of C–H bonds is a common problem. The lack of selectivity, specifically for thiazole substrates, is influenced by the palladium precatalyst and ancillary ligand. The one-factor-at-a-time approach to determine the extent in which these factors influence selectivity is not suitable for the development of an efficient and selective palladium precatalyst. In this Chapter, a chlorine bridged tri-*tert*-butyl palladacycle was designed for the systematic exploration of ancillary ligands using an HTE approach. As a result, a single component palladium precatalyst was identified for the selective direct alkenylation of thiazoles. It was also determined that the electronic features of the substrate considerably

influences the selectivity of the reaction. The study of the speciation during the reaction showed that the pivalate *tert*-butyl palladacycle precatalyst is more selective but less reactive than the previously reported (Chapter 3) precatalyst system. The single component precatalyst was applied to the synthesis of fatostatin, an investigational sterol regulatory element-binding protein (SREBP) inhibitor (Figure 4.1).

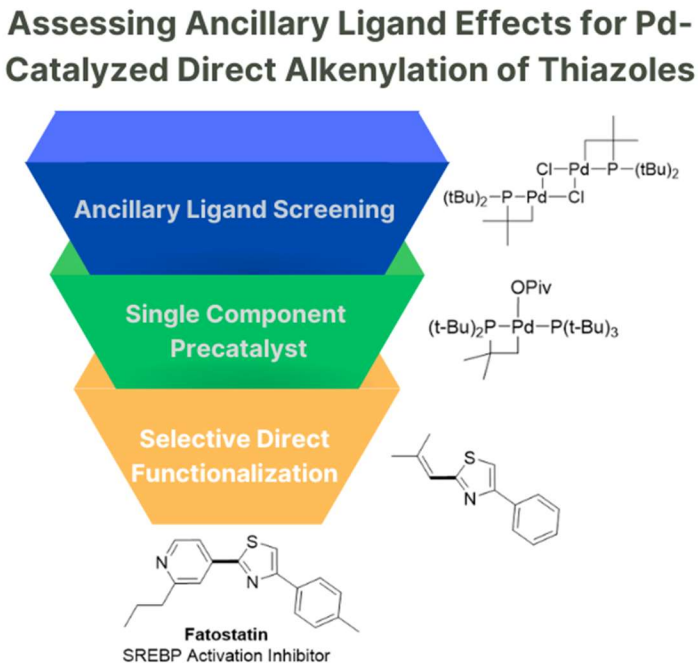

Figure 4.1. Ancillary ligand screening towards the development of a single component precatalyst for selective direct functionalization of thiazoles.

4.2 Introduction

4.2.1 Selective C–H Functionalization

As showcased in Chapters 1-3, C–H functionalization is a versatile set of reactions that allows the synthesis of simple to complex molecular scaffolds relevant to drug development and discovery. It allows functionalization at late stages of the synthesis, as it does not require pre-functionalization of the aromatic ring. However, one of the biggest challenges of C–H functionalization is achieving the desired selectivity for substrates with multiple C–H bonds. Non-selective C–H activation can result in regioisomeric species that can be hard to separate.[1] In a typical chemoselective reaction, a reagent may only have to differentiate between a small number of similar functional groups. In the case of C–H functionalization, every C–H bond in the molecule is possible a functional group.

For catalytic direct functionalization reactions, there are several approaches to control the selectivity of the reaction.[2] First, introducing steric bias by the utilization of bulky groups allows site selectivity by impeding the positions next to the sterically hindered positions and directing the catalyst towards less-hindered locations.[3] It is particularly useful for functionalizing multisubstituted benzene rings.[4] An example is the Rh-catalyzed direct arylation of anisole (Figure 4.2). While both *ortho* and *para* positions are electronically activated, the methoxy group hinders activation of the *ortho* C–H bond, giving the *para* product as the major species.[5] This approach suffers from poor selectivity when there is a steric-based competition between the incoming group and the target molecule, so it limits the functional groups that can be installed.[6]

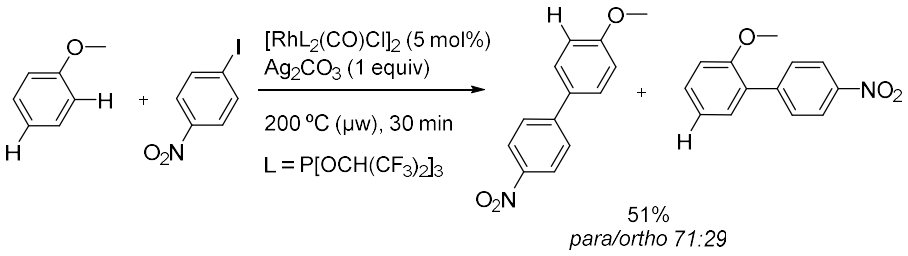

Figure 4.2. *Para*/*ortho* selective Rh-catalyzed direct arylation of anisole.

Directing groups offer another option, and can work in two different ways: they can bind to transitional metal catalyst and position it to activate a specific C–H bond, or they can introduce electronic bias in the substrate that activates specific C–H bonds. Metal coordinating directing groups usually contain heteroatoms such as nitrogen or oxygen; specific examples include pyridine, oxazoline, amide, carbonyl and hydroxy groups. In one example, Murai and co-workers developed a ketone-directed alkylation of acetophenone, where the metal catalyst coordinates to the oxygen atom and therefore activates the *ortho* C–H bond (Figure 4.3).[7]

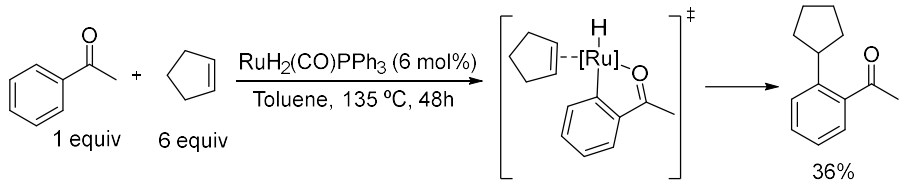

Figure 4.3. Murai's ketone-directed alkylation.

More recent strategies involve directing group free or non-directed protocols that achieve selectivity through ligand design.[8,9] Phosphines are common ligands used in organometallic C–H functionalization,[10] and their structural diversity means they can influence both catalytic activity and selectivity. The identification of suitable ligand/catalyst combinations is key to achieve high

efficiency and selectivity for a desired transformation.[11,12] However, identifying an optimal ligand from a large pool of ligand candidates is not easy. The traditional experimental approach of trial-and-error involves a feedback loop of design, synthesis, and evaluation, which is time-consuming and resource-intensive.[13] High-throughput screening techniques has emerged as an alternative to this approach, where many ligand candidates can be evaluated simultaneously.[14–16] More recently, approaches combining experimental and computational techniques can help guide ligand identification in the desired reaction using quantitative models to predict reactivity/selectivity based on structure (Figure 4.4).[17]

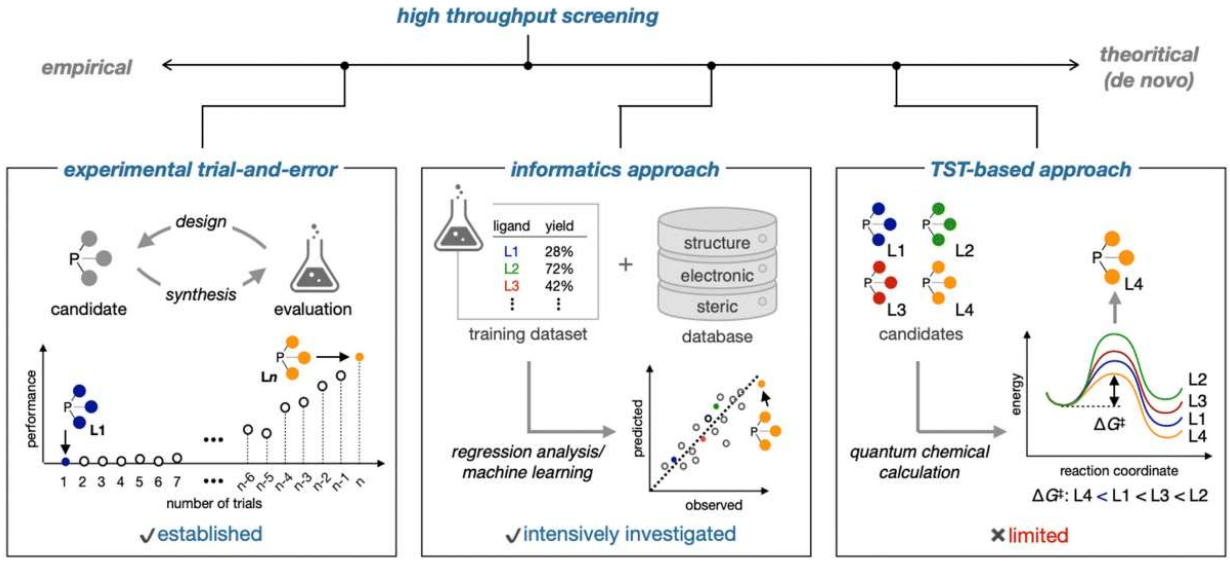

Figure 4.4. Schematic illustration of representative ligand screening approaches. (a) Conventional trial-and-error-based approach. (b) High-Throughput experiment-based approach. (c) TST-based approach. Adapted with permission from *Organic & Biomolecular Chemistry* **2023**, *21*, 3132-3142 Copyright {2023} The Royal Society of Chemistry.[13]

The ability to evaluate a wide variety of catalysts is limited by the need to synthesize and isolate them before use. To combat this, catalyst platforms that allow *in situ* assembly of the active

catalyst in a high-throughput manner can be used. This allows a rapid analysis of reactivity and selectivity without the need to isolate dozens of new precatalysts. An example is the *in situ* formation of cyclopentadienyl ligated metal complexes ($Cp^XM(LX)$) by Chang[14] for the HTE screening of both Cp and LX-type ligands (Figure 4.5). They were able to identify a rhodium catalyst system for C–H amination via multidimensional screening. The use of HTE enabled rapid examination of multiple reactions with minimum resources in a relative short period of time.

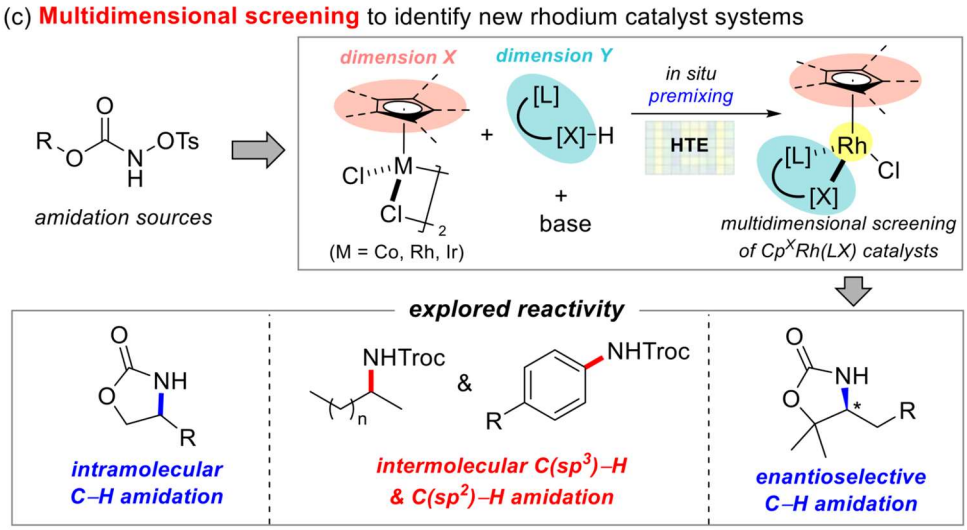

Figure 4.5. Multidimensional screening to identify efficient rhodium catalyst systems. Adapted with permission from *ACS Catalysis* **2022**, *12,* 8127-8138 Copyright {2022} American Chemical Society.

As described in Chapter 3, another factor in C–H functionalization reactions is the presence of metal-based additives. These can often lead to dual catalytic systems (where the metal additive is actually responsible for C–H activation) and/or divergent reaction outcomes. For example, Fagnou reported a regiodivergent arylation of indole, with the site-selectivity based on the choice of metal additive.[18] Silver acetate favors arylation at the C2 position, whereas copper acetate favors the C3 position (Figure 4.6).

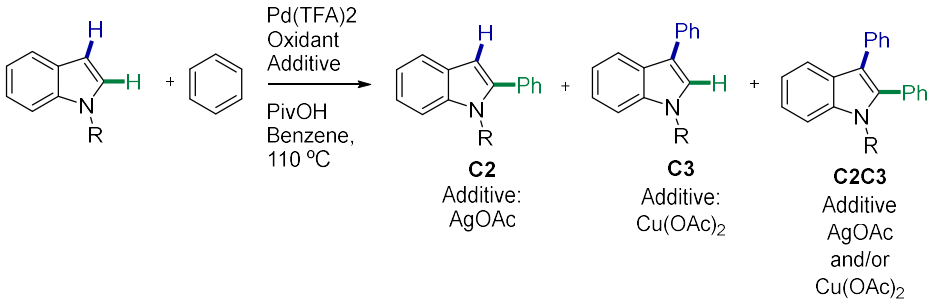

Figure 4.6. Regioselective C–H activation of indoles based on the metal additive.

4.2.2 Thiazoles in C–H Functionalization Reactions

Heterocycles are a broadly used scaffold in medicinal chemistry. Thiazole is one of the common five-membered heterocycle scaffolds present in several pharmaceutical drugs and drug candidates. Thiazole contains both nitrogen and sulfur atoms in an aromatic system, and many substituted derivatives are known. Thiazoles are present in compounds that have anticancer, analgesic, antiallergic, anti-inflammatory, antibacterial, antihypertensive, antimalarial, antipsychotic, diuretic, antifungal, hypnotic, neuroprotective, antioxidant properties, and many others (Figure 4.7).[19] The thiazole ring is also found in several natural products, including peptide alkaloids, metabolites and cyclopeptides.[20–22]

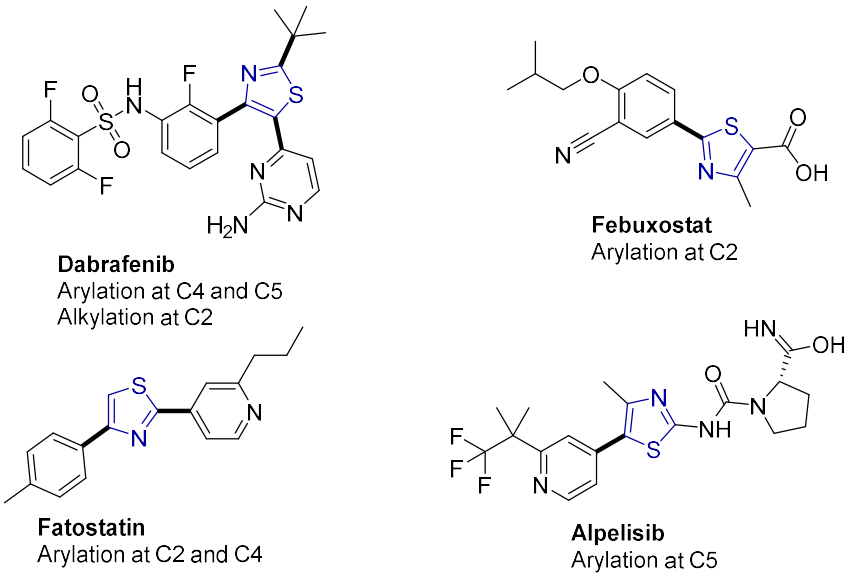

Figure 4.7. Examples of active pharmaceutical ingredients containing thiazole cores.

Traditional synthesis pathways for thiazoles include the Hantzsch synthesis, which requires the reaction between a thiourea and chloroacetone (Figure 4.8). As a result, one obtains a thiazole with an amine group at the C2 position, which limits the functionalization and diversification of thiazoles at later stages of the synthetic route. Another traditional route to thiazoles is the Cook-Heilbron synthesis (Figure 4.8). The synthesis requires carbon disulfide, which is neurotoxic. Like the Hantszch synthesis, it also results in specific substitution patterns (thiol at C2, amine at C5).

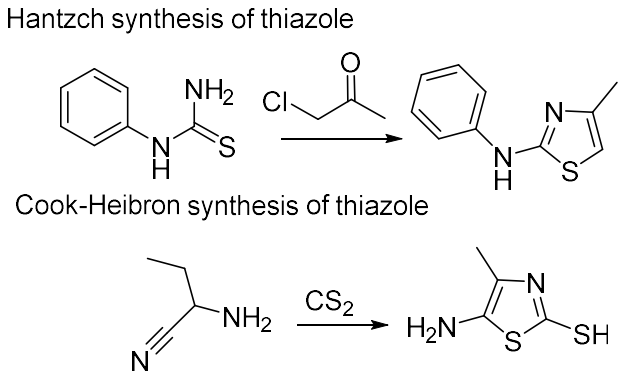

Figure 4.8. Hantzsch and Cook-Heibron synthesis of thiazoles.

As an alternative to these routes, the direct functionalization of thiazole (or its derivatives) is advantageous. Specifically, functionalization of the thiazole ring in later stages of drug synthesis is key for the development of new pharmaceutical candidates. C–H functionalization is ideal for this purpose; however, the electronically similar C–H bonds present in thiazoles present a challenge for regioselective C–H functionalization. Regioselectivity for electron-deficient arenes can be predicted from C–H bond acidities;[23] however, the pK_a values for both C5–H and C2–H are virtually identical (Figure 4.9). Based on calculated free activation energies ($\Delta G^{\ddagger}_{298K}$) for a model system, C–H activation by CMD would favor the C5 position. However the difference is small enough (2.6 kcal/mol) that both positions can be activated under the right reaction conditions.

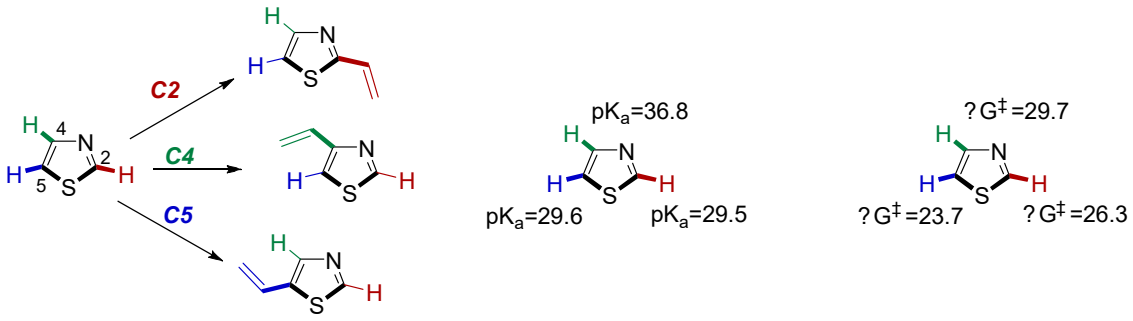

Figure 4.9. pK_a values and Gibbs free energies of activation ($\Delta G^{\ddagger}_{298K}$, kcal/mol) of the cleavage of C–H bonds for thiazole in CMD process using $Pd(C_6H_5)(PMe_3)OAc$ catalyst.

As discussed in Chapter 1, the regioselectivity of C–H activation that proceeds via concerted metallation deprotonation (CMD) is affected by the distortion and electronic interaction of the heterocycle and the catalyst.[24] Remote substituents can also affect the reactivity and regioselectivity of the reaction. For example, electron-withdrawing groups increase the acidity of C–H bonds. In the Gorelsky classification scheme,[23,25] thiazole is a Class II heterocycle, meaning that the main effect on the regioselectivity of the reaction is the interaction energy between the heterocycle and the palladium catalyst. Therefore, we hypothesized that different site selectivities should be possible by changing the metal catalyst.

Based on the C–H pK_a values and calculated $\Delta G^{\ddagger}$ for CMD at each site, the major sites for direct arylation/alkenylation of thiazoles are the C2 and C5 positions. The C5 site is more nucleophilic (Figure 4.10) while C2–H is slightly more acidic. In most reported cases, direct arylation occurs at the C5 position, but diarylation at both C2 and C5 positions is also fairly common. The selective arylation of each position is still a challenge. Reported examples achieve selectivity between the C2 and the C5 positions using diverse strategies (Figure 4.10). Many strategies for selective C5 coupling rely on blocking the C2 position.[26–29]

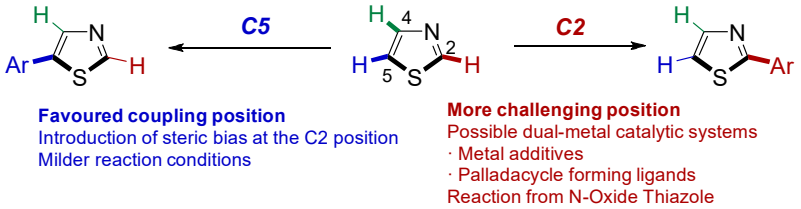

Figure 4.10. Current approaches for regioselective arylation of thiazole.

One of the approaches for changing the selectivity bias from the C5 to the C2 position is the use of thiazole *N*-oxide.[30] Other approaches involves the modification of reaction conditions. Metal-based additives (e.g. CuI and Ag_2CO_3) and specific phosphines (e.g. JohnPhos, P(*t*Bu)$_3$) can be used to favour the coupling at C2.[31–38] DFT calculations indicate that in dual metal catalyzed mechanisms (e.g. involving a Cu co-catalyst), coordination of the metal additive to the nitrogen atom switches regioselectivity from the C5 to the C2 positions.[31] Certain nickel catalysts can also selectively functionalize the C2–H bond, but they require higher catalyst loadings and blockage of the C5 position.[39–41]

The aim of this Chapter is to develop a palladium catalyst that can regioselectively alkenylate the thiazole C2 position without the need for metal-based additives or installation of directing groups.

4.3 Results and Discussion

4.3.1 Initial Observations of Direct Alkenylation Site-Selectivity for 4-Methylthiazole

During prior research on direct alkenylation of heterocycles with vinyl halides (Chapter 3), we observed the formation of two alkenylation regioisomers – C2 and C5 – when using 4-methylthiazole (**1a**) in combination with palladacycle precatalysts **I** and **II**. The ratio of these isomers depended on the reaction conditions, such as solvent, base and catalyst. Following up on these initial observations, a 96-experiment multifactor screen was designed to compare the reactivity and site-selectivity of **I** and I**I** for the coupling of **1a** and **2a** under a wide range of reaction conditions at high palladium loadings (Figure 4.11). Three solvents, with or without addition of tBuOH as a cosolvent, and eight bases were tested for each precatalyst. The solvents chosen included high boiling polar (*N*,*N*-dimethylacetamide, DMA) and non-polar (toluene and cyclopentylmethyl ether, CPME) solvents. Bases included both inorganic (K_3PO_4, KOtBu, K_2CO_3, Cs_2CO_3, Ag_2CO_3) and organic bases (diisopropylethylamine, DIPEA and 1,8-diazabicyclo(5.4.0)undec-7-ene, DBU). A "no base" setting was included to assess the need for exogenous base. Reaction mixtures were analyzed by ^{1}H NMR spectroscopy and LCMS.

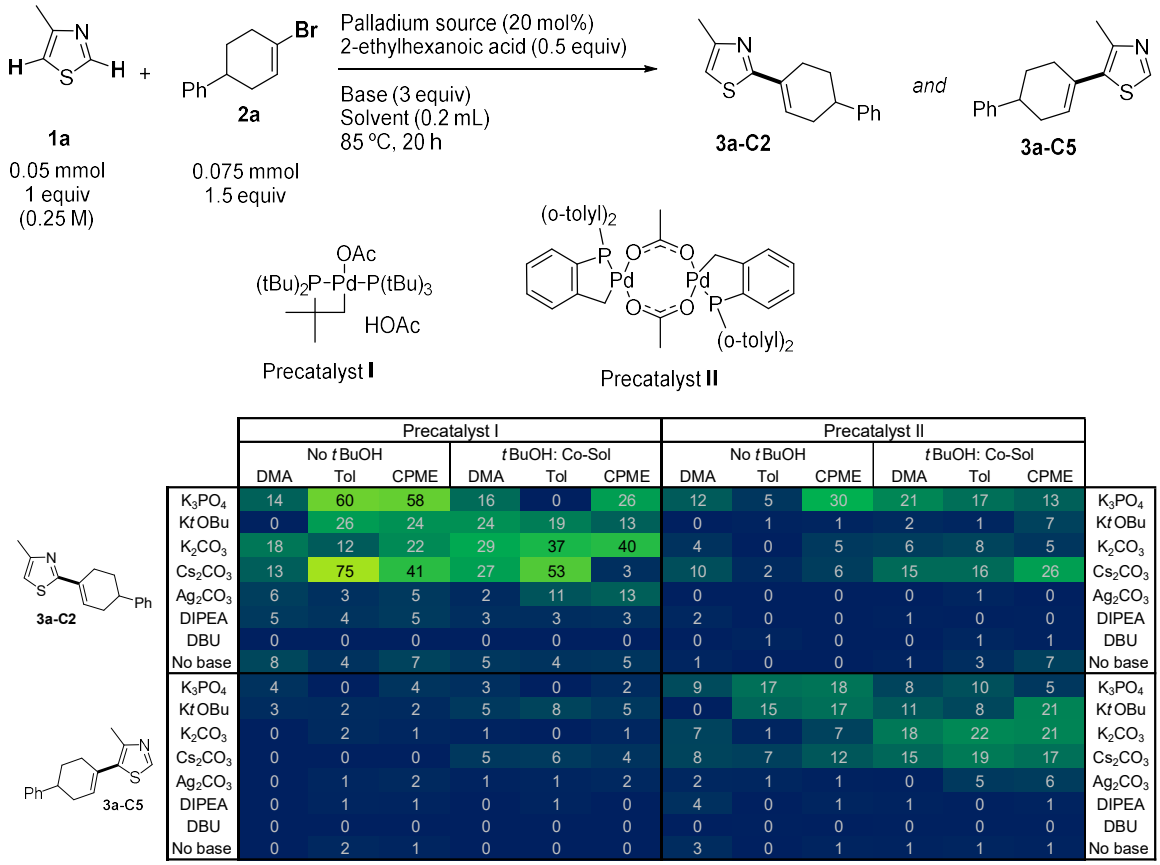

Figure 4.11. Multifactor evaluation of catalyst for the selective direct alkenylation of 4-methylthiazole, eight bases (K_3PO_4, KOtBu, K_2CO_3, Cs_2CO_3, Ag_2CO_3, DIPEA, DBU and no base), three solvents (DMA, Toluene and CPME) and two co-solvent options (no co-solvent and tBuOH as cosolvent).

An overall conclusion from this screen is that precatalyst **I** is selective for alkenylation at C2, whereas **II** is somewhat selective for C5. In terms of solvent effects, for **I** non-polar solvents appear to function best, and there is no advantage to using tBuOH as a cosolvent. When using **II**, the tBuOH cosolvent allows for higher reactivity and leads to formation of both isomers. In terms of bases, only inorganic bases lead to product formation, with potassium phosphate and cesium carbonate as the best options. Organic bases and silver carbonate are completely ineffective.

While the screening results show that precatalyst **I** forms product **3a-C2** selectively with high yields (58-75%) and moderate yields with precatalyst **II** (30%), the HTE screening was performed under high palladium loadings (20 mol%). Key examples were reproduced at lower palladium loadings (5 mol%), lower volume (0.2 mL) and base loading (1.5 equiv) (Table 4.1). Under these validation conditions, precatalyst **I** shows relatively low reaction yields (30-45%), and also lower selectivity for the C2 product.

Table 4.1 Validation condition optimization of **1a** and **2b**.

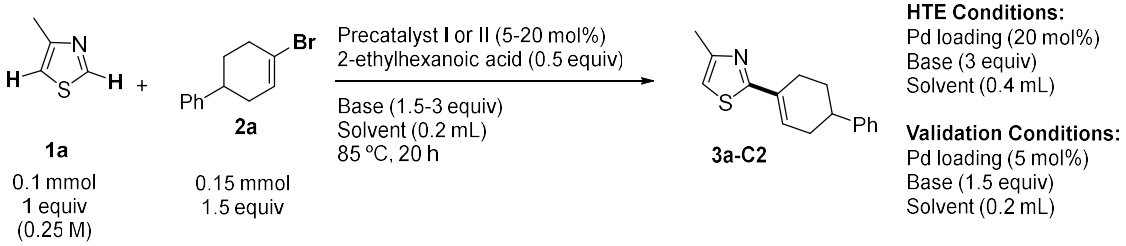

Entry	Precatalyst	Base	Solvent	HTE cond. C2 Yield	Validation cond. C2 Yield
1	I	K_3PO_4	CPME	58%	15%
2	I	K_3PO_4	Toluene	60%	15%
3	I	Cs_2CO_3	Toluene	75%	10%
4	II	K_3PO_4	CPME	30%	12%

Thus, the major factor influencing the site selectivity for direct alkenylation of **1a** is the catalyst structure. There are several differences between these two precatalysts. First, **I** is mononuclear whereas **II** is a carboxylate-bridged dimer. Second, the palladacycles are based on

two different phosphine ligands, leading to differences in metallacycle size as well as the extent of electron donation by the phosphorus center.

4.3.2 Modification of the Palladacycle Precatalysts

To further investigate catalyst-based effects on selectivity, and obtain a highly C2 selective system, a series of new palladacycles were prepared and evaluated. The general structure of these palladacycles is shown in Figure 4.12. The phosphine anchor can vary in sterics and electronics, which changes the bond strength of the Pd–P bond and also the electron density at Pd. For the metallacycle, the organic linker can vary in length, and the nature of the Pd–C bond. In the case of precatalysts **I** and **II**, the metallacycle is bonded to Pd through a CH_2 ligand, but with varied linker composition. For mononuclear palladacycles, an L-type ligand stabilizer is needed to occupy the fourth coordination site. For **I**, this is another equivalent of $P(tBu)_3$, whereas **II** does not have a ligand stabilizer (leading to its dimerization). Finally, the carboxylate is an X-type ligand that will undergo the CMD C–H activation reaction.

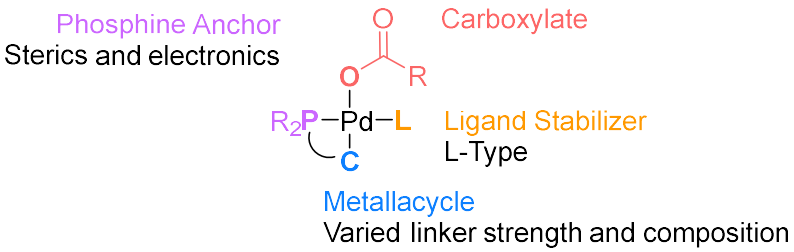

Figure 4.12. Structural features of palladacycle precatalysts.

The synthesis of palladacycles **I** and **II** can be achieved using simple reaction conditions, which involves reaction of $Pd(OAc)_2$ with either $P(tBu)_3$ (**I**) or $P(o\text{-tolyl})_3$ (**II**).[42,43] Following analogous reaction conditions, three new palladacycle precatalysts were prepared in good yields

(**III-V**, Figure 4.13). These include a dimeric version of **I** (**III**), and a monomeric version of **II** using P(o-tolyl)$_3$ as the L-type ligand stabilizer (**IV**).

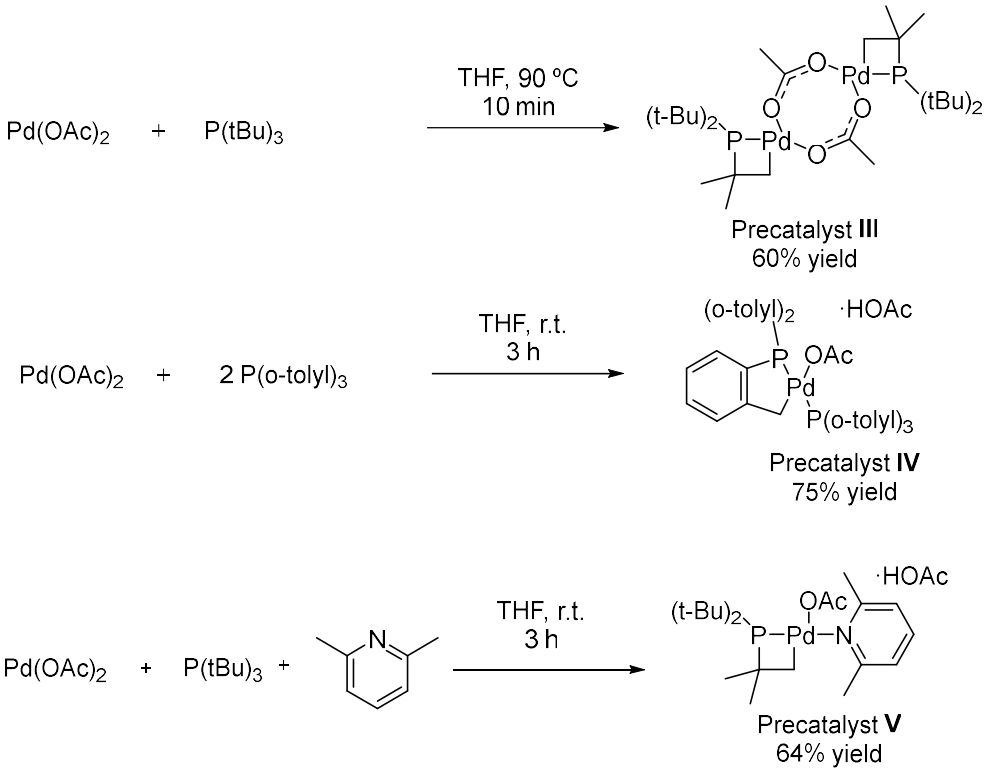

Figure 4.13. Synthesis of palladacycles **III**, **IV** and **V**.

To assess how changes to the ligand stabilizer may affect the reactivity[44] and regioselectivity of the catalyst, a version of **I** was prepared with a pyridine as the ligand stabilizer (**V**). 2,6-Dimethylpyridine (also called 2,6-lutidine) is common ligand used for cross coupling reactions.[45,46] The presence of a weaker Pd–N bond and the additional steric hindrance could make this ligand stabilizer more prone to dissociate and lead to higher reactivity. In addition to solution-phase spectroscopic characterization, **V** was characterized by X-ray crystallography (Figure 4.14). The complex adopts the expected geometry, and the structure confirms the presence of the

palladacycle unit as well as the equivalent of HOAc present as a solvate (not shown in Figure 4.14).

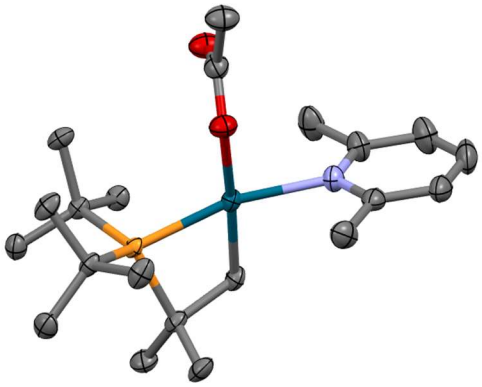

Figure 4.14. Solid-state molecular structure of **V**. Ellipsoids plotted at 50% probability. Hydrogens and acetic acid solvate not shown for clarity.

Precatalysts **I**-**V** were compared for the selective direct alkenylation of 4-methylthiazole **1a**. In all cases, we observe poor selectivity and/or reactivity with 5 mol% palladium loadings (Table 4.2, entries 1, 3, 5-7), in contrast to the results obtained at 20 mol% loading from the initial screen (Figure 4.11, and Table 4.2 entries 2 and 4). Overall, while there are some indications that altering the catalyst structure has a beneficial effect on selectivity – such as the use of 2,6-lutidine based complex **V** (entry 7) – these systems underperform relative to expectations. Accordingly, only complex **I** was further investigated to assess other factors that would improve reactivity and selectivity.

Table 4.2. Analysis of regioselectivity for the direct alkenylation of 4-methylthiazole with different palladacycle precatalysts.

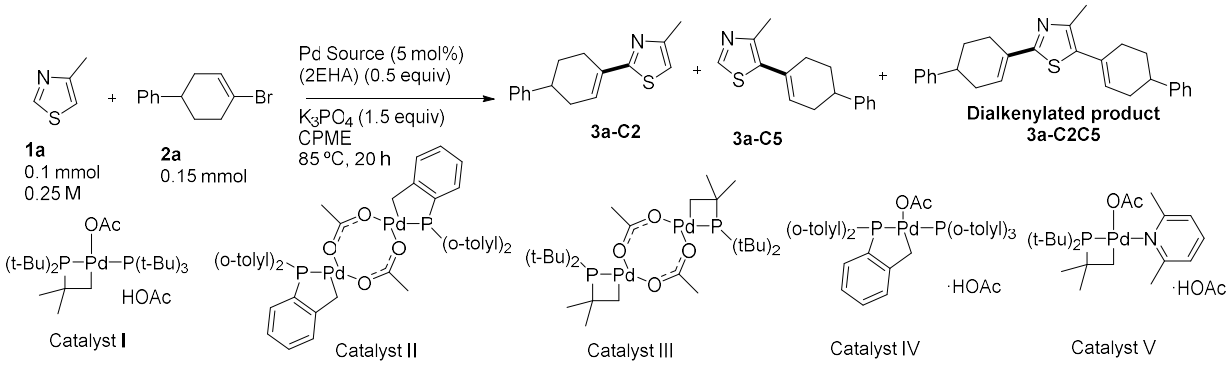

Entry	Catalyst	C2 Isomer (%)	C5 Isomer (%)	C2C5 Product (%)
1	I	15	15	8
2	I*	58	4	-
3	II	12	5	0
4	II*	30	18	-
5	III	18	15	20
6	IV	10	10	3
7	V	25	0	10

*20 mol% catalyst loading, data from Figure 4.11 (C_2C_5 not quantified).

4.3.3 Effect of Carboxylate Additive on Site-Selectivity

According to the CMD mechanism for C–H activation described in Chapter 1, the carboxylate X-type ligand is responsible for breaking the C–H bond. Also, according to the direct alkenylation catalytic cycle described in Chapter 3, the carboxylic acid additive to the reaction

mixture exchanges with the acetate ligand present on the precatalyst **I**. To further investigate catalyst effects on site-selectivity and reactivity of palladacycle precatalysts in direct alkenylation, three carboxylic acid additives were studied: acetic acid (with a primary α-carbon and already present on the precatalyst), 2-ethylhexanoic acid (more sterically hindered, used for all studies in Chapter 3), and pivalic acid [47] (the most sterically hindered, and frequently used in direct arylation) (Figure 4.15).

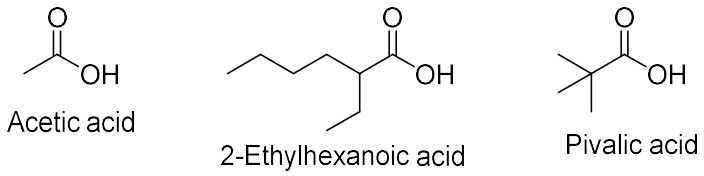

Figure 4.15. Carboxylic acid additives used to investigate carboxylate ligand effects on direct alkenylation site-selectivity.

When no carboxylate additive is added, we observe low reactivity and low selectivity, similar to when acetic acid is the additive (Table 4.3, entries 1 and 2). 2-Ethylhexanoic acid showed higher reactivity (Table 4.3, entry 3) but lower selectivity as the C2:C5:C2C5 ratio is 1.4:1:1.5. Pivalic acid exhibited the highest selectivity of all the additives (Table 4.3, entry 4) but lower reactivity as only 60% of the thiazole formed any of the products. Overall, we observed diverse selectivity and reactivity with different phosphine anchors and ligand stabilizers. For a more thorough investigation of these effects, we decided to synthesize a palladacycle core where we could modify the ligand and carboxylate and take advantage of HTE platforms.

Table 4.3. Analysis of the carboxylate on the regioselectivity of direct alkenylation of 4-methyl thiazole

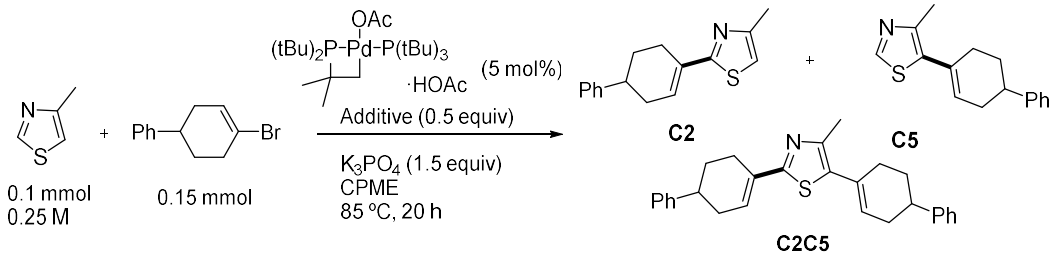

Entry	Carboxylate Additive	C2 Isomer (%)	C5 Isomer (%)	C2C5 Product (%)	Total coupling (%)
1	-	10	4	2	16
2	Acetic acid	8	2	1	11
3	2-Ethylhexanoic acid	27	20	30	77
4	Pivalic acid	45	5	10	60

4.3.4 Evaluation of ligand stabilizers and carboxylates in the HTE platform

To obtain a Pd precursor to which a variety of ligand stabilizers and carboxylate ligands could be installed *in situ*, the known chloride-bridged tri-*tert*-butylpalladacycle dimer **VI** was targeted.[48,49] Unfortunately, attempts to prepare this compound by the reported route was not successful. Instead, I developed a new approach taking advantage of precatalyst **I** as a starting material. Treating **I** with concentrated HCl (aq. 35 wt/wt%) yields **VI** in 92% yield as an off yellow white powder through a simple acid/base reaction (Figure 4.16). I also confirmed the structure of this complex by X-ray crystallography.

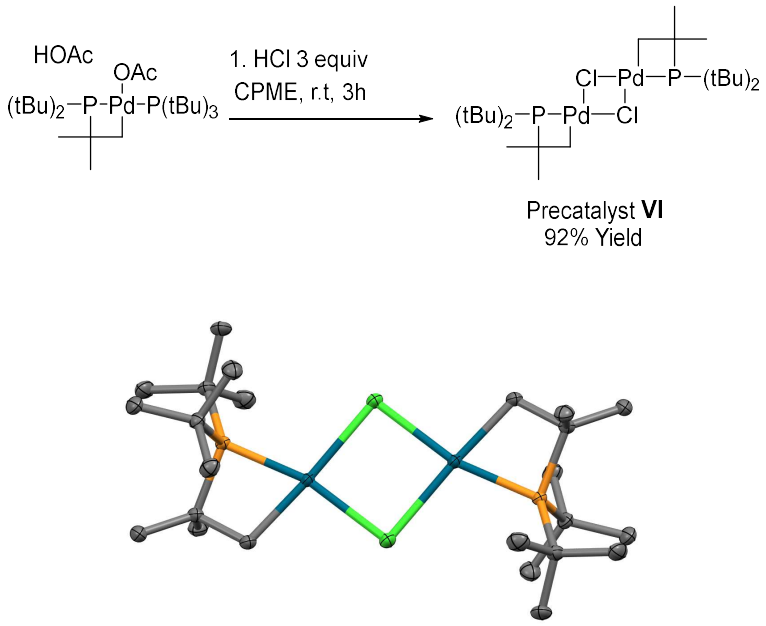

Figure 4.16. Synthesis of tri-*tert*-butylphosphine palladacycle chloride dimer **VI**, and solid state molecular structure from X-ray crystallography. Ellipsoids plotted at 50% probability. Hydrogen atoms not shown.

In solution, there are two distinct signals in the $^{31}P\{^{1}H\}$ NMR spectrum with similar chemical shifts. These are tentatively assigned to the *pseudo-trans* and *pseudo-cis* conformations

of the palladacycle (Figure 4.17). Notably, we only observe the *pseudo-trans* isomer in the solid state structure.

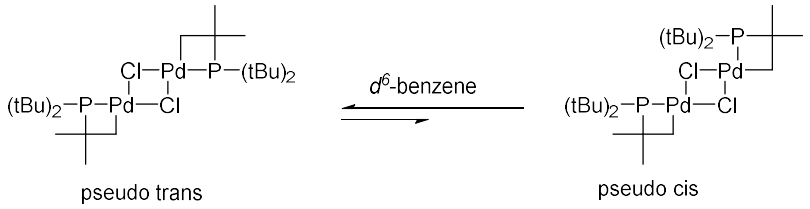

Figure 4.17. Equilibrium between the pseudo trans and pseudo cis isomers of Catalyst VI.

Using the new palladacycle chloride dimer, we undertook a multifactor screen to evaluate the combination of L-type ligands – three phosphines ($P(tBu)_3$, PPh_3 and XPhos), two nitrogen-based ligands (2,6-lutidine and TMEDA), and no ligand – and four X-type ligands – two carboxylates (2-ethylhexanoic acid and pivalic acid) and two pyridines (2-hydroxypyridine or 2(1H)-pyridone (HydroxyP) and 4-benzyloxy-2(1H)-pyridone (BenzyloxP)). These conditions were used to assess selectivity effects in the alkenylation of 4-methylthiazone (Figure 4.18).

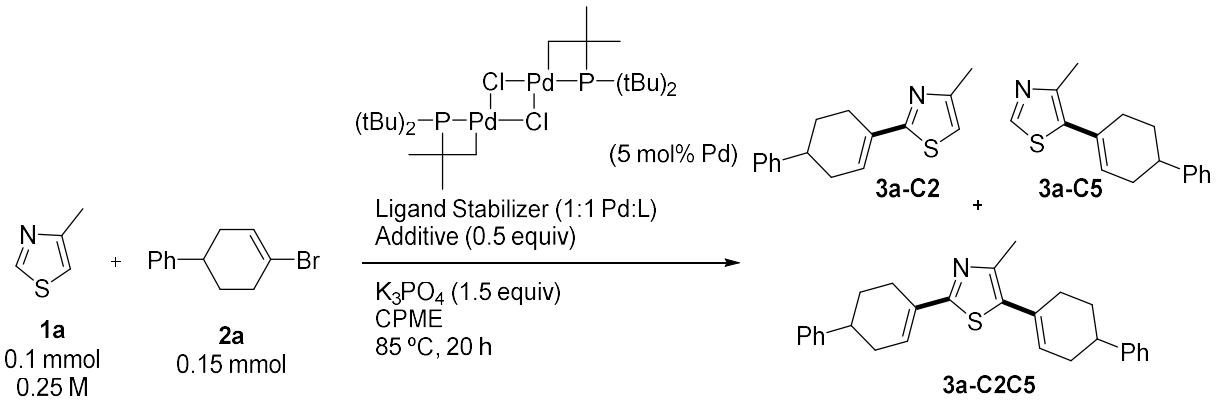

C2	None	$P(tBu)_3$	PPh_3	Xphos	Lutidine	TMEDA
2EHA	18	24	75	54	31	52
PivOH	49	42	61	32	4	40
HydroxyP	1	1	1	7	1	1
BenzyloxP	5	3	3	12	5	4

C5	None	$P(tBu)_3$	PPh_3	Xphos	Lutidine	TMEDA
2EHA	5	18	2	11	10	14
PivOH	10	7	1	8	5	9
HydroxyP	3	2	1	0	2	1
BenzyloxP	2	5	4	3	1	5

C2C5	None	$P(tBu)_3$	PPh_3	Xphos	Lutidine	TMEDA
2EHA	3	11	5	12	6	12
PivOH	11	6	2	5	4	7
HydroxyP						
BenzyloxP						

Figure 4.18. Multifactor evaluation of ligand stabilizer (None, P(*t*Bu)$_3$, PPh$_3$, XPhos, 2,6-lutidine and TMEDA) and carboxylates (2-ethylhexanoic acid, pivalic acid, 2-hydroxypyridine and 4-benzyloxypyridine), using precatalyst **VI**.

The quantification, via ^{1}H NMR spectroscopy, of the dialkenylated product when hydroxypyridone or 4-benzyloxy-2(1H)-pyridone was not possible as the signals overlap with the additives; however, the generally low reactivity of these X-type ligands make this quantification basically irrelevant. Pivalic acid is still the additive with higher selectivity, but does show lower reactivity when compared with 2-ethylhexanoic acid. In terms of L-type ligands, lutidine showed lower reactivity than the phosphine ligands P(tBu)$_3$, XPhos and PPh$_3$. Finally, while no L-type ligand is required for reactivity, improved selectivity is observed when using specific L-type additives.4.3.5 Exploring the ligand and additive effects with EDG and EWG

To follow up on the additive screen, a wider screen was designed focusing on the two carboxylates that showed reactivity: pivalic acid and 2-ethylhexanoic acid. The goal of the second screen was to evaluate if the selectivity is influenced by the L-type ligand only, or if the sterics and electronics related to the nucleophile also affect the selectivity. Eight thiazoles were explored that have substituents on the C4 position ranging from strongly electron withdrawing (4-cyanothiazole, 4-thiazole carbaldehyde and ethylthiazole-4-carboxylate) weakly withdrawing (4-(1,3-dioxolan-2-yl)thiazole), neutral (thiazole), weakly donating (4-phenylthiazole and 4-methylthiazole) and strongly donating (4-methoxythiazole) (Figure 4.19).

The screen of these eight nucleophiles forming three possible products each leads to challenges in analysis. As these products likely have protons with similar chemical shifts that could overlap in the aromatic region of the ^{1}H NMR spectrum, 1-bromo-2-methylprop-1-ene (**2b**) was chosen as the coupling partner instead of **2a** as it has a simpler structure with no aromatic rings. It would also lead to a much simpler aliphatic region, enabling quantification using the methyl signals as well as the vinyl signals. After analyzing the entire plate, each coupling product was

isolated by pooling the appropriate HTE experiments and conducting automated flash chromatography. Finally, *m/z* values were confirmed by LCMS.

In terms of total reactivity (combined % yield of all C–H alkenylation products), there is not a significant overall difference between the two carboxylate additives used for the reaction (the average yield in both cases is 35%), though pivalic acid qualitatively appears to lead the more reactive systems. Precatalyst **VI** (37% average) is more reactive than $Pd(PCy_3)_2(OAc)_2$ (17% average), especially when considering the most active systems.

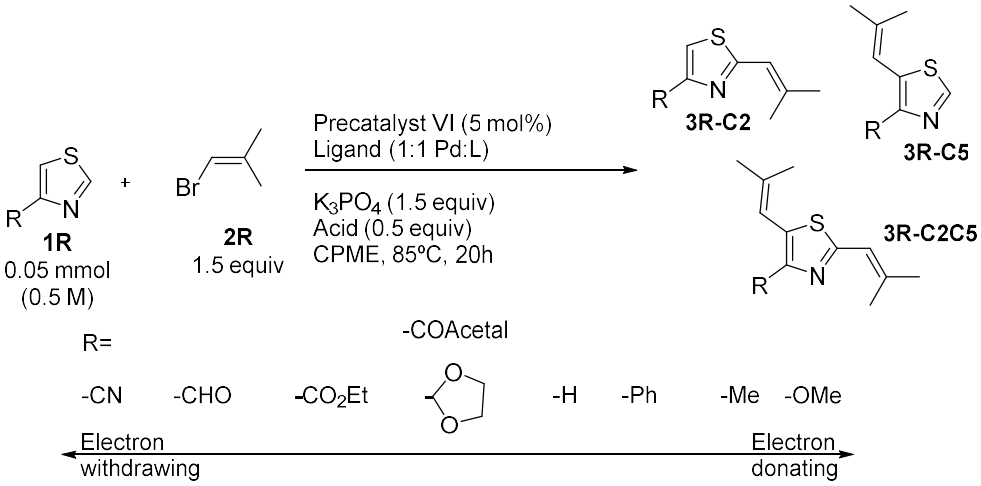

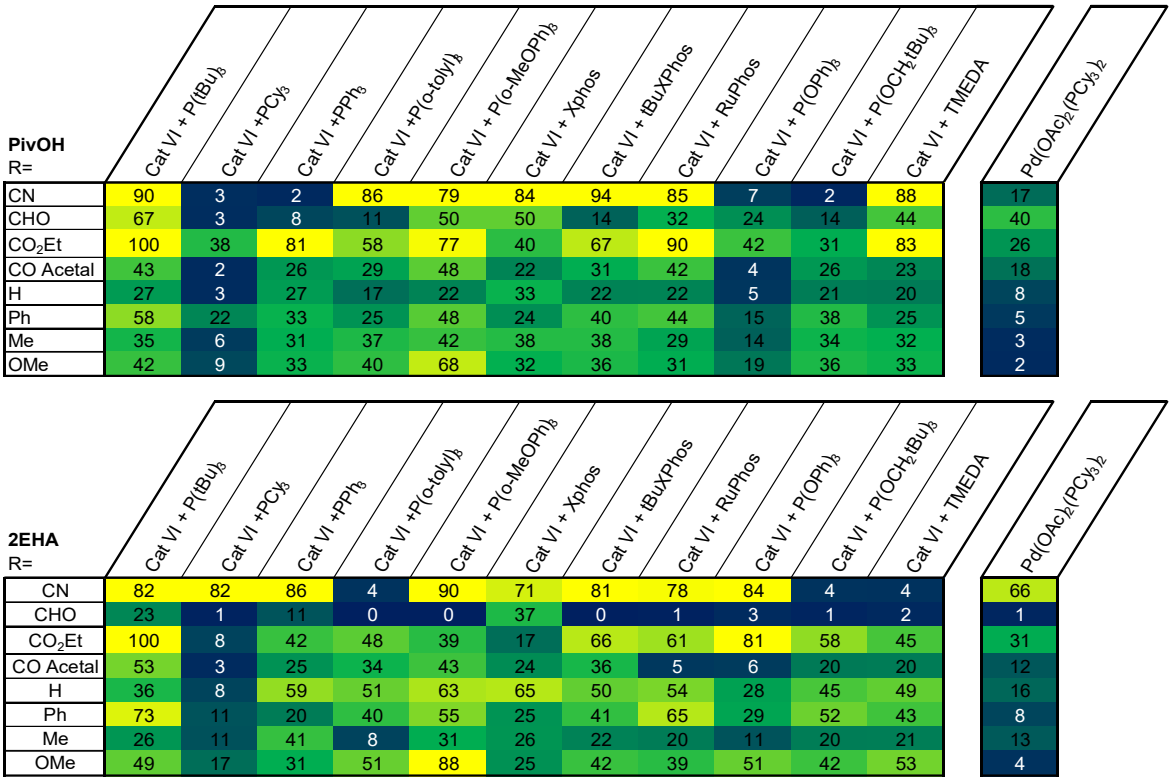

Figure 4.19. Total reactivity (% yield of **3R-C2** + **3R-C5** + **3R-C2C5**) analysis of multifactor evaluation of ligand stabilizer ($P(tBu)_3$, PCy_3 PPh_3, $P(o\text{-tolyl})_3$, $P(o\text{-MeOPh})_3$, XPhos, *t*BuXPhos, $P(OPh)_3$, $P(OCH_2tBu)_3$ and TMEDA) and carboxylates (2-ethylhexanoic acid and pivalic acid), using precatalyst **VI** or $Pd(OAc)_2(PCy_3)_2$ and eight thiazoles substituted on the C4 position (R= CN, CHO, CO_2Et, COAcetatal, H, Ph, Me and OMe).

With respect to L-type ligand effects, aryl and alkyl phosphites and TMEDA show lower reactivities than more common phosphine ligands such as P*t*Bu$_3$ or P(*o*-tolyl)$_3$. Notably, the combination of precatalyst **VI** and PCy_3 shows similar, low reactivity compared to the non-palladacycle precatalyst $Pd(PCy_3)_2(OAc)_2$ (used to emulate conditions used by Fagnou and coworkers).[50]

With respect to substrate structure, thiazoles with strong electron withdrawing groups such as (nitrile or ethyl carboxylate) show higher reactivity. Thiazole-4-carboxaldehyde (**3CHO**) shows lower reactivity than other substrates, which could indicate possible side reactions and byproduct

formation. Electron rich (**3OMe, 3Me and 3Ph**), neutral thiazole (**3H**) and slightly electron poor acetal thiazole (**3COAcetal**) showed similar reactivities across the plate.

To further interrogate these results, the C2:C5:C2C5 selectivity values for the five most reactive phosphines and $Pd(PCy_3)_2(OAc)_2$ are represented in Figure 4.20; the full screen dataset is included in Appendix C (Figure C19). $Pd(PCy_3)_2(OAc)_2$ showed preferred reactivity for the C5–H bond, consistent with prior reports,[50] whereas the palladacycle **VI** in combination with diverse ligands led to the formation of all three products for six out of the eight substrates.

Strong σ-donating phosphine ligands, such as tri-*tert*-butylphosphine or triphenylphosphine show high selectivity for C2–H bond activation with slightly electron rich thiazoles (**1H**, **1Ph** and **1Me**). Electron poor thiazoles (**1CN**, **1CHO** and **1CO$_2$Et**) are more reactive, leading to the formation of multiple coupling products. According to our investigation from Chapter 3, the formation of the dialkenylated product happens from the C2 isomer and not the C5. The reason for the low amount of C2 isomers with the electron-deficient thiazoles could be due to its conversion into the dialkenylated C2C5 product.

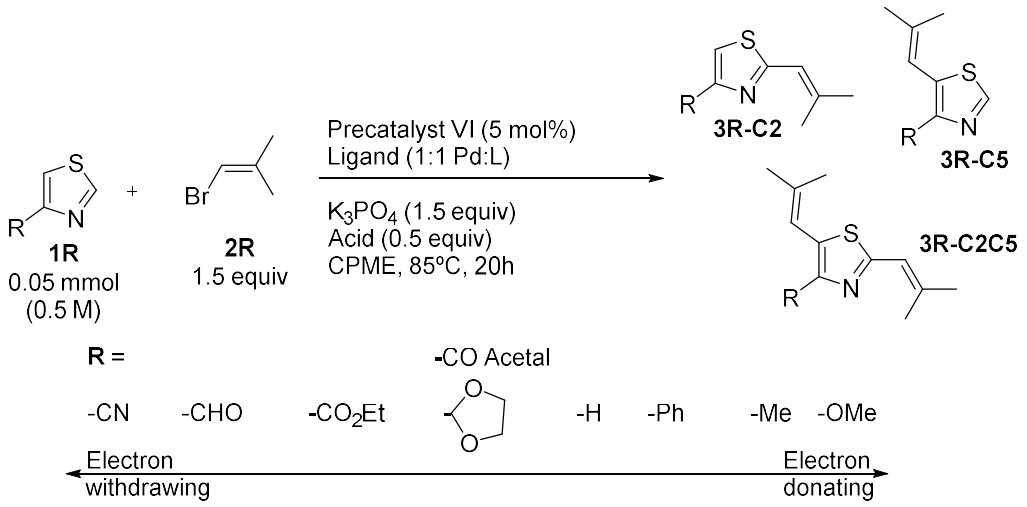

PivOH	$P(tBu)_3$			PPh_3			$P(o\text{-}MeOPh)_3$			tBuXPhos			RuPhos			$Pd(OAc)_2(PCy_3)_2$		
R=	C2	C5	C2C5	C2	C5	C2C5	C2	C5	C2C5	C2	C5	C2C5	C2	C5	C2C5	C2	C5	C2C5
CN	10	44	47	0	1	1	24	47	32	8	52	42	7	53	33	1	15	1
CHO	2	40	25	7	1	0	6	37	6	13	0	1	16	14	3	37	2	0
CO_2Et	3	53	45	3	46	32	2	47	29	14	39	14	4	47	40	2	22	2
CO Acetal	10	23	10	10	8	8	7	26	16	12	10	10	10	19	14	2	14	2
H	25	1	1	24	1	2	13	5	4	17	2	2	17	2	3	3	5	0
Ph	46	5	7	22	4	7	18	28	2	23	6	11	36	6	2	4	2	0
Me	29	3	3	23	0	8	28	11	3	30	3	5	23	2	5	1	1	1
OMe	14	11	16	28	2	4	4	37	27	12	14	11	15	10	6	1	1	0

2EHA	$P(tBu)_3$			PPh_3			$P(o\text{-}MeOPh)_3$			tBuXPhos			RuPhos			$Pd(OAc)_2(PCy_3)_2$		
R=	C2	C5	C2C5	C2	C5	C2C5	C2	C5	C2C5	C2	C5	C2C5	C2	C5	C2C5	C2	C5	C2C5
CN	4	75	7	7	58	28	6	49	41	11	57	24	13	47	30	1	64	2
CHO	13	6	3	1	5	6	0	0	0	0	0	0	0	0	0	1	0	0
CO_2Et	55	42	10	14	14	13	7	6	25	19	18	29	16	17	28	3	24	4
CO Acetal	31	14	8	17	5	4	14	24	5	11	18	6	2	2	1	1	11	0
H	26	4	5	50	2	8	28	9	27	38	3	9	39	4	11	3	13	0
Ph	61	5	7	12	5	3	11	31	14	26	9	6	45	5	15	4	3	2
Me	17	4	5	28	3	10	13	17	1	13	5	4	12	2	6	2	6	5
OMe	13	17	19	22	2	7	3	62	23	8	21	13	12	17	10	1	2	1

Figure 4.20. Multifactor evaluation of ligand stabilizer ($P(tBu)_3$, PPh_3, $P(o\text{-}MeOPh)_3$, XPhos, *t*BuXPhos) and carboxylates (2-Ethyl hexanoic acid and Pivalic acid), using precatalyst **VI** and $Pd(OAc)_2(PCy_3)_2$ and eight thiazoles substituted on the C4 position (R= CN, CHO, CO_2Et, CO Acetate, H, Ph, Me and OMe).

4.3.6 Synthesis of pivalate-derived palladacycle and reaction monitoring

To further investigate one specific combination of L and X-type ligands on the palladacycle framework, a single component palladacycle precatalyst (**VII**) was synthesized from palladium pivalate and tri-*tert*-butylphosphine following the reaction conditions from Stambuli (Figure 4.21).[42] The solid-state molecular structure was obtained *via* X-ray diffraction, confirming the structure as a monomeric palladacycle. The complex crystalizes with one equivalent of THF as a solvate.

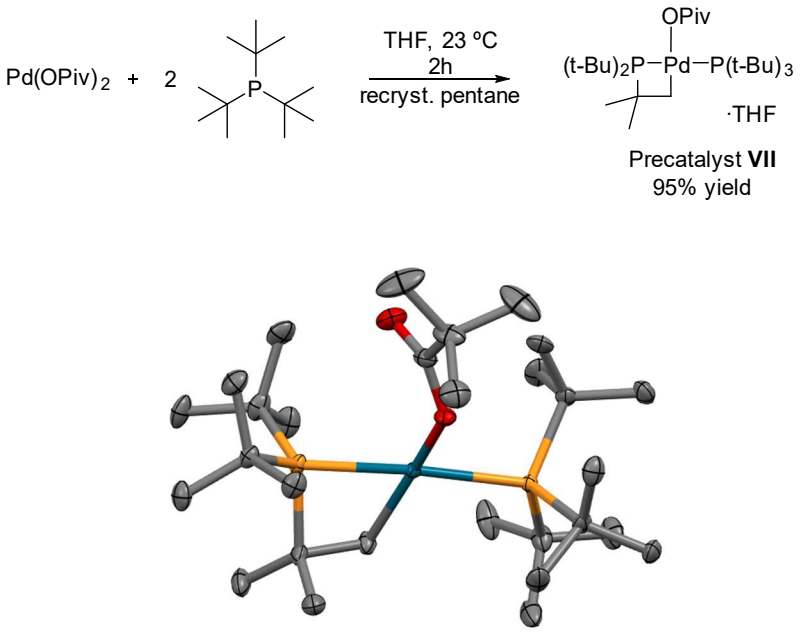

Figure 4.21. Synthesis of tri-*tert*-butylphosphine palladacycle pivalate **VII** and solid-state molecular structure from X-ray crystallography. Hydrogens and THF solvate not shown for clarity.

The effect of the carboxylate additive with precatalyst **VII** was evaluated following the same conditions as with precatalyst **I** (Table 4.4). When using the pivalate palladacycle, additional carboxylate additive is not required (Table 4.4, entries 1 and 3), and adding 2-ethylhexanoic acid leads to higher reactivity but lower selectivity, specifically the formation of more dialkenylated C2C5 product (Table 4.4, entry 2).

Table 4.4. Effect of carboxylate additive on the direct alkenylation of 4-methylthiazole with precatalyst **VII**.

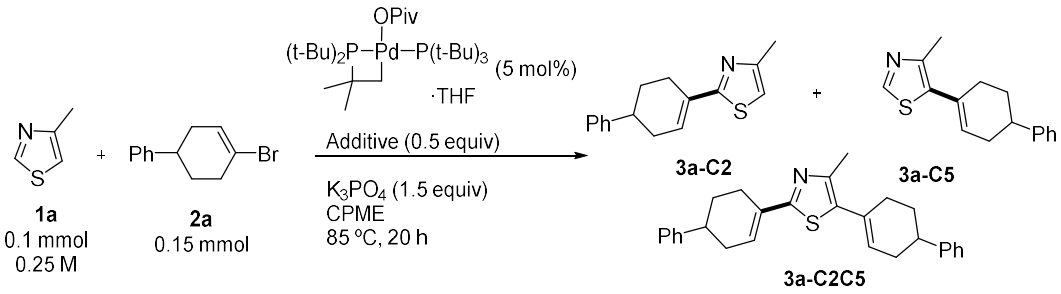

Entry	Carboxylate Additive	C2 Isomer (%)	C5 Isomer (%)	Dialkenylated product (%)	Total coupling (%)
1	None	45	0	10	55
2	2-Ethylhexanoic acid	30	15	32	77
3	Pivalic acid	45	5	10	60

To further probe the selectivity of the reaction over time, I monitored the coupling reaction progress using two different catalyst systems: precatalyst **I** with 2-ethylhexanoic acid, and precatalyst **VII** as a single component (Figure 4.22). In the case of **I** / 2-EHA, maximum **3a-C2** formation occurs at 10 h, followed by a decrease in its concentration due to the formation the dialkenylated **3a-C2C5** coupling product. In the case of precatalyst **VII**, the major product formed is **3a-C2** throughout the reaction. Thus, precatalyst **VII** exhibits higher selectivity as a result of lower reactivity toward both C5 and C2C5 alkenylation. A plot of the amount of all three products over time for the reaction with **VII** is in Appendix C (Fig. C38).

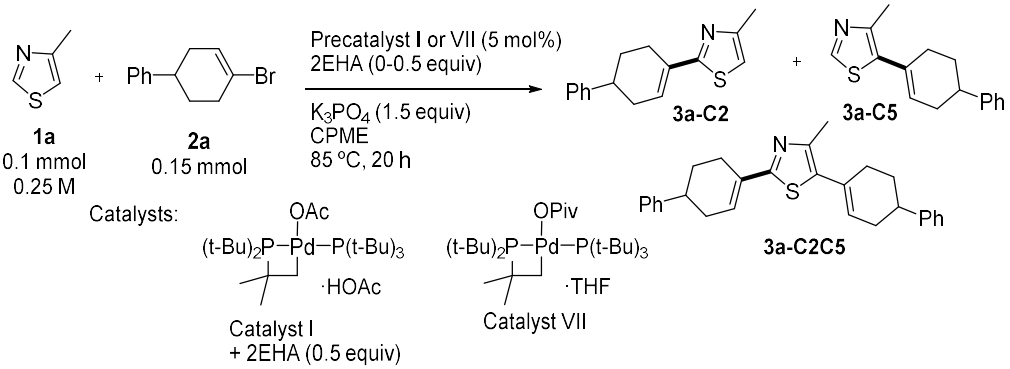

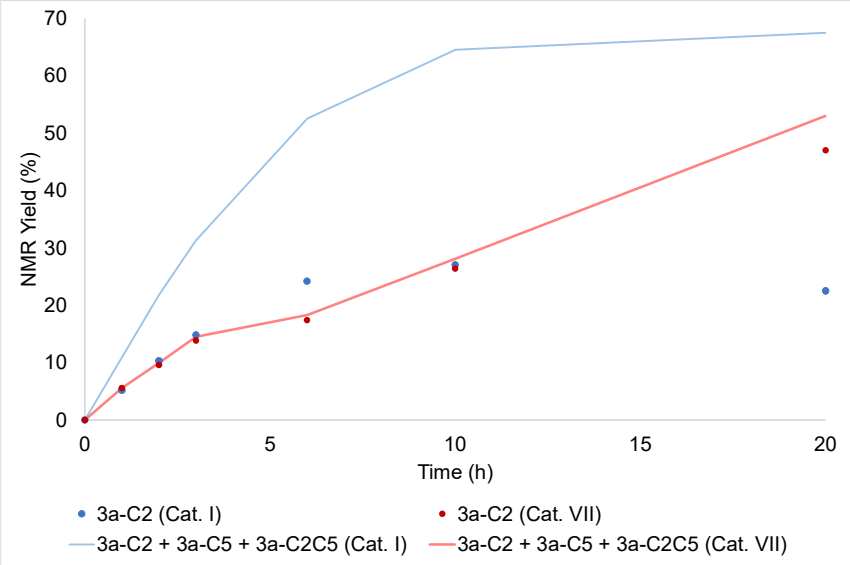

Figure 4.22. Reaction progress monitoring via ^{1}H NMR spectroscopy of direct alkenylation of 4-methylthiazole using precatalysts **I** / 2-EHA and **VII** as a single component.

4.3.7 Synthesis of Fatostatin

Finally, I applied the single component palladium precatalyst **VII** to the synthesis of fatostatin. This investigational small molecule has been shown to be active against certain cancer cell types.[51] Relevant to this work, its structure is a diarylated thiazole. Previously, Tani *et al.* prepared fatostatin by C2 selective direct arylation of 4-(*p*-tolyl)thiazole with the air sensitive $Pd(P(tBu)_3)_2$ as a precatalyst; however, their conditions include the need for a strong base (LiOtBu)

and dioxane solvent at high temperatures (100 ºC). Their isolated yield is also 53%, indicating plenty of room for improvement. Our system has a single component stable palladium precatalyst and relatively mild reaction conditions.

Starting from 4-(*p*-tolyl)thiazole, fatostatin can be accessed by C–H arylation with 4-bromo-2-propylpyridine. Performing this reaction for 72 h gives a mixture of C2, C5, and C2C5 arylated products, of which fatostatin could be isolated in 35% yield (Figure 4.23). Although the synthesis is not completely selective, further optimization of the reaction conditions, including reaction progress monitoring, would help improve the system.

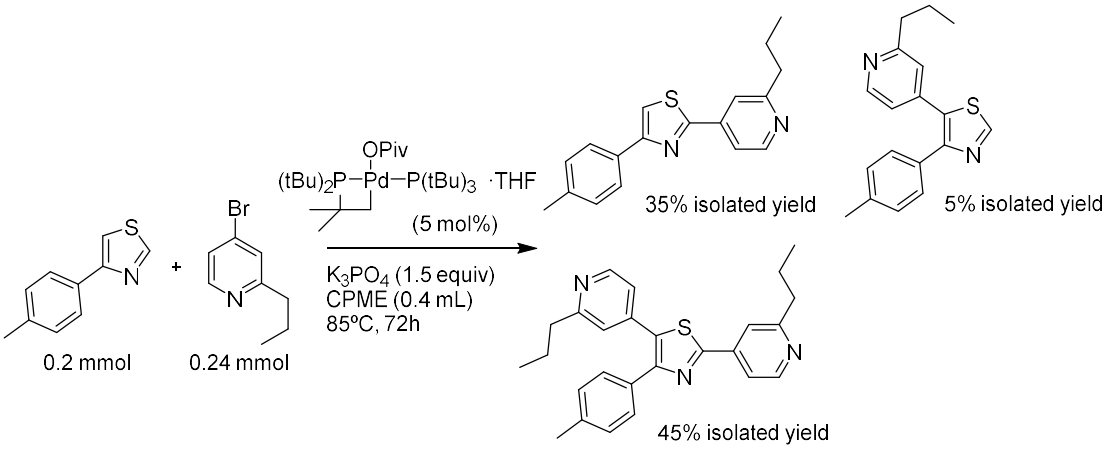

Figure 4.23. Synthesis of fatostatin *via* C–H arylation.

4.4 Conclusions

In summary, a tunable palladacycle precatalyst (**VI**) has been synthesized that can easily be substituted with diverse L and X type ligands for HTE evaluation of reactivity and selectivity for C–H functionalization reactions. Initial one-factor-at-a-time experiment design revealed an interconnection between the carboxylate X-type ligand and selectivity of the reaction. Subsequent

use of HTE techniques allowed for a more detailed exploration of the effects of both L and X-type ligands on the reaction.

HTE screening revealed the tri-*tert*-butyl phosphine and pivalic or ethylhexanoic acid combination allowed high regioselectivity on slightly electron rich thiazole rings. This led to using palladium pivalate / $P(tBu)_3$ to synthesize a single component precatalyst (precatalyst **VII**) system that also shows high selectivity. The reaction monitoring comparison with the previously developed precatalyst system showed that catalyst **VII** can selectively alkenylate thiazoles at the C2 position. This is an improvement on the current reaction conditions for the selective functionalization of C2–H bonds on thiazoles, as current examples include cocatalyst systems or otherwise less desirable reaction conditions, including high reaction temperatures, toxic solvents, and/or strong bases. Finally, the single-component precatalyst **VII** was applied to the synthesis of fatostatin, a SREBP inhibitor. Initial results are promising, though more development is needed to improve selectivity for the C2 product.

4.5 Experimental

4.5.1 General procedure for high-throughput experiments:

100 μL of 0.10 M solution of catalyst **I**, **II** or **VI** in THF and 100 μL of 0.050 M solution of 1,3,5-trimethoxybenzene (internal standard, IS) were added to 1 mL glass shell vials contained in aluminum reaction plates. The solvent was then removed by centrifugal evaporation. A micro parylene-coated stir-bar was added to each well. Inside the glovebox, ~3 equivalents of the corresponding base was added to each vial using calibrated plastic scoops: K_3PO_4 (30 mg), K_2CO_3 (20 mg) or Cs_2CO_3 (50 mg). Substrate stock solutions were prepared inside the glovebox: one containing the vinyl halide (0.65 M) and the others containing the heterocycle substrates (0.5 M) and 2-ethylhexanoic acid (0.25 M) in the desired solvent. Solvents include DMA, CPME, toluene, or TAA. 0.1 mL of each stock solution was added into the corresponding 1 mL shell vial in the aluminum reaction plates. The plates were then sealed using a screwed-down lid with a Teflon liner and rubber spacer. The reaction plates were then heated on a tumble stirrer set to 500 rpm, at 85 °C for 20 h. Upon completion, the plates were cooled to room temperature before being opened. Acetonitrile (500 μL) was added to each vial, followed by stirring for 10 minutes at room temperature to ensure complete dissolution. The samples were centrifuged for 15 minutes. Aliquots (40 μL) of each diluted reaction mixture were then transferred to 96-well plastic analysis plate, followed by the addition of 0.7 mL of acetonitrile. The samples were analyzed by LCMS, using the product/IS area ratio. The reaction plates were then dried by centrifugal evaporation, and 20-25% of the wells were analyzed by ^{1}H NMR spectroscopy to confirm product presence, and to conduct external calibration of product/IS ratios to obtain yields.

4.5.2 General procedure for reaction monitoring experiments:

Inside the glovebox, three 1-dram vials were charged with a stir bar. Then, the following components were added: heterocycle substrate (1.5 mmol, 1 equiv), vinyl halide (1.5 equiv), 1,3,5-timethoxybenzene (10 mol%, IS), followed by the corresponding catalyst mixture: **II** (5 mol%), **II** (4.5 mol%) and $Pd[P(tBu)_3]_2$ (0.5 mol%), or $Pd(PtBu_3)_2$ (5 mol%). Then, base (1.5 or 3 equivalents) and anhydrous solvent (3 mL) was added. The vial was sealed with a Teflon-lined screw cap, and the reaction mixture stirred at 85 °C for 20 h. Aliquots (10 µL) were taken in triplicate at the indicated times (0, 1, 2, 3, 6, 10 and 20 h). The aliquots were diluted with 1 mL of acetonitrile and analyzed using LCMS. Once the reactions reached completion (20 h), the solvent was evaporated under vacuum. The crude residue was redissolved in $CDCl_3$ to enable yields to be determined using ^1H NMR spectroscopy by relative integration with the internal standard.

4.5.3 General procedure for synthesis of monomer palladacycles (Catalysts I, IV)

Inside the glovebox, 4-dram vials were charged with palladium acetate (75.5 mg, 0.34 mmol, 1 equiv) and the corresponding phosphine (0.71 mmol, 2.1 equiv) were added. 400 of anhydrous THF were added and the reaction was stirred at room temperature for 3 hours. The reaction was evaporated, redissolved on the minimal amount of pentane and filtered through celite. The solution was left on the freezer inside the glovebox to allow crystallization. After 48 h the supernatant was collected and the crystals were dried under vacuum.

*4.5.4 General procedure for synthesis of catalyst **III***

Inside the glovebox, 4-dram vials were charged with palladium acetate (75.5 mg, 0.34 mmol, 1 equiv) and the corresponding phosphine (0.38 mmol, 1.1 equiv) was added. 400 µL of anhydrous toluene was added and the reaction was stirred at 90 ºC outside the glovebox between 10-30

minutes. The reaction was allowed to cool down and dried inside the glovebox. The crude was redissolved on the minimal amount of pentane and filtered through celite. The solution was left in the freezer inside the glovebox to allow crystallization. After 48 h the supernatant was collected and the crystals were dried under vacuum. The product was characterized as a white powder (60% yield). ^{1}H NMR (500 MHz, C_6D_6) δ 2.12 (s, 6H), 1.42 (m, 32H), 1.38 (s, 6H), 1.35 (m, 10H). ^{31}P{H} NMR (203 MHz, C_6D_6) δ -8.61.

*4.5.5 Procedure for synthesis of catalyst **VI***

A solution of catalyst **I** (100 mg, 0.16 mmol, 1 equiv) in anhydrous CPME (1 mL) was prepared. While the solution was stirring, 24 µL of a 35 w% aqueous solution of hydrochloric acid dissolved on 4 mL of CPME were slowly added. The reaction was allowed to stir at room temperature for 1 hour. The solution was filtered through celite and evaporated under vacuum. The product was characterized as a yellow powder (92% yield). ^{1}H NMR (500 MHz, C_6D_6) δ 1.33 (d, J = 13.8 Hz, 36H), 1.30 – 1.25 (m, 4H), 1.25 – 1.05 (m,12H). ^{31}P NMR (202 MHz, C_6D_6) δ -10.47. HRMS (ESI) m/z: $[M\text{-}C_{12}H_{26}Cl_2PPd+C_2H_2N]^+$ Calc'd for $C_{14}H_{29}NPPd$ 348.10724; found: 348.10568.

*4.5.6 Procedure for synthesis of catalyst **VII***

Inside the glovebox, a 4-dram vial was charged with palladium pivalate (105 mg, 0.34 mmol, 1 equiv) and 290 mg of a tri-*tert*-butylphosphine (0.71 mmol, 2.1 equiv) solution on toluene (w/w) 50% were added. 400 of anhydrous THF were added and the reaction was stirred at room temperature for 3 hours. The reaction was evaporated, redissolved on the minimal amount of pentane and filtered through celite. The solution was left on the freezer inside the glovebox to allow crystallization. After 48 h the supernatant was collected and the crystals were dried under

vacuum. The product was isolated as light yellow crystals. ^{1}H NMR (500 MHz, Tol) δ 2.13 (p, *J* = 2.2 Hz, 39H), 1.45 (s, 22H), 1.31 (d, *J* = 10.0 Hz, 3H). ^{31}P{H} NMR (203 MHz, Tol) δ 62.36, -8.13. HRMS (ESI) m/z: $[M\text{-}OC(CH_3)_3]^+$ Calc'd for $C_{24}H_{55}NPPd$ 511.28138; found: 511.26429

4.6 References

(1) Welch, C. J. High Throughput Analysis Enables High Throughput Experimentation in Pharmaceutical Process Research. *React. Chem. Eng.* **2019**, *4*, 1895–1911. https://doi.org/10.1039/C9RE00234K.

(2) Grover, J.; Prakash, G.; Goswami, N.; Maiti, D. Traditional and Sustainable Approaches for the Construction of C–C Bonds by Harnessing C–H Arylation. *Nat Commun* **2022**, *13*, 1085. https://doi.org/10.1038/s41467-022-28707-9.

(3) Kuhl, N.; Hopkinson, M. N.; Wencel-Delord, J.; Glorius, F. Beyond Directing Groups: Transition-Metal-Catalyzed C□H Activation of Simple Arenes. *Angew. Chem. Int. Ed.***2012**, *51*, 10236–10254. https://doi.org/10.1002/anie.201203269.

(4) Tobisu, M.; Chatani, N. Remote Control by Steric Effects. *Science* **2014**, *343*, 850–851. https://doi.org/10.1126/science.1250335.

(5) Yanagisawa, S.; Sudo, T.; Noyori, R.; Itami, K. Direct C−H Arylation of (Hetero)Arenes with Aryl Iodides via Rhodium Catalysis. *J. Am. Chem. Soc.* **2006**, *128*, 11748–11749. https://doi.org/10.1021/ja064500p.

(6) Dey, A.; Sinha, S. K.; Achar, T. K.; Maiti, D. Accessing Remote Meta- and Para-C(sp^2)−H Bonds with Covalently Attached Directing Groups. *Angew. Chem. Int. Ed.***2019**, *58*, 10820–10843. https://doi.org/10.1002/anie.201812116.

(7) Huang, Z.; Lim, H. N.; Mo, F.; Young, M. C.; Dong, G. Transition Metal-Catalyzed Ketone-Directed or Mediated C–H Functionalization. *Chem. Soc. Rev.* **2015**, *44*, 7764–7786. https://doi.org/10.1039/C5CS00272A.

(8) Lyons, T. W.; Sanford, M. S. Palladium-Catalyzed Ligand-Directed C−H Functionalization Reactions. *Chem. Rev.* **2010**, *110*, 1147–1169. https://doi.org/10.1021/cr900184e.

(9) Colby, D. A.; Tsai, A. S.; Bergman, R. G.; Ellman, J. A. Rhodium Catalyzed Chelation-Assisted C–H Bond Functionalization Reactions. *Acc. Chem. Res.* **2012**, *45*, 814–825. https://doi.org/10.1021/ar200190g.

(10) Murali, K.; Machado, L. A.; Carvalho, R. L.; Pedrosa, L. F.; Mukherjee, R.; Da Silva Júnior, E. N.; Maiti, D. Decoding Directing Groups and Their Pivotal Role in C−H Activation. *Chem. Eur. J.***2021**, *27*, 12453–12508. https://doi.org/10.1002/chem.202101004.

(11) Matsuoka, W.; Harabuchi, Y.; Maeda, S. Virtual Ligand Strategy in Transition Metal Catalysis Toward Highly Efficient Elucidation of Reaction Mechanisms and Computational Catalyst Design. *ACS Catal.* **2023**, *13*, 5697–5711. https://doi.org/10.1021/acscatal.3c00576.

(12) Melvin, P. R.; Nova, A.; Balcells, D.; Dai, W.; Hazari, N.; Hruszkewycz, D. P.; Shah, H. P.; Tudge, M. T. Design of a Versatile and Improved Precatalyst Scaffold for Palladium-Catalyzed Cross-Coupling: (H3-1-tBu-Indenyl)2(μ-Cl)2Pd2. *ACS Catal.* **2015**, *5*, 3680–3688. https://doi.org/10.1021/acscatal.5b00878.

(13) Matsuoka, W.; Harabuchi, Y.; Nagata, Y.; Maeda, S. Highly Chemoselective Ligands for Suzuki–Miyaura Cross-Coupling Reaction Based on Virtual Ligand-Assisted Screening. *Org. Biomol. Chem.* **2023**, *21*, 3132–3142. https://doi.org/10.1039/D3OB00398A.

(14) Jeong, J.; Jung, H.; Kim, D.; Chang, S. Multidimensional Screening Accelerates the Discovery of Rhodium Catalyst Systems for Selective Intra- and Intermolecular C–H Amidations. *ACS Catal.* **2022**, *12*, 8127–8138. https://doi.org/10.1021/acscatal.2c02612.

(15) Talode, J.; Kato, D.; Nagae, H.; Tsurugi, H.; Seki, M.; Mashima, K. Syntheses of SGLT2 Inhibitors by Ni- and Pd-Catalyzed Fukuyama Coupling Reactions. *J. Org. Chem.* **2020**, *85*, 12382–12392. https://doi.org/10.1021/acs.joc.0c01635.

(16) Clement, H. A.; Boghi, M.; McDonald, R. M.; Bernier, L.; Coe, J. W.; Farrell, W.; Helal, C. J.; Reese, M. R.; Sach, N. W.; Lee, J. C.; Hall, D. G. High-Throughput Ligand Screening Enables the Enantioselective Conjugate Borylation of Cyclobutenones to Access Synthetically Versatile Tertiary Cyclobutylboronates. *Angew. Chem. Int. Ed.* **2019**, *58*, 18405–18409. https://doi.org/10.1002/anie.201909308.
(17) Gensch, T.; dos Passos Gomes, G.; Friederich, P.; Peters, E.; Gaudin, T.; Pollice, R.; Jorner, K.; Nigam, A.; Lindner-D'Addario, M.; Sigman, M. S.; Aspuru-Guzik, A. A Comprehensive Discovery Platform for Organophosphorus Ligands for Catalysis. *J. Am. Chem. Soc.* **2022**, *14*, 1205–1217. https://doi.org/10.1021/jacs.1c09718.
(18) Stuart, D. R.; Villemure, E.; Fagnou, K. Elements of Regiocontrol in Palladium-Catalyzed Oxidative Arene Cross-Coupling. *J. Am. Chem. Soc*. **2007**, *129*, 12072–12073. https://doi.org/10.1021/ja0745862.
(19) Niu, Z.-X.; Wang, Y.-T.; Zhang, S.-N.; Li, Y.; Chen, X.-B.; Wang, S.-Q.; Liu, H.-M. Application and Synthesis of Thiazole Ring in Clinically Approved Drugs. *Eur. J. Med. Chem.* **2023**, *250*, 115172. https://doi.org/10.1016/j.ejmech.2023.115172.
(20) Dahiya, R.; Dahiya, S.; Fuloria, N. K.; Kumar, S.; Mourya, R.; Chennupati, S. V.; Jankie, S.; Gautam, H.; Singh, S.; Karan, S. K.; Maharaj, S.; Fuloria, S.; Shrivastava, J.; Agarwal, A.; Singh, S.; Kishor, A.; Jadon, G.; Sharma, A. Natural Bioactive Thiazole-Based Peptides from Marine Resources: Structural and Pharmacological Aspects. *Mar. Drugs* **2020**, *18*, 329. https://doi.org/10.3390/md18060329.
(21) De Souza, M. V. N. Synthesis and Biological Activity of Natural Thiazoles: An Important Class of Heterocyclic Compounds. *J. Sulphur Chem.* **2005**, *26*, 429–449. https://doi.org/10.1080/17415990500322792.
(22) Fu, P.; MacMillan, J. B. Thiasporines A–C, Thiazine and Thiazole Derivatives from a Marine-Derived Actinomycetospora Chlora. *J. Nat. Prod*. **2015**, *78*, 548–551. https://doi.org/10.1021/np500929z.
(23) Gorelsky, S. I. Origins of Regioselectivity of the Palladium-Catalyzed (Aromatic)CH Bond Metalation–Deprotonation. *Coord. Chem. Rev.* **2013**, *257*, 153–164. https://doi.org/10.1016/j.ccr.2012.06.016.
(24) Gorelsky, S. I.; Lapointe, D.; Fagnou, K. Analysis of the Concerted Metalation-Deprotonation Mechanism in Palladium-Catalyzed Direct Arylation Across a Broad Range of Aromatic Substrates. *J. Am. Chem. Soc*. **2008**, *130*, 10848–10849. https://doi.org/10.1021/ja802533u.
(25) Gorelsky, S. I.; Lapointe, D.; Fagnou, K. Analysis of the Palladium-Catalyzed (Aromatic)C–H Bond Metalation–Deprotonation Mechanism Spanning the Entire Spectrum of Arenes. *J. Org. Chem.* **2012**, *77*, 658–668. https://doi.org/10.1021/jo202342q.
(26) Turner, G. L.; Morris, J. A.; Greaney, M. F. Direct Arylation of Thiazoles on Water. *Angew. Chem. Int. Ed.* **2007**, *46*, 7996–8000. https://doi.org/10.1002/anie.200702141.
(27) Lapointe, D.; Markiewicz, T.; Whipp, C. J.; Toderian, A.; Fagnou, K. Predictable and Site-Selective Functionalization of Poly(Hetero)Arene Compounds by Palladium Catalysis. *J. Org. Chem.* **2011**, *76*, 749–759. https://doi.org/10.1021/jo102081a.
(28) Chiong, H. A.; Daugulis, O. Palladium-Catalyzed Arylation of Electron-Rich Heterocycles with Aryl Chlorides. *Org. Lett*. **2007**, *9*, 1449–1451. https://doi.org/10.1021/ol0702324.
(29) Yanagisawa, S.; Itami, K. Palladium/2,2′-Bipyridyl/Ag_2CO_3 Catalyst for C–H Bond Arylation of Heteroarenes with Haloarenes. *Tetrahedron,* **2011**, *67*, 4425–4430. https://doi.org/10.1016/j.tet.2011.03.093.

(30) Campeau, L.-C.; Bertrand-Laperle, M.; Leclerc, J.-P.; Villemure, E.; Gorelsky, S.; Fagnou, K. C2, C5, and C4 Azole N-Oxide Direct Arylation Including Room-Temperature Reactions. *J. Am. Chem. Soc.* **2008**, *130*, 3276–3277. https://doi.org/10.1021/ja7107068.
(31) Gorelsky, S. I. Tuning the Regioselectivity of Palladium-Catalyzed Direct Arylation of Azoles by Metal Coordination. *Organometallics* **2012**, *31*, 794–797. https://doi.org/10.1021/om2012612.
(32) Bellina, F.; Cauteruccio, S.; Rossi, R. Palladium- and Copper-Mediated Direct C-2 Arylation of Azoles — Including Free (NH)-Imidazole, -Benzimidazole and -Indole — Under Base-Free and Ligandless Conditions. *Eur. J. Org. Chem.* **2006**, *2006*, 1379–1382. https://doi.org/10.1002/ejoc.200500957.
(33) Tamba, S.; Okubo, Y.; Tanaka, S.; Monguchi, D.; Mori, A. Palladium-Catalyzed C−H Functionalization of Heteroarenes with Aryl Bromides and Chlorides. *J. Org. Chem.* **2010**, *75*, 6998–7001. https://doi.org/10.1021/jo101433g.
(34) Martin, T.; Verrier, C.; Hoarau, C.; Marsais, F. Direct C-2 Arylation of Alkyl 4-Thiazolecarboxylates: New Insights in Synthesis of Heterocyclic Core of Thiopeptide Antibiotics. *Org. Lett.* **2008**, *10*, 2909–2912. https://doi.org/10.1021/ol801035c.
(35) Mori, A.; Sekiguchi, A.; Masui, K.; Shimada, T.; Horie, M.; Osakada, K.; Kawamoto, M.; Ikeda, T. Facile Synthesis of 2,5-Diarylthiazoles via Palladium-Catalyzed Tandem C−H Substitutions. Design of Tunable Light Emission and Liquid Crystalline Characteristics. *J. Am. Chem. Soc.* **2003**, *125*, 1700–1701. https://doi.org/10.1021/ja0289189.
(36) Kondo, Y.; Komine, T.; Sakamoto, T. Polymer Support Assisted Selective Functionalization of Azoles Using a Palladium-Catalyzed Coupling Reaction. *Org. Lett.* **2000**, *2*, 3111–3113. https://doi.org/10.1021/ol000183u.
(37) Masui, K.; Mori, A.; Okano, K.; Takamura, K.; Kinoshita, M.; Ikeda, T. Syntheses and Properties of Donor−Acceptor-Type 2,5-Diarylthiophene and 2,5-Diarylthiazole. *Org. Lett.* **2004**, *6*, 2011–2014. https://doi.org/10.1021/ol049386z.
(38) Tani, S.; Uehara, T. N.; Yamaguchi, J.; Itami, K. Programmed Synthesis of Arylthiazoles through Sequential C–H Couplings. *Chem. Sci.* **2014**, *5*, 123–135. https://doi.org/10.1039/C3SC52199K.
(39) Amaike, K.; Muto, K.; Yamaguchi, J.; Itami, K. Decarbonylative C–H Coupling of Azoles and Aryl Esters: Unprecedented Nickel Catalysis and Application to the Synthesis of Muscoride A. *J. Am. Chem. Soc.* **2012**, *134*, 13573–13576. https://doi.org/10.1021/ja306062c.
(40) Canivet, J.; Yamaguchi, J.; Ban, I.; Itami, K. Nickel-Catalyzed Biaryl Coupling of Heteroarenes and Aryl Halides/Triflates. *Org. Lett.* **2009**, *11*, 1733–1736. https://doi.org/10.1021/ol9001587.
(41) Muto, K.; Yamaguchi, J.; Itami, K. Nickel-Catalyzed C–H/C–O Coupling of Azoles with Phenol Derivatives. *J. Am. Chem. Soc.* **2012**, *134*, 169–172. https://doi.org/10.1021/ja210249h.
(42) Henderson, W. H.; Alvarez, J. M.; Eichman, C. C.; Stambuli, J. P. Characterization, Reactivity, and Potential Catalytic Intermediacy of a Cyclometalated Tri -*Tert* -Butylphosphine Palladium Acetate Complex. *Organometallics* **2011**, *30*, 5038–5044. https://doi.org/10.1021/om2006936.
(43) Herrmann, W. A.; Brossmer, C.; Öfele, K.; Reisinger, C.-P.; Priermeier, T.; Beller, M.; Fischer, H. Palladacycles as Structurally Defined Catalysts for the Heck Olefination of Chloro- and Bromoarenes. *Angew. Chem. Int. Ed.* **1995**, *34*, 1844–1848. https://doi.org/10.1002/anie.199518441.

(44) Kurpik, G.; Walczak, A.; Gołdyn, M.; Harrowfield, J.; Stefankiewicz, A. R. Pd(II) Complexes with Pyridine Ligands: Substituent Effects on the NMR Data, Crystal Structures, and Catalytic Activity. *Inorg. Chem.* **2022**, *61*, 14019–14029. https://doi.org/10.1021/acs.inorgchem.2c01996.
(45) Hsu, Y.-C.; Shen, J.-S.; Lin, B.-C.; Chen, W.-C.; Chan, Y.-T.; Ching, W.-M.; Yap, G. P. A.; Hsu, C.-P.; Ong, T.-G. Synthesis and Isolation of an Acyclic Tridentate Bis(Pyridine)Carbodicarbene and Studies on Its Structural Implications and Reactivities. *Angew. Chem. Int. Ed.***2015**, *54*, 2420–2424. https://doi.org/10.1002/anie.201406481.
(46) Balogh, J.; Hlil, A. R.; El-Zoghbi, I.; Rafique, M. G.; Chouikhi, D.; Al-Hashimi, M.; Bazzi, H. S. Phase-Separable Polyisobutylene Palladium-PEPPSI Precatalysts: Synthesis and Application in Buchwald–Hartwig Amination. *Macromol. Rapid Commun.* **2017**, *38*, 1700214. https://doi.org/10.1002/marc.201700214.
(47) Lafrance, M.; Fagnou, K. Palladium-Catalyzed Benzene Arylation: Incorporation of Catalytic Pivalic Acid as a Proton Shuttle and a Key Element in Catalyst Design. *J. Am. Chem. Soc.* **2006**, *128*, 16496–16497. https://doi.org/10.1021/ja067144j.
(48) Clark, H. C.; Goel, A. B.; Goel, S. Facile Intramolecular Metalation of Tri-Tert-Butylphosphine in Palladium(II) Hydride Complexes. *Inorg. Chem.* **1979**, *18*, 2803–2808. https://doi.org/10.1021/ic50200a035.
(49) Goel, A. B.; Goel, S. Formation of Unusual Palladium(II) Complexes Containing Metalated Tri-*t*-Butylphosphine and Bidentate Ligands. *Inorganica Chimica Acta* **1985**, *98*, 67–70. https://doi.org/10.1016/S0020-1693(00)84913-0.
(50) Liégault, B.; Lapointe, D.; Caron, L.; Vlassova, A.; Fagnou, K. Establishment of Broadly Applicable Reaction Conditions for the Palladium-Catalyzed Direct Arylation of Heteroatom-Containing Aromatic Compounds. *J. Org. Chem.* **2009**, *74*, 1826–1834. https://doi.org/10.1021/jo8026565.
(51) Kamisuki, S.; Shirakawa, T.; Kugimiya, A.; Abu-Elheiga, L.; Park Choo, H.-Y.; Yamada, K.; Shimogawa, H.; Wakil, S. J.; Uesugi, M. Synthesis and Evaluation of Diarylthiazole Derivatives That Inhibit Activation of Sterol Regulatory Element-Binding Proteins. *J. Med. Chem.* **2011**, *54*, 4923–4927. https://doi.org/10.1021/jm200304y.

CHAPTER 5. Palladacycle Complexes Derived from BRIDP-Type Ligands and Assessment of Catalytic Reactivity

This chapter is not yet published.

Nahiane Pipaon Fernandez, Hailey Gray, Brennan Rose, Damian P. Hruszkewycz, and David C. Leitch. *Manuscript in preparation.*

Contributions:

Synthesis of palladacycles, reaction discovery and optimization, high-throughput experimentation and reaction monitoring experiments were performed by Nahiane Pipaon Fernandez. Cross-coupling products were isolated from HTE runs by Hailey Gray.

5.1 Abstract

Palladacycle complexes have been shown to be versatile precatalysts for several cross-coupling reactions. Bisalkylbiaryl phosphine ligands have been deeply studied as efficient ligands for these same reactions. BRIDP ligands were developed in 2011 by Takasago, and since then have been used in cross-coupling reactions with diverse palladium sources. This Chapter describes the formation of BRIDP-derived palladacycles using palladium acetate, and their catalytic activities as precatalysts in five of the most common cross-coupling reactions: Buchwald-Hartwig, Sonogashira, Suzuki-Miyaura, direct arylation and Heck coupling (Figure 5.1).

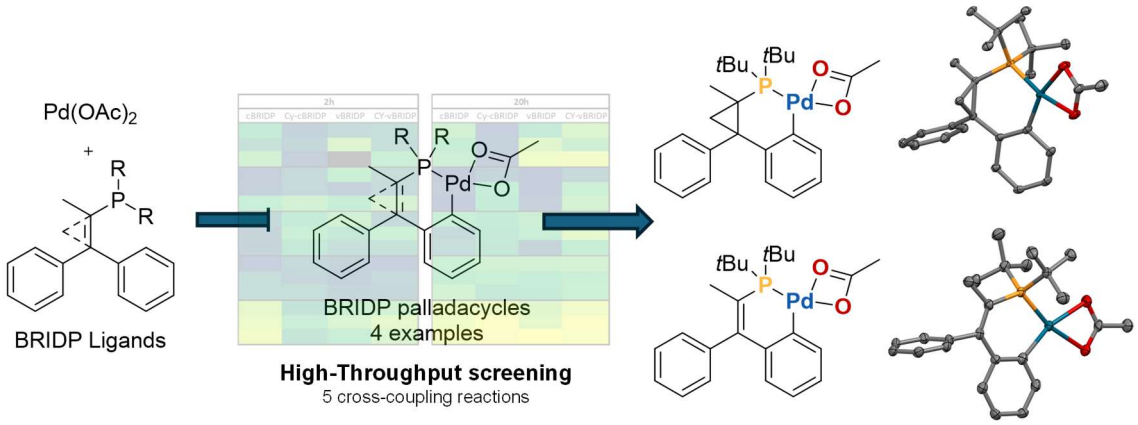

Figure 5.1. BRIDP-type ligand evaluation on cross-coupling reactions and isolation of palladacycle precatalysts.

5.2 Introduction

5.2.1 Palladium-Catalyzed Cross-Coupling

Palladium-catalyzed coupling reactions of aryl halides provide a general and reliable route to a wide range of compounds through the formation of carbon-carbon and carbon-heteroatom bonds (Figure 5.2). The 2010 Chemistry Nobel Prize was awarded to Heck, Negishi, and Suzuki for their contributions to the development of palladium-catalyzed cross-coupling reactions. In 2015 it was reported that three palladium-catalyzed cross-coupling reactions – Suzuki-Miyaura coupling, Sonogashira coupling, and Buchwald-Harwig amination – are within the top 20 reactions most commonly used in medicinal chemistry.[1] A variety of metals such as nickel, palladium or copper,[2–5] have been explored for cross-coupling reactions, but palladium catalysts remain the most widely used due to their high reactivity, functional group tolerance and stability.[6]

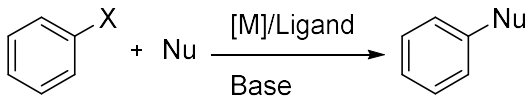

Figure 5.2. General scheme of cross-coupling reactions.

5.2.2 Mechanism of Palladium-Catalyzed Cross-Coupling

Palladium-catalyzed cross-coupling reactions proceed through three common steps, oxidative addition of a Pd(0) source, transmetallation, and reductive elimination (Figure 5.3). L_nPd^0 reacts with an aryl halide (ArX) via oxidative addition to give a Pd(II) complex, $L_nPd(Ar)(X)$. For n = 2, this 16-electron square planar intermediate is generally more stable than the palladium(0) source, but still reactive enough for the next steps. This intermediate then undergoes transmetallation with the nucleophile, generating $L_nPd(Ar)(Nu)$. The final product, (ArNu), is obtained after the reductive elimination of this intermediate and regeneration of the palladium(0) species, L_nPd^0.[7]

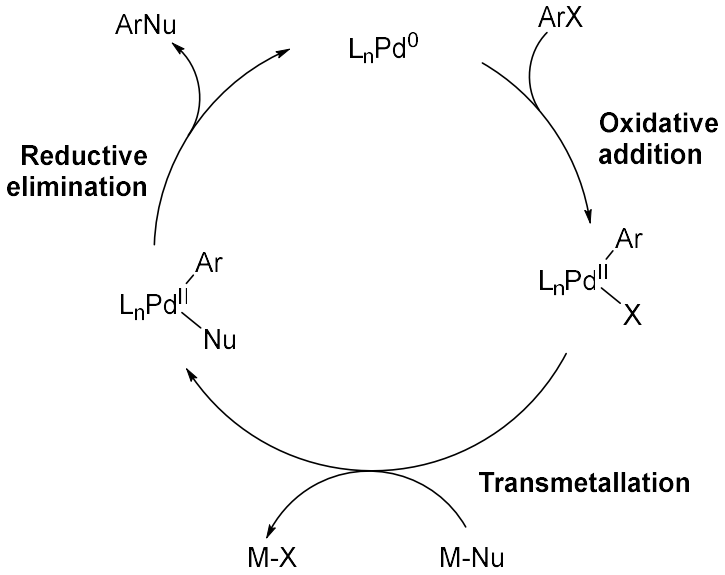

Figure 5.3. General catalytic cycle for cross-coupling reactions.

The diverse cross-coupling reaction have specific mechanistic differences, specifically in the transmetallation step. For example, in Buchwald-Hartwig C–N coupling, the amine coordinates to the metal catalyst and then gets deprotonated instead of a direct transmetallation. In Sonogashira coupling, the transmetallation involves the alkyne coordinating to the metal bond followed by a base mediated elimination of HX.[8] Suzuki-Miyaura couplings involve the use of organoborane species bonded to the nucleophile to enable the transmetallation step. In direct arylation reactions, instead of a transmetallation step, the mechanism involves salt metathesis, where the oxidative addition intermediate undergoes ligand exchange with a pivalate anion, generating $L_nPd(Ar)(OPiv)$, which then undergoes CMD (as discussed in Chapters 2-4). Finally, Heck coupling does not have a transmetallation step, but rather an alkene insertion into the Pd–Ar bond.

5.2.3 Biarylphosphines: discovery, synthesis and evolution

Since Pd-catalyzed coupling reactions were first described in the 1970s, many research groups have focused on optimization of Pd catalyst design. Multiple research groups, including pharmaceutical companies,[9] have worked on the development of air-stable biarylphosphines capable of forming palladium complexes or precatalysts that can be activated into a L_nPd^0 species under the reaction conditions.[10,11] These complexes have been explored in a wide variety of cross-coupling reactions to synthesize a wide range of products.[12–14]

Starting in 2006, the Buchwald group reported that the use of sterically hindered, electron-rich biarylphosphine ligands promote cross-coupling reactivity.[15] There are four structural features on the dialkylbiaryl phosphine ligands that affect the reactivity of the *in situ* formed active species, with BrettPhos shown as an example (Figure 5.4).[16] Bulky alkyl substituents promote the reductive

elimination step, at the same time, alkyl groups are strong σ-donors, enhancing the rate of the oxidative addition due to electron donation to the phosphine. An *ortho* substituted aryl group bonded to the phosphorous atom accelerates reductive elimination by increasing the steric bulk around it. Substituents in the *ortho* position of the second aryl ring increase the catalyst stability and prevent cyclometallation. An increase in the size of the substituents on this second aryl ring also increases the rate of catalytic coupling.[17] Lastly, the second aryl group prevents the oxidation of the phosphine into phosphine oxide.

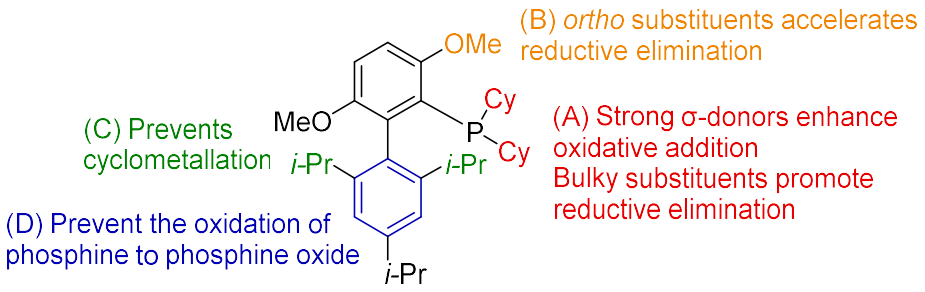

Figure 5.4. Analysis of important structural features of BrettPhos for cross-coupling reactions.

Notably, earlier work from the Buchwald group showed that biarylphosphines without the substituents on the second aryl ring form cyclometallated complexes. They found that mixing $Pd(OAc)_2$ and JohnPhos in toluene for 16 h forms an air and moisture stable solid with high catalytic activity in the amination of aryl chlorides (Figure 5.5).[18] In general, this work shows that the use of ortho unsubstituted biarylphosphines lead to C–H activated cyclometallated species. Hence, the structure of the ligand is one of the most important features for the design of the catalyst.

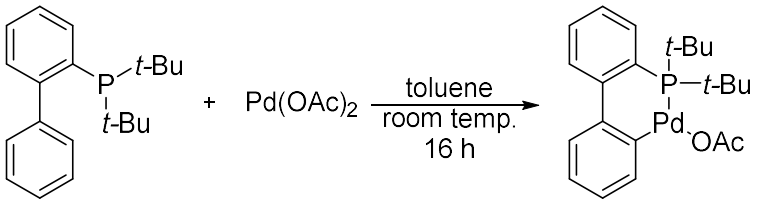

Figure 5.5. Synthesis of palladacycle from JohnPhos and palladium acetate.

5.2.4 Palladacycles

The formation of palladacyclic structures as precatalysts or as intermediates during the reaction can affect the catalytic activity. The palladium-carbon bond stabilized by the intramolecular coordination makes these compounds stable, but also facilitates the formation of Pd(0) under the catalytic reaction conditions.[19] The use of palladacycles as catalyst precursors was first reported in the 1980s[20] with the hydrogenation of C–C double bonds, by a cyclopalladated triphenyl phosphite. However, they became more popular when the Herrmann-Beller catalyst was reported for Heck coupling.[21] Other palladacycle forming catalysts have also been reported for Suzuki-Miyaura and Buchwald-Hartwig coupling. [22–24]

Palladacycles are classified into two groups, anionic four-electron donor (CY) or six-electron donor (YCY). In the dimeric conformation of CY-type palladacycles, there are two other coordination sites available for X and/or L-type donors. Depending on the identity of the other ligands, they can be neutral, cationic or anionic, as well as monomeric or dimeric (e.g. with bridging halogen or carboxylate ligands). The metalated carbon is usually an aromatic sp^2 carbon, and less commonly an sp^3 carbon (aliphatic or benzylic). The metalated ring can vary between 3 and 11 members, however the three- and four-membered palladacycles are usually less stable.[18,25,26] The YCY-type palladacycles are commonly named pincer-type palladacycles. They

are usually symmetrical with two equivalent five- or six-membered rings.[27,28] Examples of unsymmetrical pincers, with both five- and six-membered rings have also been described.[29–31]

5.2.5 BRIDP Ligands

Inspired by the 1,1-diarylethylene motif, Kobayashi and coworkers at Takasago Corporation described four BRIDP ligands in 2011.[32] They are named after the shortened form of "bridging phosphines," as they can work as a bridge between two coupling partners. They all follow the same structural scheme and specific characteristics: increased electron richness and steric bulkiness to promote the oxidative addition and reductive elimination respectively. They therefore share structural features with the biarylphosphines described above.

BRIDP ligands are easily synthesized from readily available materials. 1,1-Diarylethylene can selectively be brominated at the C2 position, the most electron rich carbon. This can later be coupled to a dialkylchlorophosphine in the presence of magnesium iodide to obtain the dialkylbiarylphosphine. This synthetic route affords the vBRIDP ligands with phosphorous-conjugated aryl groups through a vinyl bridge (Figure 5.6).

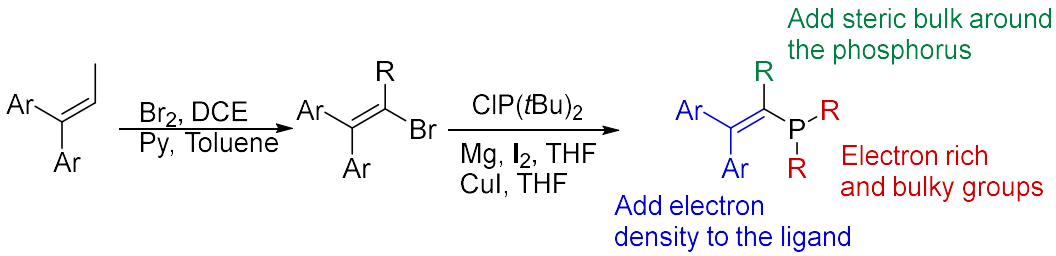

Figure 5.6. Synthesis and design of vBRIDP ligands.

Two aryl groups with electron-donating alkyl groups bonded to the phosphorous atom through the carbon-carbon double bond are responsible for the electron richness of the ligand. The two other substituents at phosphorus provide additional electron donation and steric bulk. In the initial ligands, Kobayashi and coworkers used *tert*-butyl and cyclohexyl groups to synthesize vBRIDP and Cy-vBRIDP (Figure 5.7).

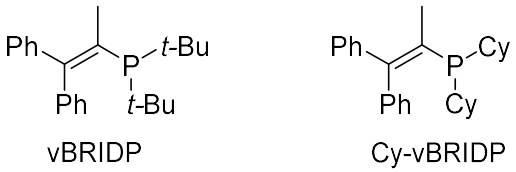

Figure 5.7. Structures of vBRIDP and Cy-vBRIDP ligands.

Common structural features of phosphines that form palladacycles include phosphines containing aryl groups at an appropriate position fixed by their spacers (including the JohnPhos palladacycle, Figure 5.5), and phosphines bearing alkyl substituents. They modified the alkene bridge with a methylcyclopropane group, increasing the hindrance on the phosphorus while maintaining the same spatial distance between the phosphorus and the aryl groups (Figure 5.8). The BRIDP ligands are colorless crystalline solids that, despite having electron-rich phosphorous centers, are air stable.

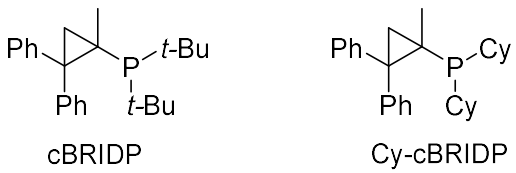

Figure 5.8. Structures of cBRIDP and Cy-cBRIDP ligands.

5.2.6 Use of BRIDP Ligands for Cross Coupling Reactions

The BRIDP ligands were originally described for Buchwald-Hartwig amination of primary amines. Kobayashi and coworkers optimized the coupling of secondary aryl amines with a series of vBRIDP phosphine derivatives. They discovered that increasing the bulkiness on the α-position of the alkene decreased the product yield, hypothesizing that larger groups impede the oxidative addition due to steric hindrance. The addition of electron donating groups on the *para* position of the aryl rings had a smaller effect but still decreased the reactivity.[33] They further explored the reactivity of Cy-vBRIDP in the coupling of primary aryl and alkyl amines, obtaining good isolated yields of the monoarylation products.

Due to the air and moisture stability of BRIDP ligands, several groups have explored their catalytic activity in surfactant-based reaction media (PS-750-M). These reaction conditions have allowed for low catalyst loading (0.5 mol%) and high reaction yields (above 85% isolated yields).[34] A similar catalytic system, combining BRIDP ligands with $[(allyl)PdCl]_2$ as the palladium source, was described for C–N coupling using ammonia equivalents (carbamates, sulfonamide and urea).[35] The same metal source has been employed under traditional Buchwald-Hartwig amination of secondary aryl amines.[36]

BRIDP ligands have also been explored in other cross-coupling reactions. In Sonogashira reactions of long chained alkynes, they have been used for cross-coupling reactions of aryl halides, under the presence of palladium acetate and the similar polyoxyethanyl-α-tocopheryl sebacate (PTC/H_2O) micellar environment.[37] The same conditions have been applied to the synthesis of donor-acceptor type thioxanthones, molecules commonly used as single-photon polymerization initiators.[38]

Another commonly studied cross-coupling reaction with BRIDP ligands is Suzuki-Miyaura coupling. Several groups have evaluated the utility of these particular dialkylbiarylphosphines as efficient catalyst ligands for the synthesis of a variety of biaryl products using palladium acetate[39] or palladium allyl chloride dimer[40] as the metal source. Other boron handles have also been explored with BRIDP ligands and palladium acetate. For example in 2016, Arai reported the coupling of potassium trifluoroborate salts as cross-coupling partners.[41]

This work reports how both vBRIDP and cBRIDP ligands undergo cyclometallation in combination with $Pd(OAc)_2$ to form palladacycles through C–H activation of one of the phenyl rings. Despite the widespread use of these ligands, these palladacycles have not been reported before. In addition to their synthesis and characterization, an evaluation of their catalytic activity in comparison to *in situ* Pd/BRIDP systems reveals where these palladacycles can be effectively used as precatalysts.

5.3 Results and Discussion

5.3.1 Synthesis of BRIDP-Derived Palladacycles

During an investigation into which phosphine ligands are able to form palladacycles, several *tert*-butyl substituted phosphine ligands were evaluated in combination with $Pd(OAc)_2$. The initial target was to identify additional four-membered palladacycles formed by C–H metalation of a *tert*-butyl methyl group. Mixing cBRIDP or vBRIDP ligands with $Pd(OAc)_2$ results in a single new phosphorous-containing species (evident in crude $^{31}P\{^1H\}$ NMR spectra). However, isolation and characterization of the resulting complexes reveals that the new metallacycle is not formed through

metalation of the *tert*-butyl group, but the *ortho* carbon on one of the phenyl rings. This is similar to the previously reported synthesis of the JohnPhos-derived palladacycle (Figure 5.5).

Using mild reaction conditions, four palladacycle derivatives were synthesized using vBRIDP and cBRIDP ligands in high yield (Figure 5.9). Recrystallization from pentane gives air-stable solids in excellent purity. X-ray crystallography was performed on two complexes: the cBRIDP (**I**) and vBRIDP (**III**) palladacycles. Both structures show a planar six-membered ring between the palladium, phosphine and aryl groups, and a κ^2-acetate ligand (Figure 5.10).

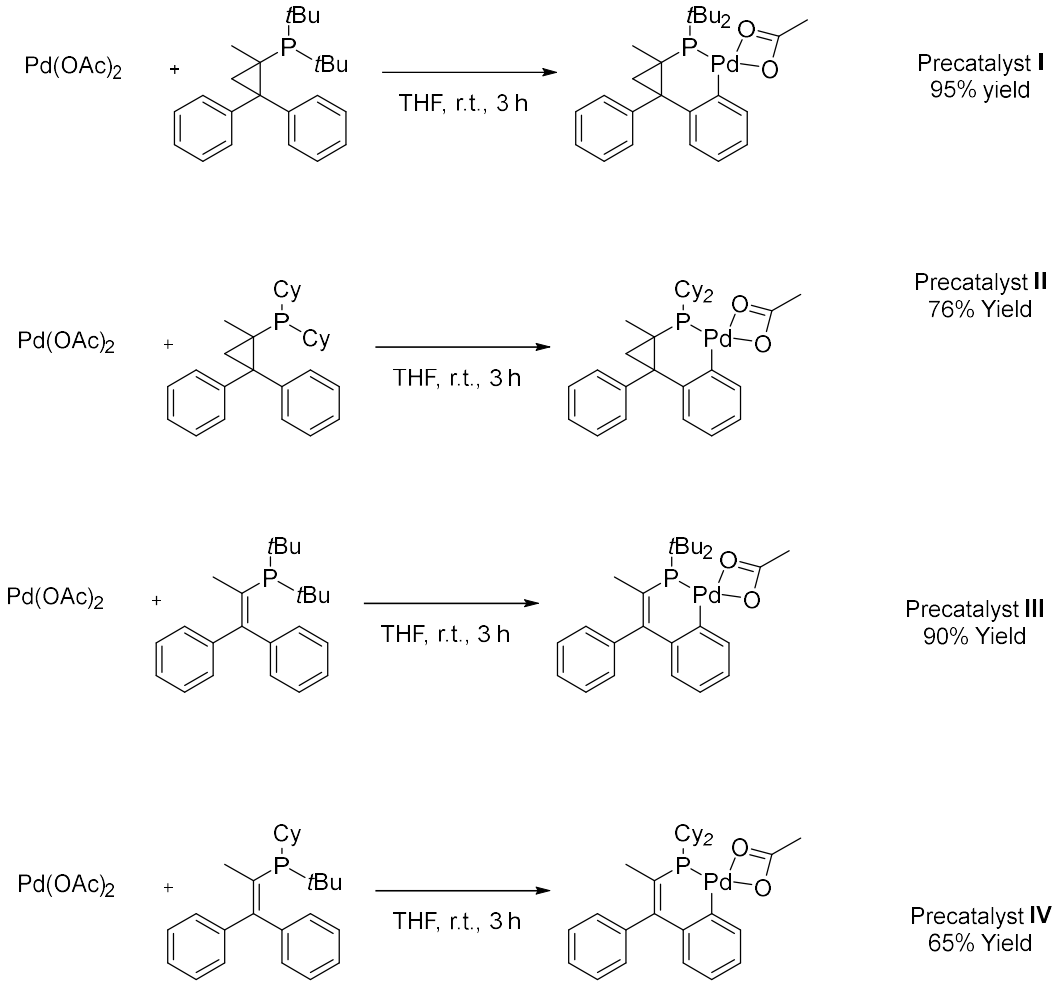

Figure 5.9. Synthesis of BRIDP palladacycles.

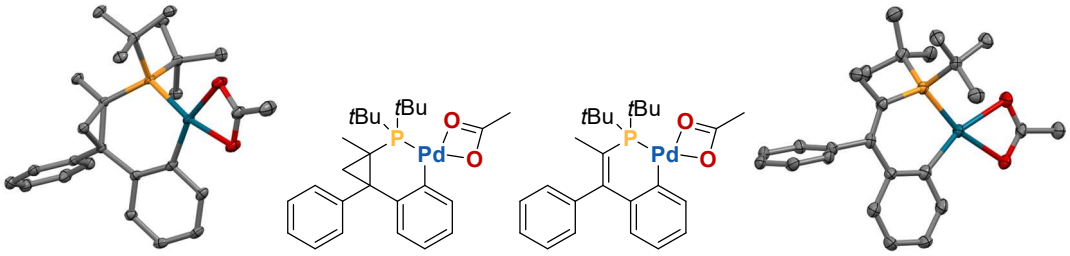

Figure 5.10. Solid-state molecular structures of precatalysts **I** (*left*) and **III** (*right*). Ellipsoids plotted at 50% probability. Hydrogens not shown for clarity.

5.2.2 Reaction monitoring of the formation of BRIDP-Palladacycles

The ease with which these palladacycles form indicated that any *in situ* combination of BRIDP ligand and $Pd(OAc)_2$ (which is common in catalysis) may simply generate the corresponding palladacycle. As cross-coupling reactions often include non-polar solvents, the formation of the palladacycles from BRIDP/$Pd(OAc)_2$ was monitored in toluene by $^{31}P\{^1H\}$ NMR spectroscopy. *tert*-Butyl phosphine containing ligands, cBRIDP (Figure 5.11) and vBRIDP (Figure 5.12) are relatively slow to form the palladacycle in toluene. While significant amounts of the palladacycle are observed after 2 hours at room temperature, even after 24 hours full conversion is not achieved. Both of these palladacycles are stable during the reaction monitoring period, with no additional ^{31}P-containing species visible.

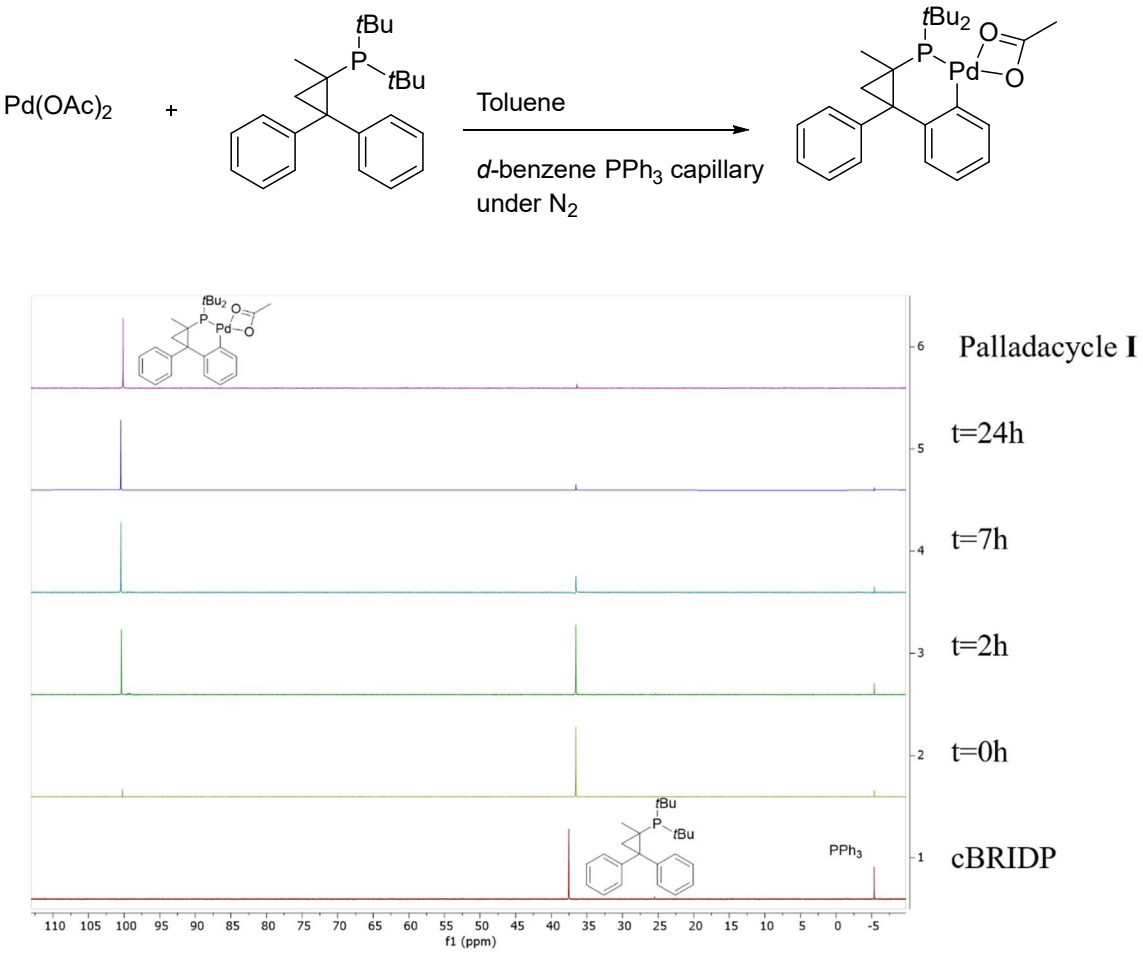

Figure 5.11. Reaction monitoring of the formation of cBRIDP palladacycle from palladium acetate and cBRIDP.

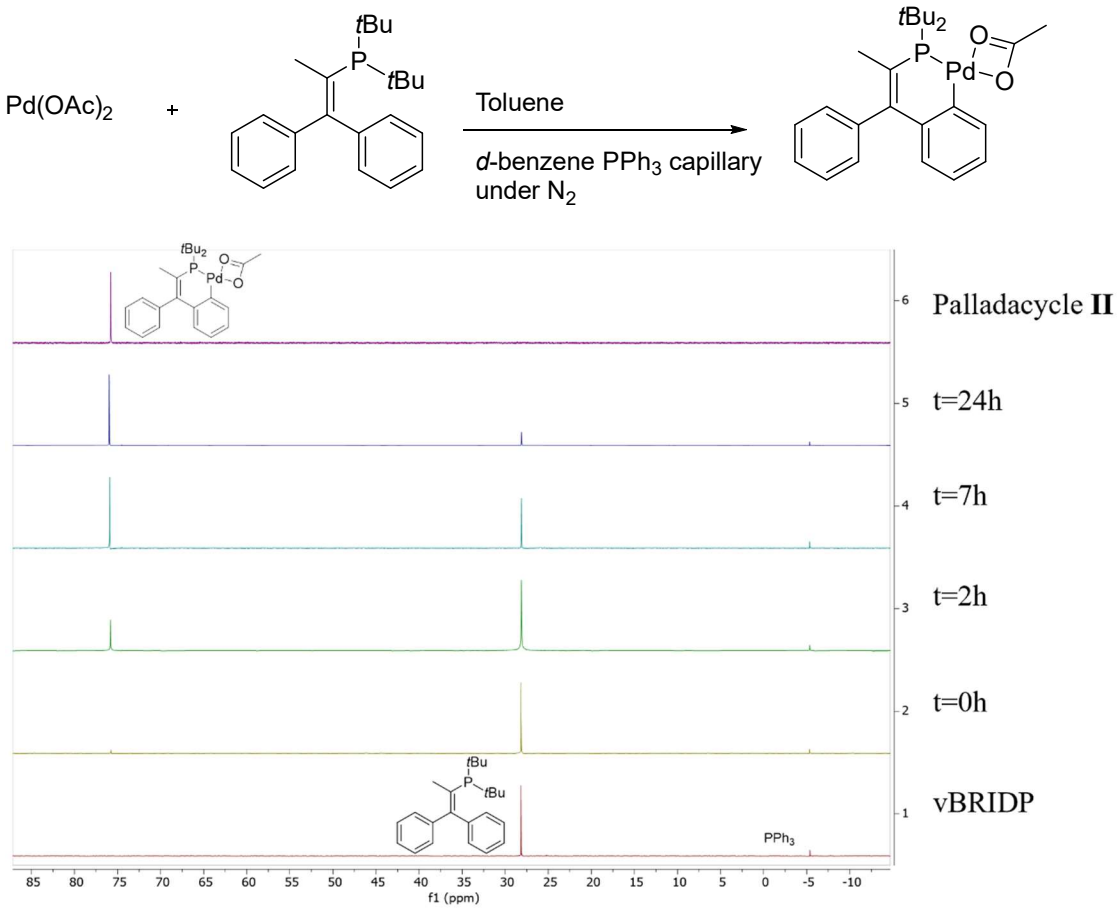

Figure 5.12. Reaction monitoring of the formation of vBRIDP palladacycle from palladium acetate and vBRIDP.

In contrast, cyclohexyl phosphine containing BRIDP ligands, Cy-cBRIDP (Figure 5.13) and Cy-vBRIDP (Figure 5.14) show rapid C–H activation and formation of palladacycle. Cy-vBRIDP shows full conversion at time = 0 h, while Cy-cBRIDP has some residual phosphine at time = 0 h. However, in both cases other ^{31}P-containing species are observed, indicating possible decomposition products. The cyclopropane containing ligand, Cy-cBRIDP, shows more decomposition products than the vinyl derivative. Overall, the different rates of palladacycle

formation and stability of the resulting species could have an impact on the catalytic activity / applicability of these BRIDP ligands.

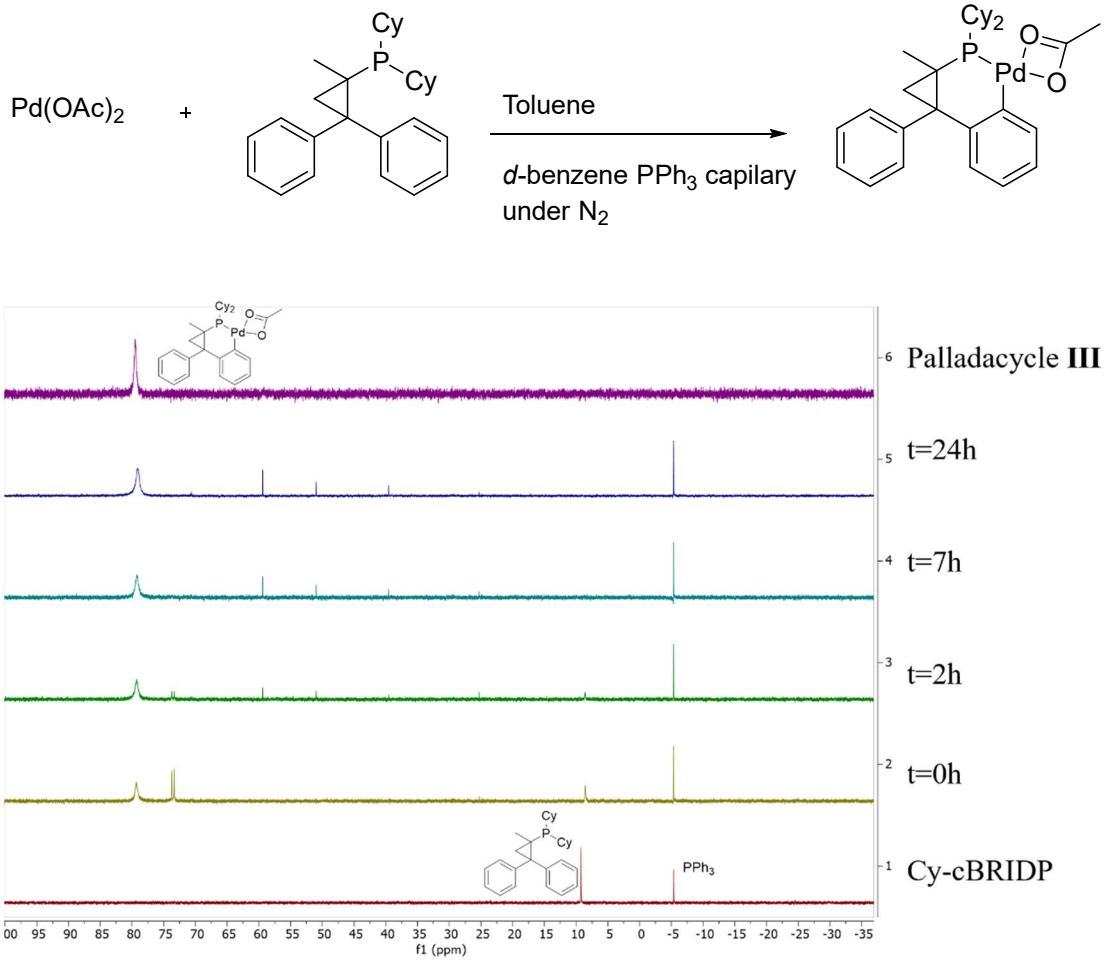

Figure 5.13. Reaction monitoring of the formation of Cy-cBRIDP palladacycle from palladium acetate and Cy-cBRIDP.

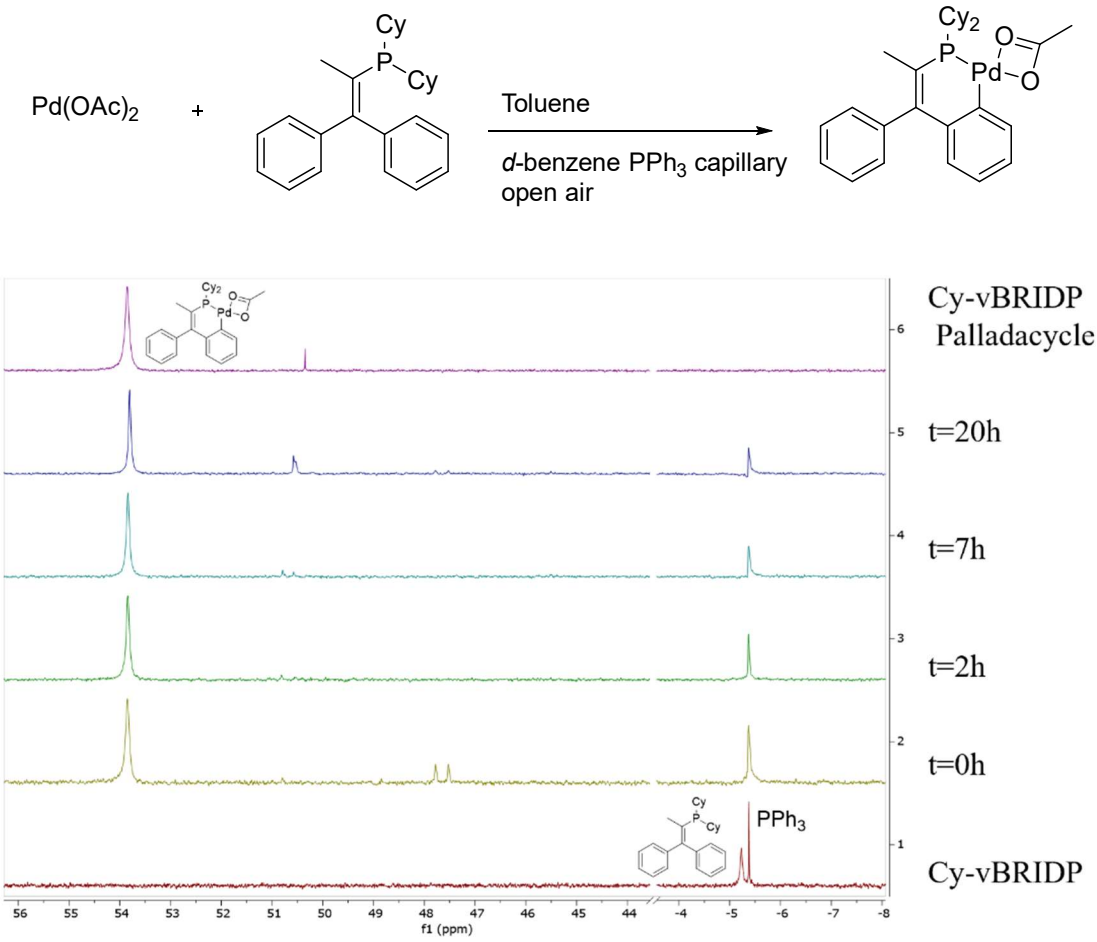

Figure 5.14. Reaction monitoring of the formation of Cy-vBRIDP palladacycle from palladium acetate and Cy-vBRIDP.

5.2.3 High-throughput experimentation for the analysis of catalytic reactivity

As described in the introduction, BRIDP ligands have been used in many catalytic reactions. The main two reported palladium sources used for the reactions are palladium acetate and allylpalladium(II) chloride dimer. To assess the relevance of these palladacycles as precatalysts, I investigated them alongside *in situ* systems using $Pd(OAc)_2$ (which is expected to generate at least some palladacycle *in situ*) and the allylpalladium(II) chloride dimer (which is reported to generate the cBRIDP-Pd(allyl)Cl complex).[42] Catalytic activity for each system was evaluated by

conversion to product after 2 h and 20 h. The most common cross-coupling reactions to use BRIDP ligands were studied, which include Buchwald-Hartwig, Sonogashira and Suzuki-Miyaura couplings. Direct arylation and Heck arylation were also included due to their relevance in pharmaceutical synthesis.

5.2.3.1 Buchwald-Hartwig Reaction

The evaluation began with a Buchwald-Hartwig amination of a secondary amine, *N*-benzylaniline. The reaction conditions were adapted from literature precedent,[33,34] and progress was monitored by ^{19}F NMR using benzotrifluoride as the internal standard. The results of the HTE screen (Figure 5.15) indicate that in this reaction, the isolated vBRIDP palladacycle shows the highest reactivity at initial stages of the reaction with a 39% yield; however, at 20 h the vBRIDP and Cy-vBRIDP combinations with $[Pd(allyl)Cl]_2$ give the highest solution yield. Across all three Pd sources, Cy-cBRIDP is completely ineffective, indicating that this specific ligand is not suitable for the Buchard-Hartwig reaction. Notably, according to the conditions in the original paper, when 1 mol% of catalyst is used the reaction needs 48 h to reach completion, whereas this study only went to 20 h.

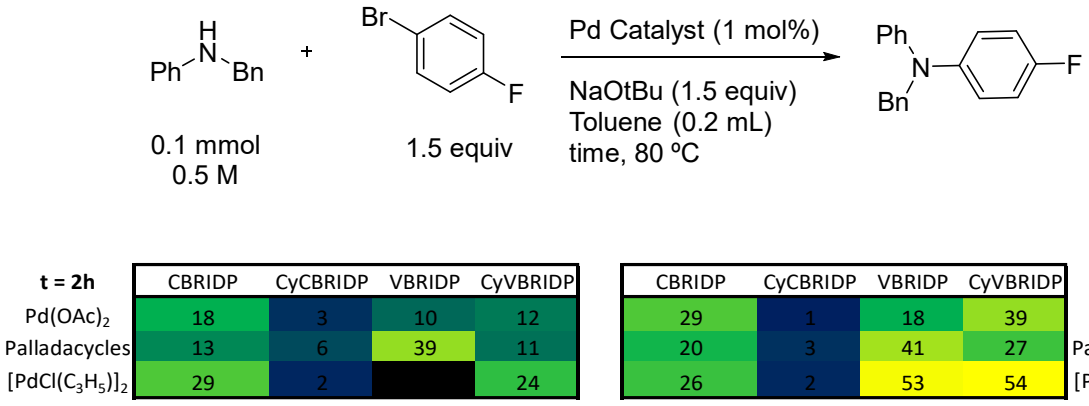

Figure 5.15. Palladium source and ligand evaluation for Buchwald-Hartwig amination of N-Benzylaniline with 1-bromo-1-fluorobenzene at 2 h and 20 h.

5.2.3.2 Sonogashira Coupling

For the Sonogashira coupling between phenylacetylene and 1-bromo-4-fluorobenzene, the reaction conditions were adapted from standard protocols.[35,37,43] The results from the Pd/ligand combinations in this coupling reveal palladacycles have lower reactivity than allylpalladium chloride dimer combinations with the same ligands (Figure 5.16). Allylpalladium chloride dimer shows good reactivity with all the ligands at the 2 h timepoint (yields vary between 21% and 32%). Cy-vBRIDP shows the highest (32% yield) reaction conversion. All of the palladacycles perform poorly relative to the other systems; however, in the case of the vBRIDP ligand, palladium acetate shows 23% product whereas the vBRIDP palladacycle only shows 3% yield at the same time. This may indicate palladacycles are inactive off-cycle species in this case.

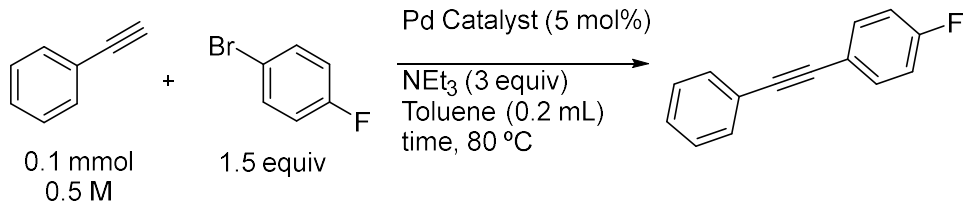

t = 2h	CBRIDP	CyCBRIDP	VBRIDP	CyVBRIDP
$Pd(OAc)_2$	1	8	23	10
Palladacycles	2	7	3	9
$[PdCl(C_3H_5)]_2$	22	29	21	32

CBRIDP	CyCBRIDP	VBRIDP	CyVBRIDP	t = 20h
0	5	0	7	$Pd(OAc)_2$
2	20	1	25	Palladacycles
0	20	3	31	$[PdCl(C_3H_5)]_2$

Figure 5.16. Palladium source and ligand evaluation for Sonogashira coupling of phenylacetylene and 1-bromo-1-fluorobenzene at 2 h and 20 h.

When the reaction is run for twenty hours, the product, 1-fluoro-4-(phenylethynyl)benzene, degrades into multiple new ^{19}F-containing species. There is complete degradation of the cross-coupling product with both di-*tert*-butyl phosphine ligands, cBRIDP and vBRIDP. Isolated cyclohexyl catalysts show less degradation that *in situ* generated palladacycles, though the degradation products were not able to be identified. Because of this complication, these catalytic comparison results are inconclusive.

5.2.3.3 Suzuki-Miyaura Coupling

For the Suzuki-Miyaura reaction evaluation, the electrophile was changed from 1-bromo-4-fluorobenzene to 2-chloro-4-fluoropyridine. The common reaction conditions for Suzuki-Miyaura reactions involve the addition of water.[39–41] However, for consistency between the reaction plates, and to minimize the additives needed in the reaction, anhydrous reaction conditions were chosen for this comparison (Figure 5.17).

In this reaction, screening of palladium and ligand sources reveals the best systems are either a palladacycle precatalyst or palladium acetate/ligand combinations. Isolated palladacycles showed slightly higher reactivity when the cyclohexylphosphine derivatives Cy-cBRIDP and Cy-vBRIDP were used compared to the tBu-based cBRIDP or vBRIDP (24-25% vs 5 or 16%). In fact, cBRIDP showed generally poor reactivity. After 20 h, the highest yielding system is the Cy-vBRIDP palladacycle, reaching 45% yield, while all of the other systems are between 4-26%.

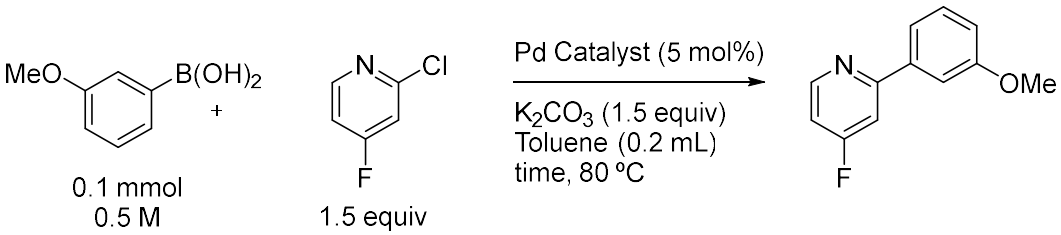

t = 2h	CBRIDP	CyCBRIDP	VBRIDP	CyVBRIDP
$Pd(OAc)_2$	8	19	29	8
Palladacycles	5	24	16	25
$[PdCl(C_3H_5)]_2$	4	17	11	13

CBRIDP	CyCBRIDP	VBRIDP	CyVBRIDP	t = 20h
24	19	26	25	$Pd(OAc)_2$
8	17	22	45	Palladacycles
10	16	4	21	$[PdCl(C_3H_5)]_2$

Figure 5.17 Palladium source and ligand evaluation for Suzuki-Miyaura coupling of 3-methoxyphenylboronic acid and 2-chloro-4-fluoropyridine at 2 h and 20 h.

5.2.3.4 Direct Arylation Reaction

Direct arylation reactions are common cross-coupling reactions that allow the formation of a wide variety of biaryl products.[44,45] Palladium acetate is a common precatalyst, and so are biaryl phosphine ligands with both *tert*-butyl and cyclohexyl R groups, such as JohnPhos, Davephos or MePhos. Currently (to the best of our knowledge), there are no reported examples of BRIDP

ligands being used specifically for direct arylation. For this reaction evaluation, the reaction conditions were standardized from the protocol developed by Fagnou (Figure 5.18).[46] Unfortunately, the reaction screening of the three palladium sources and four BRIDP ligands did not exhibit high enough yields to draw any conclusions, with generally poor reactivity in all cases. After twenty hours, moderate reaction yields are observed; however, the observed reactivity is largely the same irrespective of the catalyst system, making comparisons inconclusive.

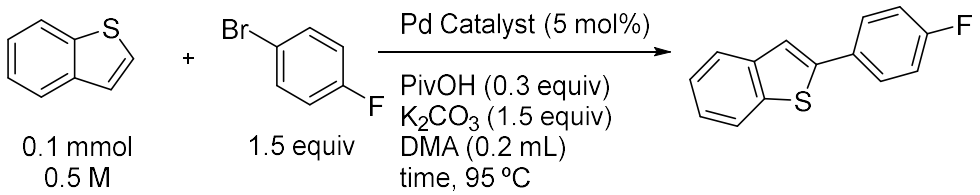

t = 2h	CBRIDP	CyCBRIDP	VBRIDP	CyVBRIDP
$Pd(OAc)_2$	1	7	3	1
Palladacycles	10	6	2	7
$[PdCl(C_3H_5)]_2$	11	11	5	6

CBRIDP	CyCBRIDP	VBRIDP	CyVBRIDP	t = 20h
26	29	29	31	$Pd(OAc)_2$
21	23	20	25	Palladacycles
31	17	19	25	$[PdCl(C_3H_5)]_2$

Figure 5.18. Palladium source and ligand evaluation for direct arylation of benzothiophene with 1-bromo-1-fluorobenzene at 2 h and 20 h.

5.2.3.5 Heck Arylation

Finally, palladium acetate is also a common palladium source in Heck arylations, though BRIDP ligands have not been reported for Heck couplings (to the best of our knowledge). The protocol for the coupling between styrene and 1-bromo-4-fluorobenzene was adapter from similar reaction conditions as for the direct arylation reaction. In the initial reactivity investigation of the reactivity of two alkenes, styrene and α-methylstyrene. Styrene yielded a single isomer, (*E*)-1-

fluoro-4-styrylbenzene, whereas α-methylstyrene showed the formation of both (*Z*)-1-fluoro-4-(2-phenylprop-1-en-1-yl)benzene and (*E*)-1-fluoro-4-(2-phenylprop-1-en-1-yl)benzene isomers. The formation of a single product with styrene led to this reaction being targeted for further study.

The HTE results show a preference for ligand but not a palladium source (Figure 5.19). cBRIDP and Cy-vBRIDP show higher product formation at 2 h independently of whether the palladacycle is generated *in situ*, used as a single component precatalyst, or if a non-palladacycle forming Pd source is used. This difference in the ligand preference disappears when the reaction is run for twenty hours, where nearly all systems reach 50-60% yield.

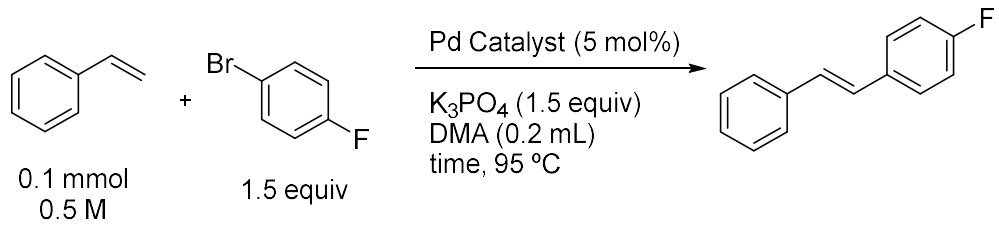

t = 2h	CBRIDP	CyCBRIDP	VBRIDP	CyVBRIDP
$Pd(OAc)_2$	45	14	26	31
Palladacycles	50	23	36	46
$[PdCl(C_3H_5)]_2$	55	15	22	36

CBRIDP	CyCBRIDP	VBRIDP	y	t = 20h
50	51	41	54	$Pd(OAc)_2$
54	62	46	60	Palladacycles
56	60	64	58	$[PdCl(C_3H_5)]_2$

Figure 5.19 Palladium source and ligand evaluation on Heck Arylation of Styrene and 1-Bromo-1-Fluorobenzene 2h and 20h

5.3 Conclusions

In summary, when palladium acetate and BRIDP ligands are combined, palladacycle species are generated through C–H metalation at a phenyl ring. The formation of these species, although fast, depends on the solvent (faster reaction in THF, slower in toluene), the alkyl groups on the phosphine (faster reaction with Cy versus tBu), and the linker group on the phosphine (faster reaction with vBRIDP than cBRIDP). The palladacycles were evaluated as single component precatalyst for several cross-coupling reactions, including some of the most common cross-coupling reactions: Suzuki-Miyaura coupling, Sonogashira reaction, and Buchwald-Hartwig amination, direct arylation, and Heck coupling. Unfortunately, BRIDP ligands did not show much reactivity for the direct arylation reaction tested; however, they did exhibit good reactivity for Heck coupling. Further optimization of the reaction conditions would reveal the chemical space that can be explored with the specific catalytic system.

Overall, under the conditions studied for these five reactions, there was not a significant difference between *in situ* formed catalyst systems from $Pd(OAc)_2$ and/or $[Pd(allyl)Cl]_2$ and the isolated BRIDP-based palladacycles. Further studies of the reactivity and suitability of these palladacycles are underway.

5.4 Experimental

5.4.1. Synthesis of BRIDP palladacycles

Inside the glovebox, 150 mg of $Pd(OAc)_2$ (0.67 mmol, 1 equiv) and the corresponding BRIDP ligand (0.80 mmol, 1.2 equiv) were added to a 4-dram vial. 7.5 mL of anhydrous THF was added to the vial and the reaction was stirred at room temperature for three hours. The reaction was filtered through celite, evaporated under vacuum and redissolved in a minimum amount of pentane. The solution was left in the freezer to allow crystallization. After 48 h, the supernatant was removed and the crystals were dried under vacuum. Products were characterized by NMR spectroscopy and HRMS (see Appendix D for details).

5.4.2 General procedure for HTE experiments

Stock solutions of palladium acetate, palladium allyl-chloride dimer, BRIDP ligands and palladacycle were prepared. A 96 well plate was charged with a 1 mL reaction vial and micro parylene-coated stir-bars were added to each well. Inside the glovebox, the corresponding base was added to each vial using calibrated plastic scoops: K_3PO_4 (30 mg), K_2CO_3 (20 mg) or a micropipette NEt_3 (41 µL). Substrate stock solutions were prepared inside the glovebox: aryl halides (1.5 M) in toluene or DMA; and corresponding nucleophile (1 M). 0.1 mL of the appropriate stock solution were added to each 1 mL shell vial in the aluminum reaction plates. The plates were then sealed using a screwed-down lid with a Teflon liner and rubber spacer. The reaction plates were then heated on a tumble stirrer set to 500 rpm, at 85 °C or 100 ºC for 2 or 20 h. Upon completion, the mixtures from the plates were filtered through celite and evaporated to dryness using centrifugal evaporation. The reactions were redissolved in deuterated chloroform and a 10 mol% trifluorotoluene stock solution was added into each cell. The reaction yields were calculated by ^{19}F NMR spectroscopy.

5.5 References

(1) Brown, D. G.; Boström, J. Analysis of Past and Present Synthetic Methodologies on Medicinal Chemistry: Where Have All the New Reactions Gone?: Miniperspective. *J. Med. Chem.* **2016**, *59*, 4443–4458. https://doi.org/10.1021/acs.jmedchem.5b01409.

(2) Mesganaw, T.; Garg, N. K. Ni- and Fe-Catalyzed Cross-Coupling Reactions of Phenol Derivatives. *Org. Process Res. Dev.* **2013**, *17*, 29–39. https://doi.org/10.1021/op300236f.

(3) Zhou, J. (Steve); Fu, G. C. Suzuki Cross-Couplings of Unactivated Secondary Alkyl Bromides and Iodides. *J. Am. Chem. Soc.* **2004**, *126*, 1340–1341. https://doi.org/10.1021/ja039889k.

(4) Kabir, M. S.; Lorenz, M.; Namjoshi, O. A.; Cook, J. M. First Application of an Efficient and Versatile Ligand for Copper-Catalyzed Cross-Coupling Reactions of Vinyl Halides with N-Heterocycles and Phenols. *Org. Lett.* **2010**, *12*, 464–467. https://doi.org/10.1021/ol9026446.

(5) Aleena, M. B.; Philip, R. M.; Anilkumar, G. Advances in Non-Palladium-Catalysed Stille Couplings. *App. Organomet. Chem.* **2021**, *35*, e6430. https://doi.org/10.1002/aoc.6430.

(6) Shaughnessy, K. H. Development of Palladium Precatalysts That Efficiently Generate LPd(0) Active Species. *Isr. J. Chem.* **2020**, *60*, 180–194. https://doi.org/10.1002/ijch.201900067.

(7) Firsan, S. J.; Sivakumar, V.; Colacot, T. J. Emerging Trends in Cross-Coupling: Twelve-Electron-Based L1Pd(0) Catalysts, Their Mechanism of Action, and Selected Applications. *Chem. Rev.* **2022**, *122*, 16983–17027. https://doi.org/10.1021/acs.chemrev.2c00204.

(8) Chinchilla, R.; Nájera, C. Recent Advances in Sonogashira Reactions. *Chem. Soc. Rev.* **2011**, *40*, 5084. https://doi.org/10.1039/c1cs15071e.

(9) Schmink, J. R.; Tudge, M. T. Facile Preparation of Highly-Functionalized, Nitrogen-Bearing Diarylmethanes. *Tetrahedron Lett.* **2013**, *54*, 15–20. https://doi.org/10.1016/j.tetlet.2012.09.112.

(10) Bruno, N. C.; Tudge, M. T.; Buchwald, S. L. Design and Preparation of New Palladium Precatalysts for C–C and C–N Cross-Coupling Reactions. *Chem. Sci.* **2013**, *4*, 916–920. https://doi.org/10.1039/C2SC20903A.

(11) Bruneau, A.; Roche, M.; Alami, M.; Messaoudi, S. 2-Aminobiphenyl Palladacycles: The "Most Powerful" Precatalysts in C–C and C–Heteroatom Cross-Couplings. *ACS Catal.* **2015**, *5*, 1386–1396. https://doi.org/10.1021/cs502011x.

(12) Ruiz-Castillo, P.; Blackmond, D. G.; Buchwald, S. L. Rational Ligand Design for the Arylation of Hindered Primary Amines Guided by Reaction Progress Kinetic Analysis. *J. Am. Chem. Soc.* **2015**, *137* (8), 3085–3092. https://doi.org/10.1021/ja512903g.

(13) Arrechea, P. L.; Buchwald, S. L. Biaryl Phosphine Based Pd(II) Amido Complexes: The Effect of Ligand Structure on Reductive Elimination. *J. Am. Chem. Soc.* **2016**, *138*, 12486–12493. https://doi.org/10.1021/jacs.6b05990.

(14) Ingoglia, B. T.; Buchwald, S. L. Oxidative Addition Complexes as Precatalysts for Cross-Coupling Reactions Requiring Extremely Bulky Biarylphosphine Ligands. *Org. Lett.* **2017**, *19*, 2853–2856. https://doi.org/10.1021/acs.orglett.7b01082.

(15) Burgos, C. H.; Barder, T. E.; Huang, X.; Buchwald, S. L. Significantly Improved Method for the Pd-Catalyzed Coupling of Phenols with Aryl Halides: Understanding Ligand Effects. *Angew. Chem. Int. Ed.* **2006**, *45*, 4321–4326. https://doi.org/10.1002/anie.200601253.

(16) Surry, D. S.; Buchwald, S. L. Dialkylbiaryl Phosphines in Pd-Catalyzed Amination: A User's Guide. *Chem. Sci.* **2010**, *2*, 27–50. https://doi.org/10.1039/C0SC00331J.

(17) Salvi, L.; Davis, N. R.; Ali, S. Z.; Buchwald, S. L. A New Biarylphosphine Ligand for the Pd-Catalyzed Synthesis of Diaryl Ethers under Mild Conditions. *Org. Lett.* **2012**, *14*, 170–173. https://doi.org/10.1021/ol202955h.
(18) Zim, D.; Buchwald, S. L. An Air and Thermally Stable One- Component Catalyst for the Amination of Aryl Chlorides. *Org. Lett.* **2003**, *5*, 2413–2415. https://doi.org/10.1021/ol034561h.
(19) Dupont, J.; Consorti, C. S.; Spencer, J. The Potential of Palladacycles: More Than Just Precatalysts. *Chem. Rev.* **2005**, *105*, 2527–2572. https://doi.org/10.1021/cr030681r.
(20) Lewis, L. N. Enhancement of Catalytic Activity through Orthometalation. Synthesis, Structure, and Catalytic Activity of a New Orthometalated Ruthenium Complex. *J. Am. Chem. Soc.* **1986**, *108*, 743–749. https://doi.org/10.1021/ja00264a028.
(21) Herrmann, W. A.; Brossmer, C.; Reisinger, C.-P.; Riermeier, T. H.; Öfele, K.; Beller, M. Palladacycles: Efficient New Catalysts for the Heck Vinylation of Aryl Halides. *Chemistry – A European Journal* **1997**, *3*, 1357–1364. https://doi.org/10.1002/chem.19970030823.
(22) Littke, A. F.; Fu, G. C. A Convenient and General Method for Pd-Catalyzed Suzuki Cross-Couplings of Aryl Chlorides and Arylboronic Acids. *Angewandte Chemie International Edition* **1998**, *37*, 3387–3388. https://doi.org/10.1002/(SICI)1521-3773(19981231)37:24<3387::AID-ANIE3387>3.0.CO;2-P.
(23) Wolfe, J. P.; Tomori, H.; Sadighi, J. P.; Yin, J.; Buchwald, S. L. Simple, Efficient Catalyst System for the Palladium-Catalyzed Amination of Aryl Chlorides, Bromides, and Triflates. *J. Org. Chem.* **2000**, *65*, 1158–1174. https://doi.org/10.1021/jo991699y.
(24) Nishiyama, M.; Yamamoto, T.; Koie, Y. Synthesis of N-Arylpiperazines from Aryl Halides and Piperazine under a Palladium Tri-Tert-Butylphosphine Catalyst. *Tetrahedron Lett.* **1998**, *39*, 617–620. https://doi.org/10.1016/S0040-4039(97)10659-1.
(25) Solé, D.; Vallverdú, L.; Solans, X.; Font-Bardía, M.; Bonjoch, J. Intramolecular Pd-Mediated Processes of Amino-Tethered Aryl Halides and Ketones: Insight into the Ketone α-Arylation and Carbonyl-Addition Dichotomy. A New Class of Four-Membered Azapalladacycles. *J. Am. Chem. Soc.* **2003**, *125*, 1587–1594. https://doi.org/10.1021/ja029114w.
(26) McPherson, H. M.; Wardell, J. L. Alkylthiomethylpalladium Compounds. *Inorganica Chimica Acta* **1983**, *75*, 37–43. https://doi.org/10.1016/S0020-1693(00)91187-3.
(27) Consorti, C. S.; Ebeling, G.; Rodembusch, F.; Stefani, V.; Livotto, P. R.; Rominger, F.; Quina, F. H.; Yihwa, C.; Dupont, J. A New Totally Flat $N(sp^2)C(sp^2)N(sp^2)$ Pincer Palladacycle: Synthesis and Photoluminescent Properties. *Inorg. Chem.* **2004**, *43*, 530–536. https://doi.org/10.1021/ic0346679.
(28) Morales-Morales, D.; Redón, R.; Yung, C.; Jensen, C. M. High Yield Olefination of a Wide Scope of Aryl Chlorides Catalyzed by the Phosphinito Palladium PCP Pincer Complex: $[PdCl\{C_6H_3(OPPri_2)_2\text{-}2,6\}]$. *Chem. Commun.* **2000**, 17, 1619–1620. https://doi.org/10.1039/B004412L.
(29) Ebeling, G.; Meneghetti, M. R.; Rominger, F.; Dupont, J. The Trans-Chlorometalation of Hetero-Substituted Alkynes: A Facile Entry to Unsymmetrical Palladium YCY‘ (Y, Y‘ = NR_2, PPh_2, $OPPh_2$, and SR) “Pincer” Complexes. *Organometallics* **2002**, *21*, 3221–3227. https://doi.org/10.1021/om011002a.
(30) Lai, S.-W.; Cheung, T.-C.; Chan, M. C. W.; Cheung, K.-K.; Peng, S.-M.; Che, C.-M. Luminescent Mononuclear and Binuclear Cyclometalated Palladium(II) Complexes of 6-Phenyl-2,2‘-Bipyridines: Spectroscopic and Structural Comparisons with Platinum(II) Analogues1,2. *Inorg. Chem.* **2000**, *39*, 255–262. https://doi.org/10.1021/ic991089g.

(31) Deeming, A. J.; Rothwell, I. P. Palladation Behaviour of 8-Methyl-, 8-Ethyl-, and 8-Isopropyl-Quinolines and Some of Their 2-Substituted Derivatives. *J. Organomet. Chem.* **1981**, *205*, 117–131. https://doi.org/10.1016/S0022-328X(00)82943-5.
(32) Suzuki, K.; Hori, Y.; Nakayama, Y.; Kobayashi, T. Development of New Phosphine Ligands (BRIDPs) for Efficient ─ Palladium Catalyzed Coupling Reactions and Their Application to Industrial Processes. *J. Synth. Org. Chem.,* **2011**, *69,* 1231-1240. https://doi.org/10.1002/chin.201215243.
(33) Suzuki, K.; Hori, Y.; Nishikawa, T.; Kobayashi, T. A Novel (2,2-Diarylvinyl)Phosphine/Palladium Catalyst for Effective Aromatic Amination. *ASC,* **2007**, *349*, 2089–2091. https://doi.org/10.1002/adsc.200700220.
(34) Ansari, T. N.; Taussat, A.; Clark, A. H.; Nachtegaal, M.; Plummer, S.; Gallou, F.; Handa, S. Insights on Bimetallic Micellar Nanocatalysis for Buchwald–Hartwig Aminations. *ACS Catal.* **2019**, *9*, 10389–10397. https://doi.org/10.1021/acscatal.9b02622.
(35) Isley, N. A.; Dobarco, S.; Lipshutz, B. H. Installation of Protected Ammonia Equivalents onto Aromatic & Heteroaromatic Rings in Water Enabled by Micellar Catalysis. *Green Chem.* **2014**, *16*, 1480–1488. https://doi.org/10.1039/C3GC42188K.
(36) Suzuki, K.; Hori, Y.; Kobayashi, T. A New Hybrid Phosphine Ligand for Palladium-Catalyzed Amination of Aryl Halides. *ASC* **2008**, *350*, 652–656. https://doi.org/10.1002/adsc.200700543.
(37) Lipshutz, B. H.; Chung, D. W.; Rich, B. Sonogashira Couplings of Aryl Bromides: Room Temperature, Water Only, No Copper. *Org. Lett.* **2008**, *10*, 3793–3796. https://doi.org/10.1021/ol801471f.
(38) Balta, D. K.; Arsu, N.; Yagci, Y.; Jockusch, S.; Turro, N. J. Thioxanthone−Anthracene: A New Photoinitiator for Free Radical Polymerization in the Presence of Oxygen. *Macromolecules* **2007**, *40*, 4138–4141. https://doi.org/10.1021/ma0628735.
(39) Suzuki, K.; Fontaine, A.; Hori, Y.; Kobayashi, T. Versatile Suzuki-Miyaura Coupling Reaction Using Diphenylvinylphosphine Ligands. *Synlett* **2007**, *20*, 3206–3208. https://doi.org/10.1055/s-2007-992371.
(40) Suzuki, K.; Sawaki, T.; Hori, Y.; Kobayashi, T. Practical and Convenient Suzuki-Miyaura Coupling Reaction and α-Arylation Using Diphenylcyclopropylphosphine Ligands. *Synlett* **2008**, *12*, 1809–1812. https://doi.org/10.1055/s-2008-1078525.
(41) Touge, T.; Arai, T. Asymmetric Hydrogenation of Unprotected Indoles Catalyzed by H6-Arene/N-Me-Sulfonyldiamine–Ru(II) Complexes. *J. Am. Chem. Soc.* **2016**, *138*, 11299–11305. https://doi.org/10.1021/jacs.6b06295.
(42) Yokoyama, N.; Nakayama, Y.; Nara, H.; Sayo, N. Synthesis of Well-Defined Diphenylvinyl(Cyclopropyl)Phosphine-Palladium Complexes for the Suzuki–Miyaura Reaction and Buchwald–Hartwig Amination. *ASC* **2013**, *355*, 2083–2088. https://doi.org/10.1002/adsc.201300332.
(43) Nazir, R.; Balčiūnas, E.; Buczyńska, D.; Bourquard, F.; Kowalska, D.; Gray, D.; Maćkowski, S.; Farsari, M.; Gryko, D. T. Donor–Acceptor Type Thioxanthones: Synthesis, Optical Properties, and Two-Photon Induced Polymerization. *Macromolecules* **2015**, *48*, 2466–2472. https://doi.org/10.1021/acs.macromol.5b00336.
(44) Ackermann, L.; Althammer, A.; Fenner, S. Palladium-Catalyzed Direct Arylations of Heteroarenes with Tosylates and Mesylates. *Angew. Chem. Int. Ed.* **2009**, *48*, 201–204. https://doi.org/10.1002/anie.200804517.

(45) Alberico, D.; Scott, M. E.; Lautens, M. Aryl−Aryl Bond Formation by Transition-Metal-Catalyzed Direct Arylation. *Chem. Rev.* **2007**, *107*, 174–238. https://doi.org/10.1021/cr0509760.
(46) Liégault, B.; Lapointe, D.; Caron, L.; Vlassova, A.; Fagnou, K. Establishment of Broadly Applicable Reaction Conditions for the Palladium-Catalyzed Direct Arylation of Heteroatom-Containing Aromatic Compounds. *J. Org. Chem.* **2009**, *74*, 1826–1834. https://doi.org/10.1021/jo8026565.

CHAPTER 6: Conclusion and Future Work:

6.1 Thesis conclusions

The objective of this thesis was to develop catalytic systems for selective direct alkenylation reactions relevant to pharmaceutical synthesis, and ideally suitable for scale-up. A common feature of these projects is modification of the traditional direct alkenylation mechanism. In Chapter 2, I developed a catalytic method to engage a novel substrate class – alkenyl pivalates – in direct alkenylation that allowed direct access to a key reaction intermediate. The C–O oxidative addition step eliminates the need for a salt metathesis step (Figure 6.1). HTE aided in discovering a palladium catalyst capable of tandem C–O/C–H activation under homogeneous conditions without the need for directing groups, co-catalysts, additives, oxidants or any other reagents.

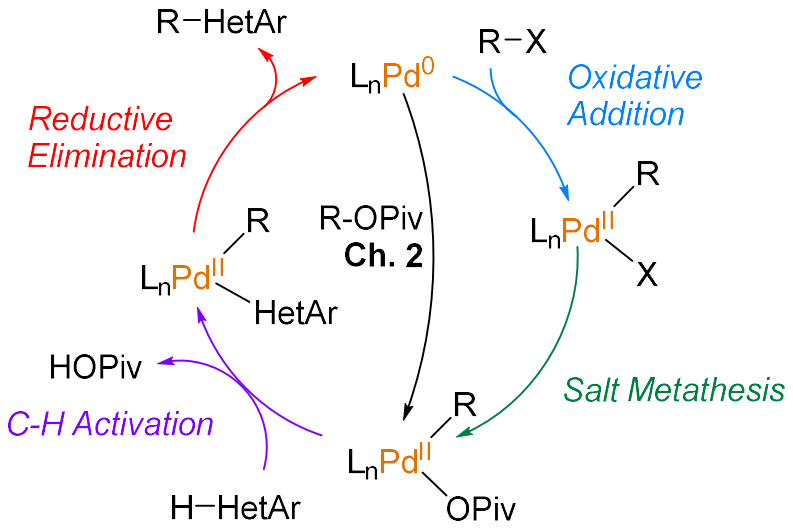

Figure 6.1. Generally accepted catalytic mechanism for Pd-catalyzed direct arylation and alkenylation reactions and mechanistic approach from Chapter 2.

The number of heterocycle classes that were suitable for the direct alkenylation reaction from Chapter 2 was limited, which we attributed to limitations in the CMD mechanism for the PCy_3-

ligated catalyst. Chapter 3 describes a different mechanistic approach that takes advantage of a dual palladium reaction mechanism and the reactivity of a palladacycle precatalyst (Figure 6.2). Extensive high-throughput experimentation for reaction optimization focused not only on the catalyst, base, and solvent, but also on the substrate class as a main factor. This work shows how a "one size fits all" approach would lead to overoptimized systems for specific substrates, and would not allow maximum exploration of the chemical space accessible in the reaction. Instead, simple modification of solvent/base combinations based on heterocycle class enabled a broader scope of reactivity. The broadly applicable reaction procedure allowed an extensive parallel-in-parallel screening, where multiple substrate combinations were evaluated under arrays of reaction conditions, mapping the reactivity for 192 individual products. Finally, the reaction was applied to the 30 g synthesis of a key intermediate for the synthesis of **GSK3368715**, a type I PRMT inhibitor under investigation for treating patients with advanced solid tumors.

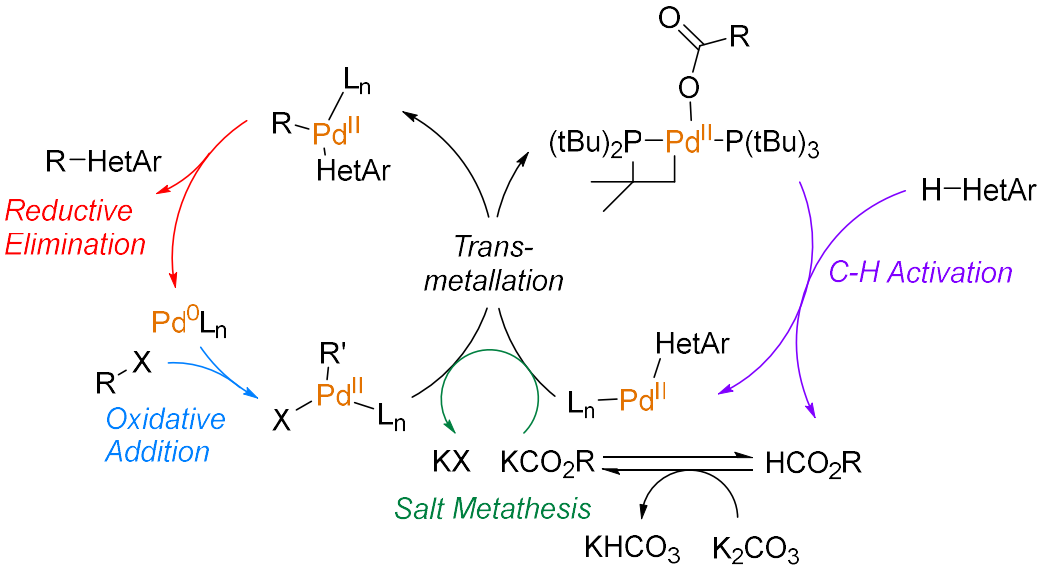

Figure 6.2. Dual metal catalyzed direct alkenylation mechanism from Chapters 3 and 4.

The reactivity and versatility of palladacycles as precatalysts was further studied in Chapters 4 and 5. In Chapter 4, I synthesized and characterized a chloride bridged palladacycle dimer that allows *in situ* modifications of the stabilizing ligand and carboxylate ligand for assessing selective C– H functionalization for thiazole substrates. The synthesis and reactivity of BRIDP-derived palladacycles was compared in Chapter 5. These compounds form readily in mixtures of BRIDP ligand and $Pd(OAc)_2$; however, their reactivity as single component precatalysts showed no significant differences compared to *in situ* systems for 5 different cross-coupling reactions. However, these studies brought to light the potential relevance of palladacycle intermediates with these ligands, showing the need to understand what the active catalytic species is when designing the catalysts and reaction conditions.

Overall, I demonstrated how HTE can be efficiently applied in research laboratories in academia, and in successful collaborations with industrial partners. The development of procedures that allow for rapid reactivity screening will help future researchers to discover new direct alkenylation and other reactions. At the same time, this work highlights the importance of including substrates as a reaction variable, changing the traditional approach to reaction scope conditions from a single combination of solvent, base, additive to a small set of four experiments to quickly assess reactivity.

6.2 Future work

6.2.1 Reversible oxidative addition of enol pivalates

Oxidative addition of organic electrophiles to Pd(0) is an important step in many palladium catalyzed cross-coupling reactions.[8,9] One of the main challenges associated with this step of the catalytic cycle is the slow activation of less reactive substrates, especially those that are not halogen-based. During the investigation of the oxidative addition of enol pivalates to $Pd(PCy_3)_2$, I discovered that the C–O activation is a reversible step. The conversion of the oxidative addition complex back into the Pd(0) species is an added kinetic challenge to achieving this transformation.

Due to the importance of cross-coupling reactions for the synthesis of pharmaceutical compounds, understanding this oxidative addition step would allow for better catalyst design and therefore optimization of synthetic procedures. The homogeneous conditions of the reaction system allowed for *in situ* study using NMR spectroscopy; however, the low solubility of the oxidative addition product and palladium (0) species required co-solvent systems with high boiling points. Initial studies using d^8-toluene as a co-solvent helped solubilize the organometallic species. However, the use of this co-solvent slowed the oxidative addition considerably, such that reaction took 14 h instead of 40 minutes to reach completion (Figure 6.3).

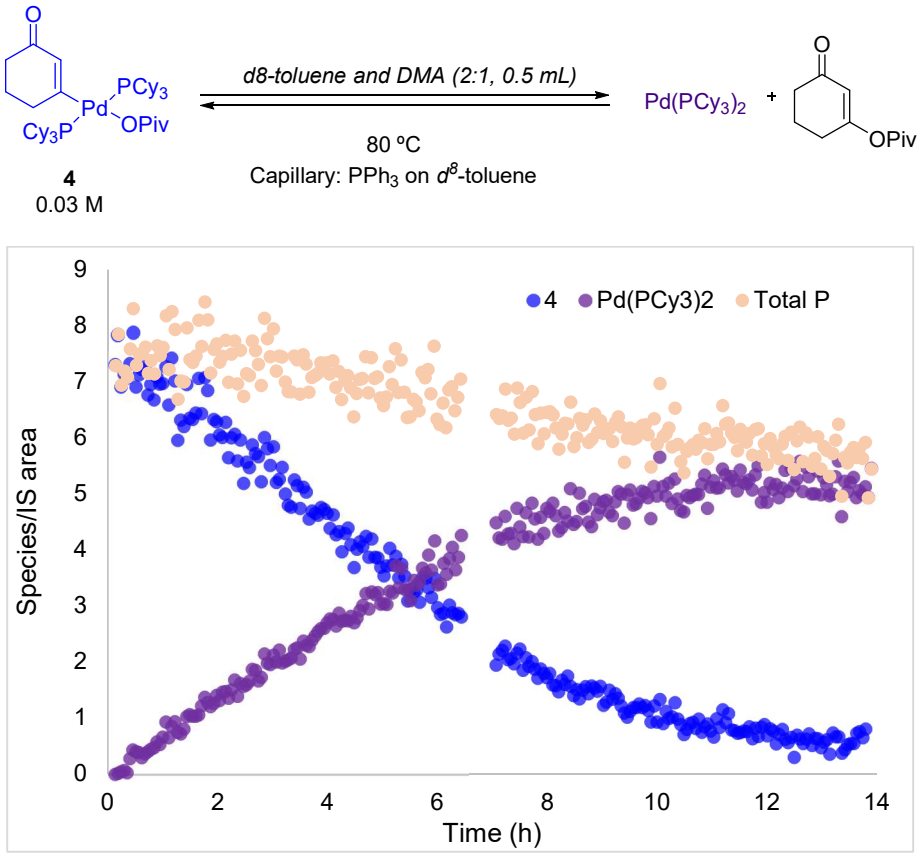

Figure 6.3. Oxidative addition monitoring by ^{31}P $\{^{1}H\}$ NMR spectroscopy using a DMA/toluene solvent mixture.

The long reaction times and the need for deuterated solvents impeded further monitoring of the reaction. The study of this oxidative addition step requires alternative techniques. One option would be to use pressurize sample infusion (PSI), a simple technique that introduces a solution to an electrospray ionization mass spectrometry (EI-MS) source. This would allow for acquisition of real-time data while maintaining an air and moisture free atmosphere for the reaction. Another possibility is to use solution-phase IR spectroscopy, taking advantage of the change to carbonyl group substitution to potentially give diagnostic signals in the carbonyl region of the spectrum.

Another potential approach would be to monitor the oxidative addition with other palladium(0) catalysts with different ligands, in diverse solvent systems and with diverse C–O

bonds. Establishing the factors that influence the rate of oxidative addition would help us better understand how to design specific ligands for specific substrates and reactions.

6.2.2 Regioselective Direct Functionalization

Although direct alkenylation is a powerful transformation, reactions that allow the synthesis of biaryl products in one single step are of more widespread importance in pharmaceutical industry. The catalytic systems described in this thesis should be interrogated under direct arylation reactions and explore if the selectivity of the functionalization is maintained. Vinyl and phenyl substrates share a lot of similarities in terms of reactivity; however, a computational study from 2006 showed that the oxidative addition of phenyl substrates is higher in energy than corresponding vinyl substrates.[8]

Now that more selective catalytic systems have been developed, it is important to assess them for late-stage functionalization of more complex organic molecules. Multiple pharmaceutical and agrochemical compounds are constituted from multiple (hetero)aromatic rings. Selectively activating not a specific C–H bond of a heterocycle, but a specific position within a larger molecule with multiple/fused heteroaromatic rings is an added challenge to direct functionalization reactions.

In this respect, initial experiments have been conducted with the aim of selectively alkenylating a thiazole in 2-(thiophen-2-yl)-thiazole. The alkenylation occurred on the C4 position of the thiazole as judged by NMR spectroscopy, which is contrary to the selectivity patterns discussed in Chapter 4. Functionalization of this specific C–H bond has been proven to be

difficult.[10] It is necessary to further study the effect of the substituents to develop specific catalytic conditions that selectively functionalize the desired C–H bond.

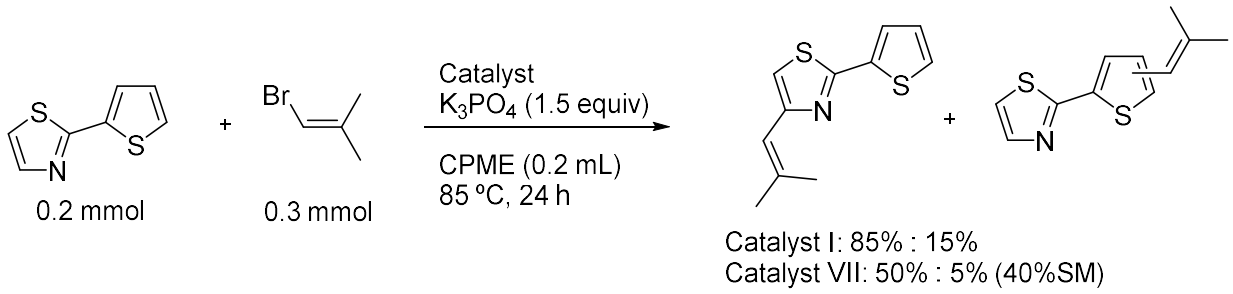

Figure 6.4. Direct alkenylation products of 2-(thiophen-2-yl)thiazole and 1-bromo-2-methylprop-1-ene.

With this goal in mind, obtaining a correlation between diverse factors on the molecule such as strength of C–H bond, electronic and steric contribution of substituents, different substitution patterns, and coupling product(s), a quantitative model could be build to predict the selectivity of the reaction. Previous work by our group and others has been successful for reaction prediction modeling of palladium-catalyzed reactions.[11] These methods involve high-throughput computational calculations of molecular descriptors. The possible transition states could also be modeled allowing to a further study into the CMD and eCMD mechanisms.

6.2.3 Development of palladium precatalysts

There are several reports in the literature where the combination of two phosphines, one that facilitates the oxidative addition step of cross coupling reaction and a second one that promotes the reductive eliminations increase the reactivity of cross-coupling reactions.[12–14] The palladacycle dimer described in Chapter 4 allows for a rapid screening of ligands. The development of other

palladium systems that can bond with different phosphines would be the next step on the development of more efficient precatalysts.

Preliminary results show that other phosphine ligands are able to form palladacyclic structures, such as the imidazolyl phosphine in Figure 6.5. The screening of ligands to make novel palladacycle precatalysts should be done hand-in-hand with the computational evaluation of these ligands and mechanistic exploration of how ligand structures lead to palladacycle formation.

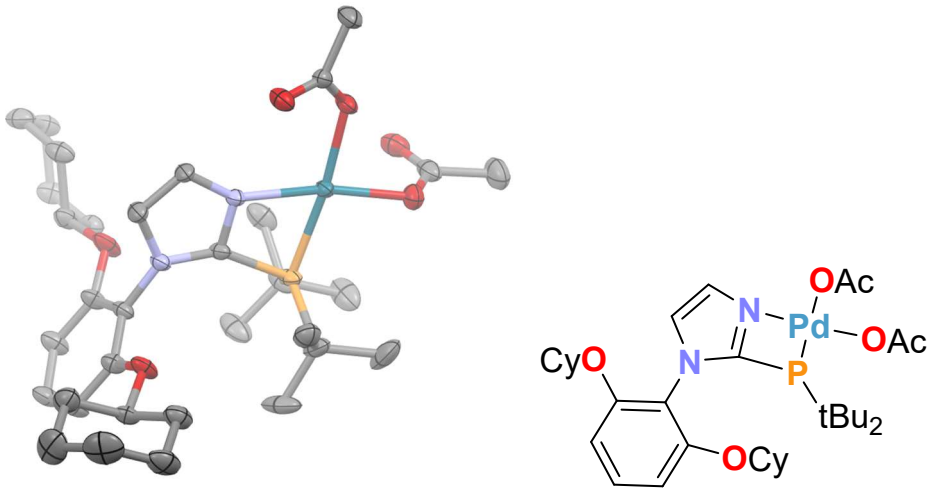

Figure 6.5. Solid-state molecular structure of 1-[2,6-Bis(cyclohexyloxy)phenyl]-2-(di-tertbutylphosphaneyl)-1H-imidazole diacetate palladacycle. Ellipsoids plotted at 50% probability. Hydrogens and THF solvate not shown for clarity.

6.2.4 High-Throughput Experimentation in Academic Research

As HTE tools keep getting more user friendly, the use of this experimental approach in academic research will become more and more prevalent. The use of HTE for reaction discovery and multiple substrate evaluation faces a major challenge in the analysis of the data. More sophisticated statistical analysis of the results and data interrogation techniques are needed in order to use this approach to its full potential.

One of the main challenges when exploring the formation of one or multiple possible products is quantification of the product formation. Common approaches include LCAP (Liquid chromatograpy area percent) and product *m/z* detection by LCMS. This can lead to the misidentification and misquantification of products. ^{1}H NMR spectroscopy also has challenges when trying to identify products. Isomers can often overlap with other functional groups or reactants present in the sample, and the acquisition and analysis of large numbers of NMR samples is expensive and time consuming. As a result, ^{1}H NMR spectroscopy is often used to confirm product formation or as an external yield calibration technique but not as the main data analysis technique.

The development of a platform that allows for a simultaneous analysis and data integration of large numbers of samples by both LCMS and ^{1}H NMR spectroscopy would allow us to fully characterize the factors involved in the reaction, in terms of selectivity and reactivity. However, due to the high volume of results that it would provide, the development of a machine learning algorithm that could collate and automatically interpret the results would be required.

6.3 References

(1) Henderson, W. H.; Alvarez, J. M.; Eichman, C. C.; Stambuli, J. P. Characterization, Reactivity, and Potential Catalytic Intermediacy of a Cyclometalated Tri -*Tert* -Butylphosphine Palladium Acetate Complex. *Organometallics* **2011**, *30*, 5038–5044. https://doi.org/10.1021/om2006936.

(2) Tan, Y.; Barrios-Landeros, F.; Hartwig, J. F. Mechanistic Studies on Direct Arylation of Pyridine N-Oxide: Evidence for Cooperative Catalysis between Two Distinct Palladium Centers. *J. Am. Chem. Soc.* **2012**, *134* (8), 3683–3686. https://doi.org/10.1021/ja2122156.

(3) Liégault, B.; Lapointe, D.; Caron, L.; Vlassova, A.; Fagnou, K. Establishment of Broadly Applicable Reaction Conditions for the Palladium-Catalyzed Direct Arylation of Heteroatom-Containing Aromatic Compounds. *J. Org. Chem.* **2009**, *74*, 1826–1834. https://doi.org/10.1021/jo8026565.

(4) Buitrago Santanilla, A.; Regalado, E. L.; Pereira, T.; Shevlin, M.; Bateman, K.; Campeau, L.-C.; Schneeweis, J.; Berritt, S.; Shi, Z.-C.; Nantermet, P.; Liu, Y.; Helmy, R.; Welch, C. J.; Vachal, P.; Davies, I. W.; Cernak, T.; Dreher, S. D. Nanomole-Scale High-Throughput Chemistry for the Synthesis of Complex Molecules. *Science* **2015**, *347*, 49–53. https://doi.org/10.1126/science.1259203.

(5) Wagen, C. C.; McMinn, S. E.; Kwan, E. E.; Jacobsen, E. N. Screening for Generality in Asymmetric Catalysis. *Nature* **2022**, *610*, 680–686. https://doi.org/10.1038/s41586-022-05263-2.

(6) Ghosh, I.; Shlapakov, N.; Karl, T. A.; Düker, J.; Nikitin, M.; Burykina, J. V.; Ananikov, V. P.; König, B. General Cross-Coupling Reactions with Adaptive Dynamic Homogeneous Catalysis. *Nature* **2023**, *619*, 87–93. https://doi.org/10.1038/s41586-023-06087-4.

(7) Dombrowski, A. W.; Gesmundo, N. J.; Aguirre, A. L.; Sarris, K. A.; Young, J. M.; Bogdan, A. R.; Martin, M. C.; Gedeon, S.; Wang, Y. Expanding the Medicinal Chemist Toolbox: Comparing Seven C(Sp2)–C(Sp3) Cross-Coupling Methods by Library Synthesis. *ACS Med. Chem. Lett.* **2020**, *11*, 597–604. https://doi.org/10.1021/acsmedchemlett.0c00093.

(8) Ariafard, A.; Lin, Z. Understanding the Relative Easiness of Oxidative Addition of Aryl and Alkyl Halides to Palladium(0). *Organometallics* **2006**, *25*, 4030–4033. https://doi.org/10.1021/om060236x.

(9) Miyaura, Norio.; Suzuki, Akira. Palladium-Catalyzed Cross-Coupling Reactions of Organoboron Compounds. *Chem. Rev.* **1995**, *95*, 2457–2483. https://doi.org/10.1021/cr00039a007.

(10) Tani, S.; Uehara, T. N.; Yamaguchi, J.; Itami, K. Programmed Synthesis of Arylthiazoles through Sequential C–H Couplings. *Chem. Sci.* **2014**, *5*, 123–135. https://doi.org/10.1039/C3SC52199K.

(11) Lu, J.; Leitch, D. C. Organopalladium Catalysis as a Proving Ground for Data-Rich Approaches to Reaction Development and Quantitative Predictions. *ACS Catal.* **2023**, *13*, 15691–15707. https://doi.org/10.1021/acscatal.3c03864.

(12) Beckers, I.; Bugaev, A.; Vos, D. D. Dual Ligand Approach Increases Functional Group Tolerance in the Pd-Catalysed C–H Arylation of N -Heterocyclic Pharmaceuticals. *Chemical Science* **2023**, *14*, 1176–1183. https://doi.org/10.1039/D2SC04911B.

(13) Wakioka, M.; Takahashi, R.; Ichihara, N.; Ozawa, F. Mixed-Ligand Approach to Palladium-Catalyzed Direct Arylation Polymerization: Highly Selective Synthesis of π-Conjugated

Polymers with Diketopyrrolopyrrole Units. *Macromolecules* **2017**, *50*, 927–934. https://doi.org/10.1021/acs.macromol.6b02679.
(14) Sato, R.; Kanbara, T.; Kuwabara, J. Air-Stable Pd(0) Catalyst Bearing Dual Phosphine Ligands: A Detailed Evaluation of Air Stability and Catalytic Property in Cross-Coupling Reactions. *Dalton Trans.* **2020**, *49*, 12814–12819. https://doi.org/10.1039/D0DT02744H.

Appendices

Appendix A: Supporting information for Chapter 2

I: General Considerations

Materials. All solvents and common organic reagents were purchased from commercial suppliers and used without further purification. $Pd(OAc)_2$, $[Pd(allyl)Cl]_2$, and $Pd(PCy_3)_2$ were purchased from Strem Chemicals and used as received. $Pd_2dba_3 \cdot CHCl_3$ was prepared according to the method of Zalesskiy and Ananikov.[1] ^{DMP}DAB–Pd–MAH was prepared using a reported procedure.[2] All phosphine ligands were purchased from Strem Chemicals and used as received. Anhydrous solvents (SureSeal) were purchased from MilliporeSigma and used as received.

Techniques. All air-free manipulations were performed under a dry nitrogen atmosphere using a MBraun glovebox. High-throughput experimentation was performed using 1 mL capacity glass shell vials in sealable aluminum reaction blocks purchased from Analytical Sales. Heating/stirring was achieved using rare-earth magnetic tumble stirrers acquired from V&P Scientific.

Centrifugal evaporation was performed using a Genevac EZ-2 (HCl compatible). The chromatography purification was performed on Biotage® Selekt SEL-2SW using Sfär Silica (60 μm) columns.

Analysis and Spectroscopy.

All NMR spectra were acquired on either a Bruker AVANCE 300 MHz spectrometer or a Bruker AVANCE Neo 500 MHz spectrometer. All ^{1}H and ^{13}C-NMR chemical shifts are calibrated to residual protio-solvents and all ^{31}P and ^{19}F NMR chemical shifts are calibrated to external standards. All NMR spectroscopic data is processed using MestreNova software.

UPLC analysis was performed using a Shimadzu Nexera X2 with a diode-array UV/Vis detector. A Raptor ARC-18 column (100 × 2.1 mm, particle size 1.8 μm) or a Waters CORTECS® UPLC® T3 column (2.1 × 30 mm, particle size 1.6 μm) were used. The eluent used is the mixture of two mobile phases. Water with 0.05% trifluoroacetic acid (TFA) was set to be the mobile phase A, and acetonitrile with 0.05% TFA was set to be the mobile phase B. All solvents used were HPLC grade.

High-resolution electrospray ionization mass spectrometric analysis was performed using a Thermo Scientific Ultimate 3000 ESI-Orbitrap Exactive Plus.

II: Preparation of Substrates

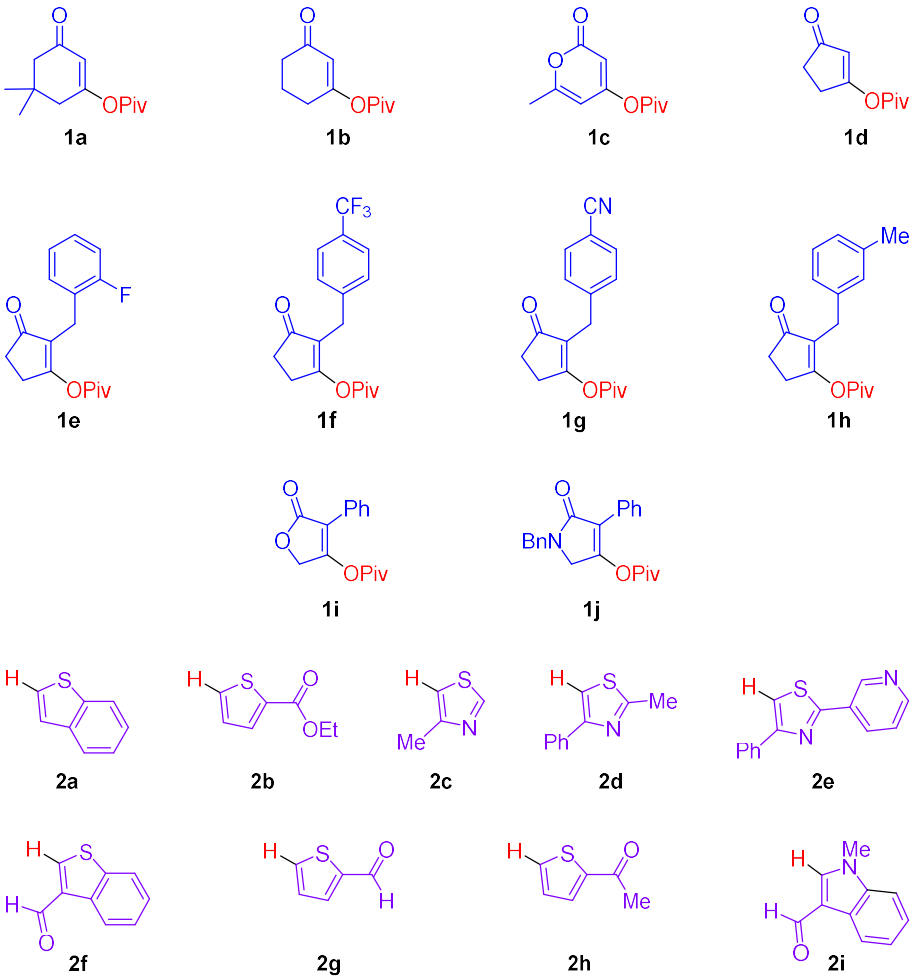

Fig. A1. Enol pivalate and heterocycle substrates

The following enol pivalate substrates were synthesized using literature procedures: 5,5-dimethyl-3-oxocyclohex-1-en-1-yl pivalate (**1a**),[3] 3-oxocyclohex-1-en-1-yl pivalate (**1b**),[3] 4-pivalyloxy-6-methyl-2-pyrone (**1c**),[4] 1-pivalyloxycyclopent-1-en-3-one (**1d**),[4] 4-pivalyloxy-3-phenylpyran-3-en-2-one (**1i**),[4] 4-pivalyloxy-1-benzyl-3-phenylpyrrolidin-3-en-2-one (**1j**).[4]

Heterocycles **2a**-**2i** were purchased from Oakwood Chemicals and MilliporeSigma and used as-received.

Enol pivalates **1e-1h** were prepared according to **general procedure 1**:

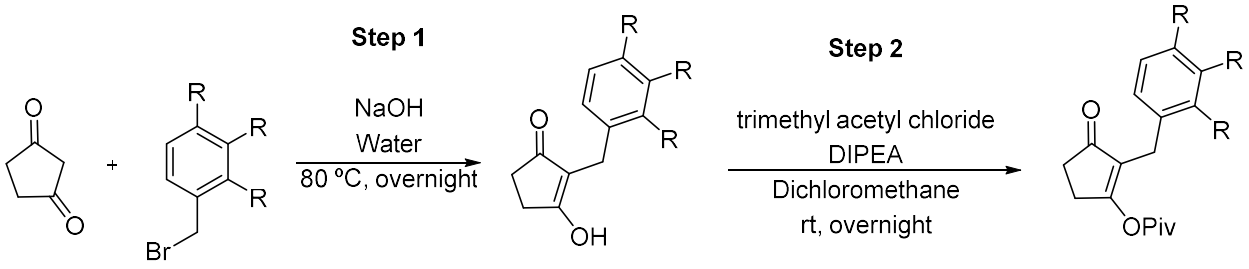

Fig. A1 General procedure 1

Step 1: Cyclopentane-1,3-dione (2.28 g, 20 mmol, 1 equiv) was dissolved in 1 M sodium hydroxide (20.0 mL, 20 mmol) in a 50 mL round-bottomed flask containing a stir bar. The corresponding benzyl bromide (21.0 mmol, 1.05 equiv) was added as a solid or liquid to the stirring solution. The flask was fitted with a condenser. The reaction mixture was heated to 80 °C and stirred overnight. The next morning, the mixture was diluted with 20 mL of water to ensure all the solids are freely suspended, and the flask was then cooled to room temperature. An amorphous white solid was observed at the bottom of the flask after cooling. The material was filtered using vacuum filtration. The solid was washed two times with TBME (20 mL) to obtain a free-flowing solid. The solid was dried *in vacuo*, giving the alkylated enol that was used without further purification.

Step 2: A 100 mL round-bottomed flask was charged with a stir bar and a slurry of the corresponding 2-alkyl-cyclopentane-1,3-dione (10 mmol, 1 equiv) in 10 mL of dichloromethane. *N*,*N*-diisopropylethylamine (3.5 mL, 20 mmol, 2 equiv) was added via a syringe with stirring. Trimethylacetyl chloride (1.5 mL, 12 mmol, 1.2 equiv) was then added with dropwise over 15 minutes. Once the addition was complete, the syringe was rinsed with DCM (0.5 mL) and the reaction mixture was stirred at room temperature overnight. The solution was washed with 1 M HCl (3 x 20 mL) and then with distilled water (3 x 10 mL). The organic phase was dried over magnesium sulfate and the volatiles were removed *in vacuo* yielding the final product. The enol pivalates were purified by automated column chromatography using a hexanes/ethyl acetate gradient eluent.

1e. 2-(2-fluorobenzyl)-3-oxocyclopent-1-en-1-yl pivalate:

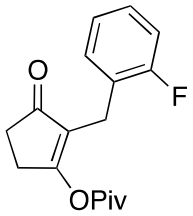

A light-yellow solid was collected (1.32 g, 46% yield over two steps).

Purified by column chromatography (Biotage® Sfär Column, 0-100% EtOAc/hexanes, eluted at 30% EtOAc).

^{1}H-NMR (500 MHz, $CDCl_3$, 292 K, ppm): δ 7.27 (m, 1H), 7.17 (m, 1H), 7.04 (m, 1H), 6.99 (m, Hz, 1H), 3.53 (s, 2H), f2.90 (m, 2H), 2.56 (m, 2H), 1.27 (s, 9H).

^{13}C-NMR (126 MHz, $CDCl_3$, 292 K, ppm): δ 205.3, 177.7, 174.3, 160.8 (d, J=245.6 Hz), 131.1 (d, J=4.1 Hz), 128.0 (d, J=8.2 Hz), 127.4, 125.03 (d, J=15.5Hz), 124.0 (d, J=3.5 Hz), 115.1 (d, J=22.0 Hz), 39.6, 34.4, 27.0, 26.8, 20.7 (d, J = 4 Hz).

^{19}F-NMR (471 MHz, $CDCl_3$, 292 K, ppm): δ -117.54.

HRMS: Calc'd for $C_{17}H_{19}FO_3$ $[M+H]^+$: 291.13910; found: 291.13903.

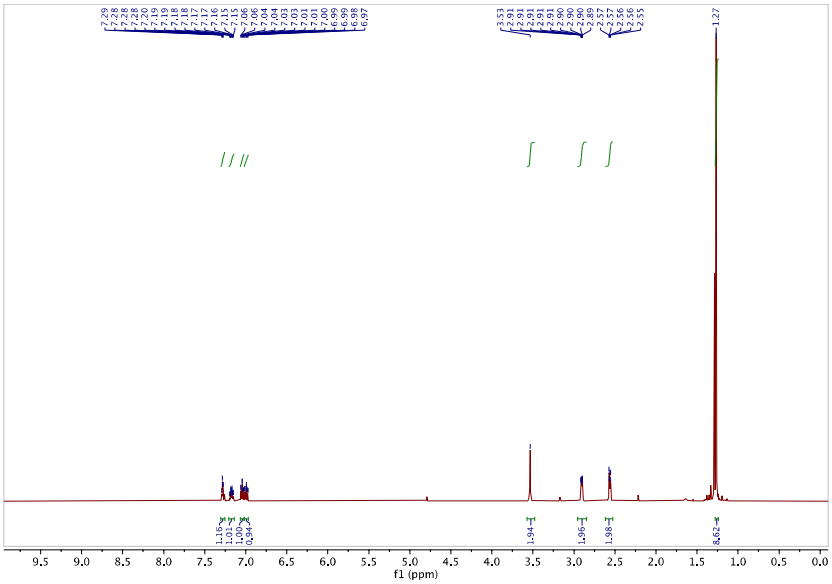

Fig. A3: ^{1}H NMR (500 MHz, Chloroform-*d*) spectrum of **1e**

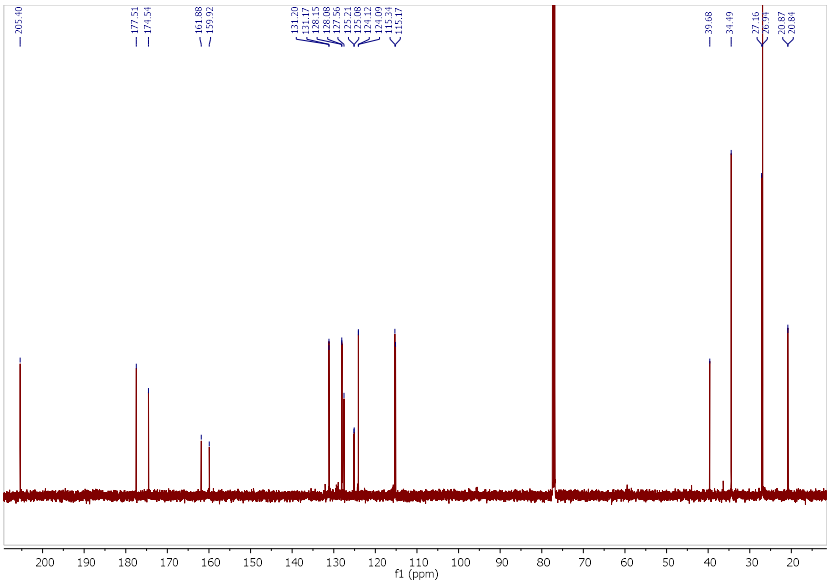

Fig. A4: $^{13}C\{^{1}H\}$ NMR (126 MHz, Chloroform-*d*) Spectrum of **1e**

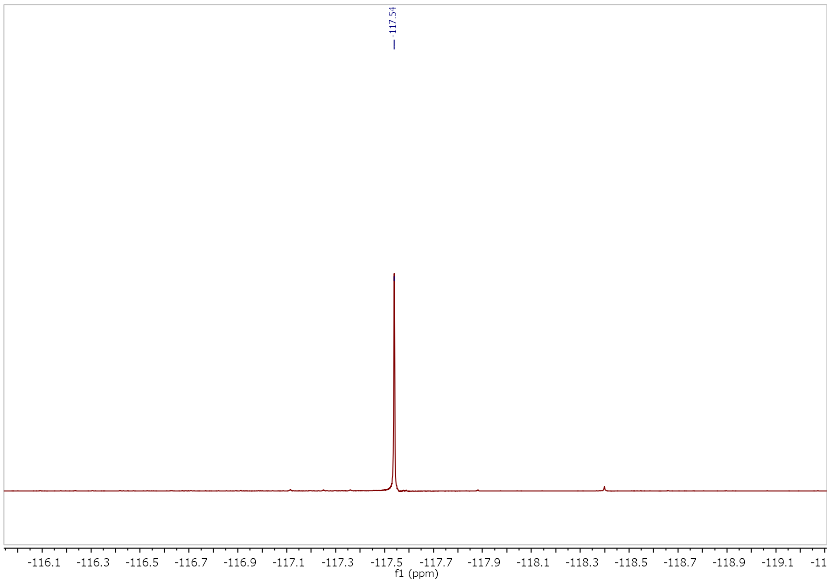

Fig. A5: ^{19}F NMR (283 MHz, Chloroform-*d*) spectrum of **1e**

1f. 3-oxo-2-(4-(trifluoromethyl)benzyl)cyclopent-1-en-1-yl pivalate:

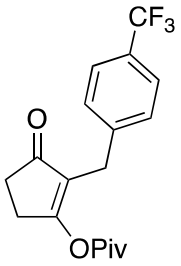

A light-yellow oil was collected (1.39 g, 41% yield over two steps).

Purified by column chromatography (Biotage® Sfär Column, 0-100% EtOAc/hexanes, eluted at 30% EtOAc).

^{1}H-NMR (500 MHz, $CDCl_3$, 292 K, ppm): δ 7.49 (d, J=8.0 Hz, 1H), 7.31 (s, 8.0 Hz, 2H), 3.52 (s, 2H), 2.9 (m, 2H), 2.55 (m, 2H), 1.24 (s, 9H).

^{13}C-NMR (126 MHz, $CDCl_3$, 292 K, ppm): δ 205.3, 177.7, 174.3, 142.5, 128.7 (q, 2JC-F = 32.8 Hz), 128.5, 125.9, 125.4 (q, 3JC-F = 3.7 Hz), 124.2 (q, 1JC-F = 272.2 Hz), 39.54, 34.38, 27.68, 27.10, 26.83.

^{19}F-NMR (471 MHz, $CDCl_3$, 292 K, ppm): δ -62.45.

HRMS: Calc'd for $C_{18}H_{19}F_3O_3$ $[M+H]^+$: 341.13590; found: 341.13587.

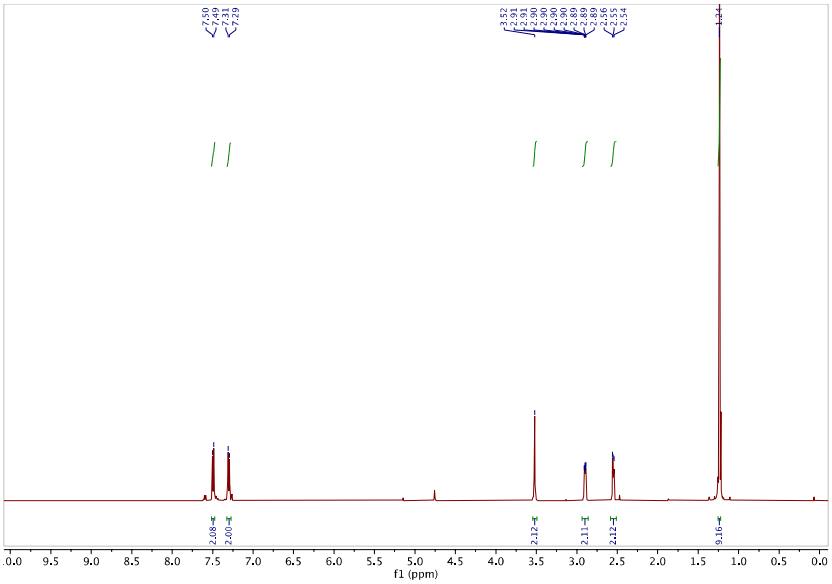

Fig. A6: ^{1}H NMR (500 MHz, Chloroform-*d*) spectrum for **1f**

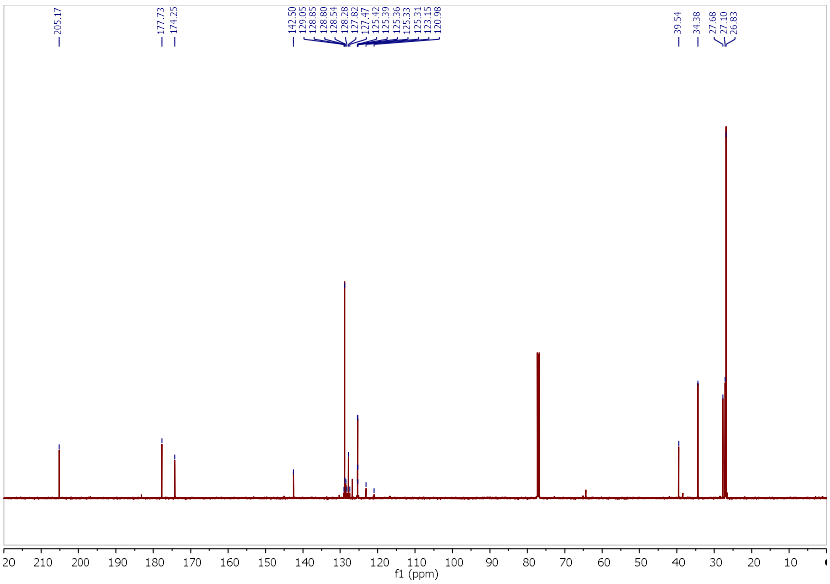

Fig. A7: $^{13}C\{^{1}H\}$ NMR (126 MHz, Chloroform-*d*) spectrum for **1f**

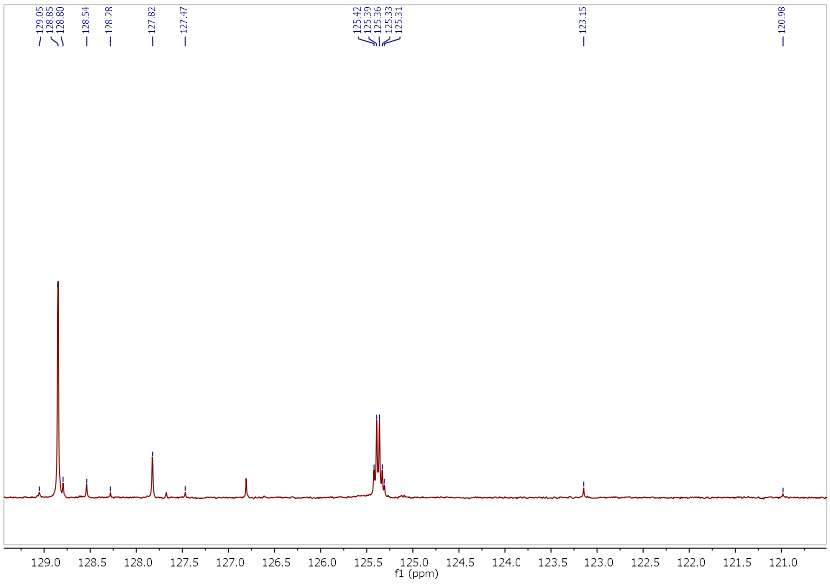

Fig. A8: Expanded (120-130 ppm) $^{13}C\{^{1}H\}$ NMR (126 MHz, Chloroform-*d*) spectrum of **1f**

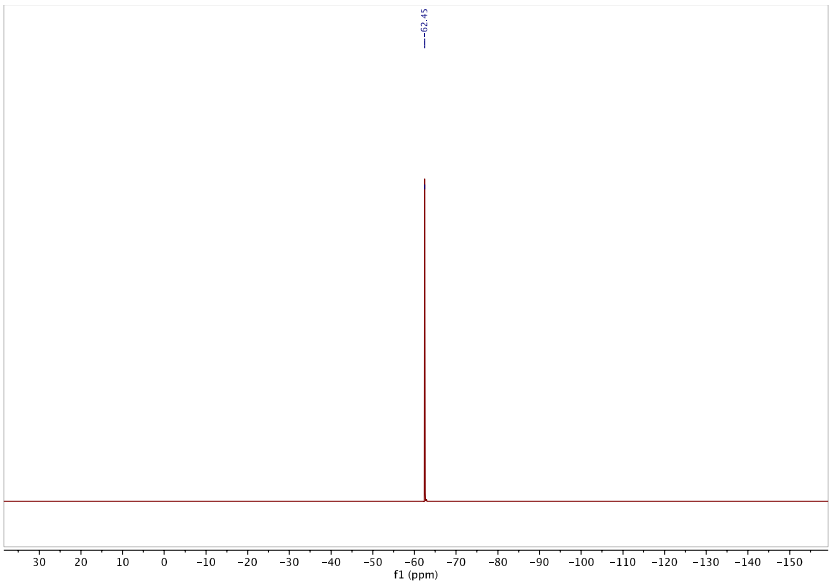

Fig. A9: ^{19}F NMR (283 MHz, Chloroform-*d*) spectrum for **1f**

1g. 2-(4-cyanobenzyl)-3-oxocyclopent-1-en-1-yl pivalate:

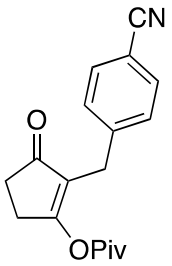

A beige powder was collected (1.72 g, 58% yield over two steps).

Purified by column chromatography (Biotage® Sfär Column, 0-100% EtOAc/hexanes, eluted at 30% EtOAc).

^{1}H-NMR (500 MHz, $CDCl_3$, 292 K, ppm): δ 7.54 (d, J = 8.3 Hz, 2H), 7.30 (d, J = 8.3 Hz, 2H), 3.52 (s, 2H), 2.91 (m, 2H), 2.56 (m, 2H), 1.26 (s, 9H).

^{13}C-NMR (126 MHz, $CDCl_3$, 292 K, ppm): δ 204.70, 177.88, 174.02, 144.02, 132.13, 129.29, 127.11, 118.75, 110.05, 39.44, 34.30, 27.85, 27.07, 26.77.

HRMS: Calc'd for $C_{18}H_{19}NO_3$ $[M+H]^+$: 298.14377; found: 298.14372

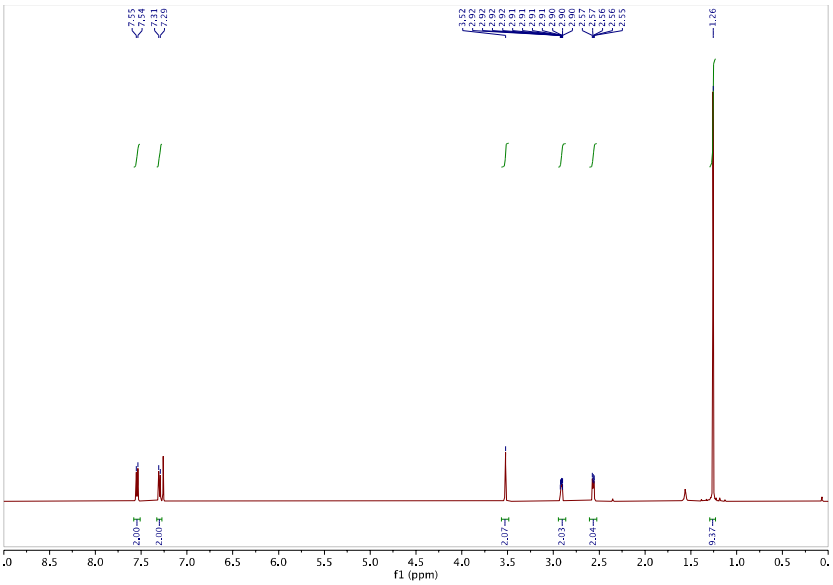

Fig. A10: ^{1}H NMR (500 MHz, Chloroform-*d*) spectrum for **1g**

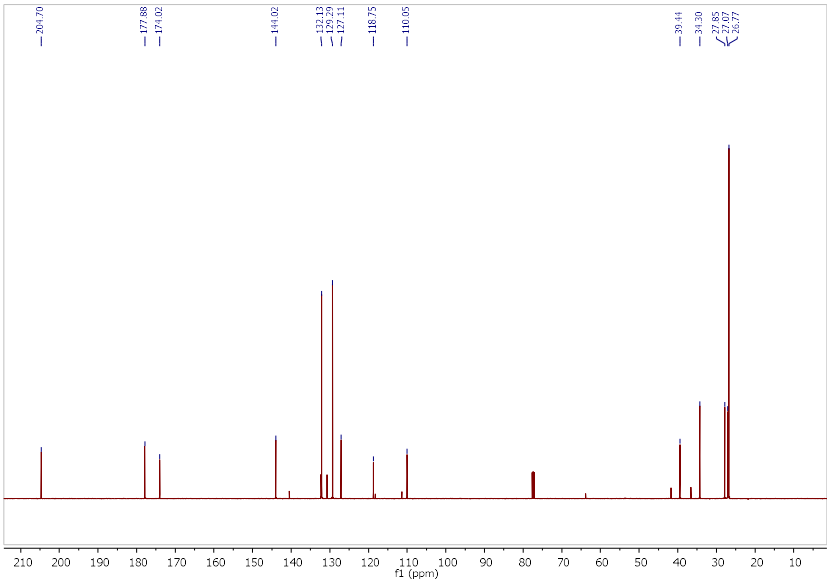

Fig. A11: ^{13}C{^{1}H} NMR (126 MHz, Chloroform-*d*) spectrum for **1g**

1h. 2-(3-methylbenzyl)-3-oxocyclopent-1-en-1-yl pivalate:

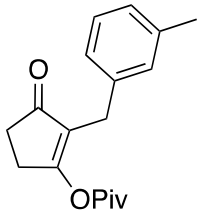

A light brown powder was collected (1.00 g, 35% yield over two steps).

Purified by column chromatography (Biotage® Sfär Column, 0-100% EtOAc/hexanes, eluted at 30% EtOAc).

^{1}H-NMR (500 MHz, $CDCl_3$, 292 K, ppm): δ 7.13 (t, J = 7.5 Hz, 1H), 7.02 (s, 1H), 6.99 (t, J = 6.5 Hz, 2H), 3.44 (s, 2H), 2.88 (m, 2H), 2.54 (m, 2H), 2.29 (s, 3H), 1.26 (S, 9H).

^{13}C-NMR (126 MHz, $CDCl_3$, 292 K, ppm): δ 205.4, 177.2, 174.4, 138.3, 138.0, 128.9, 128.3, 127.0, 125.6, 39.5, 34.4, 27.7, 27.0, 26.9, 21.4.

HRMS: Calc'd for $C_{18}H_{22}O_3$ $[M+H]^+$: 287.16417; found: 287.15416.

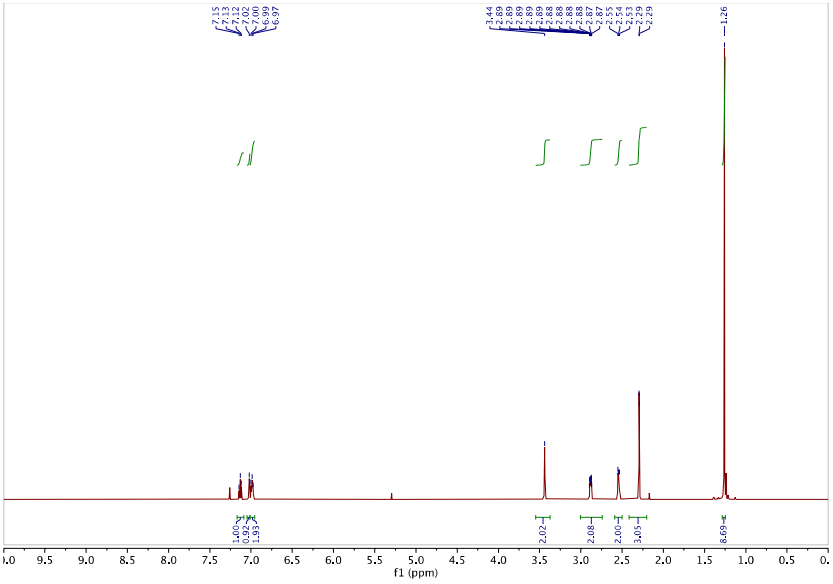

Fig. A12: ^{1}H NMR (500 MHz, Chloroform-*d*) spectrum for **1h**

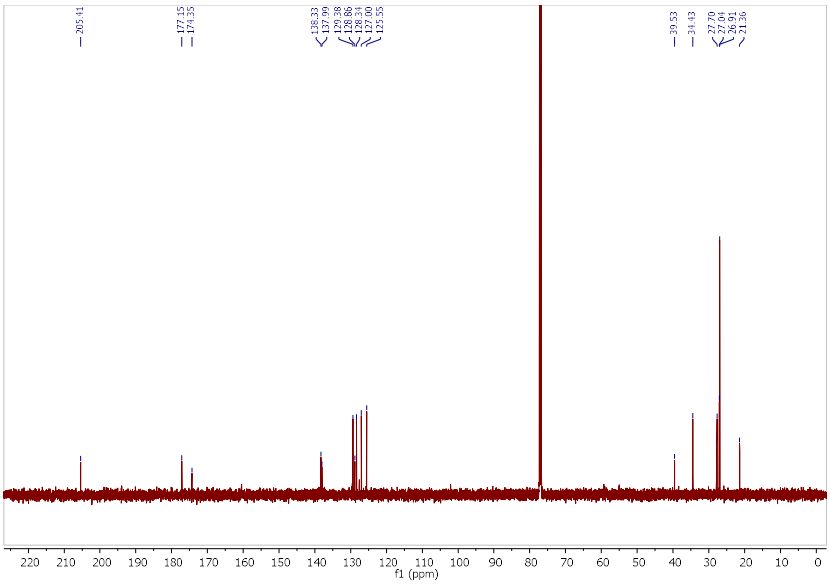

Fig. A13: $^{13}C\{^{1}H\}$ NMR (126 MHz, Chloroform-*d*) spectrum for **1h**

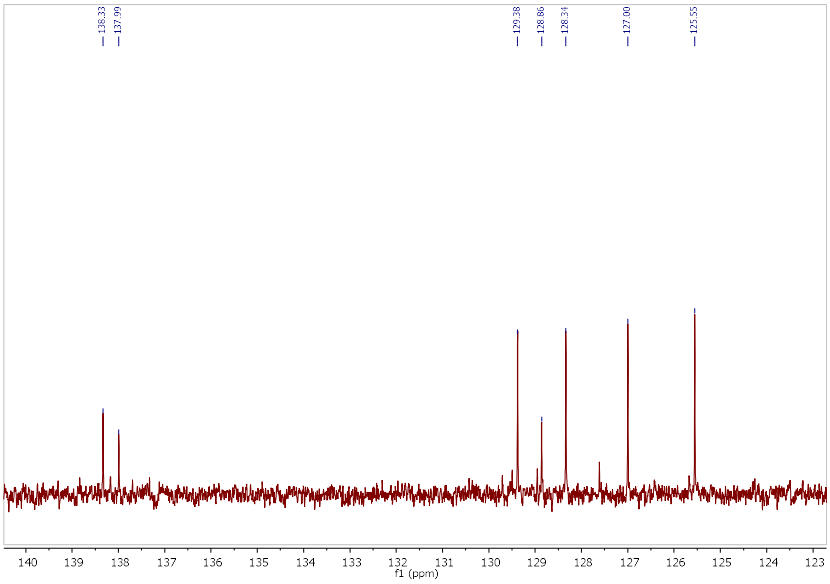

Fig. A14: Expanded (123-140 ppm) $^{13}C\{^{1}H\}$ NMR (126 MHz, Chloroform-*d*) spectrum of **1h**

III: High-Throughput Screening

Screen 1: (Figure 2.9): Palladium Sources and Phosphine Ligands

Preparation of palladium sources:

Four different palladium precatalysts were dissolved in appropriate solvents to generate the following solutions. All liquid handling was performed using a calibrated micropipette:

21.0 mg (0.0936 mmol) of palladium acetate was dissolved in 1348 μL of dichloromethane.

17.1 mg (0.0468 mmol) of allylpalladium(II) chloride dimer was dissolved in 2269 μL of acetone.

48.4 mg (0.0468 mmol) of recrystallized Pd_2dba_3•$CHCl_3$ was dissolved in 1968 μL of tetrahydrofuran.

43.9 mg of DAB-Pd-MAH (0.0936 mmol) was dissolved in 2235 μL of acetone.

These stock solutions were dispensed into 1 mL glass shell vials in a 96-well aluminum plate (24 wells for each palladium source), with each well receiving the following amounts:

40.0 μL of palladium acetate stock solution.

63.3 μL of allylpalladium chloride dimer stock solution.

56.3 μL of Pd_2dba_3•$CHCl_3$ stock solution.

63.3 μL of DAB-Pd-MAH stock solution.

The solvents were then removed by centrifugal evaporation.

Preparation of phosphine ligands:

The ratio between the Pd loading and phosphine ligands is 2:1. Inside the glovebox, 0.0624 mmol of each phosphine ligand (29.7 mg of XPhos, 17.5 mg of PCy_3, 16.4 mg of PPh_3, 22.4 mg of CataCXium A, 10.0 mg PMe(*t*-Bu)$_2$, 22.0 mg P(*o*-OMePh)$_3$) was dissolved in 600 μL of THF in 4-dram vials separately. 51.5 μL (0.0052 mmol) of each ligand stock solution was dispensed into each of four wells containing four different palladium sources. The vials were stirred at room temperature for 20 minutes and the solvents was then evaporated through using centrifugal evaporation.

Preparation and analysis of the reaction plate:

Inside the glovebox, a 20 mL vial was charged with 5,5-dimethyl-3-oxocyclohex-1-en-1-yl pivalate **1a** (269.2 mg, 1.200 mmol, 1 equiv), benzothiophene **2a** (241.6 mg, 1.799 mmol, 1.5 equiv), *N,N*-diisopropylethylamine (420 uL, 2.403 mmol, 2.0 equiv), *N,N*-dimethylacetamide (5.58 mL) and a stir bar. After being mixed well, 200 μL of this reaction stock solution was added into each well previously loaded with a stir bar. The 24-well plate was sealed, and the plate was removed from the glovebox. The plate was placed in a heat block on a tumble stirrer set to 300 rpm, and the reaction mixtures stirred for 20 hours at 100 °C. Upon completion, the plate was cooled to room temperature before being opened. Acetonitrile (500 μL) was added to each well, followed by stirring for 10 minutes at room temperature to ensure complete dissolution. Aliquots of 40 μL of each diluted reaction mixture were then transferred to 24 different HPLC vials followed by the addition of 1 mL of acetonitrile. These 24 samples were analyzed by HPLC, with solution yields of **3a** determined by UV/Vis absorbance versus a calibration curve for **3a**.

Table A1. Catalyst screening results, yields determined by ^{1}H NMR spectroscopy versus internal standard (1,3,5-trimethoxybenzene).

	$Pd(OAc)_2$	$[Pd(allyl)Cl]_2$	$Pd_2(dba)_3 \bullet CHCl_3$	DAB-Pd-MAH
XantPhos	0%	0%	0%	0%
PCy_3	22%	0%	0%	34%
PPh_3	0%	0%	0%	0%
CataCXium A	0%	0%	0%	0%
PMe(*t*-Bu)$_2$	0%	0%	0%	0%
P(*o*-OMePh)$_3$	0%	0%	0%	0%

Screen 2: (Figure 2.10): Multivariate Evaluation of Ligand, Solvent and Base

Preparation of Pd/ligand combinations:

Two stock solutions of DAB-Pd-MAH were prepared by dissolving 295.5 mg of DAB-Pd-MAH in 15.3 mL of acetone, each in a separate 20 mL vial. 242.8 µL of this stock solution was loaded into 1 mL shell vials in aluminum blocks (108 total wells). The solvent was removed by centrifugal evaporation.

Inside the glovebox, 0.154 mmol of each ligand: (1,1'-bis(diphenylphosphino)ferrocene (dppf) 85.4 mg; 1,1′-bis(diisopropylphosphino)ferrocene (dippf) 64.4 mg; 1,3-bis(diphenylphosphino)-propane (dppp) 63.5 mg; triphenylphosphine (PPh_3) 40.4 mg; DavePhos 60.6 mg; CataCXium A 55.2 mg; PMe(*t*-Bu)$_2$ 24.7 mg; SPhos 63.2 mg; XantPhos 89.1 mg; bis[(2-diphenylphosphino)phenyl] ether (DPEPhos) 82.9 mg; PCy_3 154 µL (1 M solution in toluene), P(*t*-Bu)$_3$, 154 µL (1 M solution in toluene), RuPhos 71.9 mg; JohnPhos 46.0 mg; XPhos 73.4 mg; BippyPhos 78.0 mg; P(*o*-MeOPh)$_3$ 54.3 mg; and P(*o*-MePh)$_3$ 46.9 mg) was dissolved in 1.470 mL of THF in separate 4-dram vials. 183 µL (0.0192 mmol) of each ligand stock solution was dispensed into six wells corresponding to the experimental design using one 96-well plate and one 24-well plate. The vials were stirred at room temperature for 20 minutes, before removing the volatiles by centrifugal evaporation. A micro stir bar was added to each well.

Preparation and analysis of the reaction plate:

Inside the glovebox, two 20 mL vials were each charged with 5,5-dimethyl-3-oxocyclohex-1-en-1-yl pivalate **1a** (269.2 mg, 1.2 mmol), and benzothiophene **2a** (241.6 mg, 1.8 mmol, 1.5 equiv). 5.58 mL of either CPME or DMA were added to the vials with a stir bar. After stirring to ensure complete dissolution, 200 µL of the reaction mixture stock solution was added into each well according to the experimental design. Finally the bases were added as neat liquids to each well according to experimental design: *N*,*N*-diisopropylethylamine (DIPEA, 13.9 µL) or 1,8-diazabicyclo[5.4.0]undec-7-ene (DBU, 12.0 µL). The plates were sealed and removed from the glovebox. The plates were placed in a heat block on a tumble stirrer set to 300 rpm, and the reaction mixtures stirred for 20 hours at 100 °C. Upon completion, the plates were cooled to room temperature before being opened. Acetonitrile (500 µL) was added to each well, followed by stirring for 10 minutes at room temperature to ensure complete dissolution. Aliquots of 40 µL of each diluted reaction mixture were then transferred to 24 different HPLC vials followed by the addition

of 1 mL of acetonitrile. These 24 samples were analyzed by HPLC, with solution yields of **3a** determined by UV/Vis absorbance versus a calibration curve for **3a**.

Table A2. Catalyst screening results, yields determined by HPLC area% (calibration curve for **3a**).

	DMA/No base	DMA/DIPEA	DMA/DBU	CPME/No base	CPME/DIPEA	CPME/DBU
DPPF	1%	1%	2%	1%	1%	2%
DIPPF	1%	1%	2%	1%	1%	1%
DPPP	1%	1%	1%	2%	2%	3%
PPh_3	1%	1%	2%	1%	1%	4%
DavePhos	1%	1%	1%	2%	2%	3%
CataCXium A	1%	2%	0%	2%	5%	3%
$PMe(t\text{-}Bu)_2$	2%	3%	2%	2%	2%	10%
SPhos	1%	1%	2%	2%	2%	3%
XantPhos	2%	1%	1%	2%	2%	3%
DPEPhos	1%	1%	1%	1%	1%	2%
PCy_3	33%	40%	6%	2%	2%	4%
$P(t\text{-}Bu)_3$	1%	1%	1%	2%	2%	1%
RuPhos	1%	2%	3%	3%	2%	3%
JohnPhos	1%	1%	1%	1%	1%	3%
XPhos	1%	1%	2%	2%	2%	3%
BippyPhos	1%	1%	2%	2%	2%	3%
$P(o\text{-}OMePh)_3$	3%	3%	5%	4%	0%	5%
$P(o\text{-}MePh)_3$	2%	2%	2%	2%	0%	3%

Screen 3: (Figure 2.11): Reaction Optimization

Larger-scale optimization:

Each optimization reaction was performed using this general procedure:

In the glovebox, a 1-dram vial was charged with a stir bar, **1a** (22.4 mg, 0.10 mmol) and **2a** (0.15 or 0.30 mmol). Bis(tricyclohexylphosphine)palladium(0) was added (10 mol%, 6 mol%, or 3 mol%) followed by anhydrous *N*,*N*-dimethylacetamide (0.5 mL or 0.2 mL). The vial was sealed with a Teflon-lined screw cap and removed from the glovebox. The reaction mixture was stirred at 100 °C for 20 h. After cooling to room temperature, the solvent was removed by centrifugal evaporation, followed by redissolution of the residue in $CDCl_3$ containing 1,3,5-trimethoxybenzene as an internal standard (10 mol%). The solution yield of **3a** was calculated by relative integration versus the internal standard.

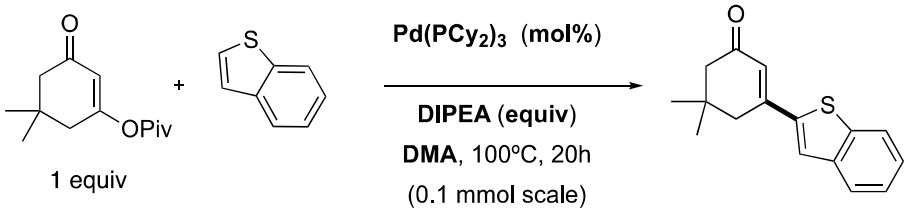

Entry	Piv/HetAr Ratio	Base quantity (equiv)	Catalyst amount (mol%)	Solvent (mL)	NMR Yield
1	1:1.5	3	3	0.5	57%
2	1:1.5	3	6	0.5	67%
3	1:1.5	3	10	0.5	66%
4	1:1.5	0	6	0.5	70%
5	1:1.5	0	6	0.2	80%
6	**1:3**	**0**	**6**	**0.2**	**91%**

Fig. A15: Larger-scale optimization results

IV: Preparative-Scale Direct Alkenylation

General Procedure

Inside the glovebox, a 1-dram vial was charged with a stir bar. The enol pivalate substrate (0.5 mmol, 1 equiv) and heterocycle substrate (1.5 mmol, 3 equiv) were added, followed by bis(tricyclohexylphosphine)palladium(0) (20.0 mg, 0.03 mmol, 6 mol%) and anhydrous *N,N*-dimethylacetamide (1 mL). The vial was sealed with a Teflon-lined screw cap, and the reaction mixture stirred at 100 °C for 20 h. After cooling to room temperature, the solvent was removed by centrifugal evaporation. The resulting crude mixture was purified by automated column chromatography using a hexanes/ethyl acetate gradient elution.

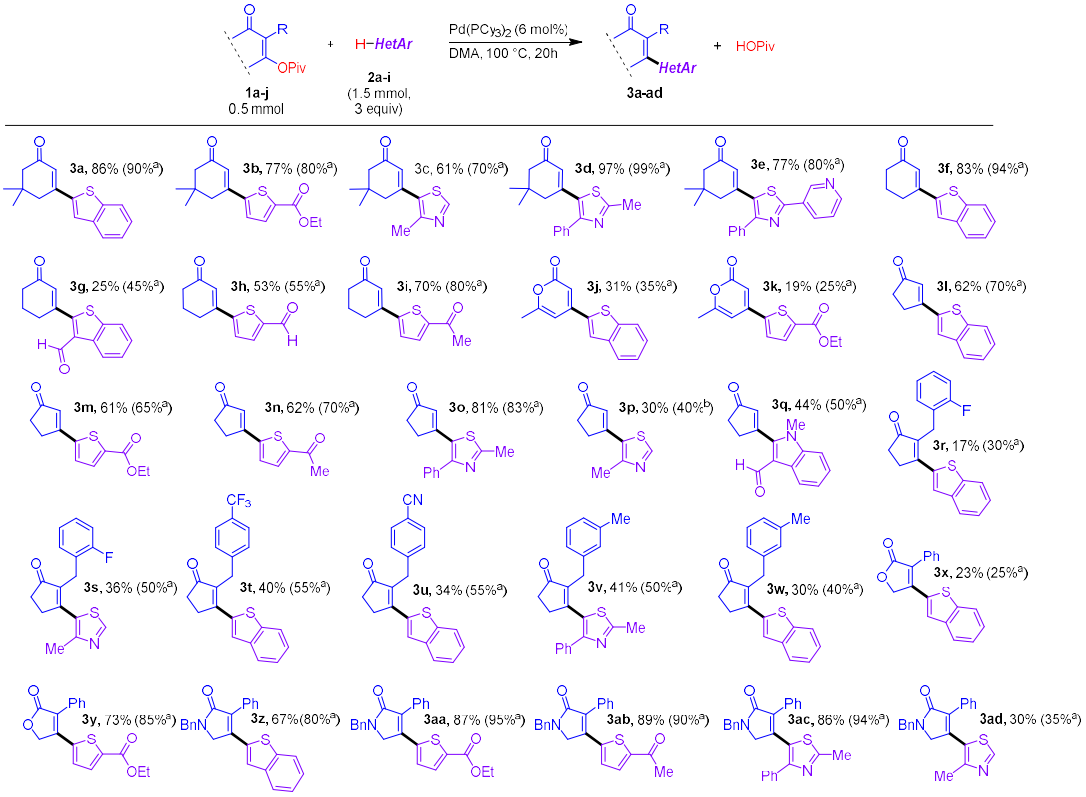

Fig. A16: Scope of the Pd-catalyzed cross-coupling of alkenyl carboxylate electrophiles with different heterocycles. [a] Solution yield by ^{1}H-NMR versus internal standard

VI Product Characterization

3a. 3-(benzo[*b*]thiophene-2-yl)-5,5-dimethylcyclohex-2-en-1-one:

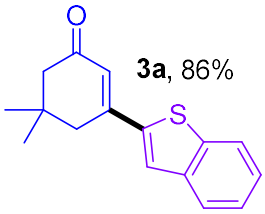

A beige solid was collected (109.7 mg, 86% yield).

Purified by column chromatography (Biotage® Sfär Column, 0-100% EtOAc/hexanes, eluted at 30% EtOAc).

^{1}H-NMR (500 MHz, $CDCl_3$, 292 K, ppm): δ 7.76 (m, 2H), 7.57 (s, 1H), 7.35 (m, 2H), 6.45 (s, 1H), 2.69 (s, 2H), 2.33 (s, 2H), 1.13 (s, 6H).

^{13}C-NMR (126 MHz, $CDCl_3$, 292 K, ppm): δ 199.41, 150.30, 142.74, 140.14, 139.73, 126.27, 124.91, 124.76, 124.48, 123.82, 122.38, 51.05, 41.50, 33.59, 28.44.

HRMS: Calc'd for $C_{16}H_{16}OS$ $[M+H]^+$: 257.09946; found: 257.09933.

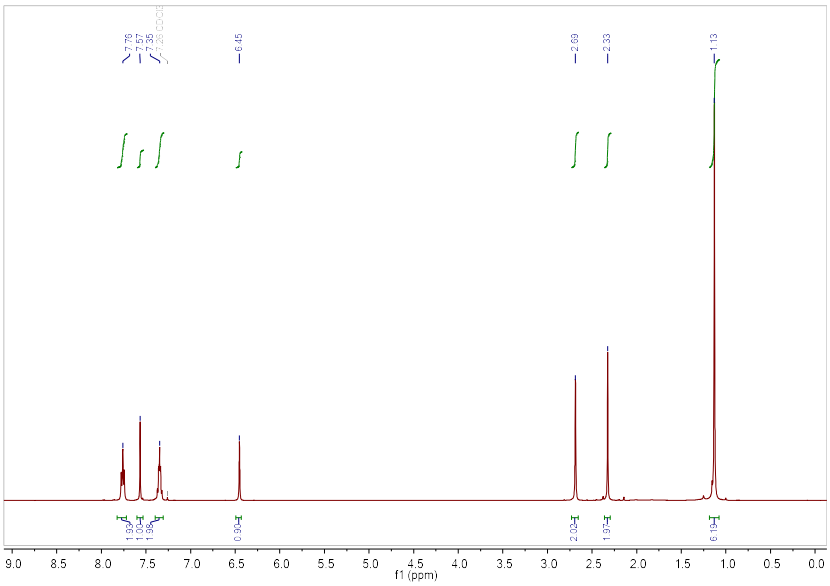

Fig. A17: ^{1}H NMR (500 MHz, Chloroform-*d*) spectrum of **3a**

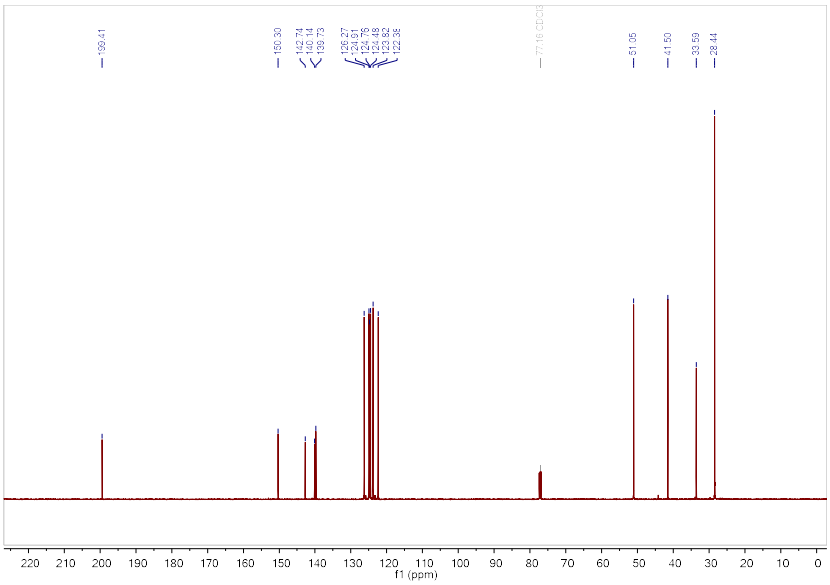

Fig. A18: $^{13}C\{^{1}H\}$ NMR (126 MHz, Chloroform-*d*) spectrum of **3a**

3b. Ethyl 5-(5,5-dimethyl-3-oxocyclohex-1-en-1-yl)thiophene-2-carboxylate:

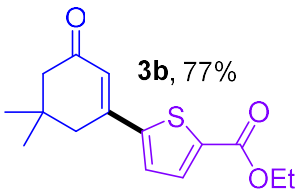

A yellow oil was collected (107.4 mg, 77% yield).

Purified by column chromatography (Biotage® Sfär Column, 0-100% EtOAc/hexanes, eluted at 35% EtOAc).

^{1}H-NMR (500 MHz, $CDCl_3$, 292 K, ppm): δ 7.70 (d, J = 4.0 Hz, 1H), 7.31 (d, J = 4.0 Hz, 1H), 6.43 (s, 1H), 4.32 (q, J = 7.2 Hz, 2H), 2.60 (ds, 2H), 2.29 (s, 2H), 1.35 (t, J = 7.1 Hz, 3H), 1.09 (s, 6H).

^{13}C-NMR (126 MHz, $CDCl_3$, 292 K, ppm): δ 199.25, 161.70, 149.22, 148.77, 135.66, 133.75, 126.99, 123.31, 61.59, 50.93, 41.94, 33.62, 28.36, 14.32.

HRMS: Calc'd for $C_{15}H_{18}O_3S$ $[M+H]^+$: 279.10495; found: 279.10487.

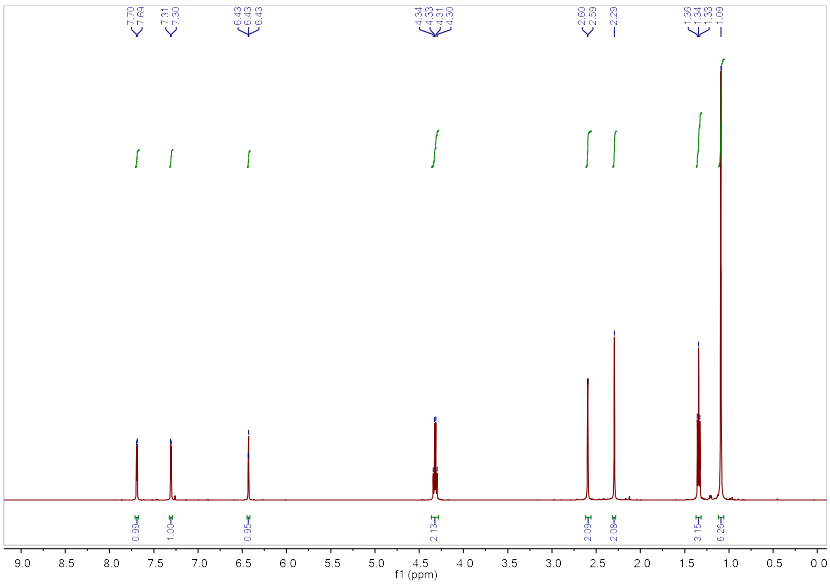

Fig. A19: ^{1}H NMR (500 MHz, Chloroform-*d*) spectrum of **3b**

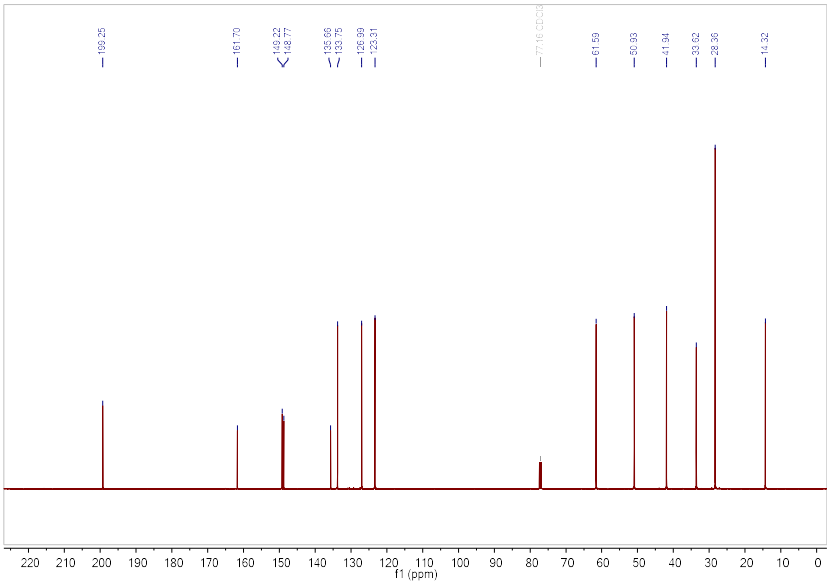

Fig. A20: ^{13}C{^{1}H} NMR (126 MHz, Chloroform-*d*) spectrum of **3b**

3c. 5,5-dimethyl-3-(4-methylthiazol-5-yl)cyclohex-2-en-1-one

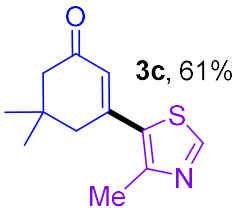

An orange oil was collected (67.0 mg, 61% yield).

Purified by column chromatography (Biotage® Sfär Column, 0-100% EtOAc/hexanes, eluted at 40% EtOAc).

^{1}H-NMR (500 MHz, $CDCl_3$, 292 K, ppm): δ 8.70 (s, 1H), 6.22 (s, 1H), 2.55 (s, 3H), 2.53 (s, 2H), 2.28 (s, 2H), 1.08 (s, 6H).

^{13}C-NMR (126 MHz, $CDCl_3$, 292 K, ppm): δ 198.96, 151.97, 151.91, 149.38, 131.56, 126.37, 50.56, 45.65, 33.88, 28.24, 18.07.

HRMS: Calc'd for $C_{12}H_{15}NOS$ $[M+H]^+$: 222.09471; found: 222.09470.

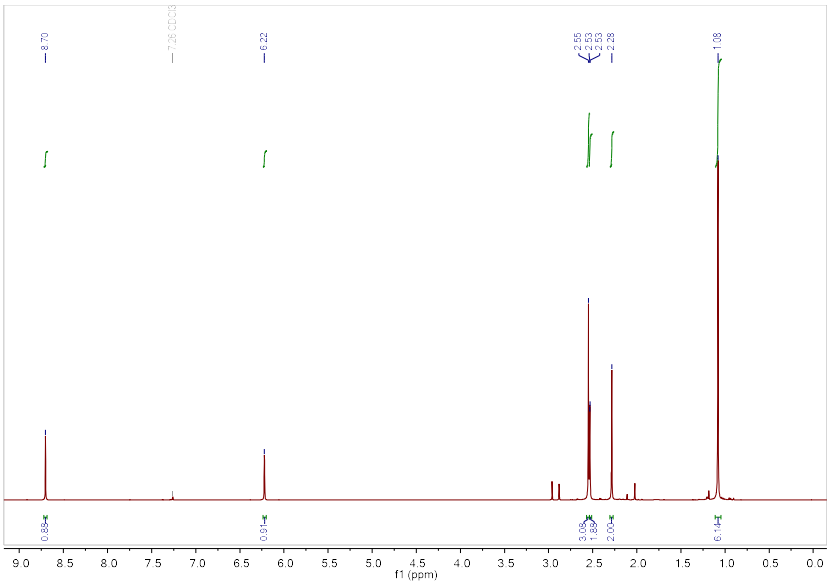

Fig. A21: ^{1}H NMR (500 MHz, Chloroform-*d*) spectrum of **3c**

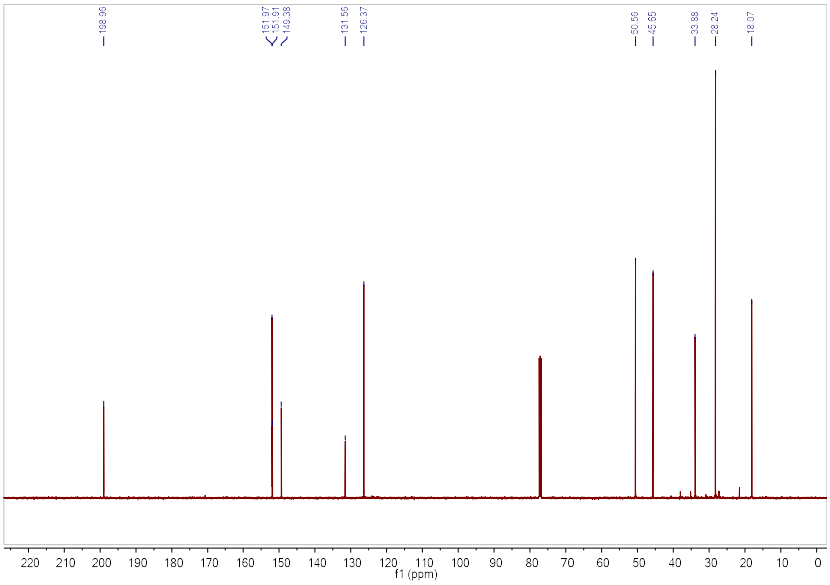

Fig. A22: ^{13}C{^{1}H} NMR (126 MHz, Chloroform-*d*) spectrum of **3c**

3d. 5,5-dimethyl-3-(2-methyl-4-phenylthiazol-5-yl)cyclohex-2-en-1-one:

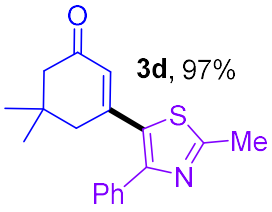

An orange solid was collected (144.6 mg, 97% yield).

Purified by column chromatography (Biotage® Sfär Column, 0-100% EtOAc/hexanes, eluted at 30% EtOAc).

^{1}H-NMR (500 MHz, $CDCl_3$, 292 K, ppm): δ 7.48 (m, 2H), 7.35 (m, 3H), 6.16 (s, 1H), 2.69 (s, 3H), 2.27 (s, 2H), 2.22 (s, 2H), 0.97 (s, 6H).

^{13}C-NMR (126 MHz, $CDCl_3$, 292 K, ppm): δ 198.87, 165.42, 152.96, 150.39, 134.93, 129.10, 128.77, 128.57, 127.97, 50.90, 43.56, 33.69, 28.04, 19.30.

HRMS: Calc'd for $C_{18}H_{19}NOS$ $[M+H]^+$: 298.12601; found: 298.12598.

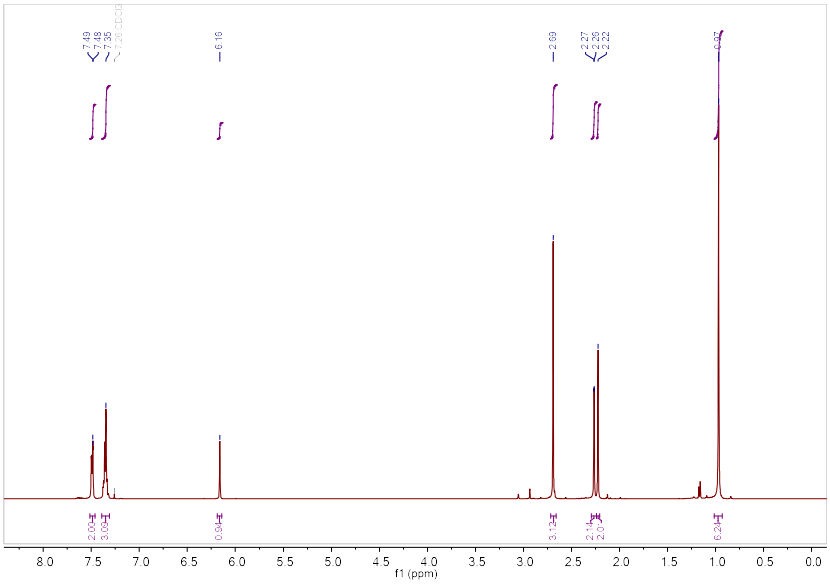

Fig. A23: ^{1}H NMR (500 MHz, Chloroform-*d*) spectrum of **3d**

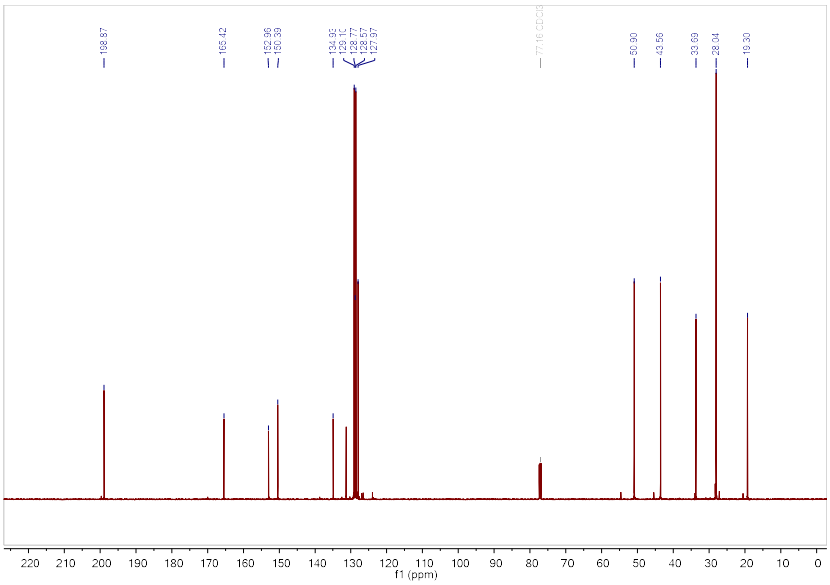

Fig. A24: $^{13}C\{^{1}H\}$ NMR (126 MHz, Chloroform-*d*) spectrum of **3d**

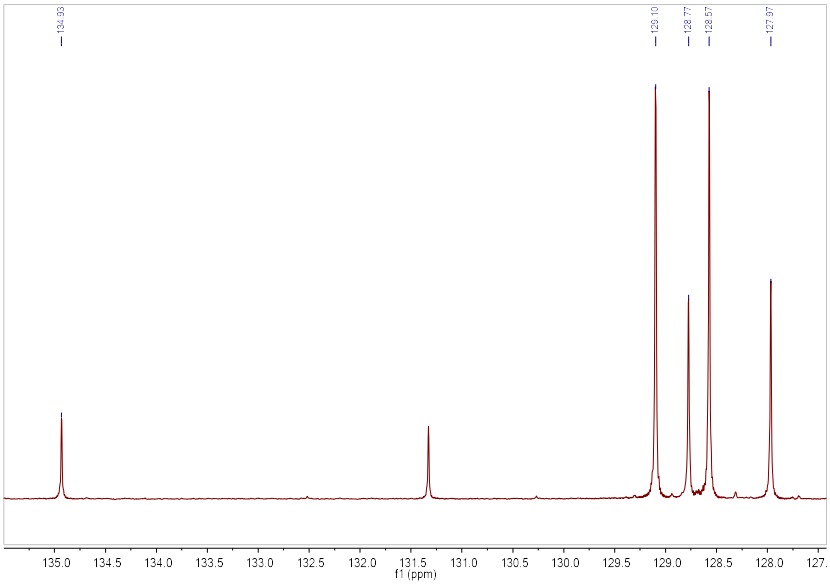

Fig. A25: Expanded (127-136 ppm) $^{13}C\{^{1}H\}$ NMR (126 MHz, Chloroform-*d*) spectrum of **3d**

3e. 5,5-dimethyl-3-(4-phenyl-2-(pyridin-3-yl)thiazol-5-yl)cyclohex-2-en-1-one:

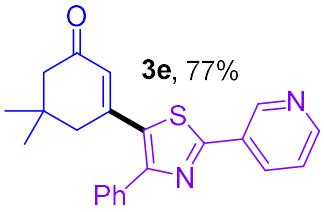

An orange oil was collected (135.6 mg, 77% yield).

Purified by column chromatography (Biotage® Sfär Column, 0-100% EtOAc/hexanes, eluted at 40% EtOAc).

^{1}H-NMR (500 MHz, $CDCl_3$, 292 K, ppm): δ 9.17 (s, 1H), 8.68 (s, 1H), 8.26 (d, J = 8.0, 1H), 7.63 – 7.56 (m, 2H), 7.45 – 7.35 (m, 5H), 6.26 (s, 1H), 2.35 (s, 2H), 2.27 (s, 2H), 1.01 (s, 6H).

^{13}C-NMR (126 MHz, $CDCl_3$, 292 K, ppm): δ 198.74, 163.14, 154.46, 151.12, 149.72, 147.63, 134.59, 133.86, 132.58, 129.24, 129.20, 129.18, 128.76, 128.72, 128.60, 127.18, 126.92, 124.18, 123.92, 50.94, 43.64, 33.82, 28.10.

HRMS: Calc'd for $C_{22}H_{20}$ $[M+H]^+$: 361.13691; found: 361.13670.

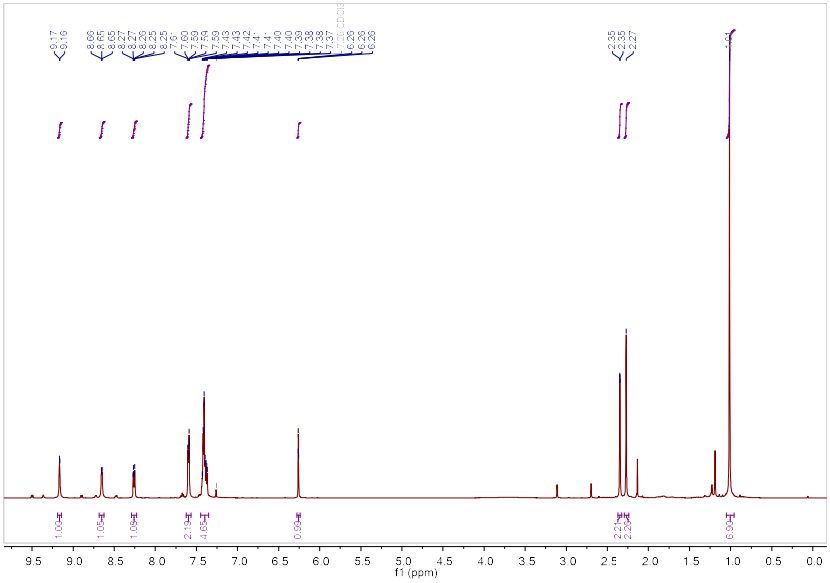

Fig. A26: ^{1}H NMR (500 MHz, Chloroform-*d*) spectrum of **3e**

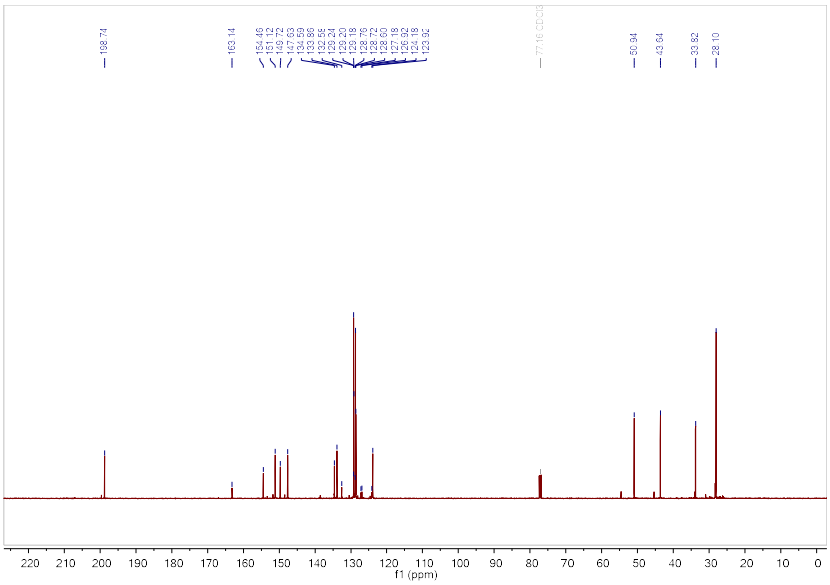

Fig. A27: $^{13}C\{^{1}H\}$ NMR (126 MHz, Chloroform-*d*) spectrum of **3e**

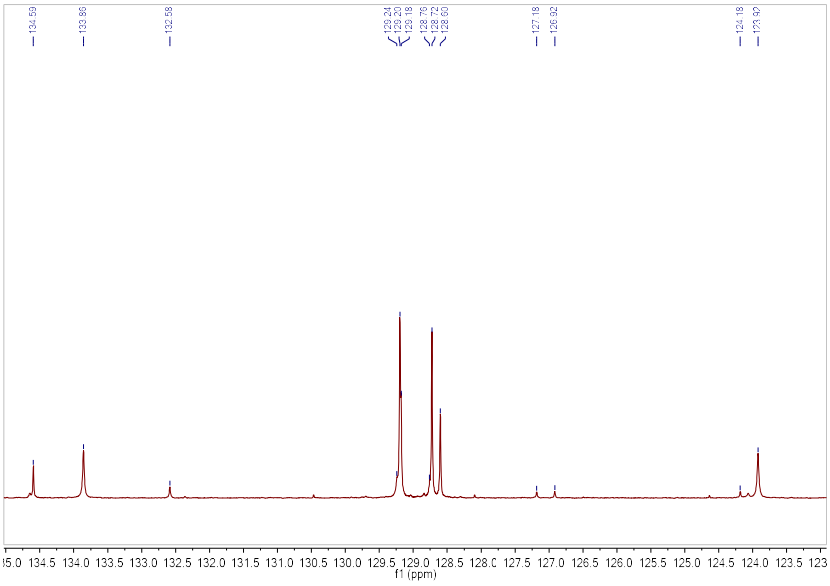

Fig. A28: Expanded (123-135 ppm) $^{13}C\{^{1}H\}$ NMR (126 MHz, Chloroform-*d*) spectrum of **3e**

3f. 3-(benzo[b]thiophen-2-yl)cyclohex-2-en-1-one

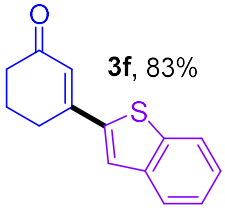

A light-yellow solid was collected (95.2 mg, 60% yield).

Purified by column chromatography (Biotage® Sfär Column, 0-100% EtOAc/hexanes, eluted at 30% EtOAc).

^{1}H-NMR (500 MHz, $CDCl_3$, 292 K, ppm): δ 7.79 – 7.75 (m, 2H), 7.56 (s, 1H), 7.35 (m, 2H), 6.45 (s, 1H), 2.83 (t, J = 7.4 Hz, 2H), 2.48 (t, J = 7.4, 2H), 2.15 (p, J=7.4 Hz, 2H).

^{13}C-NMR (126 MHz, $CDCl_3$, 292 K, ppm): δ 199.33, 152.51, 142.52, 140.19, 139.77, 126.29, 124.92, 124.82, 124.53, 122.42, 37.40, 27.57, 22.49.

HRMS: Calc'd for $C_{14}H_{12}OS$ $[M+H]^+$: 229.06817; found: 229.06814.

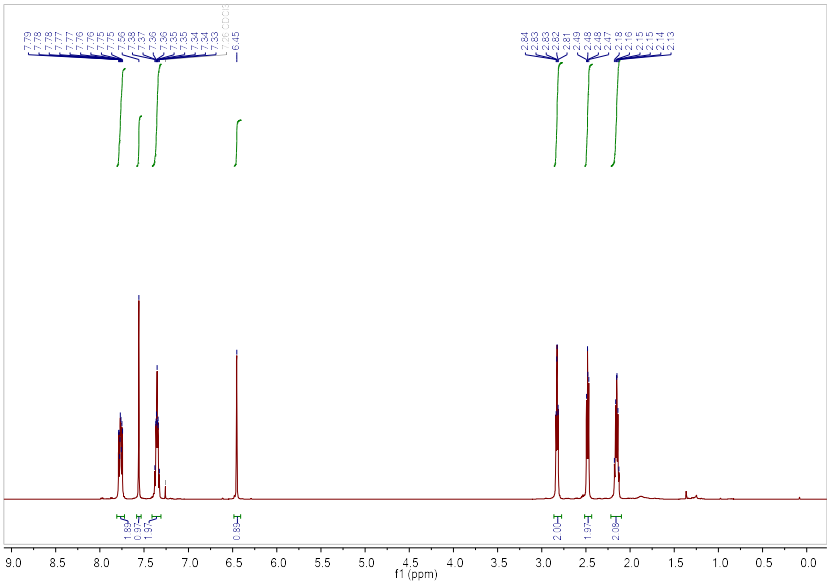

Fig. A29: ^{1}H NMR (500 MHz, Chloroform-*d*) spectrum of **3f**

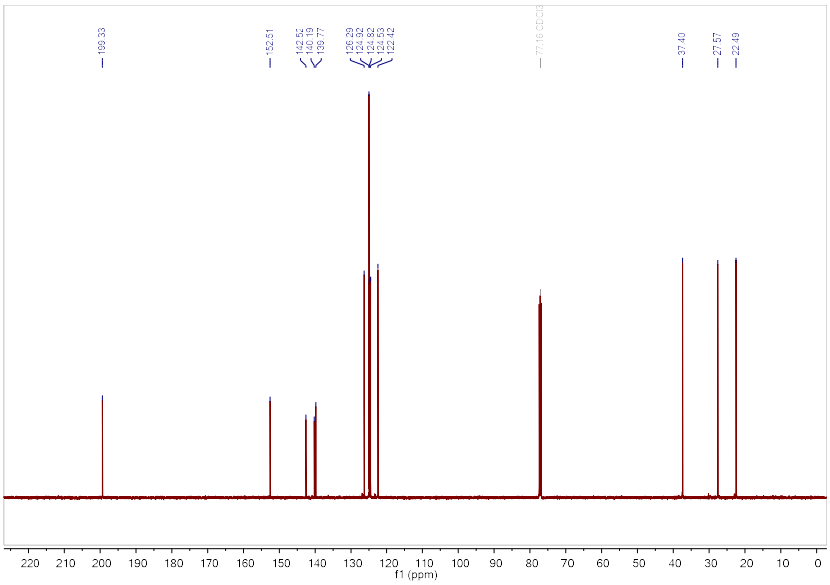

Fig. A30: $^{13}C\{^{1}H\}$ NMR (126 MHz, Chloroform-*d*) spectrum of **3f**

3g. 2-(3-oxocyclohex-1-en-1-yl)benzo[b]thiophene-3-carbaldehyde

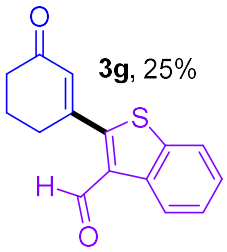

A brown solid was collected (31.9 mg, 25% yield).

Purified by column chromatography (Biotage® Sfär Column, 0-100% EtOAc/hexanes, eluted at 30% EtOAc).

^{1}H-NMR (500 MHz, $CDCl_3$, 292 K, ppm): δ 10.17 (s, 1H), 8.71 (d, J = 8.1 Hz, 1H), 7.84 (d, J = 8.0 Hz, 1H), 7.49 (ddd, J = 19.6, 8.1, 1.3 Hz, 2H), 6.29 (s, 1H), 2.84 (t, J = 6.7, 2H), 2.57 (t, J = 6.7 Hz, 2H), 2.29 – 2.21 (m, 2H).

^{13}C-NMR (126 MHz, $CDCl_3$, 292 K, ppm): δ 197.84, 185.04, 157.27, 151.48, 138.24, 136.97, 132.50, 131.67, 126.77, 126.73, 125.48, 121.96, 37.27, 32.19, 22.92.

HRMS: Calc'd for $C_{15}H_{12}O_2S$ $[M+H]^+$: 257.06308; found: 257.06297.

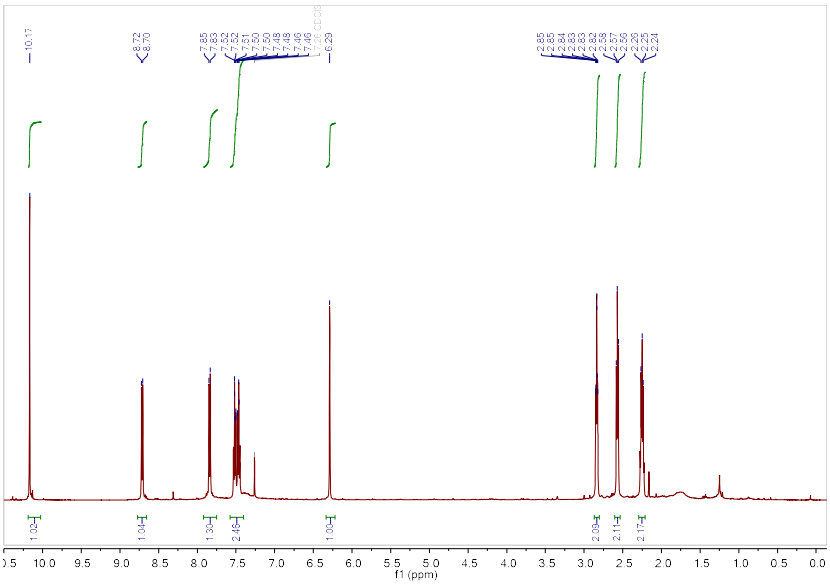

Fig. A31: ^{1}H NMR (500 MHz, Chloroform-*d*) spectrum of **3g**

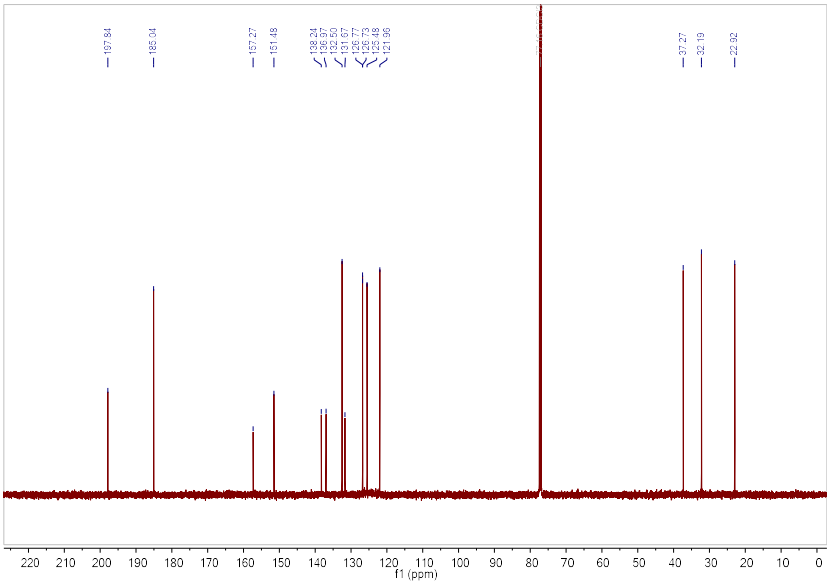

Fig. A32: ^{13}C{^{1}H} NMR (126 MHz, Chloroform-*d*) spectrum of **3g**

3h. 5-(3-oxocyclohex-1-en-1-yl)thiophene-2-carbaldehyde

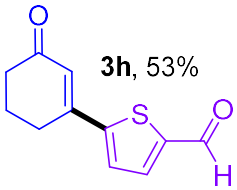

A yellow solid was collected (53.9 mg, 53% yield).

Purified by column chromatography (Biotage® Sfär Column, 0-100% EtOAc/hexanes, eluted at 50% EtOAc).

^{1}H-NMR (500 MHz, $CDCl_3$, 292 K, ppm): δ 9.91 (s, 1H), 7.73 (d, J = 4.0 Hz, 1H), 7.44 (d, J = 4.0 Hz, 1H), 6.52 (s, 1H), 2.78 (t, J = 6.1, 2H), 2.49 (t, J = 6.0 Hz, 2H), 2.18 (p, J = 6.3 Hz, 2H).

^{13}C-NMR (126 MHz, $CDCl_3$, 292 K, ppm): δ 199.05, 182.93, 151.45, 150.93, 144.78, 136.44, 127.35, 125.51, 37.31, 28.11, 22.45.

HRMS: Calc'd for $C_{11}H_{10}O_2S$ $[M+H]^+$: 207.04743; found: 207.04741.

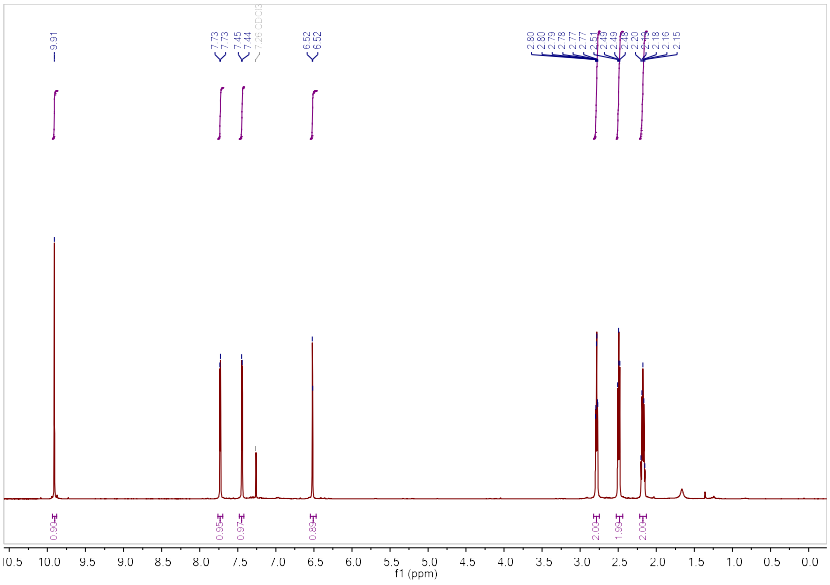

Fig. A33: ^{1}H NMR (500 MHz, Chloroform-*d*) spectrum of **3h**

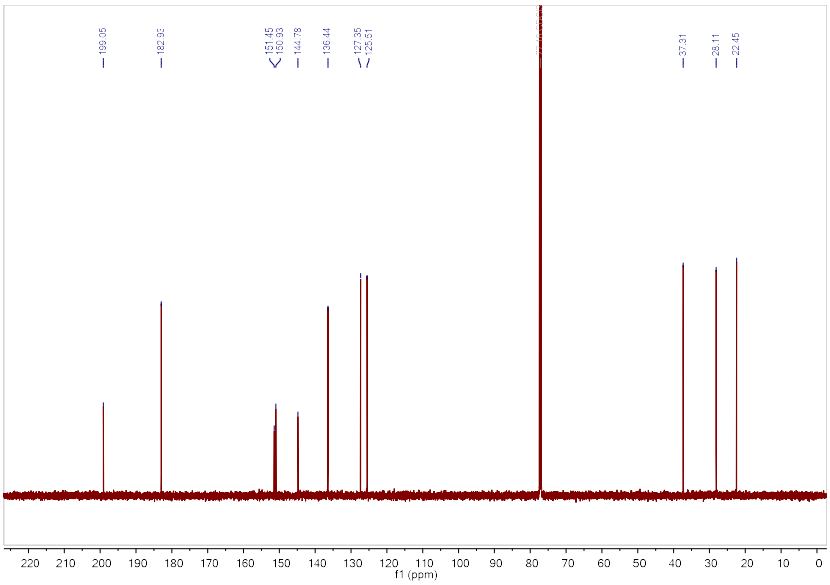

Fig. A34: $^{13}C\{^{1}H\}$ NMR (126 MHz, Chloroform-*d*) spectrum of **3h**

3i. 3-(5-acetylthiophen-2-yl)cyclohex-2-en-1-one

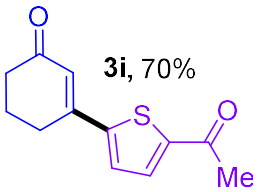

A yellow solid was collected (76.9 mg, 70% yield).

Purified by column chromatography (Biotage® Sfär Column, 0-100% EtOAc/hexanes, eluted at 60% EtOAc).

^{1}H-NMR (500 MHz, $CDCl_3$, 292 K, ppm): δ 7.62 (d, J = 4.1 Hz, 1H), 7.35 (d, J = 4.1 Hz, 1H), 6.46 (s, 1H), 2.75 (t, J = 6.1, 2H), 2.54 (s, 3H), 2.46 (t, J = 6.1 Hz, 2H), 2.14 (p, J = 6.1 Hz, 2H).

^{13}C-NMR (126 MHz, $CDCl_3$, 292 K, ppm): δ 199.11, 190.57, 151.26, 149.93, 145.63, 132.81, 127.36, 124.84, 37.26, 27.98, 26.85, 22.41.

HRMS: Calc'd for $C_{12}H_{12}O_2S$ $[M+H]^+$: 221.06308; found: 221.06306.

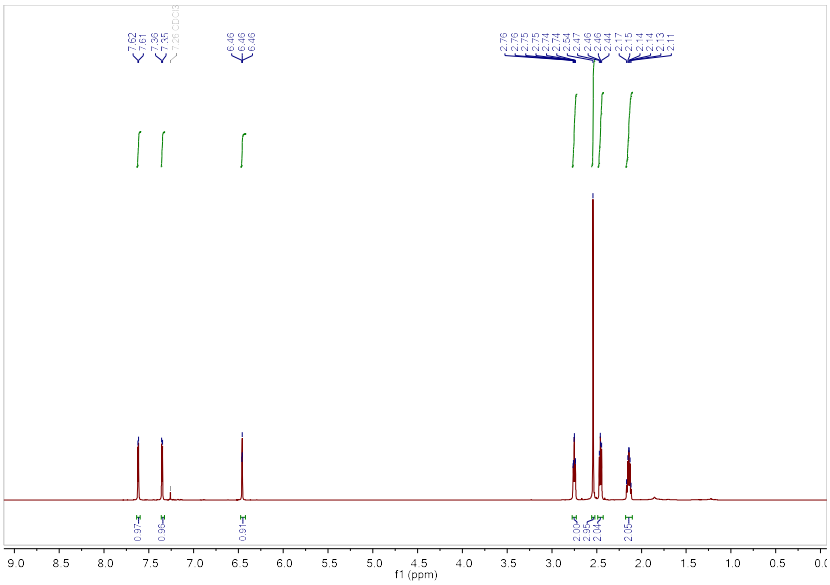

Fig. A35: ^{1}H NMR (500 MHz, Chloroform-*d*) spectrum of **3i**

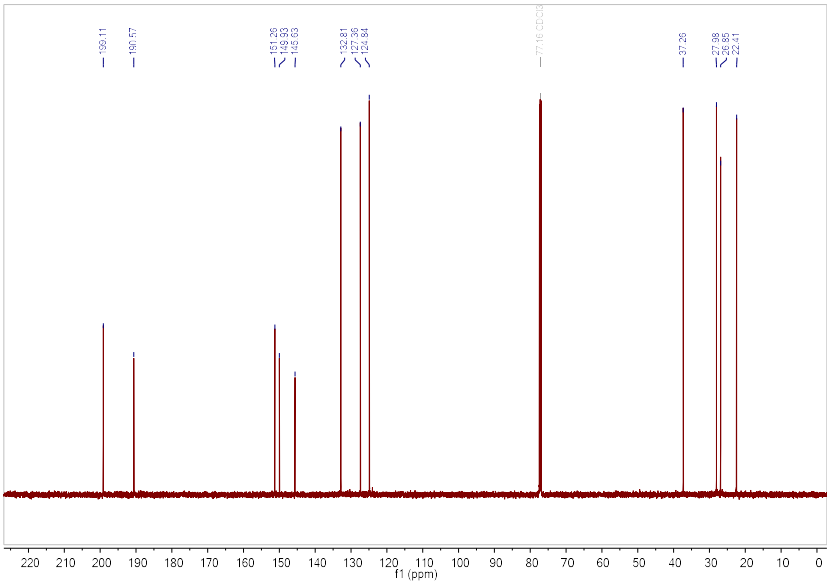

Fig. A36: ^{13}C{^{1}H} NMR (126 MHz, Chloroform-*d*) spectrum of **3i**

3j. 4-(benzo[b]thiophen-2-yl)-6-methyl-2H-pyran-2-one

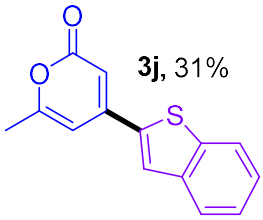

A yellow solid was collected (32.9 mg, 31 % yield).

Purified by column chromatography (Biotage® Sfär Column, 0-100% EtOAc/hexanes, eluted at 20% EtOAc).

^{1}H-NMR (500 MHz, $CDCl_3$, 292 K, ppm): δ 7.84 (m, 2H), 7.72 (s, 1H), 7.45 – 7.38 (m, 2H), 6.42 (s, 1H), 6.39 (s, 1H), 2.33 (s, 3H).

^{13}C-NMR (126 MHz, $CDCl_3$, 292 K, ppm): δ 163.10, 162.23, 148.37, 140.65, 139.75, 138.66, 126.65, 125.33, 125.03, 124.90, 122.68, 107.26, 102.23, 20.32.

HRMS: Calc'd for $C_{14}H_{10}O_2S$ $[M+H]^+$: 243.04743; found: 243.04745.

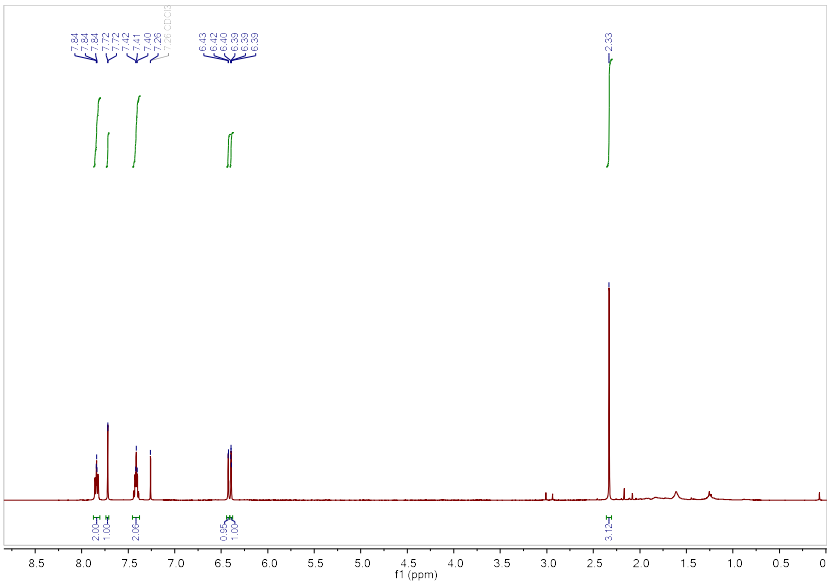

Fig. A37: ^{1}H NMR (500 MHz, Chloroform-*d*) spectrum of **3j**

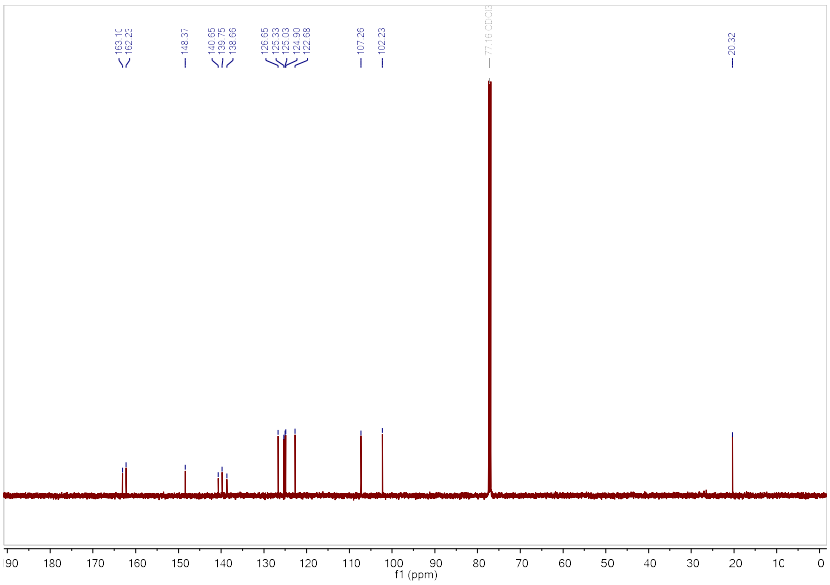

Fig. A38: $^{13}C\{^{1}H\}$ NMR (126 MHz, Chloroform-*d*) spectrum of **3j**

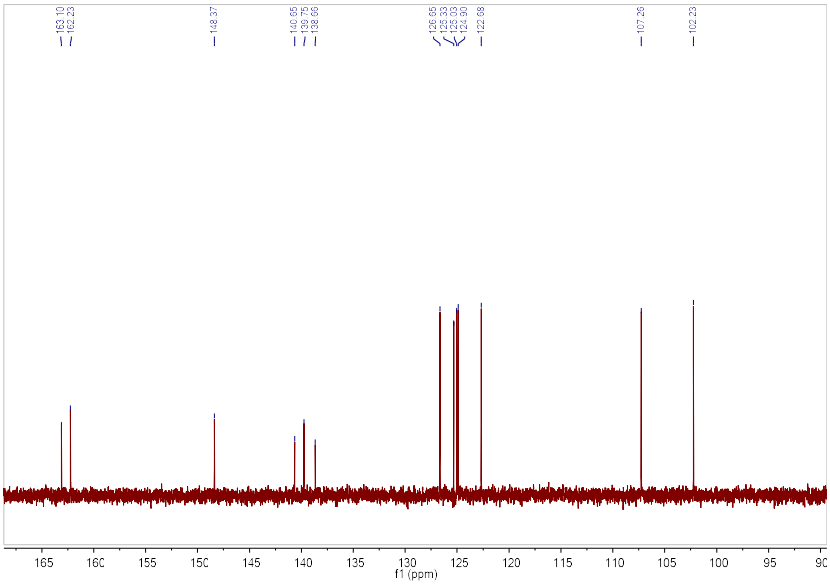

Fig. A39: Expanded (90-165 ppm) $^{13}C\{^{1}H\}$ NMR (126 MHz, Chloroform-*d*) spectrum of **3j**

3k. Ethyl 5-(6-methyl-2-oxo-2H-pyran-4-yl)thiophene-2-carboxylate

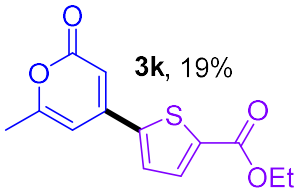

A beige solid was collected (22.0 mg, 19% yield).

Purified by column chromatography (Biotage® Sfär Column, 0-100% EtOAc/hexanes, eluted at 30% EtOAc).

^{1}H-NMR (500 MHz, $CDCl_3$, 292 K, ppm): δ 7.77 (d, J = 4.0 Hz, 1H), 7.43 (d, J = 4.0 Hz, 1H), 6.39 (s, 1H), 6.26 (s, 1H), 4.38 (q, J = 7.1 Hz, 2H), 2.31 (s, 3H), 1.39 (t, J = 7.1 Hz, 3H).

^{13}C-NMR (126 MHz, $CDCl_3$, 292 K, ppm): δ 162.85, 162.78, 161.58, 147.31, 144.46, 136.97, 134.04, 127.69, 106.91, 102.13, 61.89, 20.32, 14.41.

HRMS: Calc'd for $C_{13}H_{12}O_4S$ $[M+H]^+$: 265.05291; found: 265.05289.

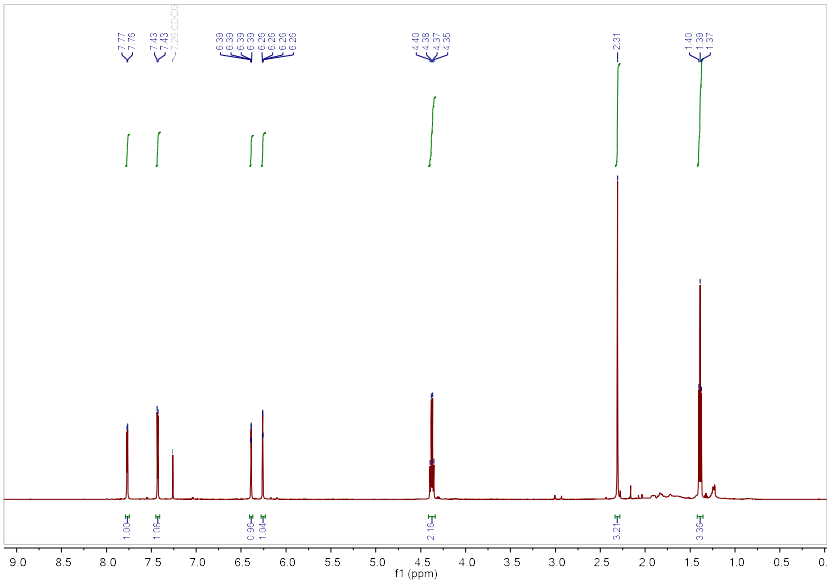

Fig. A40: ^{1}H NMR (500 MHz, Chloroform-*d*) spectrum of **3k**

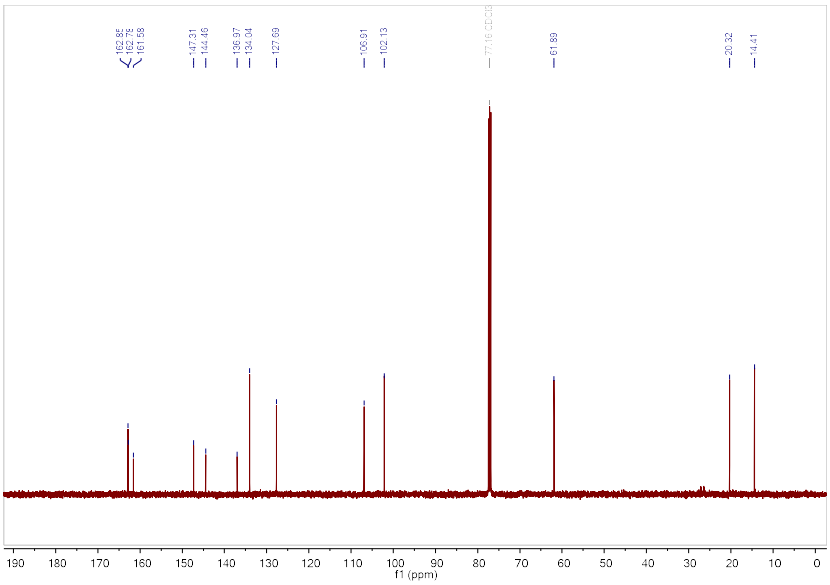

Fig. A41: $^{13}C\{^{1}H\}$ NMR (126 MHz, Chloroform-*d*) spectrum of **3k**

3l. 3-(benzo[b]thiophen-2-yl)cyclopent-2-en-1-one

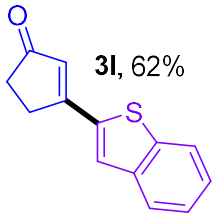

3l, 62%

An orange solid was collected (66.3 mg, 48% yield).

Purified by column chromatography (Biotage® Sfär Column, 0-100% EtOAc/hexanes, eluted at 60% EtOAc).

^{1}H NMR (500 MHz, $CDCl_3$, 292 K, ppm): δ 7.84 – 7.81 (m, 2H), 7.63 (s, 1H), 7.41 – 7.38 (m, 2H), 6.43 (s, 1H), 3.10-3.08 (m, 2H), 2.60 – 2.58 (m, 2H).

^{13}C NMR (126 MHz, $CDCl_3$, 292 K, ppm): δ 208.41, 166.74, 141.22, 139.56, 138.35, 128.15, 126.66, 125.52, 125.15, 124.93, 122.63, 35.26, 29.15.

HRMS: Calc'd for $C_{12}H_{10}OS$ $[M+H]^+$: 215.05252; found: 215.05236.

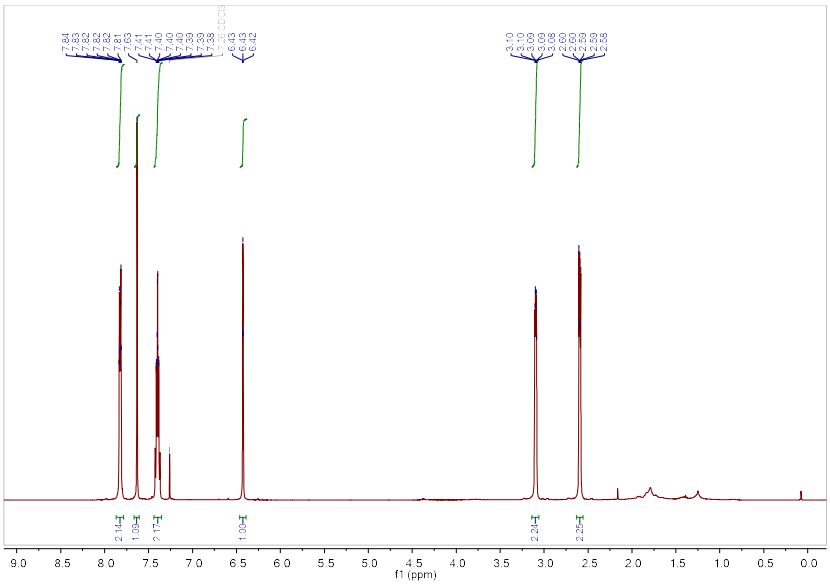

Fig. A42: ^{1}H NMR (500 MHz, Chloroform-*d*) spectrum of **3l**

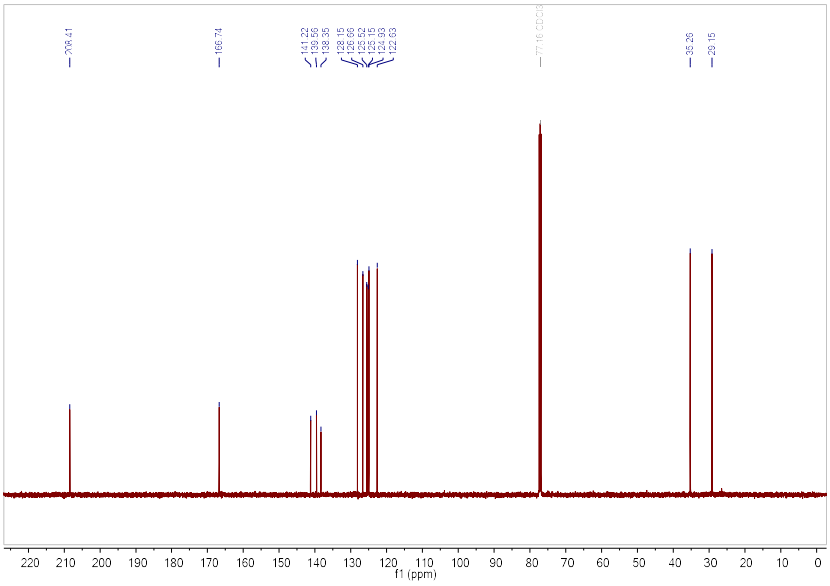

Fig. A43: ^{13}C{^{1}H} NMR (126 MHz, Chloroform-*d*) spectrum of **3l**

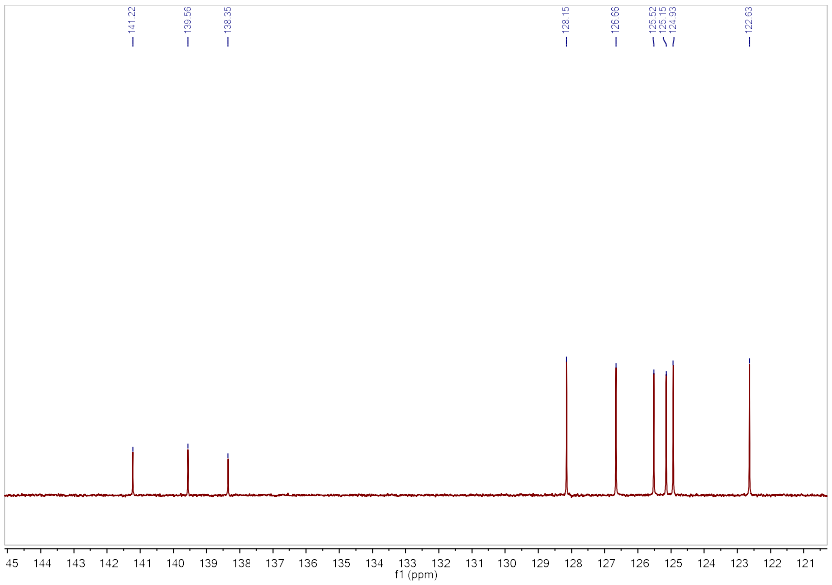

Fig. A44: Expanded (120-145 ppm) $^{13}C\{^{1}H\}$ NMR (126 MHz, Chloroform-*d*) spectrum of **3l**

3m. Ethyl 5-(3-oxocyclopent-1-en-1-yl)thiophene-2-carboxylate

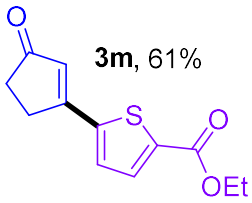

An orange solid was collected (71.7 mg, 61% yield).

Purified by column chromatography (Biotage® Sfär Column, 0-100% EtOAc/hexanes, eluted at 50% EtOAc).

^{1}H-NMR (500 MHz, $CDCl_3$, 292 K, ppm): δ 7.72 (d, J = 4.0 Hz, 1H), 7.36 (d, J = 4.0 Hz, 1H), 6.41 (s, 1H), 4.34 (q, J = 7.1 Hz, 2H), 3.00 (m, 2H), 2.58 – 2.50 (m, 2H), 1.36 (t, J = 7.2 Hz, 3H).

^{13}C-NMR (126 MHz, $CDCl_3$, 292 K, ppm): δ 208.36, 165.70, 161.89, 144.30, 137.37, 134.00, 128.57, 128.08, 62.00, 35.38, 29.48, 14.58.

HRMS: Calc'd for $C_{12}H_{12}O_3S$ $[M+H]^+$: 237.05799; found: 237.05797.

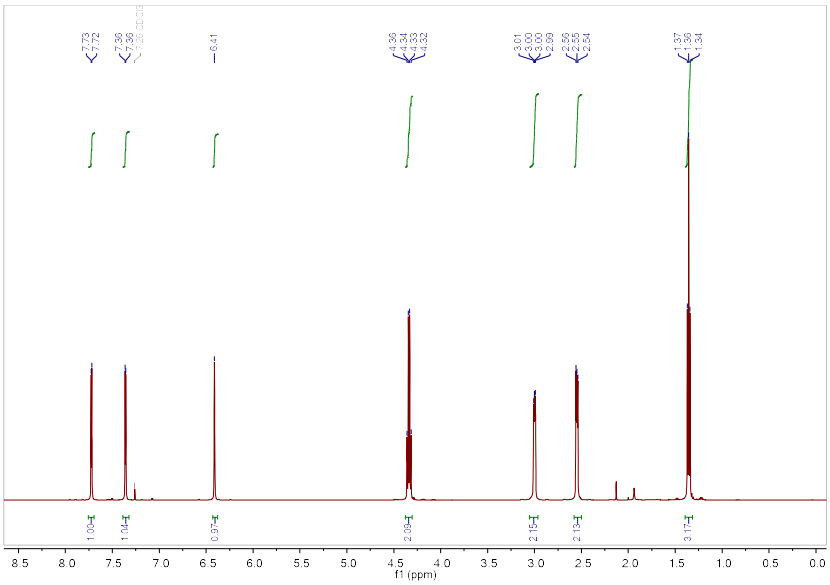

Fig. A45: ^{1}H NMR (500 MHz, Chloroform-*d*) spectrum of **3m**

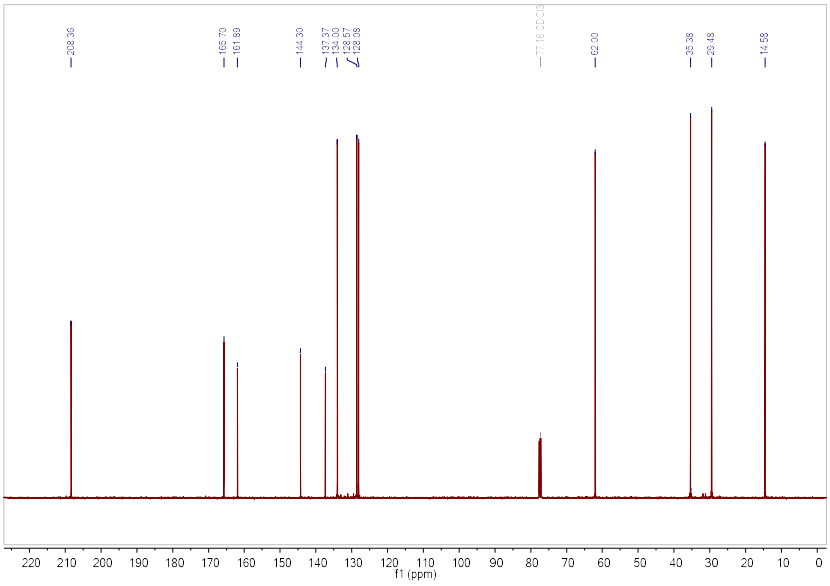

Fig. A46: ^{13}C{^{1}H} NMR (126 MHz, Chloroform-*d*) spectrum of **3m**

3n. 3-(5-acetylthiophen-2-yl)cyclopent-2-en-1-one

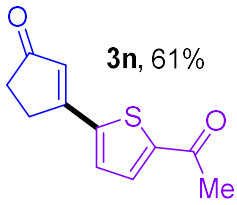

An orange solid was collected (63.2 mg, 30% yield).

Purified by column chromatography (Biotage® Sfär Column, 0-100% EtOAc/hexanes, eluted at 50% EtOAc).

^{1}H-NMR (500 MHz, $CDCl_3$, 292 K, ppm): δ 7.66 (d, J = 4.0 Hz, 1H), 7.42 (d, J = 3.9 Hz, 1H), 6.48 (s, 1H), 3.03 (m, 2H), 2.59 (m, 5H).

^{13}C-NMR (126 MHz, $CDCl_3$, 292 K, ppm): δ 208.15, 190.64, 165.35, 146.98, 145.37, 132.73, 128.69, 128.48, 35.26, 29.33, 26.99.

HRMS: Calc'd for $C_{11}H_{10}O_2S$ $[M+H]^+$: 207.04743; found: 207.04743.

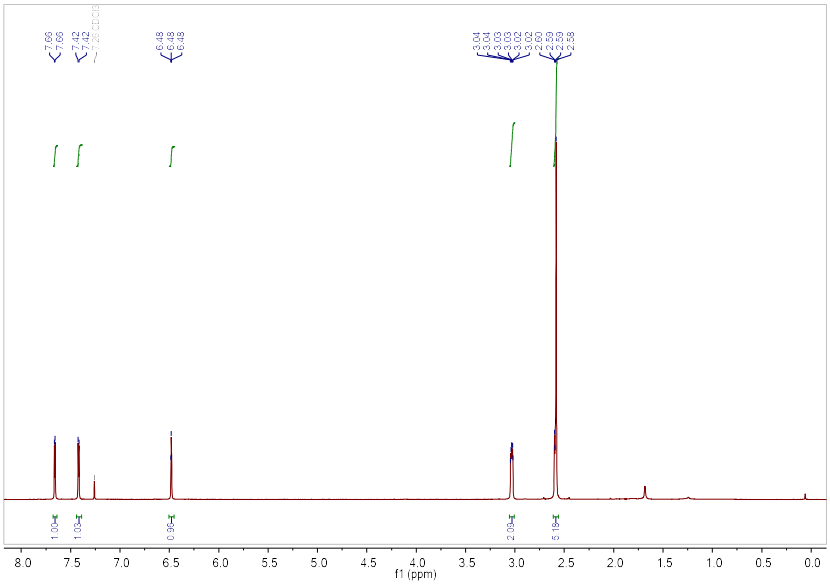

Fig. A47: ^{1}H NMR (500 MHz, Chloroform-*d*) spectrum of **3n**

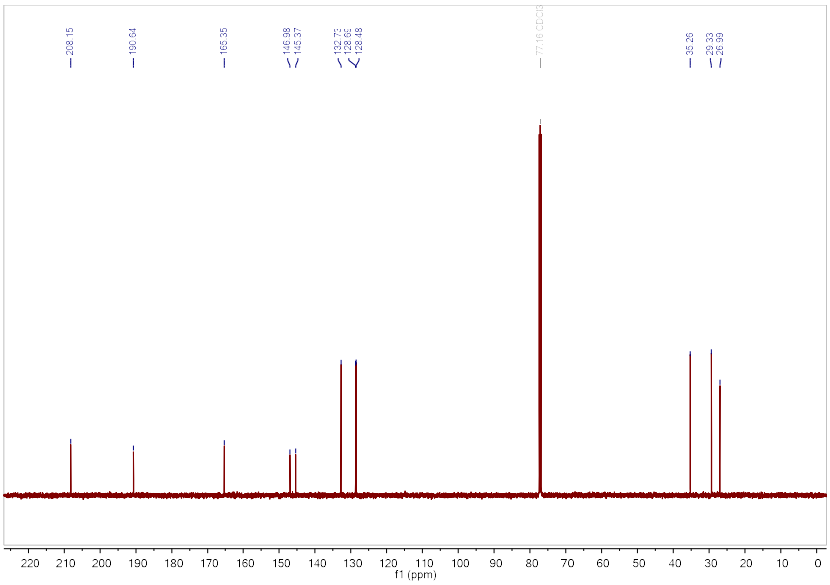

Fig. A48: $^{13}C\{^{1}H\}$ NMR (126 MHz, Chloroform-*d*) spectrum of **3n**

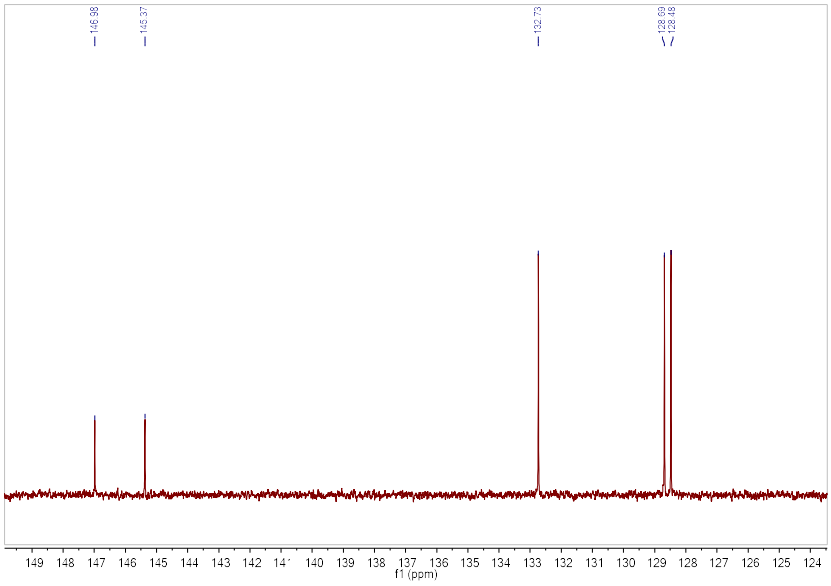

Fig. A49: Expanded (125-150 ppm) ^{13}C-NMR spectrum of **3n**

3o. 3-(2-methyl-4-phenylthiazol-5-yl)cyclopent-2-en-1-one

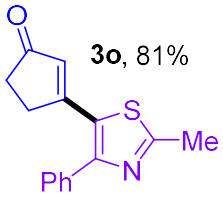

An orange solid was collected (103.6 mg, 81% yield).

Purified by column chromatography (Biotage® Sfär Column, 0-100% EtOAc/hexanes, eluted at 50% EtOAc).

^{1}H-NMR (500 MHz, $CDCl_3$, 292 K, ppm): δ 7.44 (m, 2H), 7.37 (m, 3H), 6.05 (s, 1H), 2.70 (m, 5H), 2.41 – 2.33 (m, 2H).

^{13}C-NMR (126 MHz, $CDCl_3$, 292 K, ppm): δ 208.19, 167.04, 164.71, 155.88, 135.05, 129.06, 129.03, 128.64, 128.16, 34.89, 31.66, 19.47.

HRMS: Calc'd for $C_{15}H_{13}NOS$ $[M+H]^+$: 256.07906; found: 256.07904.

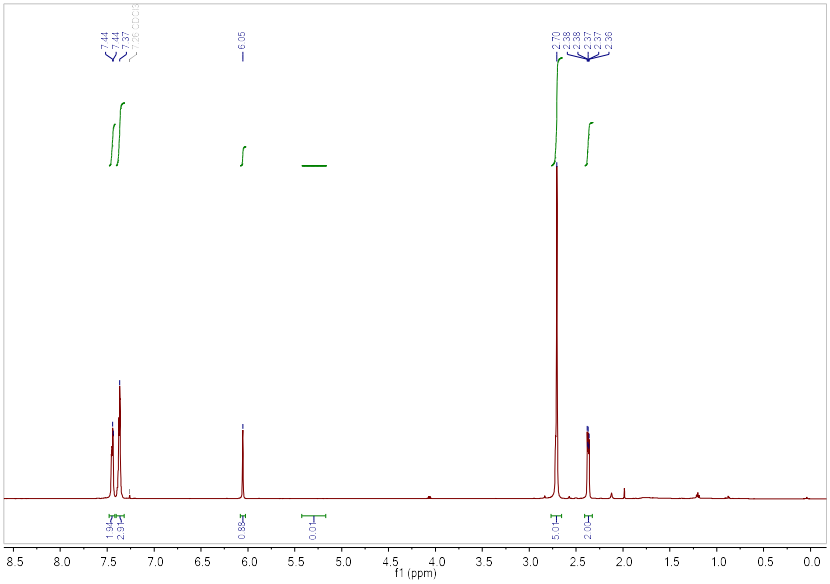

Fig. A50: ^{1}H NMR (500 MHz, Chloroform-*d*) spectrum of **3o**

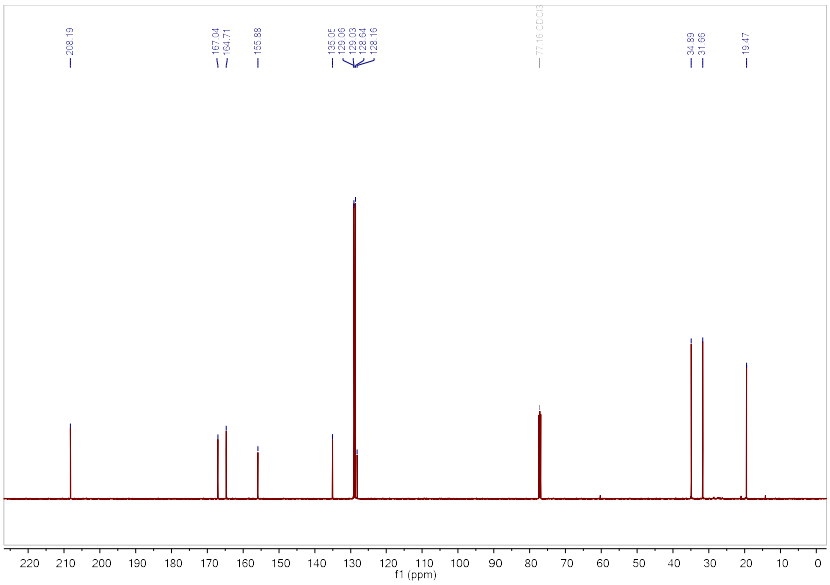

Fig. A51: $^{13}C\{^{1}H\}$ NMR (126 MHz, Chloroform-*d*) spectrum of **3o**

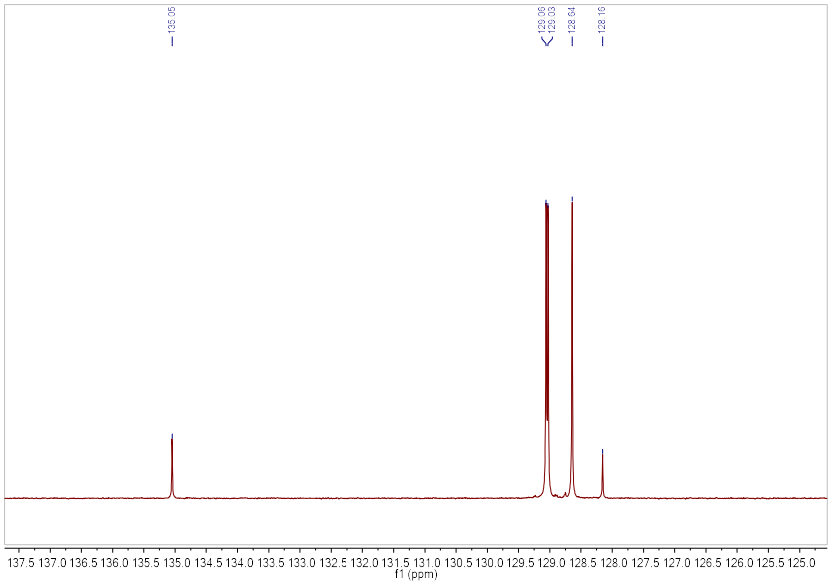

Fig. A52: Expanded (125-140 ppm) $^{13}C\{^{1}H\}$ NMR (126 MHz, Chloroform-*d*) spectrum of **3o**

3p.: 3-(4-methylthiazol-5-yl)cyclopent-2-en-1-one

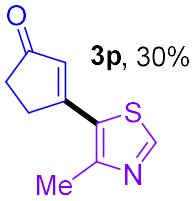

An orange solid was collected (27.2 mg, 30% yield).

Purified by column chromatography (Biotage® Sfär Column, 0-100% EtOAc/hexanes, eluted at 50% EtOAc).

^{1}H-NMR (500 MHz, $CDCl_3$, 292 K, ppm): δ 8.79 (s, 1H), 6.38 (s, 1H), 3.04 – 2.98 (m, 2H), 2.65 (s, 3H), 2.57 – 2.52 (m, 2H).

^{13}C-NMR (126 MHz, $CDCl_3$, 292 K, ppm): δ 208.38, 164.41, 154.88, 153.32, 128.72, 127.99, 34.91, 32.44, 18.42.

HRMS: Calc'd for C_9H_9NOS $[M+H]^+$: 180.04776; found: 180.04776.

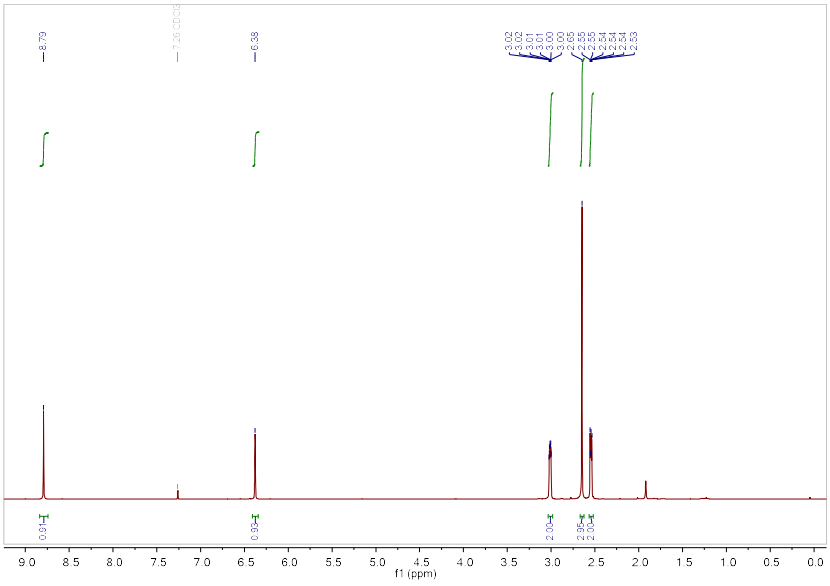

Fig. A53: ^{1}H NMR (500 MHz, Chloroform-*d*) spectrum of **3p**

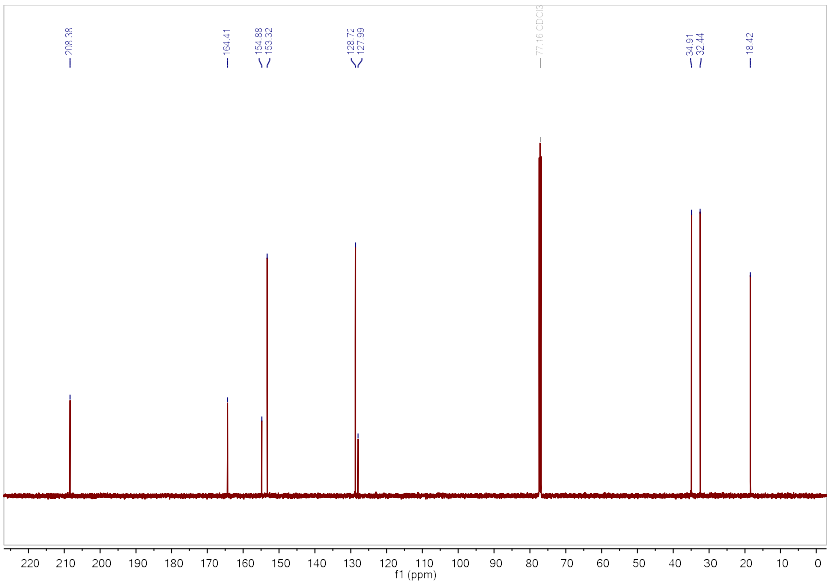

Fig. A54: $^{13}C\{^{1}H\}$ NMR (126 MHz, Chloroform-*d*) spectrum of **3p**

3q. 1-methyl-2-(3-oxocyclopent-1-en-1-yl)-1H-indole-3-carbaldehyde

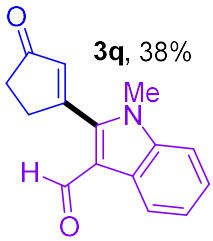

An orange solid was collected (22.7 mg, 38% yield).

Purified by column chromatography (Biotage® Sfär Column, 0-100% EtOAc/hexanes, eluted at 100% EtOAc).

^{1}H-NMR (500 MHz, $CDCl_3$, 292 K, ppm): δ 10.07 (s, 1H), 8.36 (d, J = 7.7, 1H), 7.38 (s, 2H), 7.36 (m, 1H), 6.47 (s, 1H), 3.79 (s, 3H), 3.14 (m, 2H), 2.74 – 2.67 (m, 2H).

^{13}C-NMR (126 MHz, $CDCl_3$, 292 K, ppm): δ 207.49, 184.46, 163.65, 143.66, 138.18, 137.82, 125.66, 125.12, 123.84, 122.20, 116.13, 110.11, 35.55, 33.37, 31.74.

HRMS: Calc'd for $C_{15}H_{13}NO_2$ $[M+H]^+$: 240.10191; found: 240.10187.

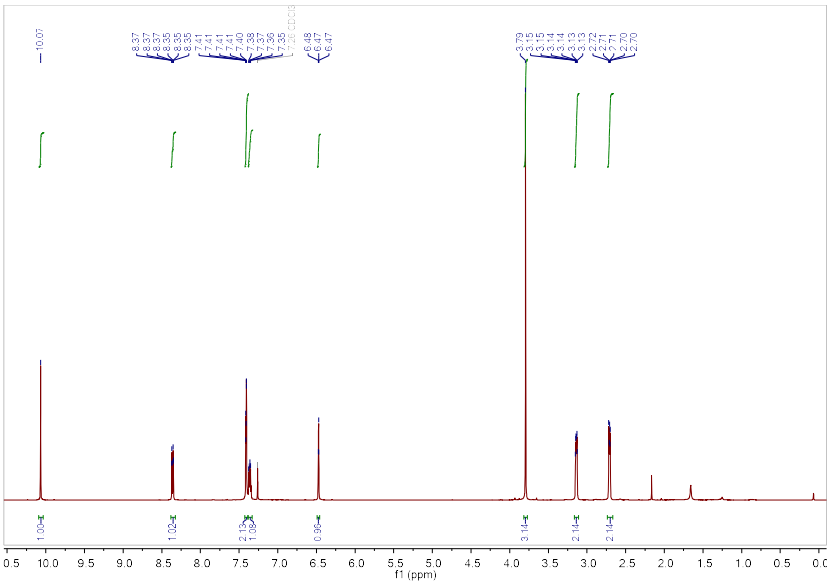

Fig. A55: ^{1}H NMR (500 MHz, Chloroform-*d*) spectrum of **3q**

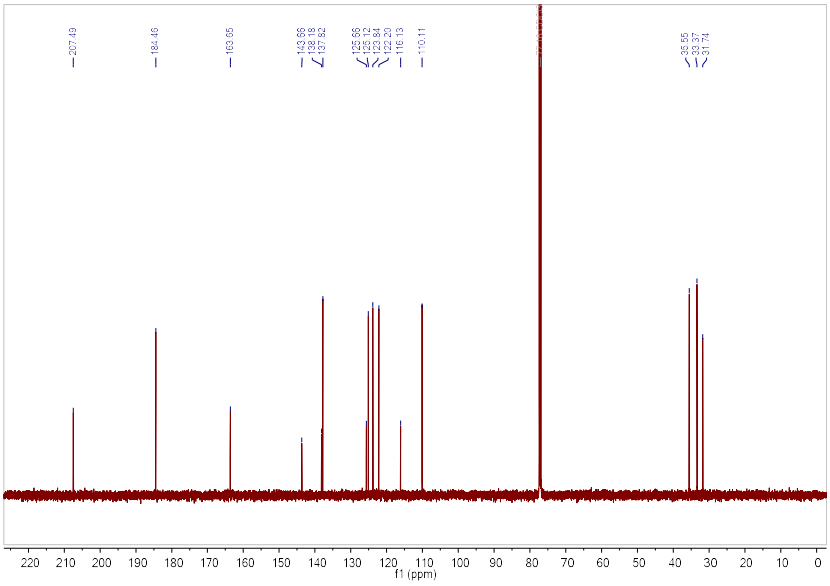

Fig. A56: ^{13}C{^{1}H} NMR (126 MHz, Chloroform-*d*) spectrum of **3q**

3r. 3-(benzo[b]thiophen-2-yl)-2-(2-fluorobenzyl)cyclopent-2-en-1-one

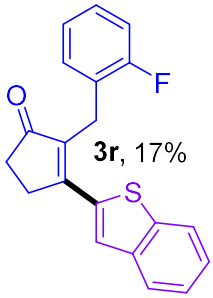

A beige solid was collected (27.6 mg, 17% yield).

Purified by column chromatography (Biotage® Sfär Column, 0-100% EtOAc/hexanes, eluted at 40% EtOAc).

^{1}H-NMR (500 MHz, $CDCl_3$, 292 K, ppm): δ 7.82 (m, 2H), 7.66 (s, 1H), 7.38 (m, 2H), 7.16 (m, 1H), 7.06 (m, 1H), 6.98 (m, 2H), 4.04 (s, 2H), 3.17 (m, 2H), 2.67 (m, 2H).

^{13}C-NMR (126 MHz, $CDCl_3$, 292 K, ppm): δ 206.2, 161.2 (d, J = 246.96 Hz), 160.5, 141.2, 138.9, 137.9, 137.0, 129.2 (d, J = 4.3 Hz), 127.9 (d, J = 8.1 Hz), 126.2, 126.0, 125.0, 124.8 (d, J = 15.7 Hz), 124.7, 124.0 (d, J = 3.5 Hz), 122.4, 115.2 (d, J = 21.9 Hz), 33.9, 29.4, 22.9

^{19}F-NMR (471 MHz, CDCl3, 292K, ppm): δ -116.72.

HRMS: Calc'd for $C_{21}H_{15}FOS$ $[M+H]^+$: 323.09004; found: 323.09002

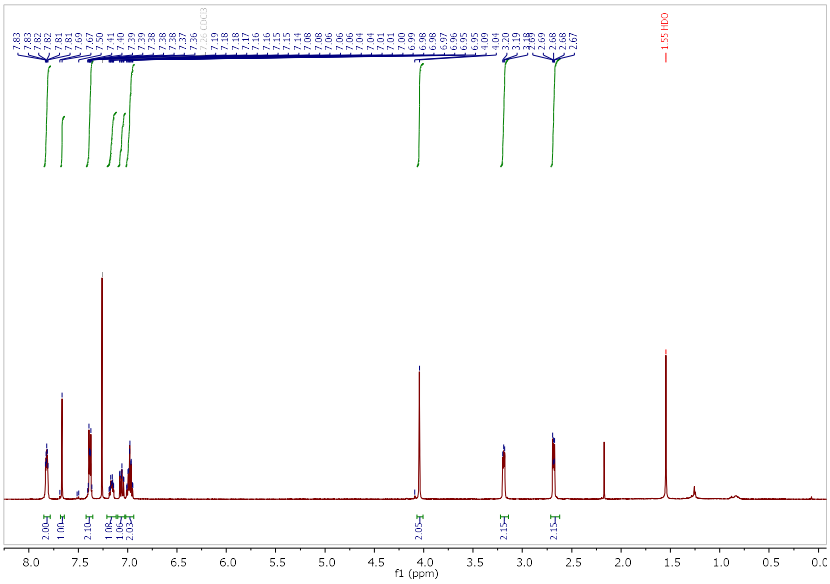

Fig. A57: ^{1}H NMR (500 MHz, Chloroform-*d*) spectrum of **3r**

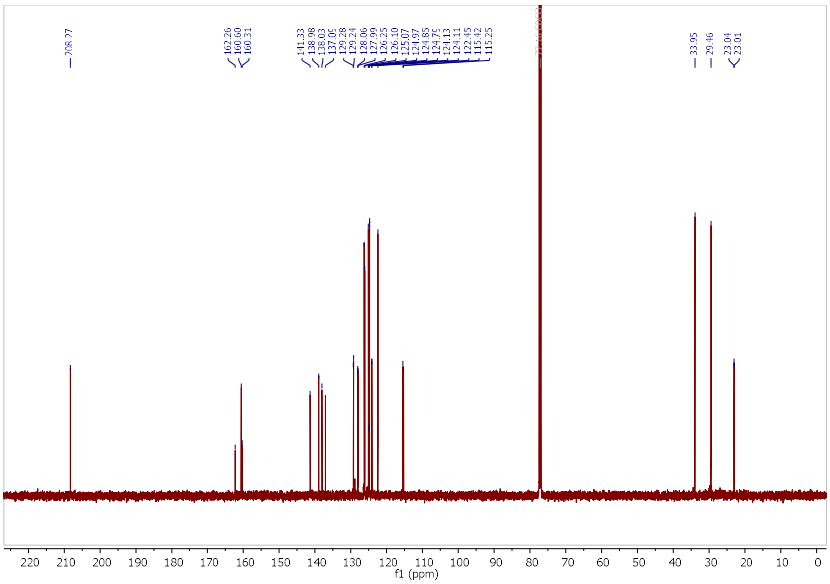

Fig. A58: $^{13}C\{^{1}H\}$ NMR (126 MHz, Chloroform-*d*) spectrum of **3r**

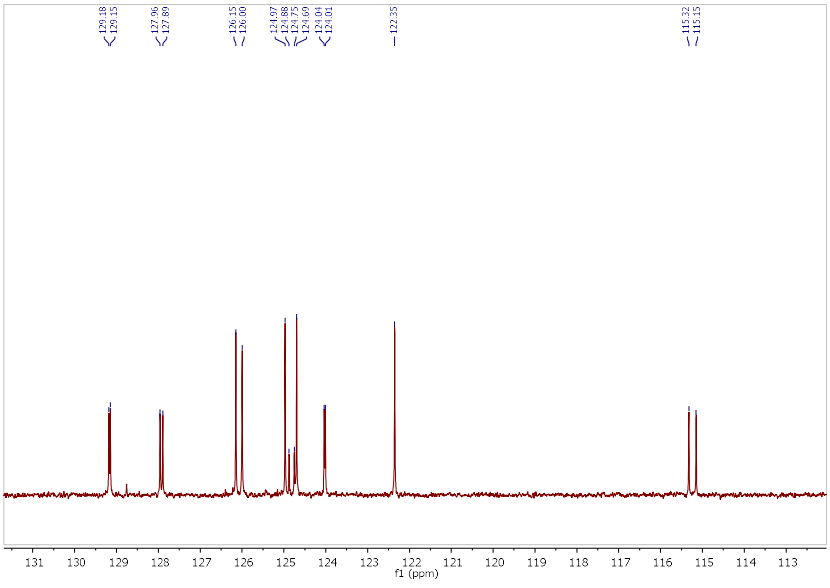

Fig. A59: Expanded (113-131 ppm) $^{13}C\{^{1}H\}$ NMR (126 MHz, Chloroform-*d*) spectrum of **3r**

3s. 2-(2-fluorobenzyl)-3-(4-methylthiazol-5-yl)cyclopent-2-en-1-one

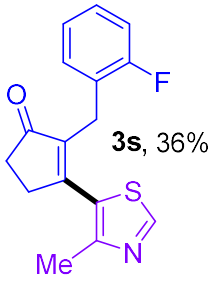

A brown oil was collected (51.7 mg, 36% yield).

Purified by column chromatography (Biotage® Sfär Column, 0-100% EtOAc/hexanes, eluted at 40% EtOAc).

^{1}H-NMR (500 MHz, $CDCl_3$, 292 K, ppm): δ 8.75 (s, 1H), 7.10 (m, 1H), 7.00 (m, 1H), 6.95-6.89 (m, 2H), 3.79 (s, 2H), 2.94 (m, 2H), 2.58 (m, 2H), 2.44 (s, 3H).

^{13}C-NMR (126 MHz, $CDCl_3$, 292 K, ppm): δ 207.5, 160.8 (d, J = 245.7 Hz), 160.7, 153.05, 151.4, 141.3, 130.1 (d, J = 4.2 Hz), 128.0 (d, J = 8.1 Hz), 126.3, 124.8 (d, J= 15.4 Hz), 123.9 (d, J = 3.6 Hz), 115.1 (d, J = 21.9 Hz), 34.3, 32.1, 23.3 (d, J = 3.6 Hz), 17.0.

^{19}F-NMR (471 MHz, CDCl3, 292K, ppm): δ-116.96.

HRMS: Calc'd for $C_{16}H_{14}FNOS$ $[M+H]^+$: 288.08529; found: 288.08521.

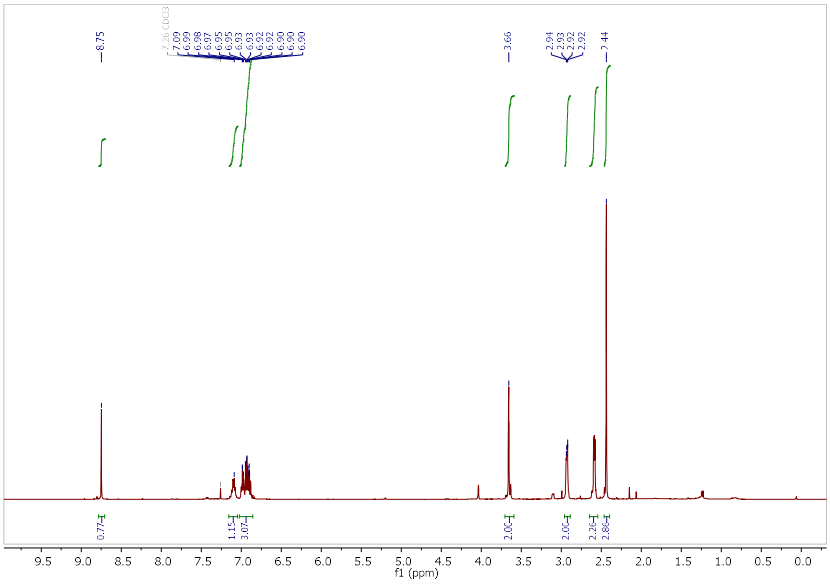

Fig. A60: ^{1}H NMR (500 MHz, Chloroform-*d*) spectrum of **3s**

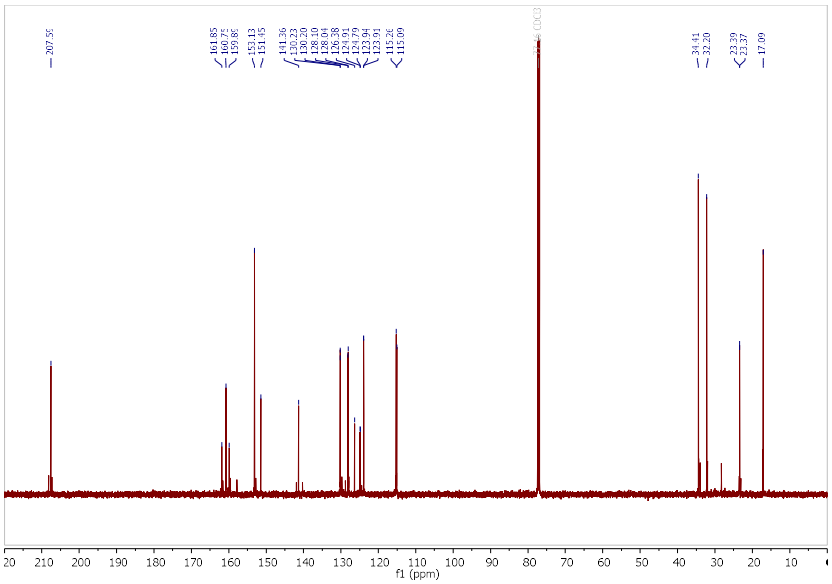

Fig. A61: $^{13}C\{^{1}H\}$ NMR (126 MHz, Chloroform-*d*) spectrum of **3s**

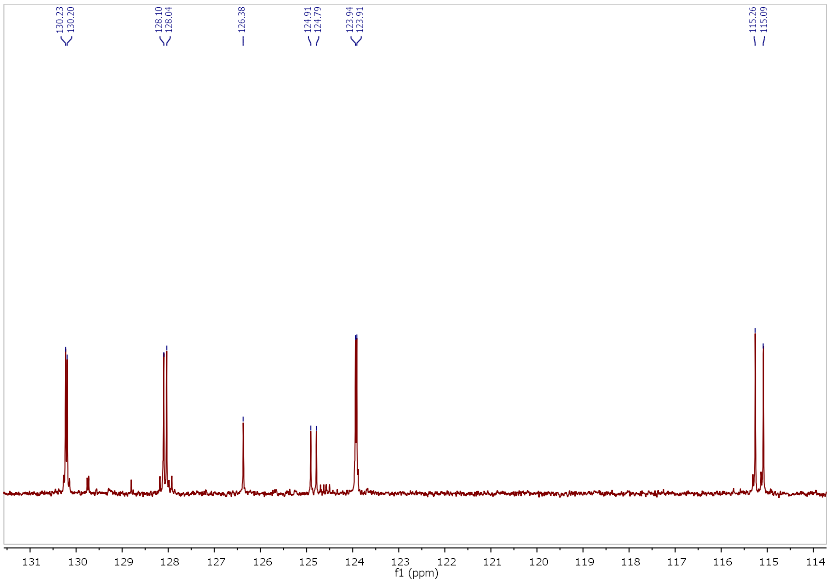

Fig. A62: Expanded (114-132 ppm) $^{13}C\{^{1}H\}$ NMR (126 MHz, Chloroform-*d*) spectrum of **3s**

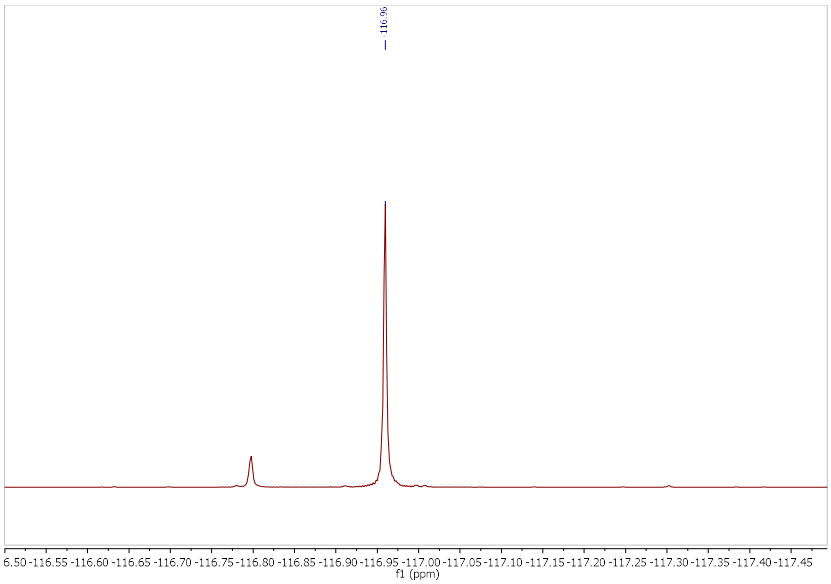

Fig. A63: ^{19}F NMR (283 MHz, Chloroform-*d*) spectrum of **3s**

3t. 3-(benzo[b]thiophen-2-yl)-2-(4-(trifluoromethyl)benzyl)cyclopent-2-en-1-one

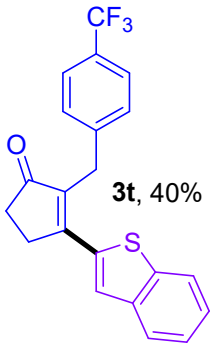

3t, 40%

A beige solid was collected (33.1* mg, 40% yield). *Used the general procedure with 0.22 mmol of enol pivalate. Purified by column chromatography (Biotage® Sfär Column, 0-100% EtOAc/hexanes, eluted at 40% EtOAc).

^{1}H-NMR (500 MHz, $CDCl_3$, 292 K, ppm): δ 7.89 – 7.80 (m, 2H), 7.68 (s, 1H), 7.51 (d, J = 8.1 Hz, 2H), 7.46 – 7.35 (m, 4H), 4.09 (s, 2H), 3.21 – 3.12 (m, 2H), 2.69 – 2.60 (m, 2H).

^{13}C-NMR (126 MHz, $CDCl_3$, 292 K, ppm): δ 208.2, 160.0, 142.3, 141.1, 138.7, 137.6, 137.5, 128.8, 128.6 (q, J = 31.5 Hz), 126.4, 126.2, 125.4 (q, J = 3.9 Hz), 125.15, 124.7, 124.3 (q, J = 272.2 Hz), 122.4, 33.8, 29.9, 29.3.

^{19}F-NMR (471 MHz, CDCl3, 292K, ppm): δ- 62.36.

HRMS: Calc'd for $C_{21}H_{15}F_3OS[M+H]^+$: 373.08685; found: 373.08681.

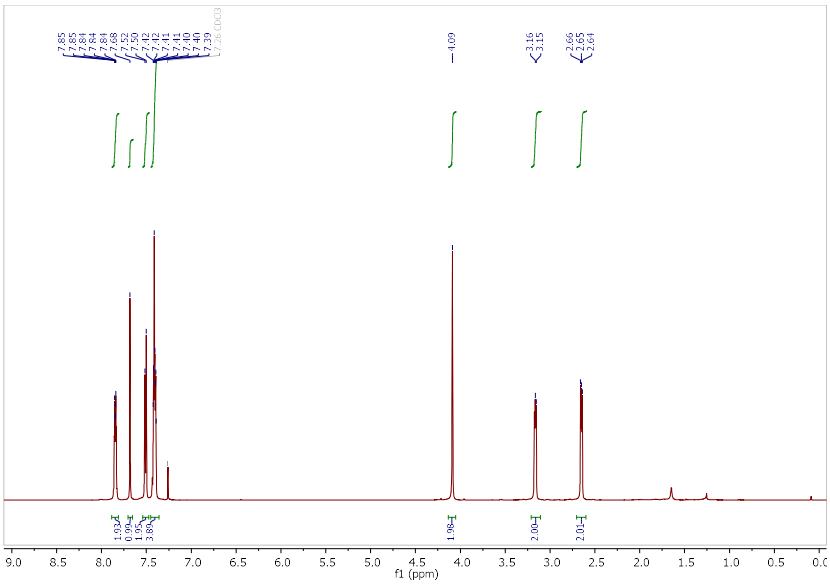

Fig. A64: ^{1}H NMR (500 MHz, Chloroform-*d*) spectrum of **3t**

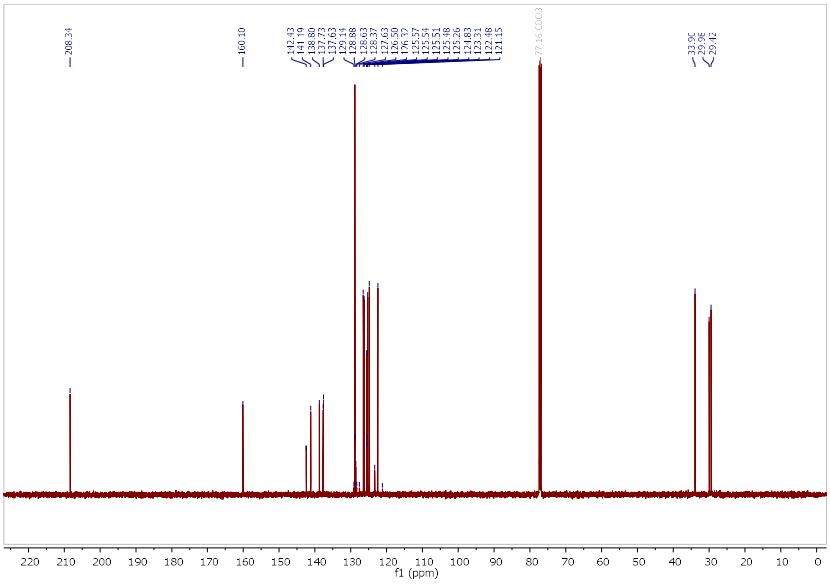

Fig. A65: ^{13}C{^{1}H} NMR (126 MHz, Chloroform-*d*) spectrum of **3t**

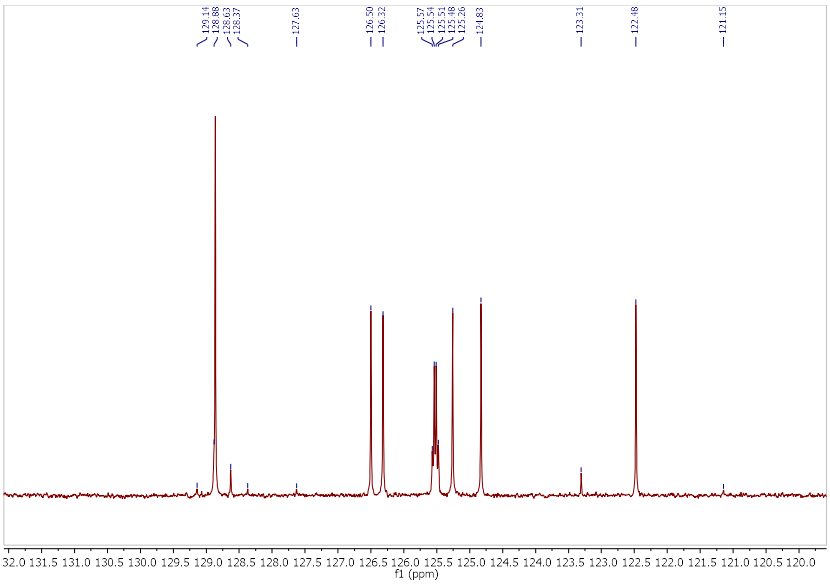

Fig. A66: Expanded (120-132 ppm) $^{13}C\{^{1}H\}$ NMR (126 MHz, Chloroform-*d*) spectrum of **3t**

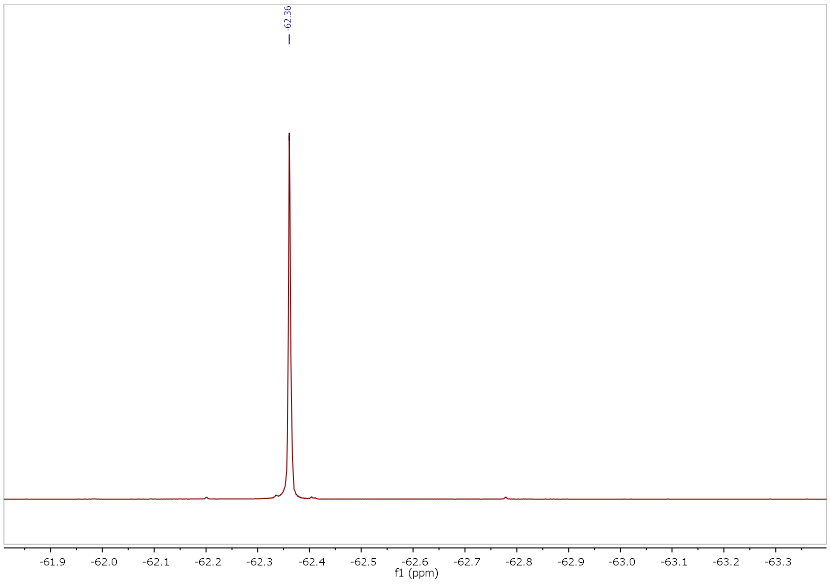

Fig. A67: ^{19}F NMR (283 MHz, Chloroform-*d*) spectrum of **3t**

3u. 4-((2-(benzo[b]thiophen-2-yl)-5-oxocyclopent-1-en-1-yl)methyl)benzonitrile

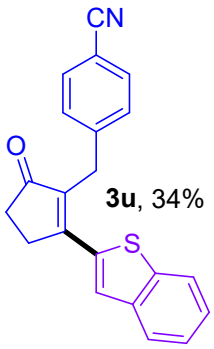

A dark orange solid was collected (55.8 mg, 34% yield).

Purified by column chromatography (Biotage® Sfär Column, 0-100% EtOAc/hexanes, eluted at 40% EtOAc).

^{1}H-NMR (500 MHz, $CDCl_3$, 292 K, ppm): δ 7.87 – 7.79 (m, 2H), 7.68 (s, 1H), 7.54 – 7.48 (m, 2H), 7.45 – 7.35 (m, 4H), 4.07 (s, 2H), 3.20 – 3.13 (m, 2H), 2.68 – 2.60 (m, 2H).

^{13}C-NMR (126 MHz, $CDCl_3$, 292 K, ppm): δ 208.15, 160.33, 143.91, 141.08, 138.63, 137.35, 136.91, 132.30, 129.27, 126.53, 126.42, 125.24, 124.79, 122.37, 119.00, 110.22, 33.77, 30.18, 29.32.

HRMS: Calc'd for $C_{21}H_{15}NOS$ $[M+H]^+$: 330.09471; found: 330.09464.

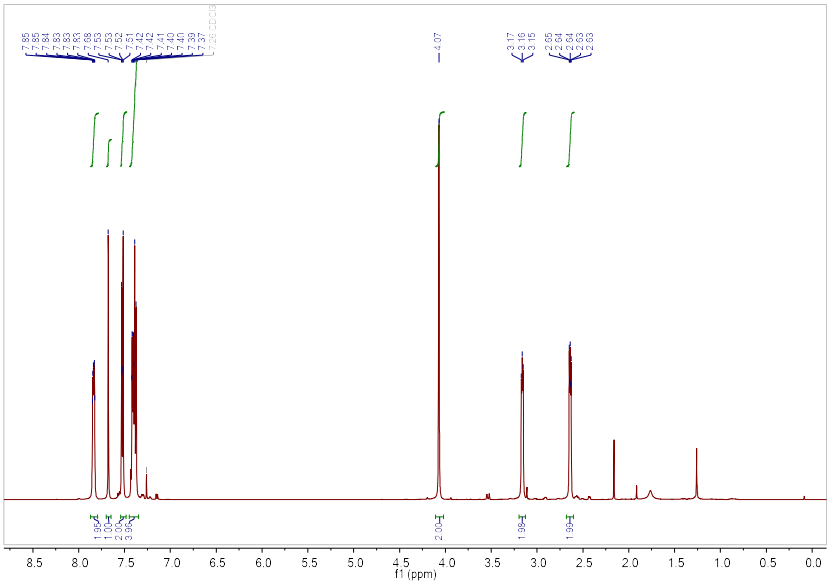

Fig. A68: ^{1}H NMR (500 MHz, Chloroform-*d*) spectrum of **3u**

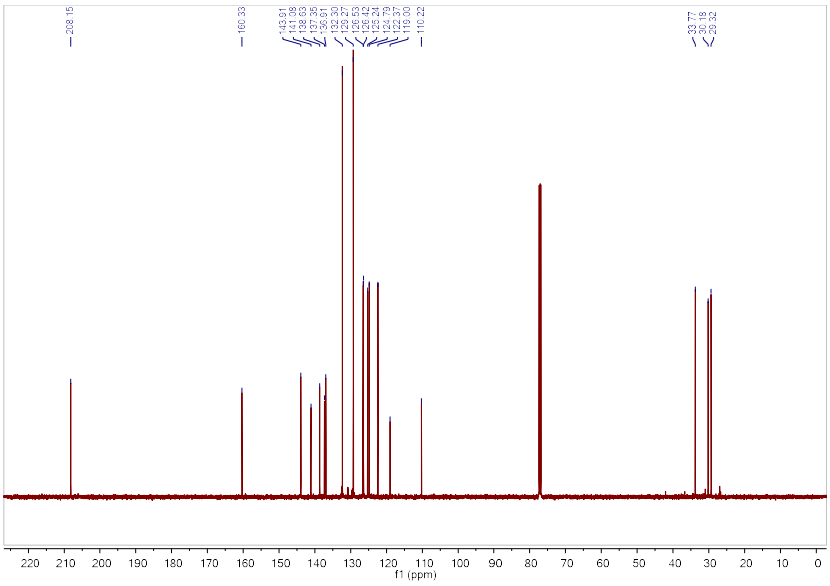

Fig. A69: $^{13}C\{^{1}H\}$ NMR (126 MHz, Chloroform-*d*) spectrum of **3u**

3v. 3-(2-methyl-4-phenylthiazol-5-yl)-2-(3-methylbenzyl)cyclopent-2-en-1-one

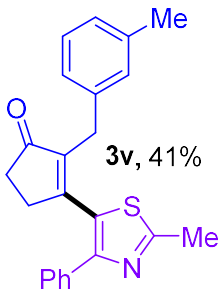

An orange oil was collected (179.7 mg, 41% yield).

Purified by column chromatography (Biotage® Sfär Column, 0-100% EtOAc/hexanes, eluted at 40% EtOAc).

^{1}H-NMR (500 MHz, $CDCl_3$, 292 K, ppm) δ 7.52 – 7.45 (m, 2H), 7.37-7.30 (m, 3H), 7.04 (t, J = 7.6 Hz, 1H), 6.92 (d, J = 7.6 Hz, 1H), 6.84 – 6.78 (m, 2H), 3.47 (s, 2H), 2.75 (s, 3H), 2.70-2.64 (m, 2H), 2.51 – 2.45 (m, 2H), 2.23 (s, 3H).

^{13}C-NMR (126 MHz, $CDCl_3$, 292 K, ppm): δ 208.06, 166.24, 160.67, 152.74, 142.97, 138.20, 137.89, 134.83, 129.33, 128.68, 128.64, 128.40, 128.24, 126.95, 126.33, 125.52, 34.43, 30.92, 29.63, 21.40, 19.31.

HRMS: Calc'd for $C_{23}H_{21}NOS$ $[M+H]^+$: 360.14166 ; found:360.14151.

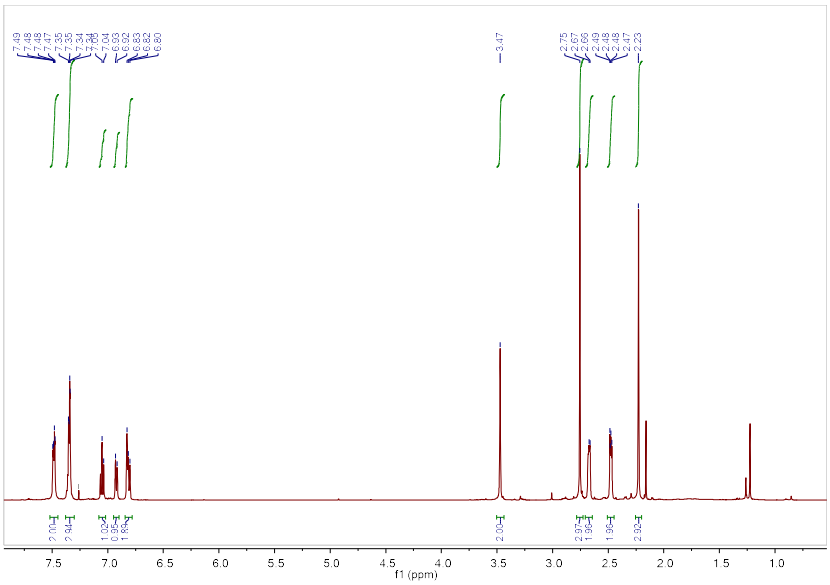

Fig. A70: ^{1}H NMR (500 MHz, Chloroform-*d*) spectrum of **3v**

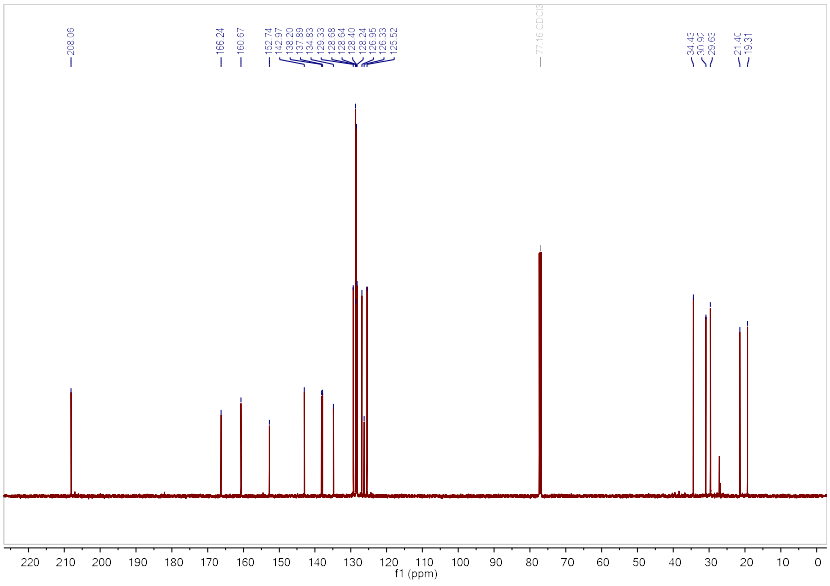

Fig. A71: ^{13}C{^{1}H} NMR (126 MHz, Chloroform-*d*) spectrum of **3v**

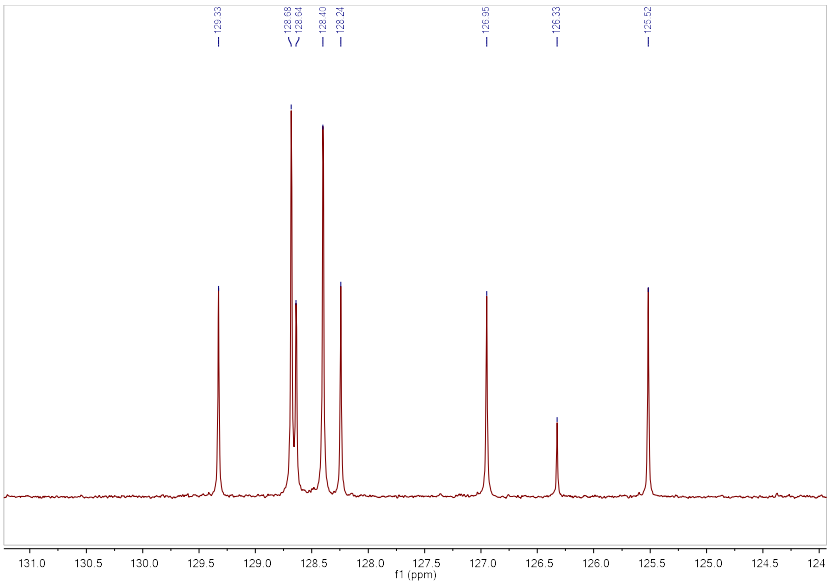

Fig. A72: Expanded (124-131 ppm) $^{13}C\{^{1}H\}$ NMR (126 MHz, Chloroform-*d*) spectrum of **3v**

3w. 3-(benzo[b]thiophen-2-yl)-2-(3-methylbenzyl)cyclopent-2-en-1-one

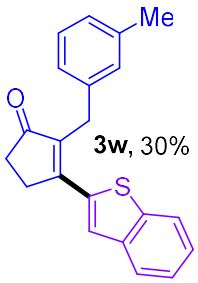

3w, 30%

A beige solid was collected (23.6* mg, 30 % yield) *Used the general procedure with 0.25 mmol of enol pivalate.

Purified by column chromatography (Biotage® Sfär Column, 0-100% EtOAc/hexanes, eluted at 30% EtOAc).

^{1}H-NMR (500 MHz, $CDCl_3$, 292 K, ppm): δ 7.87 – 7.80 (m, 2H), 7.67 (s, 1H), 7.43 – 7.36 (m, 2H), 7.14 (t, J = 7.5 Hz, 1H), 7.11 – 7.06 (m, 2H), 7.00 (d, J = 7.5 Hz, 1H), 4.01 (s, 2H), 3.16 – 3.10 (m, 2H), 2.68 – 2.61 (m, 2H), 2.30 (s, 3H).

^{13}C-NMR (126 MHz, $CDCl_3$, 292 K, ppm): δ 208.55, 159.49, 141.19, 138.95, 138.76, 138.28, 138.18, 138.09, 129.27, 128.45, 127.20, 126.19, 126.01, 125.50, 125.06, 124.71, 122.46, 33.98, 29.99, 29.39, 21.61.

HRMS: Calc'd for $C_{21}H_{18}$ $[M+H]^+$: 319.11512; found: 319.11507.

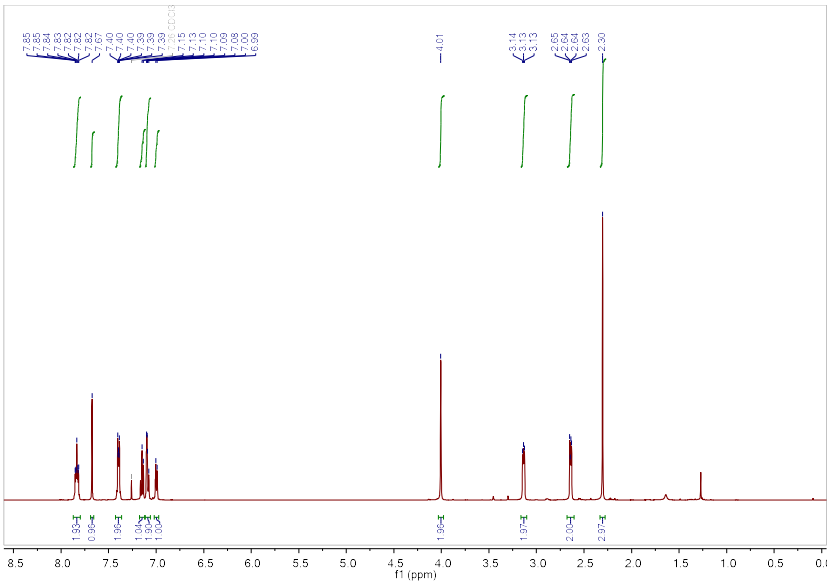

Fig. A73: ^{1}H NMR (500 MHz, Chloroform-*d*) spectrum of **3w**

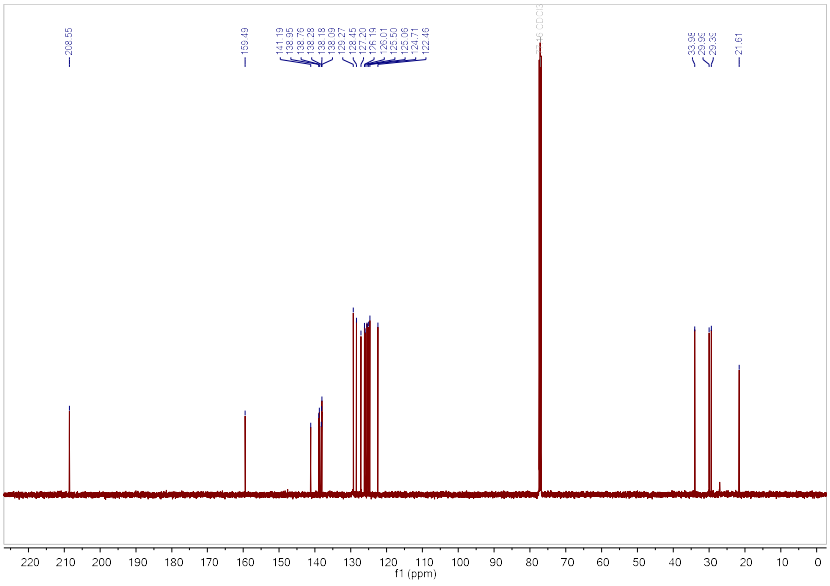

Fig. A74: ^{13}C{^{1}H} NMR (126 MHz, Chloroform-*d*) spectrum of **3w**

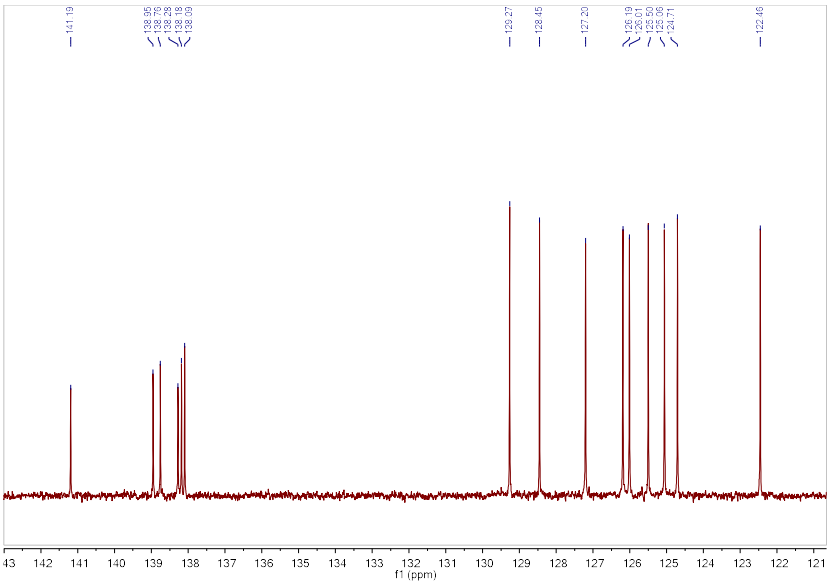

Fig. A75: Expanded (121-143 ppm) $^{13}C\{^{1}H\}$ NMR (126 MHz, Chloroform-*d*) spectrum of **3w**

3x. 4-(benzo[*b*]thiophen-2-yl)-3-phenylfuran-2(5*H*)-one:

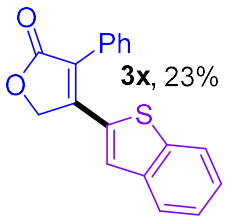

A yellow solid was collected (34.2 mg, 23% yield).

Purified by column chromatography (Biotage® Sfär Column, 0-100% EtOAc/hexanes, eluted at 25% EtOAc).

^{1}H-NMR (500 MHz, $CDCl_3$, 292 K, ppm): δ 7.80 – 7.75 (m, 1H), 7.74 – 7.70 (m, 1H), 7.50 (m, 6H), 7.40 – 7.34 (m, 2H), 5.31 (s, 2H).

^{13}C-NMR (126 MHz, $CDCl_3$, 292 K, ppm): δ 173.24, 149.79, 141.05, 138.52, 132.60, 129.84, 129.69, 129.66, 128.98, 126.74, 126.48, 125.93, 125.25, 124.70, 122.45, 70.28.

HRMS: Calc'd for $C_{18}H_{12}O_2S$ $[M+H]^+$: 293.06308; found: 293.06300.

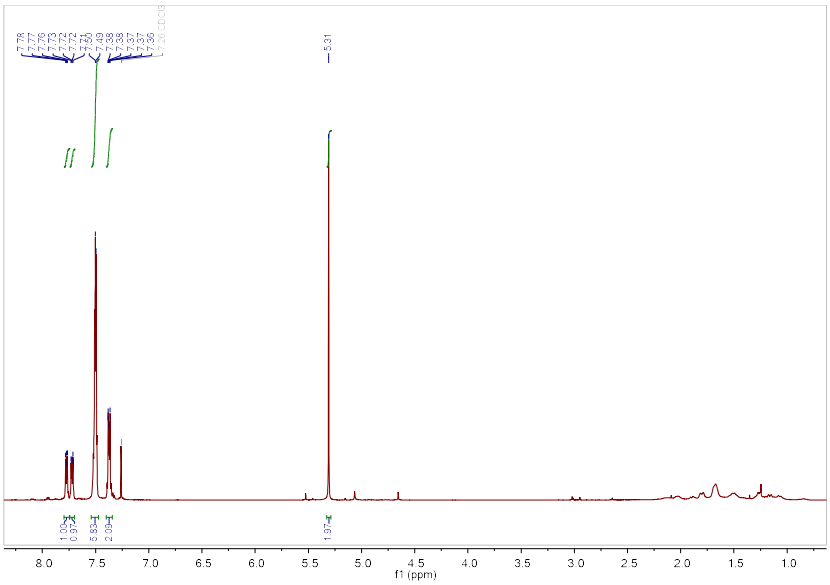

Fig. A76: ^{1}H NMR (500 MHz, Chloroform-*d*) spectrum of **3x**

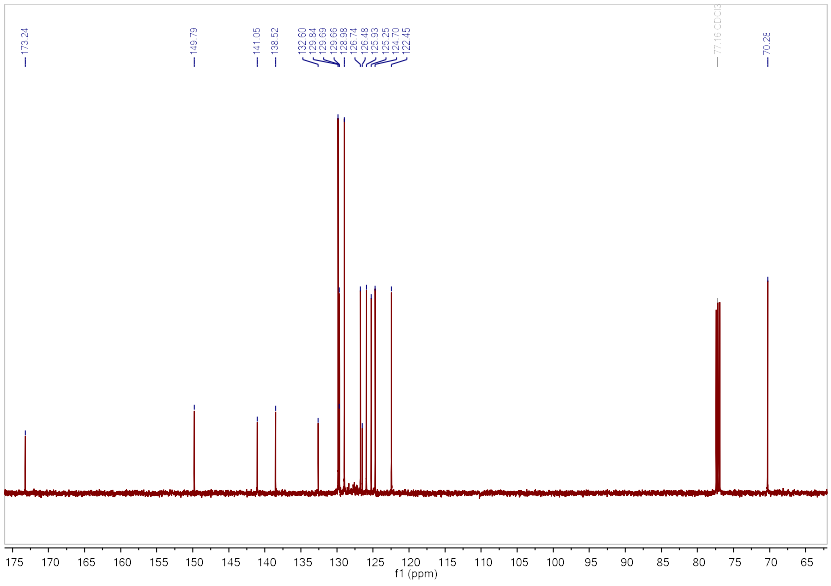

Fig. A77: ^{13}C{^{1}H} NMR (126 MHz, Chloroform-*d*) spectrum of **3x**

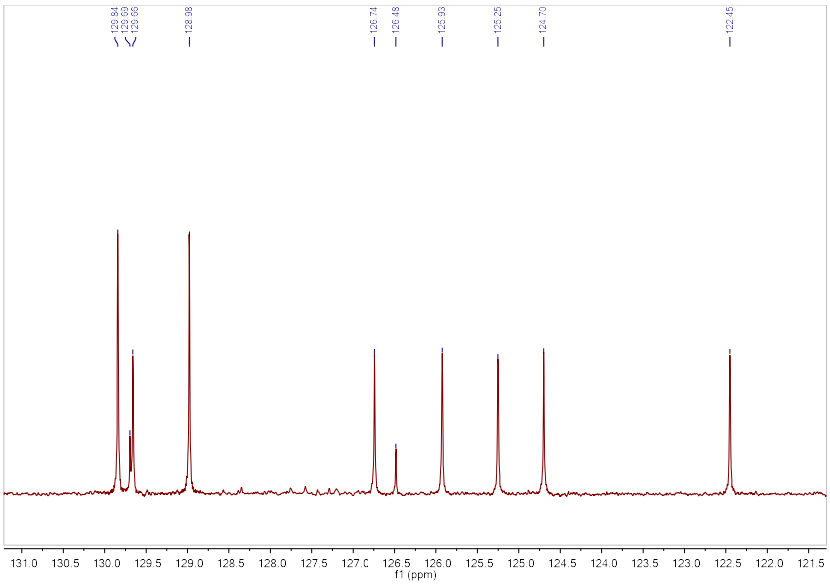

Fig. A78: Expanded (121-131 ppm) $^{13}C\{^{1}H\}$ NMR (126 MHz, Chloroform-*d*) spectrum of **3x**

3y. Ethyl 5-(5-oxo-4-phenyl-2,5-dihydrofuran-3-yl)thiophene-2-carboxylate

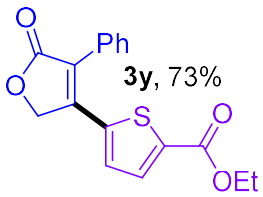

A white solid was collected (115.4 mg, 73% yield).

Purified by column chromatography (Biotage® Sfär Column, 0-100% EtOAc/hexanes, eluted at 30% EtOAc).

^{1}H-NMR (500 MHz, $CDCl_3$, 292 K, ppm): δ 7.64 (d, J = 4.0 Hz, 1H), 7.45 (m, 5H), 7.17 (d, J = 4.1 Hz, 1H), 5.18 (s, 2H), 4.30 (q, J = 7.1 Hz, 2H), 1.32 (t, J = 7.1 Hz, 3H).

^{13}C-NMR (126 MHz, $CDCl_3$, 292 K, ppm): δ 172.76, 161.43, 148.57, 138.12, 137.21, 133.05, 129.72, 129.38, 129.29, 129.11, 128.96, 126.73, 69.95, 61.76, 14.27.

HRMS: Calc'd for $C_{17}H_{14}O_4S$ $[M+H]^+$: 315.06856; found: 315.06838.

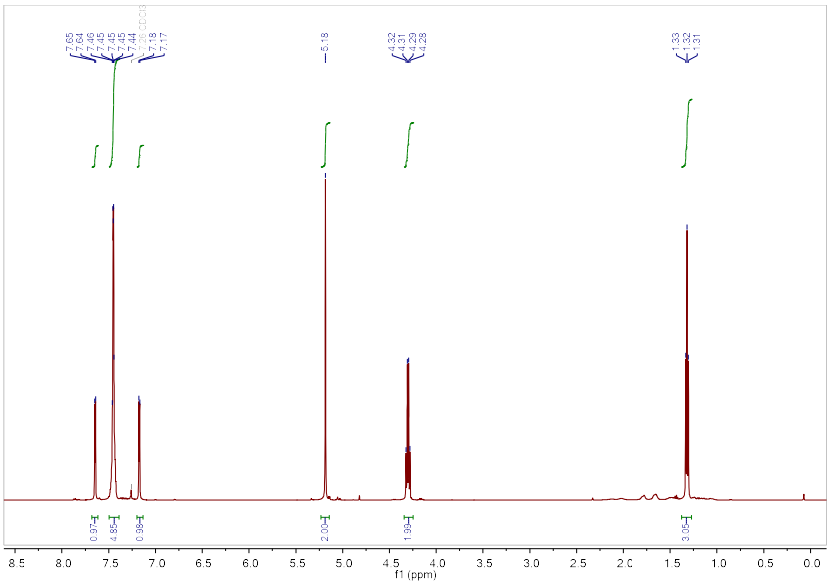

Fig. A79: ^{1}H NMR (500 MHz, Chloroform-*d*) spectrum of **3y**

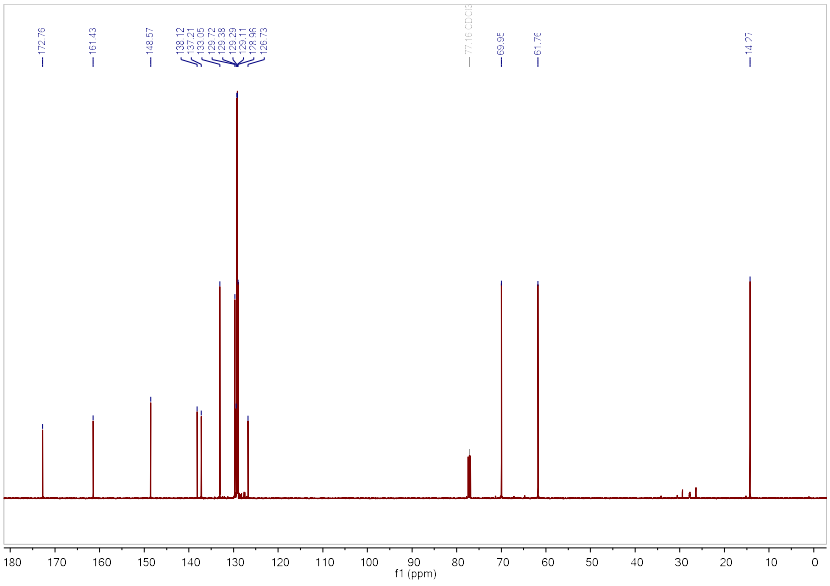

Fig. A80: ^{13}C{^{1}H} NMR (126 MHz, Chloroform-*d*) spectrum of **3y**

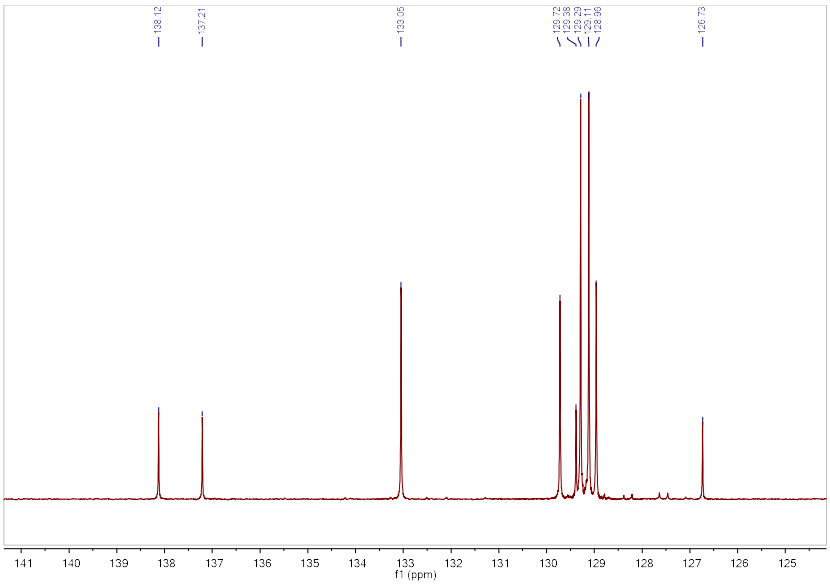

Fig. A81: Expanded (125-141 ppm) $^{13}C\{^{1}H\}$ NMR (126 MHz, Chloroform-*d*) spectrum of **3y**

3z. 4-(benzo[*b*]thiophen-2-yl)-1-benzyl-3-phenyl-1,5-dihydro-2*H*-pyrrol-2-one:

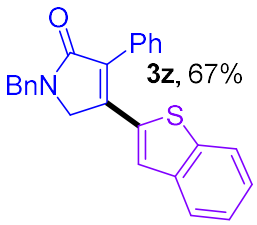

An orange solid was collected (127.9 mg, 67% yield).

Purified by column chromatography (Biotage® Sfär Column, 0-100% EtOAc/hexanes, eluted at 50% EtOAc).

^{1}H-NMR (500 MHz, $CDCl_3$, 292 K, ppm): δ 7.56 – 7.51 (m, 2H), 7.44 – 7.39 (m, 2H), 7.39 – 7.31 (m, 3H), 7.26 (s, 4H), 7.23 – 7.14 (m, 4H), 4.66 (s, 2H), 4.20 (s, 2H).

^{13}C-NMR (126 MHz, $CDCl_3$, 292 K, ppm): δ 170.49, 141.32, 140.37, 138.81, 137.22, 135.34, 133.31, 131.45, 130.04, 128.99, 128.97, 128.68, 128.41, 127.85, 125.75, 124.81, 124.06, 122.25, 51.84, 46.66.

HRMS: Calc'd for $C_{25}H_{19}NOS$ $[M+H]^+$: 382.12601; found: 382.12582.

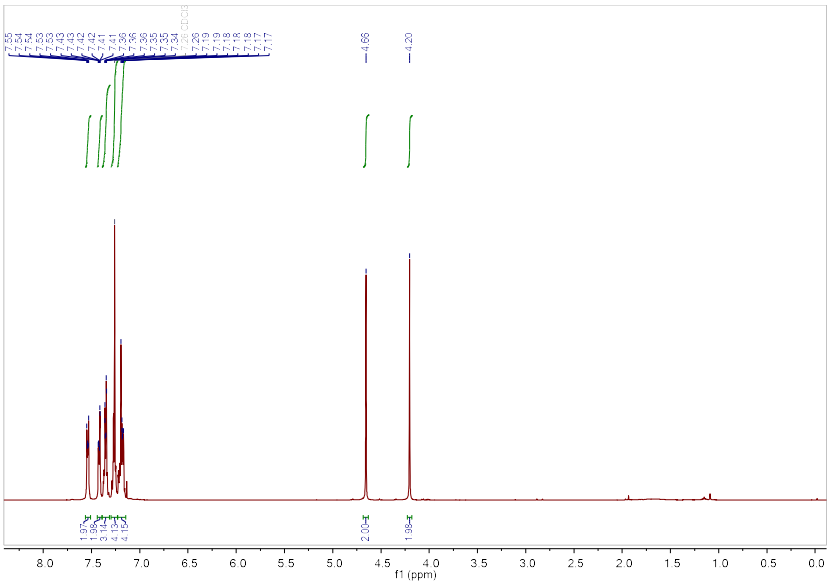

Fig. A82: ^{1}H NMR (500 MHz, Chloroform-*d*) spectrum of **3z**

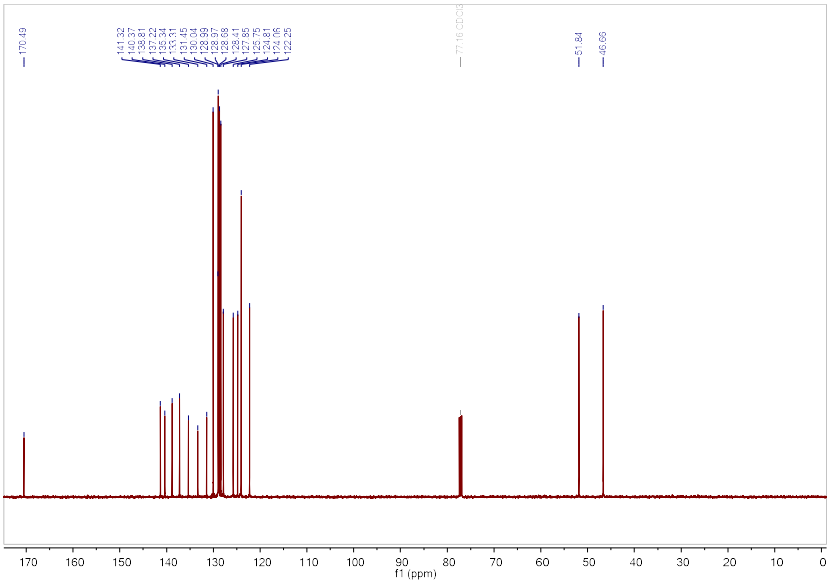

Fig. A83: ^{13}C{^{1}H} NMR (126 MHz, Chloroform-*d*) spectrum of **3z**

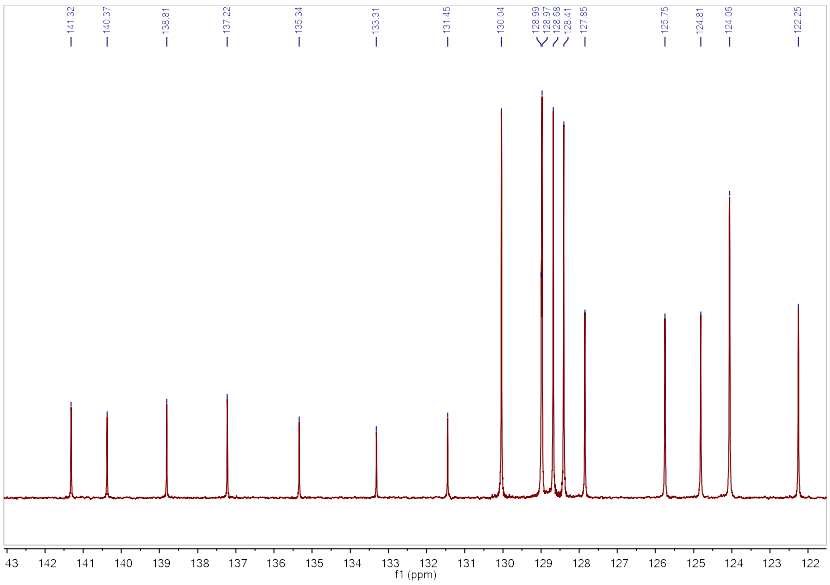

Fig. A84: Expanded (122-143 ppm) $^{13}C\{^{1}H\}$ NMR (126 MHz, Chloroform-*d*) spectrum of **3z**

3aa. ethyl 5-(1-benzyl-5-oxo-4-phenyl-2,5-dihydro-1H-pyrrol-3-yl)thiophene-2-carboxylate:

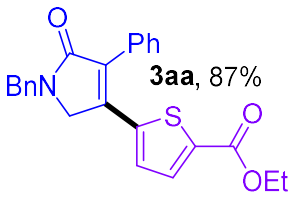

A yellow oil was collected (175.0 mg, 87% yield).

Purified by column chromatography (Biotage® Sfär Column, 0-100% EtOAc/hexanes, eluted at 50% EtOAc).

^{1}H-NMR (500 MHz, $CDCl_3$, 292 K, ppm): δ 7.57 (d, J = 4.0 Hz, 1H), 7.46 (m, 5H), 7.35 (m, H), 7.01 (d, J = 4.0 Hz, 1H), 4.74 (s, 2H), 4.29 (q, J = 7.1 Hz, 2H), 4.23 (s, 2H), 1.31 (t, J = 7.1 Hz, 3H).

^{13}C-NMR (126 MHz, $CDCl_3$, 292 K, ppm): δ 170.17, 161.78, 141.33, 140.20, 136.97, 135.02, 133.69, 133.09, 131.17, 129.52, 129.13, 128.95, 128.89, 128.36, 127.86, 127.48, 61.49, 51.67, 46.61, 14.31.

HRMS: Calc'd for $C_{21}H_{18}N_2OS$ $[M+H]^+$: 347.12126; found: 347.12109.

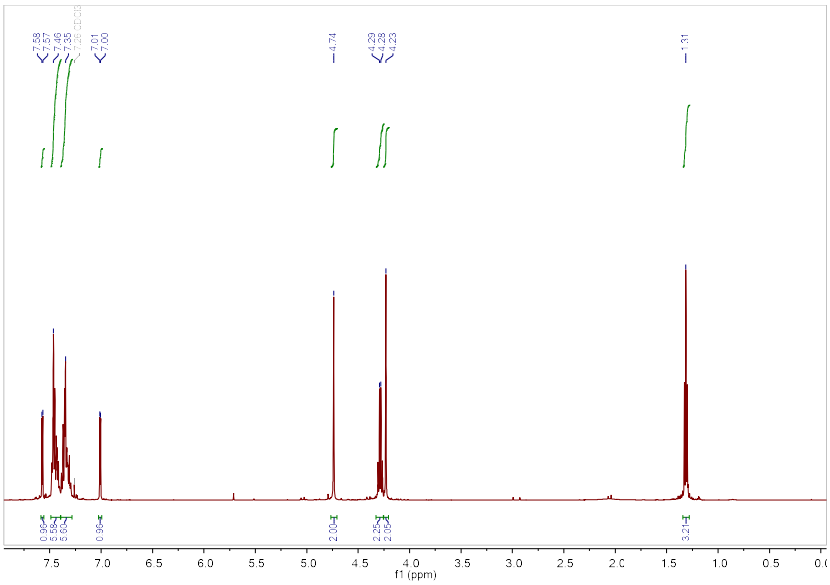

Fig. A85: ^{1}H NMR (500 MHz, Chloroform-*d*) spectrum of **3aa**

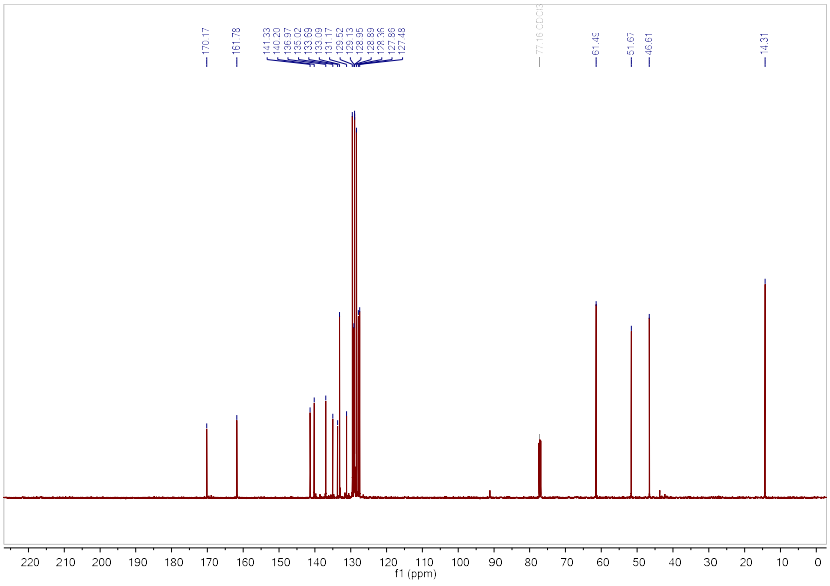

Fig. A86: ^{13}C{^{1}H} NMR (126 MHz, Chloroform-*d*) spectrum of **3aa**

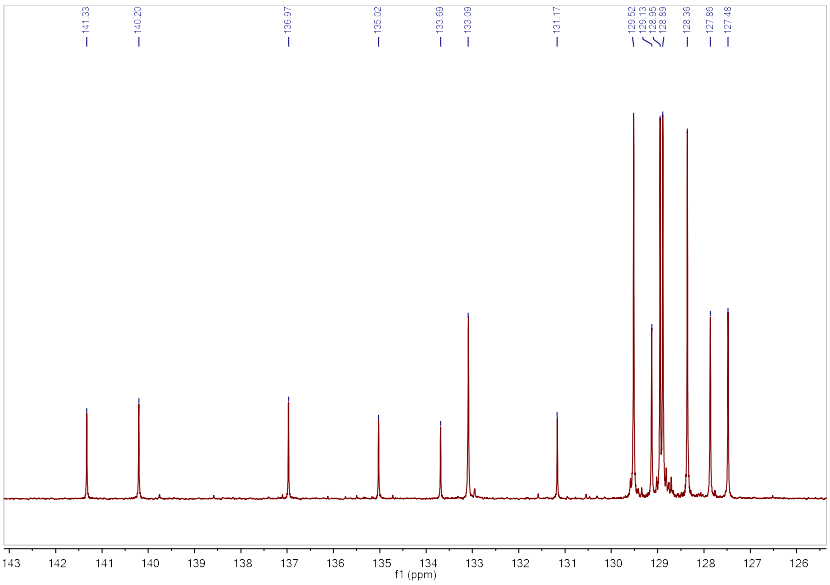

Fig. A87: Expanded (126-143 ppm) $^{13}C\{^{1}H\}$ NMR (126 MHz, Chloroform-*d*) spectrum of **3aa**

3ab. 4-(5-acetylthiophen-2-yl)-1-benzyl-3-phenyl-1,5-dihydro-2H-pyrrol-2-one

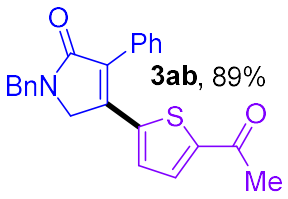

An orange solid was collected (167.8 mg, 89% yield).

Purified by column chromatography (Biotage® Sfär Column, 0-100% EtOAc/hexanes, eluted at 50% EtOAc).

^{1}H-NMR (500 MHz, $CDCl_3$, 292 K, ppm): δ 7.49 – 7.27 (m, 11H), 7.03 (d, J = 4.0 Hz, 1H), 4.73 (s, 2H), 4.23 (s, 2H), 2.45 (s, 3H).

^{13}C-NMR (126 MHz, $CDCl_3$, 292 K, ppm): δ 190.37, 169.92, 144.83, 142.62, 140.02, 136.90, 134.18, 132.20, 131.08, 129.41, 129.11, 128.87, 128.81, 128.28, 127.83, 127.79, 51.57, 46.51, 26.73.

HRMS: Calc'd for $C_{23}H_{19}NO_2S$ $[M+H]^+$: 374.12093; found: 374.02073.

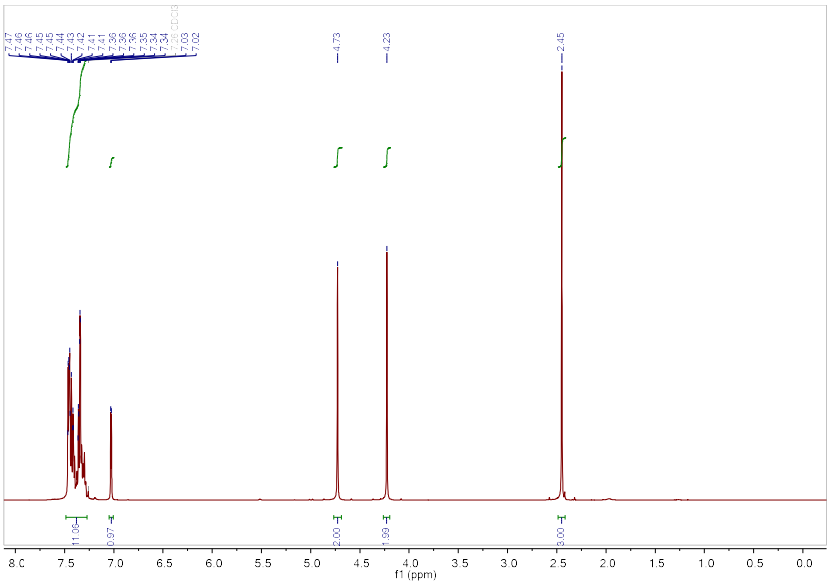

Fig. A88: ^{1}H NMR (500 MHz, Chloroform-*d*) spectrum of **3ab**

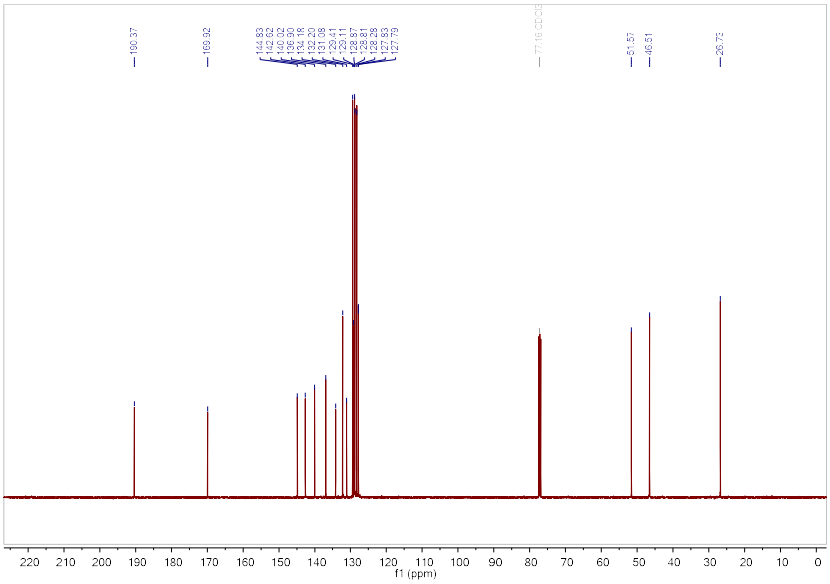

Fig. A89: ^{13}C{^{1}H} NMR (126 MHz, Chloroform-*d*) spectrum of **3ab**

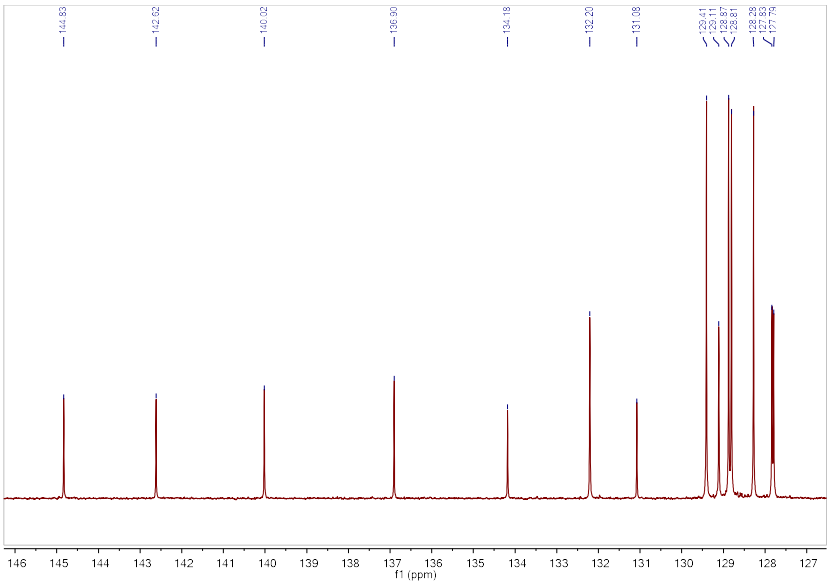

Fig. A90: Expanded (127-146 ppm) $^{13}C\{^{1}H\}$ NMR (126 MHz, Chloroform-*d*) spectrum of **3ab**

3ac. 1-benzyl-4-(2-methyl-4-phenylthiazol-5-yl)-3-phenyl-1,5-dihydro-2H-pyrrol-2-one

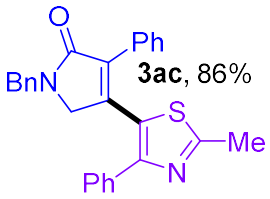

An orange solid was collected (201.8 mg, 86% yield).

Purified by column chromatography (Biotage® Sfär Column, 0-100% EtOAc/hexanes, eluted at 30% EtOAc).

^{1}H-NMR (500 MHz, $CDCl_3$, 292 K, ppm): δ 7.51 (m, 4H), 7.37 – 7.23 (m, 9H), 7.22 (m, 2H), 4.65 (s, 2H), 3.84 (s, 2H), 2.65 (s, 3H).

^{13}C-NMR (126 MHz, $CDCl_3$, 292 K, ppm): δ 169.68, 166.52, 153.33, 139.95, 137.05, 135.73, 134.43, 130.87, 129.48, 128.81, 128.69, 128.66, 128.59, 128.44, 128.37, 128.09, 127.67, 123.64, 52.01, 46.37, 27.17, 19.30.

HRMS: Calc'd for $C_{27}H_{22}N_2OS$ $[M+H]^+$: 423.15256; found: 423.15244.

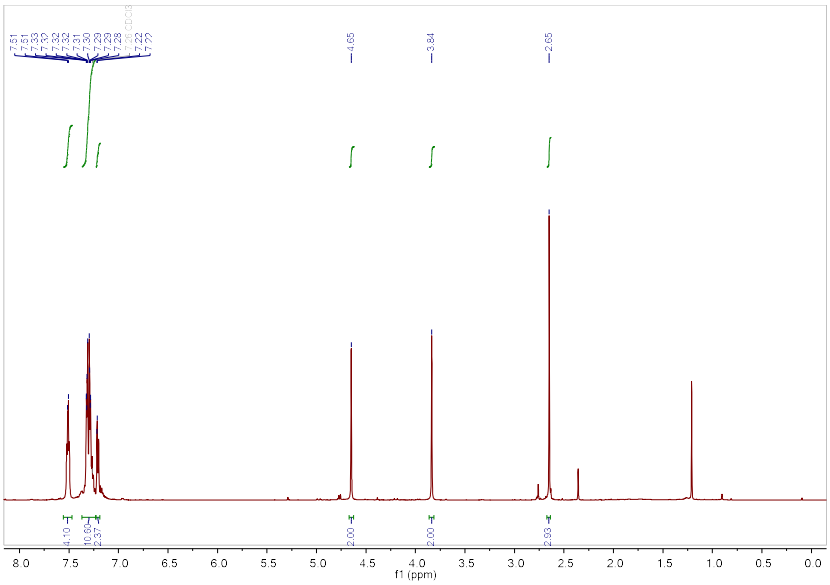

Fig. A91: ^{1}H NMR (500 MHz, Chloroform-*d*) spectrum of **3ac**

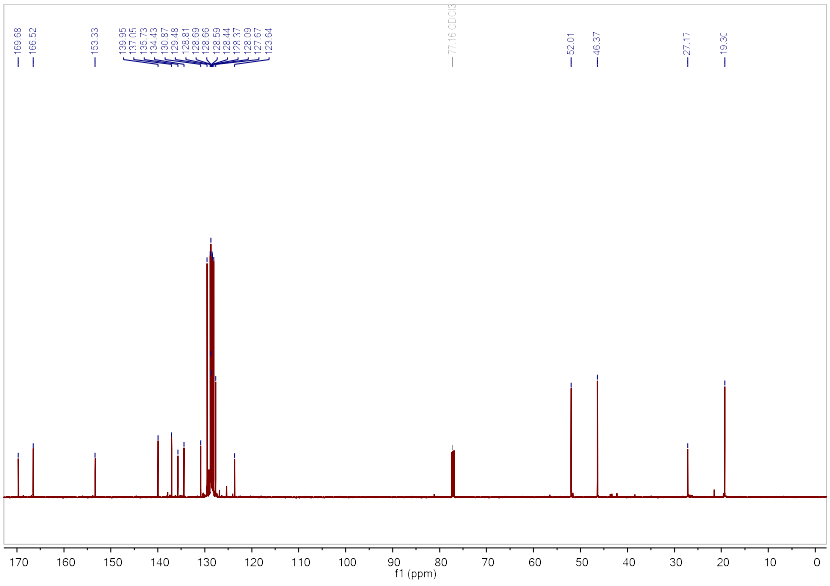

Fig. A92: ^{13}C{^{1}H} NMR (126 MHz, Chloroform-*d*) spectrum of **3ac**

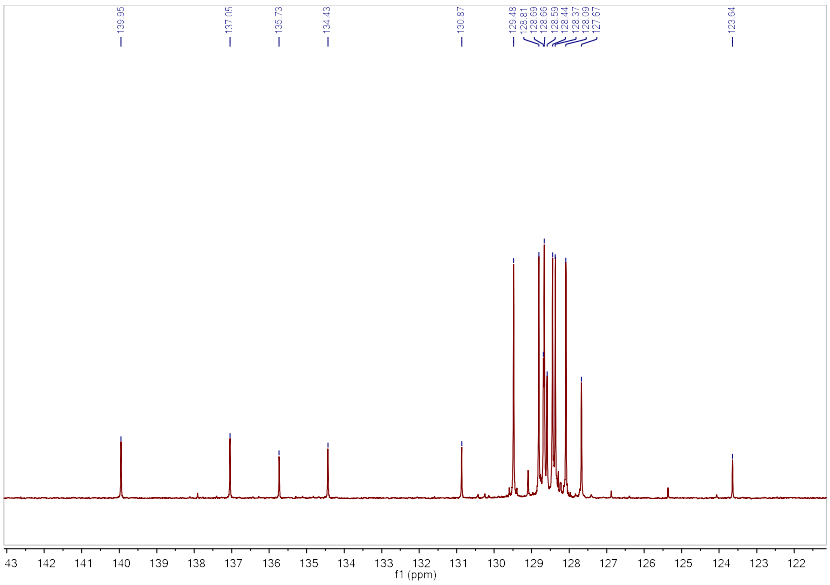

Fig. A93: Expanded (122-143 ppm) $^{13}C\{^{1}H\}$ NMR (126 MHz, Chloroform-*d*) spectrum of **3ac**

3ad. 1-benzyl-4-(4-methylthiazol-5-yl)-3-phenyl-1,5-dihydro-2H-pyrrol-2-one:

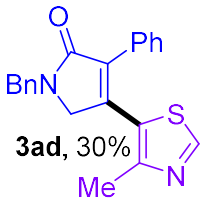

A yellow solid was collected (51.5 mg, 30% yield).

Purified by column chromatography (Biotage® Sfär Column, 0-100% EtOAc/hexanes, eluted at 50% EtOAc).

^{1}H-NMR (500 MHz, $CDCl_3$, 292 K, ppm): δ 7.47 (m, 6H), 7.35 (m, 4zH), 6.81 (s, 1H), 4.76 (s, 2H), 4.46 (s, 2H), 2.40 (s, 3H).

^{13}C-NMR (126 MHz, $CDCl_3$, 292 K, ppm): δ 170.16, 158.99, 153.33, 141.91, 137.23, 135.89, 131.13, 129.69, 129.38, 129.08, 128.95, 128.57, 127.86, 116.27, 51.60, 46.80, 17.00.

HRMS: Calc'd for $C_{24}H_{21}NO_3S$ $[M+H]^+$: 404.13149; found: 404.13142.

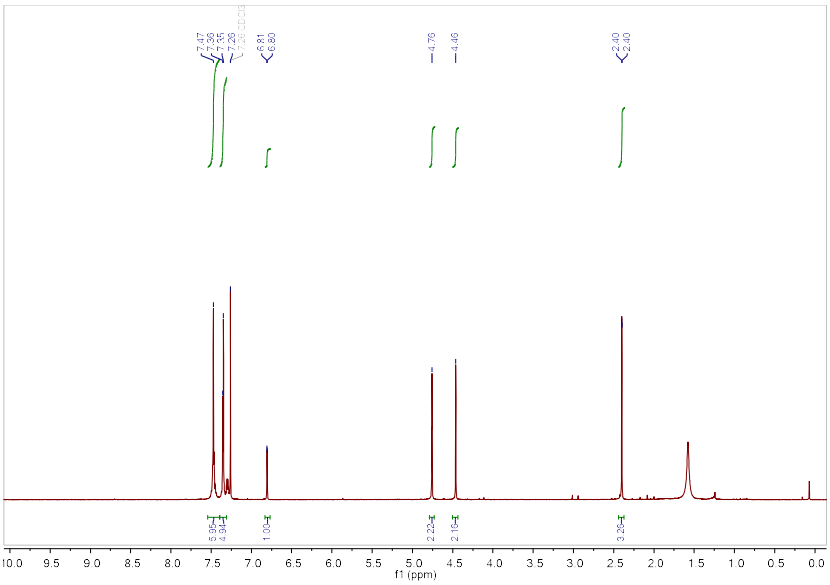

Fig. A94: ^{1}H NMR (500 MHz, Chloroform-*d*) spectrum of **3ad**

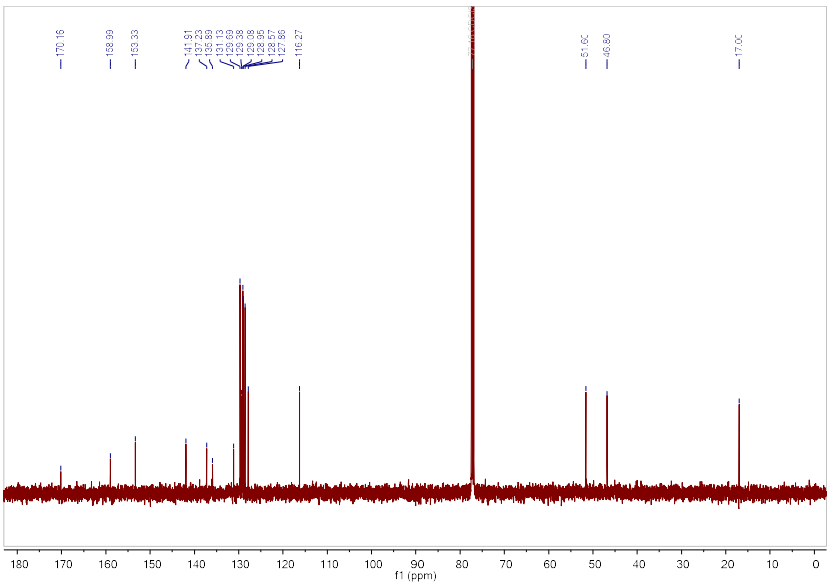

Fig. A95: ^{13}C{^{1}H} NMR (126 MHz, Chloroform-*d*) spectrum of **3ad**

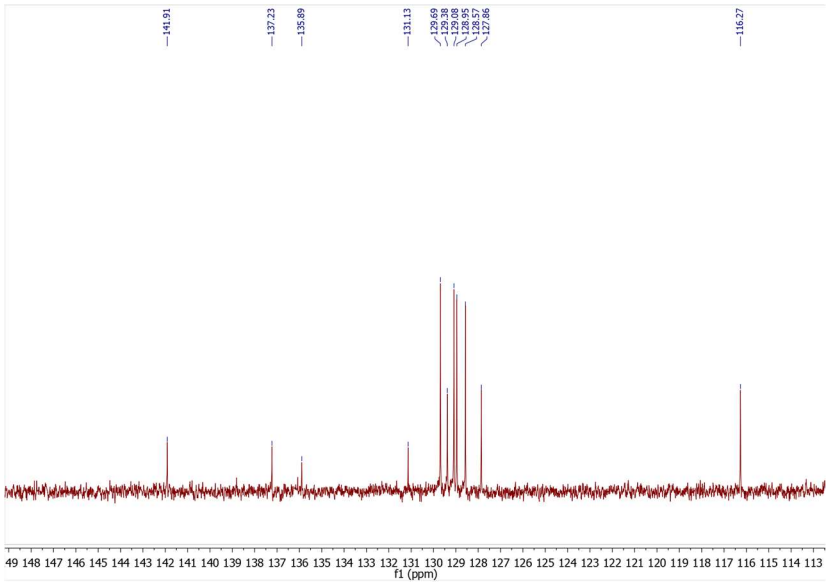

Fig. A96: Expanded (113-149 ppm) $^{13}C\{^{1}H\}$ NMR (126 MHz, Chloroform-*d*) spectrum of **3ad**

V. Mechanistic Studies

Synthesis of Pd(II) Oxidative Addition Complex **4**

Inside a nitrogen glovebox, a 4-dram vial containing a stir bar was charged with 3-oxocyclohex-1-en-1-yl pivalate **1a** (146.9 mg, 0.75 mmol, 5 equiv), bis(tricyclohexylphosphine)palladium(0) (100.0 mg, 0.15 mmol, 1 equiv), and 6 mL of anhydrous toluene. The vial was sealed with a Teflon-lined screw cap, removed from the glovebox, and stirred at 80 °C for 24h. The vial was returned to the glovebox. The reaction mixture was concentrated *in vacuo* to give a solid residue. To this was added 3 mL of anhydrous pentane followed by trituration to produce a free-flowing white solid suspended in the solvent. The suspension was stored in the freezer (-30 °C for 48 h). After this time, the suspension was centrifuged to pelletize the desired product, and the supernatant was decanted inside the glovebox. The solid was dried under vacuum to give 80.3 mg of **4** (62% yield).

4. Trimethylacetylpalladium(II)(3-oxocyclohex-1-en) bis(tricyclohexylphosphine):

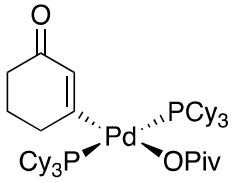

^{1}H-NMR (500 MHz, C_6D_6, 292 K, ppm): δ 6.60 (s, 1H), 3.10 (s, 2H), 2.41 (t, J = 6.6 Hz, 2H), 2.15 (d, J = 12 Hz, 11H), 2.08-1.91 (m, 6H), 1.76 (t, J = 13.9 Hz, 14H), 1.65 (s, 18H), 1.47(s, 9H), 1.37-1.16 (m, 19H), 1.02 (s, 1H).

^{13}C-NMR (126 MHz, C_6D_6, 292 K, ppm): δ 194.7 (t, $^{2}J_{C\text{-}P}$ 6.3 Hz), 190.1, 181.4, 138.1 (t, $^{3}J_{C\text{-}P}$ = 3.0 Hz), 40.4, 39.3, 38.4, 34.3 (t, $^{2}J_{C\text{-}P}$ = 8.4 Hz), 30.4 (d, $^{3}J_{C\text{-}P}$=4.3 Hz), 29.8, 28.2 (dt, $^{1}J_{C\text{-}P}$ = 20.0 Hz, $^{3}J_{C\text{-}P}$ = 5.2 Hz,), 26.8, 24.2.

^{31}P-NMR (203MHz, C_6D_6, 292 K, ppm): δ 19.35.

HRMS: Calc'd for [$C_{47}H_{82}O_3P_2Pd$ – $C_5H_9O_2$(OPiv)], 761.41660; found 761.41736.

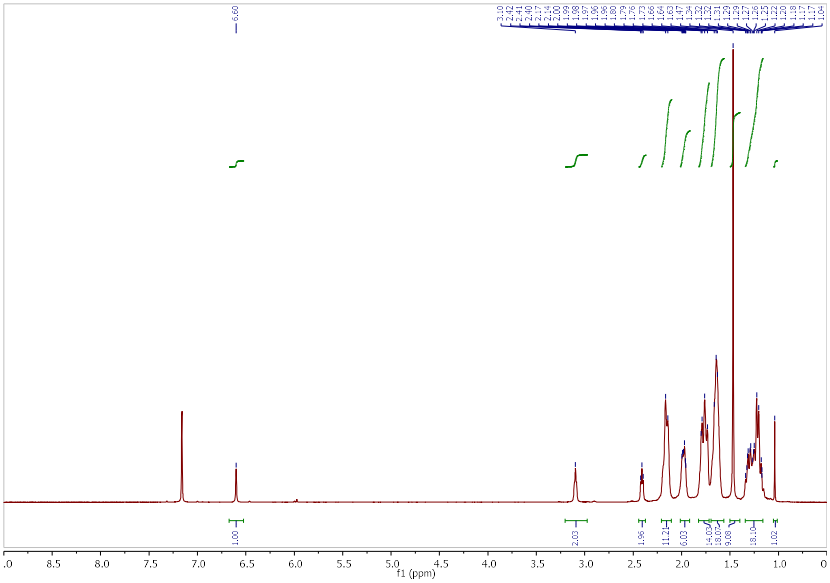

Fig. A97: ^{1}H NMR (500 MHz, C_6D_6) spectrum of **4**

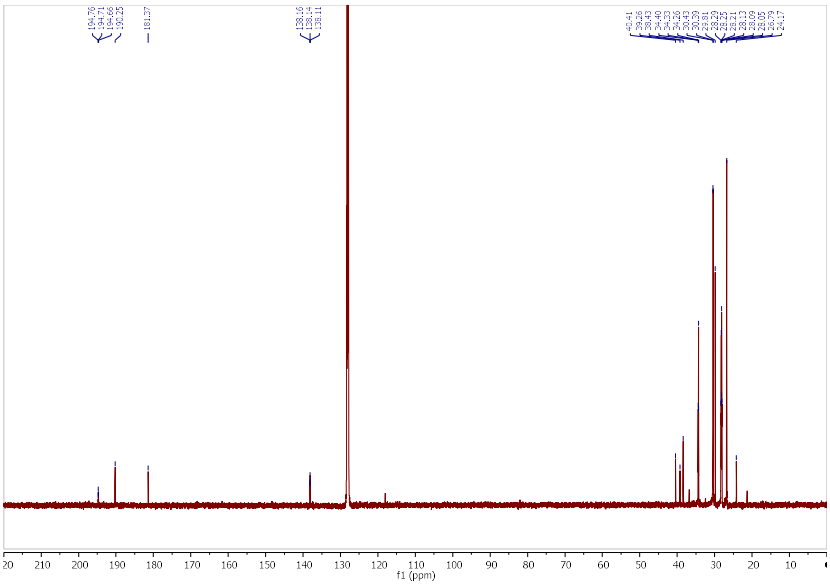

Fig. A98: $^{13}C\{^{1}H\}$ NMR (126 MHz, C_6D_6) spectrum of **4**

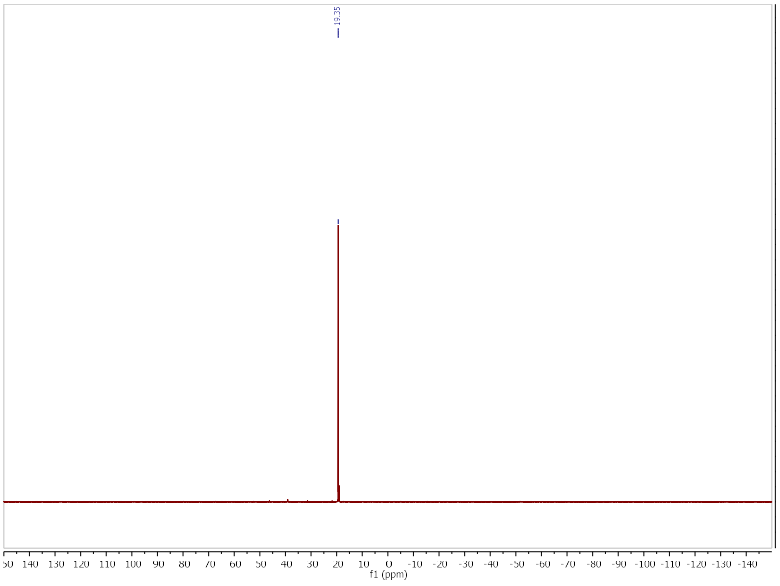

Fig. A99: ^{31}P-NMR spectrum of **4**

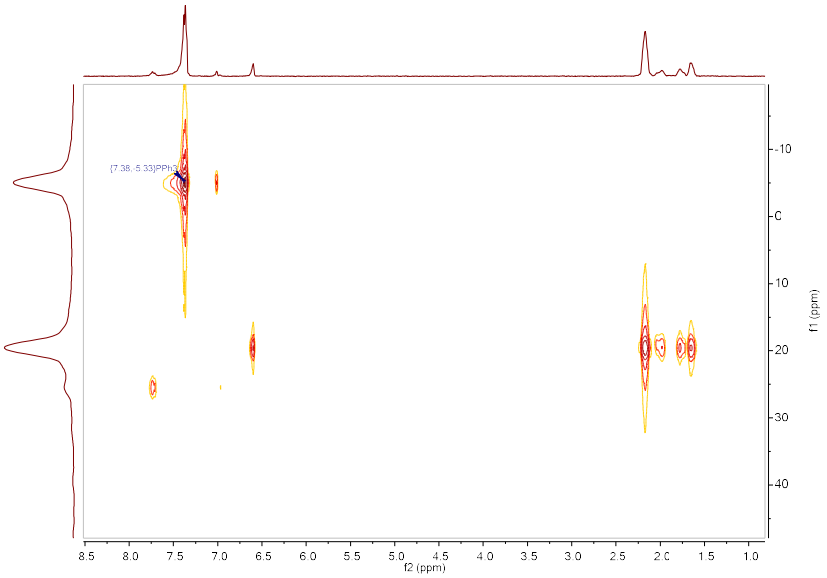

Fig. A100: ^{1}H-^{31}P-HMBC spectrum of **4**. Peak at -5.35 ppm in the ^{31}P channel is PPh_3 as an internal chemical shift standard (capillary containing PPh_3 in C_6D_6).

Oxidative Addition Reaction Monitoring in DMA/THF (Figure 2.16)

Inside the glovebox, a 1-dram vial was charged with 3-oxocyclohex-1-en-1-yl pivalate **1b** (14.7 mg, 0.075 mmol, 5 equiv) or (29.4 mg, 0.15 mmol, 10 equiv) and bis(tricyclohexylphosphine)palladium(0) (10.0 mg, 0.015 mmol, 1equiv). Anhydrous *N,N*-dimethylacetamide (0.3 mL) and anhydrous tetrahydrofuran (0.4 mL) were added; this solvent system was used to ensure complete dissolution of $Pd(PCy_3)_2$ at room temperature to enable acquisition of an accurate time zero NMR spectrum. The homogeneous solution was transferred to a J. Young NMR tube containing a sealed capillary with PPh_3 in C_6D_6 (internal ^{31}P standard). The NMR tube was sealed and removed from the glovebox. A time zero ^{31}P NMR spectrum was acquired, and then the tube was heated in an oil bath at 100 °C. After 15, 30, 45, 60, 90, 120, 180, 240 minutes, the tube was removed, cooled to room temperature, and analyzed by ^{31}P NMR spectroscopy monitoring the conversion.

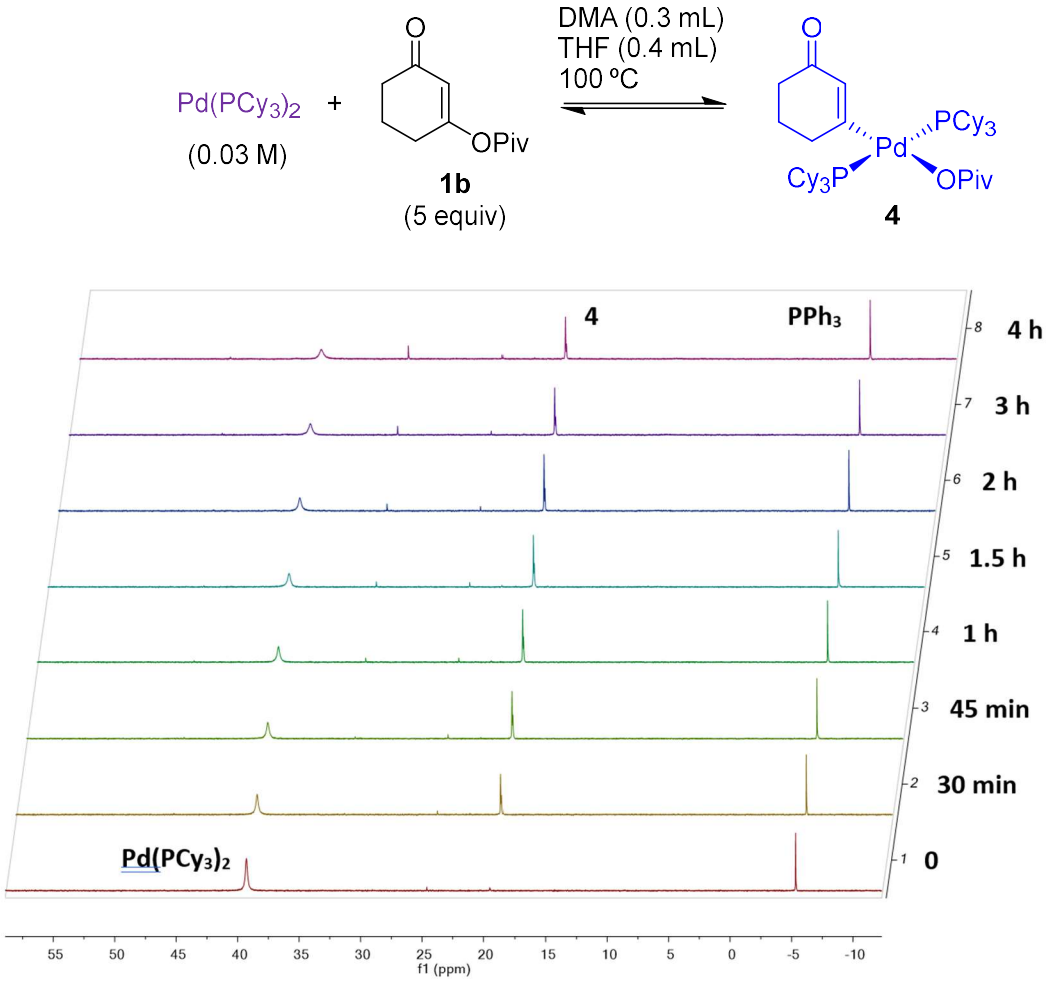

Fig. A101: ^{31}P-NMR spectroscopy monitoring of C–O oxidative addition with 5 equivalents of 3-oxocyclohex-1-en-1-yl pivalate (**1b**) and $Pd(PCy_3)_2$ in DMA/THF.

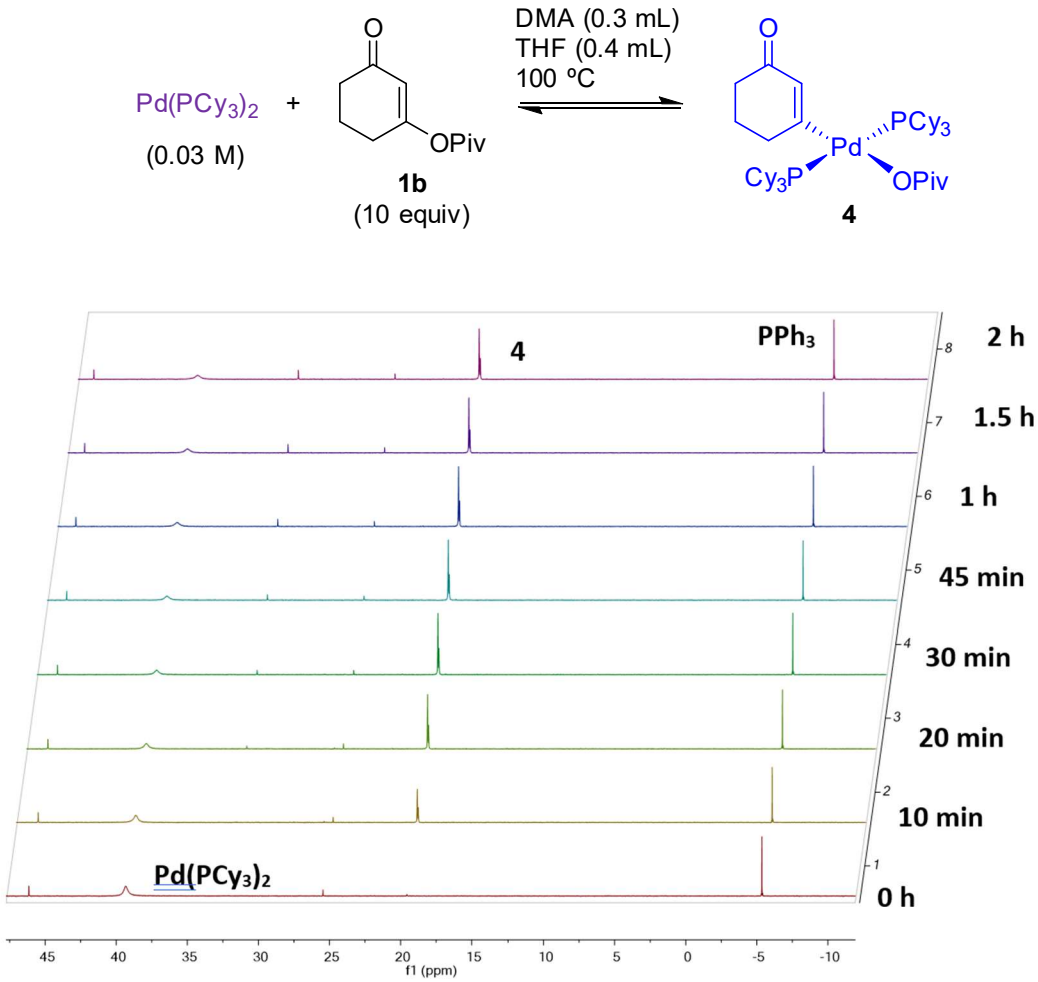

Fig. A102: ^{31}P-NMR spectroscopy monitoring of C–O oxidative addition with 10 equivalents of 3-oxocyclohex-1-en-1-yl pivalate (**1b**) and $Pd(PCy_3)_2$ in DMA/THF

C–O Reductive Elimination Reaction Monitoring (Figure 2.17)

Inside the glovebox, a 1-dram vial was charged with trimethylacetylpalladium(II)(3-oxocyclohex-1-en) bis(tricyclohexylphosphine), complex **4**, (12.9 mg, 0.015 mmol, 1 equiv). Anhydrous *N,N*-dimethylacetamide (0.3 mL) and anhydrous tetrahydrofuran (0.4 mL) were added; this solvent system was used to ensure complete dissolution of complex 4 at room temperature to enable acquisition of an accurate time zero NMR spectrum. The homogeneous solution was transferred to a J. Young NMR tube containing a sealed capillary with PPh_3 in C_6D_6 (internal ^{31}P standard). The NMR tube was sealed and removed from the glovebox. A time zero ^{31}P NMR spectrum was acquired, and then the tube was heated in an oil bath at 100 °C. After 10 min, 20 min, 45 min, 1.5 h, 1.75 h, 2.15 h, 3.15 h and 3.45 h the tube was removed, cooled to room temperature, and analyzed by ^{31}P-NMR spectroscopy monitoring the conversion. 3-oxocyclohex-1-en-1-yl pivalate **1b** was observed by LCMS comparing the starting material with the reaction crude.

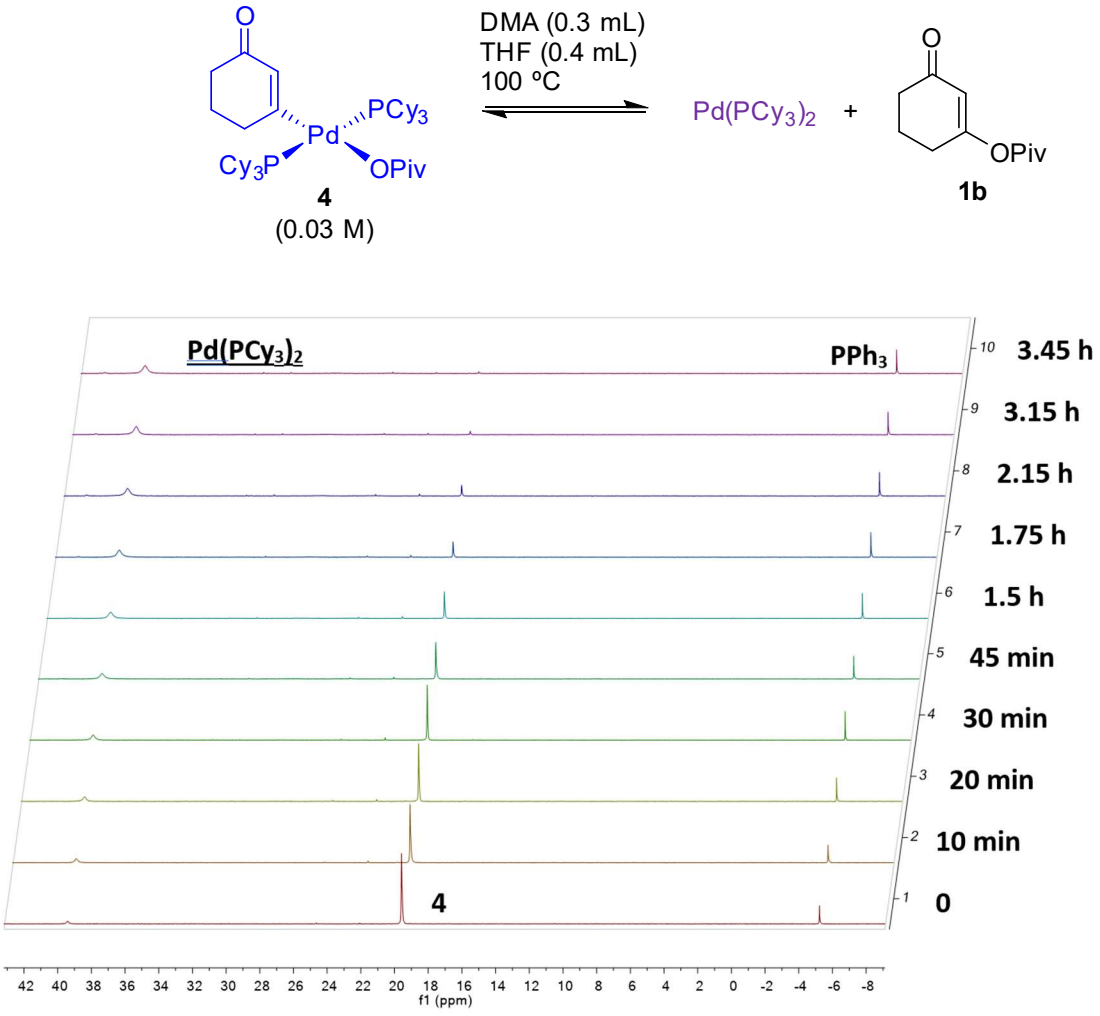

Fig. A103: ^{31}P-NMR spectroscopy monitoring of reversible C–O oxidative addition from thermolysis of complex **4** in DMA/THF.

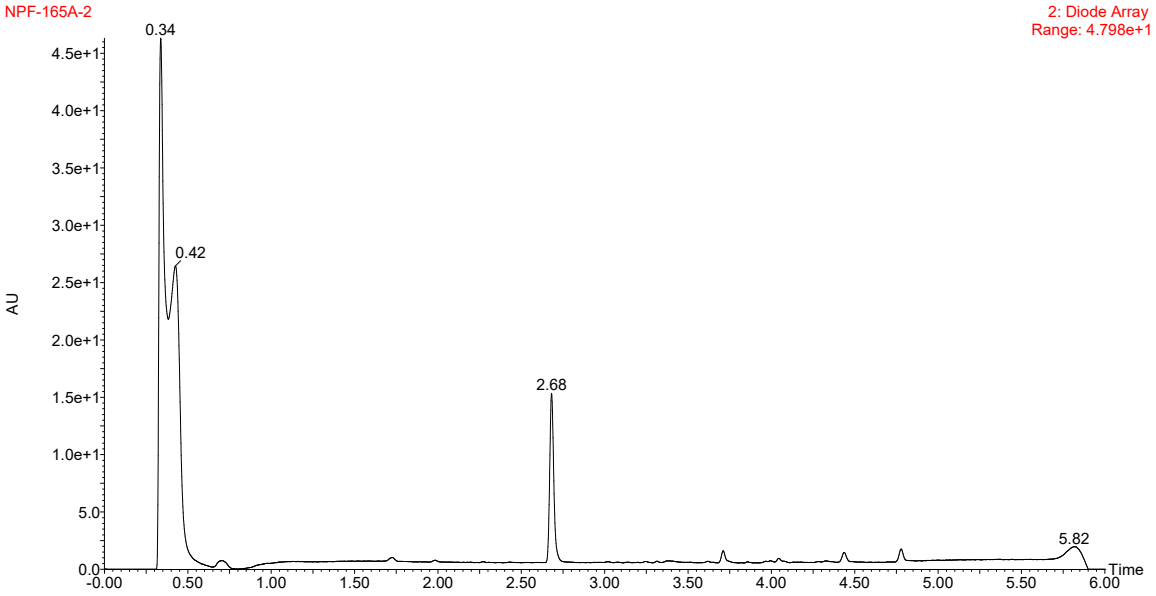

Fig. A104: LCMS chromatogram of C–O reductive elimination reaction at time = 4h.

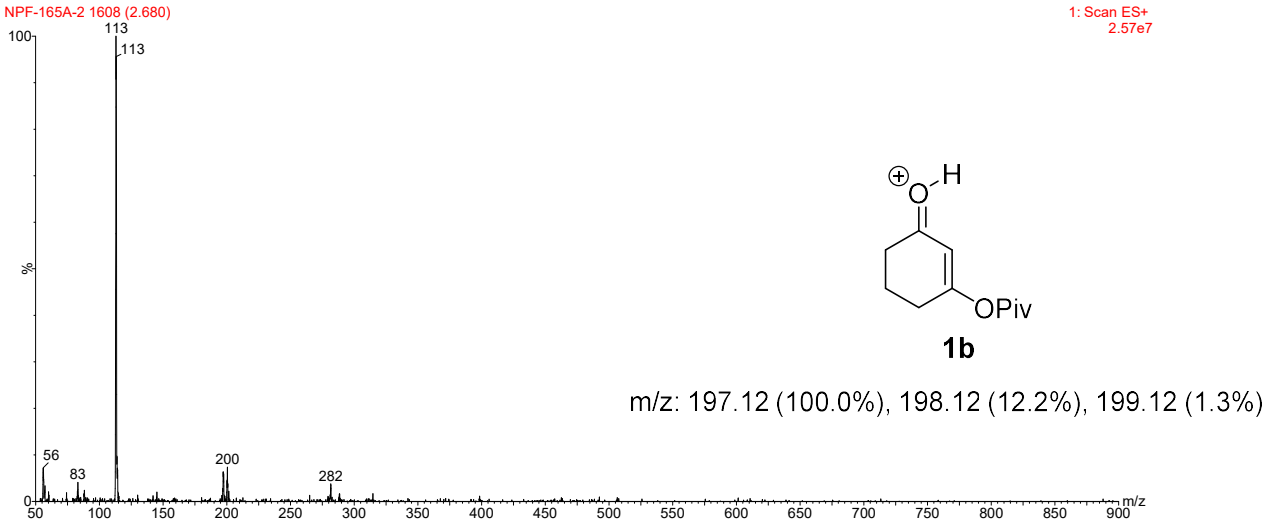

Fig. A105: ESI-MS corresponding to peak at retention time 2.66 min, with *m/z* = 197, corresponding to **1b**.

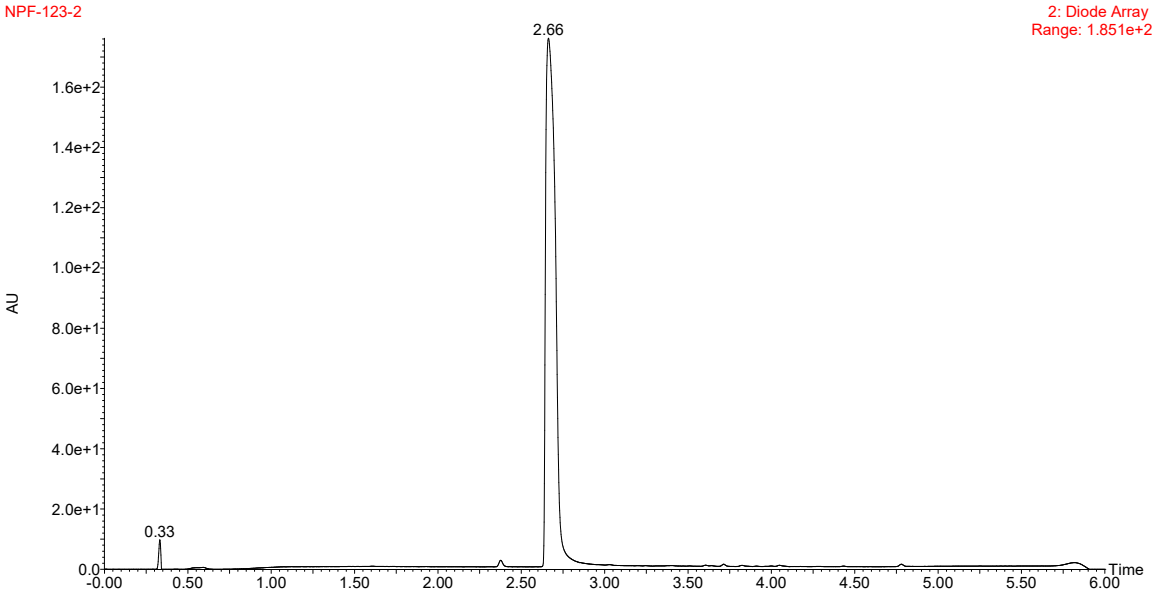

Fig. A106: LCMS chromatogram of isolated 3-oxocyclohex-1-en-1-yl pivalate **1b.** Retention time of 2.66 min matches that observed in C–O reductive elimination reaction mixture.

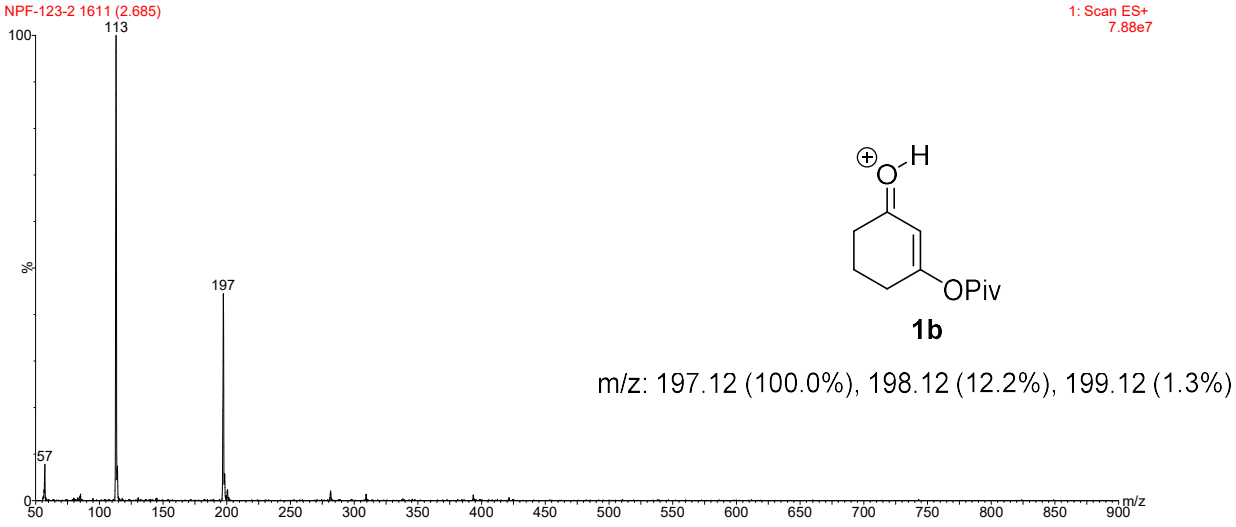

Fig. A107: ESI-MS of 3-oxocyclohex-1-en-1-yl pivalate **1b** (peak at 2.66 min retention time), with *m/z* = 197.

Concerted Metallation-Deprotonation (CMD) Reaction Monitoring (Figure 2.19)

Inside the glovebox, a 1-dram vial was charged with trimethylacetylpalladium(II)(3-oxocyclohex-1-en) bis(tricyclohexylphosphine), complex **4**, (10.4 mg, 0.012 mmol, 1 equiv) and benzothiophene (8.1 mg, 0.06 mmol, 5 equiv). Anhydrous *N,N*-dimethylacetamide (0.5 mL) and were added. The solution was transferred to a J. Young NMR tube containing a sealed capillary with PPh_3 in d^8-toluene (internal ^{31}P standard). The NMR tube was sealed and removed from the glovebox. The NMR tube was locked in the NMR and the probe was heated to 100 °C. Single scan ^{31}P-NMR spectra were acquired every 3.3 minutes to monitor the progression of the reaction.

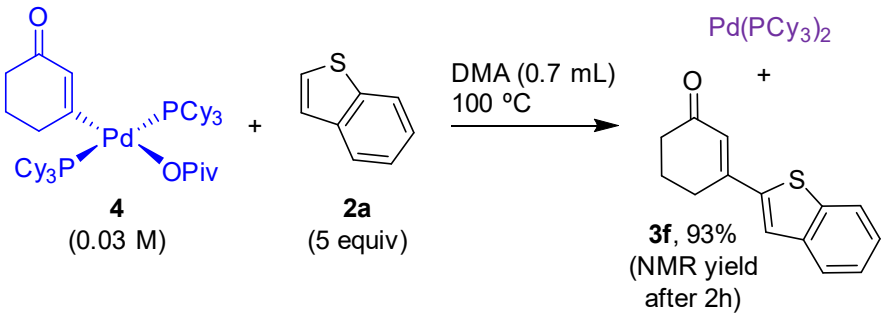

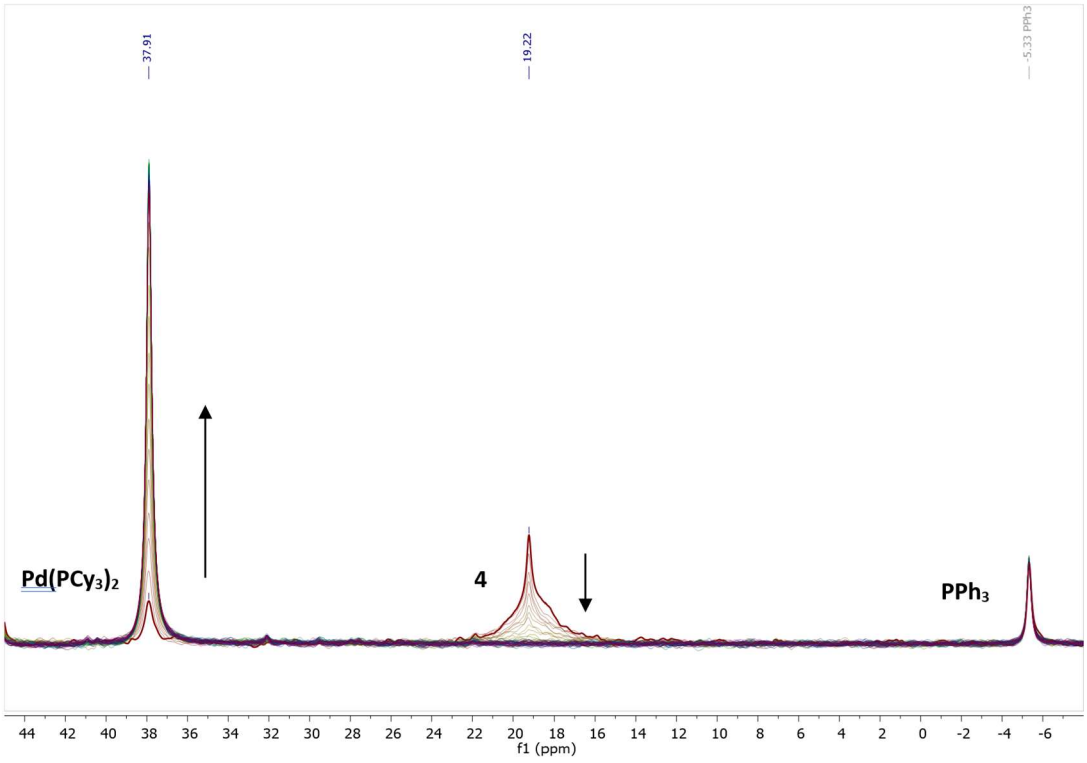

Fig. A108: CMD reaction monitoring by ^{31}P NMR spectroscopy at 100 °C (single scan spectra).

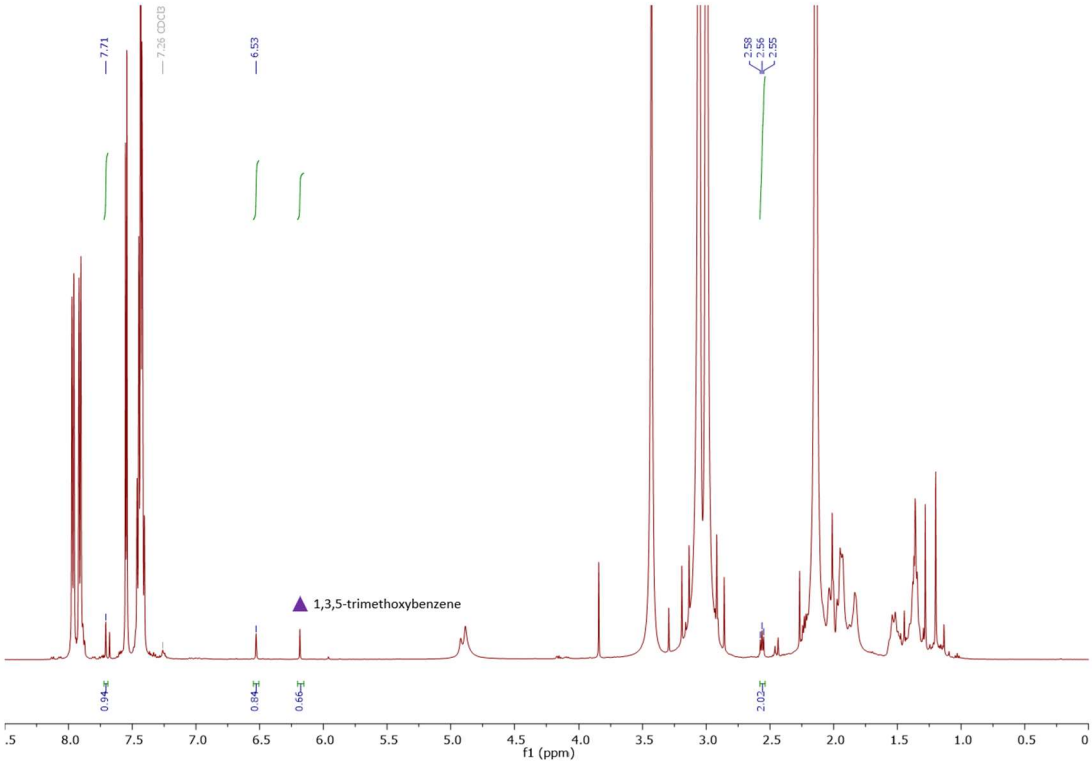

Fig. A109: ^{1}H NMR spectrum of CMD reaction at time = 2h, with quantification of product **3f** by relative integration to internal standard (1,3,5-trimethoxybenzene).
Average solution yield = [84% (s, 6.53 ppm) + 94% (s, 7.71 ppm) + 101% (dd, 2.56 ppm)] / 3 = 93%.

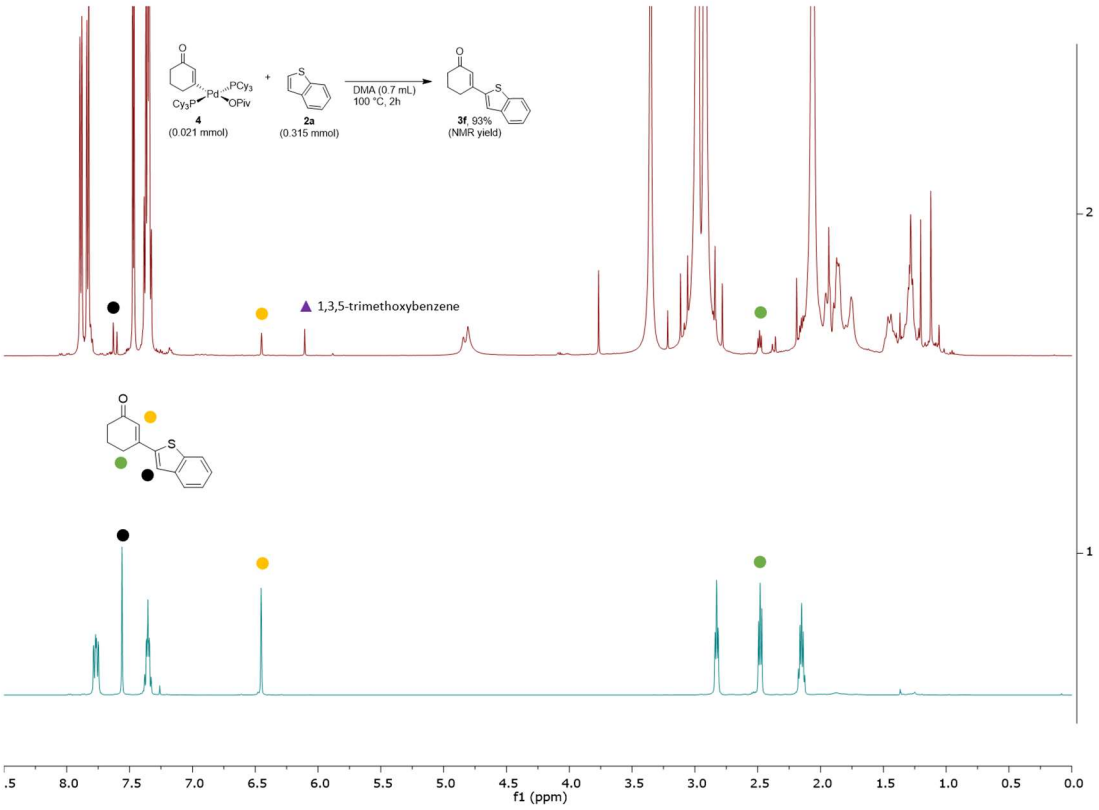

Fig. A110: Comparison of ^{1}H NMR spectrum of CMD reaction at time = 2h with isolated product **3f**.

Catalyst Resting State Observation (Figure 2.20)

Inside the glovebox, a 2-dram vial was charged with 3-oxocyclohex-1-en-1-yl pivalate **1b** (68.7 mg, 0.35 mmol, 1 equiv), benzothiophene **2a** (140.9 mg, 1.05 mmol, 3 equiv), bis(tricyclohexylphosphine)palladium(0) (14.0 mg, 0.021 mmol, 6 mol%). Anhydrous *N,N*-dimethylacetamide (0.3 mL) and anhydrous tetrahydrofuran (0.4 mL) were added; this solvent system was used to ensure complete dissolution of $Pd(PCy_3)_2$ at room temperature to enable acquisition of an accurate time zero NMR spectrum. The homogeneous solutions were transferred to two J. Young NMR tube containing a sealed capillary with PPh_3 in C_6D_6 (internal ^{31}P standard). The NMR tubes were sealed and removed from the glovebox. A time zero ^{31}P NMR spectrum was acquired, and then the tubes were heated in an oil bath at 100 °C. Every hour, the tube was removed, cooled to room temperature, and analyzed by ^{31}P-NMR spectroscopy. After 4 h, the reaction mixture in the first tube was evaporated to dryness using centrifugal evaporation, and the reaction conversion was calculated by ^{1}H-NMR spectroscopy using relative integration to 1,3,5-trimethoxybenzene (15 mol%) as internal standard, revealing 50% conversion of **1b** to **3f.**

After 24 h the reaction mixture in the second tube was evaporated to dryness using centrifugal evaporation and the reaction conversion was calculated by ^{1}H-NMR spectroscopy using relative integration to 1,3,5-trimethoxybenzene (10 mol%) as internal standard, revealing 90% conversion of **1b** to **3f**.

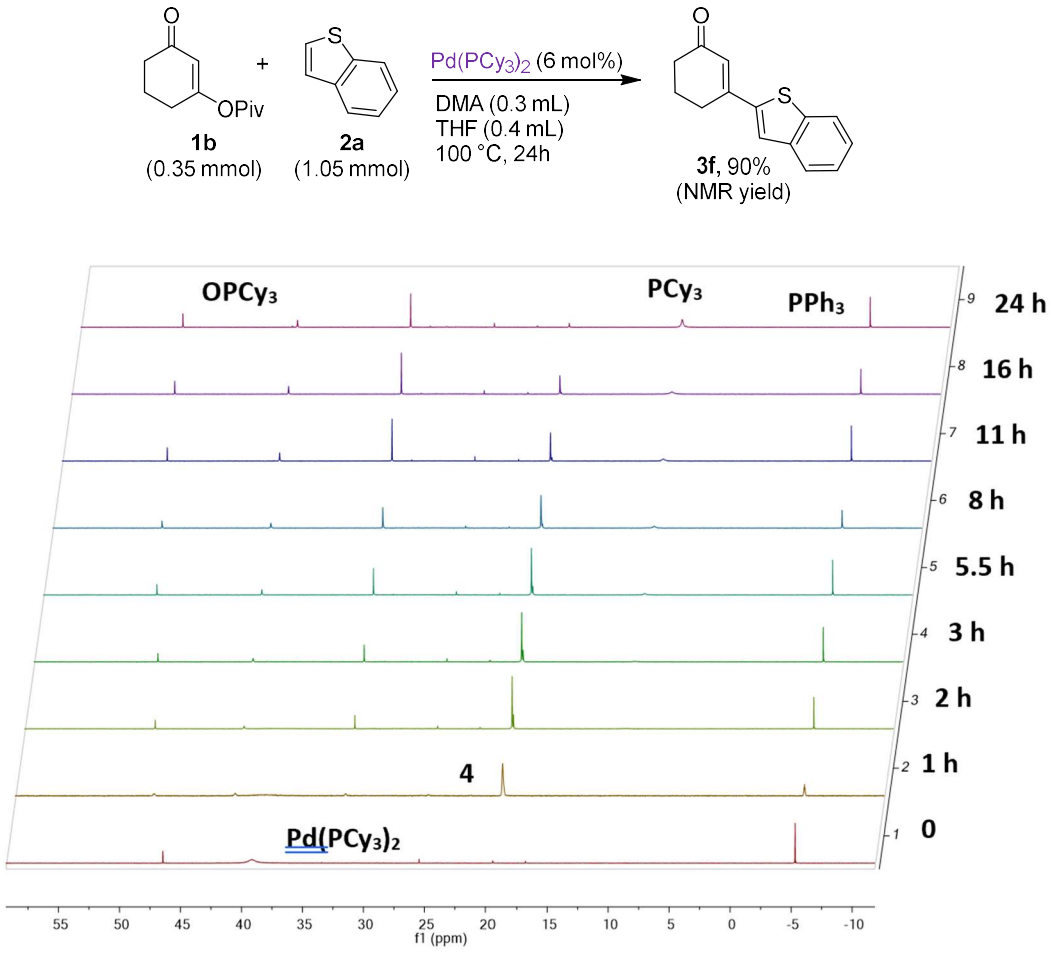

Fig. A111: ^{31}P-NMR spectroscopy reaction monitoring of catalyst resting state in DMA/THF

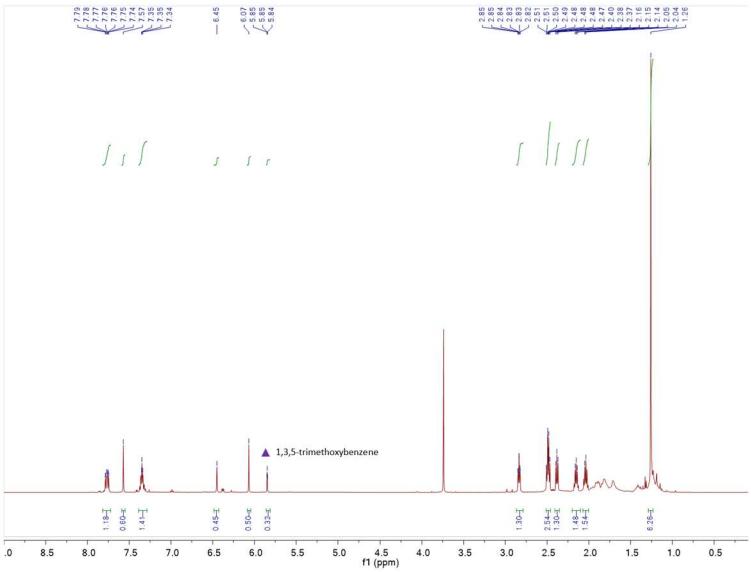

Fig. A112: ^{1}H NMR spectrum of catalytic reaction at time = 4h after solvent evaporation. Average solution yield = [45% (s, 6.45 ppm) + 60% (s, 7.57 ppm) + 65% (m, 2.83 ppm)] / 3 = 57%.

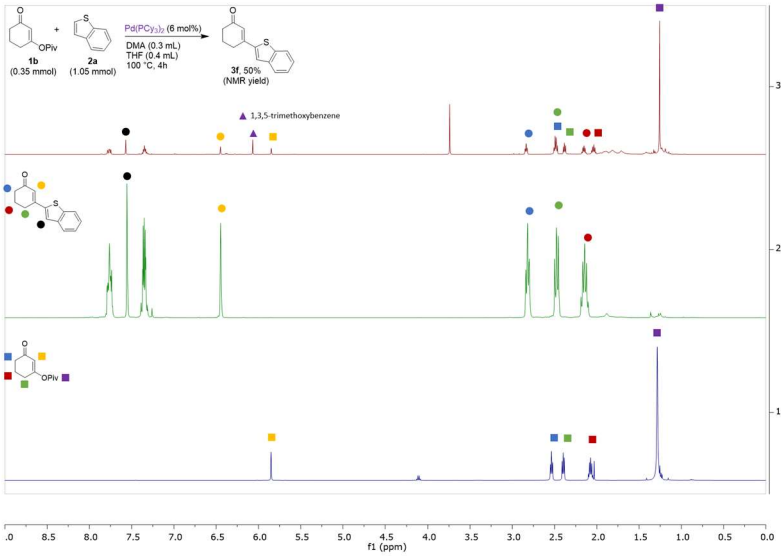

Fig. A113: ^{1}H-NMR spectra comparison of catalytic reaction at time = 4h after solvent evaporation (top), product **3f** (middle) and starting material **1b** (bottom).

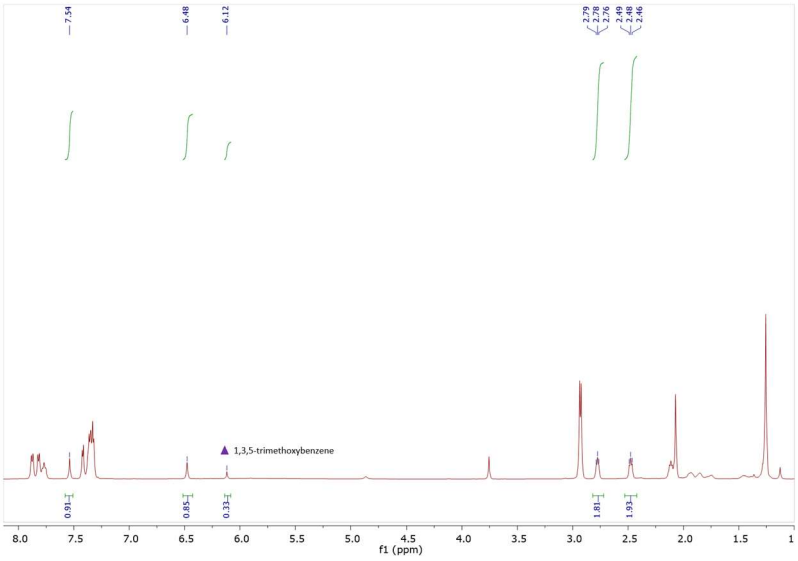

Fig. A114: [1]H NMR spectrum of catalytic reaction at time = 24h after solvent evaporation. Average solution yield = [85% (s, 6.48 ppm) + 91% (s, 7.57 ppm) + 91% (m, 2.78 ppm)] / 3 = 89%.

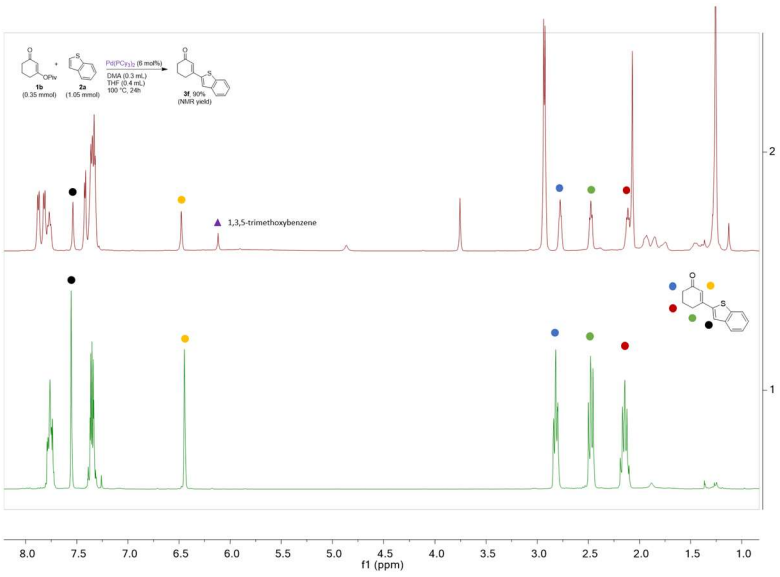

Fig. A115: [1]H-NMR spectra comparison of catalytic reaction at time = 24h after solvent evaporation (top) and product **3f** (bottom).

Addition of product 3f to bis(tricyclohexylphosphine)palladium(0)

Inside the glovebox, a 1-dram vial was charged with bis(tricyclohexylphosphine)palladium(0) (10.0 mg, 0.02 mmol, 12 mol%). Anhydrous N,N-dimethylacetamide (0.2 mL) and anhydrous tetrahydrofuran (0.3 mL) were added; The homogeneous solutions were transferred to a sealed NMR tube with a septum cap containing a sealed capillary with PPh_3 in C_6D_6 (internal ^{31}P standard). A time zero ^{31}P-NMR spectrum was acquired. A second solution was prepared dissolving product **3f** (28.5 mg, 0.125 mmol, 1 equiv) in anhydrous N,N-dimethylacetamide (0.1 mL) and anhydrous tetrahydrofuran (0.2 mL). The homogeneous solution was added to the NMR and a ^{31}P-NMR spectrum was acquired.

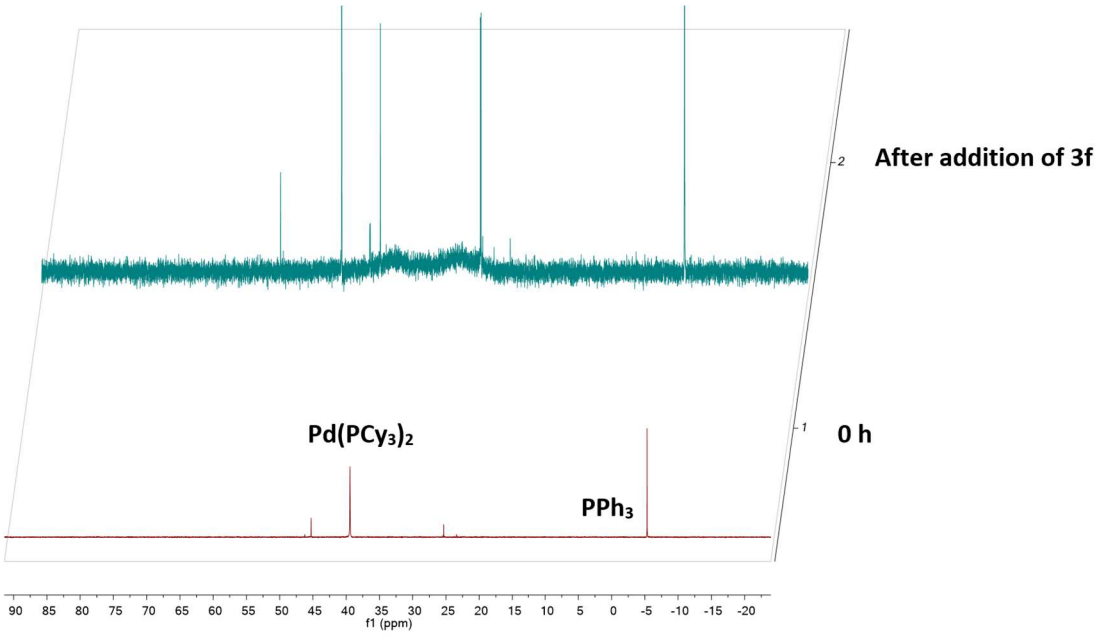

Fig. A116: ^{31}P-NMR spectrum of bis(tricyclohexylphosphine)palladium(0) in the absence (bottom) and presence (top) of product **3f**, showing two broad new signals, indicating reversible coordination.

VI: References

(1) Zalesskiy, S. S.; Ananikov, V. P. Pd $_2$ (Dba) $_3$ as a Precursor of Soluble Metal Complexes and Nanoparticles: Determination of Palladium Active Species for Catalysis and Synthesis. *Organometallics* **2012**, *31* (6), 2302–2309.

(2) Huang, J.; Isaac, M.; Watt, R.; Becica, J.; Dennis, E.; Saidaminov, M. I.; Sabbers, W. A.; Leitch, D. C. ^{DMP}DAB–Pd–MAH: A Versatile Pd(0) Source for Precatalyst Formation, Reaction Screening, and Preparative-Scale Synthesis. *ACS Catal.* **2021**, *11* (9), 5636–5646.

(3) Romanski, S.; Kraus, B.; Guttentag, M.; Schlundt, W.; Rücker, H.; Adler, A.; Neudörfl, J.-M.; Alberto, R.; Amslinger, S.; Schmalz, H.-G. Acyloxybutadiene Tricarbonyl Iron Complexes as Enzyme-Triggered CO-Releasing Molecules (ET-CORMs): A Structure–Activity Relationship Study. *Dalton Trans.* **2012**, *41* (45), 13862.

(4) Gaube, G.; Fernandez, N. P.; Leitch, D. An evaluation of palladium-based catalysts for the base-free borylation of alkenyl carboxylates. *New J. Chem.* **2021**, *45*, 20095-20098.

Appendix B: Supporting information for Chapter 3

I: General Considerations

Materials. All solvents and common organic reagents were purchased from commercial suppliers and used without further purification. $Pd(OAc)_2(PCy_3)_2$ was prepared according to the reported method.[1] Anhydrous solvents (SureSeal) were purchased from MilliporeSigma and used as received.

Preparation of 100 mesh K_3PO_4: Inside a nitrogen glovebox, anhydrous K_3PO_4 was milled in a coffee grinder for 30 seconds. The milled material was then passed through a 100 mesh sieve. The resultant 100 mesh K_3PO_4 is stable for months inside a glovebox, but it quickly absorbs water in minutes when exposed to the atmosphere.

Techniques. All air-free manipulations were performed under a dry nitrogen atmosphere using an MBraun glovebox. High-throughput experimentation was performed using 1 mL capacity glass shell vials in sealable aluminum reaction blocks purchased from Analytical Sales. Heating/stirring was achieved using rare-earth magnetic tumble stirrers acquired from V&P Scientific.

Centrifugal evaporation was performed using a Genevac EZ-2 (HCl compatible). Automated chromatography purification was performed using Biotage® Selekt SEL-2SW instruments using Sfär Silica (60 μm) columns.

Analysis and Spectroscopy.

All NMR spectra were acquired on either a Bruker AVANCE 300 MHz spectrometer or a Bruker AVANCE Neo 500 MHz spectrometer. All ^{1}H and ^{13}C-NMR chemical shifts are calibrated to residual protio-solvents and all ^{31}P and ^{19}F NMR chemical shifts are calibrated to external standards. All NMR spectroscopic data is processed using MestreNova software.

UPLC analysis was performed using a Shimadzu Nexera X2 with a diode-array UV/Vis detector. A Raptor ARC-18 column (100 × 2.1 mm, particle size 1.8 μm) or a Waters CORTECS® UPLC® T3 column (2.1 × 30 mm, particle size 1.6 μm) were used. The eluent used is a mixture of two mobile phases: water with 0.05% trifluoroacetic acid (TFA) (mobile phase A), and acetonitrile with 0.05% TFA (mobile phase B). All solvents used were HPLC grade.

LCMS was performed using a Waters Acquity class H UPLC system equipped with an autosampler, quaternary pump system, column oven, a photodiode array detector and a QDa Mass Spectrometer. The chromatogram was recorded using an ACQUITY UPLC® BEH C18 column (2.1 × 50 mm, particle size 1.7 μm) with 0.1% formic acid (FA) in water as mobile phase A and 0.1% FA in acetonitrile as mobile phase B. The data was processed using Masslynx.

High-resolution electrospray ionization mass spectrometric analysis was performed using a Thermo Scientific Ultimate 3000 ESI-Orbitrap Exactive Plus.

II: Preparation of Substrates

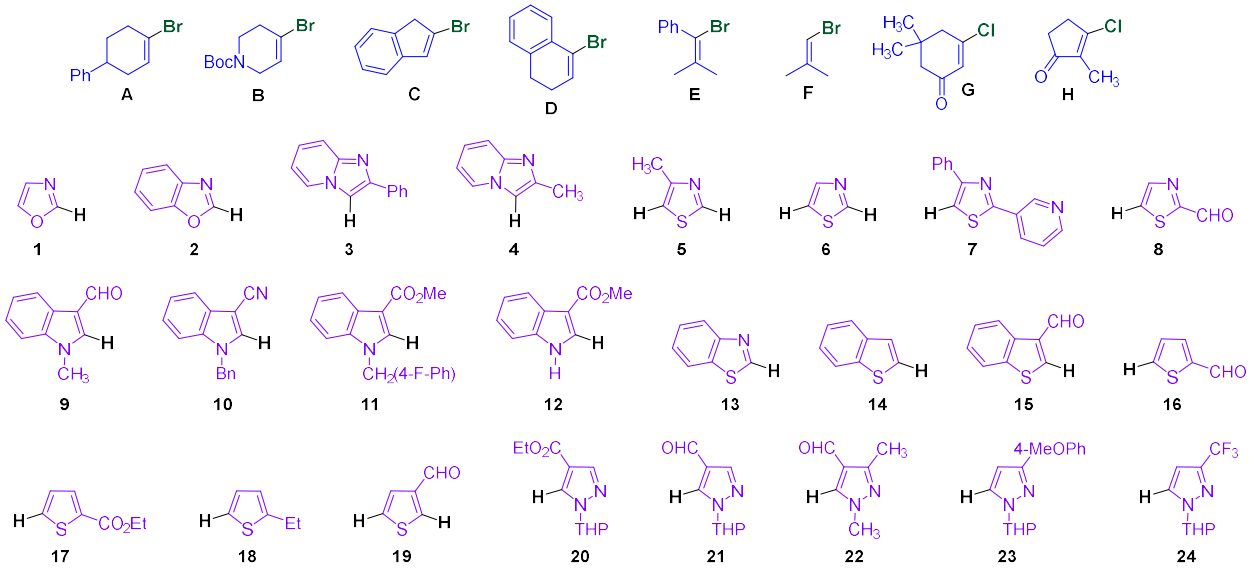

Fig. B1. Substrates used in this study.

The following vinyl halide substrates and heterocycles were synthesized using literature procedures: **D,**[2] **E,**[3] **G,**[4] **H,**[4] **10,**[5] and **4.**[6] The following heterocycles where synthesized by adapting literature procedures: **11** (*N*-benzylation),[5] and **20**, **21**, and **23** (THP protection).[7]

Vinyl halides **B**,**C** and **F** and heterocycles **1**, **2**, **5-9**, **12-19**, and **22** were purchased from Oakwood Chemicals, AK Scientific, or MilliporeSigma, and used as-received.

Synthesis of **A** (4-bromo-1,2,3,6-tetrahydro-1,1'-biphenyl)

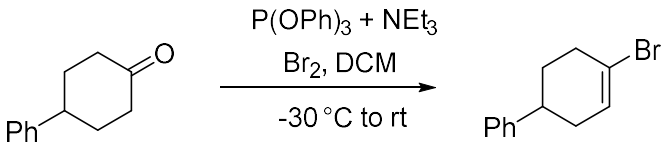

A 250 mL two-necked round bottom flask is charged with a stir bar, 4-phenylcyclohexan-1-one (0.03 mol, 5.3 g, 1 equiv), triethylamine (8.0 mL, 1.5 equiv), and triphenylphosphite (13.4 mL, 1.5 equiv). Dichloromethane (120 mL) is added, and the solution is stirred at room temperature for 5 minutes.

The reaction mixture is cooled to -25 °C using an acetonitrile/dry ice bath. Once the solution reaches the target temperature, 2 equivalents of bromine dissolved in an equal volume of dichloromethane is added to the solution dropwise via syringe. The reaction mixture is kept between -20 °C and -30 °C for 4 hours. Then, the reaction mixture is allowed to warm to room temperature over 3 hours, and stirred at room temperature overnight.

The reaction is quenched by the addition of 10% sodium thiosulfate pentahydrate solution (aqueous, 40 mL) and stirred at room temperature overnight. The mixture is then transferred to a separatory funnel and the layers separated. The organic phase is washed with water (3 x 30 mL). The organic layer is then concentrated under vacuum. NaOH solution (7 M, aqueous, 50 mL) is then added to the residue within the round bottom flask. The mixture is stirred at room temperature for 30 minutes. The reaction temperature is then raised to 50 °C using an oil bath and stirring continued overnight.

The reaction solution is transferred to a separatory funnel and extracted with hexanes until the organic layer remains colourless. The organic layers are combined and concentrated under vacuum. The resulting oil is then purified via column chromatography using 100% hexanes eluent to generate the final product 4-bromo-1,2,3,6-tetrahydro-1,1'-biphenyl[8] in 86% yield (6.1 g) as a white solid.

Synthesis of 2-phenylimidazo[1,2-*α*]-pyridine

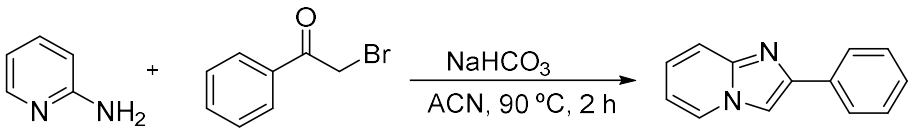

A 250 mL round-bottomed flask was charged with 2-bromoacetophenone (9.0 g, 0.045 mol, 1 equiv), 2-aminopyridine (4.3 g, 1.02 equiv) and 100 mL of acetonitrile. To the mixture, $NaHCO_3$ (7.6 g, 2 equiv) was added. The reaction was heated at reflux in an oil bath for 2 h.

The reaction mixture was filtered, and the acetonitrile was evaporated. The product was purified by recrystallization from acetonitrile to generate the title compound in 57% yield (4.90 g) as a white powder.

III: High-Throughput Screening

More extensive multivariate evaluation of solvent, base and heterocycle

Inside the glovebox, one 20 mL vial was charged with 1.321 g of precatalyst **II** and 10.5 mL of THF. Another stock solution was prepared by dissolving 206.6 mg of 1,3,5-trimethoxybenzene (internal standard) in 11.1 mL of THF. 50 µL of each stock solution was pipetted into each 1 mL glass shell vial in a 96-well aluminium plate. The solvent was evaporated by centrifugal evaporation. A micro parylene-coated stir bar was added to each vial.

Inside the glovebox, 3 equivalents of the corresponding base was added to each well. Solids K_3PO_4 (32 mg), KO*t*Bu (18 mg), K_2CO_3 (21 mg), Cs_2CO_3 (49 mg), or Ag_2CO_3 (41 mg) were added using calibrated plastic scoops. Liquids diisopropylethylamine (DIPEA) (26 µL) or 1,8-diazabicyclo[5.4.0]undec-7-ene (DBU) (22 µL) were added via micropipette.

Inside the glovebox, 4 dram vials were charged with: 4-bromo-1,2,3,6-tetrahydro-1,1'-biphenyl (**A**) (277.2 mg, 1.3 mmol), 2-ethyl hexanoic acid (71 µL, 0.5 equiv) and the corresponding heterocycle: 1-(tetrahydro-2H-pyran-2-yl)-1H-pyrazole-4-carbaldehyde (**21**) (162.1 mg, 1.0 mmol), benzothiophene (**14**) (120.8 mg, 1.0 mmol), benzoxazole (**2**) (107.3 mg, 1.0 mmol) or 4-methyl thiazole (**5**) (89.2 mg, 1.0 mmol). Then, 0.3 mL of the desired solvent – *N*,*N*-dimethylacetamide (DMA), cyclopentylmethyl ether (CPME), toluene or TAA – was added to the corresponding vial. Then, 0.05 mL of the necessary stock solution was added to each vial in the 96-well plate. Finally, 0.15 mL of the same solvent or *tert*-butanol were added to each vial to reach 0.2 mL total solvent volume.

The plates were sealed and removed from the glovebox. The plates were placed in a tumble stirrer set to 85 °C set to 500 rpm, and the reaction mixtures stirred for 20 hours. Upon completion, the plates were cooled to room temperature before being opened. Acetonitrile (500 µL) was added to each vial, followed by stirring for 10 minutes at room temperature to ensure complete dissolution. The samples were centrifuged for 15 minutes. Aliquots of 40 µL of each diluted reaction mixture were then transferred to a 96-well HPLC analysis plate followed by the addition of 0.7 mL of acetonitrile. These 96 samples were analyzed by HPLC, with solution yields of the corresponding product (versus internal standard) determined by HPLC and confirmed by ^{1}H NMR analysis.

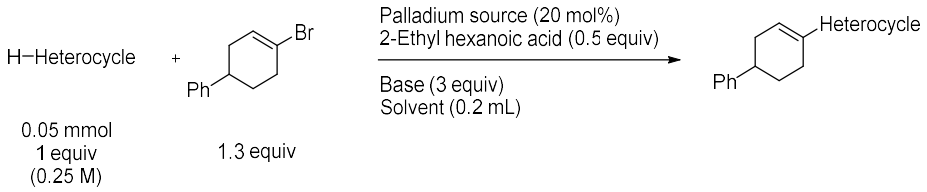

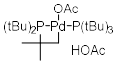

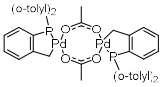

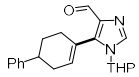

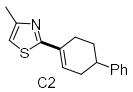

C2

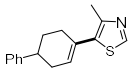

C5

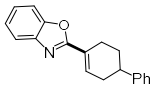

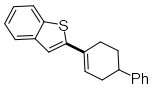

	No *t* BuOH			*t* BuOH: Co-Sol			No *t* BuOH			*t* BuOH: Co-Sol			
	DMA	Tol	CPME	DMA	Tol	CPME	DMA	Tol	CPME	DMA	Tol	CPME	
K_3PO_4	28	50	26	19	38	42	56	64	91	35	11	40	K_3PO_4
K*t* OBu	7	0	0	0	0	0	27	1	3	5	5	19	K*t* OBu
K_2CO_3	4	1	1	5	6	13	0	1	3	23	19	25	K_2CO_3
Cs_2CO_3	18	25	25	15	20	29	12	91	60	44	14	17	Cs_2CO_3
Ag_2CO_3	1	0	0	0	0	0	0	0	0	1	0	0	Ag_2CO_3
DIPEA	0	0	1	0	1	0	1	0	4	1	1	1	DIPEA
DBU	0	0	0	0	0	0	0	0	0	0	0	0	DBU
No base	0	0	0	0	0	0	1	0	0	1	0	0	No base
K_3PO_4	18	80	77	21	0	35	16	6	10	29	22	18	K_3PO_4
K*t* OBu	1	35	32	31	26	18	0	1	2	3	2	10	K*t* OBu
K_2CO_3	24	17	30	38	49	54	5	0	7	8	10	6	K_2CO_3
Cs_2CO_3	17	114	55	36	70	4	13	3	8	21	21	35	Cs_2CO_3
Ag_2CO_3	8	5	7	3	15	18	0	0	0	0	1	0	Ag_2CO_3
DIPEA	7	5	7	4	4	4	2	0	0	1	1	1	DIPEA
DBU	0	0	0	0	0	0	0	1	0	0	2	1	DBU
No base	11	5	10	7	5	6	2	0	0	1	4	9	No base
K_3PO_4	5	0	6	4	0	3	12	22	23	10	13	7	K_3PO_4
K*t* OBu	3	3	3	7	10	7	0	20	22	15	11	28	K*t* OBu
K_2CO_3	0	3	2	1	0	2	10	1	10	25	29	28	K_2CO_3
Cs_2CO_3	0	0	0	7	7	5	10	9	15	20	25	22	Cs_2CO_3
Ag_2CO_3	0	2	3	1	2	2	2	2	1	0	7	8	Ag_2CO_3
DIPEA	0	1	1	0	1	0	5	0	1	1	0	1	DIPEA
DBU	0	0	0	0	0	0	0	0	0	0	1	0	DBU
No base	0	2	1	0	0	0	3	0	1	1	2	1	No base
K_3PO_4	11	17	28	13	11	16	0	1	1	0	1	1	K_3PO_4
K*t* OBu	0	9	6	3	11	4	0	4	8	0	4	9	K*t* OBu
K_2CO_3	20	14	13	15	19	12	0	1	1	0	1	2	K_2CO_3
Cs_2CO_3	15	11	17	15	14	9	3	1	1	0	0	0	Cs_2CO_3
Ag_2CO_3	0	0	0	0	0	0	1	0	1	0	1	1	Ag_2CO_3
DIPEA	4	6	5	6	7	5	0	0	1	5	1	1	DIPEA
DBU	1	1	2	2	1	1	0	0	0	0	0	0	DBU
No base	5	7	6	7	6	6	1	0	1	1	1	1	No base
K_3PO_4	7	9	10	8	15	9	0	10	36	55	48	47	K_3PO_4
K*t* OBu	1	57	72	35	30	31	7	21	49	65	50	63	K*t* OBu
K_2CO_3	0	1	1	2	2	3	20	2	5	11	0	17	K_2CO_3
Cs_2CO_3	23	23	25	30	34	37	96	14	23	25	41	39	Cs_2CO_3
Ag_2CO_3	5	4	2	4	4	5	6	3	1	11	6	4	Ag_2CO_3
DIPEA	0	0	0	3	1	0	3	4	0	2	1	2	DIPEA
DBU	0	0	0	0	0	0	2	4	2	2	4	2	DBU
No base	1	0	1	0	0	1	0	3	2	1	1	3	No base

Fig. B2: Multifactor optimization of direct alkenylation for 4 heterocycles using two different palladacycles (II and IV). Values given are yields obtained by ^{1}H NMR spectroscopy using 1,3,5-trimethoxybenzene as an internal standard.

IV: Optimization of Reaction Conditions

Validation condition optimization

Each optimization reaction was performed using this general procedure:

In the glovebox, a 2 mL HPLC vial was charged with a stir bar, vinyl bromide **A** or **F** (0.15 mmol) and the corresponding heterocycle (0.10 mmol) and 1,3,5-trimethoxybenzene as an internal standard (10 mol%). The catalyst **I**, **II**, **III** or **IV** (5 mol%) was then added and the corresponding base (1.5, 2.25 or 3 equivalents) was added followed by anhydrous solvent: DMA, CPME, toluene or *tert*-amyl alcohol (0.2 mL). The vial was sealed with a Teflon-lined screw cap and removed from the glovebox. The reaction mixture was stirred at 85 °C using a tumble stirrer for 20 h. After cooling to room temperature, the solvent was removed by centrifugal evaporation, followed by redissolution of the residue in $CDCl_3$. The reaction mixtures were then analyzed by ^1H NMR spectroscopy. Solution yields were calculated by relative integration versus the internal standard.

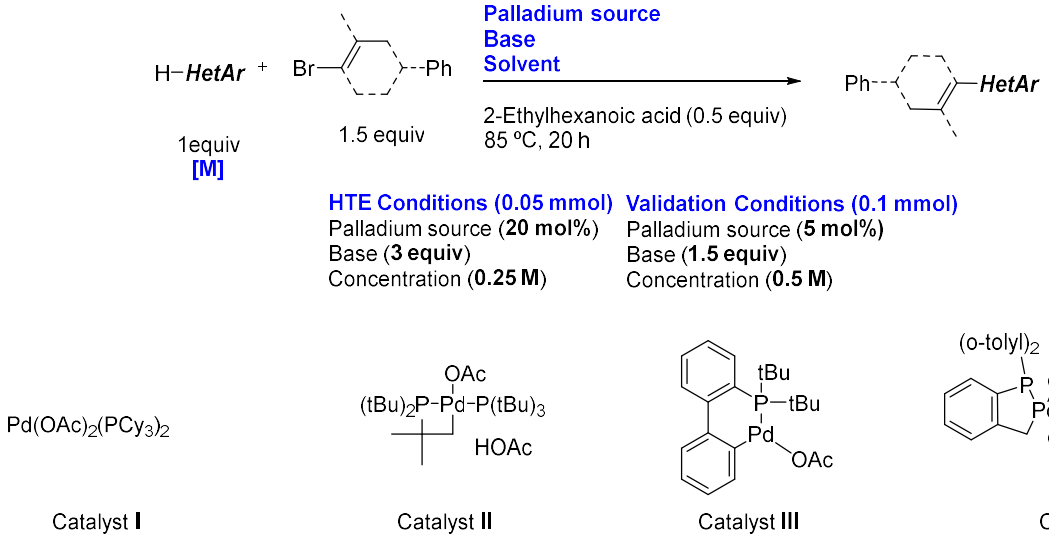

Fig. B3: Reaction optimization of Heterocycles **1, 2, 3, 5, 7, 9, 13, 14, 16, 17, 21** and **22** and vinyl halides **A** and **F** with different reaction conditions.

Table B1: Optimization of oxazole alkenylation with vinyl halide **A**.

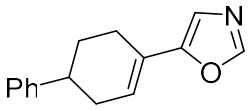

Entry	Catalyst	Base	Solvent	HTE cond. Yield	Validation cond. Yield
1	II	K_3PO_4	CPME	49%	25%
2	II	K_3PO_4	Toluene	63%	25%
3	II	K_2CO_3	TAA	58%	15%
4	II	Cs_2CO_3	TAA	54%	10%
5	I	K_2CO_3	DMA		10%
6	I	K_3PO_4	CPME		0%

Table B2: Optimization of benzoxazole alkenylation with vinyl halide **A**.

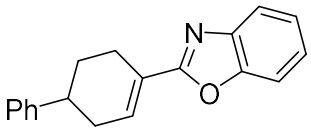

Entry	Catalyst	Base	Solvent	HTE cond. Yield	Validation cond. Yield
1	II	K_3PO_4	CPME	80%	5%
2	II	Cs_2CO_3	DMA	58%	0%
3	II	K_3PO_4	TAA	45%	5%
4	IV	KO*t*Bu	CPME	35%	2%
5	IV	KO*t*Bu	TAA	20%	0%
6	I	K_2CO_3	DMA		0%
7	I	K_3PO_4	CPME		0%

*Further optimization on page S15.

Table B3: Optimization of 2-phenylimidazo[1,2-α]pyridine alkenylation with vinyl halide **A**.

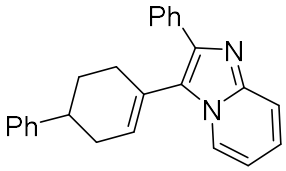

Entry	Catalyst	Base	Solvent	HTE cond. Yield	Validation cond. Yield
1	II	K_3PO_4	CPME	2%	10
2	II	Cs_2CO_3	DMA	77%	15
3	II	Cs_2CO_3	Toluene	44%	15
4	II	Cs_2CO_3	CPME	56%	60
5	II	Cs_2CO_3	TAA	100%	10

*Further optimization on page S17

Table B4: Optimization of 4-methylthiazole alkenylation with vinyl halide **A**.

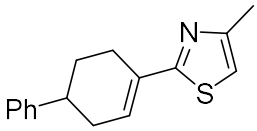

Entry	Catalyst	Base	Solvent	HTE cond. Yield	Validation cond. Yield
1	II	K_3PO_4	CPME	55%	30%
2	II	K_3PO_4	Toluene	60%	45%
3	II	Cs_2CO_3	Toluene	75%	30%
4	II	Cs_2CO_3	TAA	50%	0%
5	IV	K_3PO_4	CPME	30%	0%
6	I	K_2CO_3	DMA		20%
7	I	K_3PO_4	CPME		0%

*Further optimization on pages S18-S19.

Table B5: Optimization of 4-phenyl-2-(pyridine-3-yl)thiazole alkenylation with vinyl halide **A**.

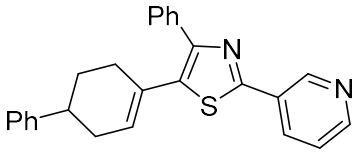

Entry	Catalyst	Base	Solvent	HTE cond. Yield	Validation cond. Yield
1	II	K_3PO_4	CPME	97%	67%
2	II	K_3PO_4	TAA	91%	83%
3	II	Cs_2CO_3	CPME	83%	75%
4	II	Cs_2CO_3	TAA	88%	90%

Table B6: Optimization of 1-Methylindole-3-carbaldehyde alkenylation with vinyl halide **A**.

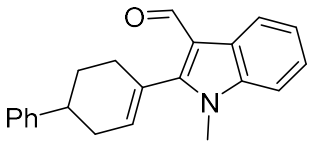

Entry	Catalyst	Base	Solvent	HTE cond. Yield	Validation cond. Yield
1	II	K_3PO_4	CPME	16%	35%
2	II	Cs_2CO_3	TAA	50%	36%
3	II	Cs_2CO_3	DMA	45%	10%
4	II	K_3PO_4	DMA	40%	75%
5	II	K_3PO_4	TAA	26%	68%
6	IV	Cs_2CO_3	TAA		34%
7	I	K_2CO_3	DMA		20%
8	I	K_3PO_4	DMA		0%

Table B7: Optimization of benzothiazole alkenylation with vinyl halide **A**.

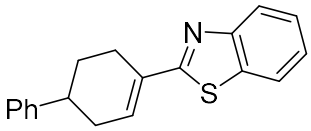

Entry	Catalyst	Base	Solvent	HTE cond. Yield	Validation cond. Yield
1	II	K_3PO_4	CPME	68%	87%
2	II	Cs_2CO_3	Toluene	70%	84%
3	II	Cs_2CO_3	TAA	100%	98%
4	II	Cs_2CO_3	DMA	59%	97%
5	II	K_2CO_3	DMA	85%	75%
6	IV	K_3PO_4	Toluene	-	0%
7	IV	Cs_2CO_3	TAA	-	0%
8	IV	K_2CO_3	DMA	-	0%
9	I	K_3PO_4	CPME	-	37%

Table B8: Optimization of benzothiophene alkenylation with vinyl halide **A**.

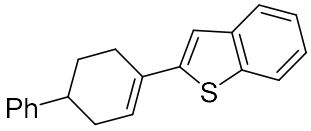

Entry	Catalyst	Base	Solvent	HTE cond. Yield	Validation cond. Yield
1	II	K_3PO_4	CPME	3%	15%
2	II	KO*t*Bu	CPME	25%	45%
3	II	KO*t*Bu	Toluene	20%	30%
4	II	Cs_2CO_3	TAA	45%	90%
5	IV	Cs_2CO_3	DMA	33%	17%
6	IV	KO*t*Bu	TAA	22%	30%
7	I	K_2CO_3	DMA		0%
8	I	KO*t*Bu	CPME		0%

Table B9: Optimization of thiophene-2-carbaldehyde alkenylation with vinyl halide **A**.

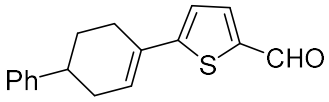

Entry	Catalyst	Base	Solvent	HTE cond. Yield	Validation cond. Yield
1	II	K_3PO_4	CPME	39%	47%
2	II	K_3PO_4	Toluene	47%	42%
3	II	K_2CO_3	TAA	37%	32%
4	II	Cs_2CO_3	CPME	24%	>95%
5	II	Cs_2CO_3	TAA	10%	85%

Table B10: Optimization of ethylthiophene-2-carboxylate alkenylation with vinyl halide **A**.

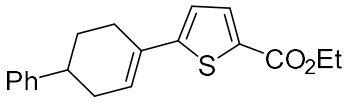

Entry	Catalyst	Base	Solvent	HTE cond. Yield	Validation cond. Yield
1	II	K_3PO_4	CPME	23%	67%
2	II	K_2CO_3	DMA	25%	34%
3	II	Cs_2CO_3	CPME	81%	84%
4	II	Cs_2CO_3	TAA	41%	87%
5	IV	K_2CO_3	DMA	-	14%
6	IV	Cs_2CO_3	CPME	-	8%
7	IV	Cs_2CO_3	TAA	-	38%
8	I	Cs_2CO_3	TAA	-	29%

Table B11: Optimization of 1-(tetrahydro-2*H*-pyran-2-yl)-1*H*-pyrazole-4-carbaldehyde alkenylation with vinyl halide **A**.

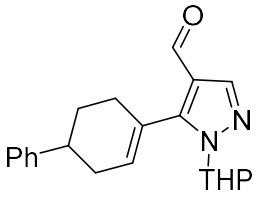

Entry	Catalyst	Base	Solvent	HTE cond. Yield	Validation cond. Yield
1	II	K_3PO_4	DMA	3%	15%
2	II	K_3PO_4	CPME	40%	30%
3	II	K_3PO_4	Toluene	31%	5%
4	II	K_3PO_4	TAA	54%	60%
5	IV	K_3PO_4	DMA	27%	25%
6	IV	K_3PO_4	CPME	100%	0%
7	IV	K_3PO_4	Toluene	92%	22%
8	I	K_2CO_3	DMA	5%	0%
9	I	K_3PO_4	CPME	39%	0%
10	III	Cs_2CO_3	Toluene	64%	10%
11	III	Cs_2CO_3	TAA	54%	19%

Table B12: Optimization of 1-(tetrahydro-2*H*-pyran-2-yl)-1*H*-pyrazole-4-carbaldehyde alkenylation with vinyl halide **F**.

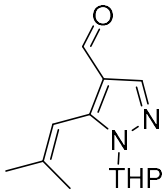

Entry	Catalyst	Base	Solvent	HTE cond. Yield	Validation cond. Yield
1	II	K_3PO_4	CPME	59%	45%
2	II	K_3PO_4	Toluene	49%	35%
3	II	Cs_2CO_3	TAA	45%	60%
4	II	Cs_2CO_3	CPME	35%	44%
5	IV	K_3PO_4	CPME	91%	16%
6	IV	Cs_2CO_3	Toluene	75%	15%
7	III	K_3PO_4	TAA	62%	8%

Table B13: Optimization of 1,3-dimethyl-1*H*-pyrazole-4-carbaldehyde alkenylation with vinyl halide **A**.

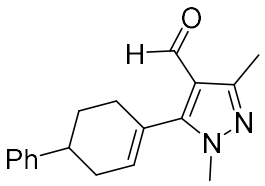

Entry	Catalyst	Base	Solvent	HTE cond. Yield	Validation cond. Yield
1	II	K_3PO_4	CPME	35%	46%
2	II	K_3PO_4	TAA	34%	84%
3	II	K_3PO_4	Toluene	50%	44%
4	II	Cs_2CO_3	CPME	80%	65%

Aggregated catalyst TON analysis of the optimization results

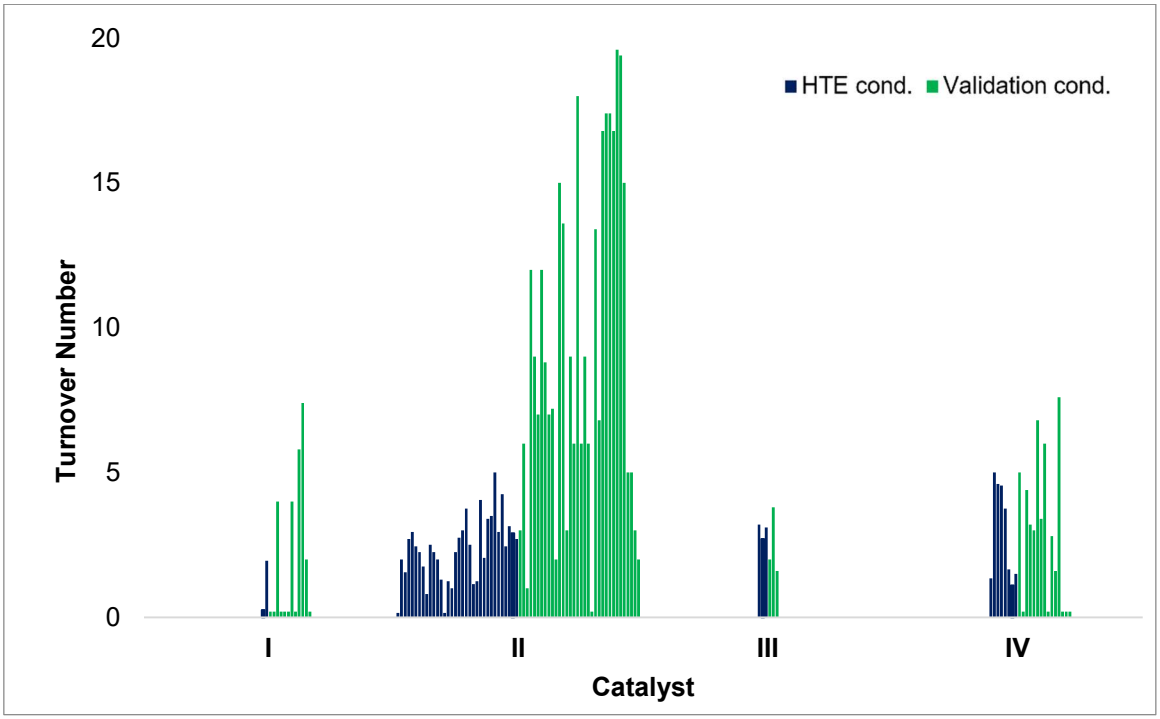

Fig. B4: Catalyst TON analysis of the optimization results from Tables S1-S13.

Full factorial DoE analysis

Inside the glovebox, HPLC vials were charged with a stir bar. The heterocycle substrate (0.1 to 0.15 mmol, 1 to 1.5 equiv) and vinyl halide (0.1 to 0.15 mmol, 1 to 1.5 equiv) were added, followed by complex **II** (5-20 mol%), the corresponding base (1.5 or 3 equivalents) and anhydrous solvents (0.2-0.4 mL). The vials were sealed with a Teflon-lined screw cap, and the reaction mixture stirred at 85 ºC for 20 h. After cooling to room temperature, the solvent was removed by centrifugal evaporation, followed by redissolution of the residue in $CDCl_3$. The product solution yields were obtained by ^1H NMR spectroscopy (calculated by relative integration versus the internal standard).

Table B14: Full factorial analysis of direct alkenylation of **2** with **A**.

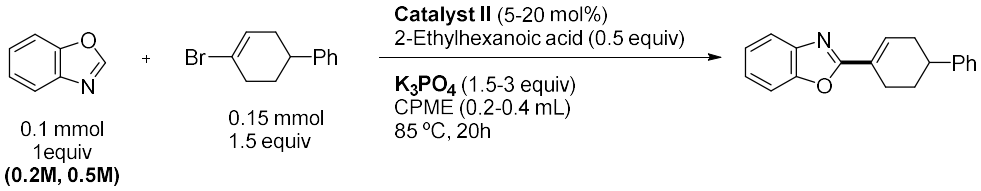

Entry	Pd loading (mol%)	Base (equiv)	Conc. [M]	NMR Yield (%)
1	5	1.5	0.5	10%
2	5	1.5	0.25	13%
3	5	3	0.5	55%
4	5	3	0.25	15%
5	20	1.5	0.5	60%
6	20	1.5	0.25	80%
7	20	3	0.5	45%
8	20	3	0.25	80%
9	12.5	2.25	0.375	33%
10	10	3	0.5	55%

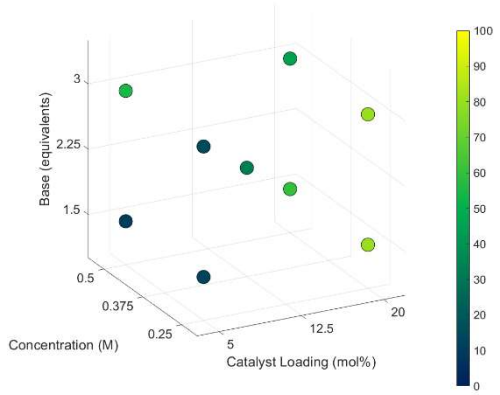

Table B15: Full factorial analysis of direct alkenylation of **3** with **A**.

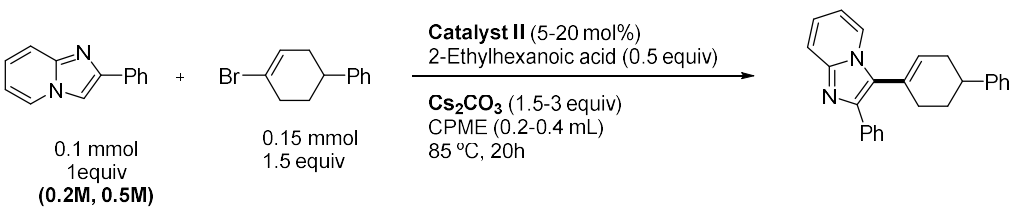

Entry	Pd loading (mol%)	Base (equiv)	Conc. [M]	NMR Yield (%)
1	5	1.5	0.5	60%
2	5	1.5	0.25	40%
3	5	3	0.5	57%
4	5	3	0.25	55%
5	20	1.5	0.5	85%
6	20	1.5	0.25	95%
7	20	3	0.5	85%
8	20	3	0.25	85%
9	12.5	2.25	0.375	75%

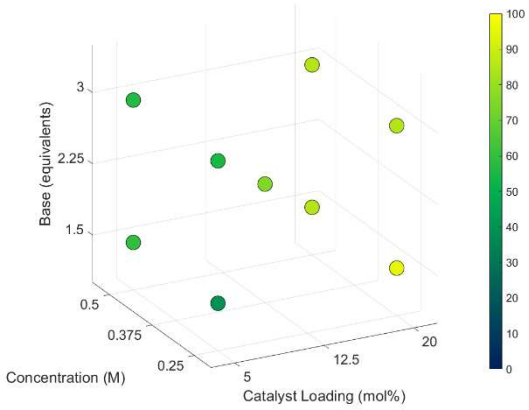

Table B16: Full factorial analysis of direct alkenylation of **5** with **A** in CPME.

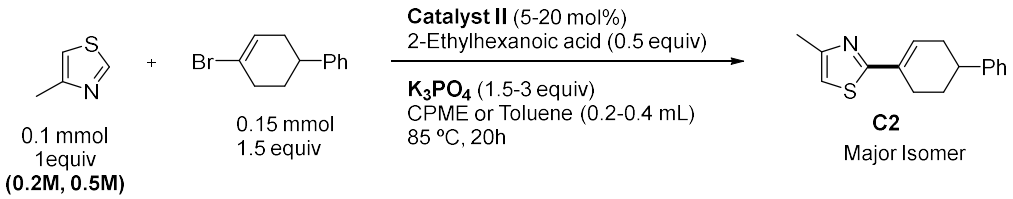

Entry	Pd loading (mol%)	Base (equiv)	Conc. [M]	NMR Yield (%)
1	5	1.5	0.5	45%
2	5	1.5	0.25	50%
3	5	3	0.5	38%
4	5	3	0.25	42%
5	20	1.5	0.5	13%
6	20	1.5	0.25	33%
7	20	3	0.5	35%
8	20	3	0.25	27%
9	12.5	2.25	0.375	33%

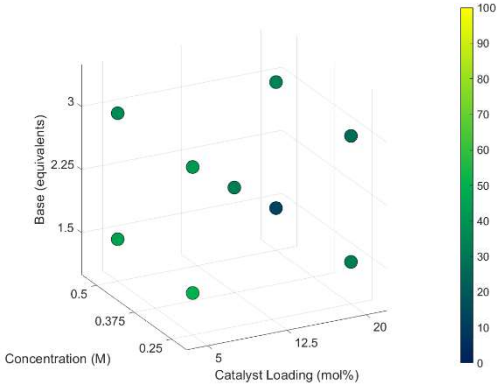

Table B17: Full factorial analysis of direct alkenylation of **5** with **A** in toluene.

Entry	Pd loading (mol%)	Base (equiv)	Conc. [M]	NMR Yield (%)
1	5	1.5	0.5	27%
2	5	1.5	0.25	30%
3	5	3	0.5	25%
4	5	3	0.25	33%
5	20	1.5	0.5	10%
6	20	1.5	0.25	15%
7	20	3	0.5	27%
8	20	3	0.25	32%
9	12.5	2.25	0.375	31%

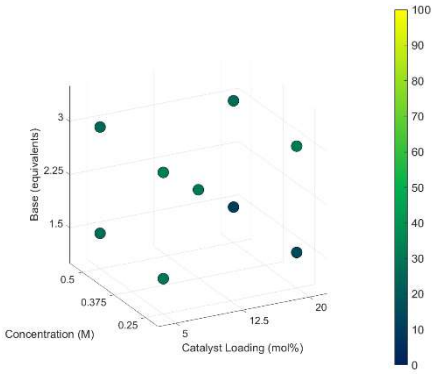

Stoichiometry optimization of direct alkenylation of 4-methylthiazole

Table B18: Stoichiometry optimization of direct alkenylation of **5** with **A**.

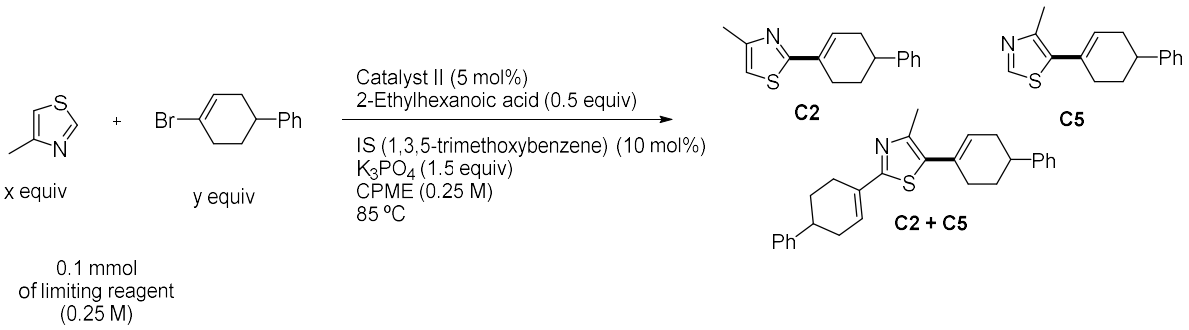

Entry	Thiazole:VinylBr	Time (h)	Conc. [M]	C_2 : C_5 : C_2+C_5	C_2 NMR Yield
1	1:1.5	20	0.25	20:8:25 2.5:1:3	20%
2	1:1.3	20	0.25	18:15:25 1:1:1.6	18%
3	1:1	20	0.25	28:9:20 3:1:2	28%
4	1.3:1	20	0.25	20:30:20 1:1.5:1	20%
5	**1.5:1**	**20**	**0.25**	**30:15:15 2:1:1**	**30%**
6	2:1	20	0.25	19:20:10 1.8:2:1	19%
7	1.5:1	10	0.25	20:10:5 2:1:0.5	20%
8	1.5:1	10	0.5	20:10:10 2:1:1	20%

V: Reaction Monitoring Experiments

Inside a glovebox, three 1-dram vials were charged with Teflon-coated stir bars. The heterocycle substrate (1.5 mmol, 1 equiv) and vinyl halide (1.5 equiv) were added, followed by internal standard (1,3,5-trimethoxybenzene, 10 mol%). Then, the corresponding precatalyst mixture was added: catalyst **II** (5 mol%), or catalyst **II** (4.5 mol%) and $Pd[P(tBu)_3]_2$ (0.5 mol%). Finally, the corresponding base (1.5 or 3 equivalents) and anhydrous solvent (3 mL) was added. The vial was sealed with a Teflon-lined screw cap, and the reaction mixture stirred at 85 °C in a hot plate for 20 h. Aliquots (3 x 10 µL) were taken at the indicated times (0, 1, 2, 3, 6, 10 and 20 h). The aliquots were diluted with acetonitrile (1 mL) and analyzed by LCMS. Once the reaction finished, the solvent was evaporated under vacuum, and the residue redissolved in $CDCl_3$. The final product solution yields were determined by ^1H NMR spectroscopy by relative integration with the internal standard.

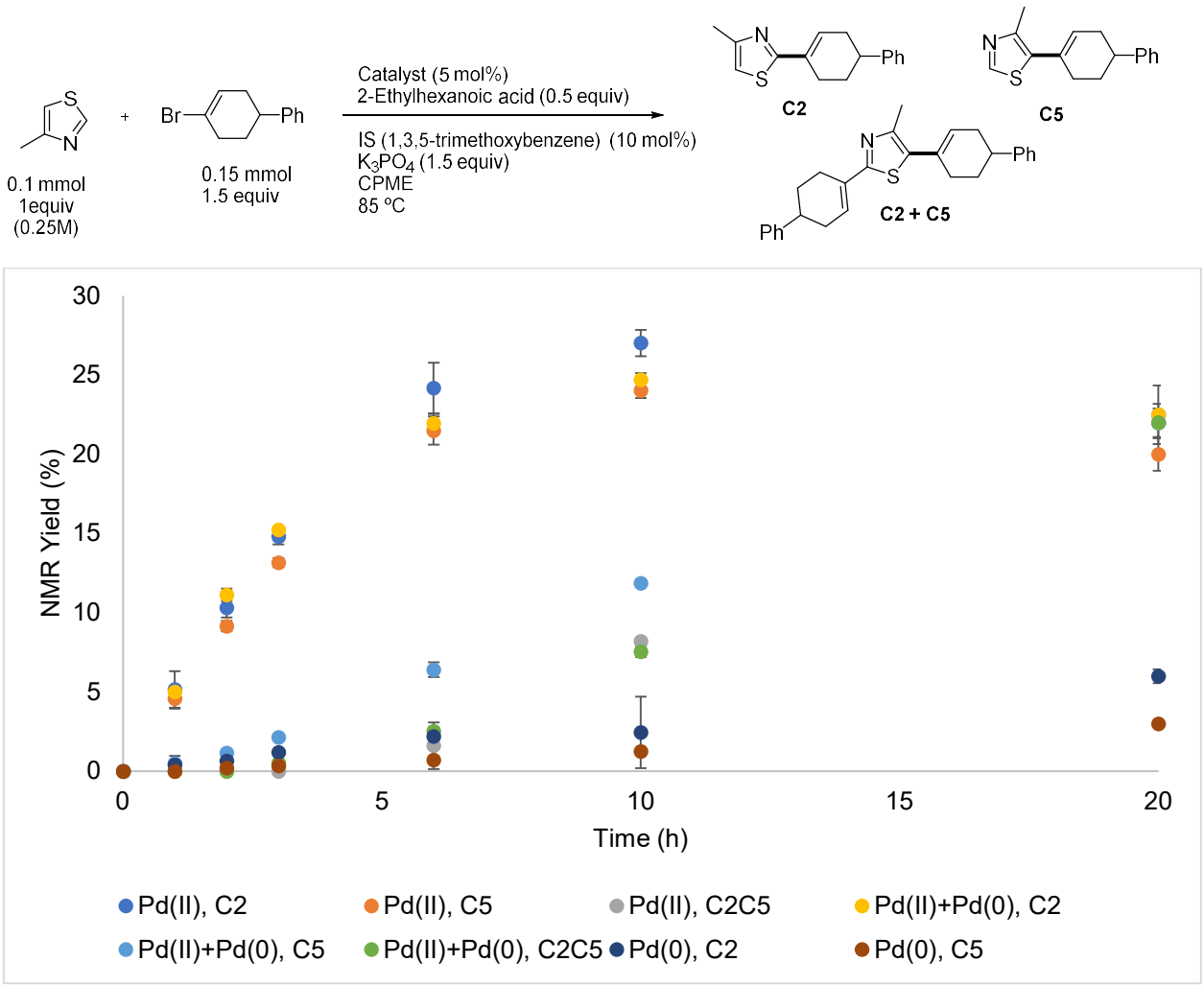

Fig. B5: Reaction progress monitoring of 4-methylthiazole (**5**) direct alkenylation with vinyl halide **A** *via* ^1H NMR spectroscopy using different precatalyst mixtures; Pd(II) 5 mol%; Pd(II) 4.5 mol% and Pd(0) 0.5 mol%; Pd(0) 0.5 mol%.

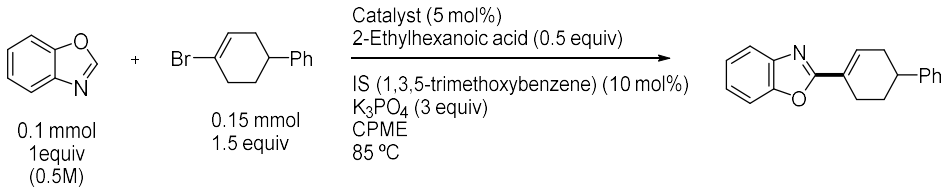

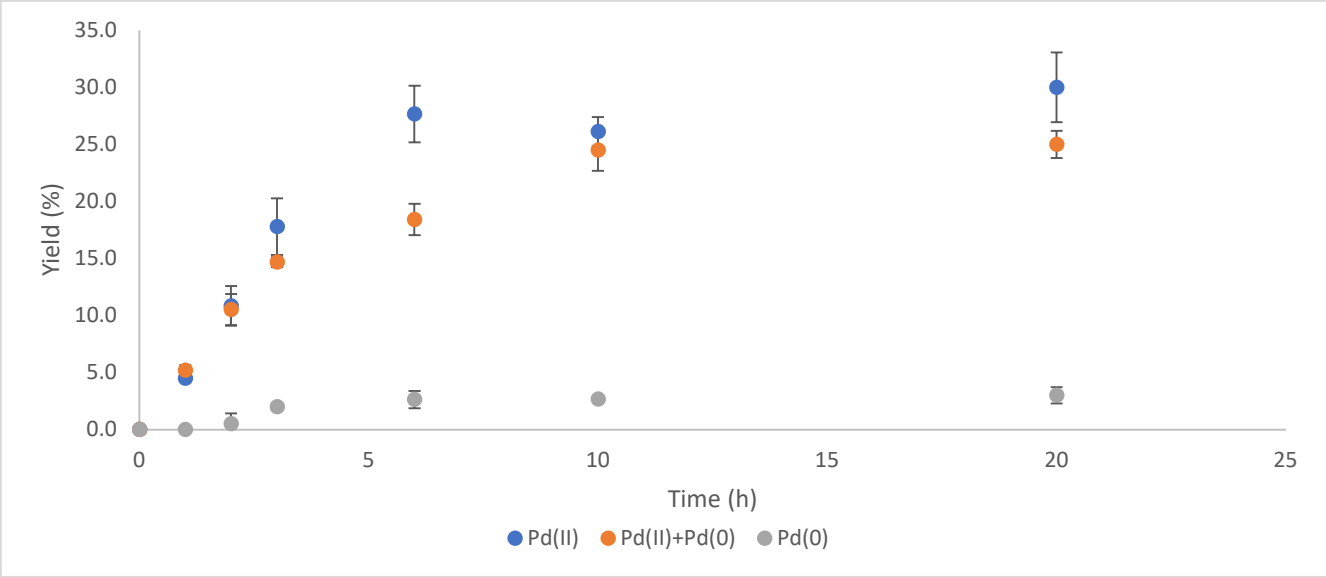

Fig. B6: Reaction progress monitoring of benzoxazole (**2**) direct alkenylation with vinyl halide **A** *via* ^{1}H NMR spectroscopy using different precatalyst mixtures; Pd(II) 5 mol%; Pd(II) 4.5 mol% and Pd(0) 0.5 mol%; Pd(0) 0.5 mol%.

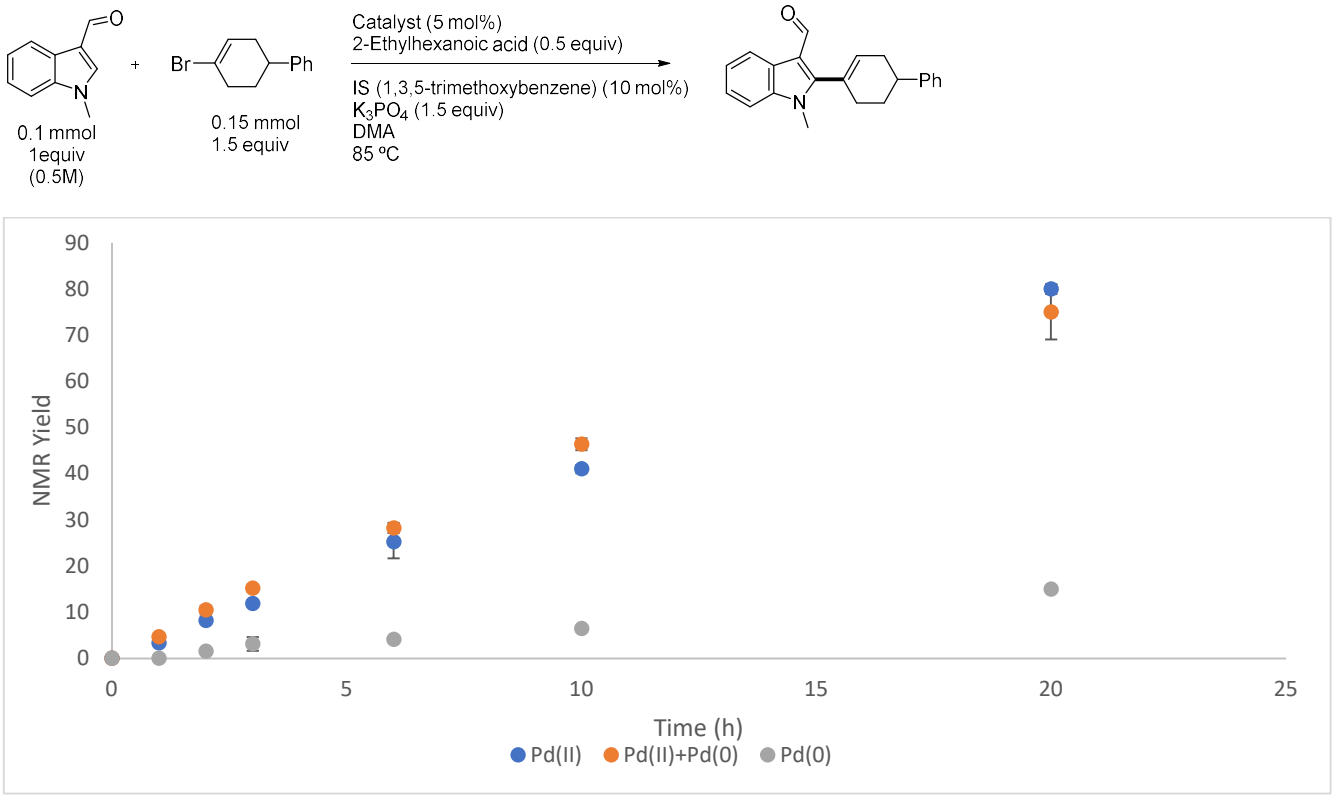

Fig. B7: Reaction progress monitoring of 1-methylindole-3-carbaldehyde (**9**) direct alkenylation with vinyl halide **A** *via* ^{1}H NMR spectroscopy using different precatalyst mixtures; Pd(II) 5 mol%; Pd(II) 4.5 mol% and Pd(0) 0.5 mol%; Pd(0) 0.5 mol%.

VI: In Situ ^{31}P NMR Spectroscopy

Reduction of palladacycle into Pd[P(*t*Bu)$_3$]$_2$

Inside a glovebox, complex **II** (6.4 mg, 0.1 mmol) was dissolved in 0.5 mL of d^8-toluene. Once the palladacycle was completely dissolved, the solution was transferred into a J. Young tube. A sealed glass capillary containing PPh_3 dissolved in d^8-toluene was added as an internal standard. The NMR tube was then sealed under N_2. The tube was heated at 85 ºC in an oil bath for 24 h before analysis by ^{31}P NMR spectroscopy.

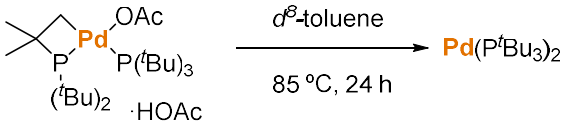

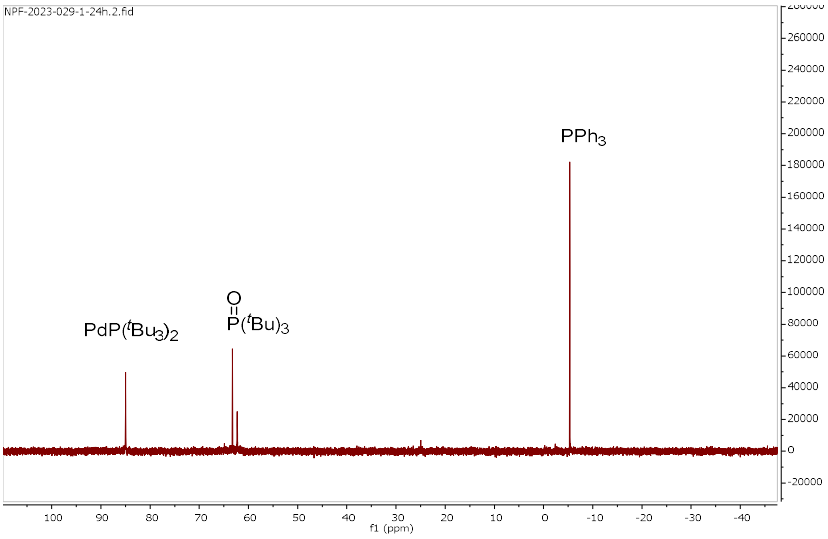

Pd (0) formation observed

Fig. B8: *In situ* reduction of complex **II** followed by ^{31}P NMR spectroscopy.

Proposed Reduction Pathway of Catalyst II into Pd[P(*t*Bu)$_3$]$_2$

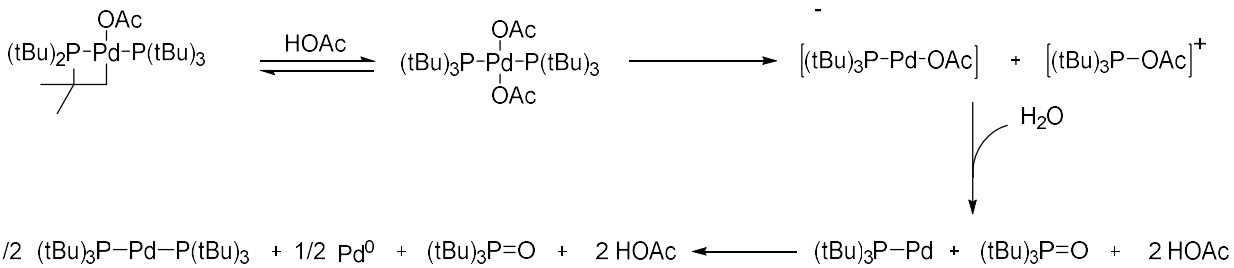

Scheme B1: Proposed pathway for *In situ* reduction of complex **II** followed by ^{31}P NMR spectroscopy.

Monitoring ^{31}P speciation during catalysis

Inside a glovebox, a 1-dram vial was charged with a stir bar. Ethyl thiophene-2-carboxylate (0.2 mmol) and 4-bromo-1,2,3,6-tetrahydro-1,1'-biphenyl (1.5 equiv) were added, followed by complex **II** (5 mol%), Cs_2CO_3 (1.5 equiv) and anhydrous *tert*-amyl alcohol (1 mL). The solution was transferred into a J-Young NMR tube containing a glass capillary of PPh_3 dissolved in d^8-toluene. The NMR tube was sealed, placed under vacuum, and heated at 85 ºC in an oil bath. The reaction progress was monitored by ^{31}P-NMR spectroscopy. After the reaction was complete, the solvent was removed by centrifugal evaporation. The coupling product formation was confirmed by ^{1}H-NMR spectroscopy.

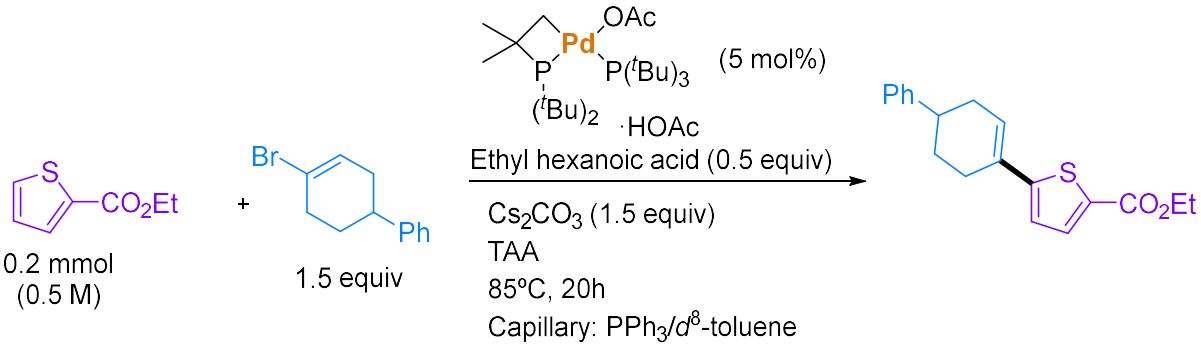

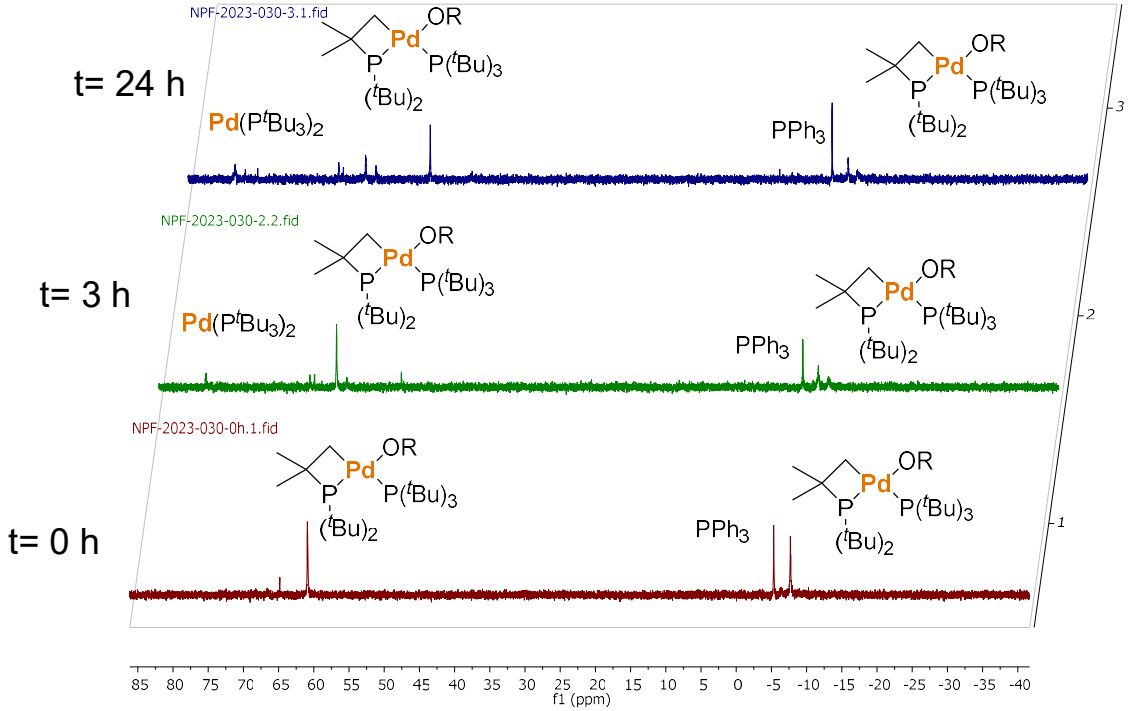

Fig. B9: Reaction monitoring by ^{31}P NMR spectroscopy of the direct alkenylation reaction between heterocycle **17** and vinyl halide **A**.

2-(1,2,3,6-Tetrahydro-[1,1'-biphenyl]-4-yl)benzo[d]oxazole (A2):

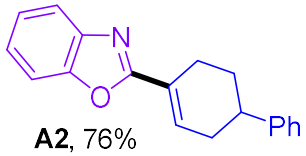

A2, 76%

Isolated by column chromatography (EtOAc : Hexanes = 20:80). Yellow solid. 104.5 mg (76%), MP: 115-116 °C.

IR ν: 3062, 2942, 1537, 1455, 1248, 741 cm^{-1}.

^{1}H NMR (500 MHz, Chloroform-*d*) δ 7.82 (dt, *J* = 7.8, 1.0 Hz, 1H), 7.60 (dt, *J* = 8.2, 1.0 Hz, 1H), 7.46 (td, *J* = 7.8, 1.4 Hz, 1H), 7.41 (td, *J* = 7.6, 1.2 Hz, 1H), 7.03 (t, *J* = 1.8 Hz, 1H), 2.91 (d, *J* = 1.8 Hz, 2H), 2.44 (s, 2H), 1.18 (s, 6H).

$^{13}C\{^{1}H\}$ NMR (126 MHz, Chloroform-*d*) δ 163.9, 150.4, 146.0, 142.1, 134.8, 128.6, 126.9, 126.4, 126.3, 124.9, 124.3, 119.9, 110.3, 39.4, 34.0, 29.4, 25.5.

HRMS (ESI) m/z: $[M+H]^+$ Calc'd for $C_{19}H_{18}NO$ 276.1383; found: 276.1384.

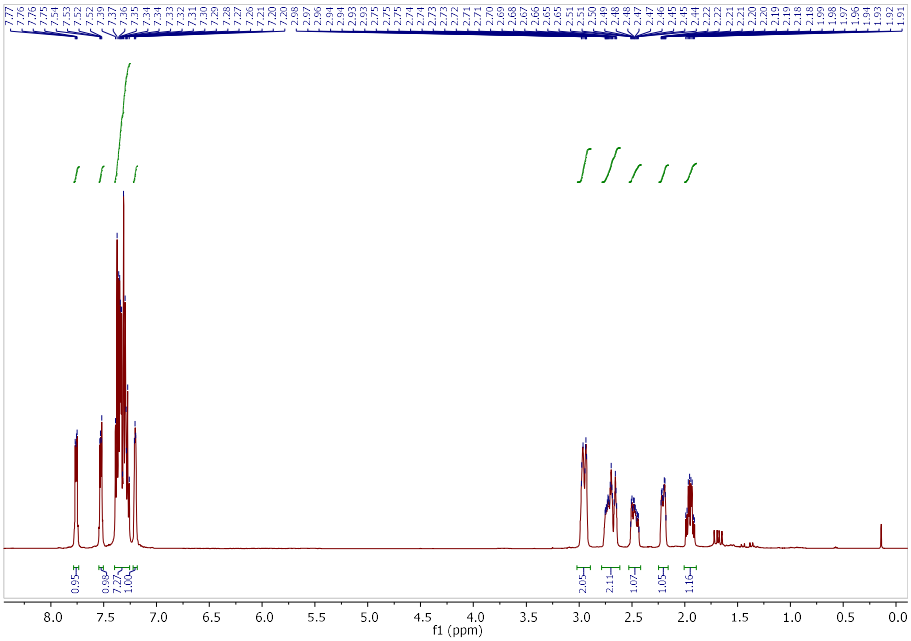

Fig. B10. ^{1}H NMR (500 MHz, Chloroform-*d*) spectrum of **A2**

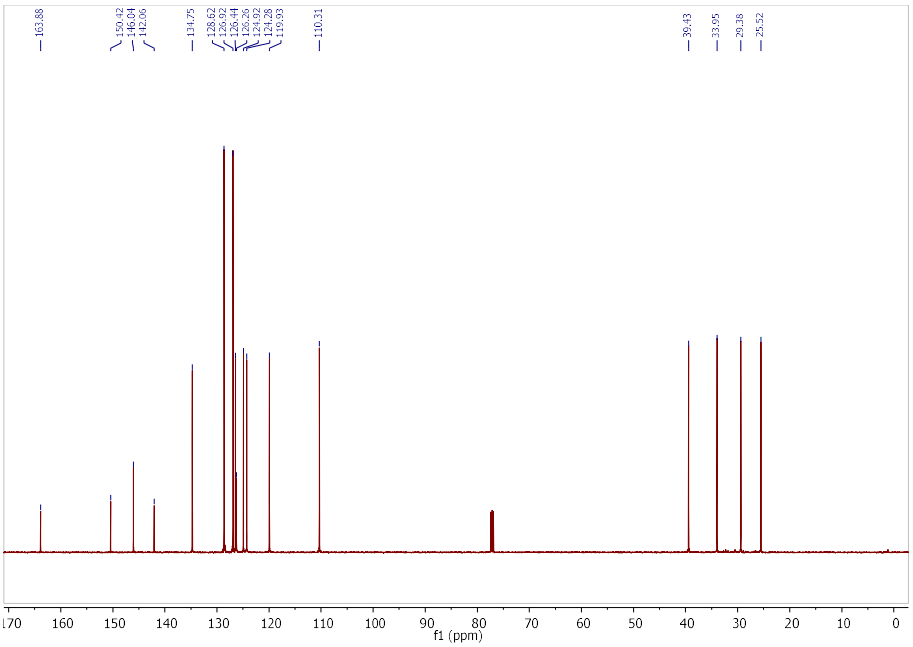

Fig. B11. $^{13}C\{^{1}H\}$ NMR (126 MHz, Chloroform-*d*) of **A2**

2-Phenyl-3-(1,2,3,6-tetrahydro-[1,1'-biphenyl]-4-yl)imidazo[1,2-a]pyridine (A3):

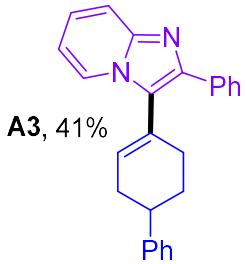

Isolated by column chromatography (EtOAc : Hexanes = 40:60). Brown oil. 71.8 mg (41%),

IR ν: 3058, 2914, 1638, 1602, 1340, 751 cm^{-1}.

^{1}H NMR (500 MHz, Chloroform-*d*) δ 8.11 (d, *J* = 6.9 Hz, 1H), 7.98 (d, *J* = 7.7 Hz, 2H), 7.66 (d, *J* = 9.0 Hz, 1H), 7.46 (t, *J* = 7.6 Hz, 2H), 7.32 (s, 1H), 7.29 (d, *J* = 8.5 Hz, 2H), 7.19 (dd, *J* = 8.7, 7.0 Hz, 1H), 6.81 (t, *J* = 6.6 Hz, 1H), 6.28 – 6.22 (m, 1H).

$^{13}C\{^{1}H\}$ NMR (126 MHz, Chloroform-*d*) δ 146.3, 144.6, 141.3, 134.8, 133.1, 128.7, 128.6, 128.2, 127.7, 127.6, 127.0, 126.5, 126.2, 124.3, 123.7, 117.7, 112.1, 39.6, 33.9, 30.3, 28.9.

HRMS (ESI) m/z: $[M+H]^+$ Calc'd for $C_{25}H_{23}N_2$ 351.1856; found: 351.1853.

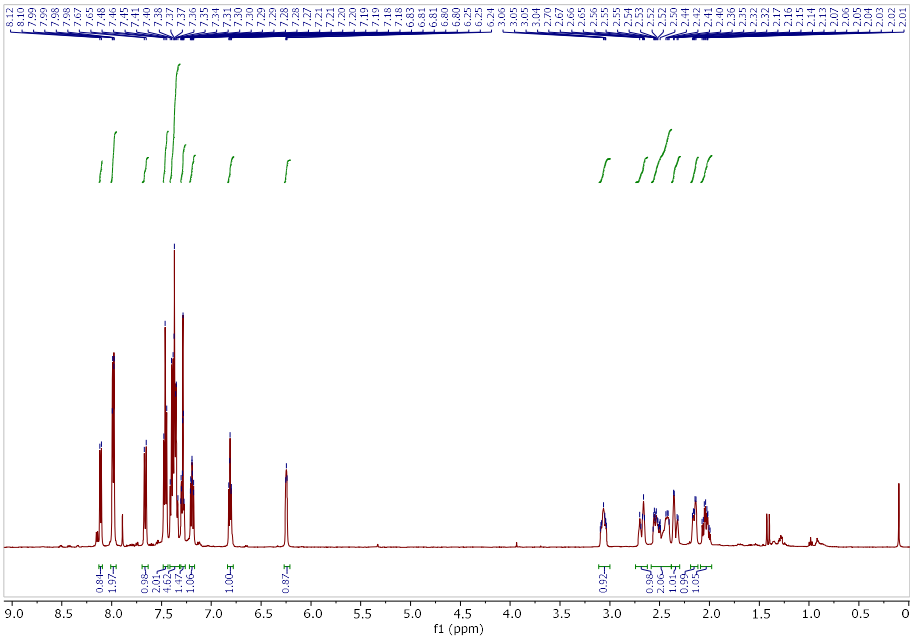

Fig. B12. ^{1}H NMR (500 MHz, Chloroform-*d*) spectrum of **A3**

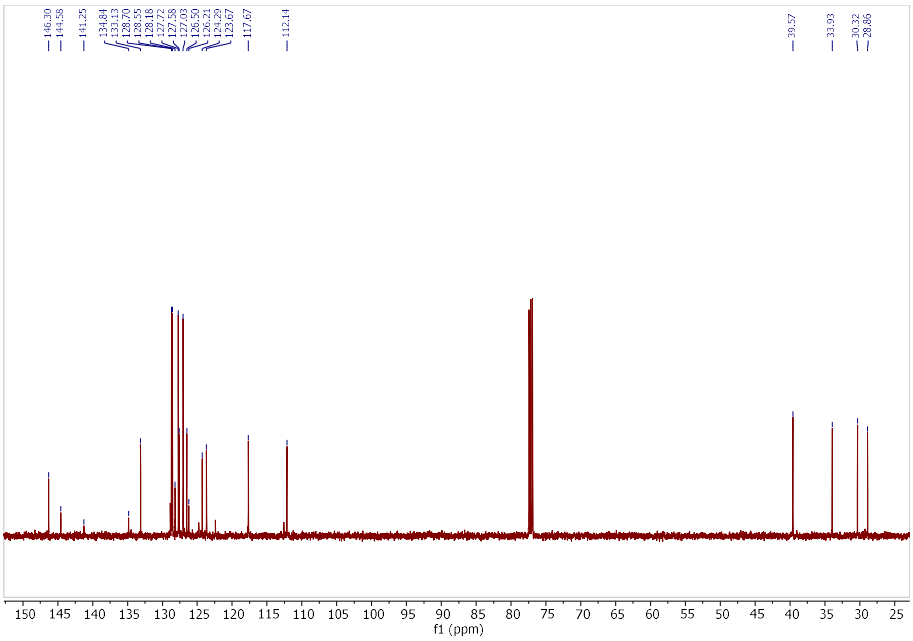

Fig. B13. $^{13}C\{^{1}H\}$ NMR (126 MHz, Chloroform-*d*) spectrum of **A3**

4-Methyl-2-(1,2,3,6-tetrahydro-[1,1'-biphenyl]-4-yl)thiazole (A5, major product, C_2 regioisomer):

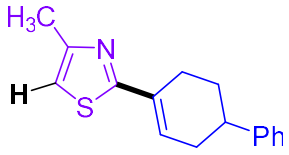

A5, 30%

Isolated by column chromatography (EtOAc : Hexanes = 8:92). Yellow oil. 38.2 mg (30%),

IR ν: 3028, 2922, 1492, 972, 754 cm^{-1}.

^1H NMR (500 MHz, Chloroform-*d*) δ 7.37 – 7.33 (m, 2H), 7.30 – 7.22 (m, 3H), 6.80 – 6.75 (m, 2H), 2.96 – 2.89 (m, 1H), 2.83 (m, 1H), 2.70 – 2.63 (m, 1H), 2.58 – 2.53 (m, 1H), 2.48 (s, 3H), 2.44 – 2.35 (m, 1H), 2.15 (m, 1H), 1.98 – 1.87 (m, 1H).

$^{13}C\{^1H\}$ NMR (126 MHz, Chloroform-*d*) δ 169.6, 152.9, 146.3, 132.2, 128.9, 128.5, 126.9, 126.3, 112.0, 39.7, 33.8, 29.6, 27.4, 17.3.

HRMS (ESI) m/z: $[M+H]^+$ Calc'd for $C_{16}H_{18}NS$ 256.1155; found: 256.1153.

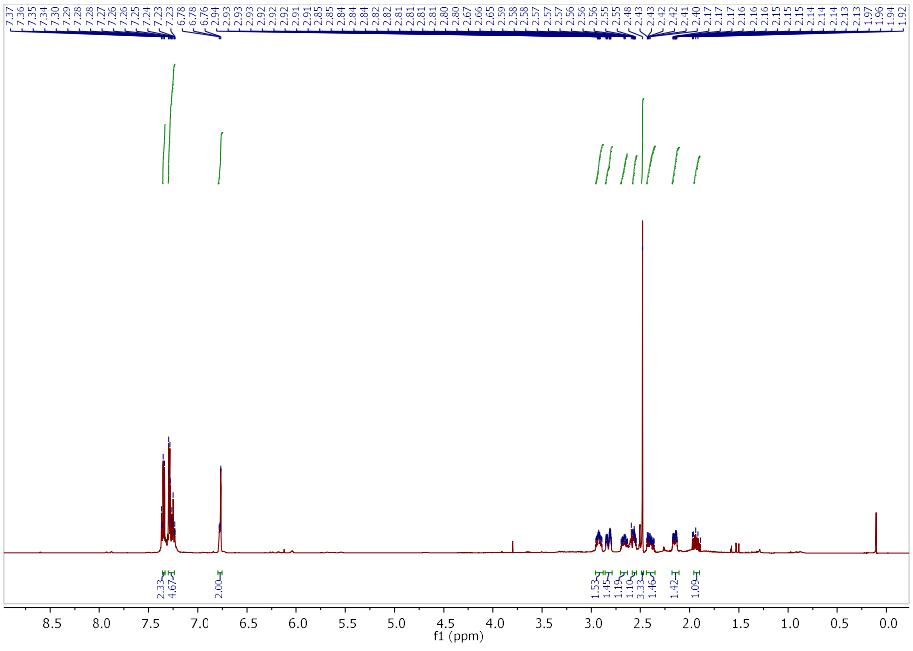

Fig. B14. ^1H NMR (500 MHz, Chloroform-*d*) spectrum of **A5, C_2 regioisomer**

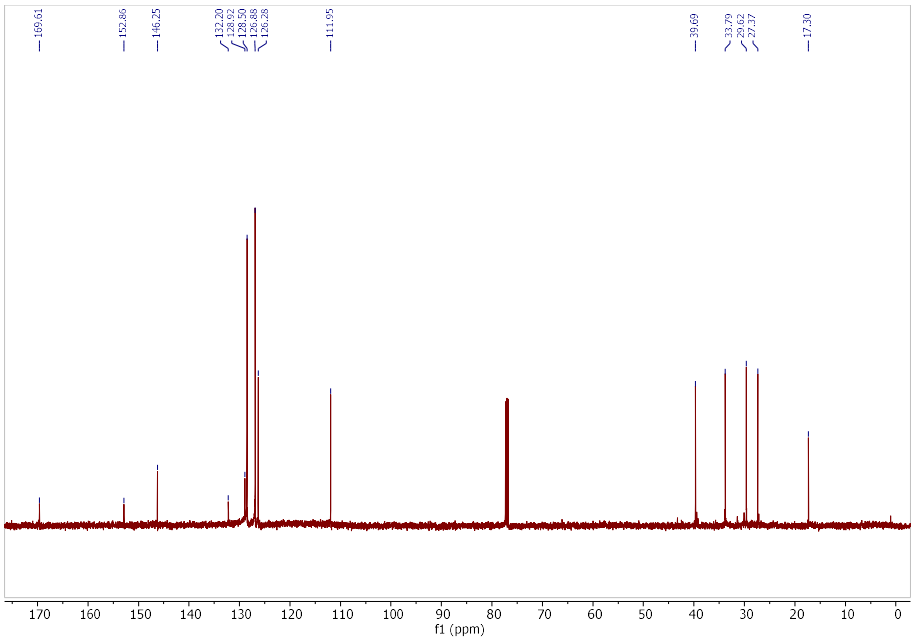

Fig. B15. $^{13}C\{^{1}H\}$ NMR (126 MHz, Chloroform-*d*) spectrum of **A5, C_2 regioisomer**

4-Methyl-5-(1,2,3,6-tetrahydro-[1,1'-biphenyl]-4-yl)thiazole (A5, minor product, C_5 regioisomer):

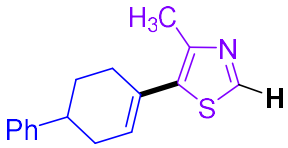

A5, 20%

Isolated by column chromatography (EtOAc : Hexanes = 15:85) Orange oil. 25.4 mg (20%),

IR ν: 3026, 2931, 1702, 1451, 1176, 698 cm^{-1}.

^1H NMR (500 MHz, Chloroform-*d*) δ 8.60 (s, 1H), 7.42 – 7.19 (m, 5H), 6.05 (dt, *J* = 5.3, 2.5 Hz, 1H), 2.92 (ddt, *J* = 11.6, 8.2, 3.0 Hz, 1H), 2.57-2.53 (m, 4H), 2.49 – 2.35 (m, 2H), 2.11 (ddq, *J* = 13.1, 5.3, 2.8 Hz, 1H), 1.96 (qd, *J* = 11.8, 5.4 Hz, 1H).

$^{13}C\{^1H\}$ NMR (126 MHz, Chloroform-*d*) δ 149.0, 147.7, 146.5, 134.2 129.2, 128.9, 128.6, 127.0, 126.4, 39.5, 33.9, 31.6, 30.2, 16.9.

HRMS (ESI) m/z: $[M+H]^+$ Calc'd for $C_{16}H_{18}NS$ 256.1155; found: 256.1154.

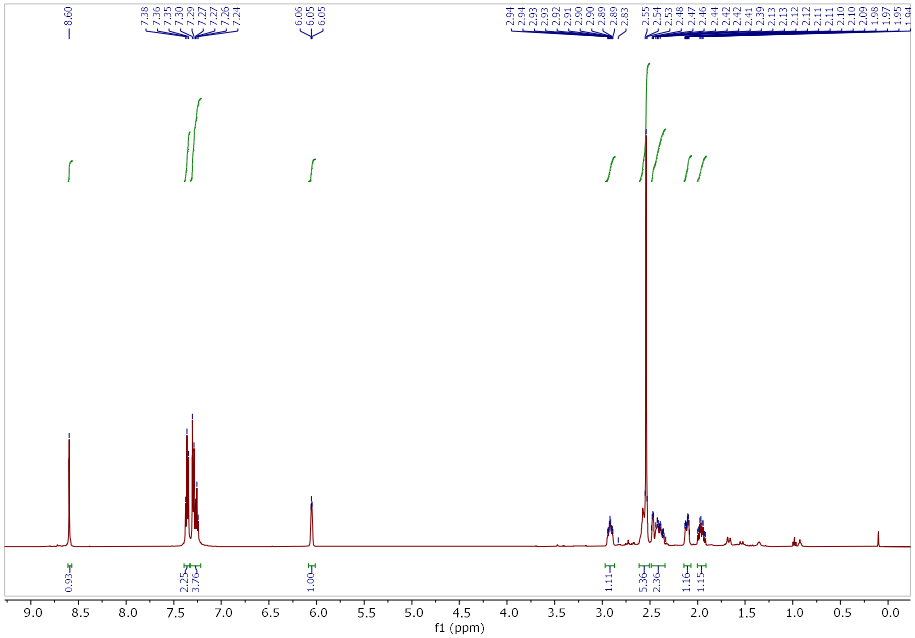

Fig. B16. ^1H NMR (500 MHz, Chloroform-*d*) spectrum of **A5, C_5 regioisomer**

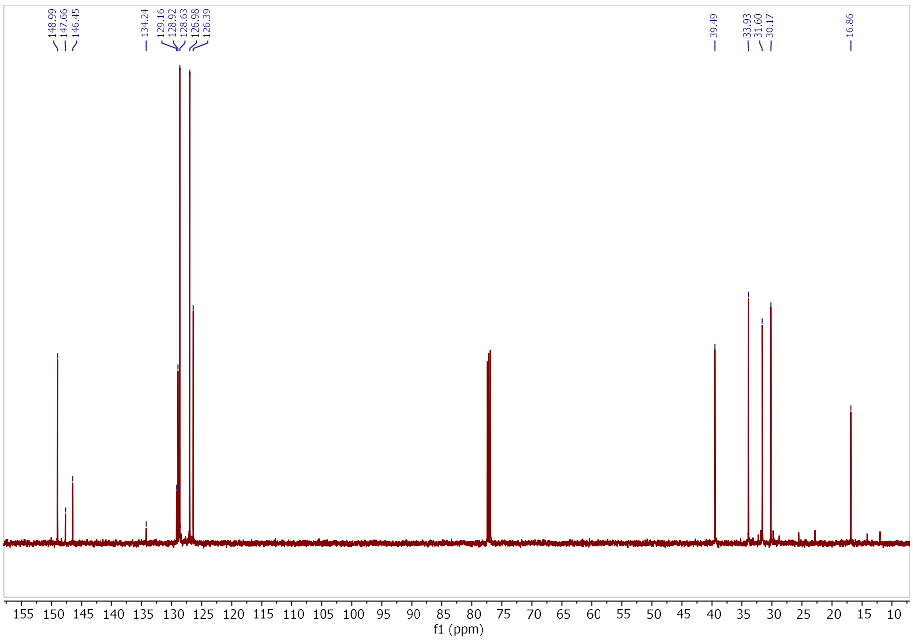

Fig. B17. $^{13}C\{^{1}H\}$ NMR (126 MHz, Chloroform-*d*) spectrum of **A5, C_5 regioisomer**

4-Methyl-2,5-bis(1,2,3,6-tetrahydro-[1,1'-biphenyl]-4-yl)thiazole (A5, dialkenylated product):

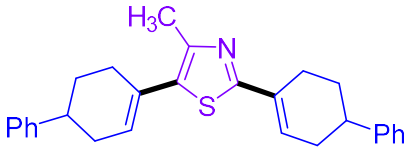

A5, 10%

Isolated by column chromatography (EtOAc : Hexanes = 10:90). Yellow oil. 20.6 mg (10%),

IR ν: 3028, 2918, 1702, 1492, 907, 697 cm^{-1}.

^{1}H NMR (500 MHz, Chloroform-*d*) δ 7.36 (m, 4H), 7.31 – 7.28 (m, 4H), 7.27 – 7.22 (m, 2H), 6.72 (m, 1H), 6.04 (m, 1H), 2.97 – 2.87 (m, 2H), 2.84 – 2.78 (m, 2H), 2.55 (m, 4H), 2.50 (s, 3H), 2.44 – 2.34 (m, 2H), 2.17 – 2.06 (m, 2H), 2.00 – 1.84 (m, 2H).

$^{13}C\{^{1}H\}$ NMR (126 MHz, Chloroform-*d*) δ 165.6, 146.4, 146.3, 133.0, 129.3, 128.8, 128.6, 128.5, 128.5, 128.4, 128.4, 39.7, 39.4, 33.9, 33.8, 31.4, 30.1, 29.6, 27.2, 16.9.

HRMS (ESI) m/z: $[M+H]^{+}$ Calc'd for $C_{28}H_{30}NS$ 412.2094; found: 412.2093.

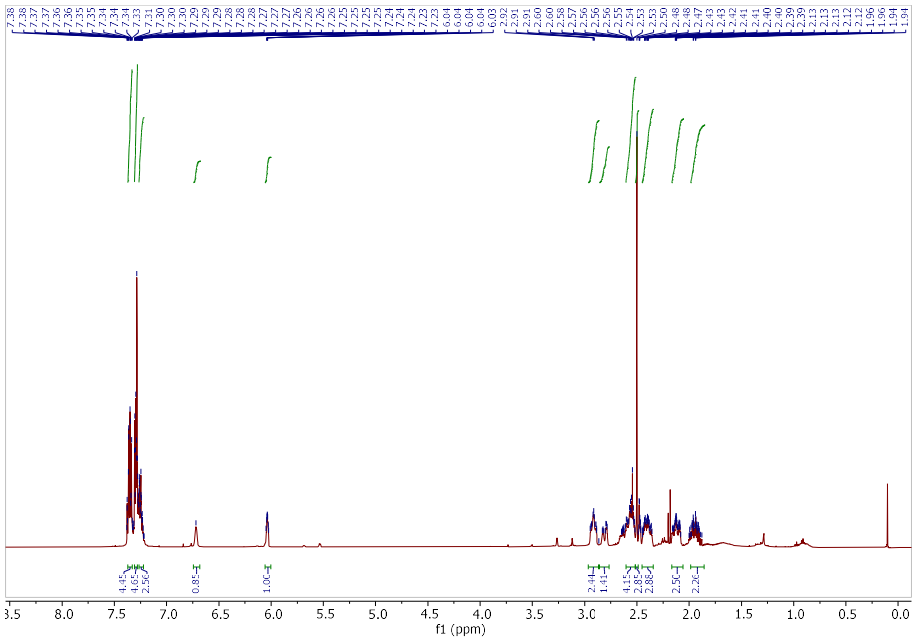

Fig. B18. ^{1}H NMR (500 MHz, Chloroform-*d*) spectrum of **A5 dialkenylated product**

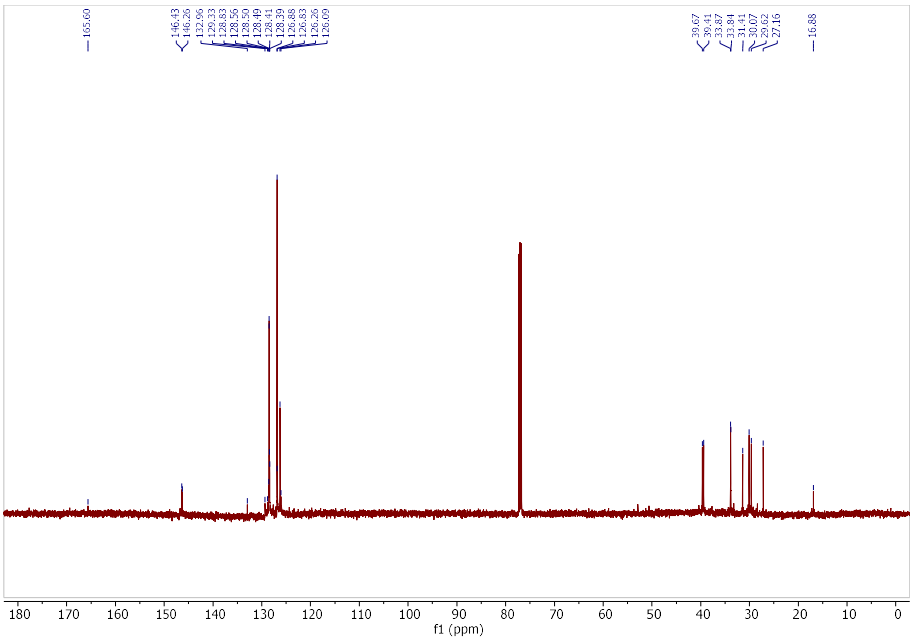

Fig. B19. $^{13}C\{^{1}H\}$ NMR (126 MHz, Chloroform-*d*) spectrum of **A5 dialkenylated product**

4-Phenyl-2-(pyridin-2-yl)-5-(1,2,3,6-tetrahydro-[1,1'-biphenyl]-4-yl)thiazole **(A7)**:

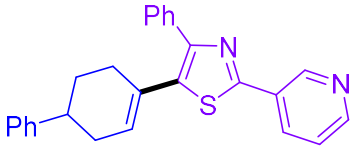

A7, 55%

Isolated by column chromatography (EtOAc : Hexanes = 40:60). Orange oil. 106.6 mg (55%).

IR ν: 3026, 2918, 1702, 1183, 695 cm^{-1}.

^{1}H NMR (500 MHz, Chloroform-*d*) δ 9.21 (d, *J* = 2.3 Hz, 1H), 8.67 (d, *J* = 4.8 Hz, 1H), 8.31 (dt, *J* = 7.9, 2.1 Hz, 1H), 7.83 (d, *J* = 7.6 Hz, 2H), 7.47 (t, *J* = 7.6 Hz, 2H), 7.44 – 7.32 (m, 4H), 7.32 – 7.24 (m, 3H), 6.24 – 6.14 (m, 1H), 2.96 – 2.88 (m, 1H), 2.53 (dt, *J* = 17.9, 5.4 Hz, 1H), 2.46 – 2.28 (m, 3H), 2.07 – 2.00 (m, 1H), 1.89 (ddt, *J* = 16.0, 11.3, 5.2 Hz, 1H).

$^{13}C\{^{1}H\}$ NMR (126 MHz, Chloroform-*d*) δ 160.3, 150.5, 150.4, 147.7, 146.2, 136.0, 135.4, 133.4, 131.1, 129.9, 129.3, 128.6, 128.5, 128.4, 128.0, 126.9, 126.3, 123.7, 39.2, 33.8, 30.0, 29.8.

HRMS (ESI) m/z: $[M+H]^+$ Calc'd for $C_{26}H_{23}N_2S$ 395.1577; found: 395.1576.

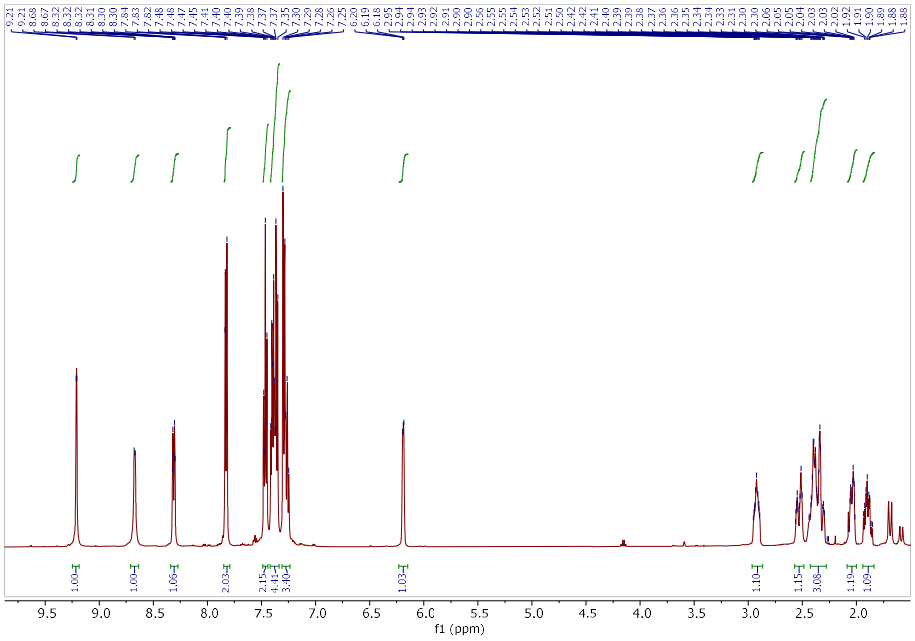

Fig. B20. ^{1}H NMR (500 MHz, Chloroform-*d*) spectrum of **A7**

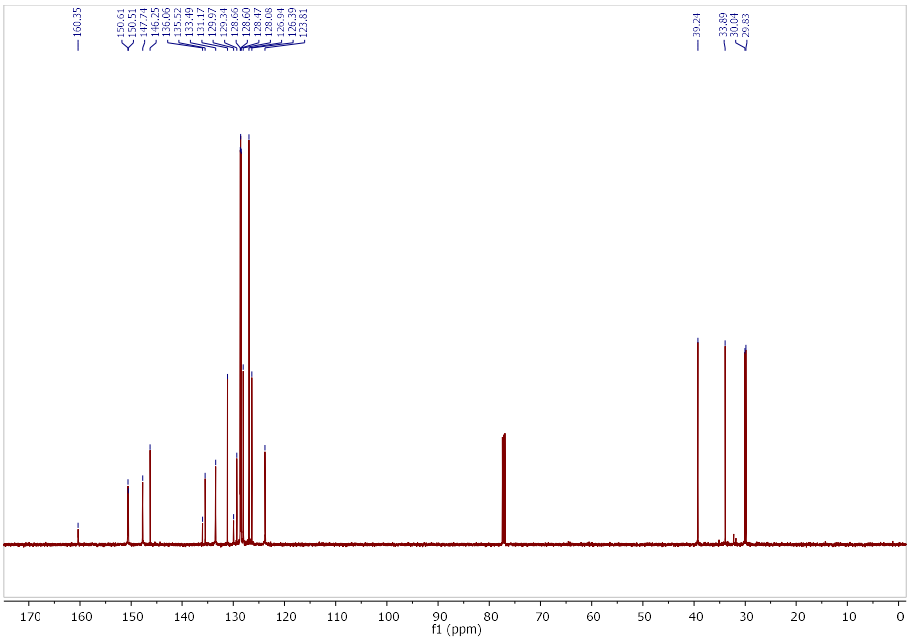

Fig. B21. $^{13}C\{^{1}H\}$ NMR (126 MHz, Chloroform-*d*) spectrum of **A7**

1-Methyl-2-(1,2,3,6-tetrahydro-[1,1'-biphenyl]-4-yl)-1H-indole-3-carbaldehyde (A9):

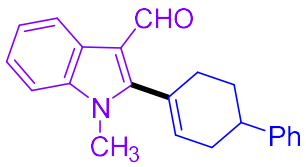

A9, 50%

Isolated by column chromatography (EtOAc : Hexanes = 25:75). Orange solid. 76.1 mg (50%). MP: 150-152 °C.

IR ν: 3028, 2912, 1649, 1381, 743 cm^{-1}.

^{1}H NMR (500 MHz, Chloroform-*d*) δ 9.99 (s, 1H), 8.45 – 8.35 (m, 1H), 7.43 – 7.33 (m, 6H), 7.32 – 7.28 (m, 1H), 6.25 – 6.10 (m, 1H), 3.74 (s, 3H), 3.09 – 3.00 (m, 1H), 2.67 (dt, *J* = 18.0, 5.4 Hz, 1H), 2.59 – 2.39 (m, 3H), 2.19 (dp, *J* = 13.1, 3.7, 3.3 Hz, 1H), 2.10 – 2.00 (m, 1H).

$^{13}C\{^{1}H\}$ NMR (126 MHz, Chloroform-*d*) δ 186.0, 154.2, 145.8, 137.2, 135.1, 128.7, 127.2, 126.9, 126.6, 125.3, 123.8, 123.1, 122.1, 114.8, 109.7, 39.3, 33.5, 30.8, 30.7, 29.8.

HRMS (ESI) m/z: $[M+H]^+$ Calc'd for $C_{22}H_{22}NO$ 316.1696; found: 316.1695.

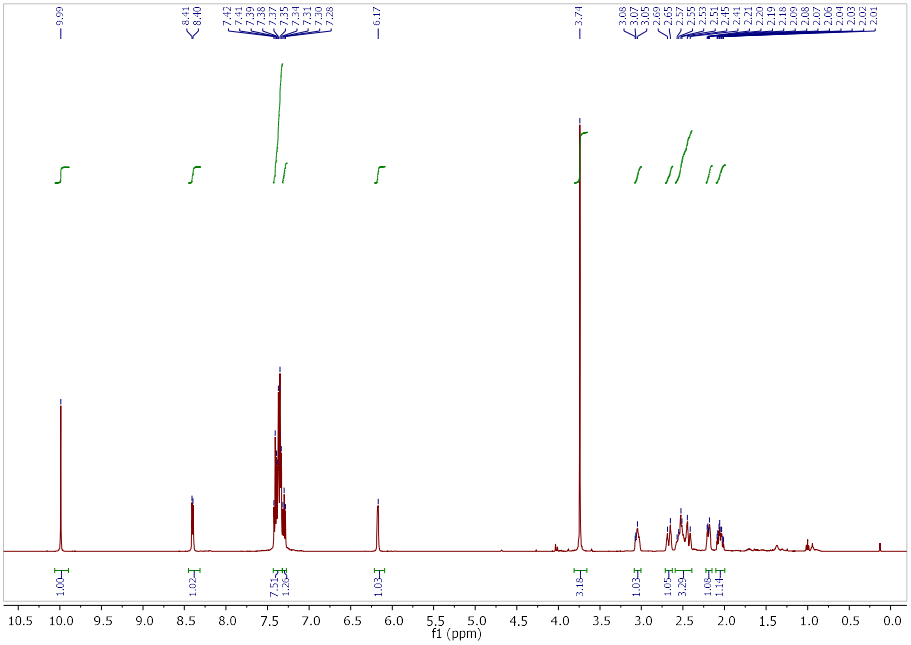

Fig. B22. ^{1}H NMR (500 MHz, Chloroform-*d*) spectrum of **A9**

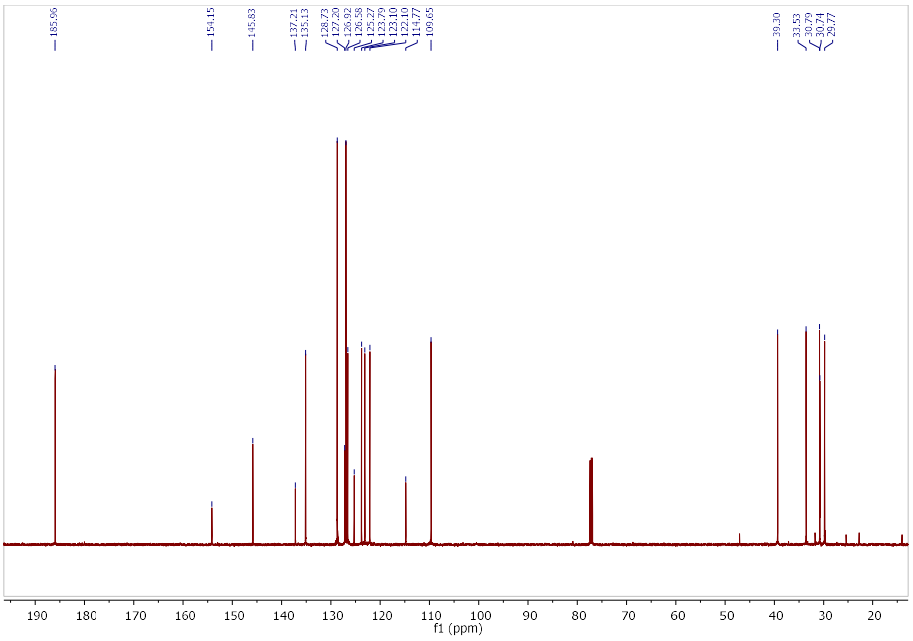

Fig. B23. $^{13}C\{^{1}H\}$ NMR (126 MHz, Chloroform-*d*) spectrum of **A9**

1-(Tetrahydro-2H-pyran-2-yl)-5-(1,2,3,6-tetrahydro-[1,1'-biphenyl]-4-yl)-1H-pyrazole-4-carbaldehyde (A21):

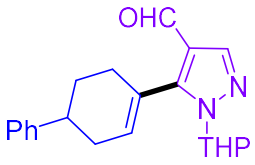

A21, 70%

Isolated by column chromatography (EtOAc : Hexanes = 40:60). Light yellow oil. 117.9 mg (70%).

IR ν: 3028, 2927, 1677, 1466, 1043, 698 cm^{-1}.

^{1}H NMR (500 MHz, Chloroform-*d*) δ 9.81 (d, *J* = 3.2 Hz, 1H), 8.01 (s, 1H), 7.38 (t, *J* = 7.5 Hz, 2H), 7.32 (d, *J* = 7.6 Hz, 2H), 7.28 (d, *J* = 7.0 Hz, 1H), 6.12 (t, *J* = 5.7 Hz, 1H), 5.29 (ddd, *J* = 27.0, 10.0, 2.6 Hz, 1H), 4.17 – 4.01 (m, 1H), 3.62 (dtd, *J* = 43.8, 11.4, 2.6 Hz, 1H), 3.01 (tt, *J* = 9.6, 4.6 Hz, 1H), 2.68 – 2.38 (m, 3H), 2.14 (dp, *J* = 9.6, 3.3, 2.9 Hz, 3H), 2.08 – 1.95 (m, 1H), 1.94 – 1.85 (m, 1H), 1.80 – 1.67 (m, 2H), 1.66 – 1.58 (m, 2H).

$^{13}C\{^{1}H\}$ NMR (126 MHz, Chloroform-*d*) δ 184.9, 184.8, 184.9, 184.8, 150.3, 150.2, 145.8, 140.1, 140.0, 134.1, 134.0, 128.7, 126.9, 126.8, 126.3, 121.3, 84.6, 84.5, 68.1, 33.5, 33.4, 30.1, 30.0, 29.7, 29.6, 24.9, 24.8, 22.7, 22.6.

HRMS (ESI) m/z: $[M+H]^+$ Calc'd for $C_{21}H_{25}N_2O_2$ 337.1911; found: 337.1912.

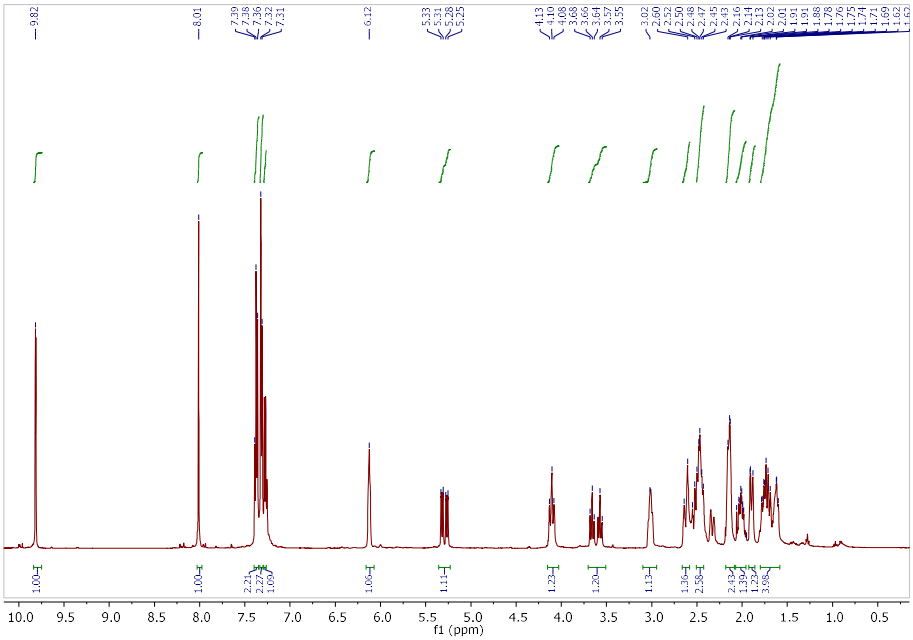

Fig. B24. ^{1}H NMR (500 MHz, Chloroform-*d*) spectrum of **A21**

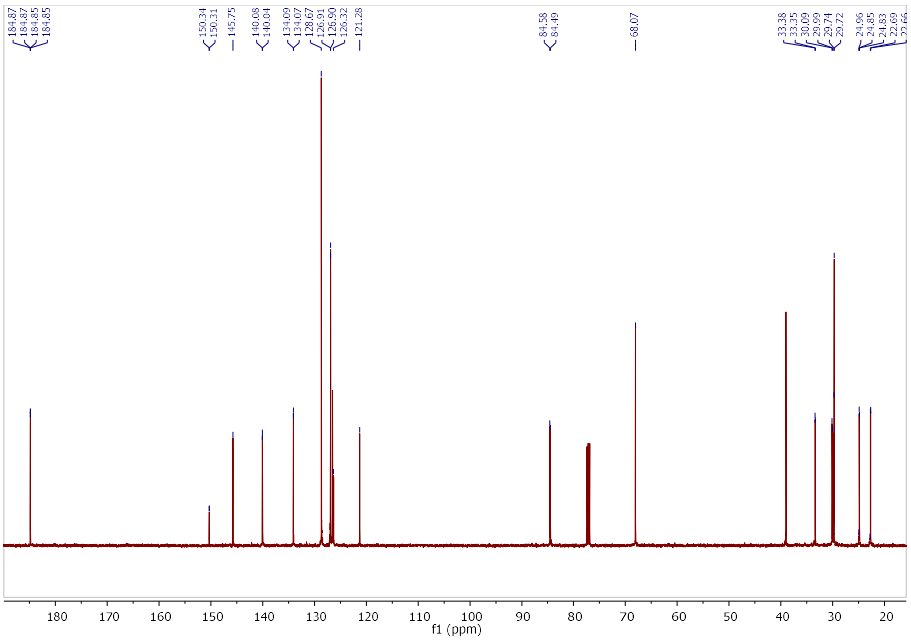

Fig. B25. $^{13}C\{^{1}H\}$ NMR (126 MHz, Chloroform-*d*) spectrum of **A21**

***tert*-Butyl 4-(2-phenyl-4-(pyridin-3-yl)thiazol-5-yl)-3,6-dihydropyridine-1(2H)-carboxylate (B7)**:

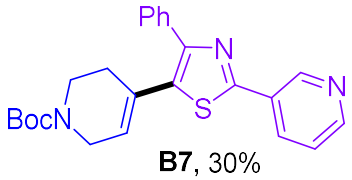

B7, 30%

Isolated by column chromatography (EtOAc : Hexanes = 30:70). Yellow oil. 60.3 mg (30%).

IR ν: 2976, 1686, 1407, 1161, 689 cm^{-1}.

^{1}H NMR (500 MHz, Chloroform-*d*) δ 9.21 (s, 1H), 8.70 (s, 1H), 8.33 (d, *J* = 8.0 Hz, 1H), 7.76 – 7.69 (m, 2H), 7.47 – 7.42 (m, 3H), 7.41 – 7.37 (m, 1H), 6.04 (s, 1H), 4.08 (s, 2H), 3.56 (t, *J* = 5.6 Hz, 2H), 2.29 (s, 2H), 1.51 (s, 9H).

$^{13}C\{^{1}H\}$ NMR (126 MHz, Chloroform-*d*) δ 163.2, 155.0, 151.3, 147.4, 145.8, 134.6, 133.9, 133.6, 129.3, 129.0, 128.8, 128.6, 128.3, 125.2, 83.3, 43.7, 29.2, 28.7, 28.5, 28.1.

HRMS (ESI) m/z: $[M+H]^+$ Calc'd for $C_{24}H_{26}N_3O_2S$ 420.1740; found: 420.1741.

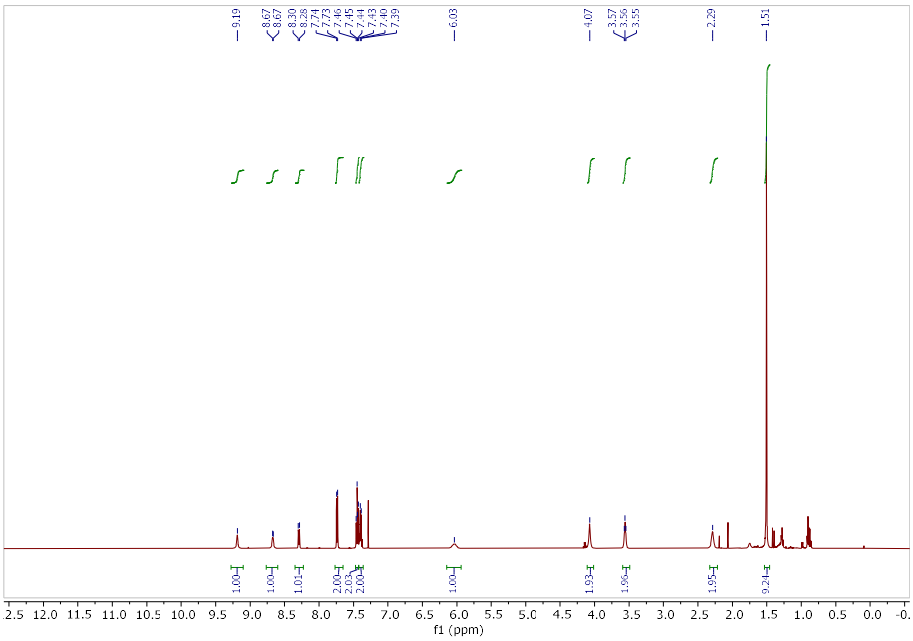

Fig. B26. ^{1}H NMR (500 MHz, Chloroform-*d*) spectrum of **B7**

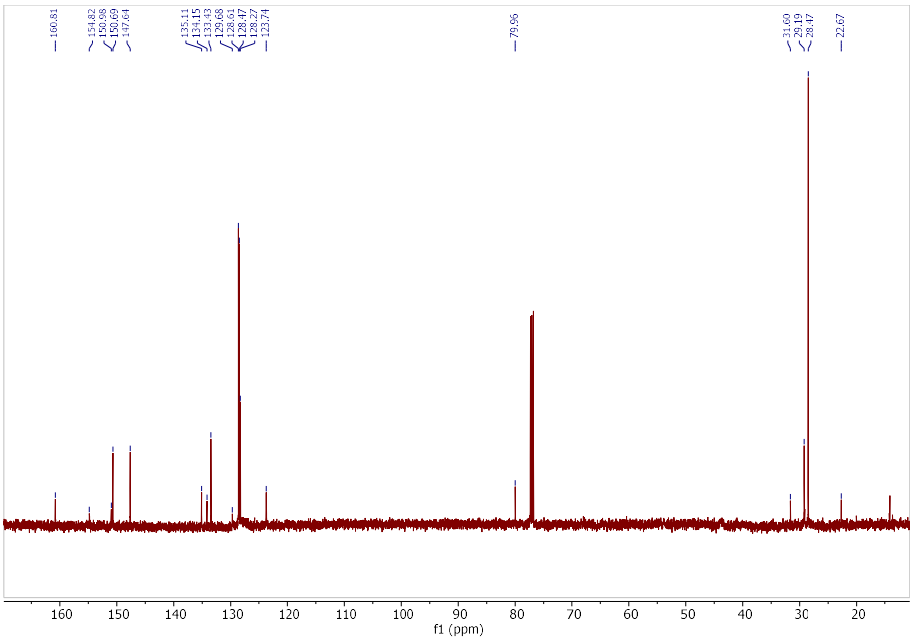

Fig. B27. $^{13}C\{^{1}H\}$ NMR (126 MHz, Chloroform-*d*) spectrum of **B7**

***tert*-Butyl 4-(benzo[d]thiazol-2-yl)-3,6-dihydropyridine-1(2H)-carboxylate (B13)**:

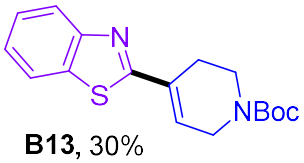

B13, 30%

Isolated by column chromatography (EtOAc : Hexanes = 10:90). Orange oil. 47.5 mg (30%).

IR ν: 2961, 1697, 1366, 1161, 785 cm^{-1}.

^{1}H NMR (500 MHz, Chloroform-*d*) δ 8.03 – 7.99 (m, 1H), 7.86 (d, *J* = 7.9 Hz, 1H), 7.49 – 7.45 (m, 1H), 7.41 – 7.35 (m, 1H), 6.70 (s, 1H), 4.20 (s, 2H), 3.69 (s, 2H), 2.84 (s, 2H), 1.52 (s, 9H).

$^{13}C\{^{1}H\}$ NMR (126 MHz, Chloroform-*d*) δ 187.8, 154.8, 153.6, 134.2, 126.2, 126.0, 125.3, 124.8, 123.1, 121.6, 121.5, 80.0, 28.5, 28.3, 26.6.

HRMS (ESI) m/z: $[M+H]^+$ Calc'd for $C_{17}H_{21}N_2O_2S$ 317.13183; found: 317.13222.

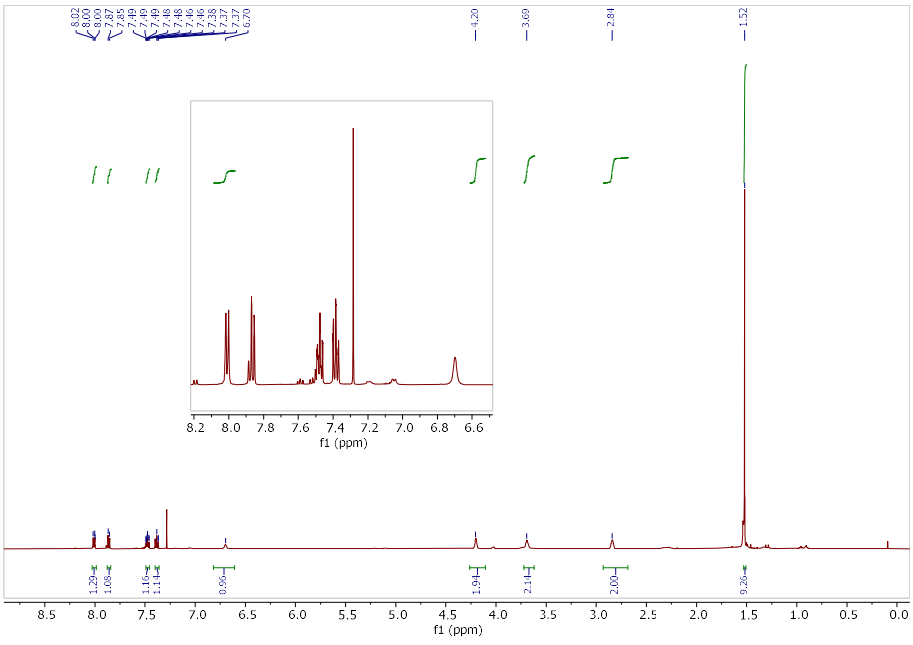

Fig. B28. ^{1}H NMR (500 MHz, Chloroform-*d*) spectrum of **B13**. Minor additional peaks are due to decomposition (product **B13** observed to decompose in solution at room temperature).

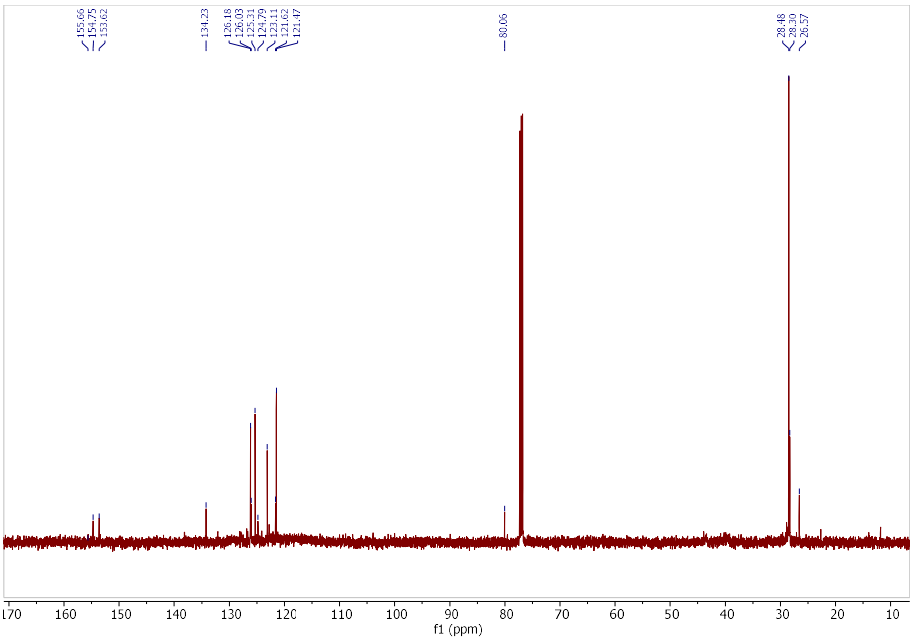

Fig. B29. $^{13}C\{^{1}H\}$ NMR (126 MHz, Chloroform-*d*) spectrum of **B13**

***tert*-Butyl 4-(3-formylthiophen-2-yl)-3,6-dihydropyridine-1(2H)-carboxylate (B19)**:

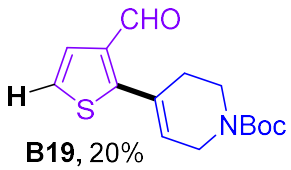

B19, 20%

Isolated by column chromatography (EtOAc : Hexanes = 25:75). Yellow oil. 29.7 mg (20%).

IR ν: 2974, 1677, 1366, 1153, 725 cm^{-1}.

^{1}H NMR (500 MHz, Chloroform-*d*) δ 9.94 – 9.93 (m, 1H), 7.48 (d, *J* = 5.4 Hz, 1H), 7.21 (dd, *J* = 5.3, 0.8 Hz, 1H), 5.98 (s, 1H), 4.15 (d, *J* = 3.0 Hz, 2H), 3.69 (t, *J* = 5.6 Hz, 2H), 2.58 (s, 2H), 1.52 (s, 9H).

$^{13}C\{^{1}H\}$ NMR (126 MHz, Chloroform-*d*) δ 185.1, 137.5, 126.8, 124.1, 46.8, 31.5, 31.2, 29.5, 28.5, 28.2, 25.2, 22.6, 13.9, 11.8.

HRMS (ESI) m/z: $[M+NH_4]^+$ Calc'd for $C_{15}H_{23}N_2O_3S$ 311.1429; found: 311.1418.

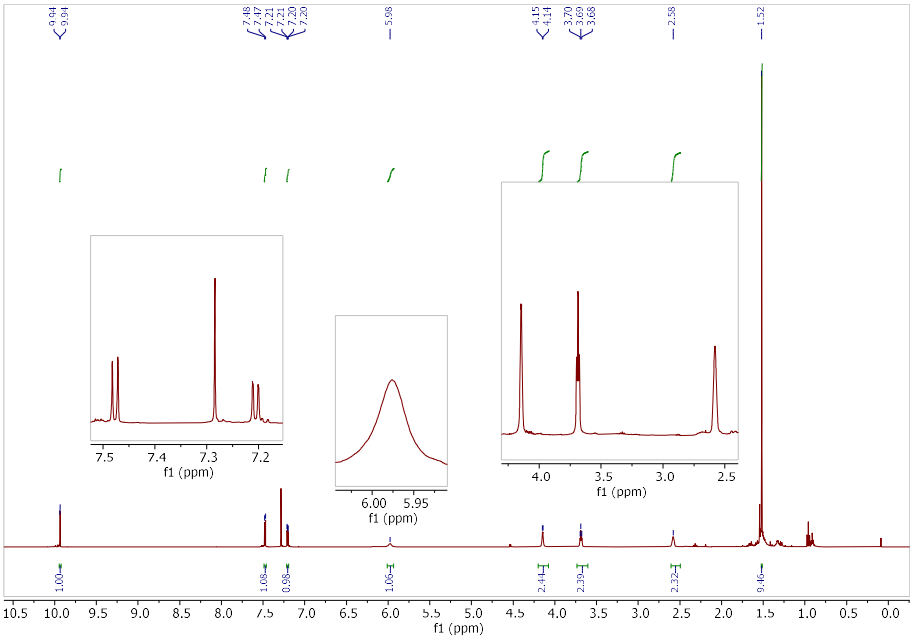

Fig. B30. ^{1}H NMR (500 MHz, Chloroform-*d*) spectrum of **B19**

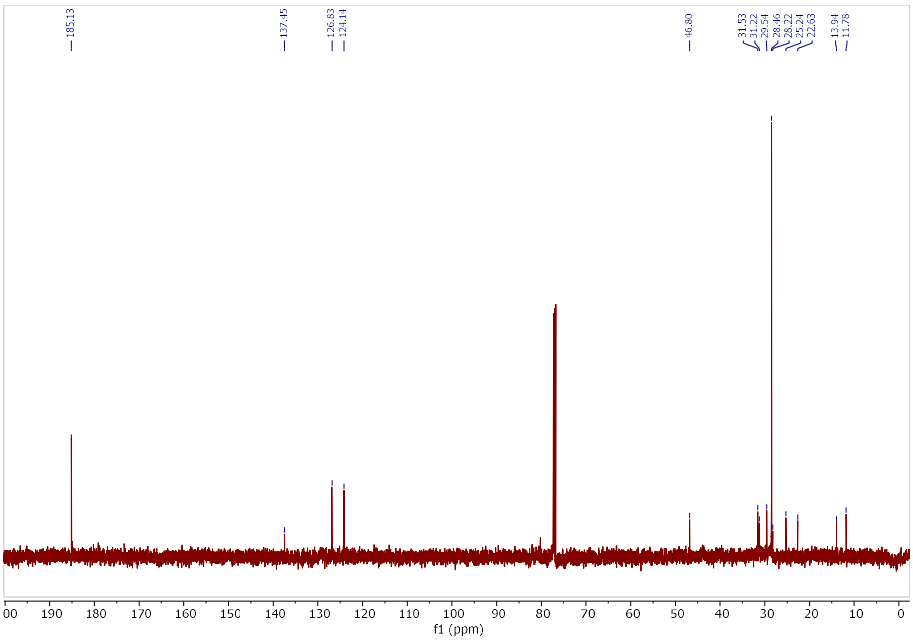

Fig. B31. $^{13}C\{^{1}H\}$ NMR (126 MHz, Chloroform-*d*) spectrum of **B19**

2-(1H-Inden-2-yl)-4-methylthiazole (C5, major product, C_2 regioisomer):

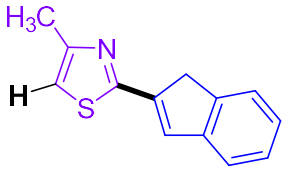

C5, 48%

Isolated by column chromatography (EtOAc : Hexanes = 15:85). Brown solid. 50.5 mg (48%). MP: 59-62 °C.

IR ν: 3052, 2922, 1561, 1135, 982, 853 cm^{-1}.

^1H NMR (500 MHz, Chloroform-*d*) δ 7.51 (m, 1H), 7.49 – 7.45 (m, 2H), 7.35 – 7.30 (m, 1H), 7.30 – 7.27 (m, 1H), 6.85 (d, *J* = 1.2 Hz, 1H), 3.99 – 3.94 (m, 2H), 2.52 (d, *J* = 1.0 Hz, 3H).

$^{13}C\{^1H\}$ NMR (126 MHz, Chloroform-*d*) δ 164.0, 153.7, 144.1, 143.2, 131.2, 126.9, 126.9, 126.1, 124.0, 122.0, 113.1, 39.6, 17.3.

HRMS (ESI) m/z: $[M+H]^+$ Calc'd for $C_{13}H_{12}NS$ 214.0685; found: 214.0686.

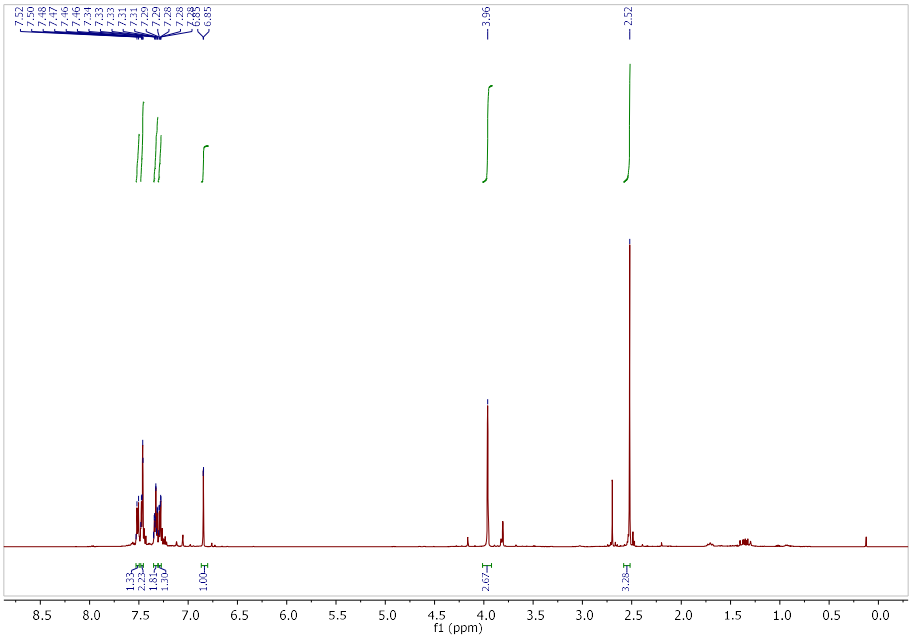

Fig. B32. ^1H NMR (500 MHz, Chloroform-*d*) spectrum of **C5**, C_2regioisomer. Minor additional signals assigned to a C_2/C_5 doubly alkenylated impurity.

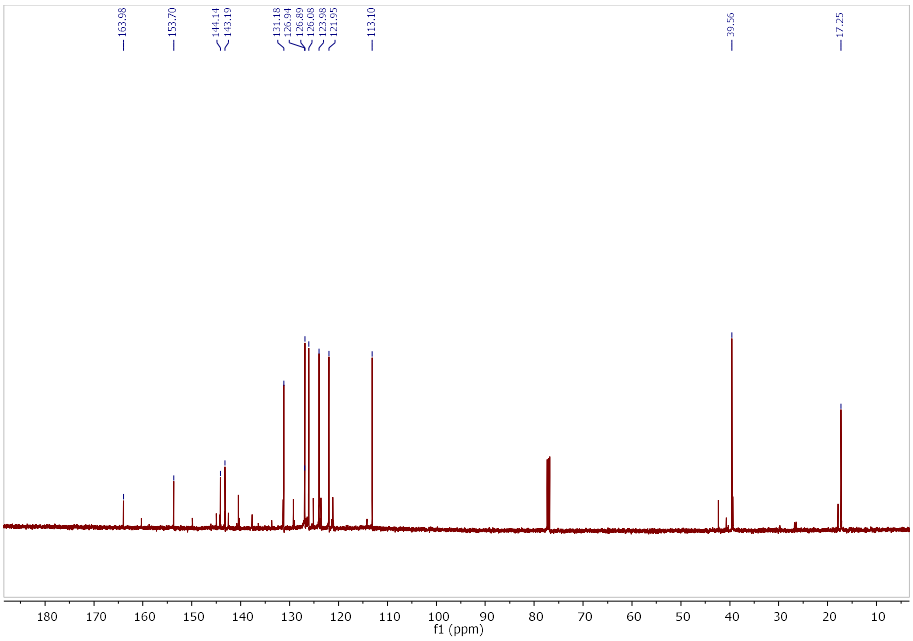

Fig. B33. $^{13}C\{^{1}H\}$ NMR (126 MHz, Chloroform-*d*) spectrum of **C5**, C_2regioisomer. Minor additional signals assigned to a C_2/C_5 doubly alkenylated impurity.

5-(1H-Inden-2-yl)-4-methylthiazole (C5, minor product, C_5 regioisomer):

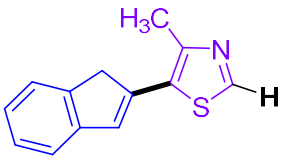

C5, 28%

Isolated by column chromatography (EtOAc : Hexanes = 17:83). Brown oil. 29.6 mg (28%)

IR ν: 3054, 2920, 1686, 1459, 937, 752 cm^{-1}.

^1H NMR (500 MHz, Chloroform-*d*) δ 8.63 (s, 1H), 7.49 (d, *J* = 7.4 Hz, 1H), 7.44 (d, *J* = 7.5 Hz, 1H), 7.32 (t, *J* = 7.4 Hz, 1H), 7.23 (td, *J* = 7.4, 1.0 Hz, 1H), 7.07 (s, 1H), 3.81 (s, 2H), 2.71 (s, 3H).

$^{13}C\{^1H\}$ NMR (126 MHz, Chloroform-*d*) δ 149.4, 144.8, 144.8, 142.5, 129.9, 129.6, 126.9, 125.2, 123.6, 121.2, 42.4, 17.5.

HRMS (ESI) m/z: $[M+H]^+$ Calc'd for $C_{13}H_{12}NS$ 214.0685; found: 214.0685.

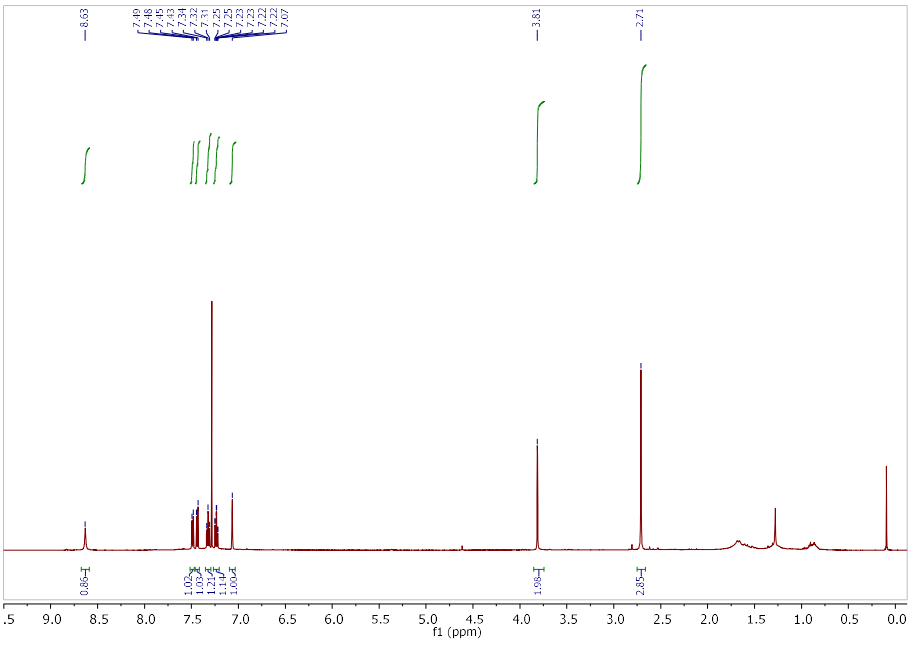

Fig. B34. ^1H NMR (500 MHz, Chloroform-*d*) spectrum of **C5**

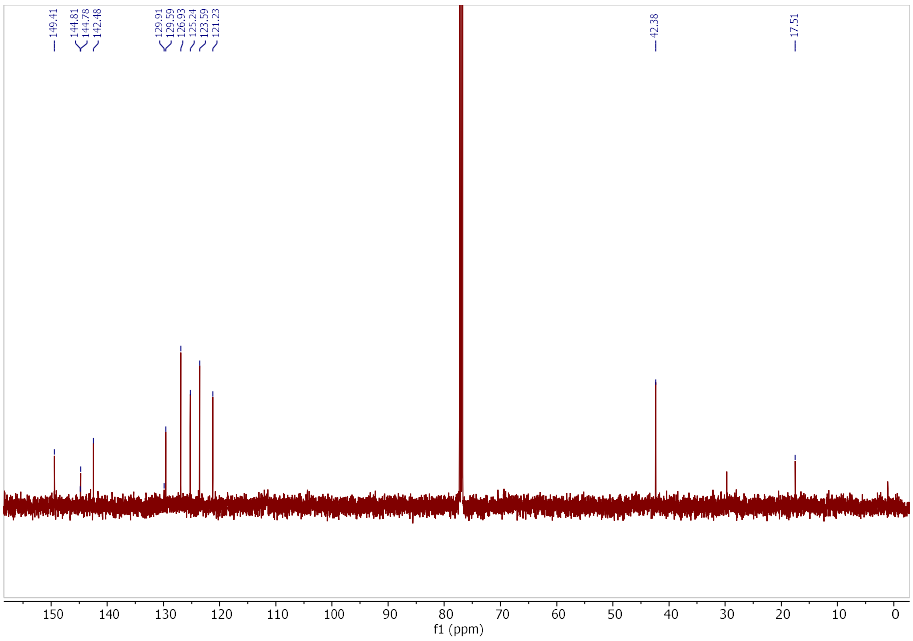

Fig. B35. $^{13}C\{^{1}H\}$ NMR (126 MHz, Chloroform-*d*) spectrum of **C5**

2-(1H-Inden-2-yl)thiazole (C6):

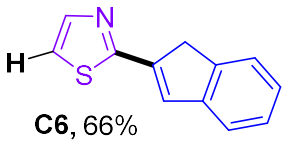

C6, 66%

Isolated by column chromatography (EtOAc : Hexanes = 22:78). Brown solid. 66 mg (66%). MP: 69-70 °C.

IR ν: 3045, 2924, 1561, 1127, 866, 702 cm^{-1}.

^{1}H NMR (500 MHz, Chloroform-*d*) δ 7.84 (d, *J* = 3.3 Hz, 1H), 7.54 – 7.50 (m, 1H), 7.49 – 7.45 (m, 2H), 7.33 (td, *J* = 7.5, 1.3 Hz, 1H), 7.31 – 7.27 (m, 2H), 4.04 – 3.87 (m, 2H).

$^{13}C\{^{1}H\}$ NMR (126 MHz, Chloroform-*d*) δ 164.7, 144.0, 143.5, 143.2, 140.3, 131.7, 126.9, 126.2, 124.0, 122.1, 118.5, 39.5.

HRMS (ESI) m/z: $[M+H]^+$ Calc'd for $C_{12}H_{10}NS$ 200.0529; found: 200.0529.

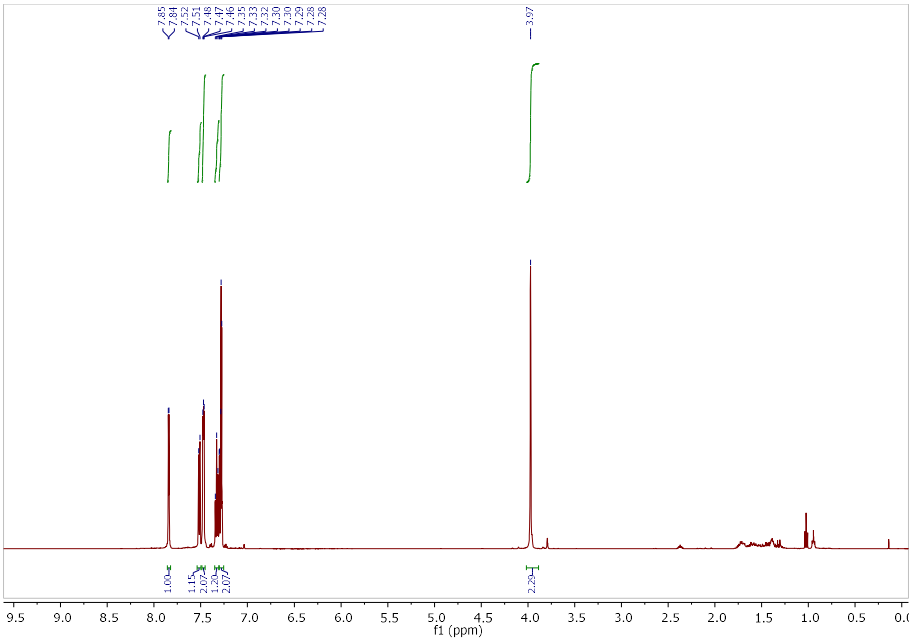

Fig. B36. ^{1}H NMR (500 MHz, Chloroform-*d*) spectrum of **C6**

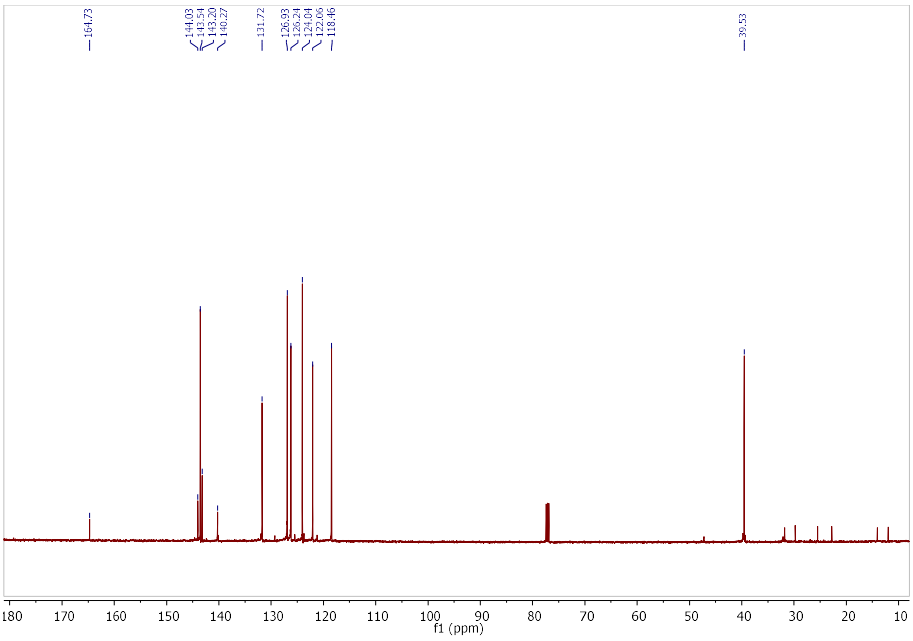

Fig. B37. $^{13}C\{^{1}H\}$ NMR (126 MHz, Chloroform-*d*) spectrum of **C6**

2-(3,4-Dihydronaphthalen-1-yl)benzo[b]thiophene-3-carbaldehyde (D15):

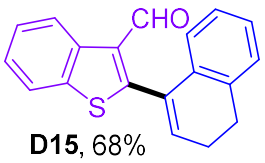

D15, 68%

Isolated by column chromatography (100% Hexanes). Yellow oil. 99.1 mg (68%).

IR ν: 3060, 2935, 2830, 1668, 1459, 1148, 730 cm^{-1}.

^{1}H NMR (500 MHz, Chloroform-*d*) δ 10.01 (s, 1H), 8.80 (d, *J* = 0.6 Hz, 1H), 7.86 (d, *J* = 8.0 Hz, 1H), 7.55 (ddd, *J* = 8.2, 7.2, 1.2 Hz, 1H), 7.47 (ddd, *J* = 8.3, 7.2, 1.3 Hz, 1H), 7.05 (d, *J* = 7.5 Hz, 1H), 6.43 (t, *J* = 4.6 Hz, 1H), 2.97 (t, *J* = 8.1 Hz, 2H), 2.58 (ddd, *J* = 8.9, 7.5, 4.7 Hz, 2H).

$^{13}C\{^{1}H\}$ NMR (126 MHz, Chloroform-*d*) δ 186.4, 159.6, 138.2, 136.5, 135.4, 135.0, 134.6, 131.9, 130.3, 128.2, 127.8, 127.0, 126.1, 125.8, 125.4, 125.0, 121.8, 27.6, 23.7.

HRMS (ESI) m/z: $[M+H]^{+}$ Calc'd for $C_{19}H_{15}OS$ 291.0844; found: 291.0847.

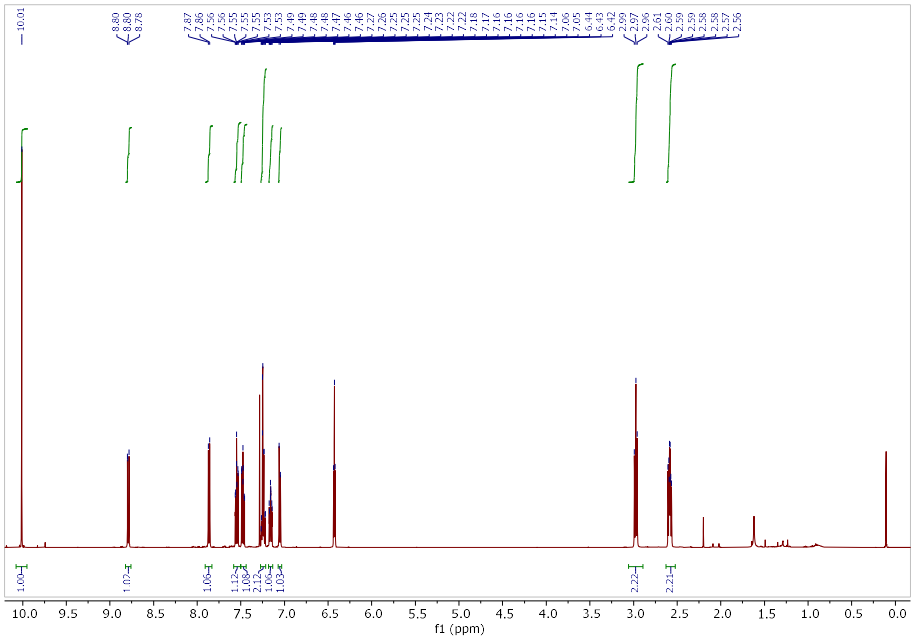

Fig. B40. ^{1}H NMR (500 MHz, Chloroform-*d*) spectrum of **D15**

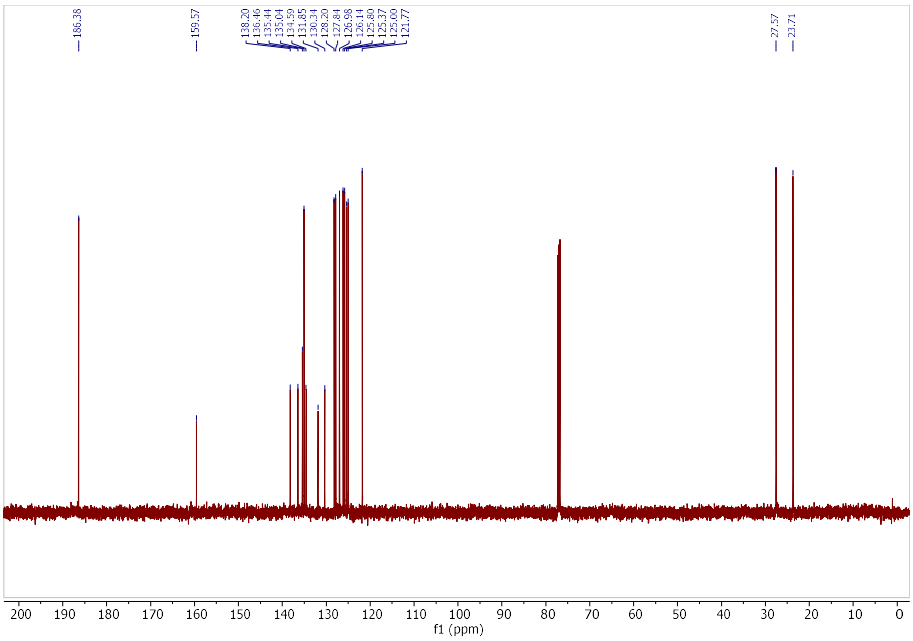

Fig. B41. $^{13}C\{^{1}H\}$ NMR (126 MHz, Chloroform-*d*) spectrum of **D15**

Ethyl 5-(3,4-dihydronaphthalen-1-yl)thiophene-2-carboxylate (D17):

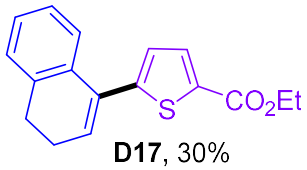

D17, 30%

Isolated by column chromatography (EtOAc : Hexanes = 5:95). Yellow oil. 41.2 mg (30%).

IR ν: 3983, 1703, 1451, 1086, 747 cm^{-1}.

^{1}H NMR (500 MHz, Chloroform-*d*) δ 7.77 (d, *J* = 3.8 Hz, 1H), 7.33 (dd, *J* = 6.8, 1.6 Hz, 1H), 7.25 – 7.17 (m, 3H), 7.06 (d, *J* = 3.8 Hz, 1H), 6.38 (t, *J* = 4.8 Hz, 1H), 4.39 (q, *J* = 7.1 Hz, 2H), 2.86 (t, *J* = 7.9 Hz, 2H), 2.53 – 2.37 (m, 2H), 1.41 (t, *J* = 7.1 Hz, 3H).

$^{13}C\{^{1}H\}$ NMR (126 MHz, Chloroform-*d*) δ 162.3, 149.8, 136.6, 133.6, 133.4, 132.7, 131.8, 130.7, 127.8, 127.7, 126.5, 126.3, 125.1, 61.1, 27.9, 23.5, 14.4.

HRMS (ESI) m/z: $[M+H]^+$ Calc'd for $C_{17}H_{17}O_2S$ 285.0949; found: 285.0950.

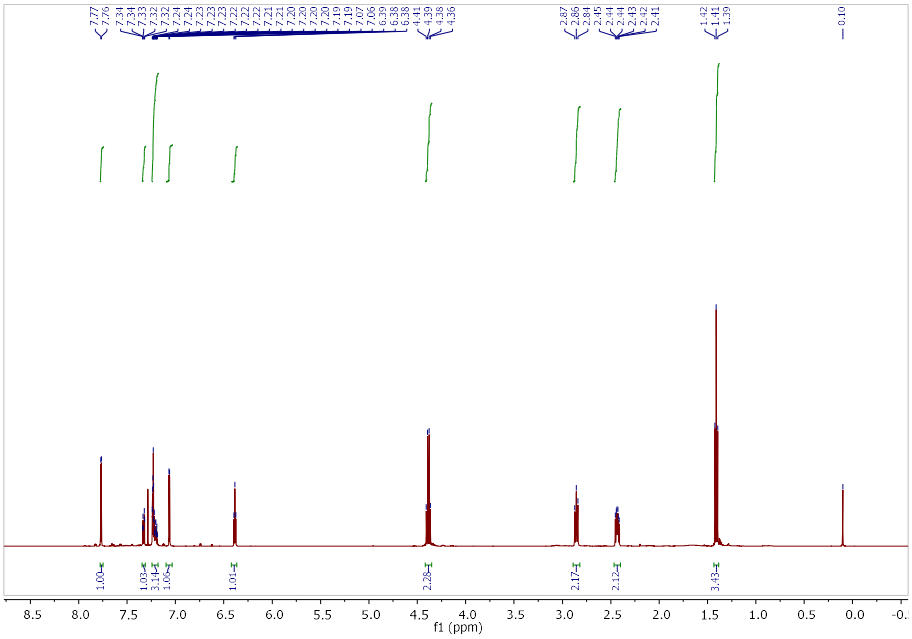

Fig. B42. ^{1}H NMR (500 MHz, Chloroform-*d*) spectrum of **D17**

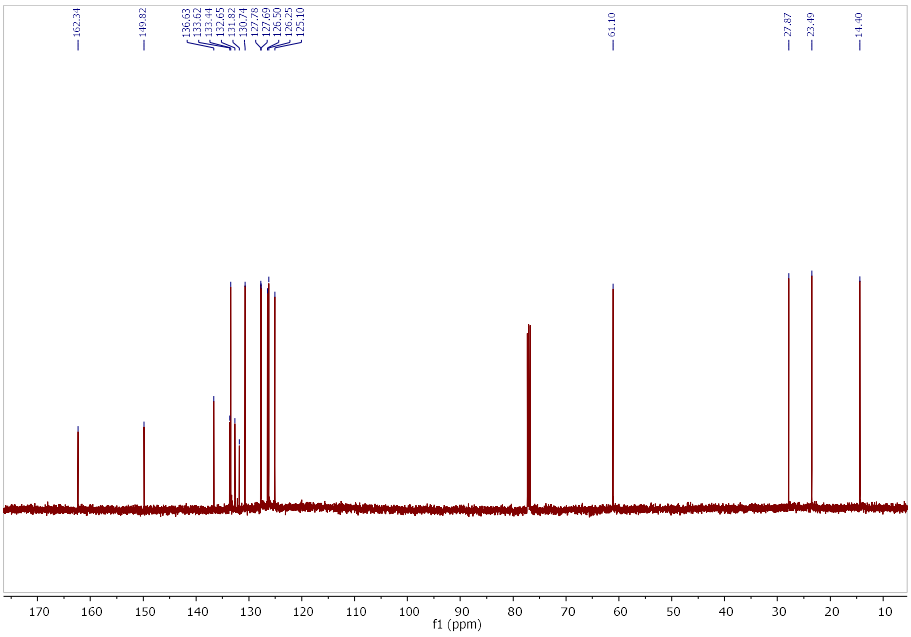

Fig. B43. $^{13}C\{^{1}H\}$ NMR (126 MHz, Chloroform-*d*) spectrum of **D17**

1-Methyl-2-(2-methyl-1-phenylprop-1-en-1-yl)-1H-indole-3-carbaldehyde (E9):

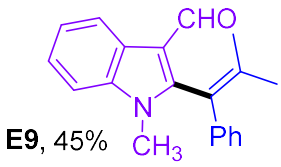

E9, 45%

Isolated by column chromatography (EtOAc : Hexanes = 30:70). Orange solid. 65.0 mg (45%), MP: 126-129 °C.

IR ν: 3050, 2729, 1641, 1373, 1045, 700 cm^{-1}.

^{1}H NMR (500 MHz, Chloroform-*d*) δ 9.99 (s, 1H), 8.45 – 8.37 (m, 1H), 7.36 – 7.31 (m, 5H), 7.29 – 7.21 (m, 2H), 3.55 (s, 3H), 2.10 (s, 3H), 1.83 (s, 3H).

$^{13}C\{^{1}H\}$ NMR (126 MHz, Chloroform-*d*) δ 186.6, 152.5, 142.0, 139.0, 137.4, 129.7, 128.5, 127.3, 125.3, 124.7, 123.6, 123.1, 122.2, 115.2, 109.7, 30.5, 23.9, 22.2.

HRMS (ESI) m/z: $[M+H]^+$ Calc'd for $C_{20}H_{20}NO$ 290.1539; found: 290.1540.

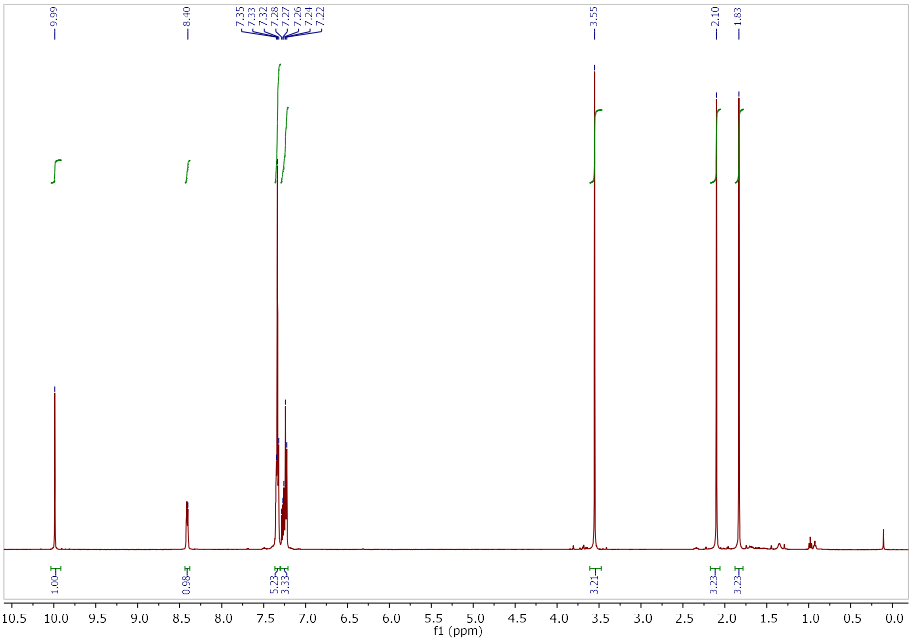

Fig. B44. ^{1}H NMR (500 MHz, Chloroform-*d*) spectrum of **E9**

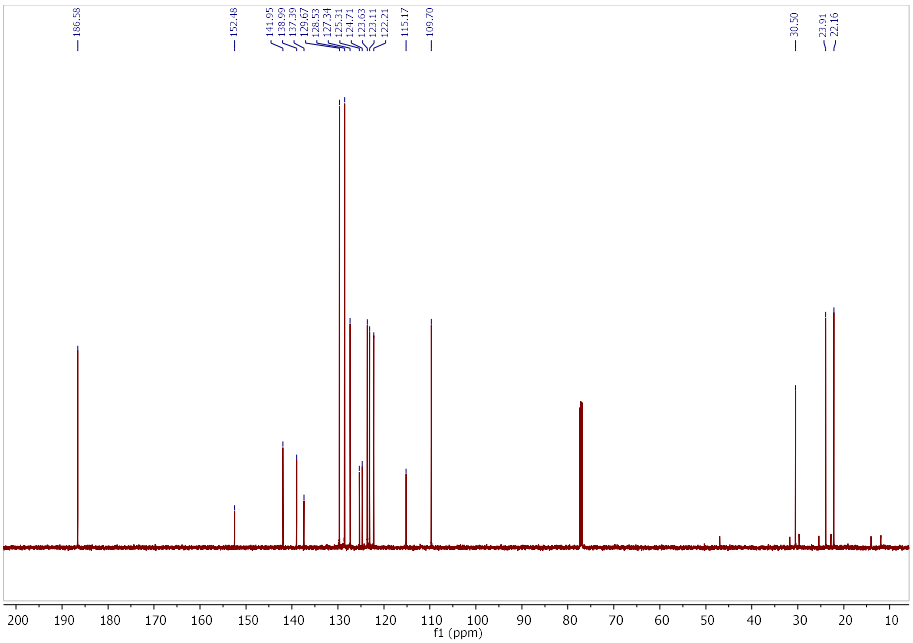

Fig. B45. $^{13}C\{^{1}H\}$ NMR (126 MHz, Chloroform-*d*) spectrum of **E9**

5-(2-Methyl-1-phenylprop-1-en-1-yl)thiophene-2-carbaldehyde (E16):

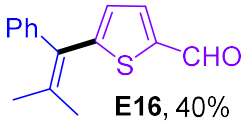

E16, 40%

Isolated by column chromatography (EtOAc : Hexanes = 25:75). Dark brown oil. 46.7 mg (40%).

IR ν: 3052, 2914, 1660, 1440, 1228, 700 cm^{-1}.

^{1}H NMR (500 MHz, Chloroform-*d*) δ 9.84 (s, 1H), 7.62 (d, *J* = 3.9 Hz, 1H), 7.37 (t, *J* = 7.4 Hz, 2H), 7.33 – 7.28 (m, 1H), 7.18 (d, *J* = 7.2 Hz, 2H), 6.85 (d, *J* = 3.9 Hz, 1H), 2.11 (s, 3H), 1.80 (s, 3H).

$^{13}C\{^{1}H\}$ NMR (126 MHz, Chloroform-*d*) δ 183.0, 155.8, 142.4, 142.2, 130.2, 129.6, 128.5, 128.3, 127.2, 24.0, 23.1.

HRMS (ESI) m/z: $[M+H]^+$ Calc'd for $C_{15}H_{15}OS$ 243.0838; found: 243.0839.

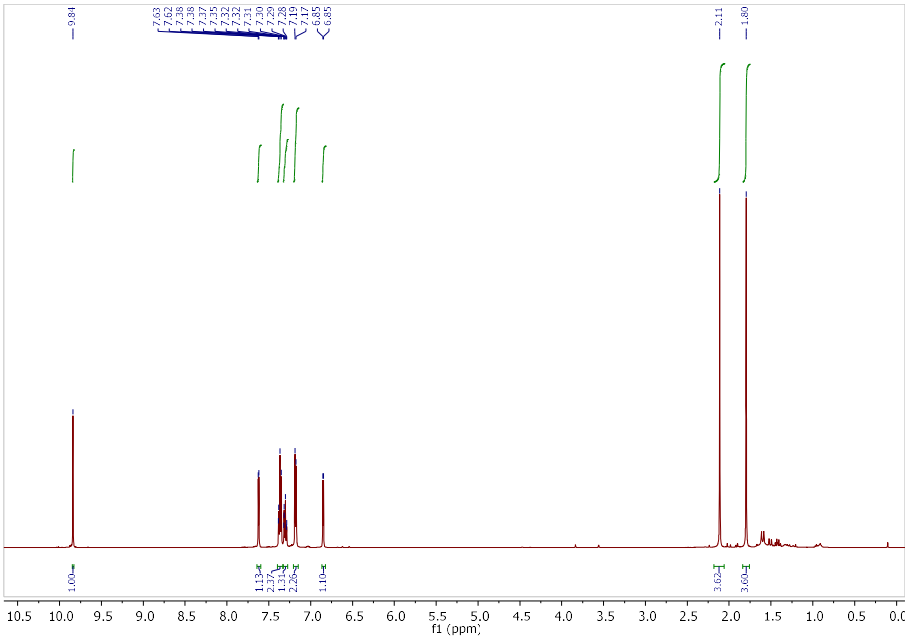

Fig. B46. ^{1}H NMR (500 MHz, Chloroform-*d*) spectrum of **E16**

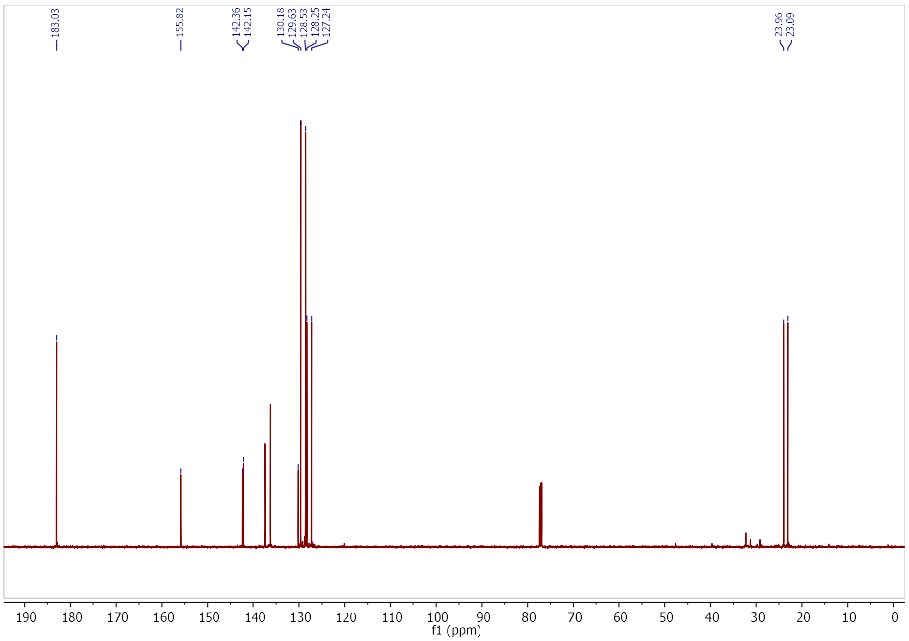

Fig. B47. $^{13}C\{^{1}H\}$ NMR (126 MHz, Chloroform-*d*) spectrum of **E16**

2-(2-Methyl-1-phenylprop-1-en-1-yl)thiophene-3-carbaldehyde (E19):

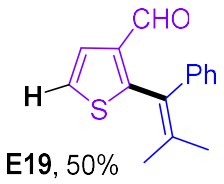

E19, 50%

Isolated by column chromatography (EtOAc : Hexanes = 10:90). Yellow oil. 60.0 mg (50%).

IR ν: 3024, 2909, 1668, 1379, 1230, 698 cm^{-1}.

^{1}H NMR (500 MHz, Chloroform-*d*) δ 9.88 (d, *J* = 0.9 Hz, 1H), 7.44 (d, *J* = 5.4 Hz, 1H), 7.36 – 7.32 (m, 2H), 7.28 – 7.24 (m, 1H), 7.23 – 7.21 (m, 3H), 1.93 (s, 3H), 1.84 (s, 3H).

$^{13}C\{^{1}H\}$ NMR (126 MHz, Chloroform-*d*) δ 185.9, 158.0, 141.3, 139.7, 137.7, 129.1, 128.4, 127.1, 126.5, 125.5, 125.0, 23.1, 22.5.

HRMS (ESI) m/z: $[M+H]^+$ Calc'd for $C_{15}H_{15}OS$ 243.0844; found: 243.0843.

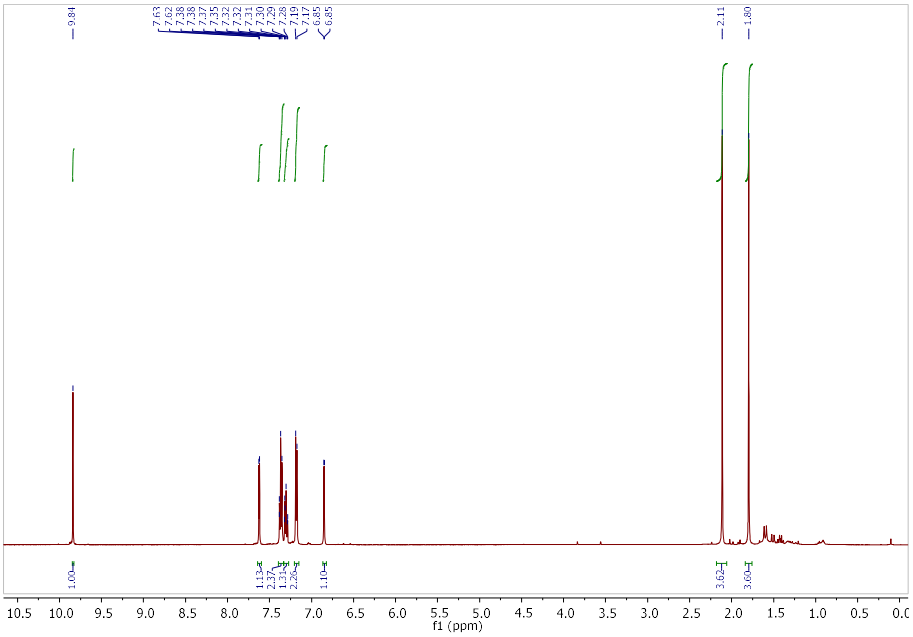

Fig. B48. ^{1}H NMR (500 MHz, Chloroform-*d*) spectrum of **E19**

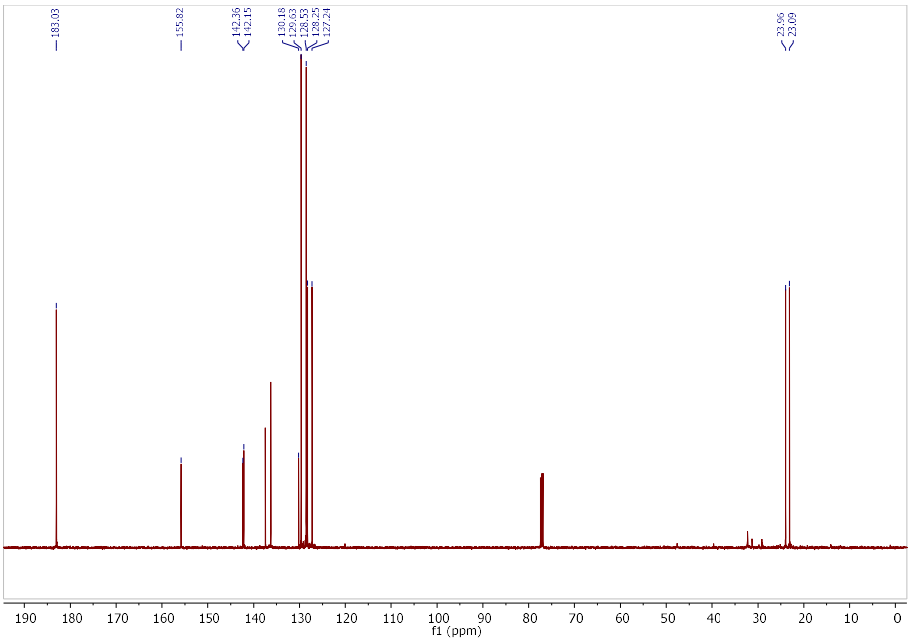

Fig. B49. $^{13}C\{^{1}H\}$ NMR (126 MHz, Chloroform-*d*) spectrum of **E19**

1-Benzyl-2-(2-methylprop-1-en-1-yl)-1H-indole-3-carbonitrile (F10):

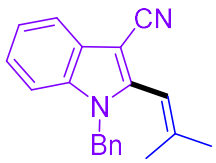

F10, 46%

Isolated by column chromatography (EtOAc : Hexanes = 20:80). Dark yellow oil. 66.0 mg (46%).

IR ν: 3032, 2916, 2214, 1654, 1451, 1183, 695 cm^{-1}.

^{1}H NMR (500 MHz, Chloroform-*d*) δ 7.80 – 7.73 (m, 1H), 7.35 – 7.25 (m, 6H), 7.06 – 7.01 (m, 2H), 6.15 – 6.11 (m, 1H), 5.33 (s, 2H), 2.02 (d, *J* = 1.5 Hz, 3H), 1.95 (d, *J* = 1.4 Hz, 3H).

$^{13}C\{^{1}H\}$ NMR (126 MHz, Chloroform-*d*) δ 147.6, 145.8, 136.2, 135.9, 129.1, 127.9, 127.7, 126.2, 123.7, 122.2, 119.4, 116.8, 111.8, 110.8, 86.5, 47.7, 26.4, 21.0.

HRMS (ESI) m/z: $[M+H]^+$ Calc'd for $C_{20}H_{19}N_2$ 287.1543; found: 287.1544.

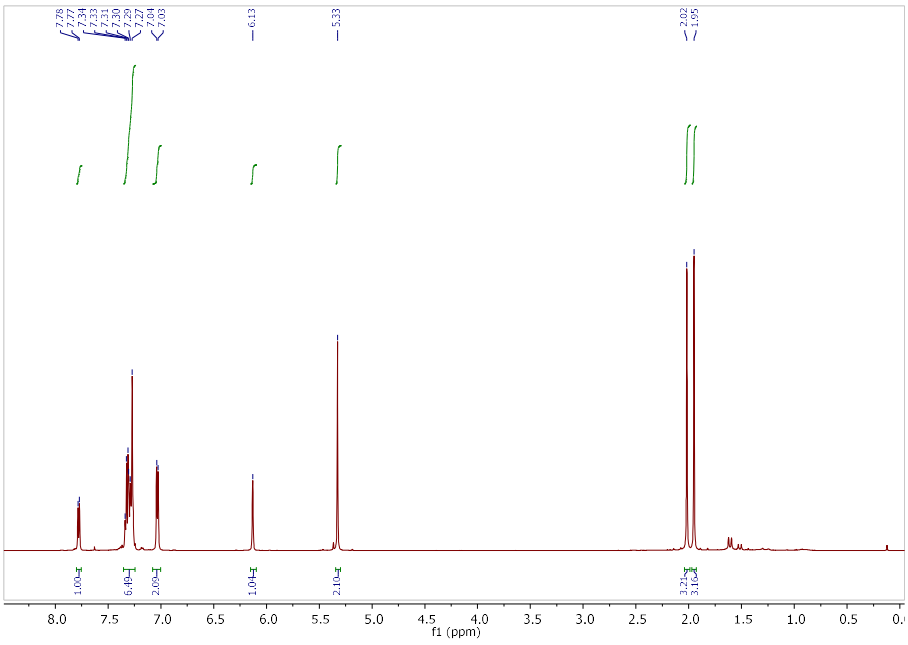

Fig. B50. ^{1}H NMR (500 MHz, Chloroform-*d*) spectrum of **F10**

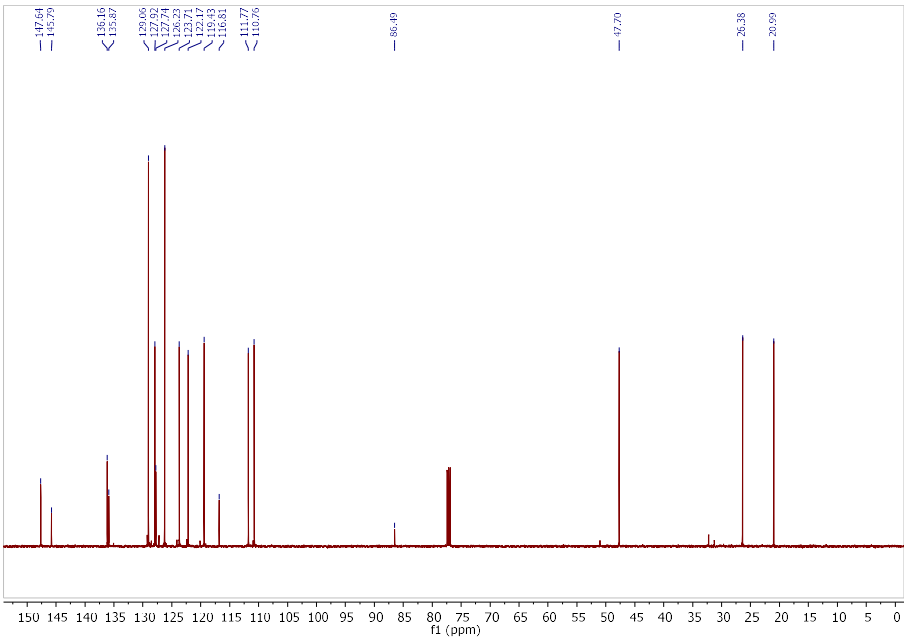

Fig. B51. $^{13}C\{^{1}H\}$ NMR (126 MHz, Chloroform-*d*) spectrum of **F10**

2-(2-Methylprop-1-en-1-yl)benzo[b]thiophene-3-carbaldehyde (F15):

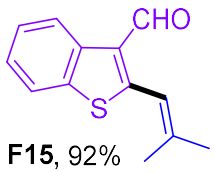

F15, 92%

Isolated by column chromatography (EtOAc : Hexanes = 20:80). Brown oil. 99.7 mg (92%)

IR ν: 2972, 1662, 1459, 751 cm^{-1}.

^{1}H NMR (500 MHz, Chloroform-*d*) δ 10.27 (s, 1H), 8.68 (d, *J* = 8.1 Hz, 1H), 7.80 (d, *J* = 8.0 Hz, 1H), 7.48 (t, *J* = 7.6 Hz, 1H), 7.40 (t, *J* = 7.5 Hz, 1H), 6.85 (s, 1H), 2.08 (s, 3H), 2.01 (s, 3H).

$^{13}C\{^{1}H\}$ NMR (126 MHz, Chloroform-*d*) δ 185.8, 157.1, 145.4, 137.9, 136.6, 129.7, 126.1, 125.5, 124.6, 121.6, 115.3, 27.4, 20.7.

HRMS (ESI) m/z: $[M+H]^{+}$ Calc'd for $C_{13}H_{13}OS$ 217.0682; found: 217.0683.

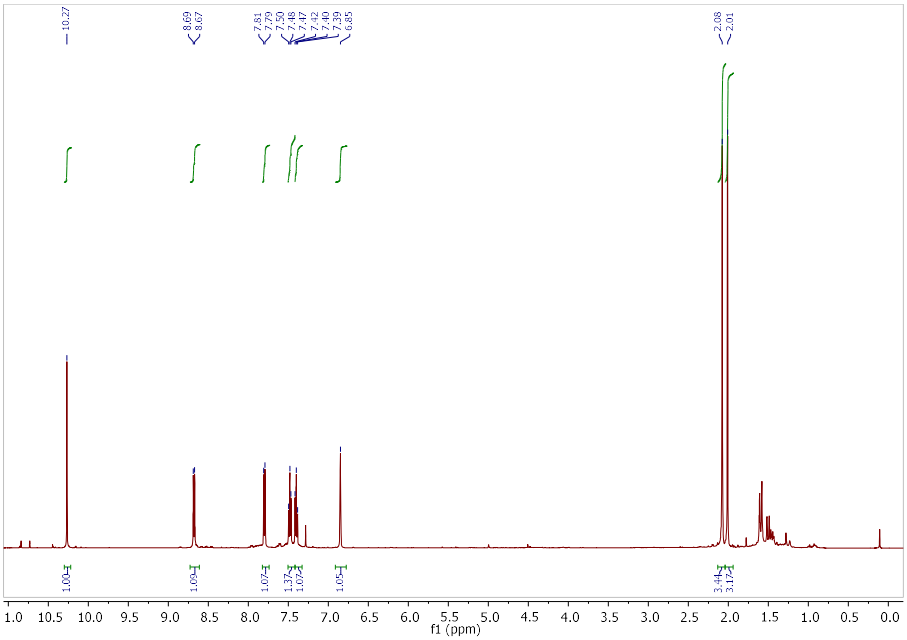

Fig. B52. ^{1}H NMR (500 MHz, Chloroform-*d*) spectrum of **F15**

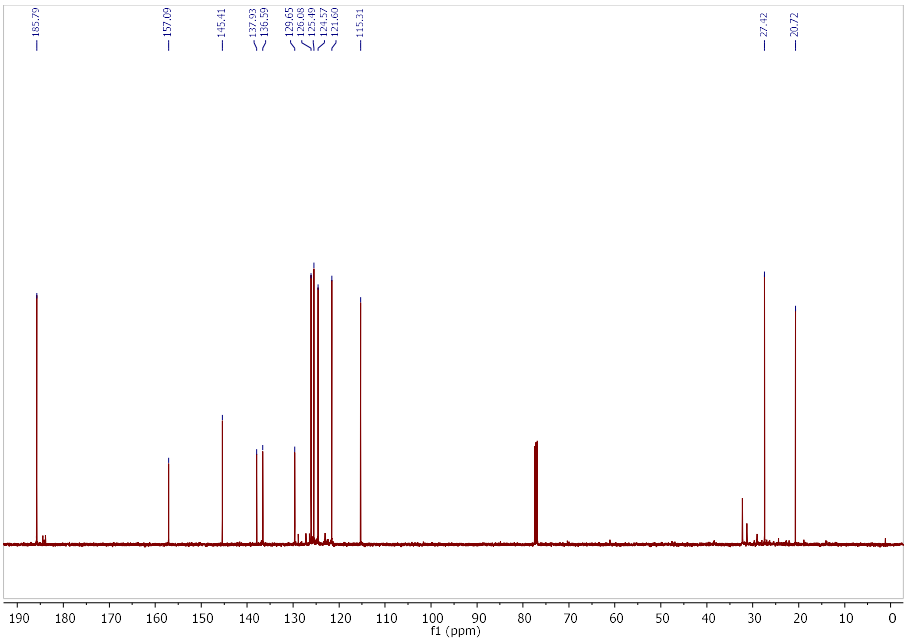

Fig. B53. $^{13}C\{^{1}H\}$ NMR (126 MHz, Chloroform-*d*) spectrum of **F15**

5-(2-methylprop-1-en-1-yl)thiophene-2-carboxaldehyde (F16):

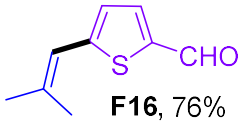

F16, 76%

Isolated by column chromatography (EtOAc : Hexanes = 20:80). Yellow solid. 63.5 mg (76%). MP: 45-49 °C

IR ν: 2969, 1638, 1441, 1208, 1042, 844, 799 cm^{-1}.

^{1}H NMR (500 MHz, Chloroform-*d*) δ 9.85 (s, 1H), 7.66 (d, *J* = 4.0 Hz, 1H), 6.97 (d, *J* = 4.0 Hz, 1H), 6.46 (m, 1H), 2.06 (s, 3H), 1.99 (s, 3H).

$^{13}C\{^{1}H\}$ NMR (126 MHz, Chloroform-*d*) δ 181.8, 150.6, 140.4, 140.1, 125.9, 117.7, 26.7, 19.6.

HRMS (ESI) m/z: $[M+H]^+$ Calc'd for $C_9H_{10}OS$ 167.0525; found: 167.0525.

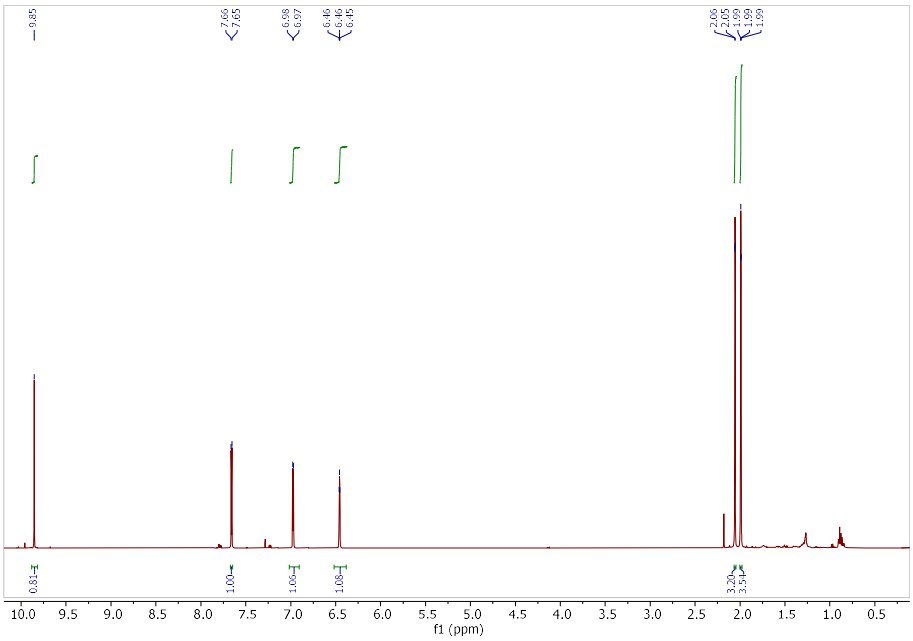

Fig. B53. ^{1}H NMR (500 MHz, Chloroform-*d*) spectrum of **F16**

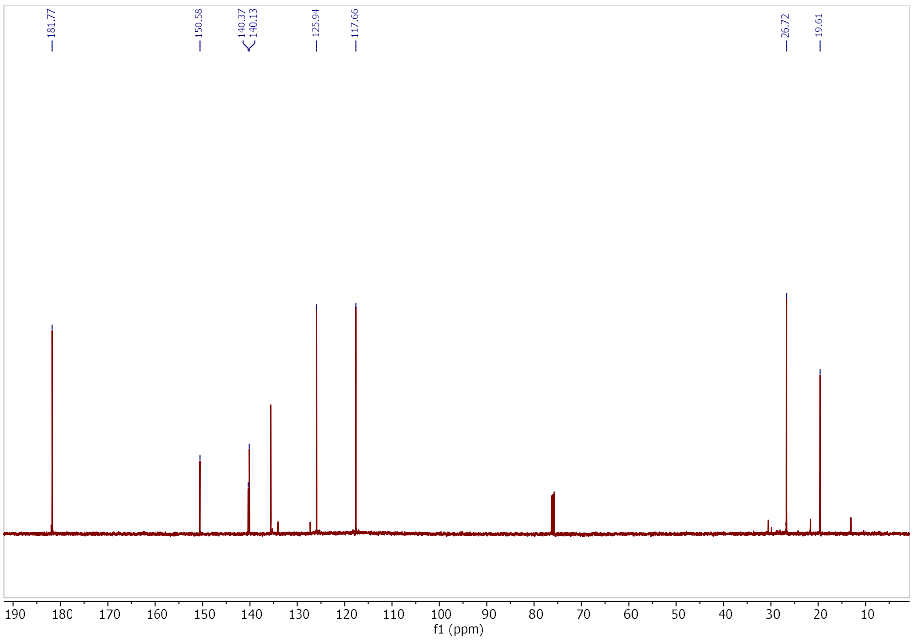

Fig. B54. $^{13}C\{^{1}H\}$ NMR (126 MHz, Chloroform-*d*) spectrum of **F16**

5-(2-methylprop-1-en-1-yl)-1-(tetrahydro-2H-pyran-2-yl)-1H-pyrazole-4-carbaldehyde (F21):

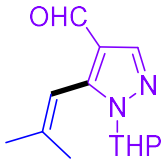

F21, 55%

Isolated by column chromatography (EtOAc : Hexanes = 20:80). Yellow oil. 64.4 mg (55%).

IR ν: 2941, 1677, 1467, 1208, 1044, 915, 729 cm^{-1}.

^{1}H NMR (500 MHz, Chloroform-*d*) δ 9.72 (s, 1H), 8.01 (s, 1H), 6.37 – 5.96 (m, 1H), 5.28 (dd, *J* = 9.9, 2.7 Hz, 1H), 4.11 – 4.06 (m, 1H), 3.65 (td, *J* = 11.3, 2.5 Hz, 1H), 2.45 (m, 1H), 2.13 (mz, 1H), 2.05 (d, *J* = 1.5 Hz, 3H), 1.89 (m, 1H), 1.78 – 1.74 (m, 1H), 1.74 (d, *J* = 1.5 Hz, 3H), 1.70 – 1.57 (m, 3H), 1.36 – 1.25 (m, 1H), 0.93 – 0.85 (m, 1H).

$^{13}C\{^{1}H\}$ NMR (126 MHz, Chloroform-*d*) δ 185.2, 147.1, 139.6, 121.6, 110.0, 84.5, 68.0, 29.5, 28.4, 25.9, 24.8, 22.5, 20.5.

HRMS (ESI) m/z: $[M+H]^+$ Calc'd for $C_{13}H_{19}N_2O_2$ 235.1441; found: 235.1441.

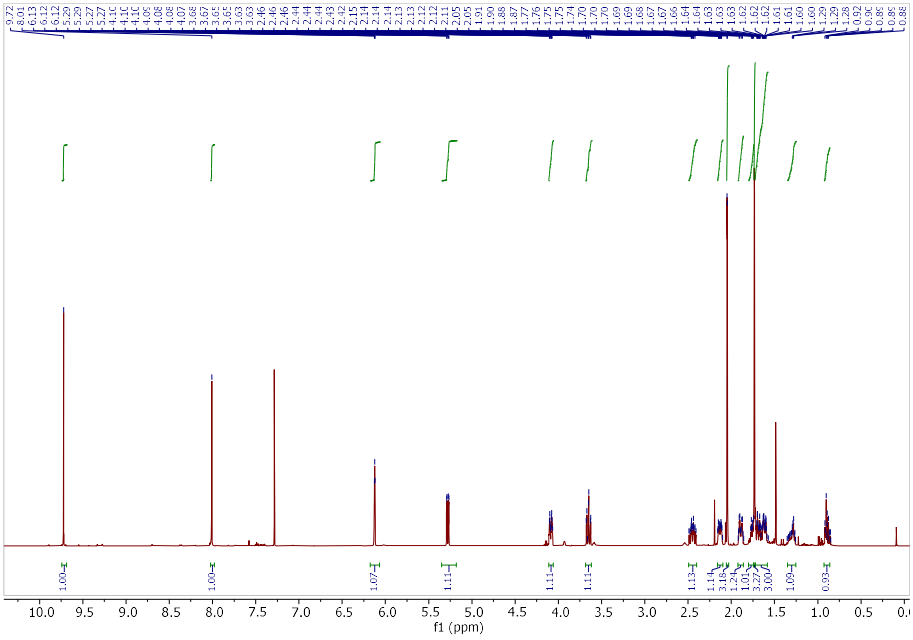

Fig. B55. ^{1}H NMR (500 MHz, Chloroform-*d*) spectrum of **F21**

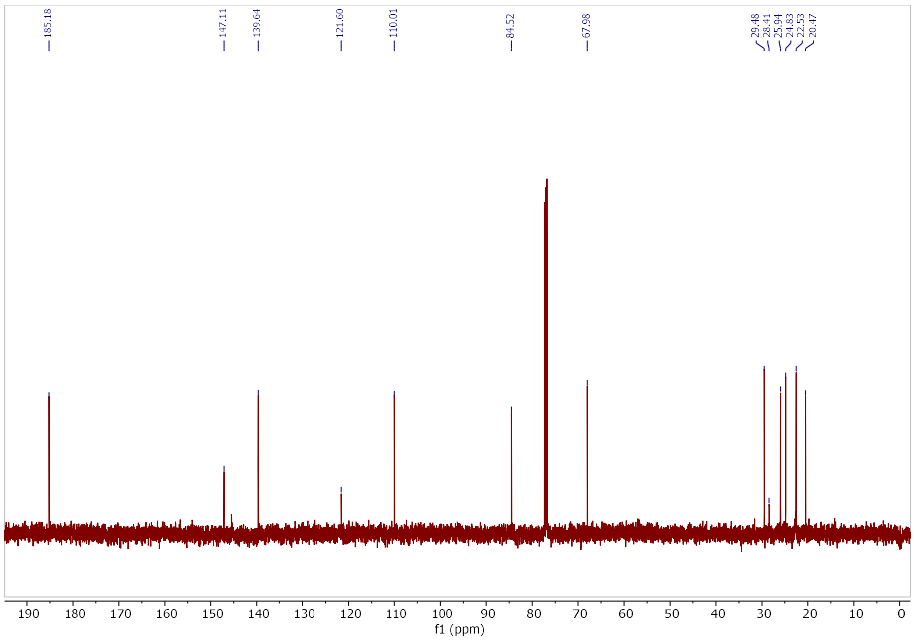

Fig. B56. $^{13}C\{^{1}H\}$ NMR (126 MHz, Chloroform-*d*) spectrum of **F21**

1,3-Dimethyl-5-(2-methylprop-1-en-1-yl)-1H-pyrazole-4-carbaldehyde (F22):

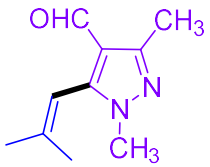

F22, 65%

Isolated by column chromatography (EtOAc : Hexanes = 40:60). Yellow oil. 58.0 mg (65%).

IR ν: 2978, 1671, 1476, 1064, 780 cm^{-1}.

^{1}H NMR (500 MHz, Chloroform-*d*) δ 9.71 (s, 1H), 6.02 (d, *J* = 1.7 Hz, 1H), 3.69 (s, 3H), 2.48 (s, 3H), 2.02 (d, *J* = 1.5 Hz, 3H), 1.71 (d, *J* = 1.4 Hz, 3H).

$^{13}C\{^{1}H\}$ NMR (126 MHz, Chloroform-*d*) δ 185.7, 150.2, 146.6, 118.5, 110.7, 36.3, 25.9, 20.6, 13.5.

HRMS (ESI) m/z: $[M+H]^{+}$ Calc'd for $C_{10}H_{15}N_2O$ 179.1179; found: 179.1179.

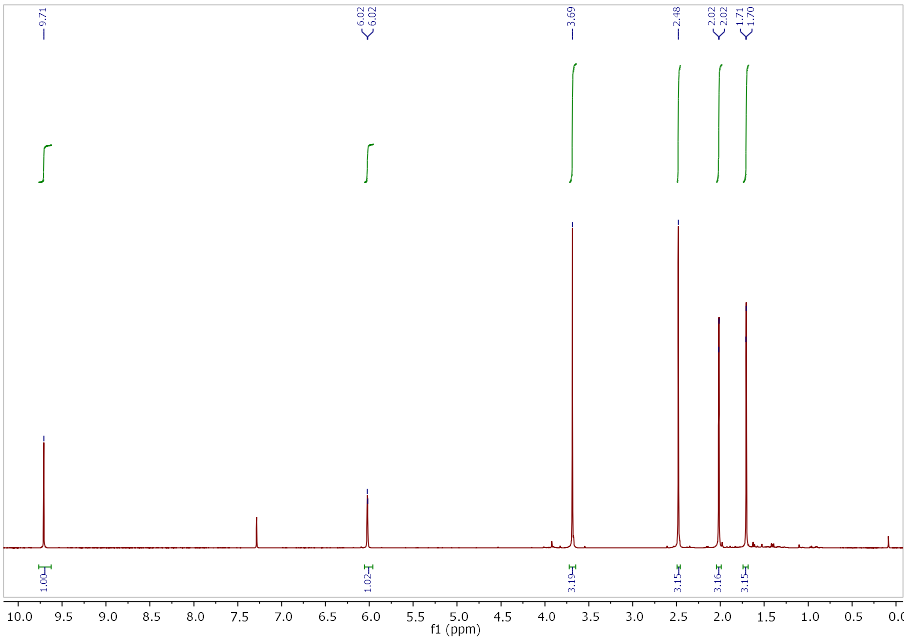

Fig. B57. ^{1}H NMR (500 MHz, Chloroform-*d*) spectrum of **F22**

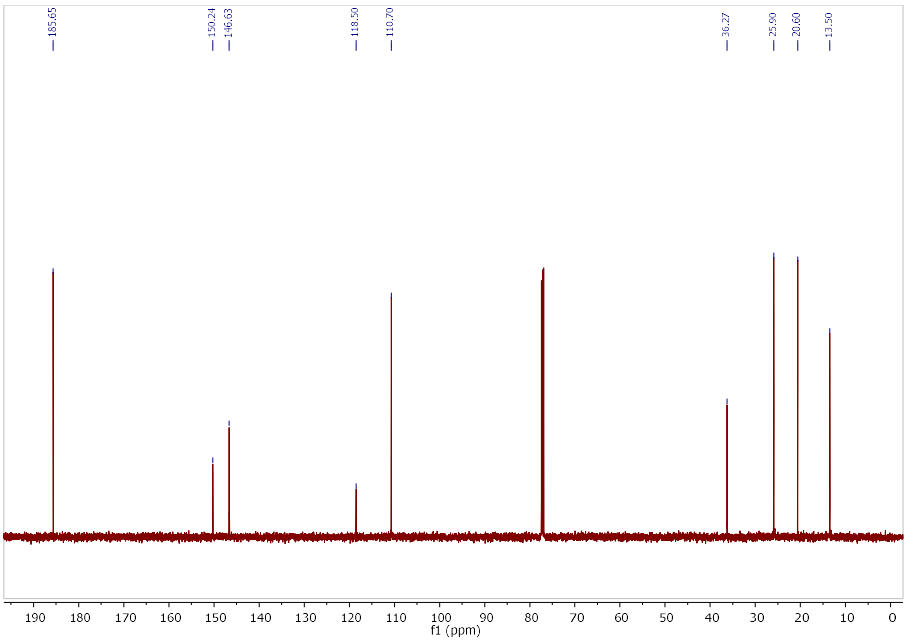

Fig. B58. $^{13}C\{^{1}H\}$ NMR (126 MHz, Chloroform-*d*) spectrum of **F22**

3-(Benzo[d]oxazol-2-yl)-5,5-dimethylcyclohex-2-en-1-one (G2):

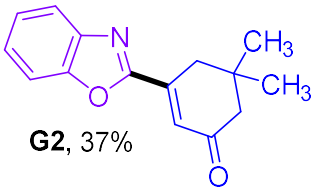

Isolated by column chromatography (EtOAc : Hexanes = 18:92). Dark red solid. 44.5 mg (37%), MP: 110-111 °C.

IR ν: 3021, 2959, 1664, 1239, 747 cm^{-1}.

^{1}H NMR (500 MHz, Chloroform-*d*) δ 7.82 (dt, *J* = 7.8, 1.0 Hz, 1H), 7.60 (dt, *J* = 8.2, 1.0 Hz, 1H), 7.46 (td, *J* = 7.8, 1.4 Hz, 1H), 7.41 (td, *J* = 7.6, 1.2 Hz, 1H), 7.03 (t, *J* = 1.8 Hz, 1H), 2.91 (d, *J* = 1.8 Hz, 2H), 2.44 (s, 2H), 1.18 (s, 6H).

$^{13}C\{^{1}H\}$ NMR (126 MHz, Chloroform-*d*) δ 199.6, 161.8, 150.8, 142.9, 141.8, 128.7, 126.9, 125.1, 120.8, 111.0, 51.5, 39.1, 33.7, 28.2.

HRMS (ESI) m/z: $[M+H]^{+}$ Calc'd for $C_{15}H_{16}NO_2$ 242.1176; found: 242.1176.

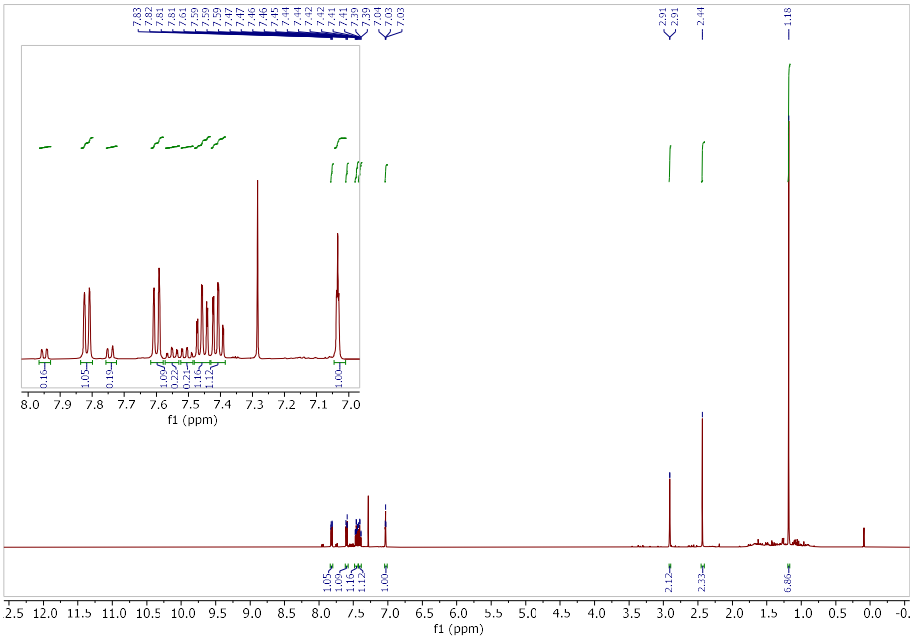

Fig. B59. ^{1}H NMR (500 MHz, Chloroform-*d*) spectrum of **G2**. The minor aromatic signals correspond to bis(benzoxazole) (8%), generated from C_2–C_2 oxidative homocoupling of benzoxazole, which co-eluted with the desired product.[10]

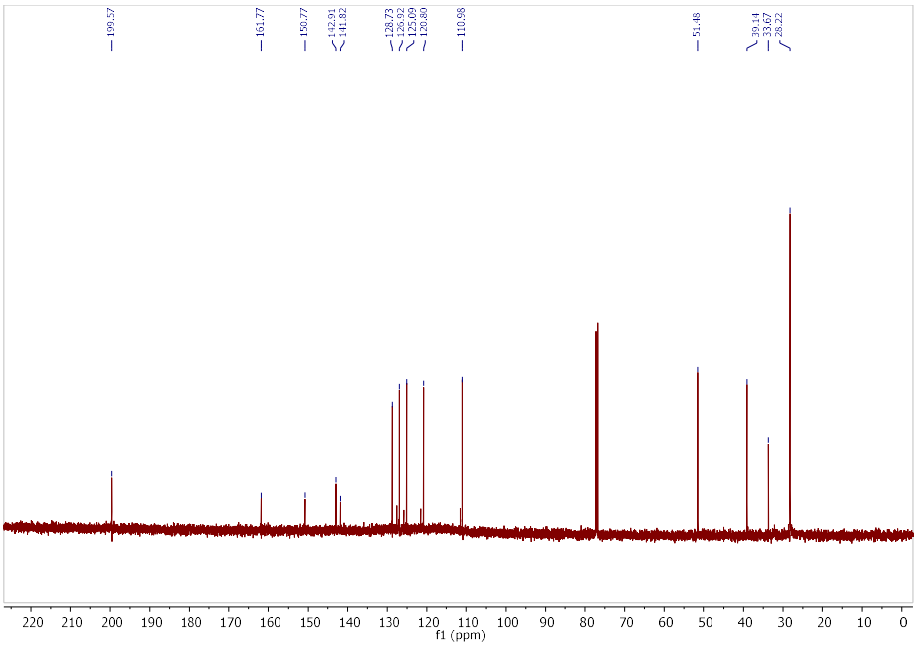

Fig. B60. $^{13}C\{^{1}H\}$ NMR (126 MHz, Chloroform-*d*) spectrum of **G2**

3-(Benzo[d]oxazol-2-yl)-2-methylcyclopent-2-en-1-one (H2):

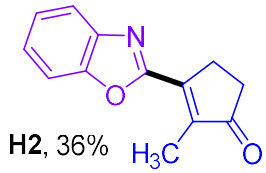

Isolated by column chromatography (EtOAc : Hexanes = 20:80). Dark yellow solid. 38.3 mg (36%). MP: 192-194 °C.

IR ν: 3080, 2927, 1692, 1443, 1239, 767 cm^{-1}.

^{1}H NMR (500 MHz, Chloroform-*d*) δ 7.85 (d, *J* = 7.0 Hz, 1H), 7.62 (d, *J* = 7.9 Hz, 1H), 7.48 – 7.38 (m, 2H), 3.14 (m, 2H), 2.65 – 2.59 (m, 2H), 2.32 (s, 3H).

$^{13}C\{^{1}H\}$ NMR (126 MHz, Chloroform-*d*) δ 209.2, 160.8, 150.7, 150.2, 143.9, 141.7, 126.8, 125.3, 121.1, 111.1, 34.0, 26.6, 10.4.

HRMS (ESI) m/z: $[M+H]^{+}$ Calc'd for $C_{13}H_{12}NO_2$ 214.0863; found: 214.0863.

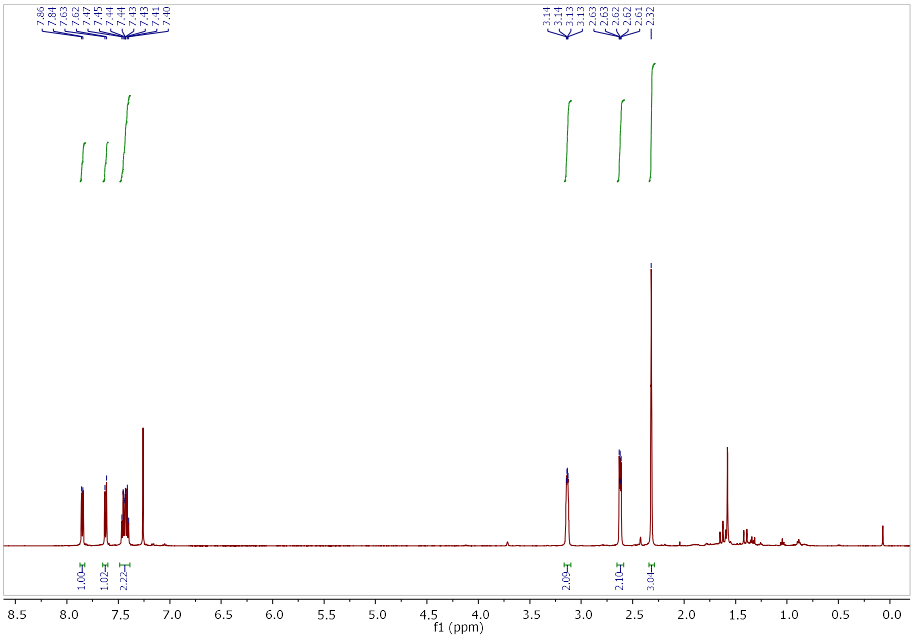

Fig. B61. ^{1}H NMR (500 MHz, Chloroform-*d*) spectrum of **H2**

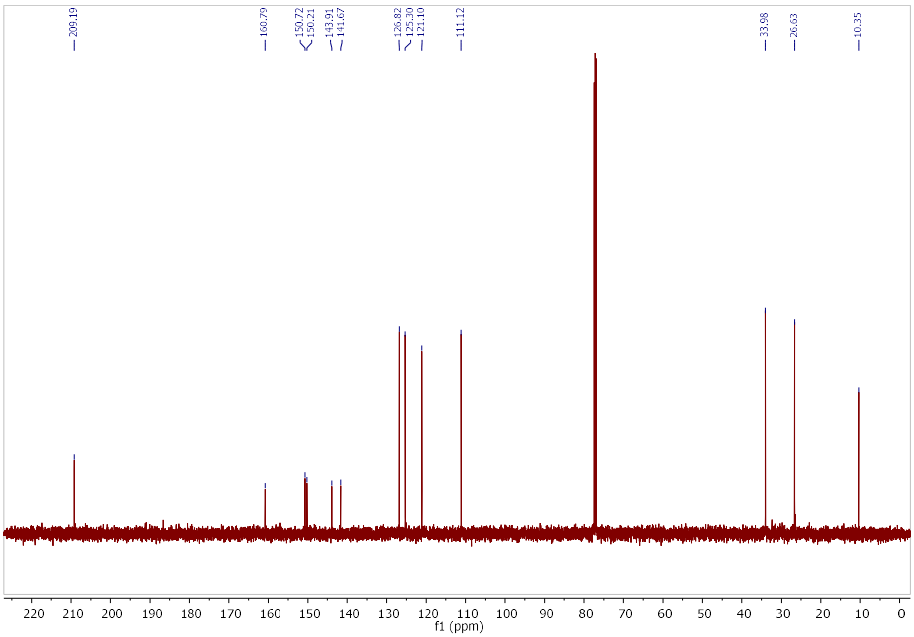

Fig. B62. $^{13}C\{^{1}H\}$ NMR (126 MHz, Chloroform-*d*) spectrum of **H2**

1-bromo-4,4-bis(ethoxymethyl)cyclohex-1-ene (2i):

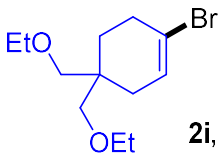

2i, 81%

^{1}H NMR (400 MHz, Chloroform-*d*) δ 5.87 (tt, *J* = 4.1, 1.7 Hz, 1H), 3.39 (q, *J* = 7.0 Hz, 4H), 3.24 – 3.14 (m, 4H), 2.33 (ttd, *J* = 6.6, 2.6, f1.8 Hz, 2H), 1.90 (dt, *J* = 4.2, 2.6 Hz, 2H), 1.59 (t, *J* = 6.5 Hz, 2H), 1.09 (t, *J* = 7.0 Hz, 6H).

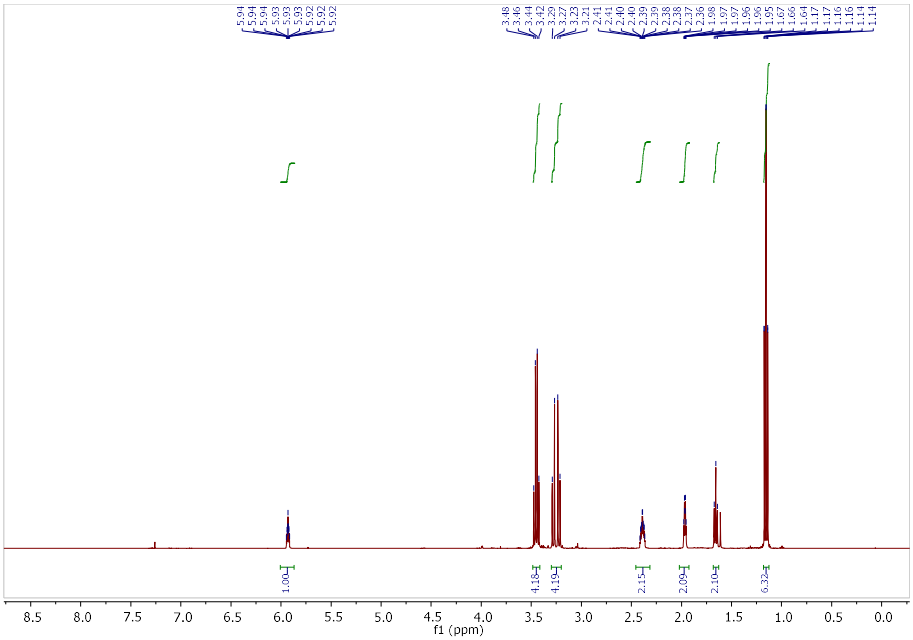

Fig. B63. ^{1}H NMR (400 MHz, Chloroform-*d*) spectrum of **2i**

2-(4,4-bis(ethoxymethyl)cyclohex-1-en-1-yl)-1-(tetrahydro-2H-pyran-2-yl)-1H-pyrrole-3-carbaldehyde (3ai):

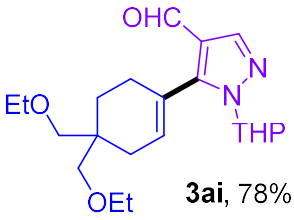

3ai, 78% assay yield

^{1}H NMR (400 MHz, Chloroform-*d*) δ 9.75 (s, 1H), 7.98 (s, 1H), 5.95 (m, 1H), 5.24 (dd, *J* = 10.0, 2.6 Hz, 1H), 4.10 (m, 1H), 3.60 (m, 1H), 3.52 (m, 4H), 3.44 – 3.32 (m, 4H), 2.56 – 2.31 (m, 2H), 2.25 (m, 1H), 2.23 – 2.08 (m, 3H), 1.92 – 1.82 (m, 1H), 1.76 (m, 2H), 1.69 (m, 1H), 1.66 – 1.56 (m, 2H), 1.22 (m, 6H).

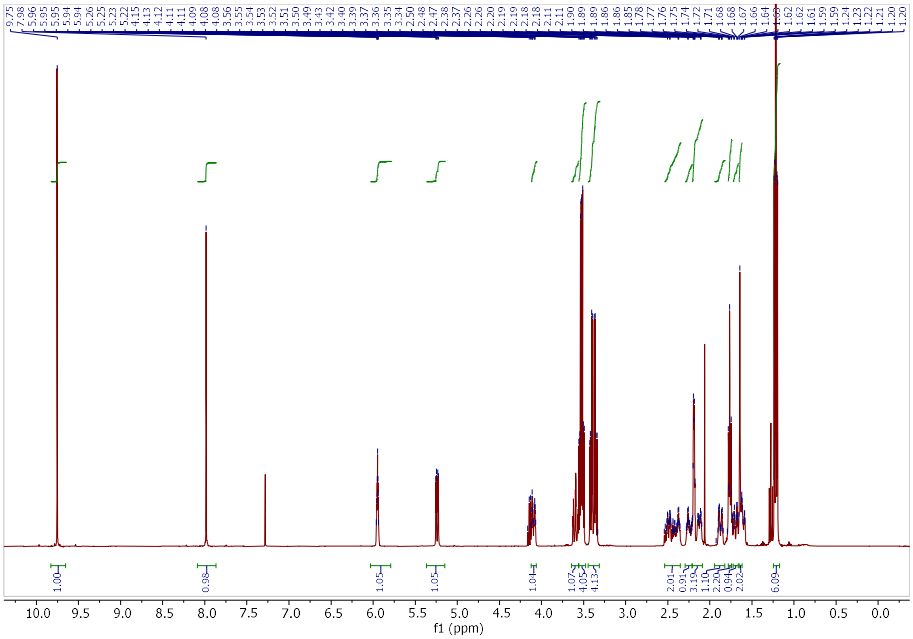

Fig. B64. ^{1}H NMR (400 MHz, Chloroform-*d*) spectrum of **3ai**

VIII: References

(1) Thirupathi, N.; Amoroso, D.; Bell, A.; Protasiewicz, J. D. Reactivity Studies of Cationic Palladium(II) Phosphine Carboxylate Complexes with Lewis Bases: Substitution versus Cyclometalation. *Organometallics* **2007**, *26*, 3157–3166. https://doi.org/10.1021/om070069g

(2) Spaggiari, A.; Vaccari, D.; Davoli, P.; Torre, G.; Prati, F. A Mild Synthesis of Vinyl Halides and Gem-Dihalides Using Triphenyl Phosphite−Halogen-Based Reagents. *J. Org. Chem*. **2007**, *72*, 2216–2219. https://doi.org/10.1021/jo061346g

(3) Jobin-Des Lauriers, A.; Legault, C. Y. Iodine(III)-Mediated Oxidative Hydrolysis of Haloalkenes: Access to α-Halo Ketones by a Release-and-Catch Mechanism. *Org. Lett.* **2016**, *18*, 108–111. https://doi.org/10.1021/acs.orglett.5b03345

(4) Mewshaw, R. E. Vilsmeier Reagents: Preparation of β-Halo-α,β-Unsaturated Ketones. *Tet. Lett.* **1989**, *30*, 3753–3756. https://doi.org/10.1016/S0040-4039(01)80646-8

(5) Patra, T.; Agasti, S.; Akanksha; Maiti, D. Nickel-Catalyzed Decyanation of Inert Carbon–Cyano Bonds. *Chem. Commun.* **2012**, *49*, 69–71. https://doi.org/10.1039/C2CC36883H

(6) Cupido, T.; Rack, P. G.; Firestone, A. J.; Hyman, J. M.; Han, K.; Sinha, S.; Ocasio, C. A.; Chen, J. K. The Imidazopyridine Derivative JK184 Reveals Dual Roles for Microtubules in Hedgehog Signaling. *Angew. Chem. Int. Ed.* **2009**, *48,* 2321–2324. https://doi.org/10.1002/anie.200805666

(7) Velankar, A. D.; Quintini, G.; Prabhu, A.; Weber, A.; Hunaeus, G.; Voland, B.; Wuest, M.; Orjeda, C.; Harel, D.; Varghese, S.; Gore, V.; Patil, M.; Gayke, D.; Herdemann, M.; Heit, I.; Zaliani, A. Synthesis and Biological Evaluation of Novel (4 or 5-Aryl)Pyrazolyl-Indoles as Inhibitors of Interleukin-2 Inducible T-Cell Kinase (ITK). *Bioorg. Med. Chem.* **2010**, *18*, 4547–4559. https://doi.org/10.1016/j.bmc.2010.04.056

(8) Likhite, N.; Ramasamy, S.; Tendulkar, S.; Sathasivam, S.; Luzung, M.; Zhu, Y.; Strotman, N.; Nye, J.; Ortiz, A.; Kiau, S.; Eastgate, M. D.; Vaidyanathan, R. Development of a Safe and Robust Process for the Large-Scale Preparation of a Vinyl Bromide from a Ketone Using a (PhO)3P/Br2-Derived Reagent. *Org. Process Res. Dev*. **2016**, *20*, 977–981. https://doi.org/10.1021/acs.oprd.6b00100

(9) Gunasekaran, P.; Yim, M. S.; Ahn, M.; Soung, N.-K.; Park, J.-E.; Kim, J.; Bang, G.; Shin, S. C.; Choi, J.; Kim, M.; Kim, H. N.; Lee, Y.-H.; Chung, Y.-H.; Lee, K.; EunKyeong Kim, E.; Jeon, Y.-H.; Kim, M. J.; Lee, K.-R.; Kim, B.-Y.; Lee, K. S.; Ryu, E. K.; Bang, J. K. Development of a Polo-like Kinase-1 Polo-Box Domain Inhibitor as a Tumor Growth Suppressor in Mice Models. *J. Med. Chem.* **2020**, *63*, 14905–14920. https://doi.org/10.1021/acs.jmedchem.0c01451

(10) Zhu, M.; Fujita, K.; Yamaguchi, R. Efficient synthesis of biazoles by aerobic oxidative homocoupling of azoles catalyzed by a copper(I)/2-pyridonate catalytic system. *Chem. Commun*. **2011**, *47*, 12876–12878. https://doi.org/10.1039/C1CC15363C

Appendix C: Supporting information for Chapter 4

I: General Considerations

Materials. All solvents and common organic reagents were purchased from commercial suppliers and used without further purification. $Pd(OAc)_2(PCy_3)_2$ was prepared according to the reported method.[1] Anhydrous solvents (SureSeal) were purchased from MilliporeSigma and used as received.

Preparation of 100 mesh K_3PO_4: Inside a nitrogen glovebox, anhydrous K_3PO_4 was milled in a coffee grinder for 30 seconds. The milled material was then passed through a 100 mesh sieve. The resultant 100 mesh K_3PO_4 is stable for months inside a glovebox, but it quickly absorbs water in minutes when exposed to the atmosphere.

Techniques. All air-free manipulations were performed under a dry nitrogen atmosphere using an MBraun glovebox. High-throughput experimentation was performed using 1 mL capacity glass shell vials in sealable aluminum reaction blocks purchased from Analytical Sales. Heating/stirring was achieved using rare-earth magnetic tumble stirrers acquired from V&P Scientific.

Centrifugal evaporation was performed using a Genevac EZ-2 (HCl compatible). Automated chromatography purification was performed using Biotage® Selekt SEL-2SW instruments using Sfär Silica (60 μm) columns.

Analysis and Spectroscopy.

All NMR spectra were acquired on either a Bruker AVANCE 300 MHz spectrometer or a Bruker AVANCE Neo 500 MHz spectrometer. All ^{1}H and ^{13}C-NMR chemical shifts are calibrated to residual protio-solvents and all ^{31}P and ^{19}F NMR chemical shifts are calibrated to external standards. All NMR spectroscopic data is processed using MestreNova software.

UPLC analysis was performed using a Shimadzu Nexera X2 with a diode-array UV/Vis detector. A Raptor ARC-18 column (100 × 2.1 mm, particle size 1.8 μm) or a Waters CORTECS® UPLC® T3 column (2.1 × 30 mm, particle size 1.6 μm) were used. The eluent used is a mixture of two mobile phases: water with 0.05% trifluoroacetic acid (TFA) (mobile phase A), and acetonitrile with 0.05% TFA (mobile phase B). All solvents used were HPLC grade.

LCMS was performed using a Waters Acquity class H UPLC system equipped with an autosampler, quaternary pump system, column oven, a photodiode array detector and a QDa Mass Spectrometer. The chromatogram was recorded using an ACQUITY UPLC® BEH C18 column (2.1 × 50 mm, particle size 1.7 μm) with 0.1% formic acid (FA) in water as mobile phase A and 0.1% FA in acetonitrile as mobile phase B. The data was processed using Masslynx.

High-resolution electrospray ionization mass spectrometric analysis was performed using a Thermo Scientific Ultimate 3000 ESI-Orbitrap Exactive Plus.

II: Preparation of Substrates

Synthesis of 4-Methoxythiazole

The procedure was adapted from literature procedure.[1]

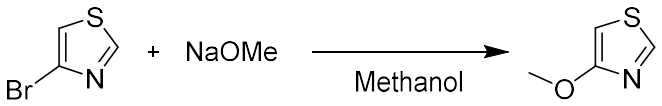

A solution of sodium methoxide on methanol (4.8 mL, 25w%) was added to a stirring solution of 4-bromothiazole (1.0 g, 6.1 mmol) in methanol (10 mL). The solution was refluxed for 24 h. The mixture was cooled to room temperature and diluted in water (20 mL). It was then extracted with diethyl ether (3 x 10 mL). The combined organic phases were washed with brine (10 mL) dried over $MgSO_4$ and evaporated. The product was purified by column chromatography with hexanes and ethyl acetate as the mobile phase. The compound was a colorless oil (0.45 mg, 64% yield).

Synthesis 4-(1,3-dioxolan-2-yl)thiazole

The procedure was adapted from literature.[2]

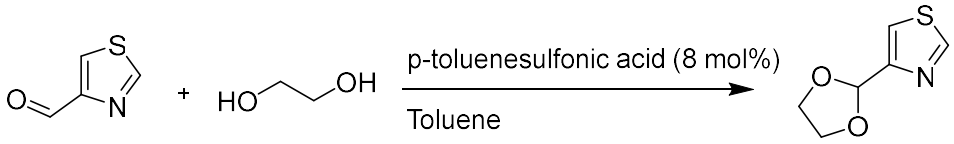

Ethylene glycol (0.76 mL, 13.6 mmol, 3.0 equiv), thiazole-4-carboxaldehyde (0.52 mg, 4.6 mmol, 1 equiv) and toluene (10 mL) were added to a round bottom flask. p-Toluenesulfonic acid (69 mg, 0.36 mmol, 8 mol%) was added to the mixture and it was refluxed overnight on a Dean-Stark apparatus. The reaction was quenched with sat. Na_2CO_3/H_2O mixture (1:1, 10 mL). The mixture was extracted with ethyl acetate (3 x 5 mL) dried over magnesium sulphate and purified on column chromatography. The product was isolated as a colorless oil (0.26 mg, 36% yield).

III: Characterization of palladacycle catalysts

Precatalyst III

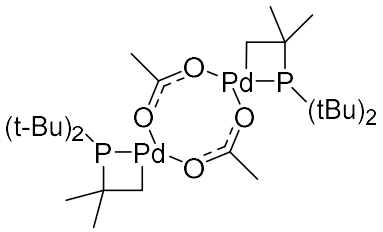

Precatalyst III

^{1}H NMR (500 MHz, C_6D_6) δ 2.12 (s, 6H), 1.42 (m, 32H), 1.38 (s, 6H), 1.35 (m, 10H).

^{31}P{H} NMR (203 MHz, C_6D_6) δ -8.61.

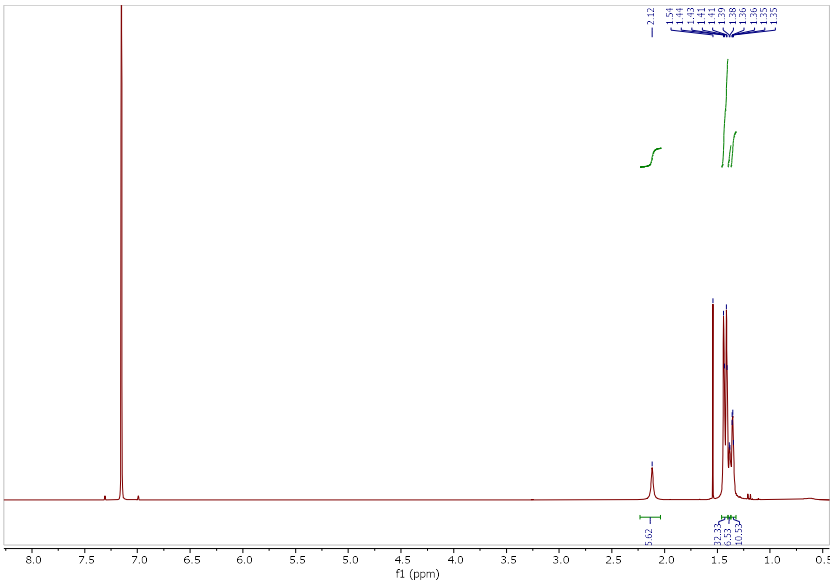

Fig. C1. ^{1}H NMR (500 MHz, C_6D_6) spectrum of **precatalyst III**

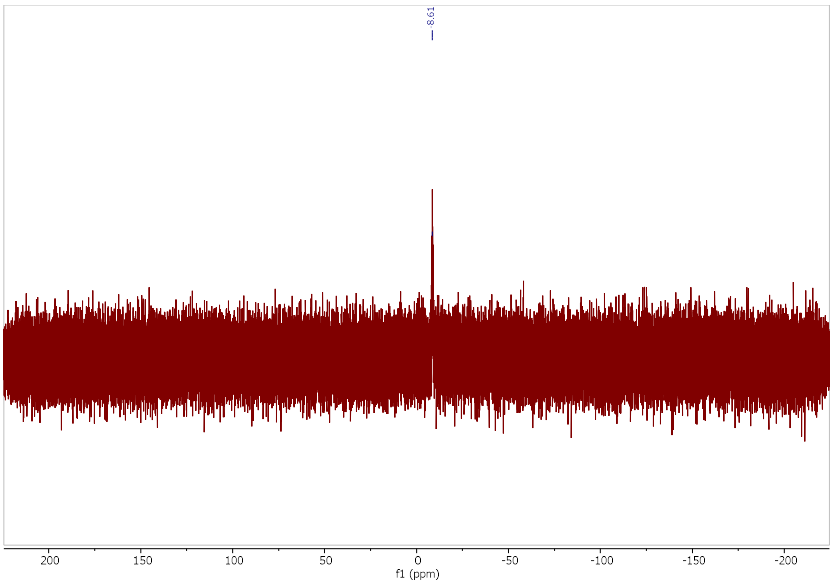

Fig. C2. $^{31}P\{H\}$ NMR (206 MHz, C_6D_6) spectrum of **precatalyst III**

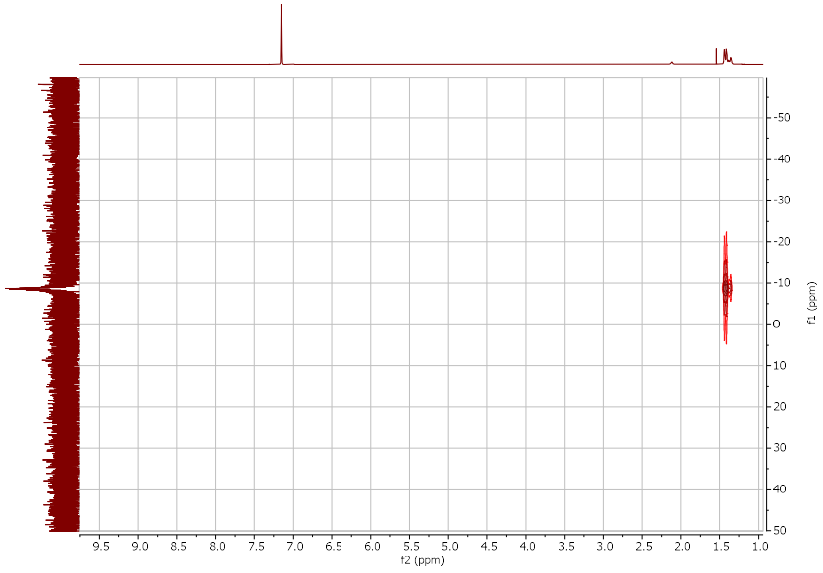

Fig. C3. ^{1}H-^{31}P-HMBC spectrum of **precatalyst III**

Precatalyst IV

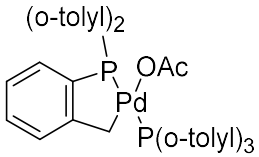

Precatalyst IV

^{1}H NMR (500 MHz, C_6D_6) δ 7.10 – 6.98 (m, 16H), 6.95 – 6.80 (m, 8H), 2.41 (s, 15H), 1.54 (s, 3H), 1.47 (s, 2H).

^{31}P{H} NMR (203 MHz, C_6D_6) δ -29.67.

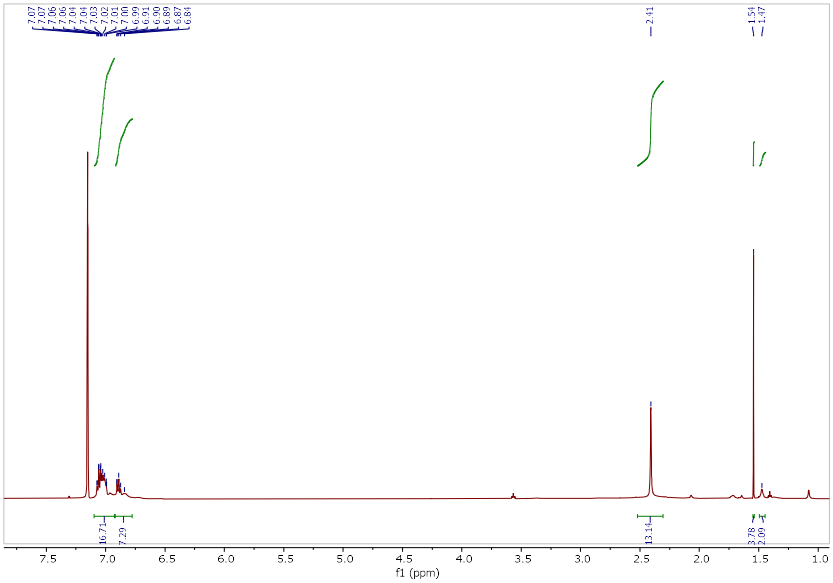

Fig. C4. ^{1}H NMR (500 MHz, C_6D_6) spectrum of **precatalyst IV**

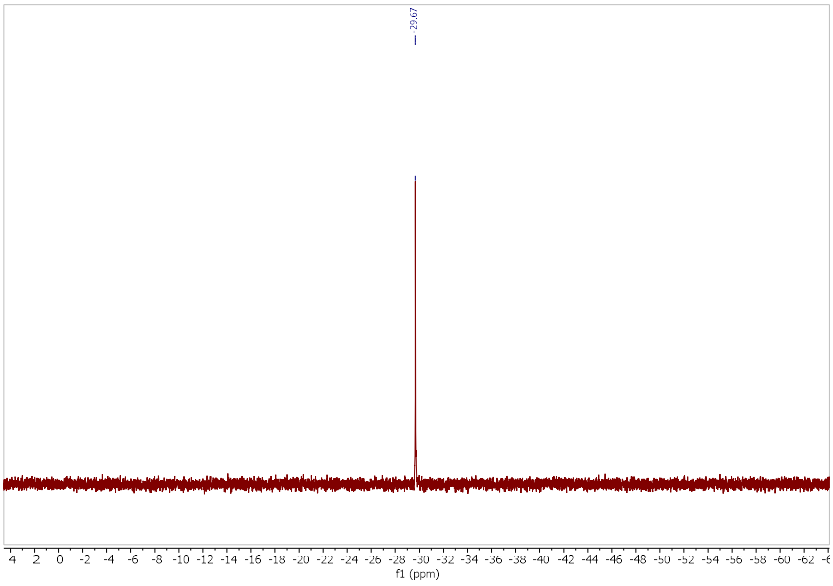

Fig. C5. $^{31}P\{H\}$ NMR (206 MHz, C_6D_6) spectrum of **precatalyst IV**

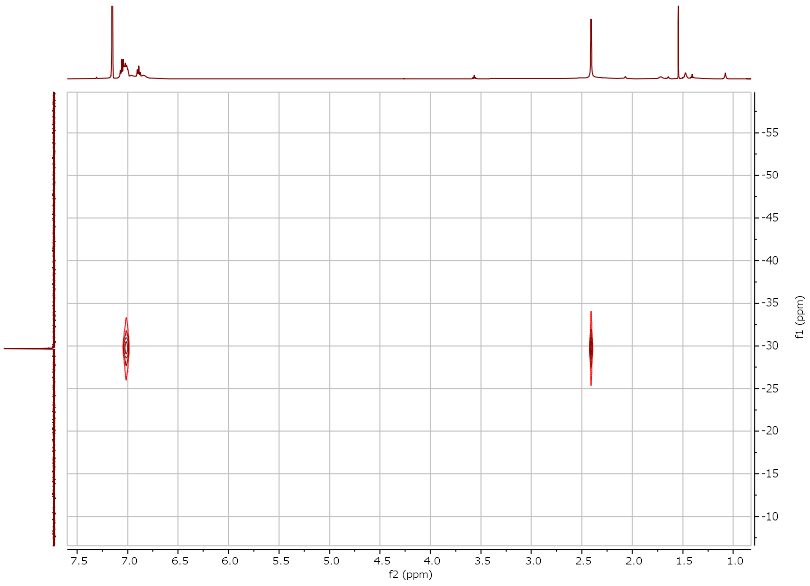

Fig. C6. ^{1}H-^{31}P-HMBC spectrum of **precatalyst IV**

Precatalyst V

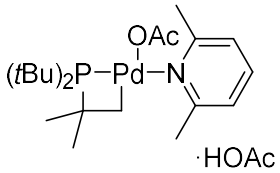

Precatalyst V

^{1}H NMR (500 MHz, C_6D_6) δ 6.87 (d, J = 7.4 Hz, 2H), 6.73 (t, J = 7.4 Hz, 1H), 2.25 (s, 6H), 2.04 (s, 4H), 1.31 (d, J = 13.6 Hz, 18H), 1.05 (d, J = 14.0 Hz, 4H).

^{13}C{H} NMR (126 MHz, C_6D_6) δ 128.18, 127.98, 36.91 (d, J = 9.6 Hz), 34.07, 31.64 (d, J = 3.4 Hz), 30.58, 17.80.

^{31}P{H} NMR (203 MHz, C_6D_6) δ -11.93.

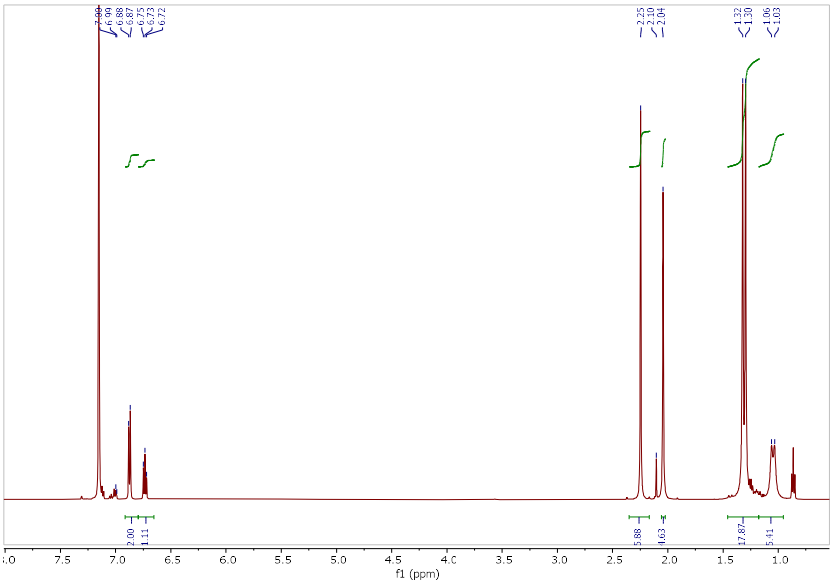

Fig. C7. ^{1}H NMR (500 MHz, C_6D_6) spectrum of **precatalyst V**

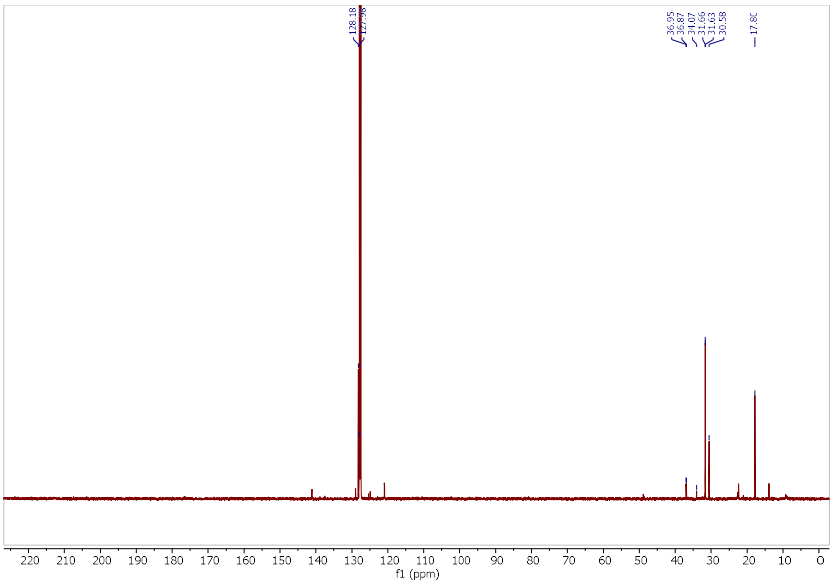

Fig. C8. $^{13}C\{H\}$ NMR (126 MHz, C_6D_6) spectrum of **precatalyst V**

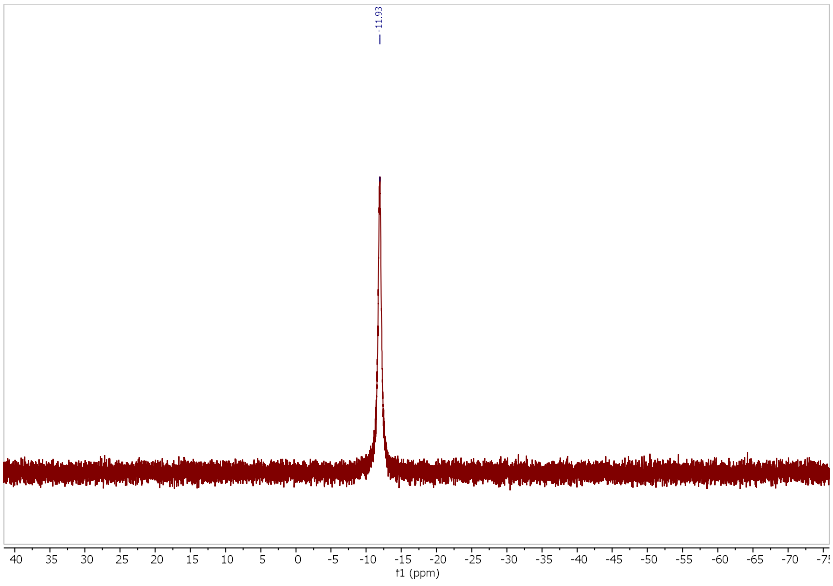

Fig. C9. $^{31}P\{H\}$ NMR (203 MHz, C_6D_6) spectrum of **precatalyst V**

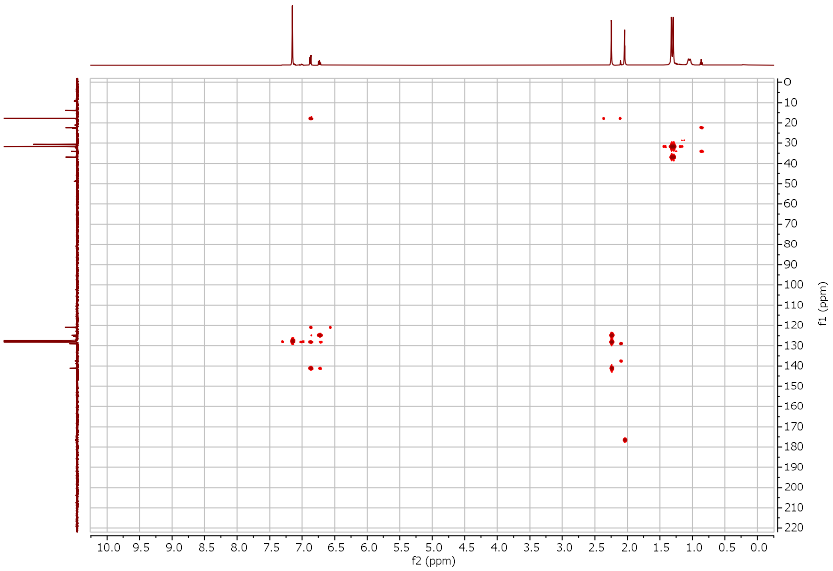

Fig. C10. ^{1}H-^{13}C–HMBC spectrum of **precatalyst V**

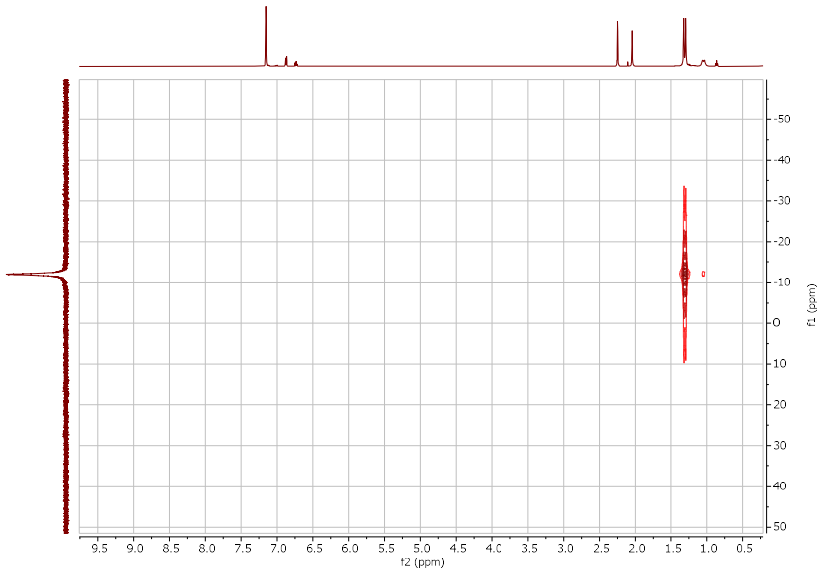

Fig. C10. ^{1}H-^{31}P-HMBC spectrum of **precatalyst V**

Precatalyst VI

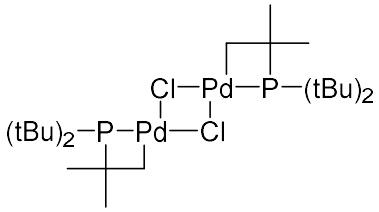

Precatalyst VI

^{1}H NMR (500 MHz, C_6D_6) δ 1.33 (d, J = 13.8 Hz, 36H), 1.30 – 1.25 (m, 4H), 1.25 – 1.05 (m,12H).

^{31}P NMR (202 MHz, C_6D_6) δ -10.47.

^{31}P{H} NMR (203 MHz, C_6D_6) δ -10.36, -10.68.

HRMS (ESI) m/z: $[M-C_{12}H_{26}Cl_2PPd+C_2H_2N]^+$ Calc'd for $C_{14}H_{29}NPPd$ 348.10724; found: 348.10568

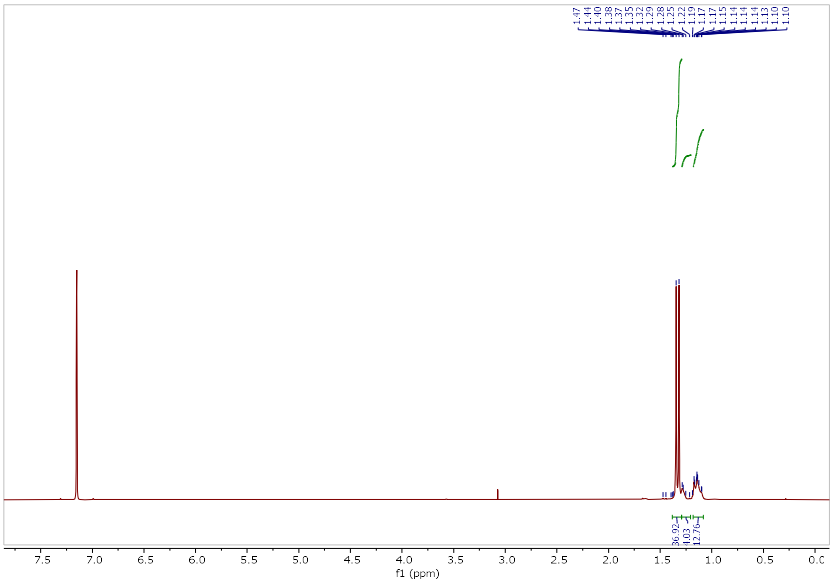

Fig. C11. ^{1}H NMR (500 MHz, C_6D_6) spectrum of **precatalyst VI**

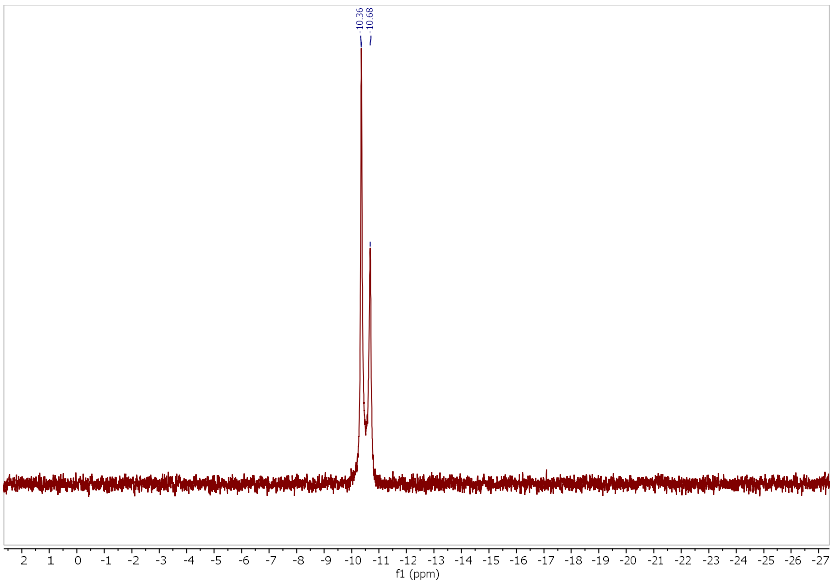

Fig. C11. $^{31}P\{H\}$ NMR (203 MHz, C_6D_6) spectrum **precatalyst VI**

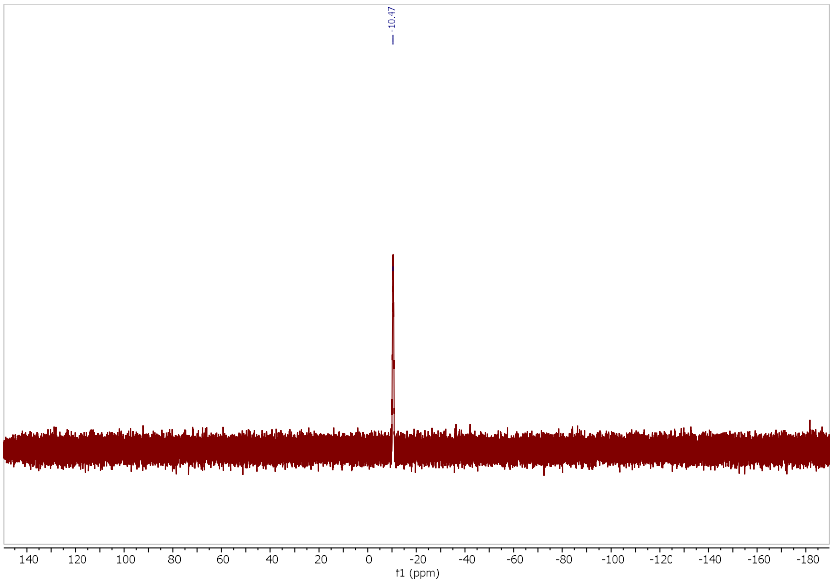

Fig. C12. ^{31}P NMR (203 MHz, C_6D_6) spectrum **precatalyst VI**

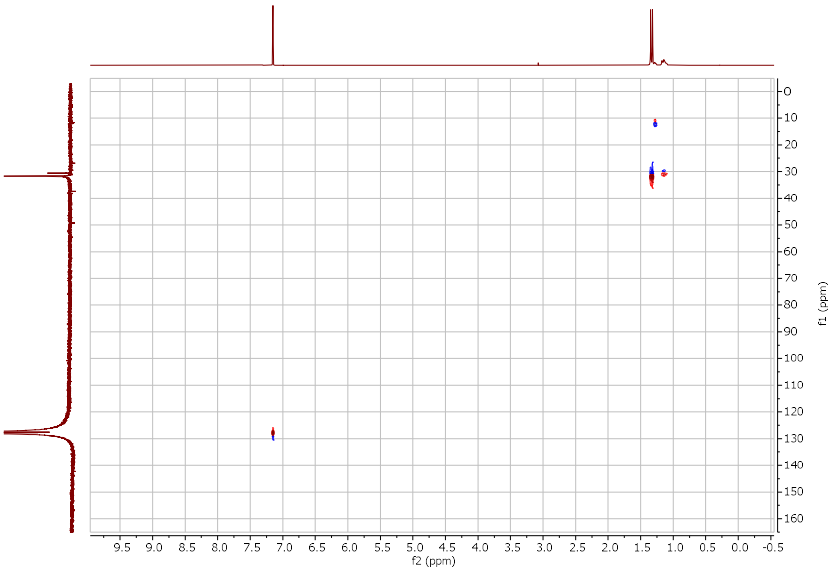

Fig. C13. ^{1}H-^{13}C–HSQC spectrum of **precatalyst VI**

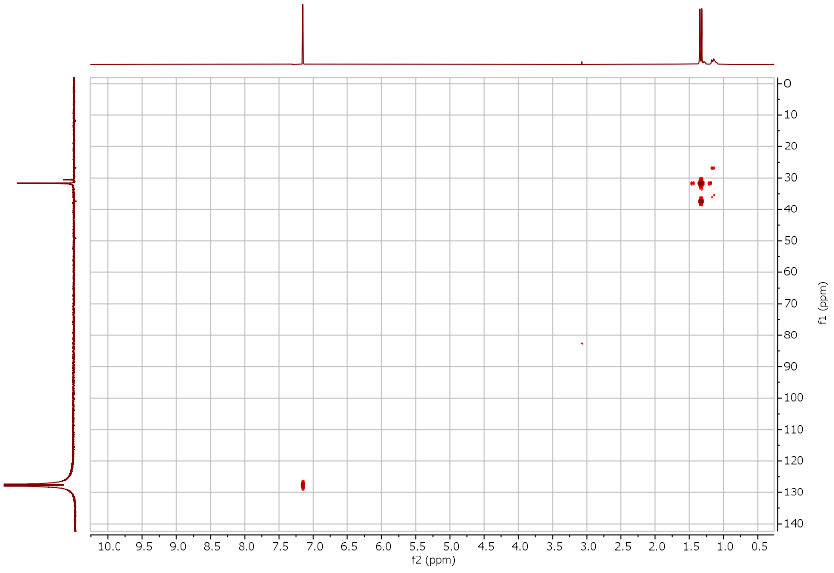

Fig. C14. ^{1}H-^{13}C–HMBC spectrum of **precatalyst VI**

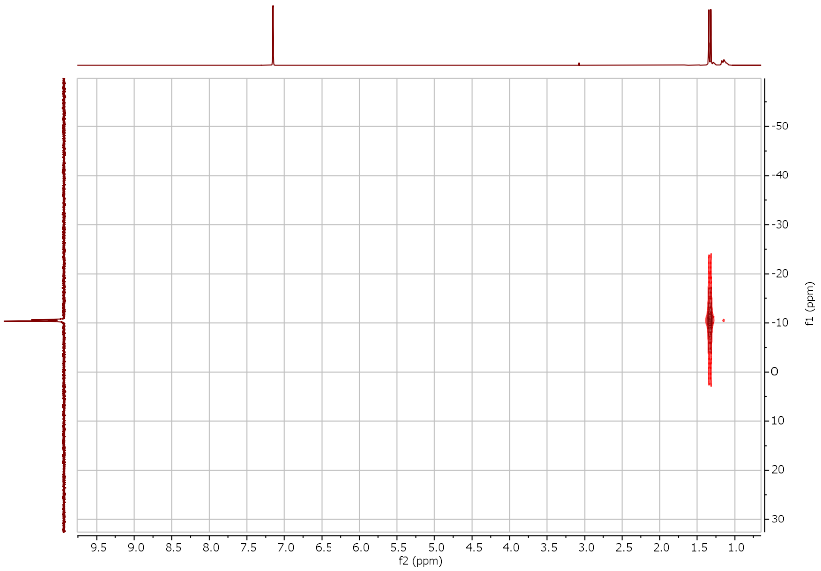

Fig. C15. ^{1}H-^{31}P-HMBC spectrum of **precatalyst VI**

Precatalyst VII

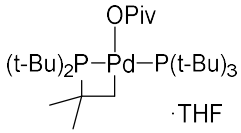

Preatalyst VII

^{1}H NMR (500 MHz, Tol) δ 2.13 (p, *J* = 2.2 Hz, 39H), 1.45 (s, 22H), 1.31 (d, *J* = 10.0 Hz, 3H).

^{31}P{H} NMR (203 MHz, Tol) δ 62.36, -8.13.

HRMS (ESI) m/z: $[M\text{-}OC(CH_3)_3]^+$ Calc'd for $C_{24}H_{55}NPPd$ 511.28138; found: 511.26429

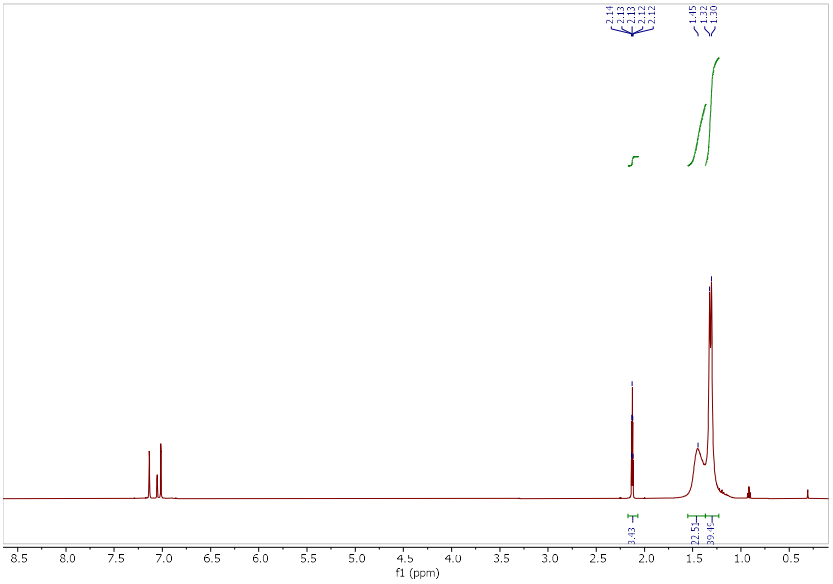

Fig. C16. ^{1}H NMR (500 MHz, C_6D_6) spectrum of **precatalyst VII**

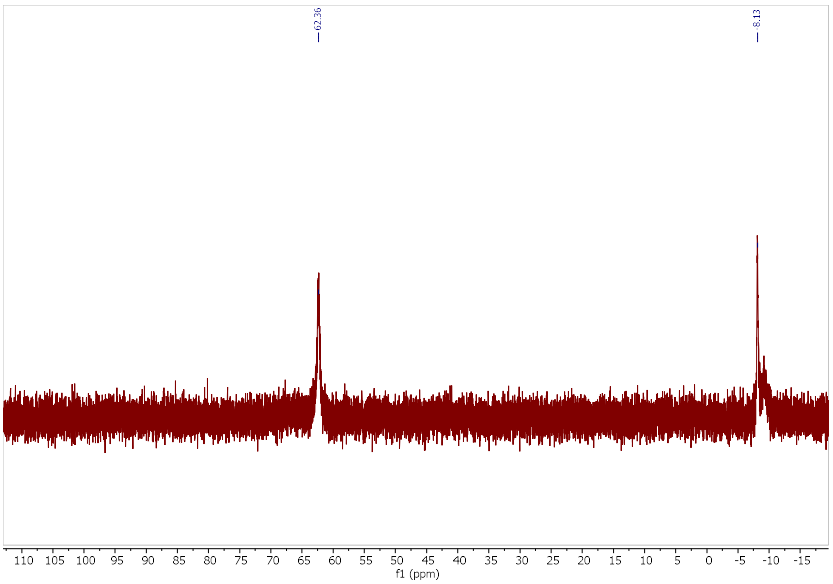

Fig. C17. $^{31}P\{H\}$ NMR (203 MHz, C_6D_6) spectrum of **precatalyst VII**

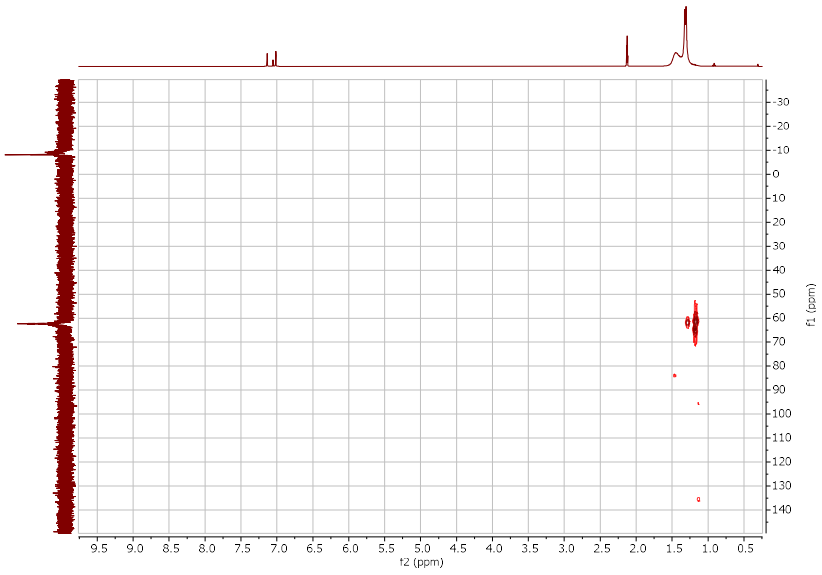

Fig. C18. ^{1}H-^{31}P-HMBC spectrum of **precatalyst VII**

PivOH	CN			CHO			CO2Et			COAcetal			H			Ph			Me			OMe		
	C2	C5	C2C5	C2	C5	C2C5	C2	C5	C2C5	C2	C5	C2C5	C2	C5	C2C5	C2	C5	C2C5	C2	C5	C2C5	C2	C5	C2C5
$P(tBu)_3$	10	44	47	2	40	25	3	53	45	10	23	10	25	1	1	46	5	7	29	3	3	14	11	16
PCy_3		2	1	1	1	1	6	28	4	1	1	0	2	1	0	6	4	12	3	1	2	6	2	1
PPh_3	0	1	1	7	1	0	3	46	32	10	8	8	24	1	2	22	4	7	23	0	8	28	2	4
$P(o\text{-}tolyl)_3$	9	52	35	11	0	0	9	37	11	10	10	8	14	2	1	17	8	1	32	2	3	21	8	11
$P(o\text{-}MeOPh)_3$	24	47	32	6	37	6	2	47	29	7	26	16	13	5	4	18	28	2	28	11	3	4	37	27
XPhos	6	54	30	6	37	6	7	25	7	10	7	5	28	2	4	17	4	3	27	2	9	24	3	4
tBuXPhos	8	52	42	13	0	1	14	39	14	12	10	10	17	2	2	23	6	11	30	3	5	12	14	11
RuPhos	7	53	33	16	14	3	4	47	40	10	19	14	17	2	3	36	6	2	23	2	5	15	10	6
P(OPh)3	1	4	3	23	1	1	19	18	5	3	1	1	3	1	1	9	4	3	11	1	2	10	6	3
$P(OCH_2tBu)_3$	0	1	1	11	1	2	7	21	3	9	10	7	16	2	3	22	9	7	28	3	3	5	20	11
TMEDA	10	52	35	17	23	3	5	44	34	12	5	6	16	2	3	18	6	1	26	3	3	11	13	10
$Pd(OAc)_2(PCy_3)_2$	1	15	1	37	2	0	2	22	2	2	14	2	3	5	0	4	2	0	1	1	1	1	1	0

2EHA	CN			CHO			CO2Et			COAcetal			H			Ph			Me			OMe		
	C2	C5	C2C5	C2	C5	C2C5	C2	C5	C2C5	C2	C5	C2C5	C2	C5	C2C5	C2	C5	C2C5	C2	C5	C2C5	C2	C5	C2C5
$P(tBu)_3$	4	75	7	13	6	3	55	42	10	31	14	8	26	4	5	61	5	7	17	4	5	13	17	19
PCy_3	14	43	39	0	0	0	0	3	1	1	2	0	5	2	1	5	6	1	5	3	3	11	4	3
PPh_3	7	58	28	1	5	6	14	14	13	17	5	4	50	2	8	12	5	3	28	3	10	22	2	7
$P(o\text{-}tolyl)_3$	0	2	2	0	0	0	8	8	32	9	20	5	41	2	7	23	10	6	5	1	1	11	24	16
$P(o\text{-}MeOPh)_3$	6	49	41	0	0	0	7	6	25	14	24	5	28	9	27	11	31	14	13	17	1	3	62	23
XPhos	9	37	34	6	27	3	5	9	3	13	9	2	53	0	12	17	6	2	16	4	6	9	6	10
tBuXPhos	11	57	24	0	0	0	19	18	29	11	18	6	38	3	9	26	9	6	13	5	4	8	21	13
RuPhos	13	47	30	0	0	0	16	17	28	2	2	1	39	4	11	45	5	15	12	2	6	12	17	10
P(OPh)3	0	49	36	1	1	1	34	33	13	4	1	1	19	5	4	20	7	3	7	2	1	11	24	16
$P(OCH_2tBu)_3$	0	4	1	1	0	0	18	17	23	10	8	2	35	3	7	36	8	7	12	5	3	6	22	14
TMEDA	0	2	2	1	1	1	17	17	10	11	7	2	40	2	7	28	8	7	12	5	4	9	28	16
$Pd(OAc)_2(PCy_3)_2$	1	64	2	1	0	0	3	24	4	1	11	0	3	13	0	4	3	2	2	6	5	1	2	1

Fig. C19. Multifactor evaluation of ligand stabilizer ($P(tBu)_3$, PCy_3, PPh_3, $P(o\text{-}tolyl)_3$, $P(o\text{-}MeOPh)_3$, XPhos, tBuXPhos, RuPhox, $P(OPh)_3$, $P(OCH_2tBu)_3$ and TMEDA) and carboxylates (2-Ethyl hexanoic acid and Pivalic acid), using precatalyst V and $Pd(OAc)_2(PCy_3)_2$ and eight thiazoles substituted on the C4 position (R= CN, CHO, CO2Et, CO Acetate, H, Ph, Me and OMe)

V: Isolated Product NMR Spectroscopy Data

2-(2-methylprop-1-en-1-yl)thiazole-4-carbonitrile (**3CN-C2**) and **2,5-bis(2-methylprop-1-en-1-yl)thiazole-4-carbonitrile** (**3CN-C2C5**) (1:1)

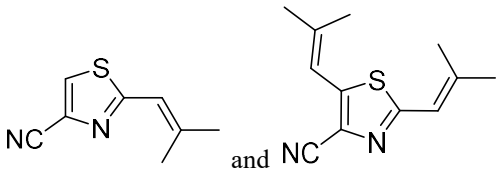

3CN-C2: ^{1}H NMR (300 MHz, $CDCl_3$) δ 8.59 (d, *J* = 0.9 Hz, 1H), 6.71 – 6.54 (m, 1H), 2.00 (dd, *J* = 1.4, 0.6 Hz, 2H), 1.95 – 1.93 (m, 2H).

3CN-C2C5: ^{1}H NMR (300 MHz, $CDCl_3$) δ 6.52 (q, *J* = 1.4 Hz, 1H), 6.34 (p, *J* = 1.4 Hz, 1H), 2.11 (dd, *J* = 1.3, 0.6 Hz, 3H), 1.97 (dd, *J* = 1.4, 0.6 Hz, 3H), 1.93 (qd, *J* = 1.0, 0.6 Hz, 6H).

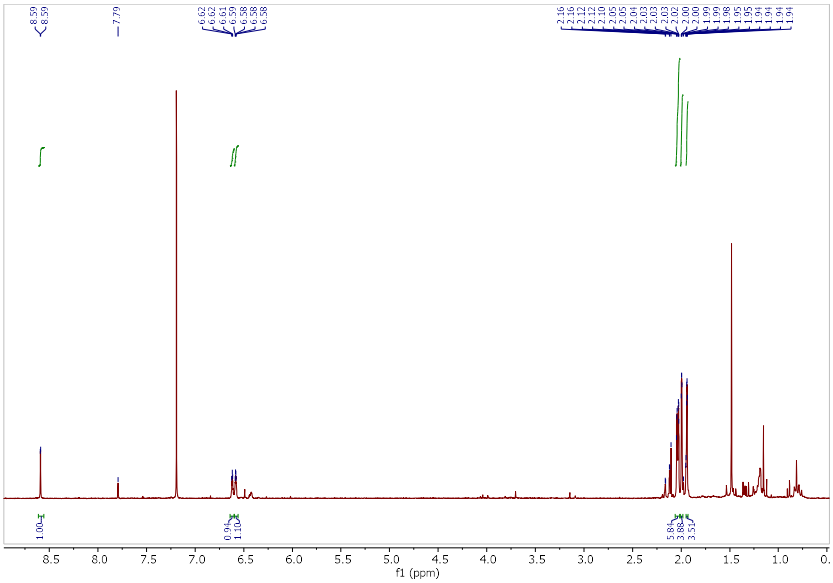

Fig. C20. ^{1}H NMR (300 MHz, Chloroform-*d*) spectrum of **3CN-C2** and **3CN-C2C5**

5-(2-methylprop-1-en-1-yl)thiazole-4-carbonitrile (3CN-C5)

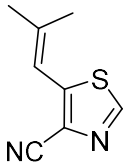

^{1}H NMR (300 MHz, $CDCl_3$) δ 8.59 (d, *J* = 0.8 Hz, 1H), 6.58 (d, *J* = 0.8 Hz, 1H), 1.99 (dd, *J* = 1.5, 0.6 Hz, 3H), 1.94 (dd, *J* = 1.3, 0.6 Hz, 3H).

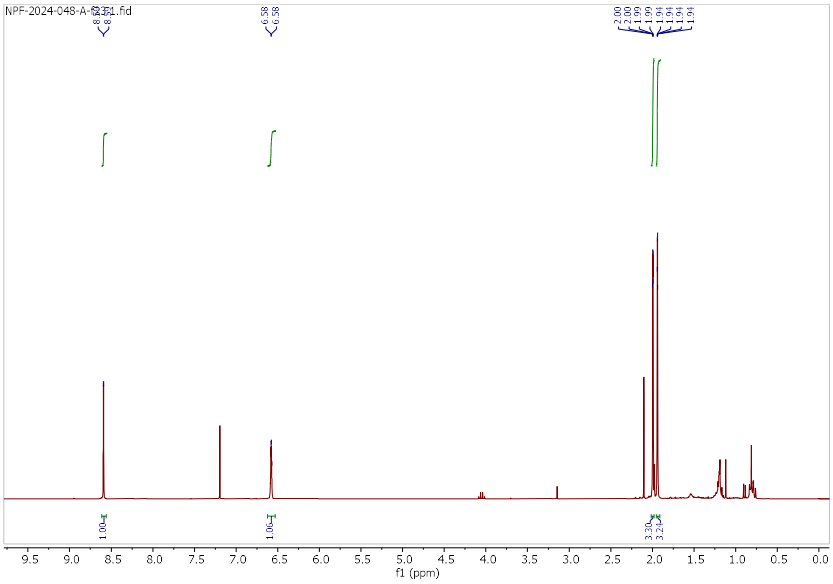

Fig. C21. ^{1}H NMR (300 MHz, Chloroform-*d*) spectrum of **3CN-C5**

2,5-bis(2-methylprop-1-en-1-yl)thiazole-4-carbonitrile (**3CN-C2C5**)

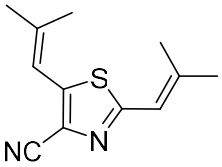

^{1}H NMR (300 MHz, $CDCl_3$) δ 6.52 (q, *J* = 1.4 Hz, 1H), 6.34 (p, *J* = 1.4 Hz, 1H), 2.11 (dd, *J* = 1.3, 0.6 Hz, 3H), 1.97 (dd, *J* = 1.4, 0.6 Hz, 3H), 1.93 (qd, *J* = 1.0, 0.6 Hz, 6H).

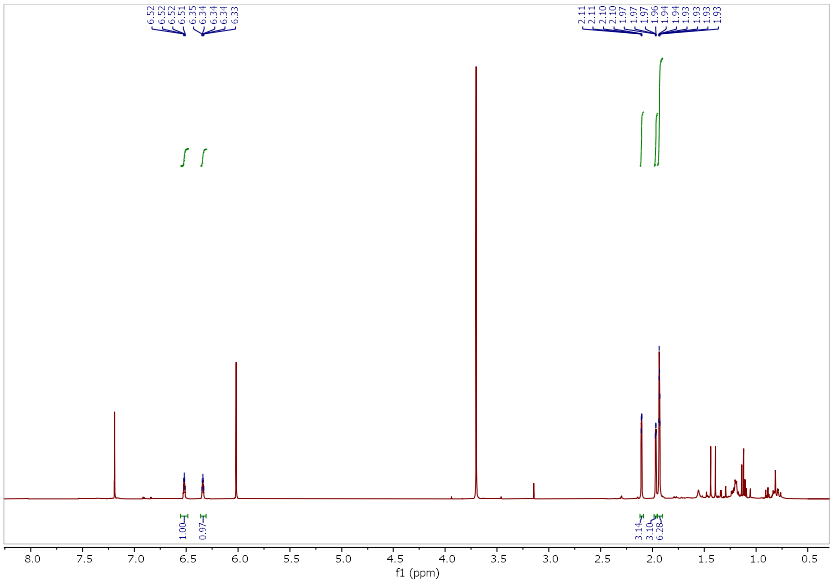

Fig. C22. ^{1}H NMR (300 MHz, Chloroform-*d*) spectrum of **3CN-C2C5.** IS, 1,3,5-trimethoxy benzene present.

2-(2-methylprop-1-en-1-yl)thiazole-4-carbaldehyde (3CHO-C2)

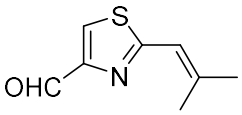

^{1}H NMR (300 MHz, $CDCl_3$) δ 10.04 (s, 1H), 8.08 (d, J = 0.7 Hz, 1H), 6.56 (s, 1H), 2.17 (s, 3H), 2.04 (s, 3H).

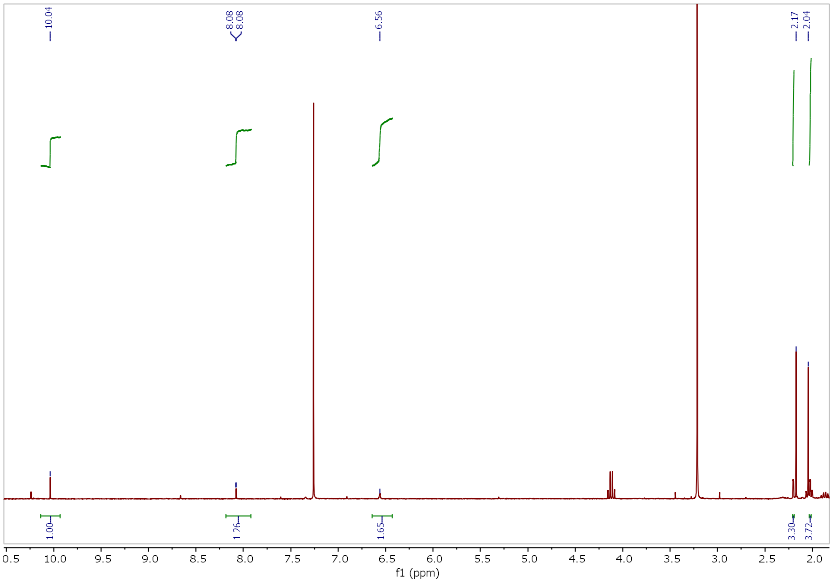

Fig. C23. ^{1}H NMR (300 MHz, Chloroform-*d*) spectrum of **3CHO-C2**

5-(2-methylprop-1-en-1-yl)thiazole-4-carbaldehyde (3CHO-C5)

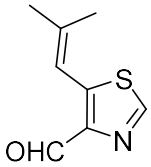

^{1}H NMR (300 MHz, $CDCl_3$) δ 10.24 (s, 1H), 8.67 (s, 1H), 7.34 (m, 1H), 2.17 (s, 3H), 2.04 (s, 3H).

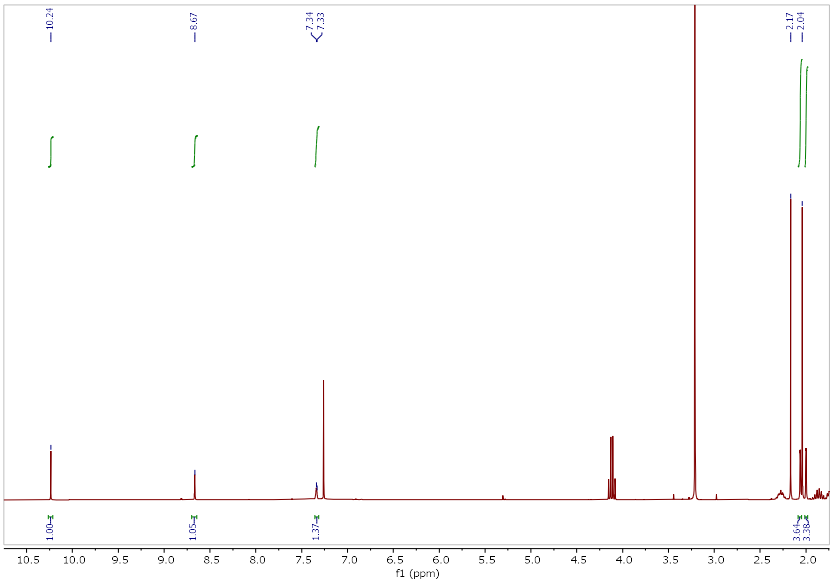

Fig. C24. ^{1}H NMR (300 MHz, Chloroform-*d*) spectrum of **3CHO-C5**

2,5-bis(2-methylprop-1-en-1-yl)thiazole-4-carbaldehyde (3CHO-C2C5)

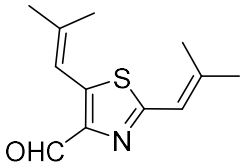

^{1}H NMR (300 MHz, $CDCl_3$) δ 10.16 (s, 1H), 7.30 – 7.27 (m, 1H), 6.48 (m, 1H), 2.18 (dd, *J* = 1.3, 0.5 Hz, 3H), 2.04 (d, *J* = 0.7 Hz, 3H), 2.02 – 1.98 (m, 6H).

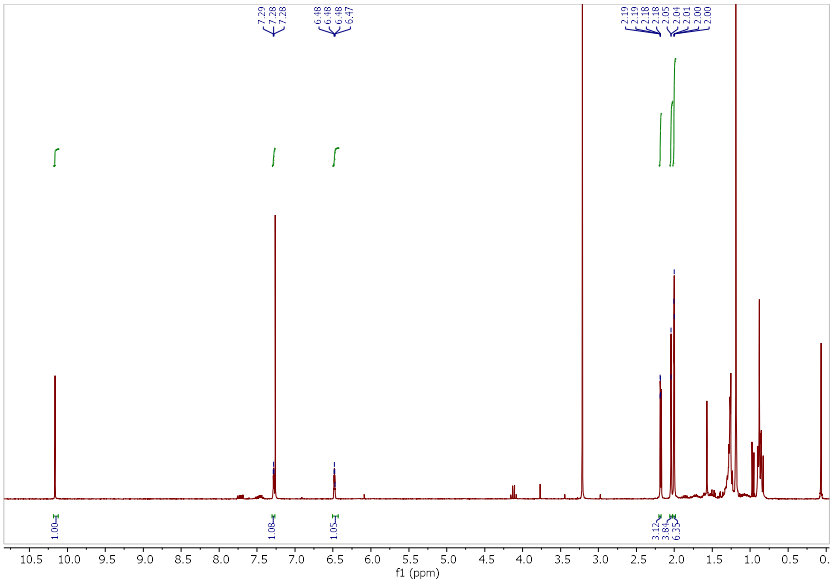

Fig. C25. ^{1}H NMR (300 MHz, Chloroform-*d*) spectrum of **3CHO-C2C5**

Ethyl 2-(2-methylprop-1-en-1-yl)thiazole-4-carboxylate (3CO$_2$Et-C2)

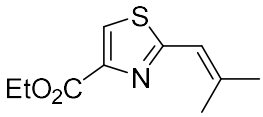

^{1}H NMR (300 MHz, $CDCl_3$) δ 8.08 (s, 1H), 6.65 (m, 1H), 4.42 (q, *J* = 7.1 Hz, 2H), 2.14 (dd, *J* = 1.3, 0.6 Hz, 3H), 2.00 (dd, *J* = 1.4, 0.6 Hz, 3H), 1.40 (t, *J* = 7.1 Hz, 3H).

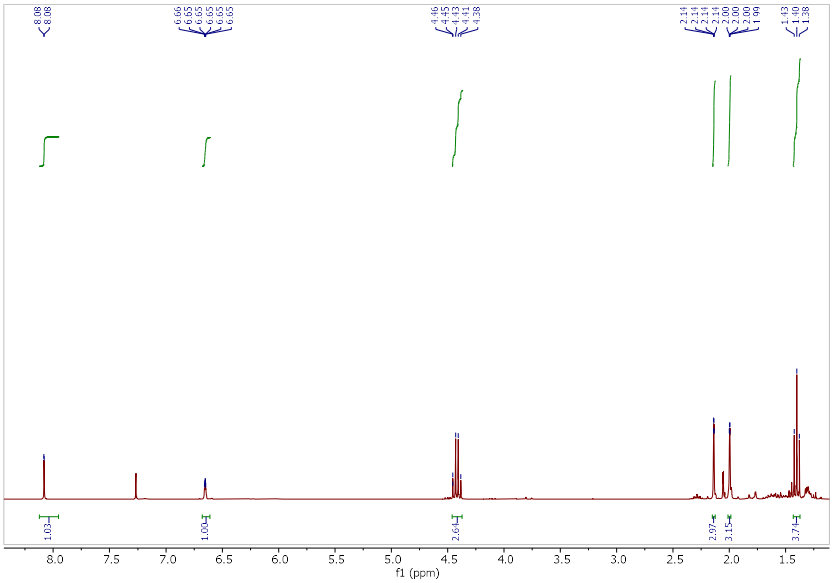

Fig. C26. ^{1}H NMR (300 MHz, Chloroform-*d*) spectrum of **3CO$_2$Et-C2**

Ethyl 5-(2-methylprop-1-en-1-yl)thiazole-4-carboxylate (3CO$_2$Et-C5)

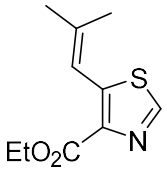

^{1}H NMR (300 MHz, $CDCl_3$) δ 8.64 (d, J = 0.6 Hz, 1H), 7.25 (m, 1H), 4.43 (q, J = 7.1 Hz, 2H), 2.03 (m, 3H), 2.01 – 1.95 (m, 3H), 1.43 (t, J = 7.1 H, 3H).

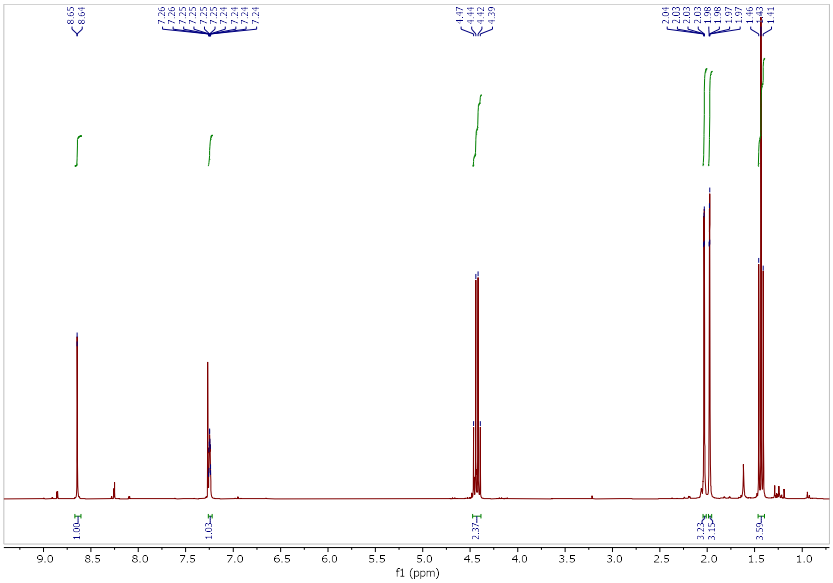

Fig. C27. ^{1}H NMR (300 MHz, Chloroform-*d*) spectrum of **3CO$_2$Et-C5**

Ethyl 2,5-bis(2-methylprop-1-en-1-yl)thiazole-4-carboxylate (3CO$_2$Et-C2C5)

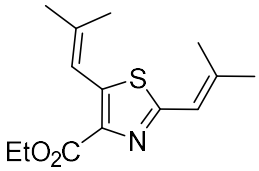

^{1}H NMR (300 MHz, $CDCl_3$) δ 7.19 (m, 1H), 6.61 – 6.55 (m, 1H), 4.41 (q, *J* = 7.1 Hz, 2H), 2.12 (d, *J* = 0.8 Hz, 3H), 2.01 (dd, *J* = 1.5, 0.6 Hz, 3H), 1.98 (dd, *J* = 1.4, 0.6 Hz, 6H), 1.40 (t, *J* = 7.1 Hz, 3H).

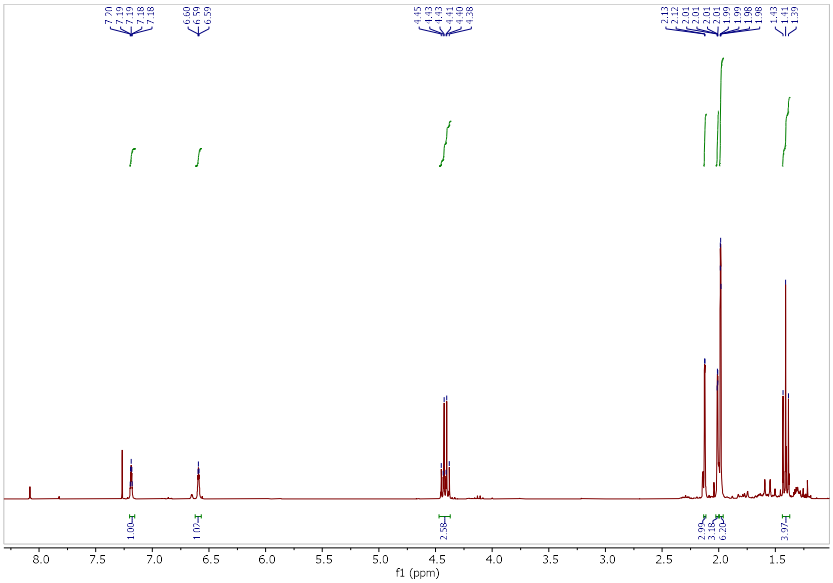

Fig. C28. ^{1}H NMR (300 MHz, Chloroform-*d*) spectrum of **3CO$_2$Et-C2C5**

4-(1,3-dioxolan-2-yl)-2-(2-methylprop-1-en-1-yl)thiazole (3COAcetal-C2)

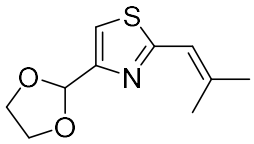

^{1}H NMR (300 MHz, $CDCl_3$) δ 8.67 (s, 1H), 6.49 – 6.38 (m, 1H), 6.05 (s, 1H), 4.34 – 4.22 (m, 2H), 4.13 – 3.99 (m, 2H), 1.95 (dd, *J* = 1.4, 0.5 Hz, 3H), 1.88 (dd, *J* = 1.3, 0.5 Hz, 3H).

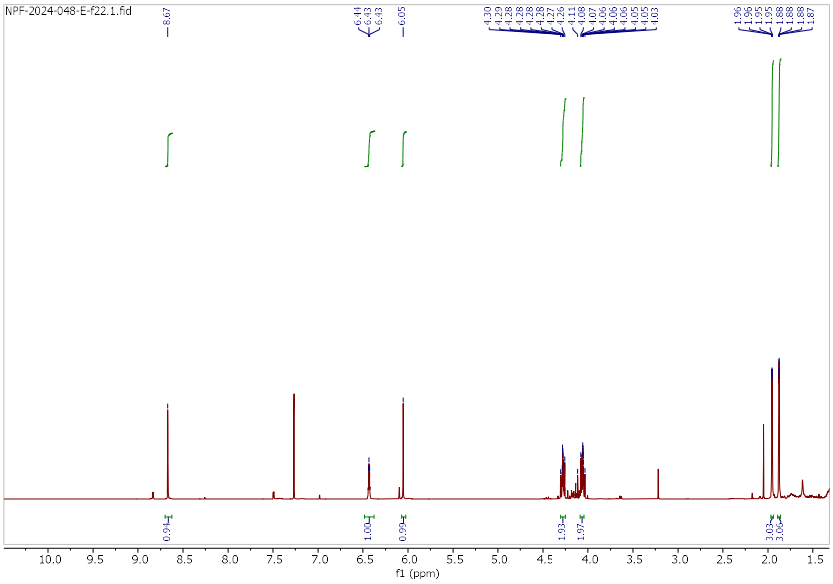

Fig. C29. ^{1}H NMR (300 MHz, Chloroform-*d*) spectrum of **3COAcetal-C2**

4-(1,3-dioxolan-2-yl)-5-(2-methylprop-1-en-1-yl)thiazole (**3COAcetal-C2**) and **4-(1,3-dioxolan-2-yl)-2,5-bis(2-methylprop-1-en-1-yl)thiazole** (1:0.33) (**3COAcetal-C2C5**)

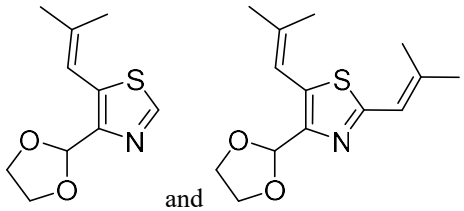

3COAcetal-C2: ^{1}H NMR (300 MHz, $CDCl_3$) δ 7.32 (s, 1H), 6.58 (s, 1H), 6.02 (d, *J* = 1.0 Hz, 1H), 4.17 – 4.13 (m, 2H), 4.05 (ddd, *J* = 6.6, 5.1, 2.1 Hz, 2H), 2.13 (d, *J* = 1.3 Hz, 3H), 1.98 (d, *J* = 1.4 Hz, 3H).

3COAcetal-C2C5: ^{1}H NMR (300 MHz, $CDCl_3$) δ 6.55 – 6.52 (m, 1H), 6.45 – 6.39 (m, 1H), 4.30 – 4.23 (m, 2H), 4.06 – 4.01 (m, 2H), 2.11 (d, *J* = 1.3 Hz, 3H), 1.96 (d, *J* = 1.4 Hz, 3H), 1.94 (d, *J* = 1.5 Hz, 3H), 1.90 (d, *J* = 1.3 Hz, 3H).

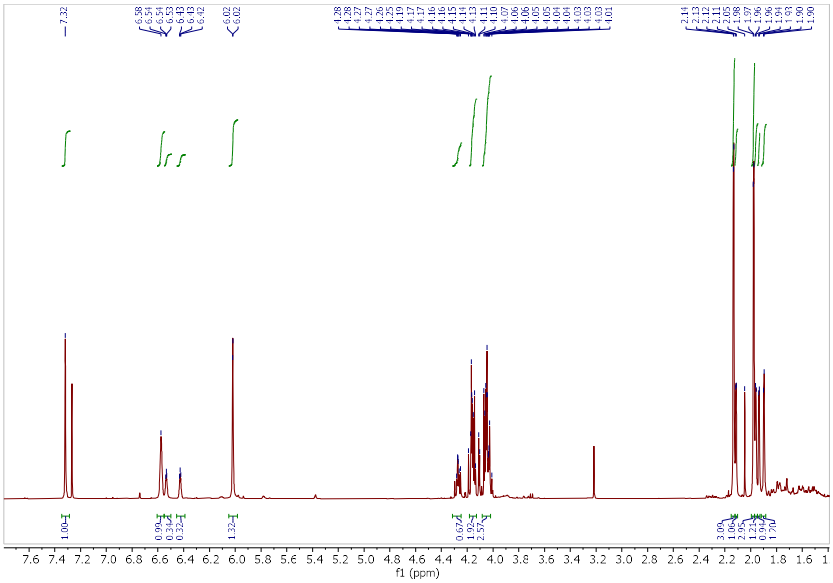

Fig. C30. ^{1}H NMR (300 MHz, Chloroform-*d*) spectrum of **3COAcetal-C5** and **3COAcetal-C2C5**

2-(2-methylprop-1-en-1-yl)thiazole (**3H-C2**) and **5-(2-methylprop-1-en-1-yl)thiazole** (**3H-C5**) (1:0.6)

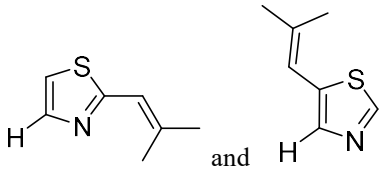

3H-C2: ^{1}H NMR (300 MHz, $CDCl_3$) δ 7.47 (s, 1H), 6.42 (h, *J* = 1.3 Hz, 1H), 6.31 – 6.22 (m, 1H), 1.89 (d, *J* = 1.3 Hz, 3H), 1.87 (d, *J* = 1.4 Hz, 3H).

3H-C5: ^{1}H NMR (300 MHz, $CDCl_3$) δ 7.70 (d, *J* = 3.3 Hz, 1H), 7.16 (dd, *J* = 3.3, 0.7 Hz, 1H), 6.50 (q, *J* = 0.7 Hz, 1H), 2.09 (dd, *J* = 1.3, 0.6 Hz, 3H), 1.92 (dd, *J* = 1.5, 0.6 Hz, 3H).

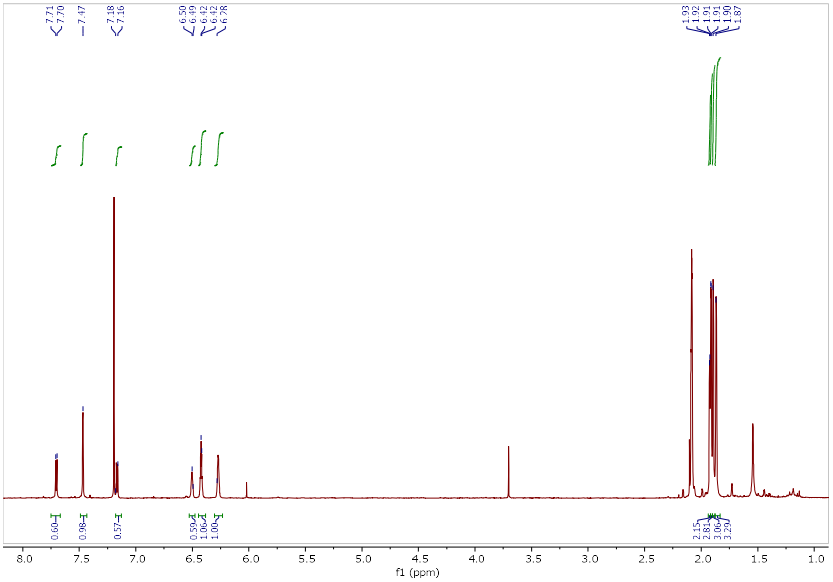

Fig. C31. ^{1}H NMR (300 MHz, Chloroform-*d*) spectrum of **3H-C5** and **3CH-C5**

5-(2-methylprop-1-en-1-yl)thiazole (3H-C5)

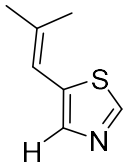

^{1}H NMR (300 MHz, $CDCl_3$) δ 7.70 (d, J = 3.3 Hz, 1H), 7.16 (dd, J = 3.3, 0.7 Hz, 1H), 6.50 (q, J = 0.7 Hz, 1H), 2.09 (dd, J = 1.3, 0.6 Hz, 3H), 1.92 (dd, J = 1.5, 0.6 Hz, 3H).

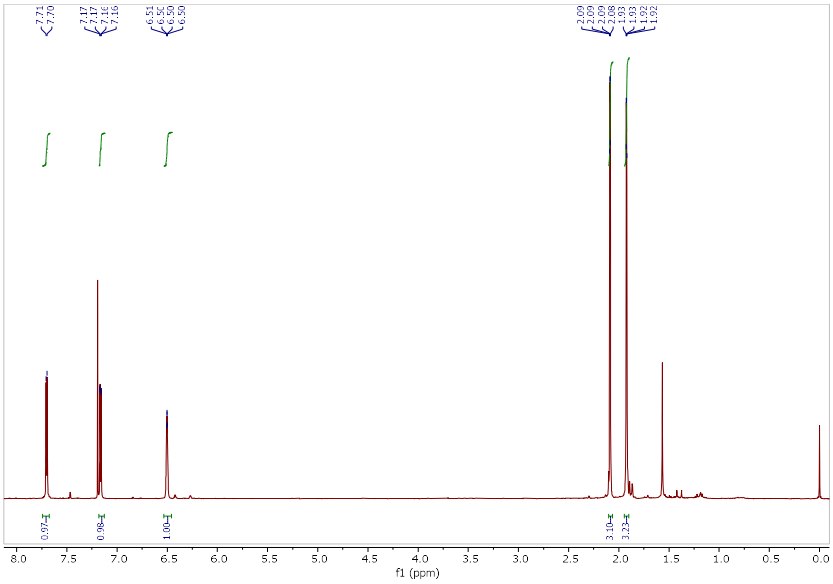

Fig. C32. ^{1}H NMR (300 MHz, Chloroform-*d*) spectrum of **3CH-C5**

4-methyl-2-(2-methylprop-1-en-1-yl)thiazole (**3Me-C2**) and **4-methyl-2,5-bis(2-methylprop-1-en-1-yl)thiazole** (**3Me-C2C5**) (1:0.12)

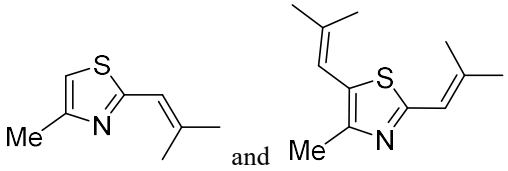

3Me-C2: ^{1}H NMR (300 MHz, $CDCl_3$) δ 7.47 (s, 1H), 6.42 (m, 1H), 6.31 – 6.22 (m, 1H), 2.08 (s, 3H), 1.89 (d, *J* = 1.3 Hz, 3H), 1.87 (d, *J* = 1.4 Hz, 3H).

3Me-C2C5: ^{1}H NMR (500 MHz, $CDCl_3$) δ 6.50 (s, 1H), 6.25 (s, 1H), 2.37 (s, 3H), 1.99 (s, 3H), 1.96 (s, 3H), 1.91 (s, 3H), 1F.79 (s, 3H).

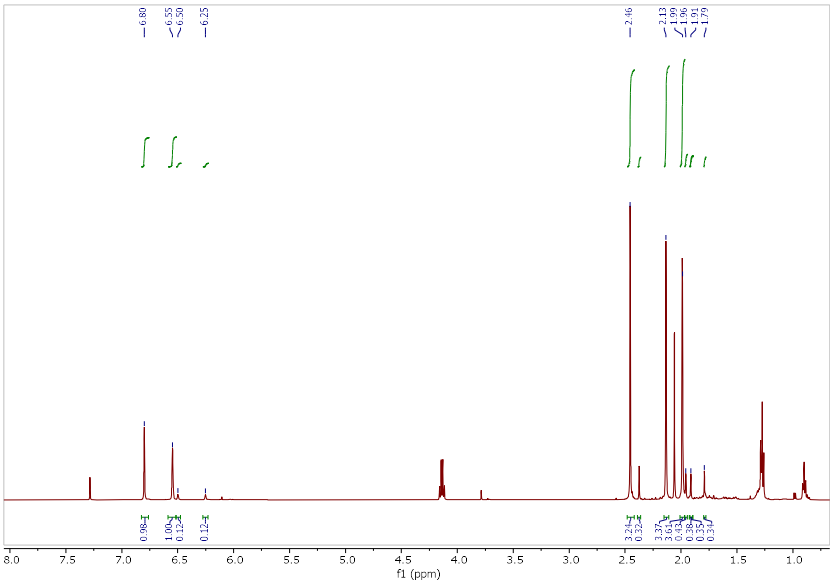

Fig. C33. ^{1}H NMR (300 MHz, Chloroform-*d*) spectrum of **3Me-C2** and **3Me-C2C5**

5-(2-methylprop-1-en-1-yl)-4-phenylthiazole (3Ph-C5)

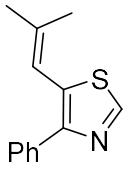

^{1}H NMR (500 MHz, $CDCl_3$) δ 8.91 (d, J = 2.0 Hz, 1H), 8.75 (s, 1H), 8.15 – 7.92 (m, 2H), 7.81 – 7.71 (m, 2H), 7.56 (d, J = 2.0 Hz, 1H), 7.46 (m, 4H), 7.42 – 7.36 (m, 2H), 6.39 (s, 1H), 1.99 – 1.94 (m, 3H), 1.92 (m, 3H).

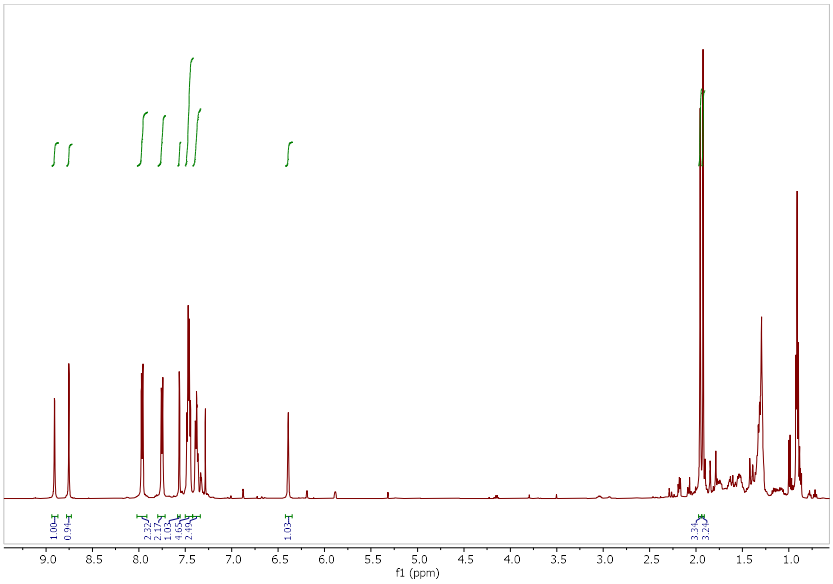

Fig. C34. ^{1}H NMR (500 MHz, Chloroform-*d*) spectrum of **3Ph-C5**

2-(2-methylprop-1-en-1-yl)-4-phenylthiazole (**3Ph-C2**) and **2,5-bis(2-methylprop-1-en-1-yl)-4-phenylthiazole** (**3Ph-C2C5**) (1:0.2)

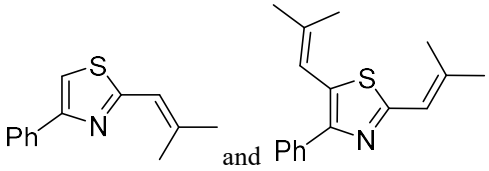

3Ph-C2: ^{1}H NMR (500 MHz, $CDCl_3$) δ 7.99 – 7.94 (m, 1H), 7.47 – 7.32 (m, 4H), 6.61 (t, J = 1.6 Hz, 1H), 2.27 (d, J = 1.3 Hz, 3H), 2.04 (d, J = 1.4 Hz, 3H).

3Ph-C2C5: ^{1}H NMR (500 MHz, $CDCl_3$) δ 7.94 – 7.89 (m, 1H), 7.51 – 7.32 (m, 4H), 6.58 (m, 1H), 6.42 – 6.36 (m, 1H), 2.23 (s, 3H), 2.03 – 2.02 (m, 3H), 1.95 (dd, J = 5.7, 1.4 Hz, 6H).

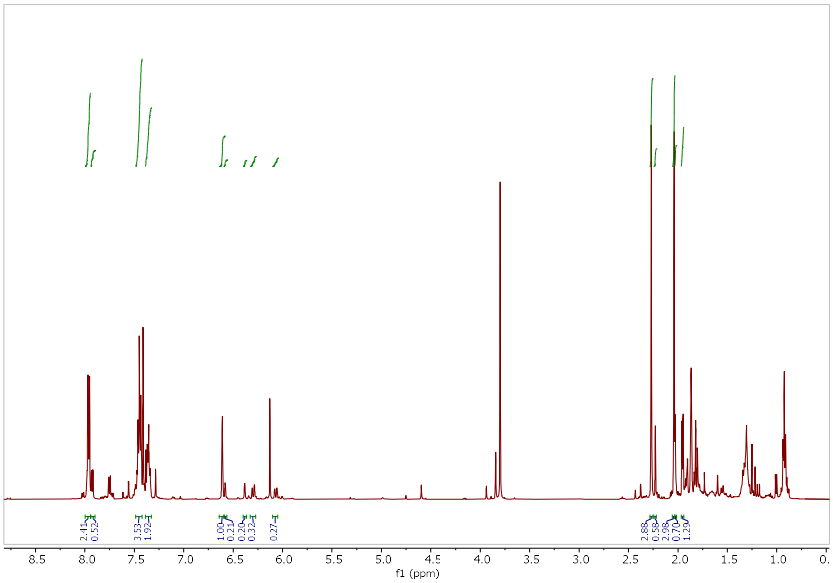

Fig. C35. ^{1}H NMR (500 MHz, Chloroform-*d*) spectrum of **3Ph-C2** and **3Ph-C2C5**

4-methoxy-2-(2-methylprop-1-en-1-yl)thiazole (3OMe-C2)

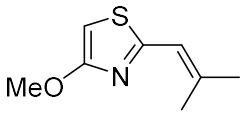

^{1}H NMR (500 MHz, $CDCl_3$) δ 6.37 (m, 1H), 6.34 – 6.26 (m, 1H), 4.06 – 4.02 (m, 3H), 2.18 (s, 3H), 2.07 (s, 3H).

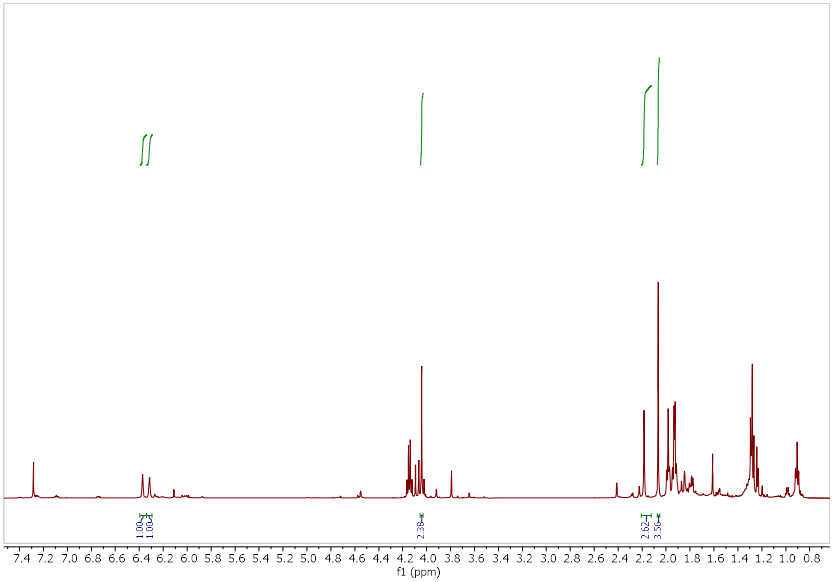

Fig. C36. ^{1}H NMR (500 MHz, Chloroform-*d*) spectrum of **3OMe-C2**

4-methoxy-5-(2-methylprop-1-en-1-yl)thiazole (3OMe-C5)

^{1}H NMR (500 MHz, $CDCl_3$) δ 8.58 (s, 1H), 6.16 (s, 1H), 3.96 (s, 3H), 2.07 (s, 6H).

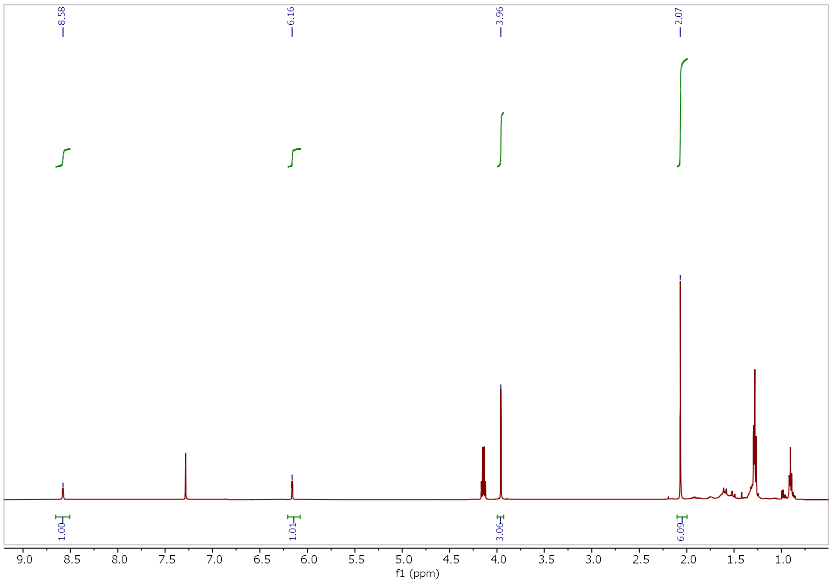

Fig. C37. ^{1}H NMR (500 MHz, Chloroform-*d*) spectrum of **3OMe-C5**

4-methoxy-2,5-bis(2-methylprop-1-en-1-yl)thiazole (**3OMe-C2C5**) and 4-methoxy thiazole

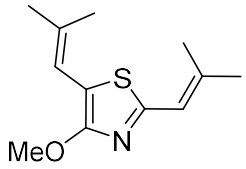

and
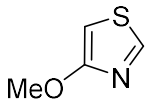

^{1}H NMR (500 MHz, $CDCl_3$) δ 6.40 (s, 1H), 6.00 (s, 1H), 3.92 (s, 3H), 2.17 (s, 3H), 2.06 (s, 3H).

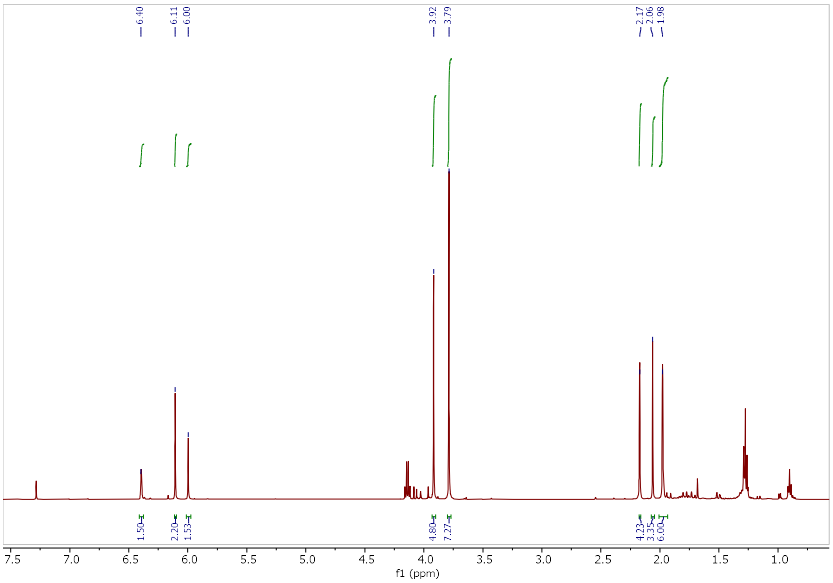

Fig. C38. ^{1}H NMR (500 MHz, Chloroform-*d*) spectrum of **3OMe-C2C5**

2-(2-propylpyridin-4-yl)-4-(p-tolyl)thiazole. Fatostatin

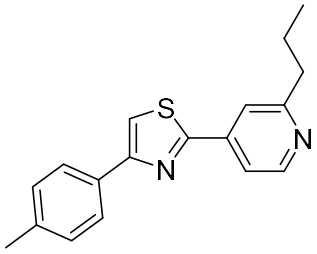

^{1}H NMR (500 MHz, $CDCl_3$) δ 8.65 (dd, *J* = 5.1, 0.8 Hz, 1H), 7.91 (d, *J* = 8.1 Hz, 2H), 7.79 (dd, J = 1.8, 0.8 Hz, 1H), 7.71 (dd, *J* = 5.2, 1.7 Hz, 1H), 7.55 (s, 1H), 7.30 (t, *J* = 0.8 Hz, 1H), 7.29 (d, *J* = 1.1 Hz, 1H), 2.99 – 2.83 (m, 2H), 2.43 (s, 3H), 1.93 – 1.81 (m, 2H), 1.04 (t, *J* = 7.3 Hz, 3H).

^{13}C NMR (126 MHz, $CDCl_3$) δ 165.3, 163.5, 157.2, 150.1, 140.7, 138.5, 131.4, 129.5, 126.4, 119.3, 117.9, 113.3, 40.5, 23.1, 21.3, 13.9.

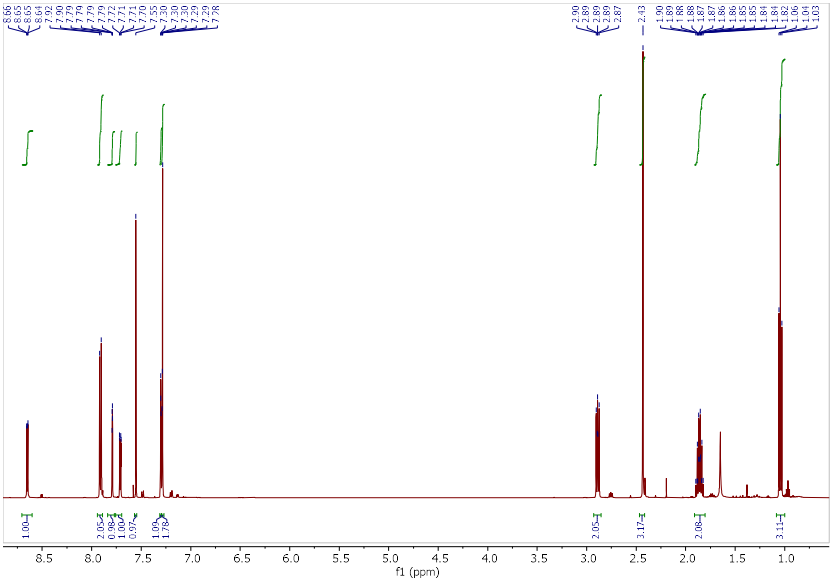

Fig. C39. ^{1}H NMR (500 MHz, Chloroform-*d*) spectrum of **2-(2-propylpyridin-4-yl)-4-(p-tolyl)thiazole**

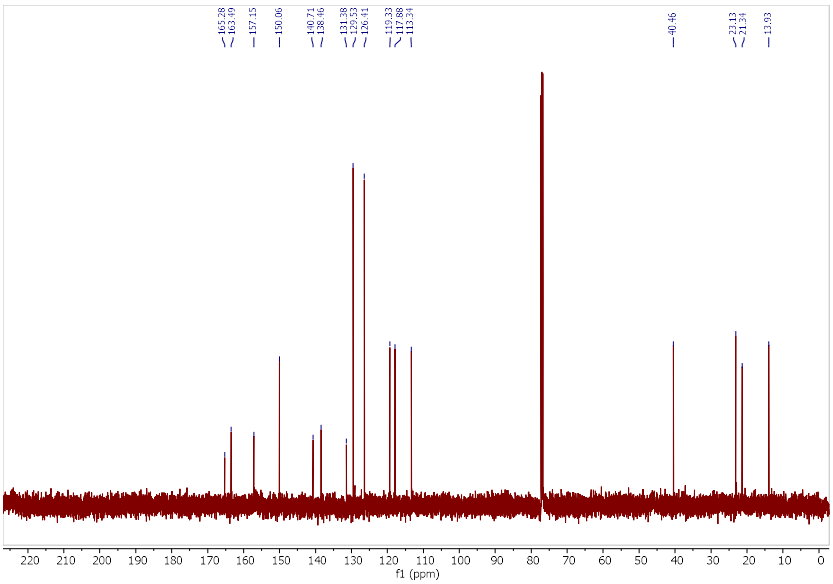

Fig. C40. $^{13}C\{^{1}H\}$ NMR (126 MHz, Chloroform-*d*) spectrum of **2-(2-propylpyridin-4-yl)-4-(p-tolyl)thiazole**

5-(2-propylpyridin-4-yl)-4-(p-tolyl)thiazole

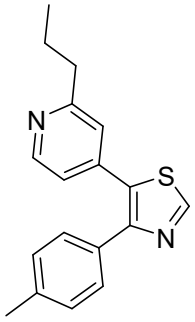

^{1}H NMR (500 MHz, $CDCl_3$) δ 8.89 (s, 1H), 8.49 (d, *J* = 5.2 Hz, 1H), 7.47 – 7.40 (m, 2H), 7.17 (d, *J* = 7.8 Hz, 1H), 7.09 (dd, *J* = 5.2, 1.7 Hz, 1H), 2.76 – 2.71 (m, 2H), 2.39 (s, 3H), 1.79 – 1.66 (m, 2H), 1.63 (s, 3H), 0.95 (t, *J* = 7.4 Hz, 4H).

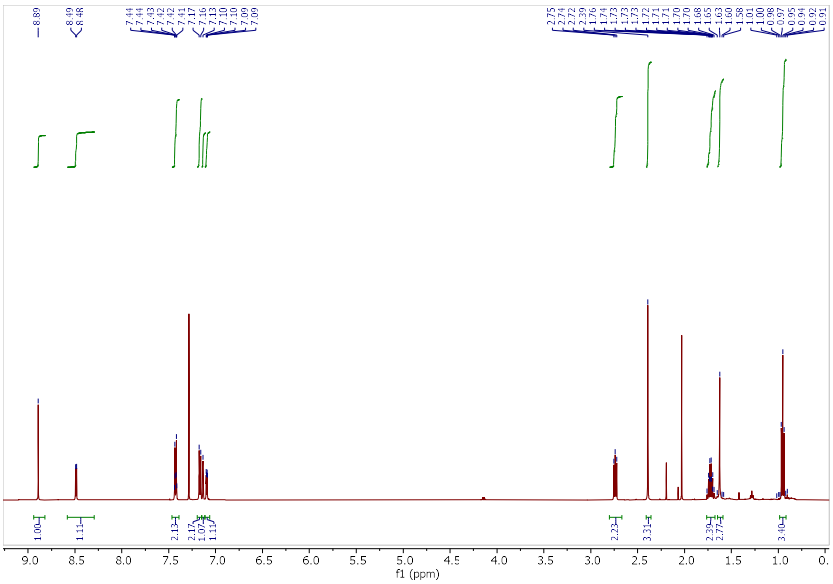

Fig. C41. ^{1}H NMR (500 MHz, Chloroform-*d*) spectrum of **5-(2-propylpyridin-4-yl)-4-(p-tolyl)thiazole**

2,5-bis(2-propylpyridin-4-yl)-4-(p-tolyl)thiazole

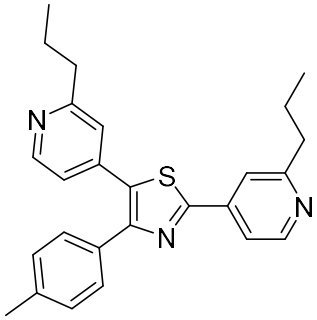

^{1}H NMR (300 MHz, $CDCl_3$) δ 8.56 (dd, *J* = 5.2, 0.8 Hz, 1H), 8.41 (dd, *J* = 5.2, 0.8 Hz, 1H), 7.67 (dd, *J* = 1.7, 0.8 Hz, 1H), 7.58 (dd, *J* = 5.2, 1.7 Hz, 1H), 7.46 – 7.35 (m, 2H), 7.17 – 7.04 (m, 3H), 7.02 (dd, *J* = 5.2, 1.8 Hz, 1H), 2.89 – 2.72 (m, 2H), 2.72 – 2.60 (m, 2H), 1.85 – 1.70 (m, 3H), 1.70 – 1.55 (m, 2H), 0.94 (t, *J* = 7.4 Hz, 2H), 0.86 (t, *J* = 7.4 Hz, 3H).

^{13}C NMR (76 MHz, $CDCl_3$) δ 164.0, 163.6, 163.01, 153.4, 150.1, 149.7, 140.2, 139.9, 138.7, 131.3, 131.1, 129.3, 129.0, 122.7, 120.9, 119.2, 117.7, 40.4, 40.3, 23.1, 22.9, 21.3, 13.9, 13.8.

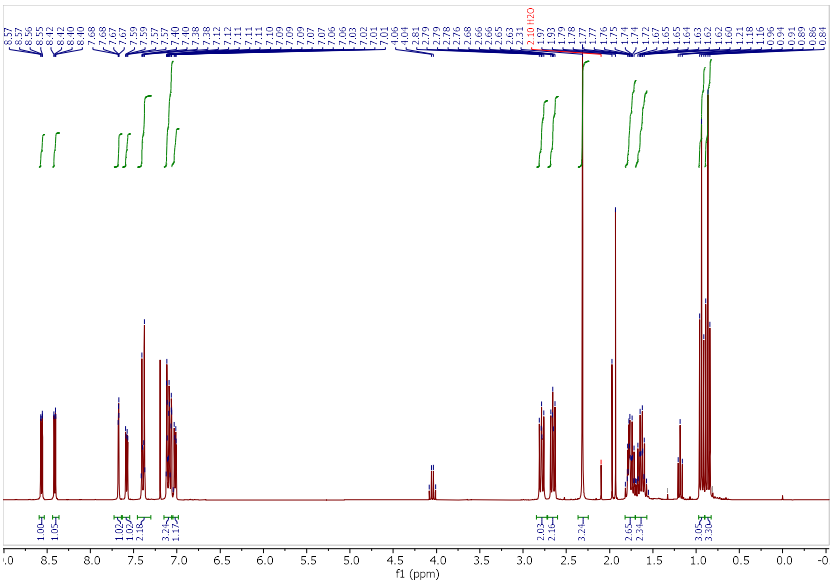

Fig. C42. ^{1}H NMR (500 MHz, Chloroform-*d*) spectrum of **2,5-bis(2-propylpyridin-4-yl)-4-(p-tolyl)thiazole**

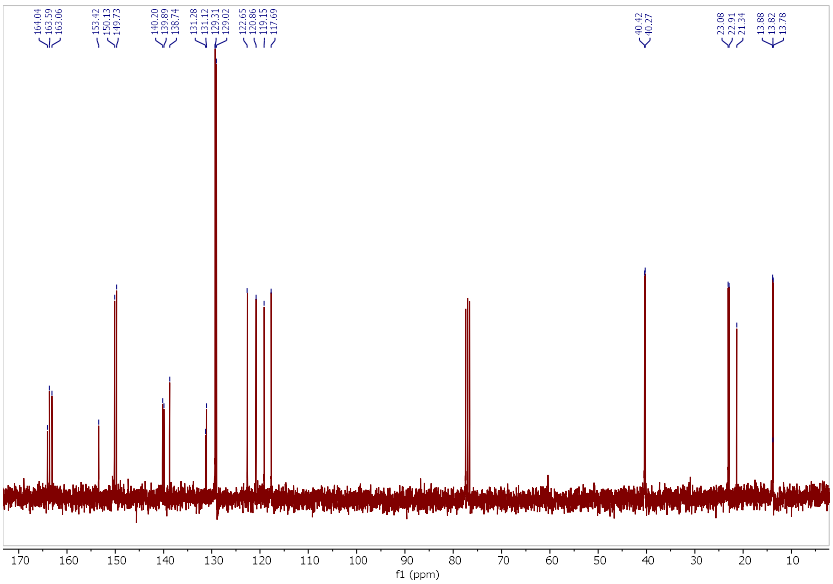

Fig. C43. ^{13}C{^{1}H} NMR (76 MHz, Chloroform-*d*) spectrum of **2,5-bis(2-propylpyridin-4-yl)-4-(p-tolyl)thiazole**

VI: Reaction Monitoring Experiments

Inside a glovebox, three 1-dram vials were charged with Teflon-coated stir bars. The heterocycle substrate (1.5 mmol, 1 equiv) and vinyl halide (1.5 equiv) were added, followed by internal standard (1,3,5-trimethoxybenzene, 10 mol%). Then, precatalyst VII (5 mol%). Finally, K_3PO_4 (1.5 equivalents) and anhydrous CPME (3 mL) was added. The vial was sealed with a Teflon-lined screw cap, and the reaction mixture stirred at 85 °C in a hot plate for 20 h. Aliquots (3 x 10 µL) were taken at the indicated times (0, 1, 2, 3, 6, 10 and 20 h). The aliquots were diluted with acetonitrile (1 mL) and analyzed by LCMS. Once the reaction finished, the solvent was evaporated under vacuum, and the residue redissolved in $CDCl_3$. The final product solution yields were determined by ^{1}H NMR spectroscopy by relative integration with the internal standard.

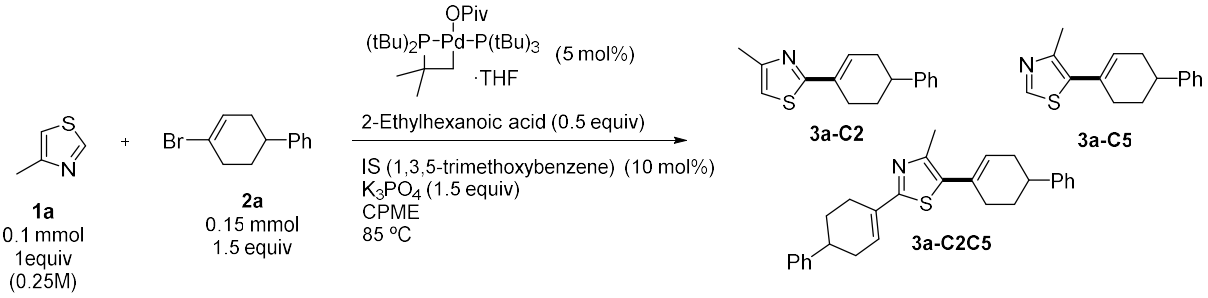

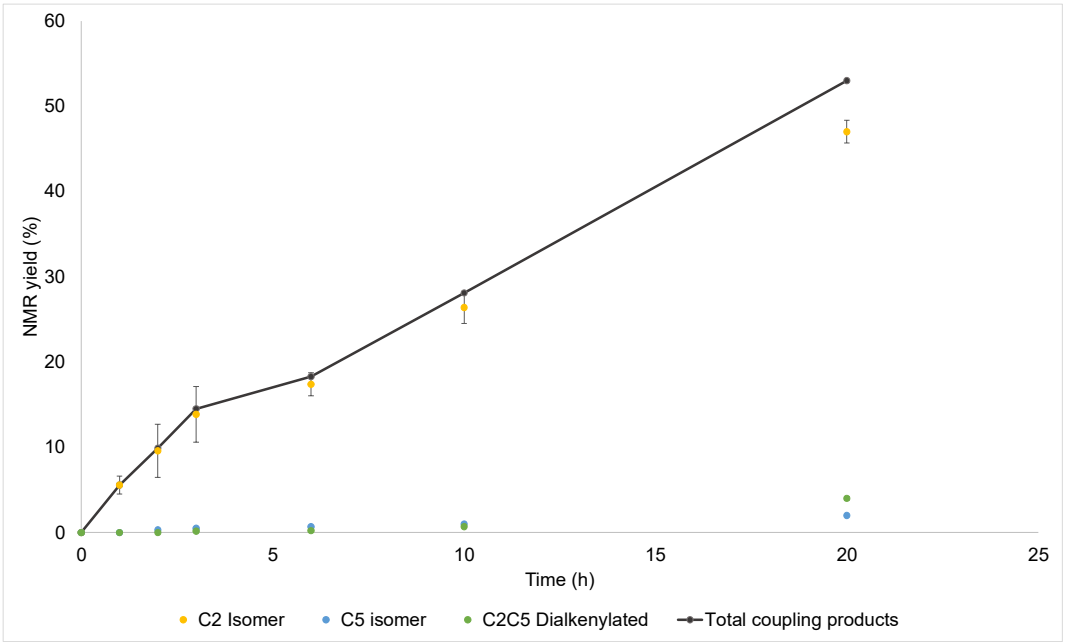

Fig. C44. Reaction progress monitoring of 4-methylthiazole (**1a**) direct alkenylation with vinyl halide **2a** *via* ^{1}H NMR spectroscopy and LCMS using different precatalyst VII

Appendix D: Supporting information for Chapter 5

I: General Considerations

Materials. All solvents and common organic reagents were purchased from commercial suppliers and used without further purification. $Pd(OAc)_2$, $[Pd(allyl)Cl]_2$, and $Pd(PCy_3)_2$ were purchased from Strem Chemicals and used as received. $Pd_2dba_3 \cdot CHCl_3$ was prepared according to the method of Zalesskiy and Ananikov.[1] ^{DMP}DAB–Pd–MAH was prepared using a reported procedure.[2] All phosphine ligands were purchased from Strem Chemicals and used as received. Anhydrous solvents (SureSeal) were purchased from MilliporeSigma and used as received.

Techniques. All air-free manipulations were performed under a dry nitrogen atmosphere using a MBraun glovebox. High-throughput experimentation was performed using 1 mL capacity glass shell vials in sealable aluminum reaction blocks purchased from Analytical Sales. Heating/stirring was achieved using rare-earth magnetic tumble stirrers acquired from V&P Scientific.

Centrifugal evaporation was performed using a Genevac EZ-2 (HCl compatible). The chromatography purification was performed on Biotage® Selekt SEL-2SW using Sfär Silica (60 μm) columns.

Analysis and Spectroscopy.

All NMR spectra were acquired on either a Bruker AVANCE 300 MHz spectrometer or a Bruker AVANCE Neo 500 MHz spectrometer. All ^{1}H and ^{13}C-NMR chemical shifts are calibrated to residual protio-solvents and all ^{31}P and ^{19}F NMR chemical shifts are calibrated to external standards. All NMR spectroscopic data is processed using MestreNova software.

UPLC analysis was performed using a Shimadzu Nexera X2 with a diode-array UV/Vis detector. A Raptor ARC-18 column (100 × 2.1 mm, particle size 1.8 μm) or a Waters CORTECS® UPLC® T3 column (2.1 × 30 mm, particle size 1.6 μm) were used. The eluent used is the mixture of two mobile phases. Water with 0.05% trifluoroacetic acid (TFA) was set to be the mobile phase A, and acetonitrile with 0.05% TFA was set to be the mobile phase B. All solvents used were HPLC grade.

High-resolution electrospray ionization mass spectrometric analysis was performed using a Thermo Scientific Ultimate 3000 ESI-Orbitrap Exactive Plus.

II: Characterization of palladacycle precatalysts

Palladacycle I

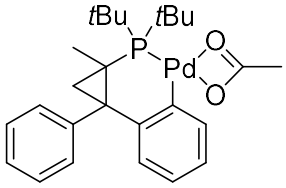

Palladacycle **I**

^{1}H NMR (500 MHz, C_6D_6) δ 8.40 (ddd, *J* = 7.9, 3.1, 1.3 Hz, 1H), 7.39 – 7.05 (m, 5H), 6.89 (ddd, *J* = 7.9, 7.0, 1.6 Hz, 1H), 6.71 (tt, *J* = 6.9, 1.1 Hz, 1H), 6.46 (dt, *J* = 7.9, 1.6 Hz, 1H), 2.61 (dd, *J* = 15.9, 5.0 Hz, 1H), 2.04 (s, 3H), 1.48 (s, 9H), 1.35 – 1.30 (m, 1H), 1.13 (d, *J* = 14.2 Hz, 9H), 0.84 (d, *J* = 7.5 Hz, 3H).

^{31}P{H} NMR (203 MHz, C_6D_6) δ 100.15.

HRMS (ESI) m/z: $[M+C_2H_5N]^+$ Calc'd for $C_{26}H_{37}NPPd$ 500.16984; found: 500.15356

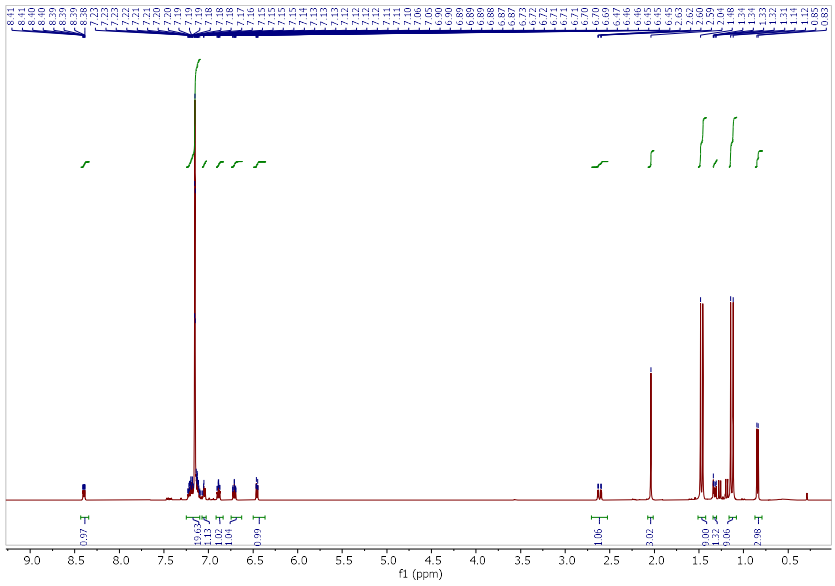

Fig. D1. ^{1}H NMR (500 MHz, C_6D_6) spectrum of **palladacycle I**

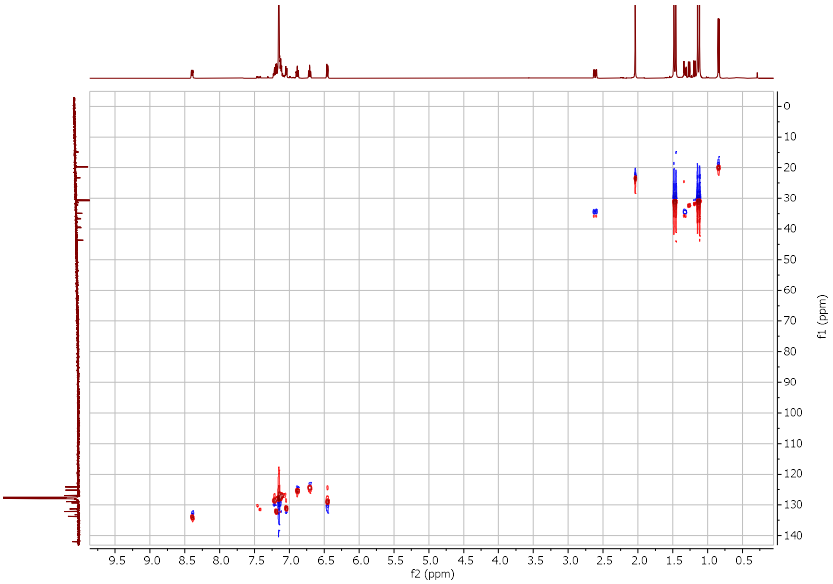

Fig. D2. ^{1}H-^{13}C–HSQC spectrum of **palladacycle I**

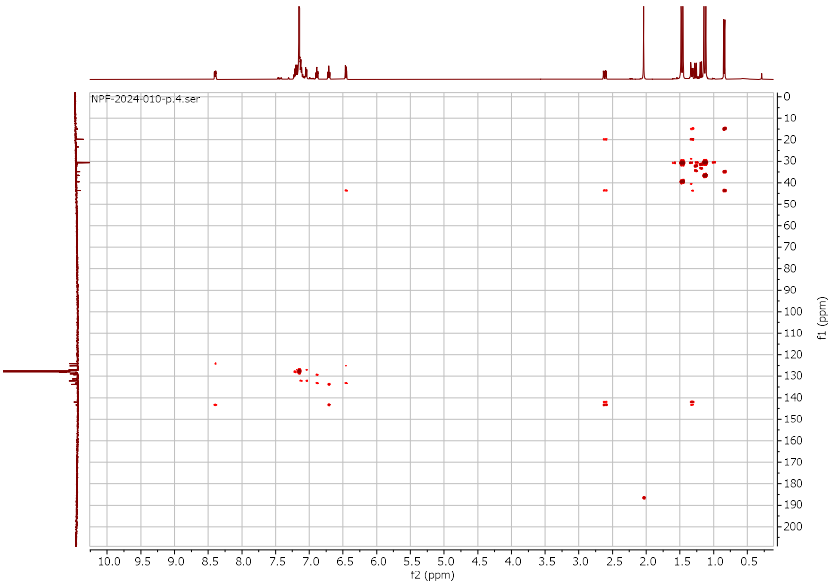

Fig. D3. ^{1}H-^{13}C–HMBC spectrum of **palladacycle I**

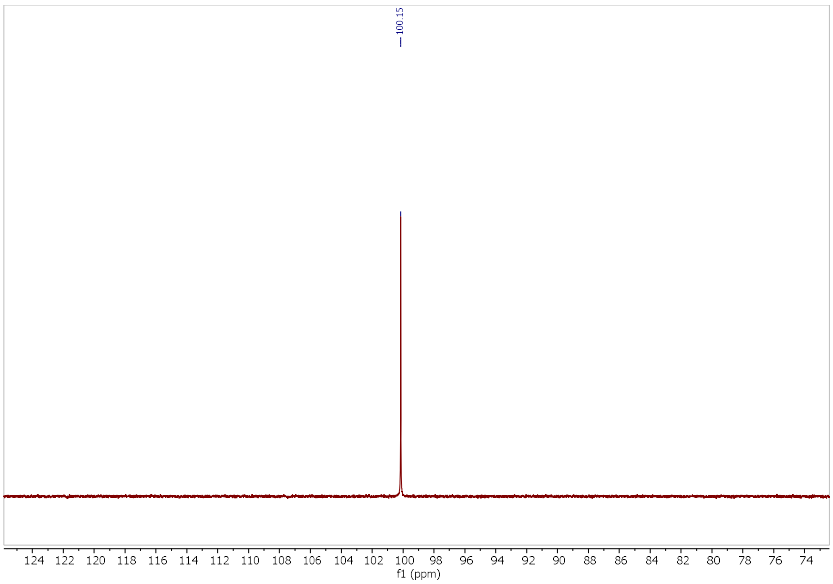

Fig. D4. $^{31}P\{H\}$ NMR (203 MHz, C_6D_6) spectrum **palladacycle I**

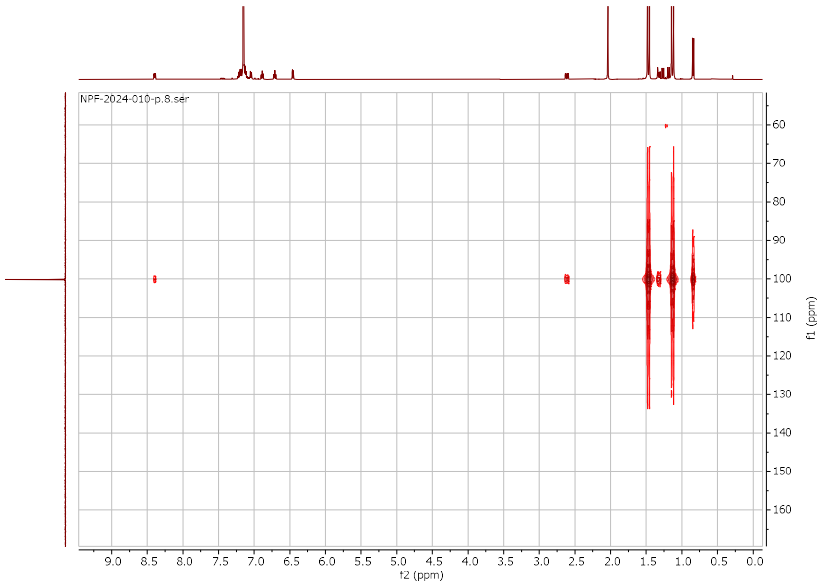

Fig. D5. ^{1}H-^{31}P-HMBC spectrum of **palladacycle I**

Palladacycle II

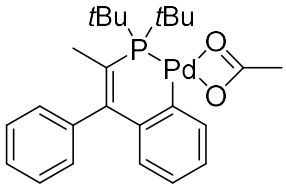

Palladacycle **II**

^{1}H NMR (500 MHz, C_6D_6) δ 8.69 (ddd, J = 8.0, 2.7, 1.1 Hz, 1H), 7.20-7.08f (m, 2H), 6.99 – 6.91 (m, 1H), 6.91 – 6.81 (m, 2H), 6.77 – 6.55 (m, 2H), 2.03 (s, 3H), 1.60 (d, J = 7.8 Hz, 3H), 1.34 (s, 9H), 1.31 (s, 9H).

^{31}P{H} NMR (203 MHz, C_6D_6) δ 75.79.

^{31}P NMR (202 MHz, C_6D_6) δ 75.80.

HRMS (ESI) m/z: $[M+C_2H_5N]^+$ Calc'd for $C_{25}H_{35}NPPd$ 486.15419; found: 486.13791

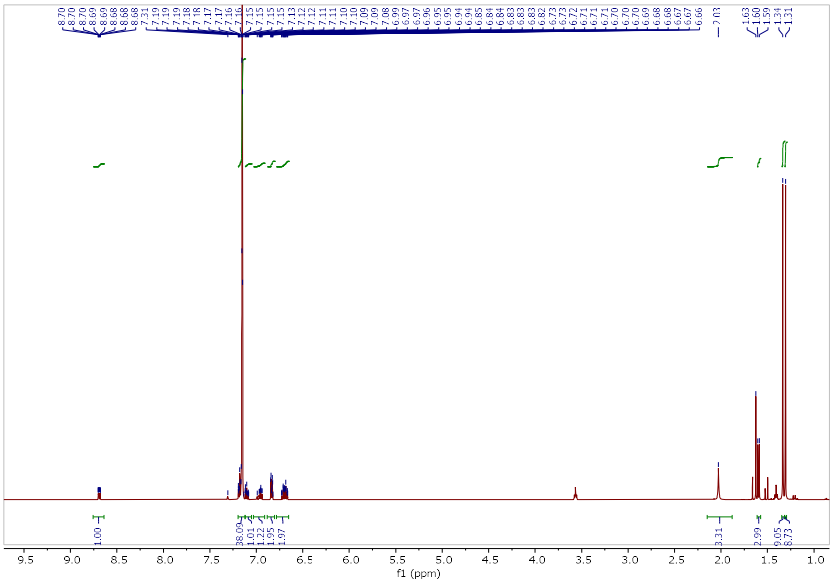

Fig. D6. ^{1}H NMR (500 MHz, C_6D_6) spectrum of **palladacycle II**

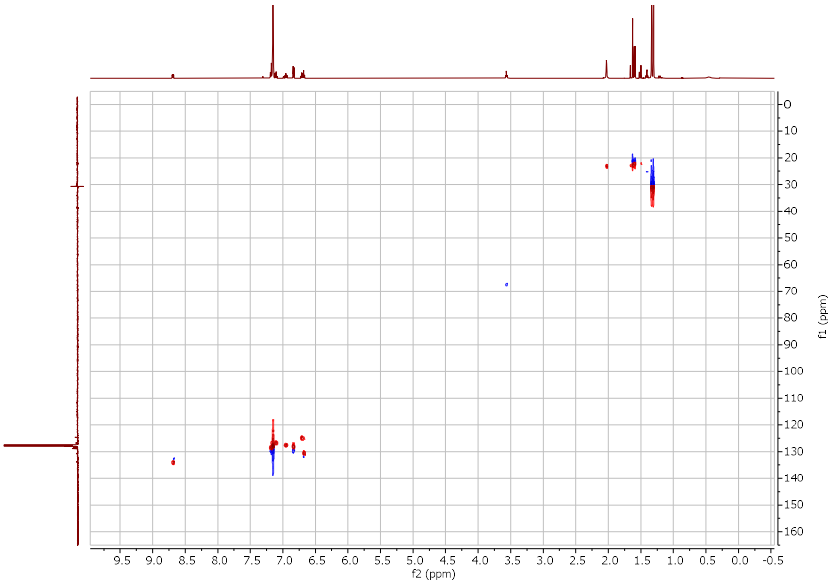

Fig. D7. ^{1}H-^{13}C–HSQC spectrum of **palladacycle II**

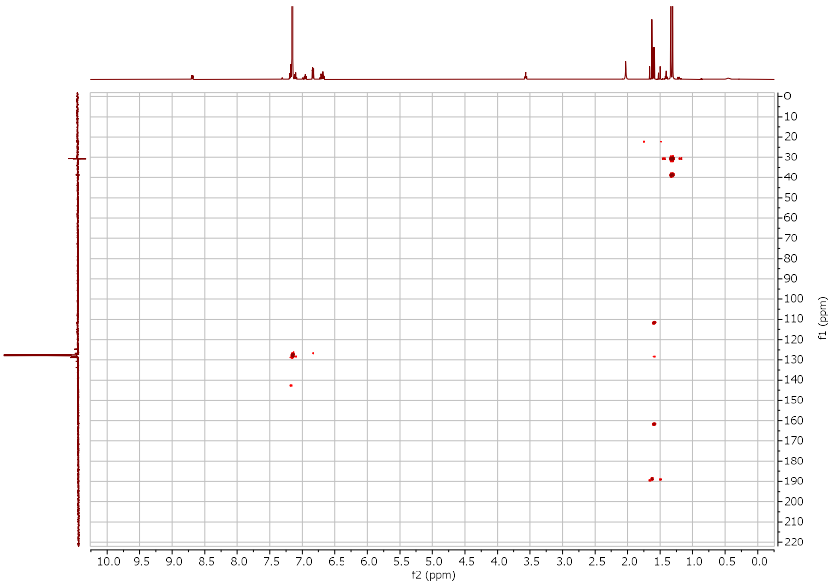

Fig. D8. ^{1}H-^{13}C–HMBC spectrum of **palladacycle II**

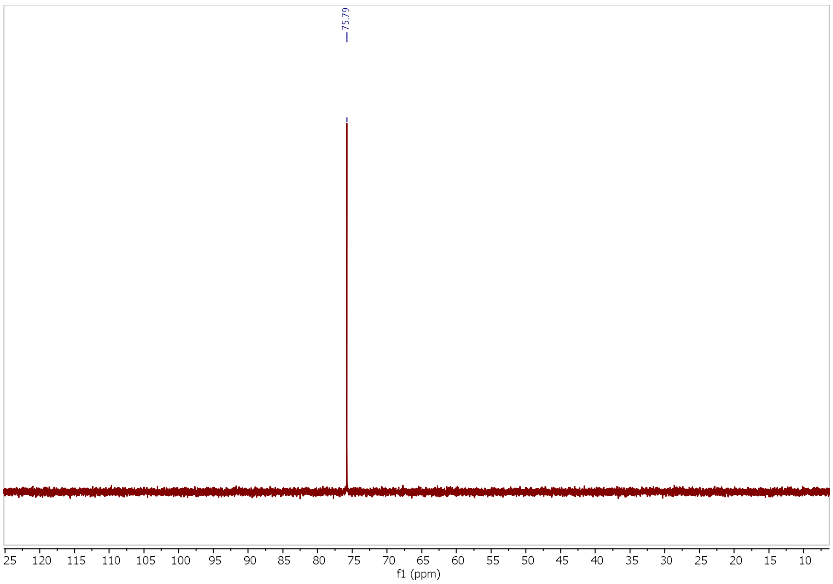

Fig. D9. $^{31}P\{H\}$ NMR (203 MHz, C_6D_6) spectrum **palladacycle II**

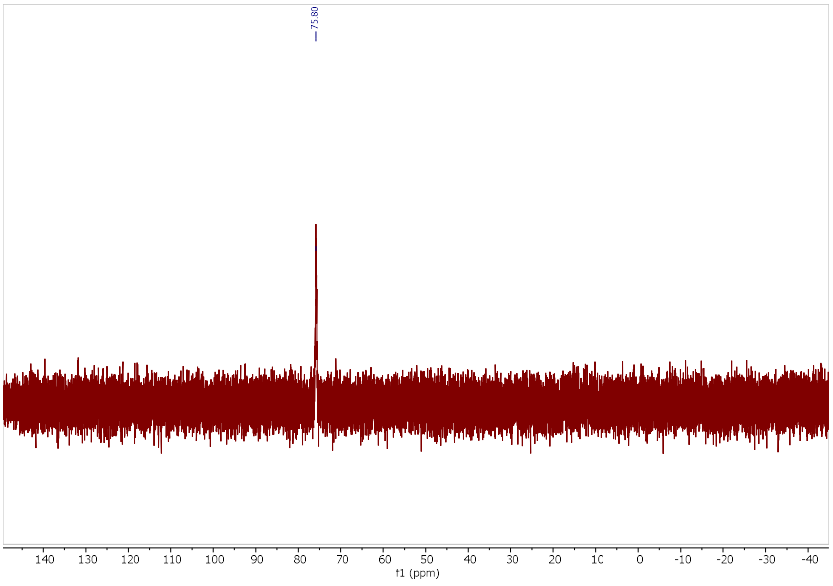

Fig. D10. ^{31}P NMR (203 MHz, C_6D_6) spectrum **palladacycle II**

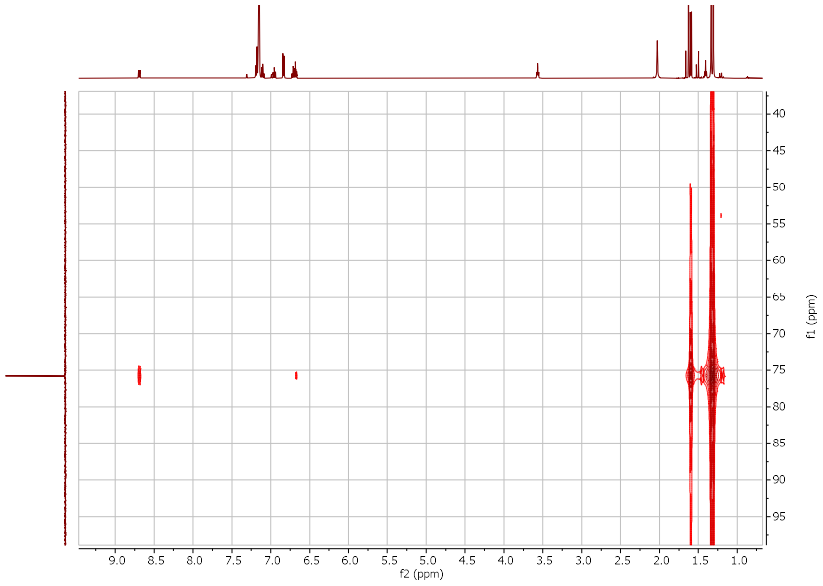

Fig. D11. ^{1}H-^{31}P-HMBC spectrum of **palladacycle II**

Palladacycle III

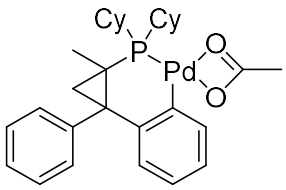

Palladacycle **III**

^{1}H NMR (500 MHz, C_6D_6) δ 8.40 (s, 1H), 7.49 – 7.05 (m, 5H), 6.88 (t, *J* = 7.4 Hz, 1H), 6.81 – 6.65 (m, 1H), 6.54 (dt, *J* = 8.0, 1.6 Hz, 1H), 3.81 – 3.42 (m, 4H), 2.00 (s, 6H), 1.94 – 1.72 (m, 4H), 1.57 – 1.45 (m, 3H), 1.47 – 1.36 (m, 4H), 1.32 – 1.13 (m, 3H), 0.91 – 0.81 (m, 3H), 0.73 (d, *J* = 8.2 Hz, 3H).

^{31}P{H} NMR (203 MHz, C_6D_6) δ 79.47.

^{31}P NMR (202 MHz, C_6D_6) δ 79.48.

HRMS (ESI) m/z: $[M+C_2H_5N]^+$ Calc'd for $C_{25}H_{35}NPPd$ 552.20114; found: 552.18460

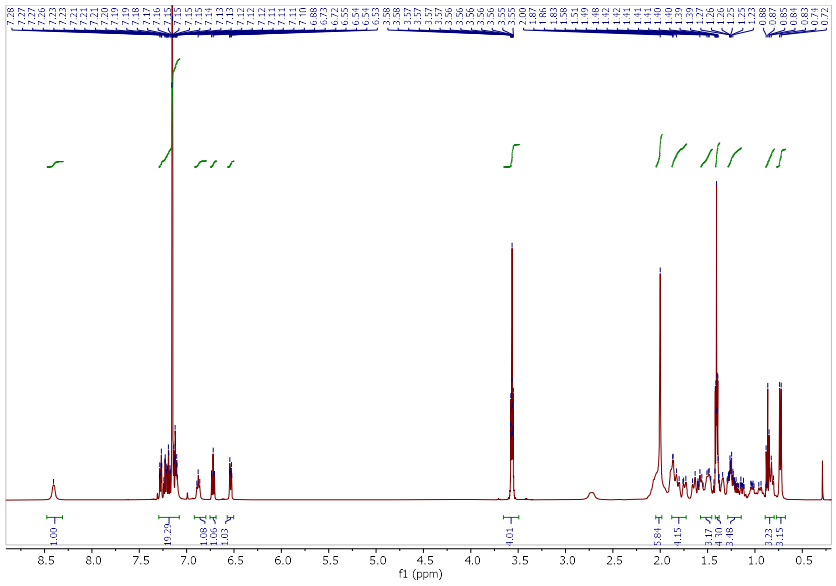

Fig. D12. ^{1}H NMR (500 MHz, C_6D_6) spectrum of **palladacycle III**

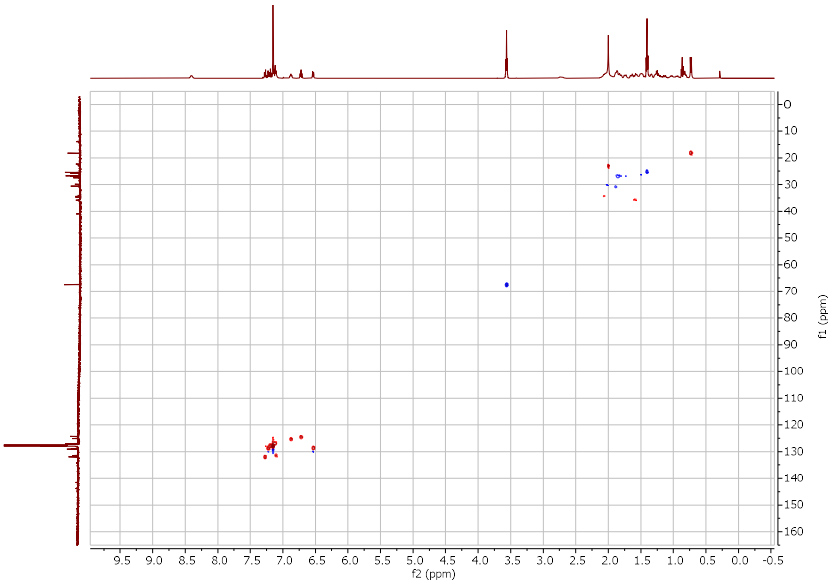

Fig. D13. ^{1}H-^{13}C–HSQC spectrum of **palladacycle III**

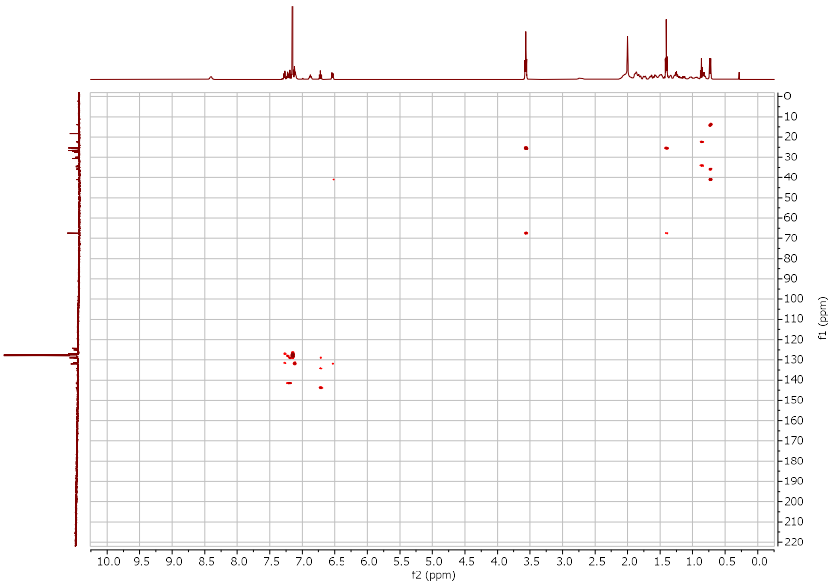

Fig. D14. ^{1}H-^{13}C–HMBC spectrum of **palladacycle III**

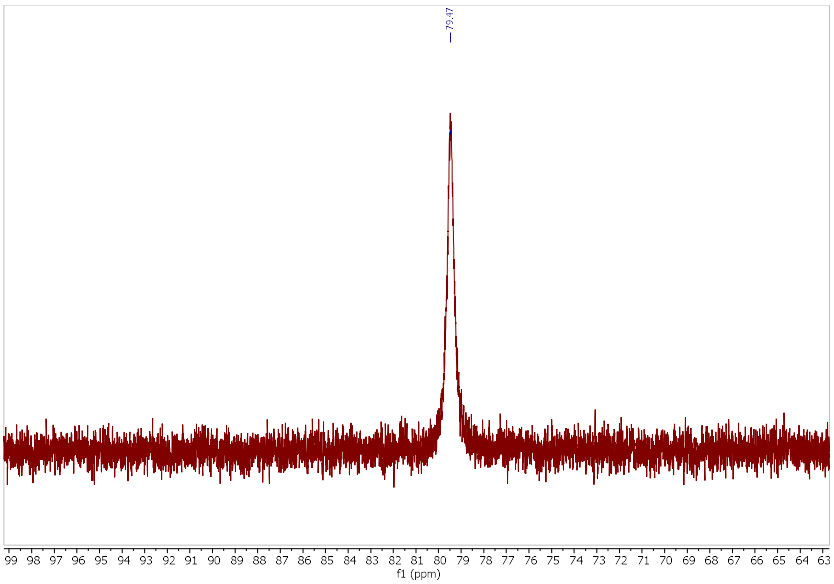

Fig. D15. $^{31}P\{H\}$ NMR (203 MHz, C_6D_6) spectrum of **palladacycle III**

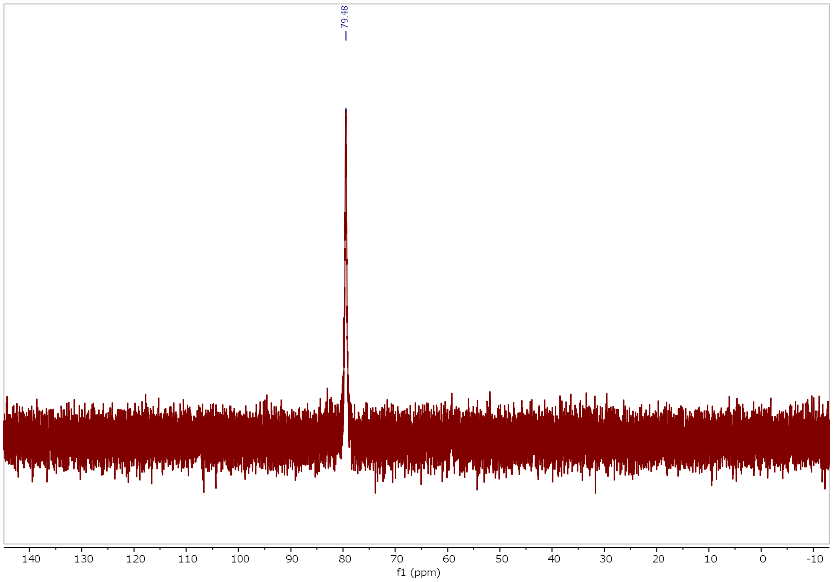

Fig. D16. ^{31}P NMR (203 MHz, C_6D_6) spectrum of **palladacycle III**

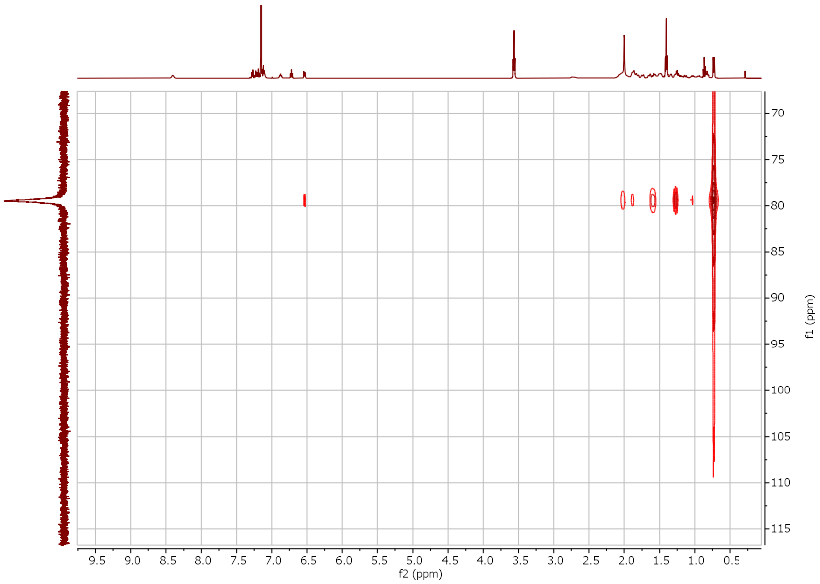

Fig. D17. ^{1}H-^{31}P-HMBC spectrum of **palladacycle III**

Palladacycle IV

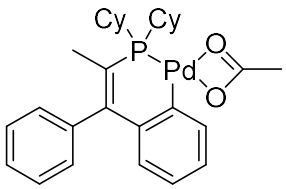

Palladacycle **IV**

^{1}H NMR (500 MHz, C_6D_6) δ 8.59 (ddd, *J* = 7.9, 2.6, 1.1 Hz, 1H), 7.31 – 7.02 (m, 3H), 6.95 (ddt, *J* = 8.0, 5.5, 1.7 Hz, 3H), 6.78 – 6.62 (m, 2H), 3.82 – 3.33 (m, 1H), 2.07 (s, 3H), 1.98 – 1.89 (m, 2H), 1.89 – 1.78 (m, 2H), 1.68 (dtq, *J* = 9.4, 6.0, 2.8 Hz, 3H), 1.54 (d, *J* = 8.7 Hz, 4H), 1.51 – 1.44 (m, 2H), 1.44 – 1.34 (m, 1H), 1.25 – 1.11 (m, 3H), 1.09 – 0.95 (m, 4H), 0.87 (t, *J* = 7.1 Hz, 3H).

^{31}P{H} NMR (203 MHz, C_6D_6) δ 53.85.

^{31}P NMR (202 MHz, C_6D_6) δ 53.85.

HRMS (ESI) m/z: $[M+C_2H_5N]^+$ Calc'd for $C_{25}H_{35}NPPd$ 538.18549; found: 538.16974

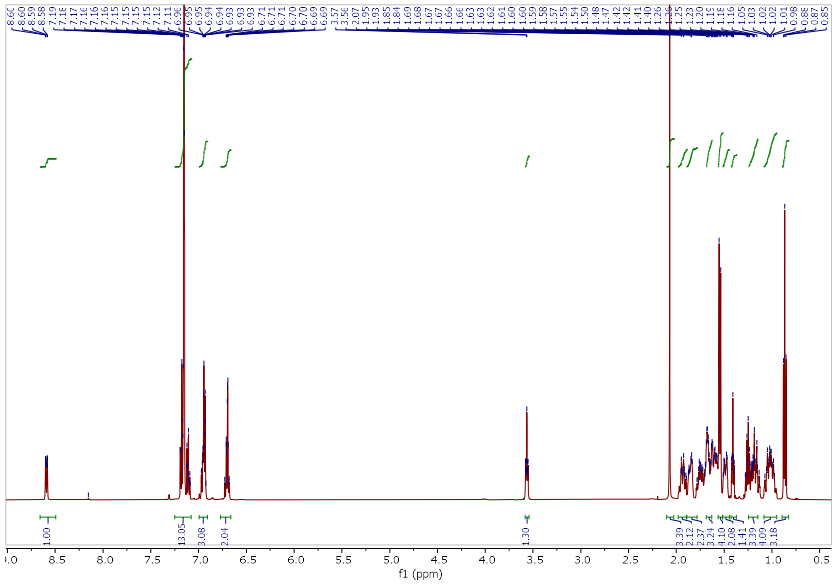

Fig. D18. ^{1}H NMR (500 MHz, C_6D_6) spectrum of **palladacycle IV**

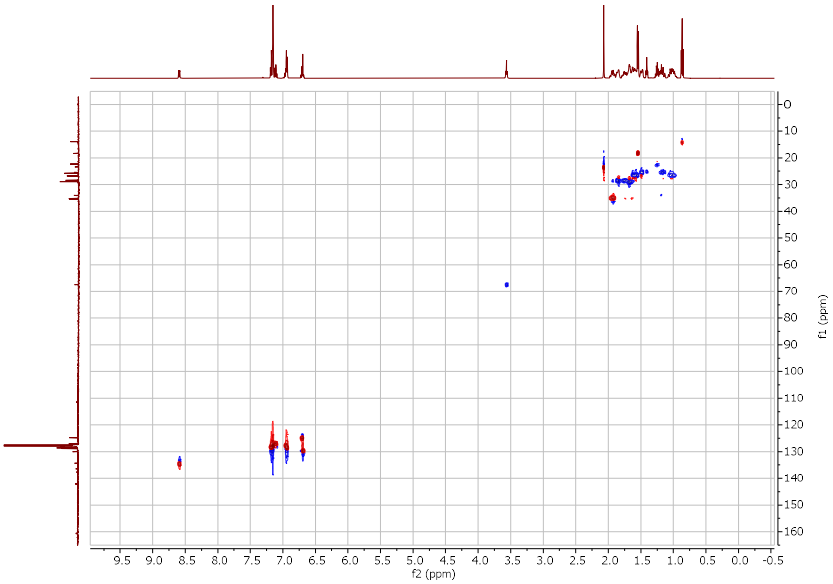

Fig. D19. ^{1}H-^{13}C–HSQC spectrum of **palladacycle IV**

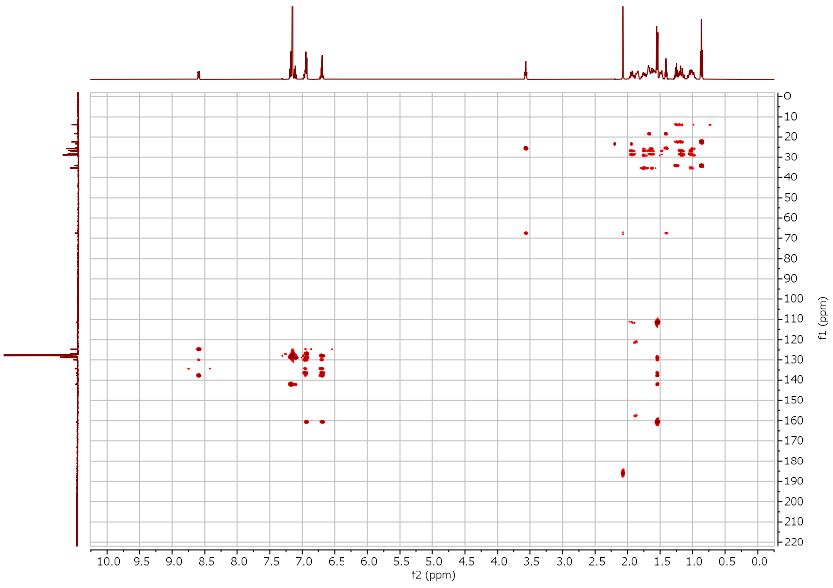

Fig. D20. ^{1}H-^{13}C–HMBC spectrum of **palladacycle IV**

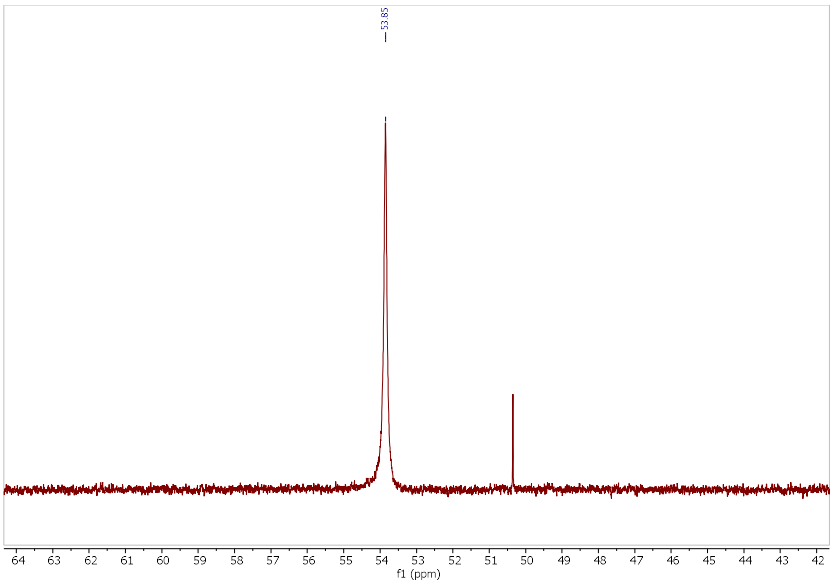

Fig. D21. $^{31}P\{H\}$ NMR (203 MHz, C_6D_6) spectrum of **palladacycle IV**

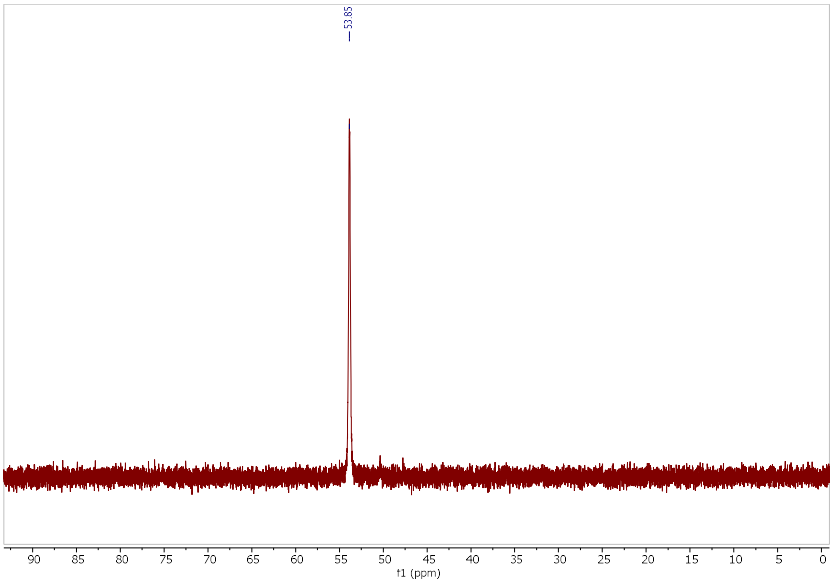

Fig. D22. ^{31}P NMR (203 MHz, C_6D_6) spectrum of **palladacycle IV**

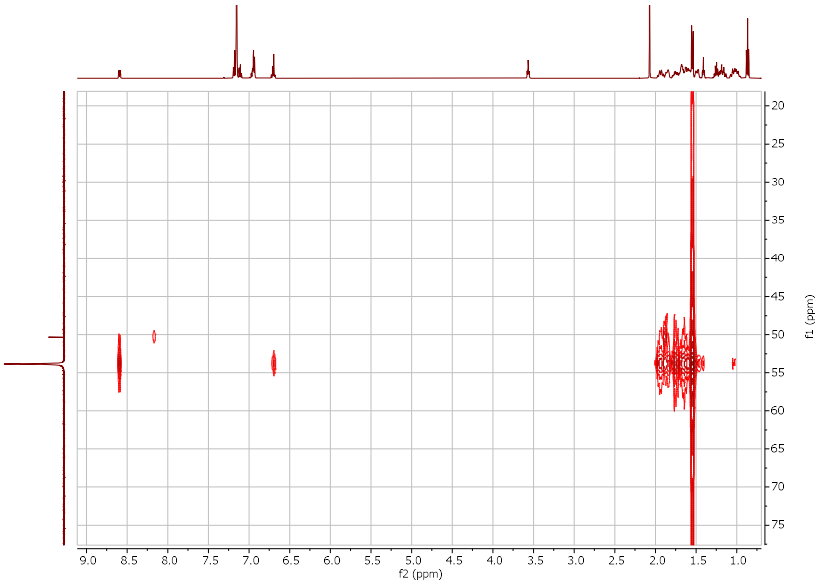

Fig. D23. ^{1}H-^{31}P-HMBC spectrum of **palladacycle IV**

III: Characterization of isolated products

N-benzyl-4-fluoro-N-phenylaniline

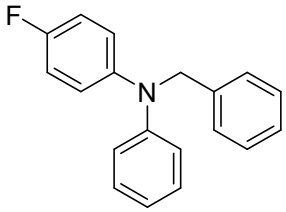

^{1}H NMR (300 MHz, $CDCl_3$) δ 7.33 – 7.18 (m, 4H), 7.18 – 7.04 (m, 3H), 7.03 – 6.94 (m, 2H), 6.94 – 6.71 (m, 5H), 4.87 (s, 2H).

^{13}C NMR (76 MHz, $CDCl_3$) δ 160.3, 157.1, 148.4, 144.1 (d, J = 2.8 Hz), 138.9, 129.4, 128.9 (d, J = 45.3 Hz), 127.5, 126.9, 126.6, 124.5 (d, J = 7.8 Hz), 120.2, 118.3, 117.6, 116.8, 116.1 (d, J = 22.3 Hz), 112.8, 56.6.

^{19}F NMR (283 MHz, $CDCl_3$) δ -120.47.

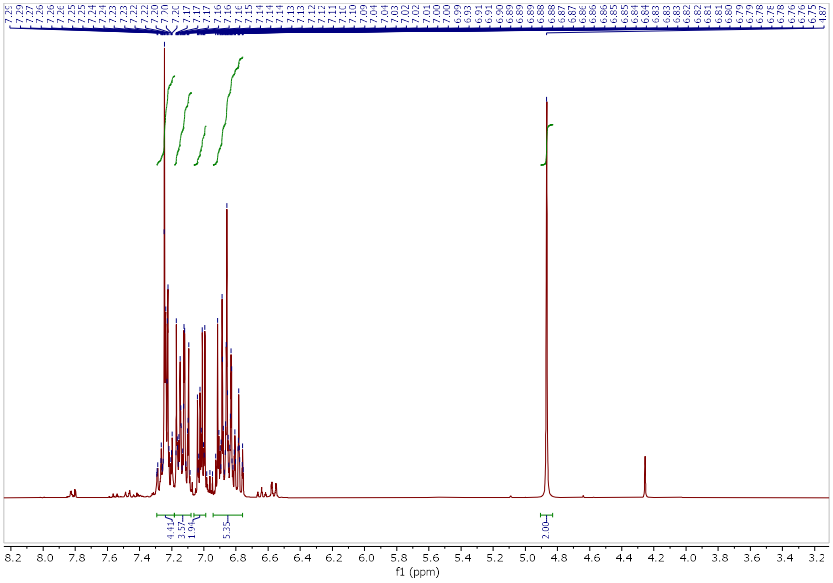

Fig. D24. ^{1}H NMR (300 MHz, Chloroform-*d*) spectrum of N-benzyl-4-fluoro-N-phenylaniline

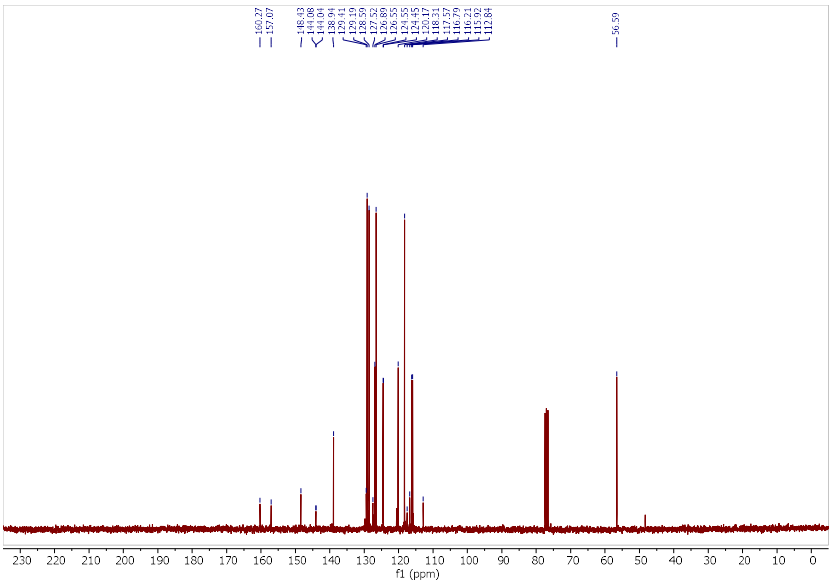

Fig. D25. ^{13}C NMR (76 MHz, Chloroform-*d*) spectrum of N-benzyl-4-fluoro-N-phenylaniline

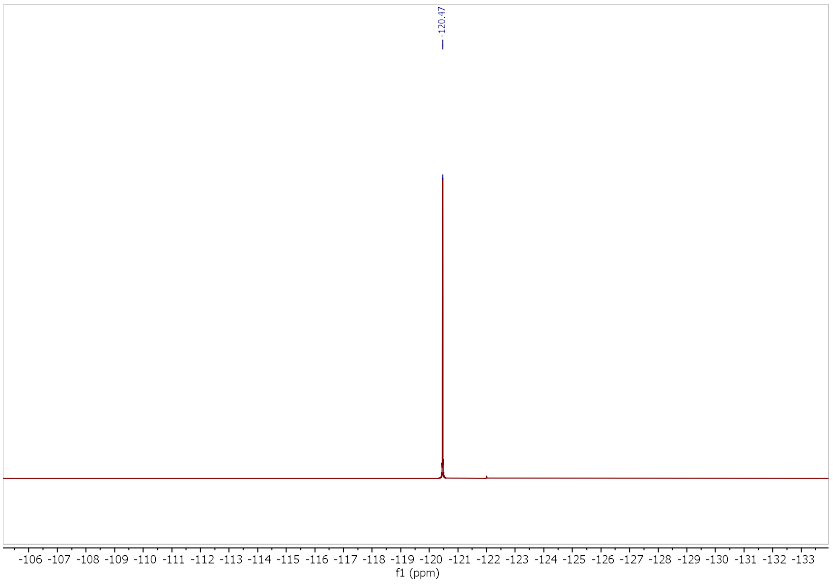

Fig. D26. ^{19}F NMR (283 MHz, Chloroform-*d*) spectrum of N-benzyl-4-fluoro-N-phenylaniline

1-fluoro-4-(phenylethynyl)benzene

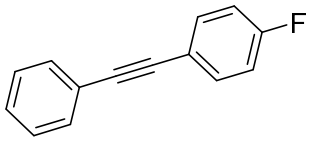

^{1}H NMR (300 MHz, $CDCl_3$) δ 7.48 – 7.41 (m, 4H), 7.30 – 7.24 (m, 3H), 7.02 – 6.92 (m, 2H).

^{19}F NMR (471 MHz, $CDCl_3$) δ -111.00.

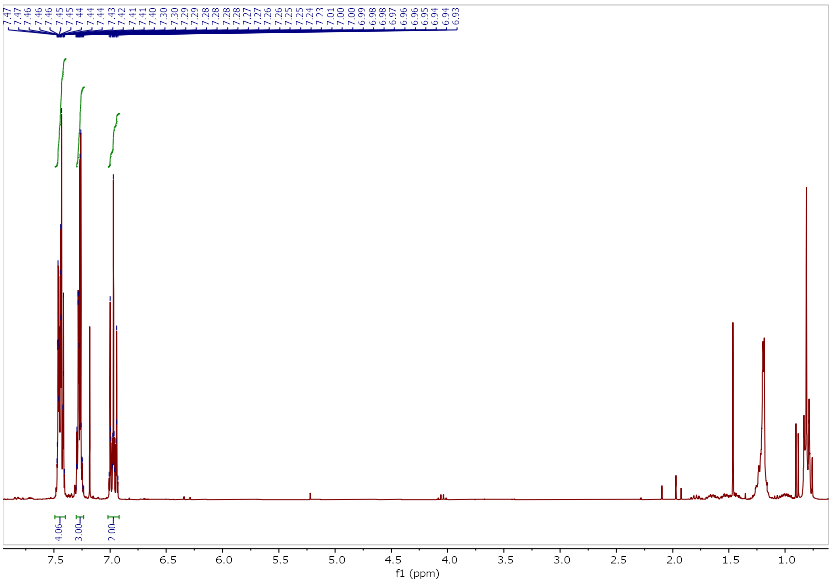

Fig. D27. ^{1}H NMR (300 MHz, Chloroform-*d*) spectrum of 1-fluoro-4-(phenylethynyl)benzene

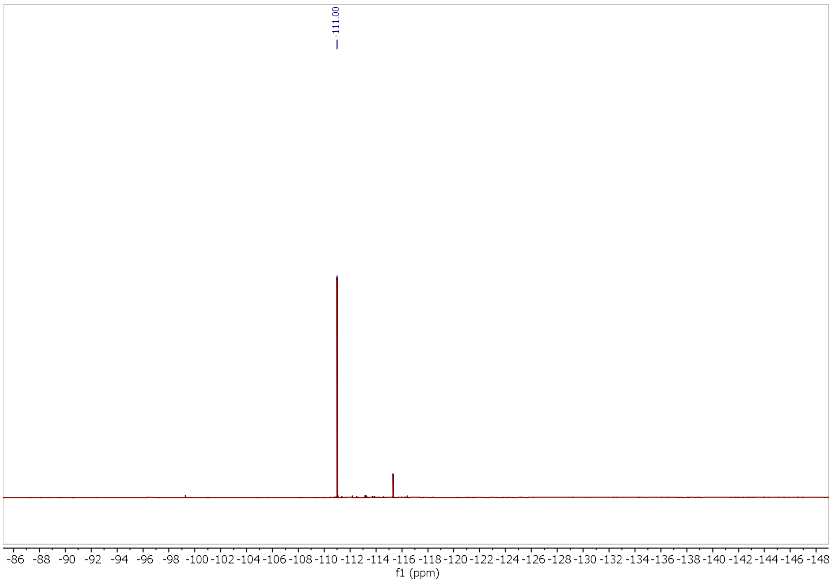

Fig. D28. ^{19}F NMR (471 MHz, Chloroform-*d*) spectrum of 1-fluoro-4-(phenylethynyl)benzene

4-fluoro-2-(2-methoxyphenyl)pyridine

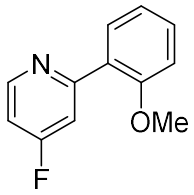

^{1}H NMR (300 MHz, $CDCl_3$) δ 8.58 (ddd, *J* = 8.8, 5.6, 0.5 Hz, 1H), 7.50 (dd, *J* = 2.6, 1.6 Hz, 1H), 7.45 (ddd, *J* = 7.7, 1.7, 1.0 Hz, 1H), 7.39 – 7.34 (m, 1H), 7.34 – 7.24 (m, 1H), 6Z.98 – 6.87 (m, 2H), 3.83 (s, 3H).

^{13}C NMR (126 MHz, $CDCl_3$) δ 170.4, 168.3, 160.5 (d, *J* = 7.1 Hz), 160.1, 151.9 (d, *J* = 7.3 Hz), 139.8 (d, *J* = 3.3 Hz), 129.9, 119.3, 115.8, 112.1, 110.1 (d, *J* = 16.5 Hz), 108.3 (d, *J* = 17.5 Hz), 55.4.

^{19}F NMR (471 MHz, $CDCl_3$) δ -102.57.

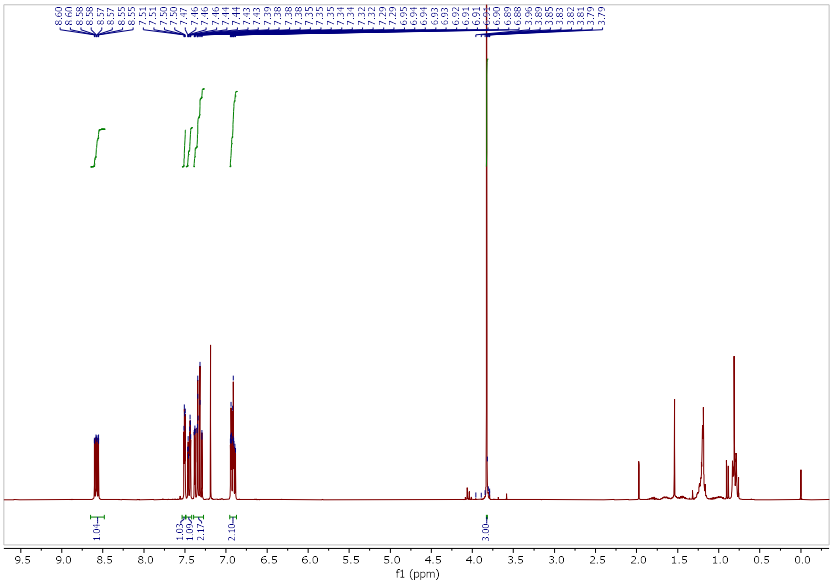

Fig. D29. ^{1}H NMR (300 MHz, Chloroform-*d*) spectrum of 4-fluoro-2-(2-methoxyphenyl)pyridine

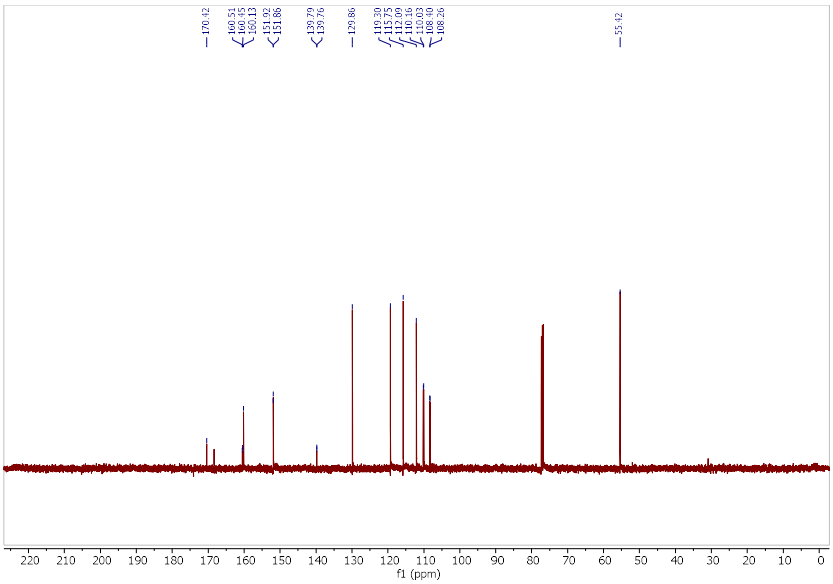

Fig. D30. ^{13}C NMR (76 MHz, Chloroform-*d*) spectrum of 4-fluoro-2-(2-methoxyphenyl)pyridine.

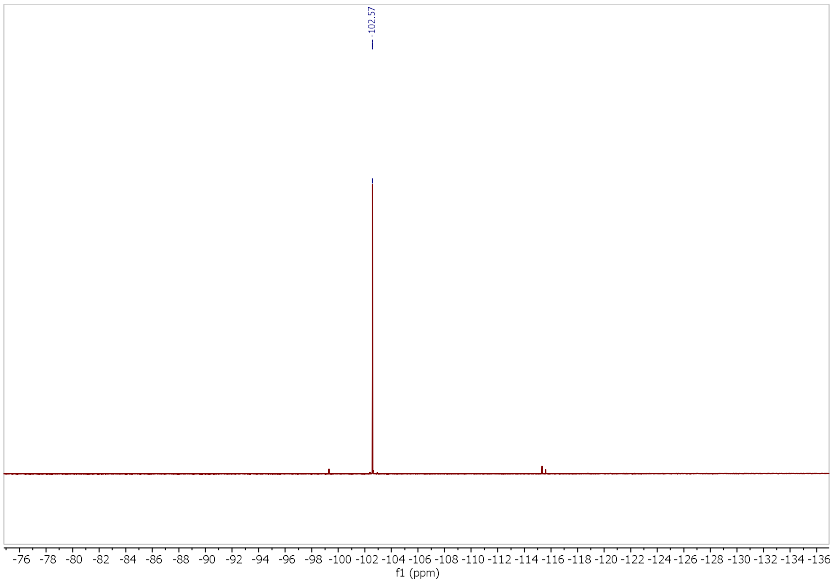

Fig. D31. ^{19}F NMR (283 MHz, Chloroform-*d*) spectrum of 4-fluoro-2-(2-methoxyphenyl)pyridine

2-(4-fluorophenyl)benzo[b]thiophene

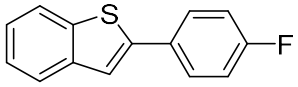

^{1}H NMR (500 MHz, $CDCl_3$) δ 7.85 (m, 1H), 7.80 (m, 1H), 7.74 – 7.67 (m, 2H), 7.50 (s, 1H), 7.39 – 7.32 (m, 2H), 7.18 – 7.11 (m, 2H).

^{13}C NMR (126 MHz, $CDCl_3$) δ 162.8 (d, J = 248.5 Hz), 143.1, 140.7, 139.46, 132.1 (d, J = 8.1 Hz), 131.3 (d, J = 8.2 Hz), 130.6 (d, J = 3.4 Hz), 128.2 (d, J = 8.2 Hz), 124.6, 124.4, 123.6, 122.28, 119.5, 116.0 (d, J = 22.0 Hz).

^{19}F NMR (283 MHz, $CDCl_3$) δ -113.36

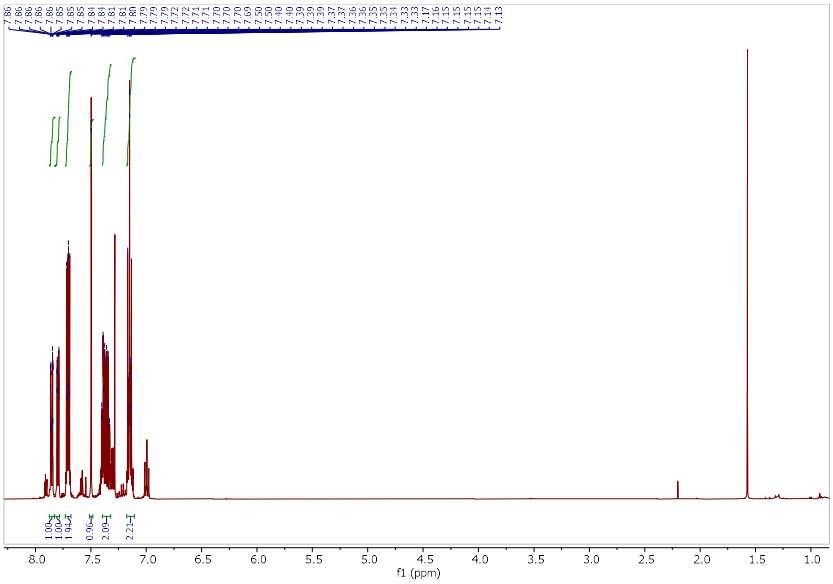

Fig. D32. ^{1}H NMR (500 MHz, Chloroform-*d*) spectrum of 2-(4-fluorophenyl)benzo[b]thiophene

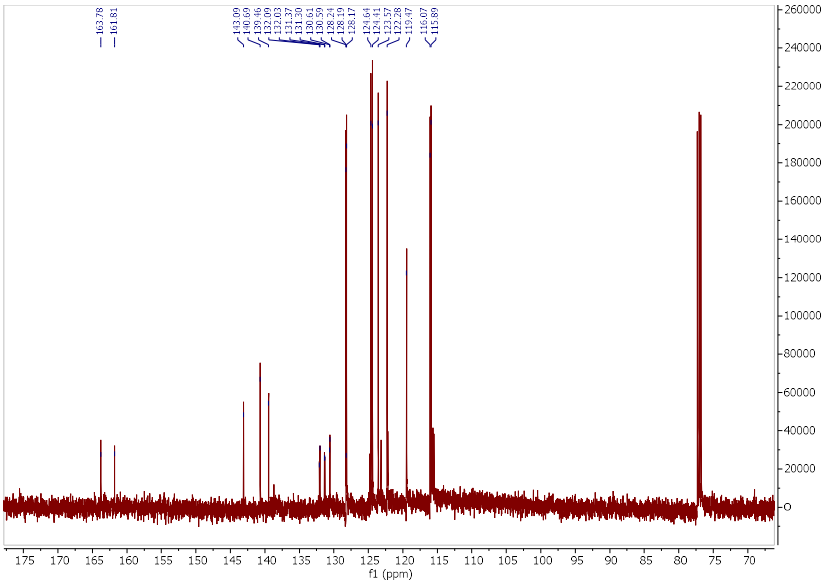

Fig. D33. ^{13}C NMR (126 MHz, Chloroform-*d*) spectrum of 2-(4-fluorophenyl)benzo[b]thiophene 4-fluoro-2-(2-methoxyphenyl)pyridine.

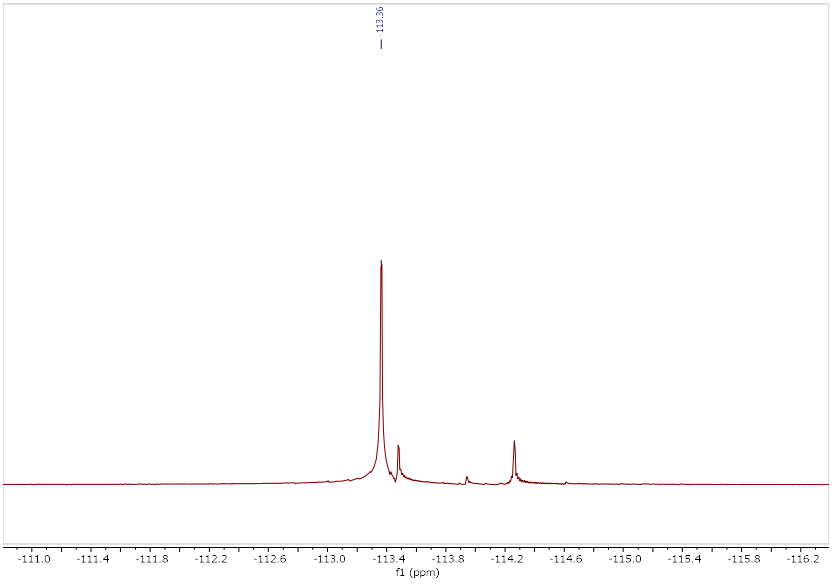

Fig. D34. ^{19}F NMR (283 MHz, Chloroform-*d*) spectrum of 2-(4-fluorophenyl)benzo[b]thiophene

(E)-1-fluoro-4-styrylbenzene

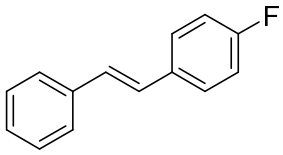

^{1}H NMR (500 MHz, $CDCl_3$) δ 7.56 – 7.48 (m, 4H), 7.43 – 7.37 (m, 2H), 7.34 – 7.28 (m, 1), 7.16 – 7.02 (m, 4H).

^{13}C NMR (126 MHz, $CDCl_3$) δ 162.4 (d, J = 247.2 Hz), 137.2, 133.5 (d, J = 3.5 Hz), 128.7, 128.5 (d, J = 2.4 Hz), 128.0 (d, J = 7.9 Hz), 127.7, 127.5, 126.5, 115.6 (d, J = 21.6 Hz).

^{19}F NMR (283 MHz, $CDCl_3$) δ -114.25.

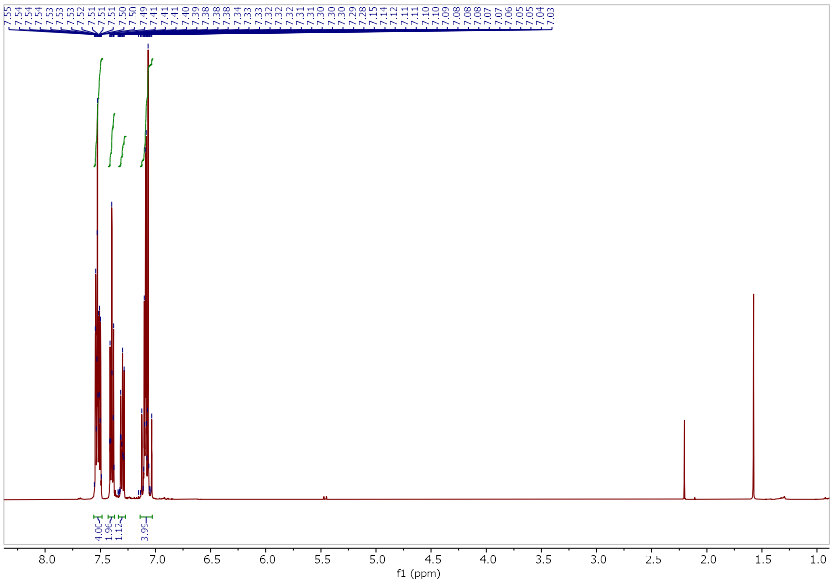

Fig. D35. ^{1}H NMR (500 MHz, Chloroform-*d*) spectrum of (E)-1-fluoro-4-styrylbenzene

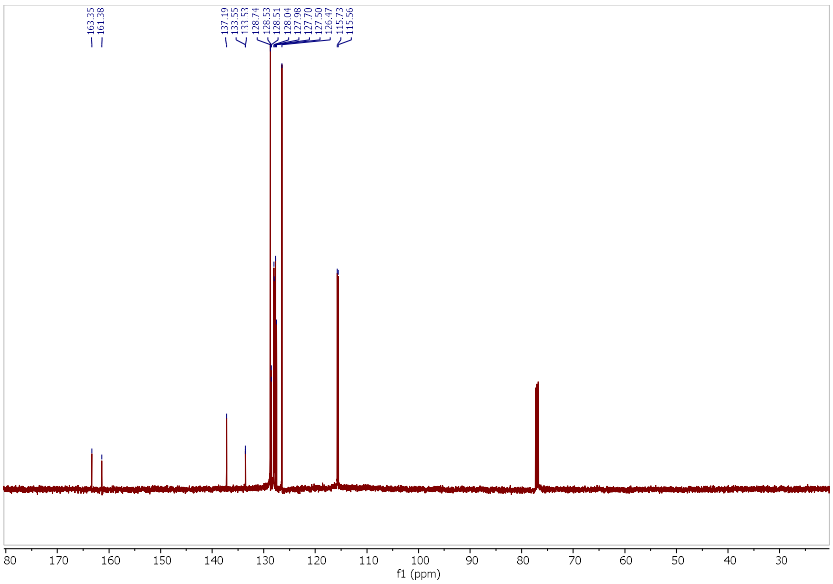

Fig. D36. ^{13}C NMR (126 MHz, Chloroform-*d*) spectrum of (E)-1-fluoro-4-styrylbenzene

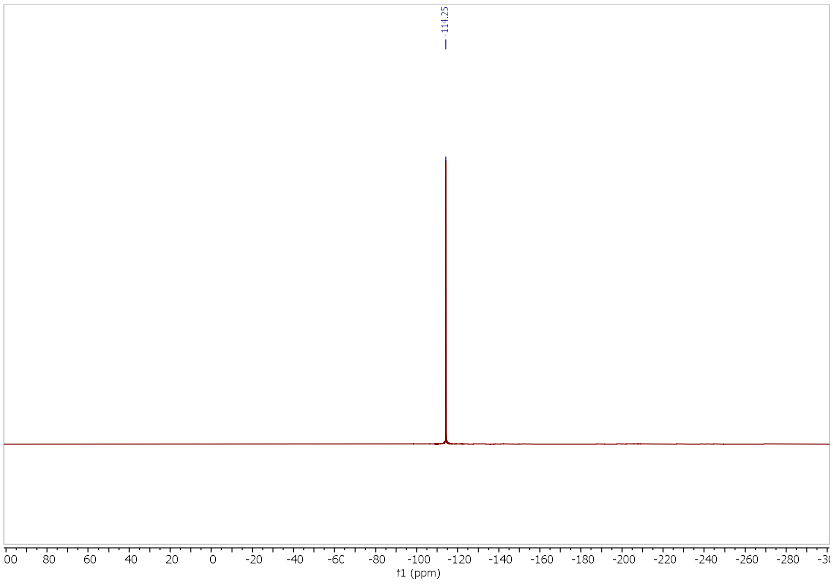

Fig. D37. ^{19}F NMR (283 MHz, Chloroform-*d*) spectrum of (E)-1-fluoro-4-styrylbenzene